Springer Series in Surface Sciences 61

Werner Wesch
Elke Wendler *Editors*

Ion Beam Modification of Solids

Ion-Solid Interaction and Radiation Damage

Springer

Springer Series in Surface Sciences

Volume 61

Series editors

Roberto Car, Princeton University, Princeton, NJ, USA
Gerhard Ertl, Fritz-Haber-Institut der Max-Planck-Gesellschaft, Berlin, Germany
Hans-Joachim Freund, Fritz-Haber-Institut der Max-Planck-Gesellschaft, Berlin, Germany
Hans Lüth, Peter Grünberg Institute, Forschungszentrum Jülich GmbH, Jülich, Germany
Mario Agostino Rocca, Università degli Studi di Genova, Genova, Italy

This series covers the whole spectrum of surface sciences, including structure and dynamics of clean and adsorbate-covered surfaces, thin films, basic surface effects, analytical methods and also the physics and chemistry of interfaces. Written by leading researchers in the field, the books are intended primarily for researchers in academia and industry and for graduate students.

More information about this series at http://www.springer.com/series/409

Werner Wesch · Elke Wendler
Editors

Ion Beam Modification of Solids

Ion-Solid Interaction and Radiation Damage

Editors
Werner Wesch
Institute of Solid State Physics
Friedrich-Schiller-University Jena
Jena
Germany

Elke Wendler
Institute of Solid State Physics
Friedrich-Schiller-University Jena
Jena
Germany

ISSN 0931-5195 ISSN 2198-4743 (electronic)
Springer Series in Surface Sciences
ISBN 978-3-319-33559-9 ISBN 978-3-319-33561-2 (eBook)
DOI 10.1007/978-3-319-33561-2

Library of Congress Control Number: 2016939918

© Springer International Publishing Switzerland 2016
This work is subject to copyright. All rights are reserved by the Publisher, whether the whole or part of the material is concerned, specifically the rights of translation, reprinting, reuse of illustrations, recitation, broadcasting, reproduction on microfilms or in any other physical way, and transmission or information storage and retrieval, electronic adaptation, computer software, or by similar or dissimilar methodology now known or hereafter developed.
The use of general descriptive names, registered names, trademarks, service marks, etc. in this publication does not imply, even in the absence of a specific statement, that such names are exempt from the relevant protective laws and regulations and therefore free for general use.
The publisher, the authors and the editors are safe to assume that the advice and information in this book are believed to be true and accurate at the date of publication. Neither the publisher nor the authors or the editors give a warranty, express or implied, with respect to the material contained herein or for any errors or omissions that may have been made.

Printed on acid-free paper

This Springer imprint is published by Springer Nature
The registered company is Springer International Publishing AG Switzerland

To Mark C. Ridgway

Preface

During the past 50 years ion beam technologies have been proven to be powerful tools in the continuously growing field of materials science. Ion beams are used for tailoring the physical and chemical properties of thin films, surfaces and interfaces. Nanostructures can be formed or modified and nanocomposite materials can be synthesised with new properties which do not exist in natural materials. In the past two decades very high-energy ion beams from accelerators usually used for nuclear and particle research became available with the parameters making them suitable for materials science. This stimulated intensive research and the use of so-called swift heavy ions in ion-beam based materials science received much attention. This was an important step to fulfil the demand for modifying more thick or buried layers. Moreover, the research in materials science with swift heavy ions induced new applications as for instance the controlled shaping of embedded nanoparticles, which could not be imagined beforehand. Besides its use in various device technologies, ion beams play an important role in a number of other fields. Examples for that are materials research and treatment of radioactive waste in nuclear fission and fusion technologies, optimization of prosthetic components and the use of ion beams in cancer treatment. Additionally, ion-beam based analytical techniques are very important not only in materials science but also in environmental studies and in the field of preservation of cultural heritage.

Ion irradiation of solids has two main effects: the introduction of foreign atoms and the energy deposition into the material. The specific application of ion beams requires a thorough knowledge of the interactions of the energetic ions with the corresponding material. These interactions determine the depth at which the ions come to rest and cause structural modifications in the material (radiation damage). The radiation damage measured after ion irradiation depends on the primary energy deposition of the ions and the external irradiation conditions and is characteristic for a given material. In some cases radiation damage results in useful changes of materials properties but typically the damage has to be reduced or removed by subsequent annealing processes in order to achieve the desired results. The choice of suitable methods for damage annealing often strongly depends on the kind and

concentration of damage produced during ion irradiation in the respective material. Consequently, the investigation of ion-beam induced damage formation is an indispensable part in the field of ion beam physics.

The fundamentals of ion–solid interaction, ion-beam induced damage formation in a broad variety of materials and theoretical description of damage formation have been subject of intensive studies of a large number of research groups around the world. This resulted in an enormous and still growing number of scientific papers. Various excellent monographs about ion beam physics appeared in recent years. Apart from the numerous scientific papers and monographs on the one hand and pure textbooks on the other, a comprehensive description of the theory of ion stopping in matter, a summary of models and the concepts that have been developed over time for characterisation of damage evolution as well as an overview of the state-of-the-art knowledge on damage formation in various classes of materials is still missing. With the present book we aim at filling this gap.

The book is organised in four parts. Part I provides the physical basics of ion–solid interaction. This includes a complete treatment of the theory of ion stopping in materials, i.e. the treatment of nuclear and electronic energy loss processes. Two further chapters give an overview about existing models for the description of damage formation due to electronic and nuclear interaction, respectively. If possible the general concepts are compared to each other and illustrated with real examples. The last chapter of this part is devoted to the physical basics of ion-beam induced synthesis of nanostructures. Part II deals with damage formation, amorphization and (re)crystallisation of semiconductors and ceramics, i.e. of covalent-ionic materials, due to nuclear energy deposition. The effect of high electronic energy deposition in solids is the topic of Part III. Structural modifications and phase transformations in crystalline insulators, metals and semiconductors are summarised. Additionally one chapter of this part reports on effects of electronic energy deposition in amorphous semiconductors. The final part, Part IV, presents selected applications of ion beams. Here the focus is on shaping and modification of nanoparticles and nanostructures and on the use of ion-beam induced effects for modification of optical materials.

It should be mentioned that not all existing literature could be taken into consideration in detail, but the contents of the various chapters are initially based on scientific results of the authors and their groups. Additional references to works of other authors are integrated. Besides well-established experimental results also possible limitations in their interpretation and open problems are addressed. In this respect the book should be suitable as material for special courses for graduate, postgraduate and Ph.D. students. Additionally it can be used as a source of information for researchers who are interested in this field.

Finally we feel the need to thank all co-authors who participated in the project with their valuable and highly interesting contributions. With extreme sadness we had to take note of the early death of our colleague, Mark C. Ridgeway, who significantly contributed not only to this book but to the field of ion beam physics in general. We shall always honour his memory.

Jena, Germany
February 2016

Werner Wesch
Elke Wendler

Contents

Part I Physical Basics

1 Ion-Solid Interaction 3
Konrad Gärtner
1.1 Introduction. 3
1.2 Elastic Ion-Atom Interaction 4
1.2.1 Ion-Atom Interaction Potential 5
1.2.2 Scattering Kinematics 8
1.2.3 Scattering Dynamics 10
1.2.4 Scattering Angles and Differential Cross Section 11
1.2.5 Transferred Energy 15
1.3 Inelastic Ion-Atom Interaction 16
1.3.1 High Energy Approach of the Transferred Energy 16
1.3.2 Low Energy Approach of the Transferred Energy 19
1.4 Ion-Amorphous Solid Interaction 22
1.4.1 Scattering Statistics 22
1.4.2 Elastic Energy Loss and Energy Loss Straggling 27
1.4.3 High Energy Inelastic Energy Loss and Energy Straggling 29
1.4.4 Low Energy Inelastic Energy Loss and Energy Straggling 37
1.4.5 Comparison of Stopping Power Theories 41
1.4.6 Energy Loss Distribution 45
1.4.7 Angular Distribution 49
1.4.8 Spatial Distributions of the Ions and the Damage 51
1.5 Ion-Crystalline Solid Interaction 55
1.5.1 Axial Channeling 55
1.5.2 Ion Range and Damage Distribution 58
1.6 Summary 59
References 60

2 Models for the Description of Track Formation . . . 63
Christian Dufour and Marcel Toulemonde
2.1 Introduction . . . 63
2.2 Electronic Energy Deposition . . . 65
2.2.1 Electronic Energy Loss . . . 65
2.2.2 Radial Energy Distribution . . . 66
2.3 Description of Track Formation . . . 69
2.3.1 Coulomb Explosion . . . 70
2.3.2 Bond Weakening (BW) Model . . . 71
2.3.3 Exciton Self-trapping (STX) Model . . . 72
2.3.4 Concept of Reduced Electronic Energy Loss . . . 73
2.3.5 A Transient Thermal Process . . . 75
2.4 Microscopic Models: Molecular Dynamics Approaches . . . 94
2.4.1 Sputtering by Electronic Excitation . . . 95
2.4.2 Track Formation . . . 96
2.4.3 Summary and Conclusions . . . 99
References . . . 100

3 Modelling Effects of Radiation Damage . . . 105
William J. Weber and Elke Wendler
3.1 Introduction . . . 105
3.2 General Remarks . . . 106
3.2.1 Origin of Radiation Damage . . . 106
3.2.2 Sources of Radiation Damage . . . 108
3.2.3 Measurement of Irradiation Damage . . . 109
3.2.4 Quantitative Analysis of Radiation Effects . . . 110
3.3 Modelling of Defect/Damage Accumulation . . . 111
3.3.1 Defect Reaction Rate Theory . . . 112
3.3.2 Effect of Temperature and Diffusion . . . 116
3.3.3 Practical Application . . . 117
3.4 Modelling of Amorphisation and Order-Disorder Phase Transformations . . . 120
3.4.1 Irradiation-Induced Amorphisation Models . . . 120
3.4.2 Amorphisation Kinetics . . . 125
3.5 Modelling of Complex Processes . . . 131
3.6 Summary . . . 134
References . . . 134

4 Synthesis of Nanostructures Using Ion-Beams: An Overview . . . 137
Giancarlo Rizza and Mark C. Ridgway
4.1 Introduction . . . 138
4.2 From Thermodynamic to Driven System . . . 139
4.2.1 Thermodynamic System . . . 139
4.2.2 Kinetic System . . . 143
4.2.3 Driven System . . . 147

4.3 On the Strategies to Synthesize Nanostructures Using Ion-Beams: The Case of Metal-Glass Nanocomposites 151
4.3.1 Ion Implantation 153
4.3.2 Limits and Drawbacks of the Implantation Technique and Some Alternative Approaches 166
4.3.3 Ion Irradiation 169
4.3.4 A Model System to Investigate the Behavior of Nanoparticles Under Irradiation 175
4.4 Conclusion 178
4.5 Appendix: Elementary Processes in Irradiated Solids 179
4.5.1 Principles of Ion-Matter Interaction 179
4.5.2 Defects and Diffusion 180
References 182

Part II Damage Formation and Amorphization by Nuclear Energy Deposition

5 Primary Processes of Damage Formation in Semiconductors 189
Elke Wendler and Werner Wesch
5.1 Introduction. 189
5.2 Rutherford Backscattering Spectrometry for Damage Analysis 191
5.2.1 General Considerations 191
5.2.2 Analysis of RBS Aligned Spectra. 193
5.3 Continuous Damage Evolution up to Amorphisation. 196
5.3.1 Typical RBS Channelling Spectra of Ion Implanted Semiconductors 196
5.3.2 Introduction of Critical Temperatures and Effect of Ion Flux 198
5.3.3 Depth Distribution of Damage and Effect of Ion Energy 205
5.3.4 Fluence Dependence and Effect of Ion Mass 208
5.3.5 Correlation of Damage Cross-Section with Primary Energy Deposition 214
5.4 Discontinuous Damage Evolution up to Amorphisation. 217
5.4.1 Damage Formation in AlAs. 217
5.4.2 Damage Formation in GaN 224
5.5 Non-amorphisable Materials 229
5.5.1 ZnO 230
5.5.2 CdTe 232
5.6 Summarising Discussion 235
References 238

6 Damage Formation, Amorphization and Crystallization in Semiconductors at Elevated Temperatures 243
James S. Williams
6.1 Introduction. 243
6.2 Si Disordering, Amorphization and Crystallisation Processes at Elevated Temperature 245
6.2.1 Dynamic Annealing and Defect Formation During Irradiation 245
6.2.2 Amorphisation Processes at Elevated Temperature 248
6.2.3 Modelling of Ion-Induced Amorphization at Elevated Temperature 250
6.2.4 Ion Beam Induced Epitaxial Crystallisation (IBIEC) 254
6.2.5 IBIEC Models 257
6.3 Irradiation of Ge at Elevated Temperatures 259
6.3.1 Disorder Formation, Amorphization and Ion-Induced Crystallization 259
6.3.2 Formation of Porous Amorphous Layers 261
6.4 Irradiation of GaAs at Elevated Temperatures 264
6.4.1 Disordering and Amorphization 264
6.4.2 IBIIA and IBIEC Processes in GaAs 266
6.5 Other Compound Semiconductors 268
6.5.1 SiC Near and Above T_c 268
6.5.2 IBIIA and IBIEC Behaviour in InP 271
6.5.3 Ternary Semiconductors and Multilayers. 272
6.5.4 Unusual Swelling and Erosion Behaviour in Ion Implanted GaN 275
6.5.5 ZnO Microstructure Following Irradiation 279
6.6 Summary and Conclusions 280
References 283

7 Defect Accumulation, Amorphization and Nanostructure Modification of Ceramics 287
Yanwen Zhang and William J. Weber
7.1 Introduction. 287
7.2 Energy Deposition Processes in Crystalline Ceramics 289
7.2.1 Damage Production from Atomic Collision Processes 291
7.2.2 Effects of Electronic Energy Loss. 291
7.2.3 Coupled Effects of Ionization and Atomic Dynamics 292
7.3 Damage Accumulation 293
7.3.1 Defect Accumulation 293
7.3.2 Irradiation-Induced Phase Transformations 294
7.3.3 Modelling Amorphization 298

7.3.4 Effect of Temperature 300
7.3.5 Effect of Electronic Energy Loss on Amorphization 303
7.4 Ionization-Induced Annealing and Ionization-Enhanced Amorphization 304
7.4.1 Ionization-Induced Annealing: Single Beam Experiments 304
7.4.2 Ion-Induced Annealing: Dual Beam Irradiations 306
7.4.3 Ionization-Enhanced Amorphization 307
7.5 Structural Modifications in Nanostructured Ceramic Matrices 308
7.5.1 Intrinsically Nanolayered Structures 309
7.5.2 Nanocrystalline Materials 311
7.6 Summary 314
References 315

Part III Damage Formation and Amorphisation by High Electronic Energy Deposition

8 Swift Heavy Ion Irradiation of Crystalline Insulators and Metals 321
Lionel Thomé
8.1 Introduction. 321
8.2 General Considerations About Electronic Energy Loss in Insulators 322
8.3 Experimental Observation of Electronic Energy Loss Effects 324
8.3.1 Direct Observation of Ion Tracks 324
8.3.2 Indirect Observation of Ion Tracks 327
8.4 Formation of Ion Tracks at Low Fluences 329
8.4.1 Track Formation in Metals and Metallic Compounds 329
8.4.2 Track Formation in Insulators 331
8.5 Structural Transformations at High Fluences 344
8.5.1 Experimental Observations of Structural Transformations 344
8.5.2 Analysis of the Build-Up of Radiation-Induced Structural Transformations with Phenomenological Models 352
8.6 Summary 356
References 357

9 Swift Heavy Ion Irradiation of Crystalline Semiconductors 365
Werner Wesch and Claudia S. Schnohr
9.1 Introduction. 365
9.2 Energy Deposition 366
9.3 Track and Damage Formation 369
9.3.1 Materials with High Radiation Resistance 369
9.3.2 Materials with Low Radiation Resistance 376
9.3.3 Threshold Values 384
9.4 Modelling of Track Formation. 386
9.4.1 Qualitative Estimations 386
9.4.2 Application of the Inelastic Thermal Spike (i-TS) Model. 388
9.5 Summary and Discussion 395
References 399

10 Swift Heavy Ion Irradiation of Amorphous Semiconductors. 403
Werner Wesch, Tobias Steinbach and Mark C. Ridgway
10.1 Introduction. 403
10.2 Plastic Deformation in Amorphous Materials. 404
10.3 Structural Modification in Amorphous Silicon (a-Si). 411
10.3.1 Ion Track Formation in a-Si 411
10.3.2 Plastic Deformation of a-Si 413
10.4 Structural Modification in Amorphous Germanium (a-Ge). 420
10.4.1 Ion Track Formation in a-Ge. 420
10.4.2 Porous Layer Formation (Multiple-Ion Irradiation) 424
10.4.3 Plastic Deformation of a-Ge 431
10.4.4 Structural Modification in Other Amorphous Semiconductors 435
10.5 Summary 437
References 437

Part IV Selected Applications of Ion Irradiation

11 Ion-Shaping of Nanoparticles 443
Giancarlo Rizza and Mark C. Ridgway
11.1 Introduction. 443
11.2 Ion-Matter Interaction for a Metal-Dielectric Nanocomposite 446
11.3 Influence of the Embedding Matrix 447
11.3.1 Influence of the Ion-Hammering. 448
11.3.2 Influence of the Ion Track. 449
11.4 Influence of the Nanoparticles 451
11.4.1 Deformation Pathways 453
11.4.2 Kinetics of the Elongation Process 455

11.4.3 Efficiency of the Ion Shaping Process: The Role of the Deposited Energy 458
11.4.4 Elongation as a Function of the Ion Flux 460
11.4.5 Elongation as a Function of the NP Concentration and Stability of the Ion-Shaped NPs 461
11.4.6 Role of Thermodynamics in the Shape Transformation 463
11.5 Toward a Phenomenological Description 464
11.6 Conclusion and Outlook 469
References 471

12 Low Energy Ion Beam Modification of Nanostructures 475
Christian Borschel and Carsten Ronning
12.1 Introduction 475
12.2 Simulations 477
12.3 Enhanced Dynamic Annealing in Nanostructures 482
12.4 Semiconductor Nanowires 484
12.4.1 Ion Beam Doping 485
12.4.2 Damage Profiles and Bending of Nanowires 489
12.5 Sputtering of Nanostructures 491
12.5.1 Static Sputtering Calculations 492
12.5.2 Dynamic Sputtering Calculations 494
12.6 Summary 497
References 498

13 Modification of Structure and Properties of Optical Crystals 501
Feng Chen and Frank Schrempel
13.1 Introduction 501
13.2 Ion Beam Induced Damage and its Effects in Optical Crystals 502
13.2.1 Damage Formation Due to Nuclear Energy Deposition 502
13.2.2 Damage Formation Due to High Electronic Energy Deposition 506
13.3 Methods for the Production of Optical Elements Based on Crystal Damage 509
13.3.1 Refractive Index Modulation and Waveguides 510
13.3.2 Crystal Ion Slicing (CIS) 512
13.3.3 Ion Beam Enhanced Etching (IBEE) 514
13.4 Application of Ion Beam Induced Effects for the Production of Optical Elements 517
13.4.1 Electro-optical Modulators 517
13.4.2 Guided-Wave Frequency Doublers 518

13.4.3 Waveguide Lasers 520
13.4.4 3D Optical Micro- and Nanostructures 523
13.5 Summary 524
References 525

Index 529

Editors and Contributors

About the Editors

Werner Wesch received his Ph.D. (1976) and postdoctoral degree (habilitation 1986) in Physics at the Friedrich-Schiller-Universität Jena, Germany. From 1992 until his retirement in 2012 he was head of the ion beam physics group at the Institut für Festkörperphysik in Jena and since 1994 university lecturer. His research interests include interaction of energetic particles with solids, ion beam modification of semiconductors and insulators due to nuclear and electronic interactions as well as structure and defect analysis by ion beams and complementary methods. He is co-author of more than 230 peer-reviewed journal papers. He was member and secretary of the International Committee of the conference series “Radiation Effects in Insulators” and member of the committees “Research with Ion Beams and Nuclear Probes” of the Bundesministerium für Bildung und Forschung (BMBF) and of the “Materials Research Program Advisory Committee” (Mat-PAC) of the Gesellschaft für Schwerionenforschung (GSI) Darmstadt.

Elke Wendler received her Ph.D. (1984) and postdoctoral degree (habilitation 1999) in Physics at the Friedrich-Schiller-Universität in Jena, Germany, dealing with radiation damage and optical properties of ion implanted semiconductors. A longer stay at the Ion Beam Centre of the University of Surrey in Guildford, UK, broadened her experience in ion beam analysis. In cooperation with researchers from various countries she has published more than 160 papers in peer-reviewed journals in the field of ion beam analysis and of ion beam modification of covalent-ionic materials. In 2014 she became a member of the International Committee of the conference series “Radiation Effects in Insulators” and “Ion Beam Modification of Materials”. Currently the ion beam physics group at the Institut für Festkörperphysik in Jena works under her leadership.

Contributors

Christian Borschel Institut für Festkörperphysik, Friedrich-Schiller-Universität Jena, Jena, Germany

Feng Chen School of Physics, Shandong University, Jinan, China

Christian Dufour Centre Interdisciplinaire de Recherche sur les Ions, les Matériaux et la Photonique (CIMAP), CEA-CNRS-ENSICAEN-Université de Caen, Caen, France

Konrad Gärtner Institut für Festkörperphysik, Friedrich-Schiller-Universität Jena, Jena, Germany

Mark C. Ridgway Research School of Physics and Engineering, Australian National University, Canberra, ACT, Australia

Giancarlo Rizza Laboratoire des Solides Irradiés, Ecole Polytechnique, CEA/DRF/IRAMIS, CNRS, Université Paris-Saclay, Palaiseau Cedex, France

Carsten Ronning Institut für Festkörperphysik, Friedrich-Schiller-Universität Jena, Jena, Germany

Claudia S. Schnohr Institut für Festkörperphysik, Friedrich-Schiller-Universität Jena, Jena, Germany

Frank Schrempel Institut für Angewandte Physik, Friedrich-Schiller-Universität Jena, Jena, Germany

Tobias Steinbach Institut für Festkörperphysik, Friedrich-Schiller-Universität Jena, Jena, Germany

Lionel Thomé Centre de Sciences Nucléaires et de Sciences de la Matière (CSNSM), Université Paris-Sud, CNRS-IN2P3, Orsay, France

Marcel Toulemonde Centre Interdisciplinaire de Recherche sur les Ions, les Matériaux et la Photonique (CIMAP), CEA-CNRS-ENSICAEN-Université de Caen, Caen, France

William J. Weber Department of Materials Science and Engineering, University of Tennessee, Knoxville, TN, USA

Elke Wendler Institut für Festkörperphysik, Friedrich-Schiller-Universität Jena, Jena, Germany

Werner Wesch Institut für Festkörperphysik, Friedrich-Schiller-Universität Jena, Jena, Germany

James S. Williams Research School of Physics and Engineering, Australian National University, Canberra, Australia

Yanwen Zhang Materials Science and Technology Division, Oak Ridge National Laboratory, Oak Ridge, TN, USA

Symbols

a	Lattice parameter, average displacement distance, screening length
a_o	Bohr radius
A	Area
A_0	Deformation yield
$b_{n,e}$	Collision diameter for nuclear (n) and electronic (e) scattering
C	Concentration
$C_{e,a}$	Heat capacity per unit volume of electronic (e) or atomic (a) system
D	Local dose, diffusion coefficient
e	Elementary charge
E	Ion energy
E_a	Thermal activation energy
E_b	Binding energy of an atom in the solid
E_d	Displacement energy
E_g	Gap energy
f	Damage fraction
F	Force
g	Electron–phonon coupling strength
G	Shear modulus, Gibbs free energy
$\hbar$	Planck constant
H	Enthalpy
j_e	Electron flux
J^*	Nucleation rate
$K_{e,a}$	Thermal conductivity of the electronic (e) or atomic (a) system
m_1, m_2, m, m_e	Mass (ion, target atom, total, electron)
M	Mobility

N	Atomic density
N_I	Ion fluence
N_{displ}^*	Number of displacements per ion and unit depth
n	Refractive index
n_e	Concentration of free electrons
n_{da}	Relative number of displaced lattice atoms
n_{dpa}	Number of displacements per lattice atom (dpa)
p	Momentum
q	Charge state
r	Distance
R	Radius
s	Impact parameter, path length
$s(t)$	Solute concentration
S	Entropy
$S_{n,e}$	Stopping power (energy loss per ion and unit depth) nuclear (n), electronic (e)
$\hat{S}$, $\hat{S}_n$, $\hat{S}_e$	Stopping cross section (total, nuclear, electronic)
S_{et}	Threshold value of electronic energy deposition
T	Temperature, transferred energy
T_m	Melting temperature
$T_{e,a}$	Temperature of electronic (e) or atomic (a) subsystem
v	Ion velocity, recrystallisation velocity
V	Ion–atom interaction potential, volume
W, W_n, W_e	Energy straggling cross section (total, nuclear, electronic)
Y	Yield of backscattered ions
Z	Atomic number
α	Linear thermal expansion coefficient
γ	Electron–phonon coupling efficiency
Γ	Displacement rate
ε	Dielectric constant, reduced energy of the ion (dimensionless)
ε^*	Effective eigenstrain
η	Shear viscosity
λ	de Broglie wavelength, electron–phonon mean free path
μ	Reduced mass, chemical potential
μ_H	Hall mobility
ν	Poisson number, Poisson rate
ν_i	Deformation velocity (i = x,y,z)
ν_s	Sound velocity
ν_x	Shear velocity
Ω	Solid angle, atomic volume
Ω^2	Energy straggling
ρ	Resistivity

ρ_e	Electron density
σ	Cross section, in-plane stress
τ_e	Mean free time between two collisions of an electron
Φ	Screening function, final scattering angle, ion flux
Ψ^2	Angular straggling

Part I
Physical Basics

Chapter 1
Ion-Solid Interaction

Konrad Gärtner

Abstract This chapter gives an introduction into the theoretical description of the physical processes which take place during the ion motion through a solid target. The interaction of the ion with the whole solid is treated as a sequence of binary collisions with free target atoms at rest. Furthermore, the elastic and inelastic contributions to the binary collisions are considered to be statistically independent and therefore they are treated separately. The elastic interaction provides changes of the energy and the direction of the ion. It is described by classical mechanics and determined by the ion-atom interaction potential. The inelastic interaction provides mainly a change of the energy of the ion which has to be described by quantum mechanics, however, also some classical approaches are presented. For amorphous solids, mainly considered here, the binary collisions can be assumed to be statistically independent and the physical quantities (e.g. energy and angular distributions) are obtained by statistics. In the case of crystalline solids, only some special effects are described.

1.1 Introduction

If an ion beam is directed onto a solid target, the ions move through the target changing continuously their direction and energy and maybe also their states of excitation and ionization. Finally, the ions come to rest within the target (implanted) or they leave the target (transmitted or reflected). During their motion through the target, the ions generate primary recoils (energetic target atoms) which generate secondary recoils and so on (collision cascade). Due to the ion and the recoils as well, target atoms can become displaced (point defects, leading also to extended defects) and excited (electronic defects) and they can be removed from the surface (sputtering). In the case of a collective energy transfer (e.g. with swift heavy ion

K. Gärtner (✉)
Institut für Festkörperphysik, Friedrich-Schiller-Universität Jena,
Max-Wien-Platz 1, 07743 Jena, Germany
e-mail: konrad.gaertner@uni-jena.de

© Springer International Publishing Switzerland 2016

W. Wesch and E. Wendler (eds.), *Ion Beam Modification of Solids*,
Springer Series in Surface Sciences 61,
DOI 10.1007/978-3-319-33561-2_1

irradiation), the structure of the solid can be changed (e.g. track formation) and more extended defect structures (e.g. voids) can be generated. Furthermore, the implanted ions and in some cases also the recoils (e.g. mixing in layered targets) cause changes of the local chemical composition.

In order to be able to understand all the possible changes of the target caused by the ion irradiation, a detailed consideration of the ion-solid interaction is required. First, the following characteristic quantities, important for the simplification of the theoretical description of the complicated interaction processes, are considered:

E_b binding energy of the atoms in the target
d_{at} average distance between the target atoms
τ_v duration of vibration of the target atoms
λ De Broglie wave length of the ion
t_I interaction time of the ion with a target atom

The binding energy E_b and the average distance of atoms d_{at} are in the order of eV and Å, respectively, and the duration of vibration τ_v is in the range of about 10^{-13} to 10^{-12} s. For ions with energies E in the order of 10 keV and above, as considered here, the relations

$$E \gg E_b$$
$$\lambda = h/(m_1 v) < 10^{-2}\,\text{Å} \ll d_{at}$$
$$t_I \lesssim d_{at}/v < 10^{-15}\,\text{s} \ll \tau_v$$

are valid, where m_1 and v are the mass and the velocity of the ion and h is the Planck constant. From this follows that the interaction of the ion with the whole solid can approximately be treated as a **sequence of classical ($\lambda \ll d_{at}$) binary collisions** with **free target atoms ($E \gg E_b$)** which do **not move during the interaction ($t_I \ll \tau_v$)**. Furthermore, as shown later, the elastic and inelastic interaction between the ion and an atom can be treated separately. They are described in Sects. 1.2 and 1.3, respectively. The theoretical description of the interaction of the ion with the whole solid, based on the elastic and inelastic binary collisions, is presented in Sect. 1.4 for amorphous solids which is also valid for polycrystalline solids (if the grain size is smaller than the ion beam diameter) and for random incidence of the ion in a crystalline solid. Special effects in the case of aligned incidence of the ion in a crystalline solid are briefly mentioned in Sect. 1.5.

1.2 Elastic Ion-Atom Interaction

With the elastic ion-atom interaction, the configurations of the electrons of the ion and the target atom remain unchanged. This means that the elastic interaction can be described by a classical two-body problem determined by the ion-atom interaction potential which is a Coulomb potential screened by the electrons of the ion and the atom. The scattering kinematics and dynamics provide the scattering angles of the

ion and the atom, the differential cross section and the energy transferred from the ion to the atom.

1.2.1 Ion-Atom Interaction Potential

During their interaction, the ion and the atom form a quasi-molecule the electronic structure of which depends on the distance r between the ion and the atom. The ion-atom interaction potential V(r) is defined as the difference of the quantum mechanical energies of the quasi-molecule for distance r and the free ion and atom

$$V(r) = E_{quasi-molecule}(r) - E_{ion} - E_{atom}. \tag{1.1}$$

Let us first consider a **single atom** with atomic number Z. The corresponding quantum mechanical energy $E_{atom} = E[\{\varphi_i\}]$ is a functional of the wave functions φ_i of all electrons i of the atom. Within the statistical model of the atom developed by Thomas [1], Fermi [2] and Dirac [3] and described in detail by Gombás [4, 5], the functional $E[\{\varphi_i\}]$ can approximately be replaced by the functional $E[\rho_e]$, where the electron density ρ_e (number of electrons per unit volume) is the sum over all $|\varphi_i|^2$. There are mainly three contributions to this energy

$$E_{atom} \approx E[\rho_e] = E_{elstat}[\rho_e] + E_{kin}[\rho_e] + E_{exch}[\rho_e], \tag{1.2}$$

the electrostatic energy, the kinetic energy and the exchange energy.

The electrostatic energy as a functional of the electron density is exactly given by

$$E_{elstat}[\rho_e] = -Z\in^2 \int d^3\mathbf{r}' \frac{\rho_e(\mathbf{r}')}{r'} + \frac{\in^2}{2} \int \frac{d^3\mathbf{r}' d^3\mathbf{r}'' \rho_e(\mathbf{r}') \rho_e(\mathbf{r}'')}{|\mathbf{r}' - \mathbf{r}''|} \tag{1.3}$$

with the abbreviation $\in^2 = e^2/(4\pi\varepsilon_0) = 14.39965$ eV Å, where e is the elementary charge and ρ_e is normalized by $\int d^3\mathbf{r}' \rho_e(\mathbf{r}') = Z$.

The kinetic energy can only approximately be expressed as a functional of the electron density. For this purpose the volume of the atom is subdivided in small cells $d^3\mathbf{r}'$ which are small enough that the potential within $d^3\mathbf{r}'$ can be assumed to be constant and large enough that the electrons within $d^3\mathbf{r}'$ can be treated statistically. The number of states dN_{ph} in the phase space $d^3\mathbf{r}'\, d^3\mathbf{p}$ is given by

$$dN_{ph} = 2\, d^3\mathbf{r}' d^3\mathbf{p}/h^3 = 8\pi\, d^3\mathbf{r}' p^2 dp/h^3 \quad \text{for } p \leq p_F \tag{1.4}$$

(the factor 2 takes into account 2 spin states) with the Fermi momentum p_F determined by the demand that the number of states in $d^3\mathbf{r}'$ must be equal to the number of electrons in $d^3\mathbf{r}'$

$$\int_0^{p_F} d\,N_{ph} = \frac{8\pi}{3h^3} d^3\mathbf{r}'\, p_F^3 = \rho_e(\mathbf{r}')\, d^3\mathbf{r}' \tag{1.5}$$

which provides

$$p_F(\mathbf{r}') = \left(\frac{3}{8\pi}\right)^{1/3} h\, \rho_e^{1/3}(\mathbf{r}'). \tag{1.6}$$

The kinetic energy of all electrons in $d^3\mathbf{r}'$ is given by

$$dE_{kin} = \int_0^{p_F} dN_{ph} \frac{p^2}{2m_e} = \frac{4\pi}{5m_e h^3} d^3\mathbf{r}' p_F^5 = \frac{3}{10}\left(\frac{3}{8\pi}\right)^{2/3} \frac{h^2}{m_e} d^3\mathbf{r}'\, \rho_e^{5/3}(\mathbf{r}') \tag{1.7}$$

(m_e is the electron mass) and the total kinetic energy reads

$$E_{kin}[\rho_e] = \kappa_{kin} \int d^3\mathbf{r}'\, \rho_e^{5/3}(\mathbf{r}') \quad \text{with} \quad \kappa_{kin} = \frac{3}{10}\left(3\pi^2\right)^{2/3} \in^2 a_0, \tag{1.8}$$

where $a_0 = \hbar^2/(m_e \in^2) = 0.529177$ Å is the Bohr radius and $\hbar = h/(2\pi)$. A similar treatment (see Dirac [3] or Jensen [6, 7]) provides the exchange energy

$$E_{exch}[\rho_e] = \kappa_{exch} \int d^3\mathbf{r}'\, \rho_e^{4/3}(\mathbf{r}') \quad \text{with} \quad \kappa_{exch} = -\frac{3}{4}\left(\frac{3}{\pi}\right)^{1/3} \in^2. \tag{1.9}$$

Now, let us return to the **ion-atom interaction potential** V(r) defined by (1.1). Within the statistical model of the atom described above, the quantum mechanical energies of the ion, the atom and the quasi-molecule are given by (1.2), (1.3), (1.8) and (1.9), where ρ_e is replaced by the electron densities $\rho_{e,1}$, $\rho_{e,2}$ and $\rho_{e,12}$ of the ion, the atom and the quasi-molecule, respectively. Now, (1.1) reads

$$V(r) = E[\rho_{e,12}(\mathbf{r}'; r)] - E[\rho_{e,1}(\mathbf{r}')] - E[\rho_{e,2}(\mathbf{r}'')], \tag{1.10}$$

with $\int d^3\mathbf{r}' \rho_{e,1}(\mathbf{r}') = Z_1 - n_{ion}$, $\int d^3\mathbf{r}'' \rho_{e,2}(\mathbf{r}'') = Z_2$ and $\int d^3\mathbf{r}' \rho_{e,12}(\mathbf{r}'; r) = Z_1 - n_{ion} + Z_2$, where Z_1 and n_{ion} are the atomic number and the degree of ionization of the ion and Z_2 is the atomic number of the target atom. The position vectors $\mathbf{r}'$ and $\mathbf{r}''$ have their origin in the nuclei of the ion and the atom, respectively. The electron density of the quasi-molecule $\rho_{e,12}(\mathbf{r}'; r)$ for a given distance r between the ion and the atom can be approximated by the superposition of the electronic densities of the free ion and free atom at distance r. This is justified because the correct electron density belongs to the minimum of $E[\rho_{e;12}(\mathbf{r}';r)]$ and therefore a deviation from the correct electron density influences the energy only slightly. It means, the accuracy of the energy is one order of magnitude better than that of the electron density.

According to the three contributions to the energies $E[\rho_e]$ (1.3), (1.8) and (1.9), the ion-atom interaction potential (1.10) is now given by

$$V(r) = V_{elstat}(r) + V_{kin}(r) + V_{exch}(r) \equiv \frac{Z_1 Z_2 \in^2}{r}\Phi(r) \quad (1.11)$$

with

$$\begin{aligned} V_{elstat}(r) = {} & \frac{Z_1 Z_2 \in^2}{r} + \in^2 \int \frac{d^3\mathbf{r}'\rho_{e,1}(r')d^3\mathbf{r}''\rho_{e,2}(r'')}{|\mathbf{r}+\mathbf{r}'-\mathbf{r}''|} \\ & - Z_2\in^2 \int \frac{d^3\mathbf{r}'\rho_{e,1}(r')}{|\mathbf{r}+\mathbf{r}'|} - Z_1\in^2 \int \frac{d^3\mathbf{r}''\rho_{e,2}(r'')}{|\mathbf{r}-\mathbf{r}''|} \end{aligned} \quad (1.12)$$

$$V_{kin}(r) = \kappa_{kin} \int d^3\mathbf{r}' \left\{ \left[\rho_{e,1}(r') + \rho_{e,2}(|\mathbf{r}+\mathbf{r}'|)\right]^{5/3} - \rho_{e,1}^{5/3}(r') - \rho_{e,2}^{5/3}(r') \right\} \quad (1.13)$$

$$V_{exch}(r) = \kappa_{exch} \int d^3\mathbf{r}' \left\{ \left[\rho_{e,1}(r') + \rho_{e,2}(|\mathbf{r}+\mathbf{r}'|)\right]^{4/3} - \rho_{e,1}^{4/3}(\rho') - \rho_{e,2}^{4/3}(r') \right\}. \quad (1.14)$$

The four contributions to V_{elstat} are directly provided by electrodynamics and V_{kin} (1.13) and V_{exch} (1.14) are obtained from (1.8), (1.9) and (1.10), where the electronic densities of the free atoms and ions are assumed to be spherical symmetric. Equation (1.11) defines also the screening function Φ which is unity for r = 0 and tends to zero for $r \to \infty$. The ion-atom interaction potential V(r) [or the screening function $\Phi(r)$] according to (1.11)–(1.14) must be calculated separately for each $Z_1 - Z_2$ combination by numerical integration. Its accuracy depends mainly on the accuracy of the electronic densities used and it is less influenced by the uncertainty of the statistical approximation. In [8], the interaction potential according to (1.11)–(1.14) is calculated using the electronic densities obtained from the electronic wave functions for atoms and ions given by Clementi and Roetti [9]. In the following, a potential calculated in this way is called 'individual potential' for short.

For simplicity, in some cases generalized expressions for the screening function are applied. Using the statistical model of the atom without exchange energy [E_{elstat} and E_{kin} according to (1.3) and (1.8)] for the calculation of the screening function and for the determination of the electron density as well, Thomas [1] and Fermi [2] obtained the screening function $\Phi_{TF}(r/a_{TF}(Z))$ for a single atom, where $\Phi_{TF}(x)$ is a universal function given numerically and the screening length $a_{TF}(Z) = 0.88534\ a_0\ Z^{-1/3}$ depends monotonously on the atomic number Z of the atom. Firsov [10, 11] and Lindhard [12] extended this screening function approximately to the interaction of two neutral atoms only by changing the screening length from $a_{TF}(Z)$ to

$$a_F(Z_1, Z_2) = \frac{0.88534\, a_0}{\left(Z_1^{1/2} + Z_2^{1/2}\right)^{2/3}} \text{ and } a_L(Z_1, Z_2) = \frac{0.88534\, a_0}{\left(Z_1^{2/3} + Z_2^{2/3}\right)^{1/2}}, \quad (1.15)$$

respectively. For convenient practical use, there exist a number of different analytical expressions of generalized screening functions $\Phi(r/a)$ with different universe functions $\Phi(x)$ and screening lengths a (see e.g. [13, 14]). Here, only two of them are mentioned. The widespread used universal ZBL screening function obtained by Ziegler, Biersack and Littmark [13] reads

$$\Phi(r) = \sum_1^4 a_i \exp\left(-b_i \frac{r}{a_{ZBL}}\right) \text{ with } a_{ZBL} = \frac{0.88534\, a_0}{Z_1^{0.23} + Z_2^{0.23}}, \quad (1.16)$$

with a_i = (0.1818, 0.5099, 0.2802, 0.02817) and b_i = (3.200, 0.9423, 0.4028, 0.2016). It has been obtained by averaging a large number of screening functions calculated for different $Z_1 - Z_2$ combinations similar to the procedure given in (1.11)–(1.14). The OCB screening function suggested by O'Connor and Biersack [15] has the same structure as that given in (1.16). However, there are only three contributions with a_i = (0.35, 0.55, 0.1) and b_i = (0.3, 1.2, 6.0) and a_{ZBL} is replaced by

$$a_{OCB} = \left[0.54 + 0.045\left(Z_1^{1/2} + Z_2^{1/2}\right)\right] a_F(Z_1, Z_2), \quad (1.17)$$

with a_F given in (1.15).

1.2.2 Scattering Kinematics

After the elastic collision of the ion of velocity **v** with a target atom at rest, the new velocity $\mathbf{v}_1'$ of the ion is smaller and it deviates from the original direction by an angle φ_1 and the target atom moves with a velocity $\mathbf{v}_2'$ at an angle φ_2 with respect to the velocity **v** (see Fig. 1.1).

The conservations of the momentum and the kinetic energy provide already some information about the velocities and angles after the collision which is independent of the ion-atom interaction potential. Because the corresponding equations become more simple, let us change from the laboratory system to the center-of-mass system which moves with the velocity $\mathbf{v}_{cm} = (m_1/m)\mathbf{v}$, where m_1 and m_2 are the masses of the ion and the target atom, respectively, and $m = m_1 + m_2$ is the total mass. The velocities of the ion and the target atom in the center-of-mass system before the collision are

Fig. 1.1 Scattering geometry

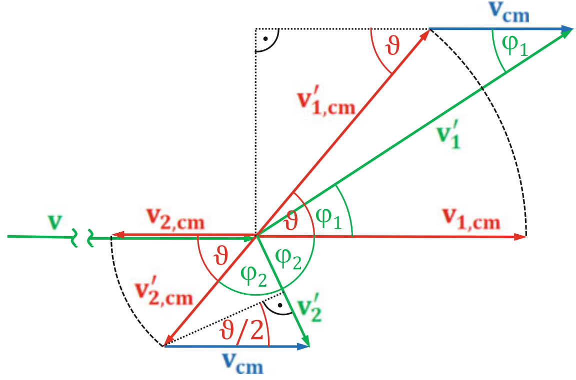

$$\mathbf{v}_{1,cm} = \mathbf{v} - \mathbf{v}_{cm} = \frac{m_2}{m}\mathbf{v} \quad \text{and} \quad \mathbf{v}_{2,cm} = -\mathbf{v}_{cm} = -\frac{m_1}{m}\mathbf{v}, \tag{1.18}$$

respectively. The conservation of the momentum in the center-of-mass system

$$m_1\,\mathbf{v}_{1,cm} + m_2\,\mathbf{v}_{2,cm} = 0 = m_1\,\mathbf{v}'_{1,cm} + m_2\,\mathbf{v}'_{2,cm} \tag{1.19}$$

means that the two velocities $\mathbf{v}'_{1,cm}$ and $\mathbf{v}'_{2,cm}$ after the collision remain anti-parallel. Under this condition the conservation of the kinetic energy in the center-of-mass system can only be fulfilled by

$$v'_{1,cm} = v_{1,cm} \quad \text{and} \quad v'_{2,cm} = v_{2,cm} = v_{cm} \tag{1.20}$$

(for $v'_{1,cm} > v_{1,cm}$ the momentum conservation requires also $v'_{2,cm} > v_{2,cm}$ which violates the energy conservation, similar for $v'_{1,cm} < v_{1,cm}$). This means that the two velocities in the center-of-mass system can only rotate by the same angle ϑ without changing their absolute value (see Fig. 1.1). The velocities $\mathbf{v}'_1$ and $\mathbf{v}'_2$ after the collision in the laboratory system are obtained by adding the velocity of the center-of-mass system $\mathbf{v}_{cm}$ to $\mathbf{v}'_{1,cm}$ and $\mathbf{v}'_{2,cm}$, respectively. Now, the scattering angles φ_1 and φ_2 in the laboratory system and the energy transferred to the target atom T_n (nuclear contribution) as functions of the scattering angle ϑ in the center-of-mass system can easily be obtained from Fig. 1.1 (for $\tan\varphi_1$ and for $v'_2 = 2v_{cm}\,\sin(\vartheta/2)$ see the upper and lower rectangular triangle, respectively) providing

$$\tan\varphi_1 = \frac{v'_{1,cm}\sin\vartheta}{v_{cm} + v'_{1,cm}\cos\vartheta} = \frac{m_2\sin\vartheta}{m_1 + m_2\cos\vartheta} \tag{1.21}$$

$$\varphi_2 = \frac{\pi - \vartheta}{2} \tag{1.22}$$

$$T_n = \frac{m_2}{2}\left(v_2'\right)^2 = T_{n,max}\sin^2\frac{\vartheta}{2} \quad \text{with} \quad T_{n,max} = \frac{4\,m_1 m_2}{m^2}\,E \tag{1.23}$$

and $E = (m_1/2)v^2$. The remaining unknown quantity ϑ depends on the ion-atom potential V(r). It will be calculated in the next section.

1.2.3 Scattering Dynamics

The classical equation of motion in the relative-coordinate system reads

$$m_r\ddot{\mathbf{r}} = -\frac{\mathbf{r}}{r}\frac{dV(r)}{dr} \quad \text{with} \quad m_r = \frac{m_1\,m_2}{m}, \tag{1.24}$$

where **r** is the vector of the distance from the atom to the ion (relative coordinates) and m_r is called reduced mass. Because the potential V depends only on $r = |\mathbf{r}|$, the energy E_r and angular momentum $\mathbf{L}_r$ in the relative-coordinate system are conserved. The conservation of the vector $\mathbf{L}_r$ means that the motion of the reduced mass takes place within a plane which is described by polar coordinates (r, φ) (see Fig. 1.2).

The scattering angle ϑ in the center-of-mass system to be determined is equal to the scattering angle ϑ shown in Fig. 1.2. It can be calculated by employing the conservation of the energy E_r and angular momentum L_r in the relative-coordinate system

$$L_r = m_r\,r^2\dot{\varphi} = m_r\,vs \rightarrow \dot{\varphi} = \frac{v\,s}{r^2} \tag{1.25}$$

$$E_r = \frac{m_r}{2}\left[\dot{r}^2 + r^2\left(\frac{v\,s}{r^2}\right)^2\right] + V(r) = \frac{m_r}{2}v^2 = \frac{m_2}{m}\,E, \tag{1.26}$$

where s is the impact parameter (see Fig. 1.2). The angular velocity $\dot{\varphi}$ (1.25) and the radial velocity $\dot{r}$ obtained from (1.26) provide

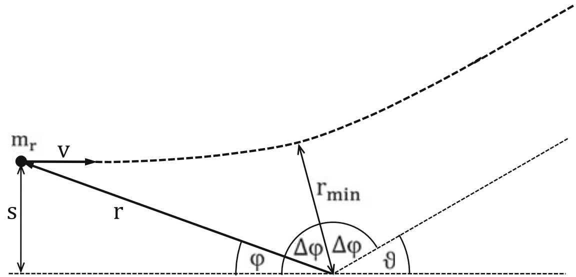

Fig. 1.2 Path r(φ) of the reduced mass m_r in relative-coordinate system

$$\frac{d\varphi}{dr} = \frac{\dot{\varphi}}{\dot{r}} = \pm\frac{s}{r^2}\left[1 - \frac{s^2}{r^2} - \frac{V(r)}{E_r}\right]^{-1/2}. \tag{1.27}$$

According to Fig. 1.2 the scattering angle ϑ is given by

$$\vartheta = \pi - 2\,\Delta\varphi = \pi - 2\int_{r_{min}}^{\infty} dr\frac{d\varphi}{dr}. \tag{1.28}$$

The insertion of $d\varphi/dr$ [(1.27), where $d\varphi/dr > 0$ for $r = r_{min}$ to ∞, see Fig. 1.2] provides

$$\vartheta(s) = \pi - 2\,s\int_{r_{min}}^{\infty}\frac{dr}{r^2}\left[1 - \frac{s^2}{r^2} - \frac{V(r)}{E_r}\right]^{-1/2} \tag{1.29}$$

with the minimum distance of approach r_{min} determined by $dr/d\varphi = 0$ corresponding to

$$1 - \frac{s^2}{r_{min}^2} - \frac{V(r_{min})}{E_r} = 0. \tag{1.30}$$

Now, the scattering angles φ_1 and φ_2 in the laboratory system and the energy T_n transferred to the target atom as functions of the impact parameter s are provided by (1.21)–(1.23) with the scattering angle $\vartheta(s)$ in the center-of-mass system given in (1.29) and (1.30).

1.2.4 Scattering Angles and Differential Cross Section

The differential cross sections in the center-of-mass system and in the laboratory system are defined by

$$\left(\frac{d\sigma}{d\Omega}\right)_{cm} = \frac{s}{\sin\vartheta}\left|\frac{ds}{d\vartheta}\right| \quad \text{and} \quad \frac{d\sigma}{d\Omega} = \frac{s}{\sin\varphi_1}\left|\frac{ds}{d\varphi_1}\right|, \tag{1.31}$$

respectively. They are related to each other by

$$\frac{d\sigma}{d\Omega} = \left(\frac{d\sigma}{d\Omega}\right)_{cm}\frac{(1-\zeta^2)^{\frac{1}{2}}}{\sin\varphi_1\cos^2\varphi_1}\,\frac{(\alpha_m+\zeta)^2}{1+\alpha_m\zeta}, \quad \text{where } \alpha_m = \frac{m_1}{m_2}$$
$$\text{and} \quad \zeta(\varphi_1) = \cos\vartheta(\varphi_1) = \cos\varphi_1\left(1-\alpha_m^2\sin^2\varphi_1\right)^{1/2} - \alpha_m\sin^2\varphi_1. \tag{1.32}$$

1.2.4.1 Coulomb Potential

For Coulomb potential [screening function Φ = 1 in (1.11)], the integral in (1.29) can be solved analytically which provides

$$\tan\left(\frac{\vartheta(s)}{2}\right) = \frac{b_n}{2\,s} \quad \text{with} \quad b_n = \frac{Z_1\,Z_2 \in^2}{E_r} = \frac{m}{m_2}\frac{Z_1\,Z_2 \in^2}{E}. \tag{1.33}$$

The scattering angles φ_1 and φ_2 are obtained from (1.21), (1.22) and (1.33) by

$$\begin{aligned} \tan\varphi_1(s) &= \frac{(1-\zeta_s^2)^{\frac{1}{2}}}{\alpha_m + \zeta_s} \quad \text{and} \quad \varphi_2(s) = \frac{\pi - \arccos(\zeta_s)}{2}, \\ \text{where } \alpha_m &= \frac{m_1}{m_2} \quad \text{and} \quad \zeta_s(s) = \cos\vartheta(s) = \frac{4\,s^2 - b_n^2}{4\,s^2 + b_n^2}. \end{aligned} \tag{1.34}$$

With the definitions of the cross sections in (1.31) and with $\varphi_1(\vartheta)$ from (1.21) and $\vartheta(s)$ from (1.33), the differential cross section for the Coulomb potential (Rutherford cross section [16]) in the center-of-mass system is given by

$$\left(\frac{d\sigma}{d\Omega}\right)_{cm}^{R} = \left(\frac{b_n}{4}\right)^2 \frac{1}{\sin^4(\vartheta/2)} = \left(\frac{m}{m_2}\frac{Z_1\,Z_2 \in^2}{4\,E}\right)^2 \frac{1}{\sin^4(\vartheta/2)} \tag{1.35}$$

and the differential Rutherford cross section in the laboratory system reads [17–19]

$$\left(\frac{d\sigma}{d\Omega}\right)^{R} = \left(\frac{Z_1\,Z_2 \in^2}{2\,E}\right)^2 \frac{\left\{\cos\varphi_1 + \left[1 - \alpha_m^2 \sin^2\varphi_1\right]^{1/2}\right\}^2}{\sin^4\varphi_1 \left[1 - \alpha_m^2 \sin^2\varphi_1\right]^{1/2}}. \tag{1.36}$$

For the impact parameter $s = b_n/2$, (1.33) provides $\vartheta = 90°$. This means that in the center-of-mass system all ions with $s < b_n/2$ (circular area with diameter b_n) are backscattered. Therefore, b_n is called collision diameter. It is also equal to the minimum distance of approach in a head-on collision $r_{min}(s = 0) = b_n$ [r_{min} defined in (1.30), b_n given in (1.33)].

1.2.4.2 Screened Coulomb Potential

Measurable quantities obtained from the scattering angles (e.g. the scattering cross section) can be used to test the validity of a given ion-atom interaction potential V(r) or screening function Φ(r). Small scattering angles are of special interest because they are most sensitive to the behavior of V(r), especially at larger distances. All generalized potentials depend smoothly on r and on Z_1 and Z_2 as well. Therefore, they cannot take into account effects caused by the shell structure of the electron density and by individual features of a given $Z_1 - Z_2$ combination. However, there

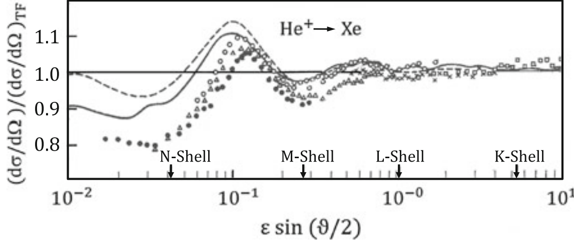

Fig. 1.3 The measured and calculated differential cross sections for the scattering of He^+ ions on Xe atoms related to the differential cross section calculated using the Thomas-Fermi screening function with the Lindhard screening length a_L (1.15) as functions of the product $\varepsilon \sin(\vartheta/2)$, where the reduced energy ε is given by $\varepsilon = a_L/b_n$ [see (1.15) and (1.33)]. The experimental data of Loftager et al. [20] belong to different energies (symbols, for details see [20]). For the theoretical results (lines) see text (note that here $\varphi_1 \approx \vartheta$ because $m_1 \ll m_2$)

is a chance to describe such effects with the potential given in (1.11)–(1.14) by using sufficiently exact individual electronic densities.

One example for shell effects is given in Fig. 1.3. It shows the differential cross section for the scattering of He^+ ions on Xe atoms (related to the differential cross section calculated using the Thomas-Fermi screening function). The theoretical result given by the full line [8] has been obtained using the individual potential (1.11)–(1.14) mentioned in Sect. 1.2.1. The dashed line represents the result of the Aarhus group [20] calculated according to (1.11)–(1.14) added by a correlation term and employing the electron density provided from the Dirac-Hartree-Fock-Slater wave functions [21]. While the cross section obtained with the Thomas-Fermi potential (here unity) provides only an average agreement with the experimental data, the results obtained with the two individually calculated potentials show the main features of the measured oscillations caused by the shell structure of the electron density of Xe.

The glancing angle scattering of atoms or ions from the surface of crystalline targets under axial surface channeling conditions is very useful to test the accuracy of a given ion-atom interaction potential V(r) especially at large distances r, where V is in the order of 1–10 eV. In this case, the projectile with energy E enters the crystal under a grazing angle of incidence φ_{in} (order of 1 degree) to the surface with the projection of its path onto the surface oriented in a low index direction. The scattered projectiles are registered on a plane perpendicular to the low index surface direction. The intensity on this plane is concentrated on a segment of a circle around the low index surface direction with pronounced maxima at the edges of this segment at azimuth angles $\pm\Theta_{rb}$. Because of the similarity with the atmospheric rainbow, this process is called rainbow scattering and Θ_{rb} is called rainbow angle (for details see [22]) which has been shown to depend not separately on the energy E and the angle of incidence φ_{in} but only on the so called transverse energy defined by $E_\perp = E \sin^2\varphi_{in}$. For the examples of the rainbow scattering of He, Ne, Ar, and N atoms from a (001)KCl surface, the rainbow angles Θ_{rb} are given in Fig. 1.4 [22].

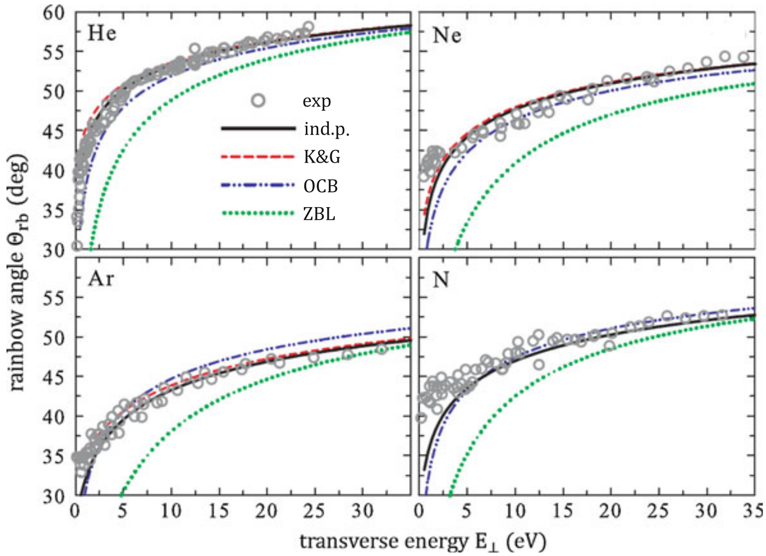

Fig. 1.4 The dependence of the rainbow angle Θ_{rb} on the transverse energy $E_\perp$ for neutral He, Ne, Ar and N atoms scattered from a (001)KCl surface around the <100> axis (all data from [22]). The experimental data are given by the circles. The lines represent the calculated rainbow angles using the individual potential [8] (*full lines*), the potential of Kim and Gordon [23, 24] (*red dashed lines*, not for N), the OCB potential [15] (*blue dash-dot-dotted lines*) and the ZBL potential [13] (*green dotted lines*), respectively

As can be seen, the rainbow angles Θ_{rb} calculated using the individual potential [8] as given in Sect. 1.2.1 and those based on the potential of Kim and Gordon [23, 24] (determined similarly to the individual potential) agree much better with the experimental data than the results obtained using the two generalized potentials [ZBL and OCB, the corresponding screening functions are given in (1.16) and (1.17)]. While in the case of the widely used ZBL potential the calculated rainbow angles underestimate the experimental results remarkably, the improved generalized OCB potential provides better results.

Another example for rainbow scattering [25] is presented in Fig. 1.5. Here, both generalized potentials (ZBL, OCB) provide rainbow angles which underestimate the measured values heavily especially for very low transverse energies. A very good agreement with the experimental data has been obtained using the individual potentials (1.11)–(1.14) for Ne-Li^+ and Ne-F^-. As can be seen in Fig. 1.5, the ionization of Li and F must be taken into account which is possible in the case of the individual potential (electron wave functions for Li^+ and F^- from [9]).

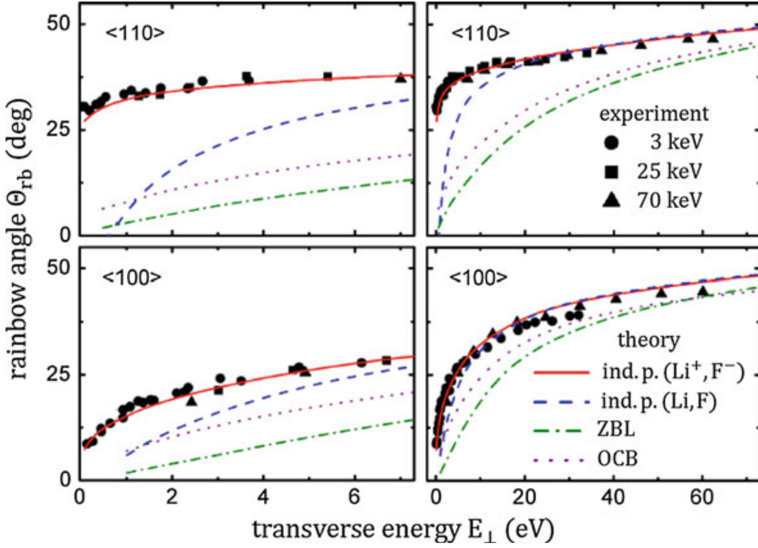

Fig. 1.5 The dependence of the rainbow angle Θ_{rb} on the transverse energy $E_{\perp}$ for neutral Ne atoms scattered from a (001)LiF surface around the < 110 > and < 100 > axis, respectively (all data from [25]). The experimental data for different energies are given by the symbols. The lines represent the calculated rainbow angles using the individual potentials [8] for the interaction of the Ne atoms with Li^+ and F^- ions (*full red lines*) and with neutral Li and F atoms (*blue dashed lines*), the ZBL potential [13] (*green dash-dotted line*) and the OCB potential [15] (*violet dotted line*). Note the different transverse energy range in the left and right hand panels

1.2.5 Transferred Energy

For a given ion-atom interaction potential V(r), the nuclear contribution to the transferred energy $T_n(s)$ as a function of the impact parameter s is obtained from (1.23) and (1.29), where the determination of $\vartheta(s)$ according to (1.29) usually requires a numerical integration. In the case of the Coulomb potential, $\vartheta(s)$ is known analytically [see (1.33)] which provides

$$T_n(s) = T_{n,max} \frac{1}{1 + (2\,s/b_n)^2} \quad \text{with} \quad T_{n,max} = \frac{4\,m_1\,m_2}{m^2} E \tag{1.37}$$

[the collision diameter b_n is given in (1.33)]. For the impact parameter s = 0, the transferred energy provides $T_n = T_{n,max}$ which is in the order of 0.1 E to E ($T_{n,max}$ = E for $m_1 = m_2$). With the ion implantation, typical values of the scattering diameter b_n may reach the order of Å but mostly they are considerably less than 1 Å and with the swift heavy ion irradiation $b_n \lesssim 10^{-3}$ Å is fulfilled. This means that the transferred energy T_n is a remarkable part of E for s = 0 and decreases rapidly with increasing impact parameter s ($T_n = 0.2\ T_{n,max}$ for $s = b_n$).

1.3 Inelastic Ion-Atom Interaction

The inelastic ion-atom interaction is characterized by changes of the configurations of the electrons of the ion and the target atom resulting mainly in an energy loss of the ion. Because of the very small electron mass, the resulting deflection of the ion is negligibly small. The main processes responsible for the energy loss are different below and above a critical energy approximately given by $E_{e,cr} \approx 22(m_1/u)\, Z_1\, Z_2^{0.4}$ keV, where u is the atomic mass unit. For ion energies above $E_{e,cr}$, the main processes are the excitation and ionization of the atom caused by the moving ion which remains unchanged. Below the critical energy $E_{e,cr}$, the probability for excitation and ionization decreases rapidly, however, the increasing interaction time allows the electrons of the ion and the target atom to exchange. This is connected with a change of their momentum and an energy transfer from the ion to the atom.

1.3.1 High Energy Approach of the Transferred Energy

1.3.1.1 Classical Treatment—Free Electrons

In order to study some general aspects, the electronic part of the transferred energy is estimated by a simple classical consideration. For the high energies ($E > E_{e,cr}$) considered here, the binding of the electrons and their orbital motion in the atom may be neglected and the ion can be assumed to be completely ionized. The remaining problem is a classical two-body collision of the **bare ion with a free electron at rest** which means that the transferred energy given in (1.37) and (1.33) can be applied by replacing the atom mass m_2 and atomic number Z_2 by the electron mass m_e and -1, respectively. The resulting classical estimation of the energy $\widehat{T}_e$ transferred to one electron of the target atom reads

$$\begin{aligned} &\widehat{T}_e(s_e) = \widehat{T}_{e,max} \frac{1}{1 + (2\, s_e/b_e)^2} \\ &\text{with } \widehat{T}_{e,max} = \frac{4\, m_e}{m_1} E = 2\, m_e\, v^2 \quad \text{and} \quad b_e = -\frac{m_1}{m_e} \frac{Z_1 \in^2}{E} \end{aligned} \tag{1.38}$$

or related to $T_{n,max}$ and b_n [(1.37) and (1.33), respectively]

$$\widehat{T}_{e,max} = \frac{m^2\, m_e}{m_1^2\, m_2} T_{n,max} \ll T_{n,max} \quad \text{and} \quad |b_e| = \frac{m_1 m_2}{m\, m_e\, Z_2} b_n \gg b_n, \tag{1.39}$$

where s_e is the impact parameter of the ion with respect to the electron and $m_e \ll m_1$ has been taken into account. The total energy transferred to all electrons of the target atom is given by

$$T_e(s) = \int dN(s, s_e)\widehat{T}_e(s_e) \quad \text{with} \int dN(s, s_e) = Z_2, \tag{1.40}$$

where $dN(s, s_e)$ is the number of electrons within s_e and $s_e + ds_e$ for a given impact parameter s (of the ion with respect to the nucleus of the target atom) which is determined by the electron density ρ_e. For impact parameters s large compared to the extension of the electron distribution, $dN(s, s_e)$ is approximately given by $Z_2\,\delta(s - s_e)ds_e$ (δ is the delta function) providing $T_e(s) \approx Z_2\widehat{T}_e(s)$. With decreasing s, the transferred energy $T_e(s)$ becomes first a bit larger and then slightly smaller than $Z_2\widehat{T}_e(s)$. The latter case can easily be proved for $s = 0$ where $dN(0, s_e) = ds_e\,2\,\pi\,s_e \int dz\,\rho_e\left(\left(s_e^2 + z^2\right)^{1/2}\right)$ has a strong maximum at $s_e = s_{e,cr} \ll b_e$. This means that $\widehat{T}_e(s_e)$ in (1.40) can approximately be replaced by $\widehat{T}_e\left(s_{e,cr}\right)$ [which is only slightly smaller than $\widehat{T}_e(0)$ because $s_{e,cr} \ll b_e$, see (1.38)] providing $T_e(0) \lesssim Z_2\widehat{T}_e(0)$. Summarizing, for a simple estimation the energy $T_e(s)$ transferred from the ion to all electrons of a target atom can be approximated by

$$T_e(s) \approx Z_2\widehat{T}_e(s) = T_{e,max}/\left[1 + (2s/b_e)^2\right] \text{ with}$$
$$T_{e,max} \lesssim Z_2\widehat{T}_{e,max} \approx \frac{1}{3600}\left(1 + \frac{m_2}{m_1}\right)^2 T_{n,max} \quad \text{and} \quad |b_e| \approx 3600\left(1 + \frac{m_2}{m_1}\right)^{-1} b_n, \tag{1.41}$$

where $\widehat{T}_{e,max}$ and b_e are taken from (1.39) and the additional simplification $Z_2 \approx m_2/(2\,u)$ (u is the atomic mass unit) is used. Taking into account all possible projectile-target combinations, the mass ratio m_2/m_1 ranges from about 0.01–100. This means that $|b_e|$ is always much larger than b_n and $T_{e,max}$ is smaller than $T_{n,max}$ for $m_2/m_1 < 59$ (most cases), only for $m_2/m_1 > 59$ it becomes larger than $T_{n,max}$. Following (1.37) and (1.41), the ratio $T_n(s)/T_e(s)$ is a unified function of the impact parameter ratio s/b_e, where the mass ratio m_2/m_1 is the only parameter. The result is depicted in Fig. 1.6. As can be seen, for all ratios $m_2/m_1 \lesssim 10$ the nuclear transferred energy T_n becomes equal to T_e at an impact parameter $s = s_0 \approx 0.008\ b_e$ and the two transferred energies differ rapidly with increasing deviation of s from s_0. This means that the total transferred energy $T(s) = T_n(s) + T_e(s)$ for $s < s_0$ is dominated by $T_n(s)$ and for $s > s_0$ it is dominated by $T_e(s)$. This fact is very important because it justifies the separate treatment of the elastic (nuclear) and inelastic (electronic) ion-atom interaction processes with respect to statistical averages. Only in the cases of m_2/m_1 considerably larger than 10 (where T_n and T_e are comparable for $s < s_0$) and physical quantities which depend nonlinearly on T, interference effects of T_n and T_e may occur which are not treated here. Though these considerations refer to high energies, the validity of the statistical independence of the nuclear and electronic ion-atom interaction processes is considered to be true for all energies (as it is usually done in the literature) which is applied in Sect. 1.4.1.3. However, for very low energies there is another effect—the coupling

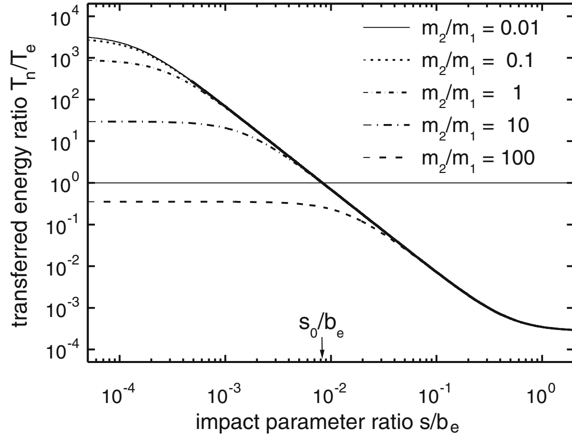

Fig. 1.6 The ratio of the nuclear transferred energy T_n and the electronically transferred energy T_e as a function of the impact parameter s related to b_e [for b_e see (1.38)] for different mass ratios m_2/m_1

of nuclear and electronic ion-atom interaction processes caused by the dependence of the electronic part of the transferred energy T_e on the shape of the trajectory determined by the nuclear interaction. This fact is approximately taken into account in Sect. 1.4.4.2 and 1.4.6.3.

1.3.1.2 Classical Treatment—Harmonically Bound Electrons

Bohr [26] considered a situation similar to that given in Sect. 1.3.1.1: the interaction of a moving **bare ion with a target electron initially at rest**, however, the electron is not free but **harmonically bound** with a binding frequency ω_b. Using a classical perturbation treatment, he obtained the energy

$$\widehat{T}_e(s_e) = \frac{2Z_1^2 \in^4 \omega_b^2}{m_e v^4} \left\{ \left[K_0\left(\frac{s_e \omega_b}{v}\right) \right]^2 + \left[K_1\left(\frac{s_e \omega_b}{v}\right) \right]^2 \right\} \tag{1.42}$$

transferred from an ion with velocity v to an electron bound with frequency ω_b as a function of the impact parameter s_e of the ion with respect to the electron (K_0 and K_1 are the zero-order and first-order modified Bessel functions, respectively).

Based on the classical stopping theory given by Bohr [26], the authors Sigmund, Mikkelsen and Schinner [27–30] presented an elaborated theoretical description of the transferred energy for high ion energies. They included the motion of the harmonically bound electrons and the screening of the ion-electron interaction potential (for dressed ions). The energy $T_e(s)$ transferred to a target atom (as a function of the impact parameter s with respect to the nucleus of the target atom) is obtained by summing up the contributions of all electrons of the target atom [similar to (1.40)] taking into account the different binding frequencies $\omega_{b,i}$. The calculation of $T_e(s)$ can only be performed numerically. For this purpose, the computer code **PASS** has been developed [27–30].

1.3.1.3 Quantum Mechanical Treatment

In principle, the transferred energy T_e due to the excitation and ionization of a target atom (electronic contribution) caused by the moving ion is given by

$$T_e(s) = \sum_n P_{n0}(s)\,(E_n - E_0), \tag{1.43}$$

where E_0 and E_n are the energies of the ground state and the excited states of the atom, respectively, and the sum runs over all states of excitation and ionization. The determination of the probability $P_{n0}(s)$ for the transition from the ground state to the excited state n of the atom caused by an ion with impact parameter s needs a quantum mechanical treatment separately for each $Z_1 - Z_2$ combination. Dettmann and Robinson [31, 32] calculated the probability $P_{n0}(s)$ for protons in first-order Born approximation using hydrogen like wave functions for the target electrons (applied to Si and Ge). Grande and Schiwietz [33–35] determined the probability $P_{n0}(s)$ also within the first-order Born approximation, however, they assumed harmonically bound target electrons. For the calculation of the transferred energy T_e as a function of the impact parameter s, Grande and Schiwietz developed the computer code **CasP** which is available from the authors as freeware. It is applicable to bare and dressed ions and to targets, where the oscillator strengths are known. Some results are given in [35] and in the references therein.

1.3.2 Low Energy Approach of the Transferred Energy

For ion energies below the critical energy $E_{e,cr} \approx 22(m_1/u)Z_1\,Z_2^{0.4}$ keV (u is the atomic mass unit), the probability for excitation is small. However, the interaction time is sufficient to allow the electrons of the atom and the ion to exchange. This process is mainly responsible for the inelastic energy loss in the low energy region. Firsov [36, 37] suggested the following model for the calculation of the energy transferred from the projectile atom (for the low energies the projectile can be assumed to be a neutral atom) to a target atom due to the exchange of electrons. During the collision, the two atoms form a quasi-molecule accompanied by an intermixing of their electrons. After the collision, some electrons previously positioned in the projectile atom belong now to the target atom and vice versa. For a simple description of this classical exchange of electrons, Firsov introduced a plane $A_F(z, s)$ (called Firsov plane in the following) perpendicular to the line between the two atoms (see Fig. 1.7) which divides the quasi-molecule in two parts defining the projectile atom domain and the target atom domain.

As can be seen in Fig. 1.7, the position of this plane depends on the coordinate z of the projectile atom and on the impact parameter s. The exchange of the electrons is expressed by the flux of electrons $\mathbf{j_e}$ perpendicular through the Firsov plane $A_F(z, s)$. Assuming the velocity $\mathbf{v_e}$ of the electrons at the Firsov plane to be

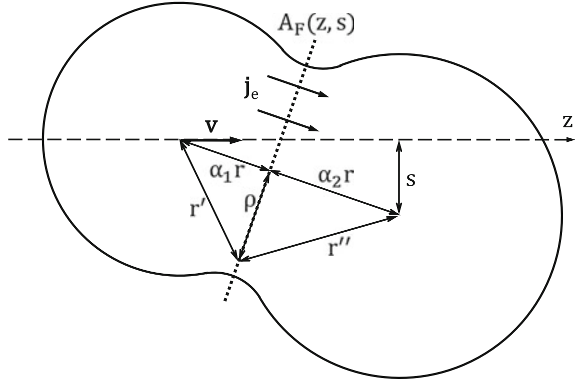

Fig. 1.7 Geometry of the quasi-molecule. The Firsov plane A_F intersects the distance $r = (z^2 + s^2)^{1/2}$ between the two atoms into $\alpha_1 r$ and $\alpha_2 r$ with $\alpha_1 + \alpha_2 = 1$

isotropically distributed, the amount of the flux $\mathbf{j_e}$ (number of electrons per unit area and unit time) reads

$$j_e = \frac{1}{2}\rho_e v_e \left(\int_0^{\frac{\pi}{2}} d\vartheta_e \sin\vartheta_e \cos\vartheta_e \right) \Big/ \left(\int_0^{\frac{\pi}{2}} d\vartheta_e \sin\vartheta_e \right) = \frac{1}{4}\rho_e v_e, \tag{1.44}$$

where ρ_e and v_e are the density (number per unit volume) and average velocity of the electrons at the Firsov plane and ϑ_e is the angle between $\mathbf{v_e}$ and $\mathbf{j_e}$. The average velocities of the electrons in the projectile and target atom are $\mathbf{v}$ and zero, respectively. This means that the exchange of one electron of the projectile atom with one electron of the target atom causes an average momentum transfer $\Delta\mathbf{p}_e = m_e\mathbf{v}$. The momentum transfers of all electrons per unit time provides the stopping force as a function of z and s

$$\mathbf{F_{st}}(z, s) = -m_e\mathbf{v} \int_{A_F(z,s)} dA\, j_e, \tag{1.45}$$

where the integral over the Firsov plane represents the number of contributing electrons per unit time. Finally, the energy transferred from the projectile atom to the target atom due to the exchange of electrons as a function of the impact parameter s is obtained by the integration of $|\mathbf{F_{st}}(z, s)|$ over the whole projectile path

$$T_e(s) = \int_{-\infty}^{\infty} dz\, F_{st}(z, s) = \frac{1}{4} m_e v \int_{-\infty}^{\infty} dz \int_{A_F(z,s)} dA\, \rho_e v_e. \tag{1.46}$$

According to the argumentation in Sect. 1.2.1, the electron density of the quasi-molecule ρ_e at the Firsov plane can be approximated by the superposition of

the electronic densities $\rho_{e,1}(r')$ and $\rho_{e,2}(r'')$ of the free atoms (see Fig. 1.7). In this case, the differential area dA on the Firsov plane is $dA = 2\pi\rho d\rho = 2\pi r'dr'$ for the projectile atom and it is $dA = 2\pi\rho d\rho = 2\pi r''dr''$ for the target atom (see Fig. 1.7), where r' runs from $\alpha_1 r$ to ∞ and r'' runs from $\alpha_2 r$ to ∞. Now, the transferred energy reads

$$T_e(s) = \frac{\pi}{2} m_e v \times \int_{-\infty}^{\infty} dz \left[\int_{\alpha_1 r(z,s)}^{\infty} dr'\, r'\, \rho_{e,1}(r')\, v_{e,1}(r') + \int_{\alpha_2 r(z,s)}^{\infty} dr''\, r''\, \rho_{e,2}(r'') v_{e,2}(r'') \right] \quad (1.47)$$

with $r(z, s) = (z^2 + s^2)^{1/2}$ (see Fig. 1.7). This formula has been proved to provide a good description of the transferred energy. The accuracy of the result is mostly influenced by the accuracy of the electron densities ($\rho_{e,1}$, $\rho_{e,2}$) and the electron velocities ($v_{e,1}$, $v_{e,2}$) used.

In the original model, Firsov [36, 37] used $\alpha_1 = \alpha_2 = 1/2$ (applicable only for $Z_1 \approx Z_2$!) and he approximated the quasi-molecule by an artificial atom with atomic number $Z_1 + Z_2$, where the electron density ρ_e and electron velocity v_e of this artificial atom are determined within the statistical model of Thomas [1] and Fermi [2]. With some additional simplifications he obtained the analytical expression

$$T_e(s) = \frac{0.35(Z_1 + Z_2)^{5/3} \in^2 / a_0}{\left[1 + 0.16(Z_1 + Z_2)^{1/3} s/a_0\right]^5} \frac{v}{v_0} \quad (1.48)$$

which depends monotonically on Z_1, Z_2 and s and does not take into account shell effects and individual properties of the atoms ($v_0 = \in^2/\hbar = 2.18769 \times 10^6$ m/s).

Modifications of the original Firsov theory are described e.g. in [38–41]. Winterbon [38] still used the relation $v_e(\rho_e)$ given by the statistical model of the atoms, however, with an improved electron density ρ_e obtained from Slater type wave functions. A further improvement was achieved by Cheshire et al. [39], Bhalla et al. [40] and Land and Brennan [41] by using

$$\rho_{e,i}\, v_{e,i} = \sum_{n,l} n_i^{(n,l)} \left|\varphi_i^{(n,l)}\right|^2 v_{e,i}^{(n,l)} \quad i = 1, 2 \quad (1.49)$$

in (1.47), where $\varphi_i^{(n,l)}$ are the Slater type wave functions of the electrons of the projectile atom (i = 1) and target atom (i = 2), respectively, for the quantum mechanical state (n, l). The corresponding velocities $v_{e,i}^{(n,l)}$ are obtained from the expectation value of the kinetic energy and $n_i^{(n,l)}$ are the occupation numbers.

1.4 Ion-Amorphous Solid Interaction

The ion-solid interaction is considered as an ensemble of ion-atom binary collisions treated by means of statistics. The kind of statistics to be used depends on the arrangement of the atoms in the solid. While in the case of amorphous solids the usual six-dimensional phase-space statistics can be applied, in the case of crystalline solids and axial or planar channeling conditions a four- or two-dimensional phase-space statistics is required (Lindhard theory, for axial channeling see Sect. 1.5.1). The statistical treatment for amorphous solids is also applicable to polycrystalline solids (if the lateral extension of the crystallites is small compared to the diameter of the ion beam) and to crystalline solids in the case of random ion incidence (no channeling effects).

Section 1.4.1 deals with the scattering statistics providing general expressions for the distributions of the energy loss and the scattering angle of the ions after having traversed a thin amorphous layer and for the corresponding averages. The special results obtained for the elastic (nuclear) scattering and for the inelastic (electronic) scattering are given and discussed in Sects. 1.4.2–1.4.7. The spatial distributions of the ions and the generated damage are preferentially determined by Monte Carlo computer simulations which is briefly described in Sect. 1.4.8.

1.4.1 Scattering Statistics

An ion with an energy E traversing a layer of an amorphous solid of thickness Δz leaves the layer with an energy lowered by ΔE and a deflection angle Φ (see Fig. 1.8). In the case of an ion beam, the different positions of entrance give rice to different ion paths resulting in distributions of ΔE and Φ. The statistical treatment for the determination of these distributions and the corresponding average values is presented in the following. The main idea of the statistical treatment and the determination of the average values was given by Bohr [42].

During the transmission, an ion undergoes a series of binary collisions with different transferred energies T (nuclear plus electronic) and scattering angles φ

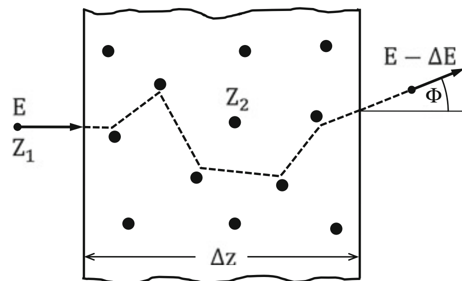

Fig. 1.8 Scattering geometry for an ion transmitting an amorphous layer of thickness Δz

(mostly only given by nuclear scattering because the deflection on the electrons can be neglected). Instead of the continuous dependence of T and φ on the impact parameter, Bohr used discrete values T_k and φ_k (k = 1, 2, 3 …) because they are more convenient for the statistical treatment. The number of binary collisions of kind k (with T_k and φ_k) and the corresponding cross sections are denoted by n_k and σ_k, respectively. From the statistical point of view, the path of one ion is characterized by a set of values (n_1, n_2, n_3 …). The probability of the occurrence of n_k collisions of kind k is given by a Poisson distribution [42]

$$P_{n_k} = \frac{\langle n_k \rangle^{n_k}}{n_k!} e^{-\langle n_k \rangle} \quad \text{with} \quad \sum_{n_k} P_{n_k} = 1 \tag{1.50}$$

and the average number of collisions of kind k is

$$\langle n_k \rangle = \sum_{n_k} P_{n_k} n_k = N \, \Delta z \, \sigma_k, \tag{1.51}$$

where N is the atomic density (number of target atoms per unit volume). Furthermore,

$$\left\langle (n_k - \langle n_k \rangle)^2 \right\rangle = \sum_{n_k} P_{n_k} (n_k - \langle n_k \rangle)^2 = \langle n_k \rangle \tag{1.52}$$

is valid.

1.4.1.1 Energy Loss Distribution and Averages

For one ion with a given ion path (n_1, n_2, n_3 …), the energy loss ΔE reads

$$\Delta E = \sum_k n_k T_k \tag{1.53}$$

and for an ion beam [ensemble of different ion paths that means different sets of values (n_1, n_2, n_3 …)], the transmission through the layer results in a distribution of ΔE characterized by the average energy loss and the energy straggling (width of the distribution). With (1.51) the average energy loss is obtained by

$$\langle \Delta E \rangle = \sum_k \langle n_k \rangle \, T_k = N \, \Delta z \sum_k \sigma_k T_k \tag{1.54}$$

and the mean square deviation (energy straggling) is given by

$$\Omega^2 \equiv \left\langle (\Delta E - \langle \Delta E \rangle)^2 \right\rangle = \sum_{k,l} \langle (n_k - \langle n_k \rangle) T_k \, (n_l - \langle n_l \rangle) \, T_l \rangle.$$

The average runs separately over all n_k and all n_l. Therefore, all contributions $l \neq k$ vanish which provides

$$\Omega^2 = \sum_k \left\langle (n_k - \langle n_k \rangle)^2 \, T_k^2 \right\rangle = \sum_k \langle n_k \rangle \, T_k^2 = N \, \Delta z \sum_k \sigma_k T_k^2, \tag{1.55}$$

where (1.51) and (1.52) are used.

Returning to the continuous description $(T_k \to T(s), \sigma_k \to d\sigma = 2\pi \, s \, ds)$, the average energy loss per unit path length dE/dz ($\Delta z \to dz$) also called stopping power S is given by

$$S = -\frac{dE}{dz} = N\widehat{S} \quad \text{with} \quad \widehat{S} = \int d\sigma \, T = 2\pi \int ds \, s \, T(s) \tag{1.56}$$

and the average energy straggling reads

$$\Omega^2 = N \, \Delta z \, W \quad \text{with} \quad W = \int d\sigma \, T^2 = 2\pi \int ds \, s \, T^2(s), \tag{1.57}$$

where $\hat{S}$ and W are the stopping cross section and the straggling cross section, respectively.

Following the derivation given by Sigmund and Winterbon [43], the full distribution of the energy loss P(ΔE, Δz) is obtained by a sum over the discrete contributions of all ion paths [all sets of values (n_1, n_2, n_3,…)]

$$P(\Delta E, \Delta z) = \sum_{n_1, n_2, n_3, \ldots} P_{n_1} \, P_{n_2} \, P_{n_3} \ldots \delta\left(\Delta E - \sum_k n_k T_k \right).$$

With the probability P_{n_k} given by (1.50) and the Fourier presentation of the δ function

$$\delta\left(\Delta E - \sum_k n_k T_k \right) = \int_{-\infty}^{\infty} \frac{d\alpha}{2\pi} \exp\left[i\alpha \left(\Delta E - \sum_k n_k T_k \right) \right],$$

the distribution P(ΔE, Δz) becomes

$$
\begin{aligned}
P(\Delta E, \Delta z) &= \int_{-\infty}^{\infty} \frac{d\alpha}{2\pi} \exp(i\alpha\,\Delta E) \prod_k \left\{ \exp(-\langle n_k \rangle) \sum_{n_k} \frac{1}{n_k!} [\langle n_k \rangle \exp(-i\alpha T_k)]^{n_k} \right\} \\
&= \int_{-\infty}^{\infty} \frac{d\alpha}{2\pi} \exp(i\alpha\,\Delta E) \prod_k \exp\{-N\,\Delta z\,\sigma_k [1 - \exp(-i\alpha T_k)]\},
\end{aligned}
\tag{1.58}
$$

where (1.51) is used. Finally, the transition to continuous values T and $d\sigma$ provides

$$
P(\Delta E, \Delta z) = \int_{-\infty}^{\infty} \frac{d\alpha}{2\pi} \exp(i\,\alpha\,\Delta E) \exp\left\{ -N\,\Delta z \int d\sigma [1 - \exp(-i\,\alpha\,T)] \right\}. \tag{1.59}
$$

This expression has first been given by Landau [44] obtained as the solution of an integro-differential equation. A second order expansion with respect to T provides the symmetric distribution

$$
P(\Delta E, \Delta z) = \frac{1}{(2\pi\Omega^2)^{1/2}} \exp\left[-\frac{(\Delta E - \langle \Delta E \rangle)^2}{2\Omega^2} \right] \tag{1.60}
$$

with $\langle \Delta E \rangle = N\,\Delta z\,\widehat{S}$ [for $\widehat{S}$ see (1.56)] and $\Omega^2 = N\,\Delta z\,W$ (1.57) which approximates the distribution given in (1.59) for a sufficiently large layer thickness Δz.

1.4.1.2 Angular Distribution and Averages

The determination of the final angle Φ for one ion is more difficult than that of ΔE because the single collision angles φ have to be added as vectors. However, in the case of an ion beam the corresponding average values are easily obtained. Because of the symmetry around the direction of ion incidence (see Fig. 1.8), the average final angle $\langle \Phi \rangle$ (vector) is zero and the mean square deviation $\langle \Phi^2 \rangle \equiv \psi^2$ is simply given analogously to Ω^2 [42] by

$$
\psi^2 = N\,\Delta z\,Q \quad \text{with} \quad Q = \int d\sigma\,\varphi^2 = 2\pi \int ds\,s\varphi^2(s), \tag{1.61}
$$

where Q is called angular straggling (or multiple scattering) cross section. Neglecting higher order averages, the angular distribution can be approximated by

$$
P(\Phi, \Delta z) = \frac{1}{\pi\psi^2} \exp\left[-\frac{\Phi^2}{\psi^2} \right] \quad \text{with} \quad \int_0^{\infty} 2\pi\,\Phi\,d\Phi\,P(\Phi) = 1. \tag{1.62}
$$

A more accurate expression for the angular distribution is given by

$$P(\Phi, \Delta z) = \int_0^\infty \frac{d\alpha}{2\pi} \alpha\, J_0(\alpha\, \Phi) \exp\left\{ -N\, \Delta z \int d\sigma [1 - J_0(\alpha\, \varphi)] \right\} \tag{1.63}$$

which is valid for small angle scattering and was first obtained by Bothe [45] (J_0 is the zero-order Bessel function of the first kind). Further derivations of this formula are presented by Wentzel [46], Scott [47] and Sigmund and Winterbon [48].

1.4.1.3 Elementary Targets and Compound Targets

As stated at the end of Sect. 1.3.1.1, with respect to the statistical averages the elastic (nuclear) and inelastic (electronic) ion-atom interaction processes can be treated separately. This means that the different cross sections for elementary targets are given by the sum of the corresponding nuclear and electronic contribution $\hat{S} = \hat{S}_n + \hat{S}_e$, $W = W_n + W_e$ and $Q = Q_n + Q_e$.

In the case of a compound target, the contributions from the different kinds of target atoms may approximately be considered to be statistically independent and not influenced by their binding (Bragg's rule). In this approximation, (1.56), (1.57) and (1.61) become

$$S = -\frac{dE}{dz} = \sum_i \left[N_i \left(\widehat{S}_{n,i} + \widehat{S}_{e,i} \right) \right] \tag{1.64}$$

$$\Omega^2 = \Delta z \sum_i \left[N_i \left(W_{n,i} + W_{e,i} \right) \right] \tag{1.65}$$

$$\psi^2 = \Delta z \sum_i \left[N_i \left(Q_{n,i} + Q_{e,i} \right) \right], \tag{1.66}$$

where $\hat{S}_{n,i}$, $W_{n,i}$ and $Q_{n,i}$ are the nuclear contributions to the stopping cross section, straggling cross section and multiple scattering cross section, respectively, for a target atom of kind i. The corresponding electronic contributions are $\hat{S}_{e,i}$, $W_{e,i}$ and $Q_{e,i}$ and N_i is the atomic density of the atoms of kind i (number of atoms of kind i per unit volume). Equations (1.64), (1.65) and (1.66) are valid if the electronic structure of the atoms in the compound target can be assumed to be the same as in the corresponding elementary targets. For some compounds, corrections to Bragg's rule are available in SRIM (see Sect. 1.4.5).

The theoretical description of the nuclear stopping cross section $\hat{S}_n$ and the nuclear straggling cross section W_n are given in the following Sections. The corresponding electronic contributions $\hat{S}_e$ and W_e are described in Sects. 1.4.3 and 1.4.4 for the high and the low energy region, respectively.

1.4.2 Elastic Energy Loss and Energy Loss Straggling

1.4.2.1 Modified Coulomb Potential

For the Coulomb potential, the transferred energy $T_n(s)$ as a function of the impact parameter s is given by (1.37). Changing from variable s to variable T_n the differential scattering cross section for nuclear (elastic) scattering $d\sigma_n = 2\pi s\, ds$ reads

$$d\sigma_n(E, T_n) = \pi \left| \frac{d(s^2)}{dT_n} \right| dT_n = \pi \left(\frac{b_n}{2} \right)^2 T_{n,max} \frac{dT_n}{T_n^2} \equiv B_n(E) \frac{dT_n}{T_n^2} \tag{1.67}$$

$$\text{with} \quad B_n(E) = \pi \frac{m_1}{m_2} \frac{(Z_1 Z_2 \in^2)^2}{E}. \tag{1.68}$$

The insertion of this scattering cross section into (1.56) provides the nuclear stopping cross section for the Coulomb potential

$$\widehat{S}_n^C(E) = \int d\sigma_n(E, T_n) T_n = B_n(E) \ln \left(\frac{T_{n,max}}{T_{n,min}} \right) \tag{1.69}$$

which is infinite for $T_{n,min} = 0$ [$T_{n,max}$ is given by (1.37)]. This means the screening of the interaction potential is essential for getting a finite $\hat{S}_n$. The most simple way of taking into account the screening is to cut the transferred energy (1.37) at the impact parameter $s = r_c$, where the cut radius r_c should be comparable with the screening length of the potential [e.g. a_{ZBL} in (1.16)]. The resulting minimum transferred energy is

$$T_{n,min} = T_n(r_c) = T_{n,max} \left[1 + \left(\frac{2r_c}{b_n} \right)^2 \right]^{-1}. \tag{1.70}$$

With this modification, the nuclear stopping cross section for the Coulomb potential is

$$\widehat{S}_n^C(E) = \pi \frac{m_1}{m_2} \frac{(Z_1 Z_2 \in^2)^2}{E} \ln \left[1 + \left(\frac{2E}{E_c} \right)^2 \right] \tag{1.71}$$

$$\text{with } \frac{2r_c}{b_n} \equiv \frac{2E}{E_c} \quad \text{and} \quad E_c = \frac{m}{m_2} \frac{Z_1 Z_2 \in^2}{r_c}. \tag{1.72}$$

In the same approximation, the nuclear straggling cross section reads

$$
\begin{aligned}
W_n^C(E) &= \int d\sigma_n(E, T_n)\, T_n^2 = B_n(E)\left(T_{n,max} - T_{n,min}\right) \\
&= 4\pi\left(\frac{m_1\, Z_1\, Z_2 \in^2}{m}\right)^2 \left\{1 - \left[1 + \left(\frac{2E}{E_c}\right)^2\right]^{-1}\right\}.
\end{aligned} \tag{1.73}
$$

While $\widehat{S}_n^C$ has a maximum at $E \approx E_c$ and decreases with increasing energy, the nuclear straggling cross section W_n^C tends to a constant value for $E \gg E_c$.

1.4.2.2 ZBL Potential—Analytical Fit

For a given ion-atom interaction potential V(r), the nuclear stopping cross section $\hat{S}_n$ and straggling cross section W_n must be calculated numerically according to (1.56) and (1.57) with $T_n(s)$ given by (1.23) and (1.29). The results obtained using the universal ZBL potential [the screening function is given in (1.16)] is presented by Ziegler, Biersack and Littmark [13]. For practical use they gave the following analytical fits to the numerical results:

$$
\begin{aligned}
&\widehat{S}_n^{ZBL}(E) = c_S \widehat{S}_r^{ZBL}(\varepsilon(E)) \quad \text{with} \\
&\quad c_S = 4\pi \frac{m_1}{m} Z_1\, Z_2 \in^2 a_{ZBL} = 84.776 \frac{m_1}{m} \frac{Z_1\, Z_2}{Z_1^{0.23} + Z_2^{0.23}}\, \text{eV}\, \text{Å}^2 \\
&\quad \widehat{S}_r^{ZBL}(\varepsilon) = \frac{\ln(1 + 1.1383\, \varepsilon)}{2(\varepsilon + 0.01321\, \varepsilon^{0.21226} + 0.19593\, \varepsilon^{0.5})} \quad \text{for } \varepsilon \leq 30 \\
&\quad \widehat{S}_r^{ZBL}(\varepsilon) = \ln(\varepsilon)/(2\varepsilon) \quad \text{for } \varepsilon > 30
\end{aligned} \tag{1.74}
$$

$$
\begin{aligned}
&W_n^{ZBL}(E) = c_W\, W_r^{ZBL}(\varepsilon(E)) \quad \text{with} \\
&\quad c_W = 4\pi\left(\frac{m_1 Z_1 Z_2 \in^2}{m}\right)^2 = 2605.6\left(\frac{m_1 Z_1 Z_2}{m}\right)^2 \text{eV}^2\, \text{Å}^2 \\
&\quad W_r^{ZBL}(\varepsilon) = \left(1 + 0.04925\, \varepsilon^{-1.6991} + 1.646\, \varepsilon^{-1.0494}\right)^{-1},
\end{aligned} \tag{1.75}
$$

where the dimensionless reduced energy ε is given by

$$
\varepsilon = \frac{a_{ZBL}}{b_n} = \frac{m_2}{m} \frac{0.88534\, a_0\, E}{\left(Z_1^{0.23} + Z_2^{0.23}\right) Z_1\, Z_2 \in^2} = \frac{m_2}{m} \frac{32.5356}{\left(Z_1^{0.23} + Z_2^{0.23}\right) Z_1\, Z_2} \frac{E}{\text{keV}}. \tag{1.76}
$$

For comparison, the results obtained using the modified Coulomb potential approximation (1.71) and (1.73) are given in the same notation.

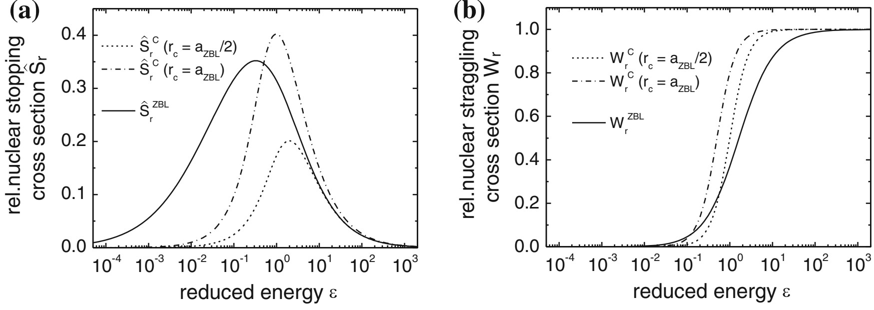

Fig. 1.9 The relative nuclear stopping cross sections $\hat{S}_r^{ZBL}$ and $\hat{S}_r^C$ (**a**) and the relative nuclear straggling cross sections W_r^{ZBL} and W_r^C (**b**) as functions of the reduced energy ε. The modified Coulomb approximations $\hat{S}_r^C$ and W_r^C (1.77) are given for two cut radii r_c. The ZBL stopping cross section $\hat{S}_r^{ZBL}$ has a maximum at $\varepsilon \approx 0.3$

$$\hat{S}_r^C(\varepsilon) = \frac{1}{4\varepsilon} \ln\left[1 + \left(\frac{2r_c}{a_{ZBL}}\varepsilon\right)^2\right] \quad W_r^C(\varepsilon) = 1 - \left[1 + \left(\frac{2r_c}{a_{ZBL}}\varepsilon\right)^2\right]^{-1} \tag{1.77}$$

As can be seen in Fig. 1.9a, the Coulomb approximation $\hat{S}_r^C(\varepsilon)$ using the cut radius $r_c = a_{ZBL}/2$ agrees well with $\hat{S}_r^{ZBL}(\varepsilon)$ for $\varepsilon > 10$, while for $r_c = a_{ZBL}$ a good agreement with $\hat{S}_r^{ZBL}(\varepsilon)$ is achieved not before $\varepsilon > 100$. The Coulomb approximation $W_r^C(\varepsilon)$ (Fig. 1.9b) agrees with $W_r^{ZBL}(\varepsilon)$ only for $\varepsilon > 100$, independent of the value of r_c. From this follows that the simple Coulomb approximations of the nuclear stopping cross section $\hat{S}_n^C(E)$ (1.71) and of the nuclear straggling cross section $W_n^C(E)$ (1.73) can be applied for $\varepsilon > 10$ and $\varepsilon > 100$, respectively, if the cut radius $r_c = a_{ZBL}/2$ is used.

1.4.3 High Energy Inelastic Energy Loss and Energy Straggling

1.4.3.1 Classical Treatment

The simplest model for the calculation of the energy loss due to ionization and excitation is based on the classical collision of a **bare ion with a single electron** of the target atom which is **initially at rest and free**. The energy $\hat{T}_e$ transferred to the electron is given by (1.38) and the corresponding differential cross section $d\sigma_e$ can easily be obtained from (1.67) and (1.68) by replacing the atom mass m_2 and atomic number Z_2 by the electron mass m_e and −1, respectively

$$d\sigma_e\left(E, \widehat{T}_e\right) = B_e(E)\frac{d\widehat{T}_e}{\widehat{T}_e^2} \quad \text{with} \quad B_e(E) = \frac{2\pi Z_1^2 \in^4}{m_e v^2}. \tag{1.78}$$

According to (1.56), the electronic stopping cross section for the interaction of the ion with all electrons of the target atom reads

$$\widehat{S}_e(E) = \sum_{i=1}^{Z_2} \int_{\widehat{T}_{e,min,i}}^{\widehat{T}_{e,max}} d\sigma_e\left(E, \widehat{T}_e\right)\widehat{T}_e = B_e(E)\sum_{i=1}^{Z_2} \ln\left(\frac{\widehat{T}_{e,max}}{\widehat{T}_{e,min,i}}\right). \tag{1.79}$$

The maximum energy transferred to one electron $\widehat{T}_{e,max} = 2m_e v^2$ [see (1.38)] is equal for all electrons, however, the minimum energy $\widehat{T}_{e,min,i}$ transferred to one electron will be shown to be different for different electrons i. For free electrons $\widehat{T}_{e,min,i}$ is zero which would provide an infinite stopping cross section. Therefore, the binding of the electrons must be taken into account which is responsible for a value $\widehat{T}_{e,min,i} > 0$. Following the concept of Bohr [42], the collisions can be subdivided in two groups, the close collisions ($\widehat{T}_{e,max} \geq \widehat{T}_e \geq I_i$ or $0 \leq s_e \leq s_{cr,i}$) and the distant collisions ($I_i > \widehat{T}_e \geq \widehat{T}_{e,min,i}$ or $s_{cr,i} < s_e \leq s_{max,i}$), where I_i is the ionization energy of the electron i. The impact parameters $s_{cr,i}$ and $s_{max,i}$ for the electron i are given by $\widehat{T}_e\left(s_{cr,i}\right) = I_i$ and $\widehat{T}_e\left(s_{max,i}\right) = \widehat{T}_{e,min,i}$ respectively.

The **close collisions result in the ionization** of the target atom. The corresponding contribution $\widehat{S}_e^{cc}(E)$ to the electronic stopping cross section is given by (1.79), where the integration interval is reduced, ranging from I_i to $\widehat{T}_{e,max}$. It provides

$$\widehat{S}_e^{cc}(E) = \frac{2\pi Z_1^2 Z_2 \in^4}{m_e v^2} \ln\left(\frac{2\, m_e\, v^2}{I}\right), \tag{1.80}$$

with I being the logarithmic average of the ionization energies I_i determined by

$$\sum_{i=1}^{Z_2} \ln(I_i) = Z_2 \ln I. \tag{1.81}$$

The **distant collisions** with an energy transfer $\widehat{T}_e < I_i$ cannot result in a removal of the electron i from the atom, however, it can **cause the excitation** of the bound electrons. Assuming the electrons to be an ensemble of harmonic oscillators, where the electron i is bound with a frequency $\omega_{b,i}$, Bohr [42] estimated the influence of the binding on the electronic stopping by introducing a dynamical cut-off energy $\widehat{T}_{e,min,i}$ in the following way. For impact parameters s_e large compared to the electronic collision diameter b_e (1.38), the interaction time t_I can be estimated by s_e/v and the duration of vibration of the electron i is about $1/\omega_{b,i}$. For $t_I = s_e/v \ll 1/\omega_{b,i}$ ($s_e \ll v/\omega_{b,i}$) the electron does approximately not move during the collision and the harmonic binding hardly

influences the energy transfer. In the other case $t_I = s_e/v \gg 1/\omega_{b,i}$ ($s_e \gg v/\omega_{b,i}$), the electron oscillates very often during the time of interaction with the effect that the transferred energy tends to zero. Therefore, the impact parameter for scattering on the electron i can approximately be cut at $s_{max,i} \approx v/\omega_{b,i}$. The corresponding minimum transferred energy $\widehat{T}_{e,min,i}$ is obtained from (1.38)

$$\widehat{T}_{e,min,i} = \widehat{T}_e(s_{max,i}) \approx \widehat{T}_{e,max}\left(\frac{b_e}{2s_{max,i}}\right)^2 = \frac{2Z_1^2 \in^4 \omega_{b,i}^2}{m_e v^4}, \tag{1.82}$$

where $s_{max,i} \gg b_e$ has been taken into account. Now, the distant collision contribution $\widehat{S}_e^{dc}(E)$ to the electronic stopping cross section is obtained from (1.79) with the integration interval ranging from $\widehat{T}_{e,min,i}$ to I_i .

$$\widehat{S}_e^{dc}(E) = \frac{2\pi Z_1^2 \in^4}{m_e v^2}\sum_{i=1}^{Z_2} \ln\left(\frac{m_e v^4 I_i}{2Z_1^2 \in^4 \omega_{b,i}^2}\right) \tag{1.83}$$

The total electronic stopping cross section $\widehat{S}_e(E)$ obtained by summing the two contributions given in (1.80) and (1.83) reads

$$\widehat{S}_e(E) = \frac{4\pi Z_1^2 \in^4}{m_e v^2}\sum_{i=1}^{Z_2} \ln\left(\frac{m_e v^3}{Z_1 \in^2 \omega_{b,i}}\right). \tag{1.84}$$

This simple estimation agrees well with the more detailed calculation of Bohr [26] (the concept is briefly described in Sect. 1.3.1.2), who found the same expression for $\widehat{S}_e(E)$ with the only difference of an additional factor 1.123 in the logarithm. While the close collision contribution $\widehat{S}_e^{cc}(E)$ to the electronic stopping cross section [(1.80) and (1.81)] is a well defined quantity, the distant collision contribution $\widehat{S}_e^{dc}(E)$ is influenced by the uncertainty of the binding frequencies $\omega_{b,i}$.

The electronic straggling cross section is not influenced by this uncertainty because $\widehat{T}_{e,min,i} = 0$ can be used without any problem (**here, the binding is of minor importance**). It provides

$$W_e(E) = \sum_{i=1}^{Z_2} \int_0^{\widehat{T}_{e,max}} d\sigma_e\left(E, \widehat{T}_e\right)\widehat{T}_e^2 = Z_2 B_e \widehat{T}_{e,max} = 4\pi Z_1^2 Z_2 \in^4. \tag{1.85}$$

1.4.3.2 First Born Approximation

The situation considered is the following. The **ion** is assumed to be **totally stripped**. Before the collision, the ion moves with velocity **v** and the target atom is in the

ground state and does not move. After the collision, the target atom has got kinetic energy which determines the nuclear energy loss (already treated in Sect. 1.4.2) and it is excited or even ionized which is responsible for the electronic energy loss considered here.

The quantum mechanical states of the target atom are given by the Schrödinger equation

$$\mathcal{H}\varphi_n(\mathbf{r}_1,\mathbf{r}_2\ldots) = E_n\varphi_n(\mathbf{r}_1,\mathbf{r}_2\ldots), \tag{1.86}$$

where $\mathcal{H}$ is the Hamilton operator, φ_n and E_n are the wave function and the energy in the state n and $\mathbf{r}_j$ is the position vector of the electron j (origin is the nucleus of the atom). The potential for the interaction of the ion with the nucleus and electrons of the target atom reads

$$V_I(\mathbf{r},\mathbf{r}_1,\mathbf{r}_2\ldots) = \frac{Z_1 Z_2 \in^2}{r} - \sum_{j=1}^{Z_2} \frac{Z_1 \in^2}{|\mathbf{r}-\mathbf{r_j}|} \tag{1.87}$$

with $\mathbf{r}$ being the vector of the distance between the ion and the nucleus of the target atom. Analogously to the classical two-body problem, the motion of the center-of-mass is separated and the dynamics in the relative-coordinate system is described by the reduced mass m_r (1.24) and the position vector $\mathbf{r}$ (for comparison see Sect. 1.2.3). The initial state of the ion-atom system in the relative-coordinate system is

$$|\mathbf{k}_0, 0\rangle = e^{i\,\mathbf{k}_0\,\mathbf{r}}\varphi_0(\mathbf{r}_1,\mathbf{r}_2\ldots) \tag{1.88}$$

with the wave vector $\mathbf{k}_0 = m_r\,\mathbf{v}/\hbar$. The initial state of the reduced mass is given by a plane wave without a lateral localization which describes the experimental situation of a lateral homogeneous ion beam.

Analogously to (1.56), the electronic stopping cross section is given by

$$\widehat{S}_e(E) = \sum_{n=1}^{\infty} \sigma_{n0}(E_n - E_0). \tag{1.89}$$

The cross section for the transition from the ground state to the excited state n in first Born approximation reads

$$\sigma_{n0} = \int d\Omega \left(\frac{m_r}{2\pi\hbar^2}\right)^2 \frac{k}{k_0} \left|\langle \mathbf{k}, n|V_I|\mathbf{k}_0, 0\rangle\right|^2 \text{ with} \tag{1.90}$$

$$\langle \mathbf{k}, n|V_I|\mathbf{k}_0, 0\rangle = \int d^3\mathbf{r}\; d^3\mathbf{r}_1\; d^3\mathbf{r}_2\ldots e^{i\,\mathbf{q}\,\mathbf{r}}\, V_I(\mathbf{r},\mathbf{r}_1,\mathbf{r}_2\ldots)\varphi_n^*(\mathbf{r}_1,\mathbf{r}_2\ldots)\varphi_0(\mathbf{r}_1,\mathbf{r}_2\ldots), \tag{1.91}$$

where $d\Omega$ is the solid angle and $\mathbf{q} = (\mathbf{k}_0 - \mathbf{k})$. The replacement of $e^{i\mathbf{qr}}$ by $\left[-q^{-2}\,\Delta_r\, e^{i\mathbf{qr}}\right]$ and the application of the Laplace operator $\Delta_r = \nabla_\mathbf{r}\nabla_\mathbf{r}$ to V_I instead to $e^{i\mathbf{qr}}$ (two-fold three-dimensional partial integration with vanishing surface integrals) provides

$$\begin{aligned}\langle \mathbf{k}, n|V_I|\mathbf{k}_0, 0\rangle &= -q^{-2}\int d^3\mathbf{r}\, d^3\mathbf{r}_1 d^3\mathbf{r}_2 \ldots e^{i\mathbf{qr}}[\Delta_r V_I]\varphi_n^*\varphi_0 \\ &= 4\pi\, q^{-2}\int d^3\mathbf{r}\, d^3\mathbf{r}_1\, d^3\mathbf{r}_2 \ldots e^{i\mathbf{qr}}\left[Z_1 Z_2 \in^2 \delta(\mathbf{r}) - \sum_{j=1}^{Z_2} Z_1 \in^2 \delta(\mathbf{r} - \mathbf{r}_j)\right]\varphi_n^*\varphi_0\end{aligned}$$

because $\Delta_r(1/r) = -4\pi\delta(\mathbf{r})$ with $\int d^3\mathbf{r}\,\delta(\mathbf{r}) = 1$. For $n > 0$ ($n = 0$ is elastic scattering!) the first term is zero because $\int d^3\mathbf{r}_1\, d^3\mathbf{r}_2 \ldots \varphi_n^*\varphi_0 = \delta_{n0}$ (Kronecker symbol) is valid and the second term provides

$$\left\langle \mathbf{k}, n|V_I|\mathbf{k}_0, 0\right\rangle = -\frac{4\pi Z_1 \in^2}{q^2}\langle n|C|0\rangle \quad \text{with} \quad C = \sum_{j=1}^{Z_2} e^{i\mathbf{qr}_j}. \tag{1.92}$$

With (1.89), (1.90) and (1.92) and the solid angle $d\Omega = 2\pi\sin\vartheta\, d\vartheta = 2\pi q\, dq/(k\, k_0)$ (ϑ is the angle between $\mathbf{k}$ and $\mathbf{k}_0$) the electronic stopping cross section provides

$$\hat{S}_e(E) = 2\pi\left(\frac{2Z_1 \in^2}{\hbar v}\right)^2 \sum_{n=0}^{\infty}\int_{q_{min,n}}^{q_{max}} \frac{dq}{q^3}\langle 0|C^*|n\rangle\langle n|C(E_n - E_0)|0\rangle \tag{1.93}$$

$$\text{with}\; q_{min,n} = \frac{E_n - E_0}{\hbar v} \quad \text{and} \quad q_{max} = \frac{2m_e v}{\hbar},$$

where $q_{min,n} = k_0 - k$ is determined by the energy conservation $E_n - E_0 = \hbar^2\left(k_0^2 - k^2\right)/(2m_r)$ assuming $k_0 + k \approx 2k_0$ for small changes of k and q_{max} is obtained from the classical maximum energy $2m_e v^2$ transferred to an electron (1.38). The lower limit $n = 1$ is replaced by $n = 0$ without any effect because the contribution for $n = 0$ is zero. With the Hamilton operator $\mathcal{H}$ of the target atom [see (1.86)], the matrix element $\langle n|C(E_n - E_0)|0\rangle$ can be expressed by $\langle n|(\mathcal{H}C - C\mathcal{H})|0\rangle$. For further analytical treatment, $q_{min,n}$ is approximately replaced by an average value $q_{min} = I/\hbar v$ with I being the average of $E_n - E_0$ called average ionization energy in the following. With this approximation, the sum in (1.93) can be performed explicitly by using the closure relation $\sum |n\rangle\langle n| = 1$ (unity operator) which provides

$$\widehat{S}_e(E) = 2\pi\left(\frac{2Z_1 \in^2}{\hbar v}\right)^2 \int_{q_{min}}^{q_{max}} \frac{dq}{q^3} \quad \langle 0|C^*[\mathcal{H}, C]|0\rangle. \tag{1.94}$$

In the commutator $[\mathcal{H}, C]$ [C is given in (1.92)], only the kinetic part of the Hamilton operator $\mathcal{H}$ provides a contribution

$$[\mathcal{H}, C] = -\frac{\hbar^2}{2m_e}\sum_{j=1}^{Z_2}\left[\Delta_j, e^{i\,\mathbf{q}\,\mathbf{r}_j}\right] = \frac{\hbar^2}{2m_e}\sum_{j=1}^{Z_2} e^{i\,\mathbf{q}\,\mathbf{r}_j}\left(q^2 - 2i\,\mathbf{q}\boldsymbol{\nabla}_j\right),$$

where Δ_j and $\boldsymbol{\nabla}_j$ are the Laplace operator and the Nabla operator, respectively, acting on the vector $\mathbf{r}_j$. Now, (1.94) reads

$$\hat{S}_e(E) = \frac{4\pi Z_1^2 \in^4}{m_e v^2}\int_{q_{min}}^{q_{max}}\frac{dq}{q^3}\left\langle 0\left|\sum_{j,k=1}^{Z_2} e^{i\mathbf{q}(\mathbf{r}_j - \mathbf{r}_k)}\left(q^2 - 2i\mathbf{q}\boldsymbol{\nabla}_j\right)\right|0\right\rangle. \tag{1.95}$$

The main contribution to the integral over q is obtained for k = j because for $k \neq j$ the exponential function oscillates around zero which diminishes the value of the integral considerably. This justifies the approximation that only the contribution for k = j is taken into account. The resulting second part $\langle 0|\mathbf{q}\,\boldsymbol{\nabla}_j|0\rangle$ of the matrix element is proportional to the average of the velocity component of the electron j in the direction of $\mathbf{q}$ which is zero. Therefore, the matrix element in (1.95) is simply $Z_2\, q^2$ and the resulting electronic stopping cross section becomes

$$\widehat{S}_e(E) = \frac{4\pi Z_1^2 Z_2 \in^4}{m_e v^2} L \quad \text{with} \quad L = \ln\left(\frac{2m_e v^2}{I}\right) \tag{1.96}$$

where L is the so called stopping number. This is the well known non-relativistic formula obtained by Bethe [49, 50] and Bloch [51, 52], where the average ionization energy I is given by

$$\ln(I) = \sum_n f_n \ln(E_n - E_0) \quad \text{with} \quad \sum_n f_n = 1 \tag{1.97}$$

with f_n being the dipole oscillator strengths. Within the statistical model of the atoms the average ionization energy is approximately given by $I(Z_2) \approx 10$ eV Z_2. More precise calculations [53] and measurements (results tabulated in [54]) show that $I(Z_2)/Z_2$ is not constant but oscillates around about $(9.9 + 5.0 \exp(-0.05\, Z_2))$ eV. It is interesting that the electronic stopping cross section $\widehat{S}_e(E)$ is twice the classical close collision stopping cross section $\widehat{S}_e^{cc}(E)$ given in (1.80) and (1.81). This agrees with the so called equipartition rule [55] which states that for high energies (where resonance occurs) the close collision contribution and the resonance contribution (distant collision contribution) are equal.

There exist some corrections to the Bethe-Bloch formula [(1.96) and (1.97)] expressed by an additional contribution ΔL to the stopping number L as follows

$$\Delta L = -\ln\left[1-\left(\frac{v}{c}\right)^2\right] - \left(\frac{v}{c}\right)^2 - \frac{C}{Z_2} - \frac{\delta}{2} + L_1 Z_1 + L_2 Z_1^2. \qquad (1.98)$$

Besides the relativistic correction, there are the shell correction C/Z_2, the density effect correction $\delta/2$, the Barkas correction L_1Z_1 and the Bloch correction $L_2\, Z_1^2$. They are described in detail by Ziegler [56], however, they are less important for the physical situations of interest here.

1.4.3.3 Dielectric Description

Lindhard [57] considered the energy loss of a **bare ion in a homogeneous and isotropic medium**, the properties of which are given by the dielectric constant $\varepsilon(k, \omega)$ and the permeability $\mu(k, \omega)$ as functions of the amount of the wave vector $\mathbf{k}$ and of the frequency ω. Instead of the functions $\varepsilon(k, \omega)$ and $\mu(k, \omega)$, Lindhard used the longitudinal and transversal dielectric constants defined by

$$\varepsilon^l(k,\omega) = \varepsilon(k,\omega) \quad \text{and} \quad \varepsilon^{tr}(k,\omega) = \varepsilon(k,\omega) + (kc/\omega)^2[1 - 1/\mu(k,\omega)] \qquad (1.99)$$

and formulated the electromagnetic field equations for the Fourier transform $U(\mathbf{k},\omega)$ of the electric potential and the Fourier transform $\mathbf{A}^{tr}(\mathbf{k},\omega)$ of the transverse component of the vector potential with ε^l and ε^{tr} (see [57]). For instance the equation for $U(\mathbf{k},\omega)$ (Poisson equation) is given by

$$\varepsilon^l(k,\omega)\varepsilon_0\, k^2 U(\mathbf{k},\omega) = \rho_{ch}(\mathbf{k},\omega), \qquad (1.100)$$

where $\rho_{ch}(\mathbf{k}, \omega)$ is the Fourier transform of the density of the electric charge $\rho_{ch}(\mathbf{r}, t)$ (different from ρ_e which is the number of electrons per unit volume!). For a bare ion of an electric charge Z_1e moving with a velocity $\mathbf{v}$, the charge density is

$$\rho_{ch}(\mathbf{r},t) = Z_1 e\, \delta(\mathbf{r} - \mathbf{v}t) = Z_1 e \int \frac{d^3\mathbf{k}}{(2\pi)^3} \int_{-\infty}^{\infty} d\omega\, \delta(\omega - \mathbf{k}\mathbf{v}) \exp[i(\mathbf{k}\mathbf{r} - \omega t)] \qquad (1.101)$$

(the Fourier presentation of the δ function is used) providing the corresponding Fourier transform

$$\rho_{ch}(\mathbf{k},\omega) = 2\,\pi\, Z_1 e\, \delta(\omega - \mathbf{k}\mathbf{v}). \qquad (1.102)$$

This charge density causes an electric potential $U(\mathbf{r}, t)$ given by its Fourier transform $U(\mathbf{k}, \omega)$ according to (1.100). The corresponding electric field $\mathbf{E}(\mathbf{r}, t) = -\nabla U(\mathbf{r}, t)$ ($-\partial\mathbf{A}/\partial t$ can be neglected in the non-relativistic case) at the position $\mathbf{r} = \mathbf{v}t$ of the bare ion is (note that the application of ∇ provides $i\mathbf{k}$)

$$\mathbf{E}(\mathbf{v}t, t) = -\int \frac{d^3\mathbf{k}}{(2\pi)^3} \int_{-\infty}^{\infty} \frac{d\omega}{2\pi} i\,\mathbf{k}\,U(\mathbf{k}, \omega) \exp[i(\mathbf{k}\mathbf{v}t - \omega t)]. \tag{1.103}$$

The insertion of U(**k**, ω) from (1.100) with $\rho_{ch}(\mathbf{k}, \omega)$ given in (1.102) and the integration over ω provides

$$\mathbf{E}(\mathbf{v}t, t) = -i \frac{Z_1 e}{8\pi^3 \varepsilon_0} \int d^3\mathbf{k} \frac{\mathbf{k}}{k^2\, \varepsilon^l(k, \mathbf{k}\mathbf{v})} \tag{1.104}$$

and the resulting force on the bare ion is

$$\mathbf{F_{st}} = Z_1 e\, \mathbf{E}(\mathbf{v}t, t) = -\frac{\mathbf{v}}{v} i \frac{Z_1^2 e^2}{8\pi^3 \varepsilon_0} \int d^3\mathbf{k} \frac{\mathbf{k}\mathbf{v}}{v} \frac{1}{k^2\, \varepsilon^l(k, \mathbf{k}\mathbf{v})}. \tag{1.105}$$

It is anti-parallel to the velocity **v** because the contribution to the integral for **k** ⊥ **v** is zero. With $\omega \equiv \mathbf{k}\mathbf{v} = kv\ \cos\xi$ (ω runs from −kv to kv) and $d^3\mathbf{k} = 2\pi k^2 dk\ d(\cos\xi) = 2\pi k^2 dk\ d\omega/(kv)$, the electronic stopping power reads

$$S_e = |\mathbf{F}_{st}| = \frac{Z_1^2 \in^2}{\pi v^2} \operatorname{Im}\left\{ \int_0^{\infty} \frac{dk}{k} \int_{-kv}^{kv} d\omega \frac{\omega}{\varepsilon^l(k, \omega)} \right\}. \tag{1.106}$$

Replacing ħω by $(\hbar\omega)^2$ (or ω by $\hbar\omega^2$) provides the electronic straggling according to [57]

$$\Omega_e^2 = \Delta z \frac{Z_1^2 \hbar \in^2}{\pi v^2} \operatorname{Im}\left\{ \int_0^{\infty} \frac{dk}{k} \int_0^{kv} d\omega \frac{2\,\omega^2}{\varepsilon^l(k, \omega)} \right\}. \tag{1.107}$$

Note that (1.106) and (1.107) are derived for bare ions [see (1.101)]. This means that the screening due to the electrons of the ion is neglected. Therefore, the two formulae for S_e and Ω_e^2 are valid only for high ion energies or completely stripped ions.

Now, the formulae given by (1.106) and (1.107) are applied to a homogeneous electron gas of density ρ_e (number of electrons per unit volume). For very high ion energies where the motion of the electrons is less important, **a gas of electrons at rest** can be assumed. In this case, the integrations can be performed analytically which provide [57]

$$S_e = \frac{4\pi Z_1^2 \in^4}{m_e v^2} \rho_e \ln\left(\frac{2 m_e v^2}{\hbar\, \omega_{pl}(\rho_e)} \right) \quad \text{and} \tag{1.108}$$

$$\Omega_e^2 = \Delta z\, 4\pi Z_1^2 \in^4 \rho_e \tag{1.109}$$

with the plasma frequency $\omega_{pl}(\rho_e) = (4\pi \in^2 \rho_e/m_e)^{1/2}$. Considering all electrons of a target atom to be free ($\rho_e = N Z_2$), the electronic straggling (1.109) agrees exactly with the classical result for free electrons given by (1.57) and (1.85) and the

electronic stopping power (1.108) agrees formally with the Bethe-Bloch formula [(1.96) and (1.97)]—only the mean ionization energy I is replaced by the plasma excitation energy $\hbar\omega_{pl}$. Note that (1.108) and (1.109) are applicable only for very high energies, where $2m_e v^2 \gg \hbar\omega_{pl}$.

For lower (but still high) energies the motion of the target electrons must be taken into account. In the case of a Fermi distribution of the electrons at temperature T = 0 K, the longitudinal dielectric constant ε_l reads [57]

$$\varepsilon^l(k,\omega,\rho_e) = 1 + \frac{3\omega_{pl}^2}{k^2 v_F^2}(f_1(u,z) + i f_2(u,z)) \quad \text{with} \quad u = \frac{\omega}{k\,v_F} \quad \text{and} \quad z = \frac{k}{2\,k_F} \tag{1.110}$$

$$\text{and} \quad f_1(u,z) = \frac{1}{2} + \frac{1}{8z}\left[1-(z-u)^2\right]\ln\left|\frac{z-u+1}{z-u-1}\right| + \frac{1}{8z}\left[1-(z+u)^2\right]\ln\left|\frac{z+u+1}{z+u-1}\right| \tag{1.111}$$

$$\begin{aligned} f_2(u,z) &= \tfrac{\pi}{2}u && \text{for } z+u<1 \\ f_2(u,z) &= 0 && \text{for } |z-u|>1 \\ f_2(u,z) &= \tfrac{\pi}{8z}\left[1-(z-u)^2\right] && \text{else,} \end{aligned} \tag{1.112}$$

with the plasma frequency $\omega_{pl}(\rho_e) = (4\pi\,\epsilon^2\rho_e/m_e)^{1/2}$ and the Fermi wave number k_F and Fermi velocity v_F given by $k_F(\rho_e) = m_e v_F/\hbar = p_F/\hbar = (3\pi^2\rho_e)^{1/3}$ [for p_F see (1.6)]. With this longitudinal dielectric constant, the electronic stopping power S_e and the electronic straggling Ω_e^2 for a bare ion penetrating a **gas of moving electrons at zero temperature** can be obtained by numerical integration of (1.106) and (1.107).

In the low energy region, (1.106) and (1.107) can be applied only for completely stripped ions. For dressed ions and low energies, the inelastic energy loss and energy straggling is treated in the following Sections.

1.4.4 Low Energy Inelastic Energy Loss and Energy Straggling

1.4.4.1 Firsov Theory

With the approximated transferred energy $T_e(s)$ (1.48) obtained within the original Firsov model [36, 37] (see Sect. 1.3.2), the electronic stopping cross section and the straggling cross section read

$$\widehat{S}_e = 2\pi \int_0^\infty ds\, s\, T_e(s) = 7.159(Z_1 + Z_2)\in^2 a_0 \frac{v}{v_0}$$
$$= 10.95(Z_1 + Z_2)\left(\frac{E/\text{keV}}{m_1/u}\right)^{1/2} \text{eV}\,\text{Å}^2 \tag{1.113}$$

and

$$W_e = 2\pi \int_0^\infty ds\, s\, T_e^2(s) = 3.491\,(Z_1 + Z_2)^{8/3}\left(\frac{E/\text{keV}}{m_1/u}\right) \text{eV}^2\text{Å}^2. \tag{1.114}$$

Because of the simplifications used with the derivation of (1.48), the cross sections given by (1.113) and(1.114) are valid only for ratios Z_1/Z_2 not far from unity.

1.4.4.2 Modified Firsov Theory

With the transferred energy $T_e(s)$ given in (1.47) and the improved expressions for the electron densities and velocities according to (1.49), the electronic stopping cross section $\widehat{S}_e = 2\pi \int ds\, s\, T_e(s)$ provides

$$\widehat{S}_e = \pi^2 m_e v \sum_{i=1}^{2} \sum_{n,l} n_i^{(n,l)}\, v_{e,i}^{(n,l)} \int_{s_0}^\infty ds\, s \int_{-\infty}^\infty dz \int_{\alpha_i r(z,s)}^\infty dr'\, r' \left|\varphi_i^{(n,l)}(r')\right|^2 \tag{1.115}$$

with $r(z, s) = (z^2 + s^2)^{1/2}$ (for α_i see Fig. 1.7). In the low energy region considered here, the angular deflection (due to nuclear scattering) for very low impact parameter s cannot be neglected which means that the straight line trajectory of the ion as assumed in the Firsov theory (see Fig. 1.7) is not true. This fact is approximately taken into account by introducing a minimum impact parameter $s_0 > 0$. Cheshire et al. [39] determined s_0 by $\varphi_1(s_0) = \Phi_{max,exp}$, where $\varphi_1(s)$ is given by (1.21) and (1.29) and $\Phi_{max,exp}$ is the maximum exit angle registered by the detector. Bhalla et al. [40] and Land and Brennan [41] used s_0 as a fit parameter to get optimum agreement with the experimental data and they found $s_0 = 2.11\ a_0$ to be the best choice.

By twofold exchange of the sequence of the integrations, it is possible to perform two integrations analytically. The change from variable $z = (r^2 - s^2)^{1/2}$ to variable r provides

$$\int_{s_0}^\infty ds\, s \int_{-\infty}^\infty dz \int_{\alpha_i r(z,s)}^\infty \cdots = 2 \int_{s_0}^\infty ds\, s \int_s^\infty \frac{dr\, r}{(r^2 - s^2)^{1/2}} \int_{\alpha_i r}^\infty \cdots$$
$$= 2 \int_{s_0}^\infty dr\, r\left(r^2 - s_0^2\right)^{1/2} \int_{\alpha_i r}^\infty \cdots,$$

where the last expression is obtained by the exchange of the sequence of the two integrations over r and s $(r = s \ldots \infty, s = s_0 \ldots \infty \rightarrow s = s_0 \ldots r, r = s_0 \ldots \infty)$ and the integration over s. The insertion of this expression in (1.115) and the exchange of the sequence of the two remaining integrations over r' and r $(r' = \alpha_i r \ldots \infty, r = s_0 \ldots \infty \rightarrow r = s_0 \ldots r'/\alpha_i, r' = \alpha_i s_0 \ldots \infty)$ and the integration over r result in the final formula for the stopping cross section

$$\widehat{S}_e = \frac{2}{3}\pi^2 m_e v \sum_{i=1}^{2} \frac{1}{\alpha_i^3} \sum_{n,l} n_i^{(n,l)} v_{e,i}^{(n,l)} \int_{\alpha_i s_0}^{\infty} dr' \, r' \left[(r')^2 - (\alpha_i s_0)^2\right]^{\frac{3}{2}} \left|\varphi_i^{(n,l)}(r')\right|^2 \quad (1.116)$$

as given by Land and Brennan [41] (for α_i see Fig. 1.7). A similar formula was already obtained by Bhalla et al. [40].

1.4.4.3 Theories of Lindhard-Scharff and Tilinin

Lindhard and Scharff [58] used a different approach for the determination of the low energy electronic energy loss. They referred to the description of the stopping of an ion in an electron gas given by Lindhard [57] and presented a formula for the stopping cross section showing a linear dependence on the ion velocity. However, they did never publish a derivation of this formula. In order to understand this linear dependence on the ion velocity, a description given by Bonderup [59] is very helpful and briefly discussed in the following. The target electrons move with velocities $\mathbf{v}_e$ in the laboratory system, where the velocities are distributed within the Fermi sphere $|\mathbf{v}_e| \leq v_F$ and the average velocity is zero. Because of the small mass of the electrons, the center-of-mass velocity of the ion-electron system is equal to the ion velocity $\mathbf{v}$ and the velocity of an electron in the center-of-mass system is $\mathbf{v}_e - \mathbf{v}$ (see Sect. 1.2.2).

This means, the distribution of the electron velocities in the center-of-mass system is given by a sphere with the radius v_F and the center shifted by $-\mathbf{v}$. For low energies ($v \ll v_F$) as considered here, the situation is visualized in Fig. 1.10 (the edge of the Fermi sphere is given by the thick solid line). Due to the collision of the ion with an electron, the electron velocity changes. According to (1.20) the velocities of the ion and of the electron in the center-of-mass system do not change their amounts, they change only their direction. This means that the velocities of the electrons in the center-of-mass system after the collision must keep within a sphere of radius $v_F + v$, the edge of which is marked by the dashed line in Fig. 1.10. Because all states in the inner white sphere in Fig. 1.10 are occupied, the only allowed velocity changes are those from the sickle formed left volume (dark grey) to the sickle formed right volume (light grey) as shown by the two grey arrows. The corresponding average change of the momentum of one electron can be estimated by $\Delta\mathbf{p}_e \approx m_e v_F \; \mathbf{v}/v$ (because of the symmetry the components perpendicular to $\mathbf{v}$ vanish). The relative part of the electrons which take part in the scattering process (dark grey volume divided by the total volume of the Fermi sphere) is

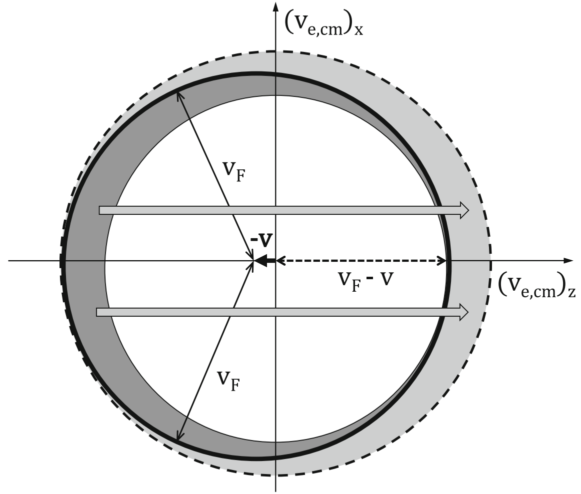

Fig. 1.10 Electron velocity distributions in the center-of-mass system (situation for $v \ll v_F$)

$\left[v_F^3 - (v_F - v)^3\right]/v_F^3 \approx 3v/v_F$ for $v \ll v_F$ and the number of participating electrons per unit volume is given by $\rho_{e,p} = \rho_e 3v/v_F$. With the effective volume $dV_\sigma = \sigma(v_F)v_F dt$ for the ion-electron scattering (the velocity of the participating electrons in the hatched volume is approximately given by v_F and $\sigma(v_F)$ is the cross section for the scattering on these electrons), the average change of the momentum of all participating electrons is $dp = |\Delta\mathbf{p}_e|\, \rho_{e,p}\, dV_\sigma$ and the stopping power reads

$$S_e = -\frac{dE}{dz} = \frac{dp}{dt} \approx 3m_e v_F\, \rho_e \sigma(v_F) v \propto v. \tag{1.117}$$

The main result is that the proportionality of the stopping power to the ion velocity can be explained by the velocity dependence of the relative part of electrons participating in the collision. Taking into account also the scattering of the target atom on the projectile electrons and applying the statistical model of atoms, Lindhard and Scharff [58] presented the following formula for the electronic stopping cross section

$$\widehat{S}_e = S_e/N = \frac{8\pi\, a_0 \in^2 Z_1 Z_2\, \zeta}{\left(Z_1^{2/3} + Z_2^{2/3}\right)^{3/2}} \frac{v}{v_0} = \frac{38.45\, Z_1 Z_2\, \zeta}{\left(Z_1^{2/3} + Z_2^{2/3}\right)^{3/2}} \left(\frac{E/\text{keV}}{m_1/u}\right)^{1/2} \text{eV}\,\text{Å}^2, \tag{1.118}$$

with a factor

$$\zeta = \zeta_{LS} = Z_1^{1/6} \tag{1.119}$$

obtained by fitting the experimental data. A similar formula was derived by Tilinin [60] with the only difference that the factor ζ is not a fitting function but it is determined by an integral (see [60]), where the integrand depends on the interatomic interaction potential. The resulting factor

$$\zeta = \zeta_T(Z_1/Z_2, E) \qquad (1.120)$$

is a function of the energy E and it depends symmetrically on Z_1 and Z_2. For the Thomas-Fermi interaction potential used, Tilinin found $\zeta_T \lesssim 1$ which is smaller than the fitting function ζ_{LS} of Lindhard and Scharff.

1.4.5 Comparison of Stopping Power Theories

In order to compare the results of the different stopping power theories, a few examples are presented. The energy dependence of the electronic and nuclear stopping power is shown in Fig. 1.11 for H, He, Si and Au ions in InP which covers the range of light to heavy ions in a material of interest in following Parts. According to (1.64) the electronic and nuclear stopping power for the compound target InP are obtained by $S_e = N_{In}\widehat{S}_{e,In} + N_P\widehat{S}_{e,P}$ and $S_n = N_{In}\widehat{S}_{n,In} + N_P\widehat{S}_{n,P}$, respectively, with $N_{In} = N_P = 1.99 \times 10^{22}$ atoms/cm^3 (corresponds to the mass density of 4.81 g/cm^3). The electronic stopping cross sections $\widehat{S}_{e,In}$ and $\widehat{S}_{e,P}$ for the different theories are given by (1.96) using I = 10 eV Z_2 and (1.113), (1.118), (1.119) and (1.120) and the nuclear stopping cross sections $\widehat{S}_{n,In}$ and $\widehat{S}_{n,P}$ are obtained from (1.74) and (1.76). In addition, the electronic stopping powers S_e calculated with TRIM (1985–1990) or SRIM (1991–2013) [61] are depicted in Fig. 1.11. The determination of the corresponding stopping cross sections is very briefly described in the following. For hydrogen ions, the stopping cross section $\widehat{S}_{e,H}$ is given by an analytical function fitted to all available experimental data. For all the other ions, the scaling rule $\widehat{S}_e(v, Z_2) = Z_{1,eff}^2\widehat{S}_{e,H}(v, Z_2)$ is used (v is the ion velocity). The description of the effective atomic number $Z_{1,eff}$ (effective charge) of the ion is based on the Brand-Kitagawa theory [62] and partially fitted to experimental data. In the low energy region, $S_e \propto v^\alpha$ is used with the parameter $\alpha \lesssim 1$ fitted to the experimental data. A detailed description of the electronic stopping cross sections used in TRIM or SRIM is given in [13]. With respect to the electronic stopping power, the different versions of TRIM and SRIM differ mainly by the fitting parameters used which had been updated according to the state-of-the art experimental data. As can be seen in Fig. 1.11, the TRIM-88 results and the SRIM-2003 results do not differ much and both agree well with the small number of experimental data [63, 64] which exist for the H and He ions. Calculations using SRIM-2013 provided the same stopping powers as that obtained with SRIM-2003.

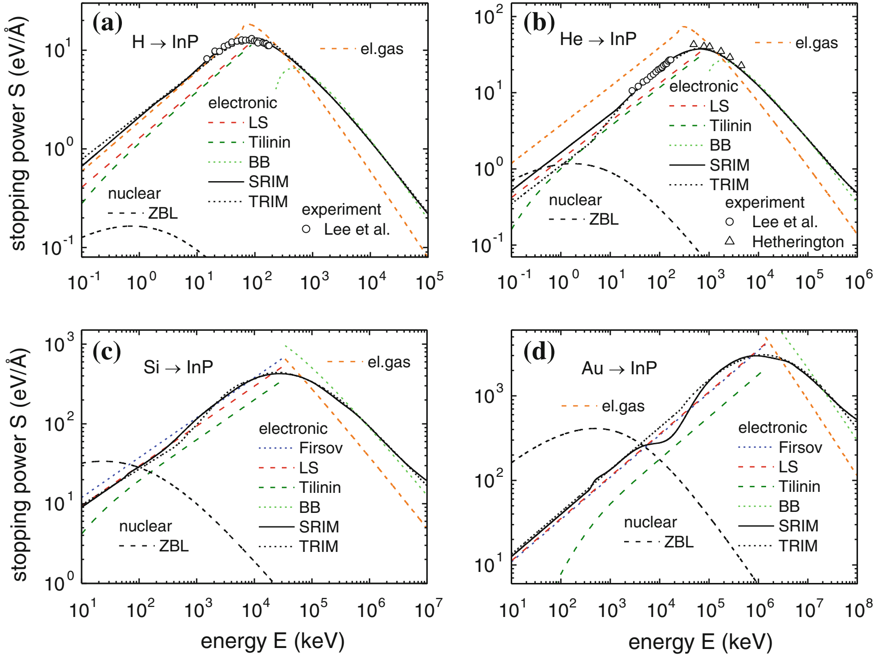

Fig. 1.11 The energy dependence of the stopping powers S = −dE/dz of H (**a**), He (**b**), Si (**c**) and Au (**d**) ions in InP. The electronic stopping powers S_e obtained using SRIM-2003 and TRIM-88 and the formulae of Firsov [36, 37], Lindhard-Scharff (LS) [58], Tilinin [60] and Bethe-Bloch (BB) [49–52] and S_e numerically calculated for an electron gas (see text) are given by different lines. The experimental data (note that $S_{exp} \approx S_{e,exp}$) of Lee and Hart [63] and of Hetherington [64] are depicted by symbols. For comparison the nuclear stopping powers S_n^{ZBL} according to the ZBL formula [(1.74) and (1.76)] are added (note that in (**d**) the Firsov and LS stopping powers are equal)

For the comparison of the different stopping power theories, the SRIM results are considered as reference data like experimental data. The critical energy $E_{e,cr} \approx 22\,(m_1/u)\,Z_1\,Z_{2,av}^{0.4}$ keV introduced in Sect. 1.3 (u is the atomic mass unit, Z_2 is replaced by the average atomic number $Z_{2,av} = 32$) is 89, 705, 3.4×10^4 and 1.4×10^6 keV for H, He, Si and Au ions, respectively. As can be seen in Fig. 1.11, they agree well with the positions of the maxima of the electronic stopping power obtained by SRIM. The low energy electronic stopping cross section formula of Lindhard and Scharff [58] [(1.118) and (1.119)] provides reasonable results for the He, Si and Au ions up to an energy of about 0.1 $E_{e,cr}$ (see Fig. 1.11b–d), but for the H ions the stopping power is too small. The results obtained using the formula of Firsov [36, 37] [see (1.113)] agree also well with the SRIM data in the case of Si and Au ions (Fig. 1.11c, d), however, this formula is not applicable to H → InP and He → InP because Z_1/Z_2 is too far from unity (therefore not shown in Fig. 1.11a, b). The theory of Tilinin [60] [see (1.118) and (1.120)] underestimates

the electronic stopping power for all four examples considered. As can be seen in Fig. 1.11, the Bethe-Bloch formula can be applied for energies above about 10 $E_{e,cr}$, however, for much higher energies and heavy ions the electronic stopping power becomes slightly lower than that obtained using SRIM. This small difference cannot be explained by the corrections to the Bethe-Bloch formula given by (1.98) because they are negligible in this energy region.

In order to study the amount of stopping in an electron gas, the electronic stopping power according to (1.106), (1.110)–(1.112) was calculated for an electron gas with constant density $\rho_e = 18\ N_{InP}$ ($N_{InP} = N_{In} = N_P = 1.99 \times 10^{22}$ InP molecules/cm^3). This density is obtained by the assumption that the 13 weakly bound electrons per In atom (3d(10), 5 s(2), 5p(1)) and the 5 weakly bound electrons per P atom (3 s(2), 3p(3)) form the free electron gas. The results are added in Fig. 1.11. Note that they belong to completely stripped ions [(1.106) is valid for a point charge Z_1e, see (1.101)] which means that the screening of the ion-electron interaction is not taken into account. In the high energy region $E \gg E_{e,cr}$ the screening is less important which makes the electron gas results reliable. As can be seen in Fig. 1.11, the stopping power in the electron gas for $E \gg E_{e,cr}$ is about 40–60 % of the Bethe-Bloch stopping power for all four ions. This means, the weakly bound electrons in the InP (18 per molecule) contribute about 40–60 % to the electronic stopping power. The fact that the ratio is approximately independent of the kind of the ion proves the screening of the ion-electron interaction to have no remarkable influence on S_e in the high energy region. In the low energy region $E \ll E_{e,cr}$, the screening heavily influences the stopping power in the electron gas. For Si and Au ions, S_e is much too large and therefore not depicted in Fig. 1.11 for $E < E_{e,cr}$. In the low energy region, the stopping power in the electron gas is reliable only for H ions because they are bare ions. As can be seen in Fig. 1.11a, surprisingly, the electron gas stopping power of H ions agrees very well with the SRIM data. This means that the electronic energy loss of H in InP for $E \ll E_{e,cr}$ can also be understood as the electron gas stopping contribution of the 18 weakly bound electrons per InP molecule.

In the low energy region $E \ll E_{e,cr}$ ($v \ll v_{e,cr} = 0.94\, Z_1^{1/2} Z_2^{0.2}\, v_0 \gtrsim v_0$ with $v_0 = \epsilon^2/\hbar = 2.1877 \times 10^6$ m/s), the energy dependence of the electronic stopping power is in most cases well described by a proportionality to the velocity v. Therefore it is sufficient to measure the electronic stopping power only for one typical velocity within this energy region, usually at $v \lesssim v_0$. This has been done for a large variety of projectile-target combinations ([65–70] and references in [70]). The results show that the electronic stopping cross section $\widehat{S}_e$ for a fixed velocity v does not depend monotonously on Z_1 and Z_2 but it reveals pronounced oscillations which cannot be described by the theories of Firsov, Lindhard and Scharff and Tilinin. However, using the modified Firsov theory and taking into account electron structure effects, it is possible to explain the Z_1- and Z_2- oscillations of $\hat{S}_e$ [39–41, 71]. Two examples are given in Figs. 1.12 and 1.13. As can be seen in both figures, the results obtained using the formulae of Firsov [36, 37] (1.113) and Tilinin [60] [(1.118) and (1.120)] form approximately the upper and lower envelope of the

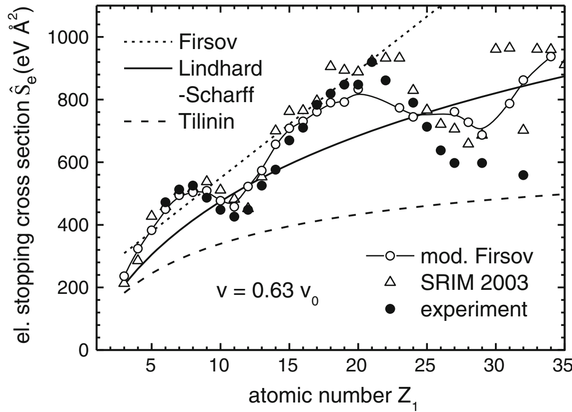

Fig. 1.12 The Z_1-dependence of the stopping cross section $\hat{S}_e$ in carbon ($Z_2 = 6$) for ions of velocity $v = 0.63\ v_0$. The full dots represent the experimental data of Fastrup, Hvelplund and Sautter [66, 67]. The theoretical results of Firsov [36, 37], Lindhard-Scharff (LS) [58] and Tilinin [60] are given by different lines. The values of $\hat{S}_e$ obtained from SRIM-2003 and that obtained by Cheshire et al. [39] within the modified Firsov theory are presented by *symbols* (the line connecting the modified Firsov results is only added to guide the eye)

oscillating experimental data and the results of Lindhard and Scharff [58] [(1.118) and (1.119)] are positioned in between. The modified Firsov theory results given in Fig. 1.12 were obtained by Cheshire et al. [39] using (1.115) and simple Hartree-Fock wave functions, and those given in Fig. 1.13 were obtained by Land and Brennan [71] using (1.116) and the wave functions given by Clementi and Roetti [9]. As can be seen in Figs. 1.12 and 1.13, the stopping cross sections provided by the modified Firsov theory agree well with the experimental data. The deviations for heavy ions ($Z_1 > 25$) in Fig. 1.12 may be a consequence of the too simple wave functions used by Cheshire et al. [39]. The electronic stopping cross sections calculated using SRIM-2003 are added for comparison. In Fig. 1.12. they show an agreement with the experimental data similar to those of the modified Firsov theory and in Fig. 1.13 the modified Firsov theory results agree better with the measured stopping cross sections than the SRIM results do.

Summarizing, with respect to the application the following can be stated. The nuclear stopping cross section has a maximum at an energy $E_{n,cr} \approx 0.01\, Z_1 Z_2 \left(Z_1^{0.23} + Z_2^{0.23}\right) m/m_2\, \text{keV}$ [corresponds to $\varepsilon \approx 0.3$, see Fig. 1.9 and (1.76)] and the electronic stopping cross section has a maximum at an energy $E_{e,cr} \approx 22\,(m_1/u)\, Z_1\, Z_2^{0.4}\, \text{keV}$ (u is the atomic mass unit). For the nuclear stopping cross section, the formula obtained using the ZBL potential [(1.74) and (1.76)] is a reasonable approximation. The remarkable incorrectness of the ZBL potential for large distances as shown in Sect. 1.2.4.2 has a minor influence on the stopping cross section because the latter one is an integral quantity. In general, the electronic stopping cross sections obtained using SRIM are the most reliable ones because they are fitted to a lot of experimental data. However, for a few cases in the low

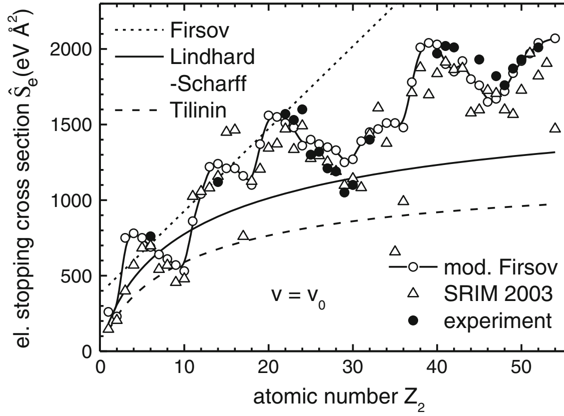

Fig. 1.13 The Z_2-dependence of the stopping cross section $\hat{S}_e$ of N ions ($Z_1 = 7$) with velocity $v = v_0$ (E = 350 keV). The *full dots* represent the experimental data of Land et al. [70]. The theoretical results of Firsov [36, 37], Lindhard-Scharff (LS) [58] and Tilinin [60] are given by different lines. The values of $\hat{S}_e$ obtained from SRIM-2003 and that obtained by Land et al. [71] within the modified Firsov theory are presented by *symbols* (the line connecting the modified Firsov results is only added to guide the eye)

energy region (see Fig. 1.13) there are remarkable deviations from the measured stopping cross sections. In these cases the electronic stopping cross section for energies $E \ll E_{e,cr}$ $(v \ll v_{e,cr} = 0.94\, Z_1^{1/2} Z_2^{0.2}\, v_0)$ can be obtained by $\hat{S}_e(v) = \hat{S}_{e,mc}(v_{mc})\, v/v_{mc}$, where $\hat{S}_{e,mc}(v_{mc})$ is the stopping cross section measured or calculated for the velocity v_{mc}. For a large number of projectile-target combinations ($Z_1 = 6 \ldots 54$, $Z_2 = 1 \ldots 54$) the electronic stopping cross sections at $v_{mc} = v_0$ have been calculated and tabulated by Land and Brennan [71]. For $Z_1 = 7$ the reliability of these data has already been demonstrated in Fig. 1.13. For a very simple estimation of the electronic stopping cross section at low energies ($E < 0.1\ E_{e,cr}$) without taking into account the oscillations and at high energies ($E > 10\ E_{e,cr}$), the Lindhard-Scharff formula [(1.118) and (1.119)] and the Bethe-Bloch formula [(1.96) and (1.97)], respectively, can be used.

1.4.6 Energy Loss Distribution

The general formula for the energy loss distribution $P(\Delta E, \Delta z)$ is given in (1.59) as an integral. It has been derived by Landau [44] and it is valid for layer thicknesses Δz small enough that the change of the differential cross section $d\sigma$ with the energy is not significant. Because of the oscillation of the integrand, the numerical integration is not trivial. There exist a number of publications dealing with the evaluation of (1.59) for high ion energies where the electronic energy loss dominates (see references in [43]). The results for two situations are given in Sects. 1.4.6.1 and 1.4.6.2. In the case of medium

and low ion energies, the calculation of the energy loss distribution is more difficult because also the nuclear energy loss must be taken into account where the corresponding differential cross section is not given analytically. In addition, the dependence of the electronic energy loss on the deflection angle must be taken into account for low energies. A few approximations of the energy loss distribution for low energies are presented in Sect. 1.4.6.3.

1.4.6.1 High Energy Region and Small Layer Thickness (Landau Distribution)

For high ion energies $E \gg E_{e,cr} \approx 22\,(m_1/u)\,Z_1\,Z_2^{0.4}\,keV$(u is the atomic mass unit), the nuclear energy loss can be neglected, the differential cross section $d\sigma_e$ for electronic scattering is given by (1.78) and the electronic energy loss can be obtained from the Bethe-Bloch formula [(1.96) and (1.97)]. For this case, Landau [44] evaluated his formula (1.59) with the simplification that the maximum transferred energy is infinite. He received the energy loss distribution

$$P(\Delta E, \Delta z)\,d(\Delta E) = P_L(\lambda(\Delta E, \Delta z))\,d\lambda = [P_L(\lambda(\Delta E, \Delta z))/\xi]\,d(\Delta E) \qquad (1.121)$$

which depends only on one dimensionless parameter—the Landau parameter

$$\lambda(\Delta E, \Delta z) = \frac{(\Delta E - \langle \Delta E \rangle)}{\xi} - \ln(\kappa) - 0.4228\,(\mathrm{non-relativistic\,case}) \qquad (1.122)$$

$$\text{with}\ \xi = \frac{\Omega_e^2}{2\,m_e v^2} = \Delta z\,N\frac{2\pi\,Z_1^2\,Z_2 \in^4}{m_e v^2}\ \text{and}\ \langle \Delta E \rangle = \Delta z\,N\,\widehat{S}_e \qquad (1.123)$$

and the reduced thickness

$$\kappa = \frac{\xi}{2\,m_e v^2} = \Delta z\,N\frac{\pi\,Z_1^2\,Z_2 \in^4}{(m_e v^2)^2}, \qquad (1.124)$$

where Ω_e^2 and $\widehat{S}_e(E)$ are given by (1.57), (1.85) and (1.96), (1.97), respectively. The function $P_L(\lambda)$ (Landau distribution) has been calculated numerically by Börsch-Supan [72]. Later, Lindhard [73] obtained the analytical expression

$$P_L(\lambda) = \frac{1}{y^{1/2}\,(1+y)^{3/2}}\left[1 + \frac{y^2}{2 + 7y + 6y^2 + 2y^3}\right]\exp\left(\frac{1}{2+2y} - \frac{1}{y}\right) \qquad (1.125)$$

with $y(\lambda)$ implicitly determined by $\lambda = y + \ln y - 1/(2+2y) - 0.4228$ which agrees very well with the numerical results. Because of the simplification of the infinite maximum transferred energy, the Landau distribution is **valid only for very small layer thicknesses** according to $\kappa \lesssim 0.01$ (as demonstrated in the following Fig. 1.14a).

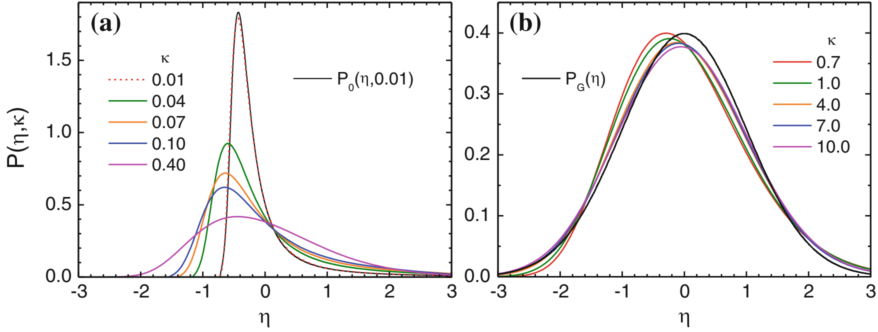

Fig. 1.14 The energy loss distribution $P(\eta, \kappa)$ (1.127) depicted over the relative deviation of the energy loss from its average value $\eta = (\Delta E - \langle \Delta E \rangle)/\Omega_e$ obtained from the Vavilov distribution $P_V(\lambda, \kappa, \beta = 0)$ of Seltzer and Berger [76] (non-relativistic case) for different reduced thicknesses $\kappa = 0.01$ to 0.4 (a) and $\kappa = 0.7$ to 10 (b). The Gaussian distribution $P_G(\eta)$ (1.128) and the Landau distribution $P_0(\eta, \kappa)$ for $\kappa = 0.01$ (1.129) [with $P_L(\lambda)$ given by (1.125)], both expressed as functions of η, are added

1.4.6.2 High Energy Region (Vavilov Distribution)

Vavilov [74, 75] evaluated the Landau formula (1.59) under the same conditions as given in Sect. 1.4.6.1, however, without the simplification of an infinite maximum transferred energy. The resulting distribution also depends on the Landau parameter $\lambda(\Delta E, \Delta z)$ but in addition it depends also directly on Δz [or the reduced thickness $\kappa \propto \Delta z$ given in (1.124)]. Seltzer and Berger [76] calculated and tabulated the Vavilov distribution $P_V(\lambda, \kappa, \beta)$ for the relativistic ($\beta = v/c$) and non-relativistic ($\beta = 0$) case. Using the relative deviation of the energy loss from its average value

$$\eta = \frac{\Delta E - \langle \Delta E \rangle}{\Omega_e} = \kappa^{1/2}(\lambda + \ln(\kappa) + 0.4228) \tag{1.126}$$

instead of λ [obtained from (1.122)–(1.124)], the energy loss distribution in the non-relativistic case ($\beta = 0$) reads

$$P(\eta, \kappa)d\eta = P_V(\lambda(\eta), \kappa, 0)\, d\lambda = \left[P_V(\lambda(\eta), \kappa, 0)/\kappa^{1/2}\right] d\eta. \tag{1.127}$$

It is shown in Fig. 1.14 for all values of κ given in the tables of Seltzer and Berger [76]. The electronic energy loss straggling $\Omega_e^2 = \Delta z\, N\, 4\pi\, Z_1^2 Z_2 \in^4$ is given by (1.57) and (1.85). For large values of κ, the energy loss distribution $P(\eta, \kappa)$ tends to the Gaussian distribution (1.60) expressed as a function of η

$$P_G(\eta)d\eta = \frac{1}{(2\pi)^{1/2}} \exp\left(-\frac{1}{2}\eta^2\right) d\eta, \tag{1.128}$$

and for very small values of κ it becomes equal to the Landau distribution, also expressed as a function of η

$$P_0(\eta, \kappa)\, d\eta = \left[P_L(\lambda(\eta))/\, \kappa^{1/2}\right] d\,\eta. \tag{1.129}$$

As can be seen in Fig. 1.14, the Vavilov distribution is well approximated by the Landau distribution for $\kappa \lesssim 0.01$ and the Gaussian distribution may roughly be used for $\kappa \gtrsim 1$, however, there remains an asymmetry of a few percent up to $\kappa = 10$.

1.4.6.3 Low Energy Region

In the case of very low energies, where nuclear scattering is dominant, Lindhard and Nielsen [77] published exact analytical solutions of the energy loss distribution $P(\Delta E, \Delta z)$ for a simplified nuclear scattering cross section. The authors used the so called power law cross section $d\sigma_n = C_m\, dT_n/T_n^{1+m}$ with the free parameters C_m and $0 < m < 1$ which very roughly simulates a screened Coulomb potential (for $m = 1$ this cross section is equal to the Coulomb cross section given in (1.67) with $C_m = B_n$).

Using a more realistic ion-atom interaction potential (the Thomas-Fermi potential [1, 2]) and including the electronic energy loss, Meyer et al. [78] calculated the energy loss distribution applying two simplifications. First, the nuclear scattering cross section is calculated within the small angle approximation introduced by Lindhard et al. [79]. Second, the electronic energy loss T_e is independent of the energy but it depends on the scattering angle of the ion φ_1 which means that electronic scattering and nuclear scattering are coupled. Because the Thomas-Fermi potential used is a generalized one, the resulting energy loss distribution $P(\Delta E,\Delta z) = C_P\, f_1\left(\tau, \widetilde{Q}\right)$ is also given by a generalized function $f_1\left(\tau, \widetilde{Q}\right)$ of the dimensionless reduced thickness $\tau = C_{\Delta z}\Delta z$ and the dimensionless reduced energy loss $\widetilde{Q} = C_{\Delta E}\Delta E$ (the correction function f_2 mentioned in [78] can be neglected). The function $f_1\left(\tau, \widetilde{Q}\right)$ is tabulated in [78]. The coefficients C_P, $C_{\Delta z}$ and $C_{\Delta E}$ depend on the atomic numbers and masses of the ion and the target atom and on the parameters of the electronic energy loss (see [78]). The results show that with respect to the energy loss distribution for very low energies [$\varepsilon \ll 1$, see (1.76)], the nuclear and electronic scattering cannot be treated separately.

A very useful method for the determination of the energy loss distribution is the Monte Carlo (MC) computer simulation. The advantage of the simulation is that no simplifications of the nuclear and electronic scattering are necessary. A widely used MC code is TRIM (later SRIM) which is very briefly described in Sect. 1.4.8.2. This code uses the ZBL potential for nuclear scattering and realistic energy dependent electronic energy losses, however, the dependence of the electronic energy loss on the nuclear scattering angle is not taken into account. For example,

Goebl et al. [80] applied TRIM to calculate the energy distribution of 10 keV He transmitted through a 600 Å Ag film.

1.4.7 *Angular Distribution*

1.4.7.1 Nuclear Scattering

The general formula for the angular distribution derived by Bothe [45] is given in (1.63). Because of the small mass of the electrons, the scattering angle due to scattering on electrons is negligibly small compared to that caused by nuclear scattering. Therefore, in most cases (where channeling does not occur) only the nuclear scattering must be considered. That means, the single scattering angle φ and the differential cross section $d\sigma$ in (1.63) are given by the scattering angle φ_1 of the ion in the laboratory system and the nuclear differential cross section $d\sigma_n$, respectively, both determined by the interatomic interaction potential V(r) [see (1.21), (1.29) and (1.31)]. For a generalized potential (e.g. Thomas-Fermi potential) with the Lindhard screening length a_L (1.15), the angular distribution can also be generalized

$$P(\Phi, \Delta z) = \frac{1}{2\pi}\left(\frac{E\,a_L}{2\,Z_1 Z_2 \in^2}\right)^2 f_1\left(\widetilde{\Phi}, \tau\right) \tag{1.130}$$

$$\text{with } \widetilde{\Phi} = \frac{E\,a_L}{2\,Z_1 Z_2 \in^2}\Phi \text{ and } \tau = \Delta z\, N\, \pi\, a_L^2. \tag{1.131}$$

The function $f_1\left(\widetilde{\Phi}, \tau\right)$ was first introduced and calculated for the Thomas-Fermi potential by Meyer [81]. Later calculations of $f_1\left(\widetilde{\Phi}, \tau\right)$ have been performed by Sigmund and Winterbon [82] and by Amsel et al. [83] for the Thomas-Fermi potential [1, 2] and the Lenz-Jensen potential (see e.g. [14]) as well. Figure 1.15 visualizes the function $f_1\left(\widetilde{\Phi}, \tau\right)$ for the Thomas-Fermi potential in two different presentations. The relative function $f_{1,rel}\left(\widetilde{\Phi}/\widetilde{\Phi}_{1/2}, \tau\right) = f_1\left(\widetilde{\Phi}, \tau\right)/f_1(0, \tau)$ over $\widetilde{\Phi}/\widetilde{\Phi}_{1/2}$ is shown in Fig. 1.15a, where the values of $f_1\left(\widetilde{\Phi}, \tau\right)$ are obtained from the tables given by Sigmund and Winterbon [82]. The maximum value $f_1(0, \tau)$ and the half width angle $\widetilde{\Phi}_{1/2}(\tau)$ of the distribution $f_1\left(\widetilde{\Phi}, \tau\right)$ [82] are well approximated by

$$f_1(0, \tau) = \exp\left\{\sum_{n=0}^{5} c_n (\ln\, \tau)^n\right\} \quad \text{and} \quad \widetilde{\Phi}_{1/2}(\tau) = \exp\left\{\sum_{n=0}^{5} d_n (\ln\, \tau)^n\right\} \tag{1.132}$$

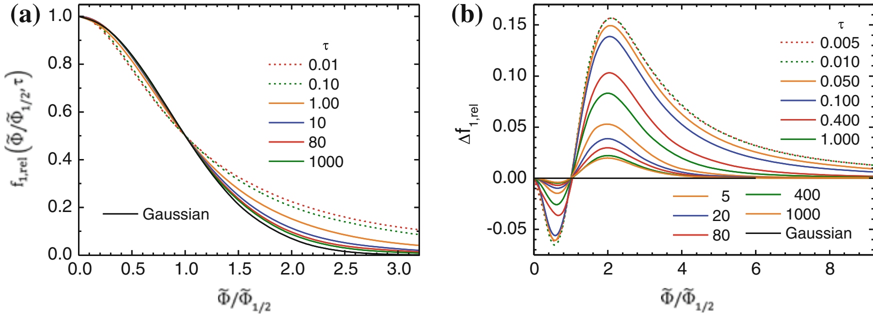

Fig. 1.15 The relative angular distribution $f_{1,rel}\left(\tilde{\Phi}/\tilde{\Phi}_{1/2}, \tau\right) = f_1\left(\tilde{\Phi}, \tau\right)/f_1(0, \tau)$ (**a**) and its deviation $\Delta f_{1,rel}$ (see text) from the Gaussian distribution (**b**) depicted over the ratio $\tilde{\Phi}/\tilde{\Phi}_{1/2}$ for different reduced thicknesses τ. For $f_1(0, \tau)$ and $\tilde{\Phi}_{1/2}(\tau)$ see (1.132) (all data obtained from $f_1\left(\tilde{\Phi}, \tau\right)$ given in [82])

with $c_n = \{2.126, -1.708, 0.128, -0.0116, -0.000662, 0.000128\}$
and $d_n = \{-1.166, 0.947, -0.0832, 0.00646, 0.000728, -0.000105\}$.

In the same notation, the Gaussian distribution (1.62), valid for very large values of τ, reads

$$f^G_{1,rel}\left(\tilde{\Phi}/\tilde{\Phi}_{1/2}\right) = \exp\left(-\ln 2\, \tilde{\Phi}/\tilde{\Phi}_{1/2}\right). \tag{1.133}$$

For comparison, it is added in Fig. 1.15a. As can be seen, the angular distributions for different values τ differ from the Gaussian distribution mainly by their pronounced tails. Even for τ = 1000, a small tail remains. In order to visualize the deviations from the Gaussian distribution more distinctly, especially for larger angles, the difference

$$\Delta f_{1,rel}\left(\tilde{\Phi}/\tilde{\Phi}_{1/2}, \tau\right) = f_{1,rel}\left(\tilde{\Phi}/\tilde{\Phi}_{1/2}, \tau\right) - f^G_{1,rel}\left(\tilde{\Phi}/\tilde{\Phi}_{1/2}\right)$$

is shown in Fig. 1.15b. For more details about the theoretical description of the angular distribution of ions after having passed a target layer see the review article of Amsel et al. [83].

1.4.7.2 Electronic Scattering

The electronic scattering contributes significantly to the angular distribution of the ions only in the case, where the nuclear scattering is considerably suppressed (e.g. with channeling). Because of the very small single scattering angles, the angular distribution is well described by the Gaussian distribution given in (1.62). In the

case of **bare ions** with charge Z_1e, the required mean square deviation Ψ^2 (angular spread) can be obtained within the dielectric description of Lindhard [57] by

$$\psi^2 = -\Delta z \frac{2\,Z_1^2 \in^2 \hbar}{\pi\, m_1^2\, v^4}\, \mathrm{Im}\left\{ \int_0^\infty \frac{dk}{k} \int_0^{kv} d\omega\, \frac{k^2 - \omega^2/v^2}{\varepsilon^l(k,\omega)} \right\}. \qquad (1.134)$$

The formalism is already described in Sect. 1.4.3.3. For the scattering on an electron gas of density ρ_e (number of electrons per unit volume), the longitudinal dielectric constant $\varepsilon^l(k, \omega, \rho_e)$ is given by (1.110)–(1.112), and (1.134) can be evaluated numerically.

1.4.8 Spatial Distributions of the Ions and the Damage

1.4.8.1 Analytical Description

An energetic ion incident in an amorphous target undergoes a lot of collisions with the target atoms, each resulting in a change of its direction and energy and of the generation of a recoil target atom. Each recoil atom with an energy larger than the displacement energy E_d generates further recoil atoms resulting finally in a collision cascade. After a path length l_p, the ion starting with velocity $\mathbf{v}$ at the position $\mathbf{r} = 0$ on the target surface (x-y plane) comes to rest in a volume $d^3\mathbf{r}$ at $\mathbf{r}$ ($r = |\mathbf{r}| < l_p$). The different paths of the ions caused by the different impact positions result in a spatial distribution $P_{ion}(\mathbf{r}, \mathbf{v})$ of the ions determined by the integro-differential equation [84–86]

$$-\mathbf{e}\,\nabla_r\, P_{ion}(\mathbf{r},\mathbf{v}) = N \int d\sigma\, [P_{ion}(\mathbf{r},\mathbf{v}) - P_{ion}(\mathbf{r},\mathbf{v}')], \qquad (1.135)$$

where $\mathbf{e} = \mathbf{v}/v$, ∇_r is the Nabla operator, $\mathbf{v}'$ is the ion velocity after the collision with a target atom and $d\sigma$ is the corresponding differential cross section. The distribution P_{ion} is normalized by $\int d^3\mathbf{r} P_{ion}(\mathbf{r}, \mathbf{v})=1$.

A suitable measure for the damage caused by the ion irradiation has been proved to be the energy deposited into nuclear processes. According to Sigmund et al. [87], the corresponding quantity $F(\mathbf{r}, \mathbf{v})\, d^3\mathbf{r}$ is defined as the average energy located in the volume element $d^3\mathbf{r}$ at the position $\mathbf{r}$, minus the energy contained in electronic excitation or ionization, at the end of the slowing-down cascade. Thus, integrating over the whole space provides $\int d^3\mathbf{r} F(\mathbf{r}, \mathbf{v}) = \nu(E)$, where ν is the total amount of nuclear deposited energy which is smaller than the ion energy E. The basic equation for the nuclear deposited energy distribution $F(\mathbf{r}, \mathbf{v})$ given by Lindhard et al. [88] and Winterbon et al. [89] reads

$$-\mathbf{e}\,\nabla_r\, F(\mathbf{r},\mathbf{v}) = N\int d\sigma[F(\mathbf{r},\mathbf{v}) - F(\mathbf{r},\mathbf{v}') - F_0(\mathbf{r},\mathbf{v}'')] \tag{1.136}$$

which is similar to (1.135), however, it is inhomogeneous and therefore more complicated. The quantities $\mathbf{v}'$ and $\mathbf{v}''$ are the velocities of the ion and the target atom, respectively, after the collision and the inhomogeneity $F_0(\mathbf{r}, \mathbf{v})$ is the nuclear deposited energy distribution for the case of the irradiation with a target atom ($Z_1 = Z_2$) given by the homogeneous equation

$$-\mathbf{e}\,\nabla_r\, F_0(\mathbf{r},\mathbf{v}) = N\int d\sigma_0[F_0(\mathbf{r},\mathbf{v}) - F_0(\mathbf{r},\mathbf{v}') - F_0(\mathbf{r},\mathbf{v}'')]. \tag{1.137}$$

The ion distribution $P_{ion}(\mathbf{r}, \mathbf{v})$ and the nuclear deposited energy distribution $F(\mathbf{r}, \mathbf{v})$ can be characterized by their moments which are determined by integral equations obtained from (1.135)–(1.137) [84–89]. For instance, in the case of a homogeneous ion beam with large lateral extension and incidence normal to the surface (x-y plane), the ion distribution $P_{ion}(z, E)$ depends only on the depth z and the energy (or the amount of the velocity). It can be characterized by its moments $\langle z^n\rangle(E) = \int dz\, z^n\, P_{ion}(z, E)$, where the most prominent ones are the projected range $R_p(E) = \langle z\rangle(E)$ and the straggling of the projected range $\Delta R_p(E) = \left(\langle z^2\rangle(E) - R_p^2(E)\right)^{1/2}$. A quantity to be obtained very easily is the total range $R_t > R_p$ given by

$$R_t(E) = \langle l_p\rangle = \int_0^E \frac{dE'}{S(E')}, \tag{1.138}$$

where $S(E) = S_n(E) + S_e(E)$ is the total energy loss per unit path length. For more about analytical descriptions of the energy losses and of the ion and damage distributions see e.g. [13, 59, 90–92].

1.4.8.2 Computer Simulation

The analytical descriptions given above are very useful to study the ion distribution $P_{ion}(\mathbf{r}, \mathbf{v})$ and the nuclear deposited energy distribution $F(\mathbf{r}, \mathbf{v})$ and their moments for simplified ion-atom interaction potentials and electronic energy losses (see e.g. [84–89]). Nowadays, for practical application the distributions $P_{ion}(\mathbf{r}, \mathbf{v})$ and $F(\mathbf{r}, \mathbf{v})$ (or a related quantity, e.g. the vacancy distribution) are mainly obtained by computer simulation. For the cases of ion irradiation considered here (see Sect. 1.1), where the ion energy is large enough that the binding of the target atoms can be neglected in first approximation, the Monte Carlo (MC) computer simulation based on binary collisions can be applied. MC codes follow the ion trajectory (sufficient for ion distribution) and the recoil trajectories (necessary for the damage distribution) as sequences of binary collisions. This requires the knowledge of the scattering angles $\varphi_1(s)$ and $\varphi_2(s)$ of the colliding atom and the recoil atom, respectively, and of the nuclear and

electronic part of the transferred energy $T_n(s)$ and $T_e(s)$ as functions of the impact parameter s for all combinations of colliding pairs (ion and different kinds of target atoms). In the case of amorphous targets as considered here, the impact parameter s is determined by random numbers according to the probability of the occurrence of the impact parameter s (see e.g. [93]). For energies $E \gg E_{n,cr} \approx 0.01\, Z_1 Z_2 \left(Z_1^{0.23} + Z_2^{0.23}\right) m/m_2\, keV$ [maximum of nuclear stopping power, see Fig. 1.9 and (1.76)], noticeable scattering angles occur only after a path length Δl_p large compared to the interatomic distance in the target. In this case, only one nuclear collision is considered within the path length Δl_p and the electronic part of the transferred energy $T_e(s)$ is replaced by a continuous energy loss $S_e\, \Delta l_p$, where S_e is the electronic stopping power of the moving atom. The advantages of the computer simulation are: all information about the collision cascade is available, the target geometry can be complicated (e.g. layered targets, spatial distribution of target elements) and no simplified descriptions of the binary collision quantities $\varphi_1(s)$, $\varphi_2(s)$, $T_n(s)$, $T_e(s)$ or S_e are necessary. The scattering angles $\varphi_1(s)$ and $\varphi_2(s)$ and the nuclear transferred energy $T_n(s)$ as functions of the impact parameter s are determined by the ion-atom interaction potential V(r) according to (1.21)–(1.23) and (1.29). For V(r), a generalized potential [e.g. (1.11) and (1.16)] or a more accurate individual potential calculated numerically according to (1.11)–(1.14) can be used. However, the latter one requires much more computing time. The electronic stopping power $S_e(E, Z_1, Z_2)$ is sufficiently well known for all Z_1, Z_2 and energies E (see Sect. 1.4.5), but this is not true for the electronic part of the transferred energy $T_e(s, E, Z_1, Z_2)$ as function of the impact parameter s. For low energies ($E \ll E_{e,cr}$) there is the analytic formula of Firsov (1.48), however, it is limited to $Z_1 \approx Z_2$. In order to get an analytical expression of $T_e(s, E, Z_1, Z_2)$ for the low energy region which is more reliable than that given in (1.48), Oen and Robinson [94] suggested the semi-empirical formula

$$T_e(s, E, Z_1, Z_2) = \frac{K_{OR}(Z_1, Z_2, E)}{a_L^2(Z_1, Z_2)} \exp\left[-\frac{0.3\, r_{min}(s, E)}{a_L(Z_1, Z_2)}\right] E^{1/2}, \tag{1.139}$$

where $a_L(Z_1, Z_2)$ is the Lindhard screening length (1.15), $r_{min}(s, E)$ is the minimum distance of approach determined by the ion-atom interaction potential V(r) according to (1.30) and $K_{OR}(Z_1, Z_2, E)$ is a fitting function obtained by the demand that T_e should provide the correct stopping cross section $\hat{S}_e(E, Z_1, Z_2) = 2\pi \int ds s T_e(s, E, Z_1, Z_2)$ according to (1.56). In the approximation $r_{min}(s, E) \approx s$, K_{OR} does not depend on E and both, T_e and $\hat{S}_e$ are proportional to $E^{1/2}$. Equation (1.139) is therefore usually applied to low energies where $\hat{S}_e \sim E^{1/2}$ is valid. A similar expression, applicable to all energies, has been suggested by Posselt [95]

$$T_e(s, E, Z_1, Z_2) = \widehat{S}_e(E) \exp\left[-\frac{0.3\, C_P r_{min}(s, E)}{a_{ZBL}(Z_1, Z_2)}\right] \Big/ \int ds\, 2\pi s \exp\left[-\frac{0.3\, C_P r_{min}(s, E)}{a_{ZBL}(Z_1, Z_2)}\right], \tag{1.140}$$

where $\hat{S}_e$ is the ZBL stopping cross section [13] as used in TRIM / SRIM, $a_{ZBL}(Z_1, Z_2)$ is the ZBL screening length (1.16) and C_P is an empirical parameter given in [95] for Si targets. The advantage of the two formulae (1.139 and 1.140) is that they provide the correct stopping power. With respect to the simulation of the ion and damage distributions in amorphous targets, this is more important than their inaccuracy of the impact parameter dependence. With respect to the impact parameter dependence, the most reliable values of the transferred energies $T_e(s, E, Z_1, Z_2)$ for $E \ll E_{e,cr}$ can be obtained using the modified Firsov theory, however, this needs individual numerical calculations (see (1.47) and (1.49)] for each $Z_1 - Z_2$ combination. In the high energy region ($E \gg E_{e,cr}$) the electronic part of the transferred energy $T_e(s, E, Z_1, Z_2)$ can be calculated numerically using the PASS code (Sigmund and Schinner [27–30]) or the CasP code (Grande and Schiwietz [33–35]), the physical backgrounds of which are briefly given in Sect. 1.3.1.

There are a number of different MC computer simulation codes mentioned for instance in [14]. The most prominent one is the TRIM (1985–1990)/SRIM (1991–2013) code [61]. The physical background described in [13, 93] is essentially the same for all versions of TRIM / SRIM, there are only small changes in the electronic stopping powers caused by fitting newer experimental stopping data. The situation with SRIM-2003 is described by Ziegler in [96]. Obviously, no further changes of the stopping powers have been made in the following versions up to SRIM-2013. The scattering angles and the nuclear transferred energy are determined using the ZBL potential [13] given in (1.11) and (1.16). For the determination of the spatial distribution of the ions and of the defects, two energies are important: the displacement energy E_d necessary for a target atom to leave its lattice site and the final energy E_f which causes an atom to stop. Let us consider a nuclear collision in a space cell i at position $\mathbf{r}_i$. The colliding atom with energy E transfers an energy T_n to the recoil atom and it has the energy $E' = E - T_n$ after the collision. If $T_n > E_d$ and $E' > E_d$ is fulfilled, the recoil leaves its lattice site which means that a vacancy is generated in the space cell i. In the case of $T_n > E_d$ and $E' < E_d$ the recoil also leaves its lattice place, however, the colliding atom is captured to the lattice site which is called replacement collision and no vacancy is generated. For small transferred energies $T_n < E_d$, the recoil is unable to leave its lattice site and T_n only enhances the thermal vibration energy (phonon energy). Finally, if the energy of the colliding atom after the collision E' is smaller or equal to E_f, the colliding atom comes to rest in the space cell i. The spatial distribution of the ions is determined by the number of ions stopped in the space cell i at position $\mathbf{r}_i$ and the vacancy distribution (damage distribution) is given by the number of vacancies generated in the space cell i at position $\mathbf{r}_i$. Usually, the space cell i is a depth layer $z_i \ldots z_{i+1}$ with small thickness d. For a detailed description of TRIM / SRIM and its output see [13].

For very low ion energies (in the order of keV or less), the binding of the target atoms must be taken into account which means that the MC computer simulation based on binary collisions cannot be applied. In this case, the much more computer time consuming molecular dynamics (MD) computer simulations must be used. However, this is not the topic of this book.

1.5 Ion-Crystalline Solid Interaction

In contrast to amorphous targets, the atoms in a crystalline target are well ordered and the binary collisions are no longer statistically independent. Especially, there is a strong correlation of the succeeding collisions if the angle ψ between the actual velocity of the ion and a low index direction or a low index plane of the crystal lattice is smaller or about a critical angle (typically $\lesssim 1°$). The correlation consists in the fact that the impact parameters of succeeding collisions do not change much and consequently a small angle collision is mostly followed by a small angle collision. Therefore, such ions remain in a low index axial channel (axial channeling) or in a low index planar channel (planar channeling) of the crystal until they suffer a series of deflections with increasing angles (dechanneling). The small angle collisions are connected with large impact parameters s and small transferred energies T(s) which means that channeled ions have a lower energy loss per unit path length than ions moving in an amorphous target. For ions incident under an angle ψ lower than the critical angle, a remarkable part of the ions become channeled. Because of their lower energy loss, the depth distribution of the ions and the damage distribution are extended to larger depths and the reduction of the nuclear transferred energy leads to a smaller amount of the damage.

1.5.1 Axial Channeling

The basic concept for an analytical description of the ion motion in a crystalline target under axial and planar channeling conditions was given by Lindhard [97]. Here, only his description of axial channeling is presented which is more important for application (analysis of defects in crystals). It is based on a four-dimensional phase-space statistics, where the elements of the statistics are not atoms but strings of atoms in the low index direction considered. The crystalline target is an ensemble of parallel atomic strings (define the z-direction), statistically distributed in the x-y-plane (transverse space).

First, an **idealized crystal** is considered. It consists of idealized atomic strings without thermal vibrations of the string atoms and the scattering of the ions on the target electrons is not taken into account. In this case the equation of motion of an ion along an atomic string is approximately given by [97]

$$\frac{d\mathbf{p}}{dt} = -\frac{\mathbf{r}}{r}\frac{dU}{dr} \text{ with } U(r) = \frac{1}{d}\int_{-\infty}^{\infty} dz\, V\left[\left(r^2 + z^2\right)^{1/2}\right], \tag{1.141}$$

where $\mathbf{r} = (x, y)$, $\mathbf{p} = (p_x, p_y)$ are the transverse coordinates and momentum (differently defined than in previous Sections !), U(r) is the continuous string potential, V is the ion-atom interaction potential as given in Sect. 1.2.1 and d is the average distance between two succeeding atoms in the string. The momentum p_z in the

direction of the string is approximately constant $p_z \approx m_1 v$ (v is the initial ion velocity, $p_x, p_y \ll m_1 v$). From (1.141) follows that the so called transverse energy

$$E_\perp = \frac{p^2}{2m_1} + U(r) = E\psi^2 + U(r) \tag{1.142}$$

is constant ($p = |\mathbf{p}| = m_1 v \sin\psi \approx m_1 v\, \psi$ because the angle between the actual velocity of the ion and a low index direction $\psi \lesssim 1°$, $E = m_1 v^2/2$) and there exists a minimum distance of approach of the ion to the string $r_{min}(E_\perp)$ given by $U(r_{min}) = E_\perp$. A more detailed treatment [97] shows that the transverse energy $E_\perp$ is approximately conserved for

$$E_\perp \lesssim E\psi_1^2 \quad \text{with } \psi_1 = \left(\frac{2Z_1 Z_2 \in^2}{E\,d}\right)^{1/2}, \tag{1.143}$$

where ψ_1 is a characteristic or critical angle for axial channeling.

Assuming a constant probability within the transverse energy shell ($E_\perp \ldots E_\perp + dE_\perp$) in the transverse phase space (**r**, **p**) (that means the equilibrium is reached), the statistical average of a physical quantity f(**r**, **p**) in the four-dimensional phase space (note that the motion in z-direction is not a statistical one but determined by $z = vt$ and $p_z = m_1 v$) is obtained by

$$\langle f\rangle(E_\perp) = \int_{r_{min}(E_\perp)}^{r_0} \frac{dr\,2r}{r_0^2 - r_{min}^2(E_\perp)} \int_0^{2\pi} \frac{d\varphi_r}{2\pi} \int_0^{2\pi} \frac{d\varphi_p}{2\pi} f\left[r, \varphi_r, p(E_\perp, r), \varphi_p\right] \tag{1.144}$$

[97] with $p(E_\perp, r) = \{2m_1[E_\perp - U(r)]\}^{1/2}$ according to (1.142). The radius r_0 is given by the area belonging to one string $\pi r_0^2 = 1/(Nd)$ and (r, φ_r) and (p, φ_p) are the polar coordinates of **r** and **p.** According to Lindhard [97], the equilibrium in the transverse energy shell is reached after a depth $z_{eq} \approx 1000$ atomic layers or less, which limits the validity of (1.144) to depths $z > z_{eq}$.

For an ion incident in the crystalline target under an angle ψ_{in} with respect to a low index direction, the passage through the surface (z = 0) causes a distribution of transverse energies

$$g(E_\perp, z = 0) = \int_0^{r_o} \frac{dr\,2r}{r_0^2} \delta\left(E_\perp - E\psi_{in}^2 - U(r)\right), \tag{1.145}$$

where δ is the delta function. In the case of the idealized crystal, this distribution does not change with increasing depth because the transverse energy is conserved (channeling).

In the **real crystal**, the **transverse energy is not conserved**. It changes caused by scattering on the thermally vibrating lattice atoms, on the target electrons and on different kinds of defects if present. Therefore, also the distribution $g(E_\perp, z)$ of the

transverse energy changes with depth (dechanneling) described by the integro-differential equation (master equation) [97]

$$\frac{\partial g(E_\perp, z)}{\partial z} = \int_0^\infty dE'_\perp \left[P(E_\perp, E'_\perp, z) g(E'_\perp, z) - P(E'_\perp, E_\perp, z) g(E_\perp, z)\right]. \quad (1.146)$$

The probability $P(E'_\perp, E_\perp, z)\, dE'_\perp$ for the transition of the transverse energy $E_\perp$ to $E'_\perp \ldots E'_\perp + dE'_\perp$ at depth z is determined by all scattering processes mentioned above which are responsible for the dechanneling. The distribution $g(E_\perp, z)$ is derived by solving (1.146) with the initial distribution given by (1.145).

A quantity of interest in following Chapters is the Rutherford backscattering minimum yield $\chi_{min}(z)$ as a function of the depth z. It is obtained from the distribution $g(E_\perp, z)$ for normal incidence [$\psi_{in} = 0$ in (1.145)] by

$$\chi_{min}(z) = \int_0^\infty dE_\perp\, g(E_\perp, z) \pi_{in}(E_\perp), \quad (1.147)$$

where π_{in} is the relative probability (with respect to an amorphous target) of an ion with transverse energy $E_\perp$ to hit a thermally vibrating lattice atom

$$\pi_{in}(E_\perp) = \frac{r_0^2}{r_0^2 - r_{min}^2(E_\perp)} \int_{r_{min}(E_\perp)}^{r_0} dP_{th}(r) \quad (1.148)$$

and $dP_{th}(r)$ is the spatial distribution of the thermally vibrating atoms. For details and more information concerning the theory of Lindhard and its application see [97, 98].

The two problems of the Lindhard theory are the difficulty of the numerical solution of (1.146) for realistic transition probabilities and the limitation of its validity to depths $z > z_{eq} \approx 1000$ atomic layers as mentioned above. Therefore, a modified master equation approach has been developed [98–100] which is more easy to handle numerically and overcomes the problem for small depths $z < z_{eq}$. It is based on the Lindhard theory mentioned above, however, discrete transverse energy intervals i are used instead of the continuous transverse energy $E_\perp$. This means that the distribution $g(E_\perp, z)$ becomes an array $g_i(z)$ and the transition probability $P(E'_\perp, E_\perp, z)$ describing the dechanneling becomes a matrix $P_{j,i}(z)$. Three contributions to $P_{j,i}(z)$, caused by the scattering on lattice atoms, electrons and point defects, are taken into account. The contributions from the elastic scattering of the ion on thermally vibrating lattice atoms and on point defects (displaced lattice atoms) are calculated using the individual ion-atom interaction potential [8] according to (1.11)–(1.14). Opposite to amorphous targets, in the case of crystalline targets and channeling conditions, the scattering of the ions on the target electrons must be taken into account because the nuclear scattering is remarkably suppressed. The corresponding contribution to $P_{j,i}(z)$ is determined using the angular spread (1.134) given

by Lindhard [57]. The problem that the Lindhard theory is not valid for depths $z < z_{eq}$ (the equilibrium in the transverse energy shell is only reached at $z \approx z_{eq}$) is overcome in the following way. For perfect crystals (no defects), the minimum yield $\chi_{min,sim}(z_{eq})$ at depth z_{eq} is determined by computer simulation using the individual potential [8] for the nuclear scattering and the angular spread given by (1.134) for the additional angular deflection due to electronic scattering. Then, the initial distribution $g_i(0)$ is modified in this way that the calculated minimum yield $\chi_{min}(z_{eq})$ is equal to the simulated minimum yield $\chi_{min,sim}(z_{eq})$ at depth z_{eq}. It has been shown that $z_{eq} = 3000$ Å is a good choice [100] (the results are insensitive to a small variation of the value of z_{eq}). Due to this modification of the master equation approach, a good agreement of the calculated minimum yield with completely simulated and measured $\chi_{min}(z)$ for perfect crystals has been obtained [100].

The modified master equation approach of the dechanneling [98–100], briefly described above, is the basis for the computer code DICADA (Dechanneling In Crystals And Defect Analysis). It takes into account two different depth distributions $n_{da1}(z)$ and $n_{da2}(z)$ of point defects (displaced atoms) of different kinds. The different kinds of point defects considered are: displaced atoms randomly distributed within the lattice cell; displaced atoms with a fixed displacement distance with and without thermal vibration; and displaced atoms with up to 10 different displacement distances. Using DICADA it is possible to calculate the Rutherford backscattering minimum yield $\chi_{min}(z)$ as a function of the depth z for the perfect crystal or for crystals with point defects if the defect distribution $n_{da1}(z)$ (and $n_{da2}(z)$ if present) and the parameters for the corresponding kinds of point defects are known. Vice versa, it is possible to calculate $n_{da1}(z)$ if $\chi_{min}(z)$ is measured, $n_{da2}(z)$ is known or not present and the parameters for the kinds of point defects are known (defect analysis). A full description of the physical background and the input and output of DICADA is given in [99, 100].

1.5.2 Ion Range and Damage Distribution

The spatial distributions of the ions and of the damage in crystalline targets are nowadays mainly determined by computer simulation. For the cases of ion irradiation considered here, where the ion energy is large enough that the binding of the target atoms can be neglected, the computer simulation based on binary collisions can be applied. It is similar to the MC computer simulation for amorphous targets described in Sect. 1.4.8.2. In both cases, the interatomic interaction potential (provides the scattering angles and the nuclear transferred energy) and the electronic energy loss are required. The main difference is that in the case of crystalline targets the impact parameters are not fully chosen by means of statistics but they are mainly determined by the lattice sites of the crystal lattice. There is only a slight statistical influence given by the deviation of the position of the target atoms from the lattice sites due to their thermal vibrations. Another difference concerns the electronic energy loss. In comparison with amorphous targets, for crystalline targets

the impact parameter dependence of the electronic part of the transferred energy $T_e(s)$ must be known more accurately because small impact parameters are suppressed due to the channeling effect; that means a continuous energy loss cannot be used at all. There exist some binary collision computer codes for crystalline targets mentioned in [14]. The most used codes are MARLOWE [101] developed by Robinson, Torrens and Oen [94, 102, 103] and Crystal-TRIM developed by Posselt [95, 104]. Usually, the MARLOWE code uses the Moliere potential [105] but it also allows the alteration of the potential function. The electronic part of the transferred energy $T_e(s)$ is given by (1.139). Because of the limited validity of (1.139), MARLOW can only be applied to the low ion energy region $E \ll E_{e,cr}$. The Crystal-TRIM code is based on the ZBL potential [13] given in (1.11) and (1.16) and on the electronic part of the transferred energy $T_e(s)$ given by (1.140). It can be applied for all ion energies, however, only for targets, where the parameter sets for $T_e(s, E, Z_1, Z_2)$ are known (for Si in [95]). Both codes simulate the whole collision cascade and therefore they are able to provide the full information about the spatial distributions of the ions and the damage (displaced atoms). For details concerning the physical background and the application of MARLOW and Crystal-TRIM see [94, 102, 103] and [95, 104], respectively.

1.6 Summary

In the ion energy range considered here, the interaction of the ion with the whole solid can be described as a sequence of binary collisions where the elastic (nuclear) and inelastic (electronic) contributions to the binary collisions can be treated separately. There exist two characteristic ion energies $E_{n,cr} \approx 0.01 Z_1 Z_2 \left(Z_1^{0.23} + Z_2^{0.23}\right)(m_1 + m_2)/m_2$ keV and $E_{e,cr} \approx 22(m_1/u) Z_1 Z_2^{0.4}$ keV (u is the atomic mass unit) for the nuclear and electronic scattering, respectively, where the ratio $E_{e,cr}/E_{n,cr}$ varies between about 100 and 3000 for all possible projectile-target combinations.

The nuclear scattering is determined by the ion-atom interaction potential. For ion energies $E \gg E_{n,cr}$ it can be approximated by the Coulomb potential between the two nuclei, however, in the case of $E \lesssim E_{n,cr}$ the screening due to the electrons of the ion and target atom must be taken into account. The nuclear stopping cross section has a maximum for $E \approx E_{n,cr}$.

The processes responsible for the electronic scattering are quite different for ion energies below and above $E_{e,cr}$. While the excitation and ionization of the target atom is the dominating process for $E \gg E_{e,cr}$, the classical exchange of the electrons of the ion and the target atom mainly determines the electronic scattering for $E \ll E_{e,cr}$. Near the maximum of the electronic stopping cross section, positioned at $E \approx E_{e,cr}$, both processes are important for the electronic scattering. Because $E_{e,cr} \gg E_{n,cr}$ is true for all projectile-target combinations, the nuclear contribution to the stopping can always be neglected for $E \gtrsim E_{e,cr}$.

Besides the introduction into the physical processes of the ion-solid interaction, some formulae and figures are given for practical use.

References

1. L.H. Thomas, Proc. Cambridge Phil. Soc. **23**, 542 (1927)
2. E. Fermi, Z. Phys. **48**, 73 (1928)
3. P.A.M. Dirac, Proc. Cambridge Phil. Soc. **26**, 376 (1930)
4. P. Gombás, *Die statistische Theorie des Atoms* (Springer, Wien, 1949)
5. P. Gombás, Handbuch der Physik **36**, 109 (1956)
6. H. Jensen, Z. Physik **89**, 713 (1934)
7. H. Jensen, Z. Physik **93**, 232 (1935)
8. K. Gärtner, K. Hehl, Phys. Stat. Sol. (b) **94**, 231 (1979)
9. E. Clementi, C. Roetti, At. Data Nucl. Data Tables **14**, 177 (1974)
10. O.B. Firsov, Zh Eksp, Teor. Fiz. **33**, 696 (1957)
11. O. B. Firsov, Zh. Eksp. Sov. Phys.-JETP 6 (1958) 534
12. J. Lindhard, V. Nielsen, M. Scharff, Mat. Phys. Med. Dan. Vid. Selsk. **36**, 10 (1968)
13. J.F. Ziegler, J.P. Biersack, U. Littmarck, *The Stopping and Range of Ions in Solids*, vol. 1 (Pergamon Press, New York, 1985)
14. W. Eckstein, *Computer Simulation of Ion-Solid Interactions*. Springer Series in Materials Science, vol. 10 (Springer, Berlin, 1991)
15. D.J. O'Connor, J.P. Biersack, Nucl. Instr. and Meth. B **15**, 14 (1986)
16. E. Rutherford, Phil. Mag. **21**, 669 (1911)
17. C.G. Darwin, Phil. Mag. **27**, 499 (1914)
18. J.F. Ziegler, R.F. Lever, Thin Solid Films **19**, 291 (1973)
19. W.K. Chu, J.W. Mayer, M.A. Nicolet, *Backscattering Spectrometry* (Academic Press, INC, New York, 1978)
20. P. Loftager, J.E. Andersen, personal communication, similar results as given in P. Loftager, F. Besenbacher, O.S. Jensen, V.S. Sørensen, Phys. Rev. A **20**, 1443 (1979)
21. D.A. Liberman, D.T. Cromer, J.T. Waber, Comp. Phys. Commun. **2**, 107 (1971)
22. U. Specht, M. Busch, J. Seifert, A. Schüller, H. Winter, K. Gärtner, R. Wlodarzyk, M. Sierka, J. Sauer, Phys. Rev. B **84**, 125440 (2011)
23. G. Gordon, Y.S. Kim, J. Chem. Phys. **56**, 3122 (1972)
24. Y.S. Kim, R.G. Gordon, J. Chem. Phys. **60**, 4323 (1974)
25. A. Schüller, K. Gärtner, H. Winter, EPL **81**, 37007 (2008)
26. N. Bohr, Phil. Mag. **25**, 10 (1913)
27. H.H. Mikkelsen, P. Sigmund, Nucl. Instr. Meth. **B27**, 266 (1987)
28. A. Schinner, P. Sigmund, Eur. Phys. J. D **56**, 41 (2010)
29. A. Schinner, P. Sigmund, Eur. Phys. J. D **56**, 51 (2010)
30. A. Schinner, P. Sigmund, Eur. Phys. J. D **58**, 105 (2010)
31. K. Dettmann, M.T. Robinson, Phys. Rev. B **10**, 1 (1974)
32. K. Dettmann, Z. Physik A **272**, 227 (1975)
33. G. Schiwietz, P.L. Grande, Nucl. Instr. Meth. **B153**, 1 (1999)
34. P.L. Grande, G. Schiwietz, Nucl. Instr. Meth. **B195**, 55 (2002)
35. P.L. Grande, G. Schiwietz, Nucl. Instr. Meth. **B267**, 859 (2009)
36. O.B. Firsov, Zh Eksp, Teor. Fiz. **36**, 1517 (1959)
37. O. B. Firsov, Zh. Eksp. Sov. Phys.-JETP 36 (1959) 1076
38. K.B. Winterbon, Canad. J. Phys. **46**, 2429 (1968)
39. I.M. Cheshire, G. Dearnaley, J.P. Poate, Proc. Roy. Soc. **A311**, 47 (1969)

40. C.P. Bhalla, J.N. Bradford, G. Reese, in *Atomic Collision Phenomena in Solids*, ed. by D.W. Palmer, M.W. Thompson, P.D. Townsend (North-Holland, Amsterdam, 1970), p. 361
41. D.J. Land, J.G. Brennan, Nucl. Instr. Meth. **132**, 89 (1976)
42. N. Bohr, Mat. Fys. Medd. Dan. Vid. Selsk. 18 (1948) No.8
43. P. Sigmund, K.B. Winterbon, Nucl. Instr. Meth. **B12**, 1 (1985)
44. L. Landau, J. Phys. USSR **8**, 201 (1944)
45. W. Bothe, Z. Phys. **5**, 63 (1921)
46. G. Wentzel, Ann. Phys. **69**, 335 (1922)
47. W.T. Scott, Rev. Mod. Phys. **35**, 231 (1963)
48. P. Sigmund, K.B. Winterbon, Nucl. Instr. Meth. **119**, 541 (1974)
49. H.A. Bethe, Ann. Phys. **5**, 325 (1930)
50. H.A. Bethe, Z. Phys. **76**, 293 (1932)
51. F. Bloch, Ann. Phys. **16**, 285 (1933)
52. F. Bloch, Z. Phys. **81**, 363 (1933)
53. W.K. Chu, D. Powers, Phys. Lett. **40A**, 23 (1972)
54. Stopping Powers for Electrons and Positrons, ICRU Report No. 37 (1984)
55. J. Lindhard, A.Winter, Mat. Fys. Medd. Dan. Vid. Selsk. **34**, 4 (1964)
56. J.F. Ziegler, J. Appl. Phys/Rev. Appl. Phys. **85**, 1249–1272 (1999)
57. J. Lindhard, Mat. Phys. Med. Dan. Vid. Selsk. 28 (1954) No.8
58. J. Lindhard, M. Scharff, Phys. Rev. **124**, 128 (1961)
59. E. Bonderup, *Penetration of Charged Particles Through Matter*. Lecture Notes (Aarhus, 1978)
60. I.S. Tilinin, Phys. Rev. A **51**, 3058 (1995)
61. SRIM available online: www.srim.org
62. W. Brandt, M. Kitagawa, Phys. Rev. **25B**, 5631 (1982)
63. S.R. Lee, R.R. Hart, Nucl. Instr. Meth. **B28**, 470 (1987)
64. D.W. Hetherington, Nucl. Instr. Meth. **B115**, 319 (1996)
65. J.H. Ormrod, H.E. Duckworth, Can. J. Phys. **41**, 1424 (1963)
66. B. Fastrup, P. Hvelplund and C. A. Sautter, Mat. Phys. Med. Dan. Vid. Selsk. 35 (1966) No.10
67. P. Hvelplund, B. Fastrup, Phys. Rev. **165**, 408 (1968)
68. F. Eisen, Can. J. Phys. **46**, 561 (1968)
69. D. Ward, H.R. Andrews, I.V. Mitchell, W.N. Lennard, R.B. Walker, N. Rud, Can. J. Phys. **57**, 645 (1979)
70. D.J. Land, D.G. Simons, J.G. Brennan, M.D. Brown, Phys. Rev. A **22**, 68 (1980)
71. D.J. Land, J.G. Brennan, At. Data Nucl. Data Tables **22**, 235 (1978)
72. W. Börsch-Supan, J. Res. Natl. Bur. Stand. **65B**, 245 (1961)
73. J. Lindhard, Phys. Scr. **32**, 72 (1985)
74. P.V. Vavilov, Zh Eksp, Teor. Fiz. **32**, 920 (1957)
75. P.V. Vavilov, Zh Eksp, Sov. Phys. JETP **5**, 749 (1957)
76. S.M. Seltzer, M.J. Berger, in *Studies in penetration of Charged Particles in Matter*, vol. 1133 (National Academy of Sciences, the National Research Council Publications, 1964), p. 187
77. J. Lindhard, V. Nielsen, Mat. Phys. Med. Dan. Vid. Selsk. **38**, 9 (1971)
78. L. Meyer, M. Klein, R. Wedell, Phys. Stat. Sol. (B) **83**, 451 (1977)
79. J. Lindhard, V. Nielsen, M. Scharff, Mat. Phys. Med. Dan. Vid. Selsk. **36**, 10 (1968)
80. D. Goebl, K. Khalal-Kouache, D. Roth, E. Steinbauer, P. Bauer, Phys. Rev. A **88**, 032901 (2013)
81. L. Meyer, Phys. Stat. Sol. (b) **44**, 253 (1971)
82. P. Sigmund, K.B. Winterbon, Nucl. Instr. Meth. **119**, 541 (1974)
83. G. Amsel, G. Battistig, A. L'Hoir, Nucl. Instr. Meth. **B201**, 325 (2003)
84. J. Lindhard, M. Scharff, H. E. Schiøtt, Mat. Phys. Med. Dan. Vid. Selsk. **33**, 14 (1963)
85. J.B. Sanders, Can. J. Phys. **46**, 455 (1968)
86. U. Littmark, J.F. Ziegler, Phys. Rev. A **23**, 64 (1981)

87. P. Sigmund, M.T. Matthies, D.L. Phillips, Radiat. Eff. **11**, 39 (1971)
88. J. Lindhard, V. Nielsen, M. Scharff, P.V. Thomsen, Mat. Phys. Med. Dan. Vid. Selsk. **33**, 10 (1963)
89. K. B. Winterbon, P. Sigmund, J.B. Sanders, Mat. Phys. Med. Dan. Vid. Selsk. **37**, 14 (1970)
90. P. Sigmund, *Particle Penetration and Radiation Effects*, vol. 2. Springer Series in Solid State Science (Springer International Publishing, Switzerland 2014)
91. M.A. Kumakhov, F.F. Komarov, *Energy loss and Ranges in Solids* (Gordon & Breach Science Publishers, New York, 1981)
92. M. Nastasi, J.W. Mayer, J.K. Hirvonen, *Ion-Solid Interactions: Fundamentals and Applications* (Cambridge University Press, Cambridge, 1996)
93. J.P. Biersack, L.G. Haggmark, Nucl. Instr. Meth. **174**, 257 (1980)
94. O.S. Oen, M.T. Robinson, Nucl. Instr. Meth. **132**, 647 (1976)
95. M. Posselt, Radiat. Eff. **130**(131), 87 (1994)
96. J.F. Ziegler, Nucl. Instr. Meth. **B219–220**, 1027 (2004)
97. J. Lindhard, Mat. Fys. Medd. Dan. Vid. Selsk. **34**, 14 (1965)
98. K. Gärtner, Chapter 1 in *High Energy Ion Beam Analysis in Solids*, ed. by G. Götz, K. Gärtner (Akademie-Verlag Berlin, 1988)
99. K. Gärtner, Nucl. Instr. Meth. **B132**, 147 (1997)
100. K. Gärtner, Nucl. Instr. Meth. **B227**, 522 (2005)
101. MARLOW available online: www.oecd-nea.org/tools/abstract/detail/psr-0137
102. M.T. Robinson, I.M. Torrens, Phys. Rev. B **9**, 5008 (1974)
103. M.T. Robinson, Phys. Rev. B **40**, 10717 (1989)
104. M. Posselt, Nucl. Instr. Meth. **B96**, 163 (1995)
105. G. Molière, Z. Naturforsch. **A2**, 133 (1947)

Chapter 2
Models for the Description of Track Formation

Christian Dufour and Marcel Toulemonde

Abstract The different models developed to describe track formation induced by swift heavy ions will be presented. The macroscopic ones are the Coulomb explosion model, the bond weakening (BW) model, the exciton self-trapping (STX) model, the concept of reduced electronic energy loss, the analytical thermal spike model, the IDEA (Ionization Diffusion-Explosion-Amorphization) model, the inelastic thermal spike model (i-TS) and to finish microscopic descriptions using molecular dynamic (MD) calculations. All the models were applied to describe the track formation in different kinds of materials (metals, semiconductors or insulators), while additionally the i-TS model and MD calculations were used to describe the sputtering yield. It will be shown that the initial energy deposition plays an important role in the different descriptions and that there is no simple link between the energy deposited in the electronic and later in the atomic system. The large number of models presented here shows by itself that we are far away from a complete description of track formation. So the ambition here is just to give a present status of the different models.

2.1 Introduction

When irradiating a material with swift heavy ions, four stages have to be considered as depicted in Fig. 2.1. In the following it will be tried to describe how the energy deposited in the electrons in 10^{-16} s induces a nanometric transformation of the irradiated material called ion track. Such track is a discontinuous or continuous trail of defects [1] resulting from a dense electronic excitation, deposited in a short time and in nanometric space. Experimental results of track formation in various

C. Dufour · M. Toulemonde (✉)
Centre Interdisciplinaire de Recherche sur les Ions, les Matériaux et la Photonique (CIMAP), CEA-CNRS-ENSICAEN-Université de Caen, 14070 Caen, France
e-mail: toulemonde@ganil.fr

C. Dufour
e-mail: christian.dufour@ensicaen.fr

© Springer International Publishing Switzerland 2016

W. Wesch and E. Wendler (eds.), *Ion Beam Modification of Solids*,
Springer Series in Surface Sciences 61,
DOI 10.1007/978-3-319-33561-2_2

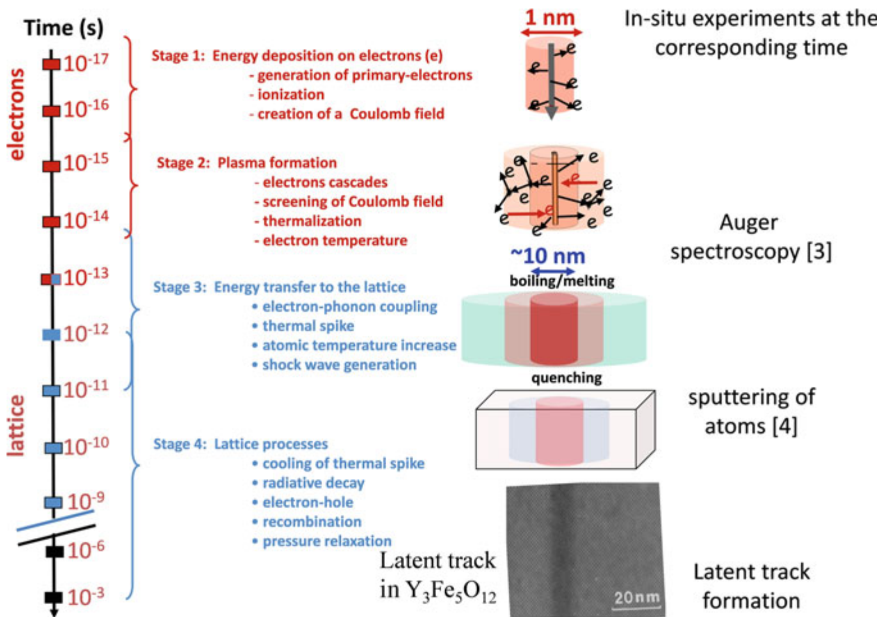

Fig. 2.1 Description of the different processes related to the energy deposition to the electrons and its relaxation to the lattice atoms. This figure is a combined picture from the paper of Zhang et al. [2] and of a track observed in $Y_3Fe_5O_{12}$ [161]. The column called "in situ experiments" account for Auger spectroscopy that probes the electron temperature at 10^{-14} s [162] and for atom sputtering [163] that probes indirectly the atomic temperature between 10^{-13} and 10^{-11} s. Tracks are observed in rest, i.e. after at least one day

materials will be reported in Part III of this book. As compared to nuclear collisions for which damage results from a direct atom–atom interaction, the track resulting from this electronic excitation is a four step process (Fig. 2.1) [2]: first, the incident ions transfer their energy to the electrons of the target by ion-electron collisions, second by electron-electron collisions this energy is shared among other cold electrons, third it is transferred to the lattice by electron-phonon coupling and fourth it dissipates among the atoms, inducing a spike along the ion trajectory. The energy is deposited in the electrons within 10^{-16} to 10^{-15} s and then transferred to the lattice atoms within 10^{-13} to 10^{-11} s. Our goal in this chapter is to present the different models that have been proposed to describe the latent track formation resulting from this four step process. A lot of questions are still open because it is not possible to make experiments within this short time scale within a nanometer volume and furthermore to develop microscopic models taking into account electron and atom motion at the same time. So it is necessary to proceed step by step in order to present the models that can provoke more clever experiments.

2.2 Electronic Energy Deposition

2.2.1 Electronic Energy Loss

Before any model development, it is necessary to know the slowing down of an ion per unit length (dE/dx). During a collision the incident ion with an energy E_i can transfer an energy E_e to electrons of the target with a probability $\sigma(E_i,E_e)$ [3–6]. The average energy $\langle E_{eav} \rangle$ deposited in the electronic system over a path length *dr,* small enough to allow a single collision, is

$$\langle E_{eav} \rangle = N\,dr \int_0^{E_{em}} E_e\,\sigma(E_i, E_e) dE_e \qquad (2.1)$$

where N is the number of scattering centers per unit volume, E_{em} the maximum energy transfer to the electrons, calculated by the kinematics of an ion-electron collision. Therefore the energy loss of the incident ion (dE/dx) is equal to $\langle E_{eav} \rangle$/dr. Consequently the energy deposited to the target electrons is $S_e = -$dE/dx. The probability $\sigma(E_i, E_e)$ is deduced from Coulomb interaction between the incident ion and the electrons of the target atoms, described by Bohr [4] and Lindhard et al. [5, 6]. All descriptions take into account the effective charge states Z_1^* of the incident ions which are the result of a competition between electron stripping and electron capture determined by the ion velocity compared to the electron velocity of the target atoms. The evolution of the effective ion charge state as a function of its velocity is described either microscopically [7, 8] or macroscopically [9]. A continuous model of the energy loss process is based on the well known theories of Bohr and Lindhard, Scharff and Schiøtt [5, 6] and the electronic energy deposited in the target $S_e = -$dE/dx is calculated with the SRIM (Stopping and Ranges of Ions in Matter) code [10, 11]. The parameters necessary for calculations in the framework of this code have to be determined experimentally from fits of energy loss measurements. In a more recent development limited only to the electronic energy loss (the CasP code [8, 12]), the main input data are the projectile screening function, in the case of dressed ions, the electron density and the set of oscillator strengths for each sub-shell. The authors proposed a general interpolation procedure between close and distant collisions by introducing additive connecting functions. Thus, expressions derived for small and large impact parameters can be smoothly joined to a simple expression valid for all impact parameters.

The differences of the values of the electronic energy deposition per ion and unit length, S_e, calculated with the SRIM and CasP codes are illustrated in Fig. 2.2 for the example of Xe irradiation in CaF_2. The main features are on the one hand a difference by around ±10 % of S_e for beam energy larger than 1 MeV/u, and on the other hand a variation by a factor of 2 of S_e at energies around 0.01 MeV/u. Such variation in the electronic energy loss in this low energy regime depends strongly on the stopping material in which the atoms are slowing down [13]. It should be mentioned that in the lower energy range (around 0.005 MeV/u) the absolute value

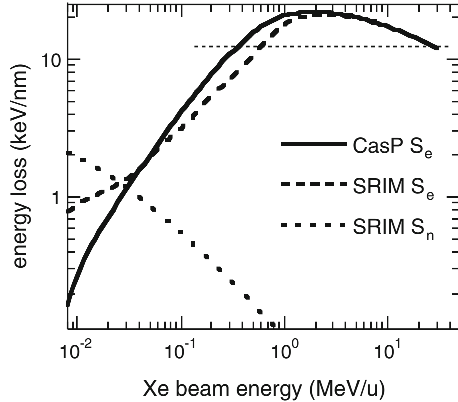

Fig. 2.2 Nuclear and electronic energy losses for Xe in CaF_2: comparison of the electronic energy loss calculated by SRIM [14] and by CasP [164]. The horizontal dotted line at $\sim$12 keV nm^{-1} shows that same electronic energy loss can be reached with two different ion velocities

of electronic energy loss is smaller than the nuclear energy deposition per ion and unit length, S_n, as seen in Fig. 2.2 [14]. It should be noted that recent measurements of particle ranges in materials [15] at $\sim$0.025 MeV/u are in favor of the CasP code [12]. Moreover such predictions have been confirmed by Sigmund [16, 17] since the electronic stopping cross section may be determined from the inverted ion-target system by applying the concept of reciprocity. The principle of reciprocity is based on the invariance of the inelastic excitation in ion-atom collisions against interchange of projectile and target, and is applicable in the low-velocity regime ($E < 0.025$ MeV/u) where the projectiles are neutral and the probability for electron loss is small. These differences can alter drastically any quantitative track description if the exact values of the electronic energy loss are not taken into account.

2.2.2 Radial Energy Distribution

For a given nominal S_e value, the energy density deposited in the electronic system strongly depends on the ion velocity, called velocity effect [18–26]. The target volume in which the kinetic energy of the ions is deposited to the kicked-off electrons of the target, the so-called δ-ray electrons, becomes larger with increasing ion velocity. Using Monte Carlo (MC) calculations, Katz and Kobetich [19, 20] and Fain et al. [21] have determined the radial distribution of the energy deposited in the electrons by calculating the evolution of the kinetic energy in the electron cascades as a function of the radial distance ($\sim$1 μm) and the time ($\sim 10^{-15}$ to 10^{-14} s) [22, 23]. These Monte-Carlo calculations have been updated by Kraft and Krämer [24] and Gervais and Bouffard [23]. The calculations stop when the energy given to an electron by a collision is smaller than the ionization potential which is in the order of 10 eV. Figure 2.3a presents the evolution of the dose in Gray versus the radial distance from the ion axis. Gray is usually defined as the energy deposited per

kilogram of matter (J/kg). The unit (J/kg) can be expressed in eV/at. These curves result from Monte Carlo calculations [25] for the same value of electronic energy loss (~ 11.3 keV nm^{-1}) at two different ion energies per nucleon in mica. Since the volume in which the energy is deposited is smaller at low energy than at high energy, the energy density deposited in the electrons is the larger the lower the ion energy is.

Fitting the results of Monte Carlo calculations [19, 20], an analytical formula has been proposed by Zhang et al. [22] and Waligorski et al. [26] that describes the energy distribution versus the radial distance from the ion axis,

$$D_0(r) = (B/r)\,(1 - (r + r_0)/(r_m + r_0))^{1/\alpha}/(r + r_0). \tag{2.2}$$

Here $D_0(r)$ is the dose deposited at a radial distance r from the ion path, r_0 is the range of electrons having the ionization energy of the target, r_m is the maximum range of the δ ray electrons in the considered matter and α is a constant depending on the velocity of the incident particle. The dose distribution $D_0(r)$ is corrected by a factor (1 + $K(r)$) to take into account the missing dose at small radial distances (~ 1 nm) [26], leading to an energy A(r) given to the electrons per unit volume

$$A(r) = D_0(r)\,(1 + K(r)) \tag{2.3}$$

with B a normalization constant ensuring that the integration of $A(r)$ over the radial distance is equal to S_e in cylinder geometry.

$A(r)$ can be calculated versus the radius for each material [22]. Figure 2.3b shows the fraction of S_e deposited in the electronic system versus the radial distance from the ion trajectory for vitreous SiO_2 irradiated with different ion energies per nucleon [27].

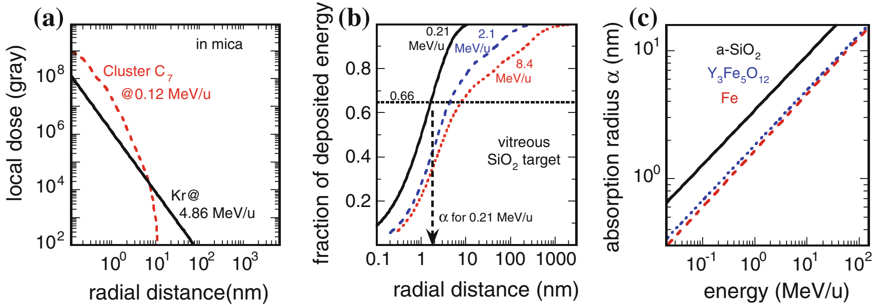

Fig. 2.3 **a** Radial distribution of the energy deposited in the electrons in mica for two different beam energies (from Bouffard et al. [25]). The lines are fits of the calculation results. **b** Fraction of energy deposited in the electrons of vitreous SiO_2 irradiated at different energies as a function of radial distance from ion trajectory [27]. The calculations assume cylindrical geometry and are based on Monte Carlo calculations [26]. **c** Evolution of a cylinder radius α in which 66 % of the initial energy is deposited in the electrons, versus beam energy for vitreous SiO_2 (a-SiO_2), $Y_3Fe_5O_{12}$ and Fe

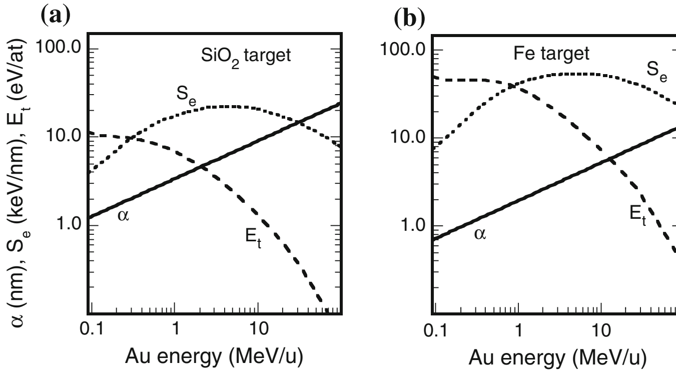

Fig. 2.4 S_e, α, and the energy deposited in the electrons (E_t) versus beam energy for Au irradiation of **a** vitreous SiO_2 and **b** Fe

To estimate the effect of the ion velocity, a cylinder of radius α in which 66 % of the electronic energy loss is stored, has been defined (Fig. 2.3b). This criterion assumes that ~2/3 of the energy deposited in the electrons is located in the core of the track and ~1/3 in the halo of the track as shown in [27]. As it can be seen in Fig. 2.3b, the deposition radius increases with increasing energy, i.e. larger ion velocities lead to electronic energy deposition in a larger volume resulting in a lower energy density. Figure 2.3c shows α values as a function of the specific beam energy for different materials. These α values follow roughly a power law of the specific energy ($\alpha \sim E^{0.4}$), i.e. seem to be almost proportional to the ion velocity. It should be noted that the extrapolation of the analytical formula of the radial energy distribution from Waligorski et al. [26] to low energies ($E < 0.1$ MeV/u) is questionable and in this energy regime new Monte Carlo calculations are needed.

As an example, S_e and the absorption radius α are plotted in Fig. 2.4 versus the Au energy for an irradiation of vitreous SiO_2 (Fig. 2.4a) and pure Fe (Fig. 2.4b). The energy E_t deposited in the electrons is equal to the electronic energy loss S_e divided by $\pi\alpha^2$, the area in which the slowing down energy of the ion is given to the electrons normalized with the atomic density of the material. E_t is shown in Fig. 2.4 in eV/at for SiO_2 and Fe. At 1 MeV/u the energy deposited in the electrons is $E_t \sim 7$ eV/at for SiO_2 and ~40 eV/at for Fe (Fig. 2.4) corresponding to 5.6×10^4 and 3.2×10^5 J cm^{-3}, respectively. Assuming a mean value of ~2×10^5 J cm^{-3} this leads to a power of ~2×10^{19} W cm^{-3} within a time of 10^{-14} s. Such a power has to be compared to femtosecond laser irradiation: as an example, melting of Ni is expected when it is irradiated by a femtosecond laser (200 fs) with a power of 0.43 J/cm^2 [28]. The depth of the light absorption is in the order of 10^{-6} cm in a metal and so the energy density is 4.3×10^5 J/cm^3, i.e. a power of ~2×10^{18} W/cm^3 which is one order of magnitude lower than that for ion irradiation. So, as already mentioned [29, 30], it is reliable to take advantage of experiments and models developed to describe the transformation of matter by femtosecond lasers in order to understand track formation and sputtering due to ion

irradiation. However, the main difference in these two processes of electronic excitation is the geometry and the size: with ions this energy is deposited in a cylinder with some nanometer radius, while fs laser irradiation has a planar geometry with a beam spot of ~1 μm and a minimum depth of light absorption of ~10 nm. Such change in the geometry influences the cooling rate which is one order of magnitude larger in cylinder geometry as compared to a planar one.

2.3 Description of Track Formation

The track in a material is a trail of damage resulting from a nanometric, dense and shortly created electronic excitation and was observed for the first time by Silk and Barnes [31]. Defects created by individual electronic excitation as observed by classical irradiations (gamma irradiation or low Z ions) are not considered.

The electronic energy loss S_e with its radial distribution is the initial stage of any track description which will be presented now. Several macroscopic models have been proposed: Coulomb explosion [32–34], reduced electronic energy loss [25], self-trapped excitons [35–38], bond weakening [39, 40] and the thermal spike model developed by Szenes [41, 42] considering only the process starting when the energy is already transferred to the atoms. Then Canut and Ramos [43] introduced the concept of effective electronic energy loss by analytically solving the diffusion equation for the temperature distribution of the electrons and considering the energy transfer to the atoms. Toulemonde et al. [27, 44], Trautmann et al. [45], Meftah et al. [46, 47], Dufour et al. [48, 49] and Wang et al. [50] have numerically solved [51] the complete two coupled differential equations describing heat diffusion within the electronic and atomic subsystems of the solid. The thermal spike model is subject of intense research [27, 30] in order to study its strengths and weaknesses or to develop alternative models [52, 53]. It is not the aim of this chapter to describe all the models in detail, but we shall summarize recent detailed reviews [29, 37, 53] by giving an overview about the various models with the focus on the main physical phenomena the models are based on.

All these models cover several fields of physics: the ionization stage resulting from the ion-electron collisions leads to a positive charge along the ion path which is described by atomic physics [54]. This results in the creation of a high electric field which exists only for a short time due to its rapid screening by the returning electrons [32] and also in a distribution of the energy deposited in the electrons. These two processes induce then atomic motion which is described by a solid state physics approach [55–57]. The following response of the atomic lattice to the perturbation is a problem of mechanics [58–60]. And finally, the resulting structural modifications and possible atomic motion have to be explained in the framework of solid state physics. This clearly shows that the description of track formation is a complex problem [61–63].

At the end of this chapter molecular dynamics calculations will be shortly described in order to illustrate the development of microscopic models [2, 62, 64–67].

2.3.1 Coulomb Explosion

Ejection of electrons by ion-electron collisions leads to the appearance of ionized target atoms, creating a Coulomb field along the ion path. The ion motion under this electric field that exists during a limited time (less than 10^{-13} s) may induce tracks in materials. Such a model was developed by Fleischer et al. [32] to explain that hard insulators (like Al_2O_3) and metallic materials are insensitive to ion irradiation in the electronic energy loss regime. The volume in which such an electric field is created is as narrow as 1 nm^3 [63] and the created Coulomb field acts in a short time ($\sim 10^{-14}$ s) as recently measured by Schiwietz et al. [68, 69] and Rzadkiewicz et al. [70].

The model describes under which condition a repulsive Coulomb force is sufficient to prevail over the lattice bonding forces. This local force is equal to $n^2e^2/\varepsilon a_0^4$ where n is the average ionization, ε the dielectric constant of the considered material and a_0 the mean atomic spacing. If this force is larger than the mechanical strength $\sigma_M \sim Y/10$ (Y the Young modulus) then atomic motion is expected.

With the availability of large accelerator facilities, in the 1980s it was shown that pure metals [48, 71] and insulators like Al_2O_3 [72, 73] are really sensitive to electronic excitation which could not be explained by the model descibed by Fleischer et al. [32]. So the Coulomb explosion model was extended by Lesueur and Dunlop [33]. They estimate the space charge created by an incident ion during a time scale defined by the electron gas response. The ionized radius was calculated leading to a dimensionless quantity $\eta = Z_1^* \times v_0/v$ where Z_1^* is the effective charge of the incident ion, v its velocity and v_0 the Bohr velocity. This quantity η is proportional to $S_e^{0.5}$ since S_e is proportional to the square of the incident ion charge. The model was applied to pure metallic materials (Ti and Fe) for which the existence of a displacive transformation associated with a soft mode in the phonon spectrum seems to favour efficient energy transfers between highly excited electrons and target atoms [74]. The experimental damage cross sections are plotted versus η and fitted with a power law of η^8, i.e. to S_e^4 (solid lines in Fig. 2.5a for Ti [75] and Fe [76]). Such a law is expected since the calculated kinetic energy E_{kin} received by the atoms during the Coulomb explosion follows roughly a power law ($E_{kin} \sim S_e^4$) [33]. The model was also applied with success to high T_c superconductors by Iwase et al. [34]. In that case $(\Delta c/c_0)/\Delta N_I$ which is the relative increase of the c-axis lattice parameter per incident ion normalized by the initial value of the lattice parameter c_0 with the ion fluence defined as N_I is plotted versus dJ/dx where dJ/dx is the deposited energy per unit lenght with J the potential energy resulting from primarily ionized atoms [32] (Fig. 2.5b). dJ/dx is a parameter proportional to S_e. As can be seen $(\Delta c/c_0)/\Delta \Phi$ is proportional to $(dJ/dx)^4$ and thus to S_e^4 as proposed in the case of Coulomb explosion [33] developed for metallic materials.

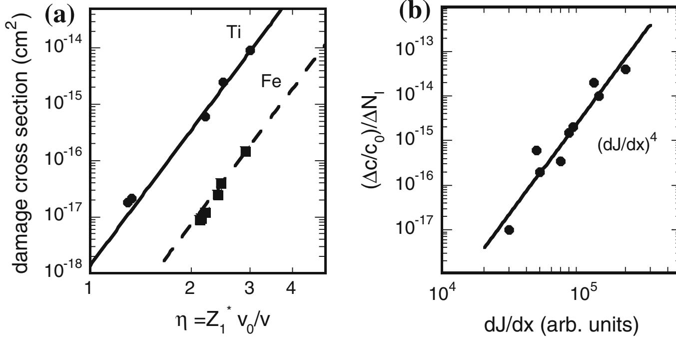

Fig. 2.5 **a** Cross section for damage creation in Ti and Fe by electronic excitation versus η from Lesueur and Dunlop [33]. The lines are proportional to η^8, i.e. proportional to S_e^4. **b** For high T_c superconductors, $(\Delta c/c_0)/\Delta N_I$ is plotted versus dJ/dx, and the solid line represents a $(dJ/dx)^4$ dependence (after Iwase et al. [34])

It should be noted that, as suggested by Fleischer's original Coulomb explosion model, that this electric field exists in a time range of 10^{-14} to 10^{-13} s in order to be efficient. Based on this time Itoh et al. [37] have calculated the energy transferred to the atoms and they suggest that rather a little fraction of the initial deposited energy is transferred to the atoms ($\sim$ some 10^{-3} of S_e) along the ion path in agreement with the calculations of Lesueur and Dunlop [33].

2.3.2 Bond Weakening (BW) Model

Electron excitation can affect interatomic forces, leading to material modification as suggested earlier. The bond weakening is a natural extension of earlier ideas showing a strong dependence of the crystal structure on the corresponding electronic structure of the material [77]. Such a model was developed by van Vechten et al. [39] and Combescot et al. [78] to explain laser annealing of defects in Si by nanosecond laser pulses. But it has appeared that the electron–hole pair concentration created by the laser light absorption may be too small to be critical to ensure a thermal annealing. Then to explain such annealing a transient thermal process was suggested and quantitatively developed [79, 80]. This model was able to describe quantitatively the time and depth of melting. The comparison with experiments was performed by measuring the time of melting by in situ reflectivity and the depth of melting by impurity diffusion [81–83]. The measurement of light reflectivity provides also the evolution of the surface reflectivity versus temperature of the solid [82].

More recent calculations for Si, Ge and GaAs by Stampfli and Bennemann [40] find that the excitation (and hence loss) of valence electrons by 15 % induces lattice instability within 100 fs [84], consistent with recent time-resolved x-ray diffraction measurements following a femtosecond laser pulse [85] in Bi. It is certainly true

that excitation from bonding valence orbitals to antibonding conduction band orbitals leads to very rapid structural rearrangements in systems like Bi [86]. Extended discussions regarding this phenomenon are given by Duffy et al. [53] and by Klaumünzer [30].

2.3.3 *Exciton Self-trapping (STX) Model*

Excited electrons and holes polarize the surrounding lattice creating a distortion which, associated with the excited carrier, is called a polaron. Two kinds of polarons do exist [87], the one linked to a free motion of the carriers in the lattice and the second that can be trapped by the created distortion and is called self-trapped exciton. In halides [88] like in LiF [89–93] and oxides, particularly crystalline quartz [91], this phenomenon has been observed under swift heavy ion irradiation [88–93]. Atomic motion is the result of the transfer of the stored electronic energy to the lattice by emission of several phonons. This process was studied in several materials by Itoh and Stoneham [36]. They conclude that in insulators self-trapping of excitons influences the critical energy deposition for track formation. According to this study, the critical energy loss amounts to 3–5 keV nm^{-1} in materials where excitons are self-trapped, as e.g. in crystalline quartz. In materials in which self-trapping of excitons does not occur like in metallic materials and III-V and group IV semiconductors the critical energy deposition for track formation reaches values near 20 keV nm^{-1}. The difference can be ascribed to a strong localization of electronic excitation energy along the ion path in halides while it is delocalized in the case of free excitons.

A quantitative development of the model has been done for crystalline SiO_2 by Itoh [91] in order to describe amorphous ion tracks observed by Meftah et al. [46]. It is assumed that this exciton mechanism is efficient only if the number of self-trapped excitons is equal to the number of the SiO units. Suppose that $D(r)$ is the dose deposited per unit area in a coaxial cylindrical shell of a thickness of a molecular layer, at a distance r from the path of the ion as calculated by Zhang et al. [22]. The initial dose distribution $D_0(r)$ transferred to the electrons is mainly governed by the secondary ionization by δ ray electrons [see (2.2)]. The number $p(r)$ of self-trapped excitons per unit area produced at a distance $\boldsymbol{r}$ from the ion path is given by $p(r) = D_0(r)/W$, where W is the energy necessary to excite all SiO_2 electrons. For the calculation of the cylinder radius in which all SiO_2 electrons are excited a value larger than W = 38 eV was assumed. This value which is larger than the optical gap energy of crystalline SiO_2 ($\sim$9 eV [94]) was used since the energy to create an electron-pair is around three times the optical band gap. The results of the calculation are compared with experimental results by Meftah et al. [46] in Fig. 2.6, in which the experimental track radii (dots) as well as the calculated ones (full line) are plotted as a function of electronic energy loss S_e. The good agreement between experiment and calculation confirms the suitability of the model for the description of ionization induced damage formation in SiO_2.

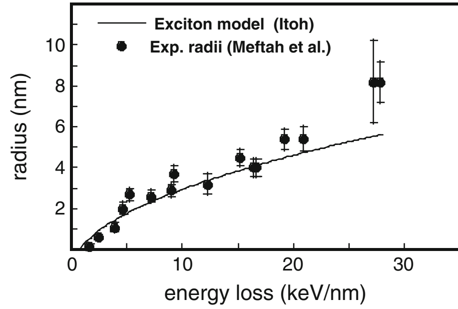

Fig. 2.6 Experimental radii in c-SiO_2 from Meftah et al. [46] compared to calculations in the framework of the exciton model from Itoh [90]

2.3.4 Concept of Reduced Electronic Energy Loss

The concept of reduced electronic energy loss was introduced by Bouffard et al. [25] in order to take into account the fact that for the same electronic energy loss the track radii are larger for low beam energy (<0.6 MeV/u) than the radii resulting for high beam energy (>2.7 MeV/u) as observed in mica (Fig. 2.7a).

The main difference is that at low ion energy the energy deposited in the electrons is spread out into a smaller volume than at high energy. As an example the maximum energy transfer per ion to electrons for a beam energy of 0.1 MeV/u is around 200 eV, while at 10 MeV/u it is 20 keV. Using the Monte Carlo model described by Gervais and Bouffard [23], the calculated radial dose $D_{MC}(r)$ does not give the corresponding energy loss with satisfactory accuracy. Thus the radial dose distribution has been normalized assuming that

$$D(r) = \frac{dE/dx}{\int_0^\infty 2\pi r D_{MC}(r')dr'} D_{MC}(r) \tag{2.4}$$

where $D(r)$ is the local dose at a distance r from the ion path (Fig. 2.3a).

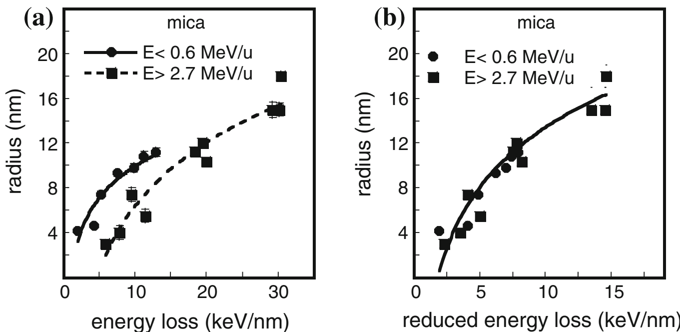

Fig. 2.7 Experimental track radii in mica versus (**a**) electronic energy loss, (**b**) reduced electronic energy loss. The data presented in the two pictures are from Bouffard et al. [25]. The lines are there to guide the eye

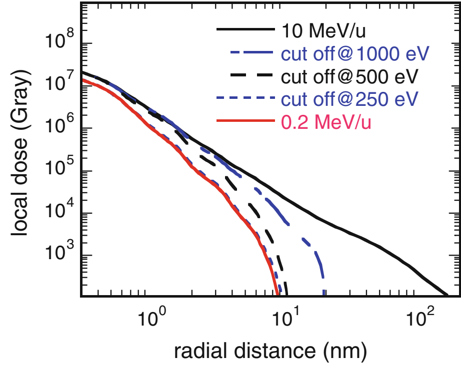

Fig. 2.8 Evolution of the radial distribution of the dose as function of cut-off energy, $E_{cut\text{-}off}$, of primary electrons for a beam energy of 10 MeV/u Kr in mica. The *red line* shows the evolution of the radial dose for 0.2 MeV/u without any cut-off. Figure extracted from Bouffard et al. [25]

Since the track radius R_t is in the order of 5 nm the dose deposited at larger distance ($r > R_t$) is not efficient to create a track. Consequently, only electrons having energy lower than the so-called cut-off energy $E_{cut\text{-}off}$ will be considered. The evolution of the radial dose distribution for Kr irradiation in mica is plotted as function of the radial distance r for several values of this cut-off energy in Fig. 2.8, showing that it becomes efficient for $T_{cut\text{-}off} \leq 1000$ eV. It is shown that for a cut-off energy of 250 eV the local dose distribution for 10 MeV/u Kr ions becomes the same as that for 0.2 MeV/u. Such an agreement is the result of neglecting the dose given to the atoms by electrons with energy larger than 250 eV.

The reduced energy loss $S_{e\text{-}red}$ is then calculated (Fig. 2.7b) using (2.1) [3], with E_{em} replaced by $E_{cut\text{-}off}$.

$$S_{e-red} = -\left(\frac{dE}{dx}\right)_{red} = N \int_{0}^{E_{cut-off}} E_e \sigma(E_i, E_e) dE_e \tag{2.5}$$

where $\sigma(E_i,E_e)$ is the differential cross section for electron emission. Independent of the cut-off energy, between 100 and 500 eV the dose distribution remains nearly unchanged (Fig. 2.8). By choosing $E_{cut\text{-}off} = 200$ eV, the track radii versus the reduced electronic energy loss lie on the same curve for all ion energies (Fig. 2.7b). So, the difference in radii between high and low beam energies (Fig. 2.7a) disappears if only the energy which is deposited near the ion path is considered instead of the total electronic energy loss.

This model developed by Bouffard et al. has been proposed as a possible model to predict the experimental track radii directly from the initial energy deposition of the electrons as obtained by Monte Carlo calculation without any other radial expansion of the initial energy. It is disappointing that, to our knowledge, this model up to now was applied only for mica.

2.3.5 A Transient Thermal Process

The thermal spike was proposed by Desauer [95] and reconsidered for insulators by Chadderton and Montagu-Pollock [96] and for metals by Seitz and Koehler [97]. The main idea of this model is to suppose that the energy deposited in the lattice can be described by a transient thermal process acting in the electronic and atomic subsystems. We denote it more specifically as the inelastic thermal spike (i-TS) model [44–51] to emphasize the difference with the elastic collision spike model which is valid in the nuclear energy loss regime [98]. In the i–TS model, the energy deposited in the electrons by the slowing down of the incident ions diffuses within the electron subsystem by electron-electron interactions before being transferred and finally localized in the lattice system via the electron–phonon coupling. The heat diffusion in the electron and in the lattice subsystems versus time t and space r (in cylindrical geometry) is described by the following two coupled differential equations [99]:

$$C_e(T_e)\frac{\partial T_e}{\partial \mathrm{t}} = \frac{1}{r}\frac{\partial}{\partial r}\left[rK_e(T_e)\frac{\partial T_e}{\partial r}\right] - g(T_e - T_a) + A(r) \tag{2.6}$$

$$C_a(T_a)\frac{\partial T_a}{\partial t} = \frac{1}{r}\frac{\partial}{\partial r}\left[rK_a(T_a)\frac{\partial T_a}{\partial r}\right] + g(T_e - T_a) \tag{2.7}$$

where $T_{e,a}(r,t)$, $C_{e,a}(r,t)$ and $K_{e,a}(r,t)$ are the temperature, the heat capacity per unit volume (called specific heat in the following) and the thermal conductivity of the electronic (e) and atomic (a) subsystem, respectively. $A(r)$ is the energy deposited into the electronic system [26]. The only free parameter in this model is the electron–phonon coupling strength g [55].

At present different ways exist to explore the heat diffusion equations for describing the occurring physical processes and calculating experimentally accessible quantities:

I The so-called analytical thermal spike (a-TS) model proposed by Szenes [41, 42] provides an analytical solution of the differential equation for the atomic system (2.7) ignoring the way the energy is transferred to the atoms. This model was extended by Trinkaus [58] to describe the anisotropic growth in amorphous materials under swift heavy ion irradiation (see Chap. 10).

II The ionization diffusion-explosion-amorphization (IDEA) model by Canut and Ramos [43] takes into account the energy diffusion to the electrons prior to its transfer to the atoms by providing an analytical solution of the differential equation for the electronic system (2.6).

III In the inelastic thermal spike (i-TS) model [44–51] a complete numerical solution of the system of differential equations [(2.6) and (2.7)] is given taking into account the coupling between the electronic and atomic subsystems.

IV Finally, in the exciton decay model [38] it is assumed that the energy delivered by the thermal spike leads to the formation of bound excitons. Their nonradiative decay results in the creation of point defects.

The different approaches mentioned will be discussed in the following subsections taking into account the energy criterion to create a track that will change with the model proposed.

2.3.5.1 The Analytical Thermal Spike (a-TS) Model

Within the analytical thermal spike (a-TS) model [41, 42, 100] the various ion-induced physical effects are determined by the maximum temperature, and the actual time evolution of the temperature spike is not considered. It is assumed that the ion-induced temperature increase $\Delta T(r,t)$ can be approximated by a Gaussian distribution function, which is an analytical solution of (2.7):

$$\Delta T(r,t) = \gamma S_e/\pi\rho c a^2(t) e^{-(r^2/a^2(t))} \tag{2.8}$$

where ρ and c are the density and the heat capacity, γS_e is the fraction of S_e deposited in the thermal spike with an efficiency of γ and $a(t) = a(0) + 4Dt$ where $a(0)$ is the initial width of the radial distribution of the temperature approximated by a Gaussian function in the phonon system, Dt is the squared value of energy diffusion length versus time of the considered material with a thermal diffusivity D. Szenes [41] had assumed that the maximum track size is reached at $t = 0$, and $\Delta T(r,0)$ is calculated only with $a(0)$.

A typical temperature distribution is plotted versus the radius for $Y_3Fe_5O_{12}$ in Fig. 2.9. The track radius R_m in $Y_3Fe_5O_{12}$ can be found using the temperature distribution defined at time $t = 0$,

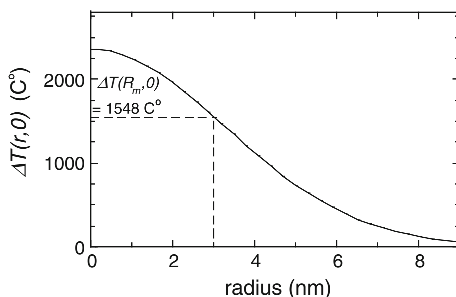

Fig. 2.9 Radial temperature distribution for $Y_3Fe_5O_{12}$, irradiated with an ion energy of 1 MeV/u and with S_e = 10 keV nm^{-1}. $\Delta T(r,0) = 2350\ \exp(-r^2/a(0)^2)$ with $\gamma = 0.35$, $\rho = 5.18$ g cm^{-3}, c = 0.68 J K^{-1} cm^{-3} and $a(0)^2$ = 21.6 nm^2 [41, 42]. At the melting temperature $\Delta T(R_m,0)$, the radius is equal to 2.9 nm in agreement with that measured by Meftah et al. [18]

$$\Delta T(R_m, 0) = T_0 = T_m - T_{ir} \tag{2.9}$$

where T_{ir} (usually 300 K) is the irradiation temperature and T_m = 1848 K the melting temperature. Here the energy needed to make the solid to liquid phase change is ignored. Such assumption is surprising since it has been shown by Rethfeld et al. [101] that the shorter the energy deposition time the larger is the temperature to melt the material. But it is presumed in this model that the electronic energy deposition induces a decrease of the bonding strength in the irradiated material as it was proposed by Van Vechten et al. [39] (see Sect. 2.3.2 in this chapter). The two free parameters of the model are the fraction γ of S_e deposited in the atoms, and $a(0)$ the initial Gaussian width.

Under these assumptions, two simple equations for the track radius R can be derived from (2.8):

$$R^2 = a^2(0)\ln(\mathrm{S_e}/\mathrm{S_{et}}) \text{ for } \mathrm{S_e} < 2.7\,\mathrm{S_{et}} \tag{2.10}$$

$$R^2 = (a^2(0)S_e)/(2.7S_{et}) \text{ for } S_e > 2.7\,\mathrm{S_{et}} \tag{2.11}$$

where S_{et} is the electronic energy loss threshold for track formation. This threshold is the most important parameter and can be deduced either by fitting the track radii near the threshold [41, 42] using (2.10) or directly by plotting the damage cross section σ, which can be calculated from experimentally determined track radii, versus the electronic energy deposition S_e. The extrapolation of the resulting $\sigma(S_e)$ curve then yields the threshold value S_{et} [27] (see also Chap. 9). $a(0)$ can also be deduced from (2.10) and (2.11) since it is equal to the measured radius for S_e = 2.7 S_{et}. Knowing S_{et} and $a(0)$, track radii can be fitted. In the a-TS model, the criteria for track formation are on one hand the energy to reach the melting temperature and on the other hand the fraction γ of S_e which is deposited to the atoms to create a track. The efficiency γ is given by

$$S_{et} = (\pi\rho c T_0 a^2(0))/\gamma \tag{2.12}$$

if $a(0)$ is known or, by substituting $a^2(0)$ from (2.11) in (2.12), can be determined according to

$$\gamma = 2.7\pi\rho c T_0 R^2/S_e. \tag{2.13}$$

According to Szenes, the most important features of the a-TS model are that the initial Gaussian width is uniformly $a(0)$ = 4.5 nm and that the efficiency is $\gamma \sim 0.4$ at low and $\gamma \sim 0.17$ at high ion velocities, respectively. Thus there is no free parameter characteristic for various insulators at low and high ion velocities in this model (for details see [41, 42]).

The a-TS model, first developed for insulators [41, 42], was extended to polymers [102], to biological samples [103], as well as to materials with highly anisotropic electrical conduction [104].

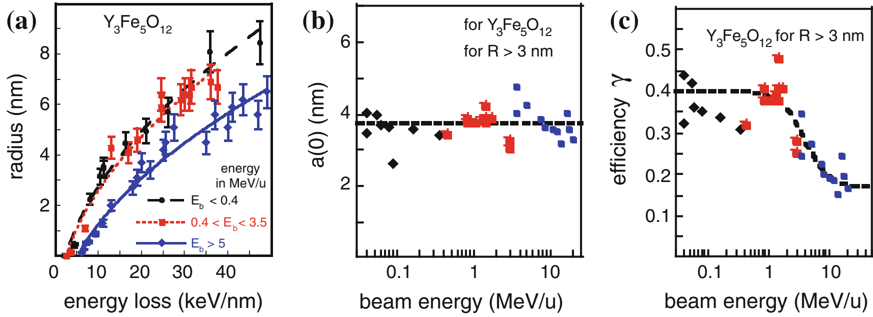

Fig. 2.10 **a** Experimental track radius versus electronic energy loss in $Y_3Fe_5O_{12}$ for three different ranges of beam energy (the lines are square root fits of the experimental radii for the corresponding beam energy; figure extracted from Toulemonde et al. [109]). **b** Evolution of a(0) versus beam energy from (2.11). **c** Evolution of the efficiency versus beam energy (figure extracted from Szenes [41, 42] from 2.12 and 2.13. For (**b**) and (**c**), the lines are there to guide the eyes

In order to illustrate the determination of $a(0)$ and γ, the measured track radii of $Y_3Fe_5O_{12}$ for which track formation is extensively studied [18, 105–107], will be analyzed in more detail. The measured radii are plotted in Fig. 2.10a for various groups of beam energies E_b versus the electronic energy deposition. By extrapolation to the radius $R = 0$, the threshold values of the electronic energy deposition are $S_{et} = 4$ keV nm^{-1} for $E_b < 3.5$ MeV/u and 7 keV nm^{-1} for $E_b > 5$ MeV/u (from Fig. 2.13 in [18]). Then the measured R values at $2.7 \times S_{et}$ are $\sim$3 nm whatever the beam energy is (Fig. 2.10a). In order to verify such $a(0)$ determination the width is calculated using (2.11) for experimental radii > 3 nm with the corresponding S_e values in Fig. 2.10a. In these cases continuous tracks are formed in $Y_3Fe_5O_{12}$ [107].

The result leads to a mean value of $a(0) = 3.8 \pm 0.4$ nm independent of the beam energy. This value is larger than the value of 3 nm determined from $S_e = 2.7 \times S_{et}$ but lower than the mean value of 4.5 nm deduced by Szenes from the analysis of track data in several materials ($Y_3Fe_5O_{12}$, $BaFe_{12}O_{19}$, $SrFe_{12}O_{19}$, $MgFe_2O_4$, $NiFe_2O_4$, and $ZnFe_2O_4$) [41, 42]. The experimental values of the radii at low (Fig. 2.11a) and high ion energies (Fig. 2.11b) are compared with the description in the framework of the Szenes model using three values of $a(0)$: 3, 3.8 and 4.5 nm. The results confirm that the value $a(0) = 3.8$ nm seems to give the best agreement with the experimental data for ion energies below $\sim$3.5 MeV/u (Fig. 2.11a), whereas for energies of $\sim$15 MeV/u the best agreement is reached for $a(0)$ between 3.8 and 5.0 nm (Fig. 2.11b), surrounding the 4.5 nm deduced by Szenes. With (2.13), it is possible to calculate the efficiency γ for the track radii larger than 3.0 nm for all the beam energies using $\rho = 5.15$ g cm^{-3}, $c = 0.68$ J g^{-1} K^{-1} and $T_m = 1848$ K. This leads to $\gamma = A\ R^2/S_e$, with $A = 2.7\pi r c T_0 = 0.29$ keV nm^{-3}, which is plotted versus the beam energy in Fig. 2.10c. Three regimes may be defined: for $E_b < 2$ MeV/u, γ is constant and equal to 0.4, then for E_b between 2 and 10 MeV/u there is a transition regime with γ decreasing smoothly from 0.4 to 0.17

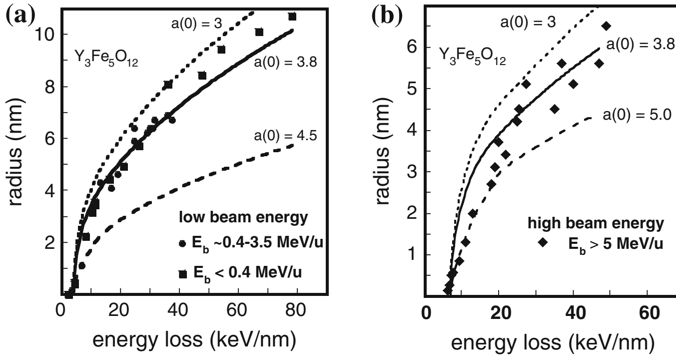

Fig. 2.11 Experimental radii versus electronic energy loss for $Y_3Fe_5O_{12}$ irradiated with various ion energies compared to radii calculated in the ATS model using different values of the initial width a(0) in nm. **a** For beam energy less than 3.5 MeV/u, using S_{et} = 4 keV nm^{-1} [18, 106] and **b** for beam energy ~15 MeV/u, using S_{et} = 7 keV nm^{-1} [17]

and afterwards, for energies larger than 10 MeV/u, γ seems to stay constant and equal to 0.17. This is in agreement with the velocity effect [18] since the energy density deposited in the atoms decreases with beam energy.

Using the model of Szenes [41], Moll et al. [108] analyzed the measured radii in pyrochlores ($Gd_2Ti_{2-x}Zr_xO_7$ for x = 0, 1 and 2) which have been irradiated with ions at energies between 10 and 6.5 MeV/u. Since the experimental electronic energy loss threshold for track formation is $S_{et} \sim 13$ keV nm^{-1} (Fig. 2.12) for each material, the track radii belong to an electronic energy loss range below $S_e = 2.7 \times S_{et} = 35$ keV nm^{-1} and the radii are fitted using the square root of (2.10). The best fits to the data (Fig. 2.12) provide the following values of the parameters: $a(0) = 5.8$ nm and $S_{et} = 13.2$ keV nm^{-1} leading to $\gamma = 0.32$ for $Gd_2Ti_2O_7$, $a(0) = 4.9$ nm and $S_{et} = 13.2$ keV nm^{-1} leading to $\gamma = 0.26$ for

Fig. 2.12 Variation of the radius R as a function of the electronic energy loss, S_e, in pyrochlore samples irradiated with Kr and Xe at energies larger than 6.5 MeV/u. The lines are fits to the data in the framework of the model of Szenes (data extracted from Moll et al. [108]) (for $Gd_2Ti_2O_7$: S_{et} = 13.2 keV nm^{-1} and a(0) = 4.9 nm, and for $Gd_2Zr_2O_7$: S_{et} = 13.8 keV nm^{-1} and a(0) = 4.1 nm)

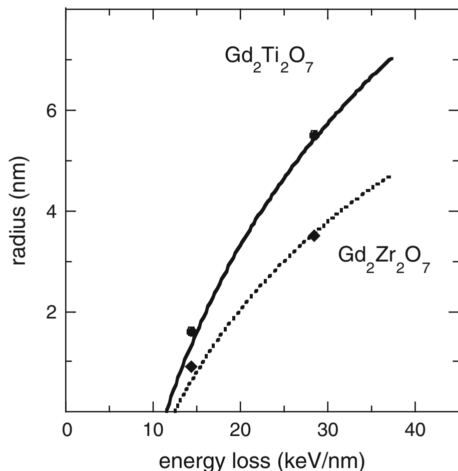

Gd_2TiZrO_7 and $a(0)$ = 4.1 nm and S_{et} = 13.8 keV nm^{-1} leading to γ = 0.20 for $Gd_2Zr_2O_7$. It should be noted that $a(0)$ varies from 5.8 to 4.1 nm which encircles the value of 4.5 nm determined by Szenes as observed for the high energy regime in $Y_3Fe_5O_{12}$ (Fig. 2.11b). The efficiency γ is varying from 0.32 to 0.20. This is not expected since the efficiency should be smaller than 0.2 for beam energies larger than 6 MeV/u (Fig. 2.10c) according to the model of Szenes [41, 42].

Consequently, the a-TS model gives a quantitative description of track radii in insulating materials provided that the Gaussian width $a(0)$ at time t = 0 can be deduced from the knowledge of the threshold value S_{et} for track formation ($a(0)$ equals the track radius at S_e = 2.7 S_{et}) as well as from the track size for S_e larger than 2.7 S_{et} for a specific beam energy. The efficiency γ, with the knowledge of $a(0)$ [(2.11) and (2.12)], determines the fraction of S_e deposited in the track. It does not take into account the latent heat energy needed for the phase change from solid to liquid which is based on the assumption that for track formation the melting temperature of the corresponding material is exceeded. However, with the knowledge of $a(0)$ and γ, this model provides an initial temperature distribution of the atomic system. This has been successfully used by Klaumünzer [30] to describe the anisotropic growth in amorphous silica, using γ = 0.6.

2.3.5.2 The Ionization Diffusion-Explosion-Amorphization (IDEA) Model

In the model developed by Canut and Ramos [43], it is assumed that the damage evolution via collective electronic excitations takes place in four steps. The model takes into account the energy deposition in the electrons by an analytical solution of (2.6) governing the energy diffusion to the electrons.

(1) The first stage concerns the interaction of the incident ions with the electrons of the lattice. The resulting ionization process is caused by the energy density $A(r)$ initially deposited in the electronic system [26] (see Sect. 2.2.2).

(2) The energy density W initially deposited in the electrons diffuses via electron-electron collisions before its transfer to the lattice according to

$$\frac{\partial W(r,t)}{\partial t} = \frac{D}{r}\frac{\partial}{\partial r}\left[r\frac{\partial W(r,t)}{\partial r}\right] + A(r) \quad (2.14)$$

After the diffusion process has finished, the final energy density profile will be given by $W_1(r) = W(r, \tau)$ at a time τ. By integration of (2.14), $W_1(r)$ is obtained,

$$W_1(r) = \frac{1}{2D\tau}\int_0^{r_m} uW_0(u)I_0\left(\frac{ru}{2D\tau}\right)e^{-\frac{r^2+u^2}{4D\tau}}du \quad (2.15)$$

where I_0 is the zero order hyperbolic Bessel function, τ is the duration of the diffusion process, D the energy diffusivity of the electrons and r_m is the

maximum radius of the energy distribution ($W(r, 0) = 0$ *for* $r > r_m$). τ should be in the order of the phonon period $\sim 10^{-12}$ s, and the diffusion length L_d characteristic for the material is defined by $L_d^2 = 2D\tau$. The integration of (2.15) is described in detail in [43].

(3) At the end of the diffusion stage the energy is transferred to the atomic system, in analogy with an explosion mechanism, if $W_1(r)$ exceeds a critical density W_c at the radius $r = r_1$. Here it is assumed that the part of the $W_1(r)$ distribution below W_c ($r > r_1$) does not create irreversible atomic disorder. Therefore an effective electronic stopping power S_e^* which represents the energy per unit length deposited in this "hot" region is defined according to

$$S_e^* = \int_0^{r_1} 2\pi r W_1(r) dr \tag{2.16}$$

(4) In this stage an equipartition of energy above W_c is assumed resulting in an extension of the cylinder where energy deposition occurs from r_1 to a final value r_e, the effective radius of the track. That means that the atoms excited within r_1 share their energy with atoms in the larger radius r_e. At the end of this amorphization process the radial density of deposited energy $W_e(r)$ inside the track is equal to the critical energy density $W_c = W_1(r_1)$ leading to a cross section $\sigma = S_e^*/W_c$.

The model was successfully applied to $LiNbO_3$ [43] and $Y_3Fe_{15}O_{12}$ [109, 110]. As example, in the following the application of the model to $Y_3Fe_{15}O_{12}$ irradiated with cluster and single ions will be briefly described.

Using cluster ion irradiation with its very low particle velocity ($\sim$0.05 MeV/u) and very high electronic energy loss, the kinetic energy given to electrons by ion-electron collisions is very low and consequently the initial energy deposition can be approximated by a Dirac distribution. In that case, (2.15) may be approximated by

$$W_1(r) = \frac{S_e}{2\pi L_d^2} e^{(-r^2/2L_d^2)} \tag{2.17}$$

Using (2.16) with the assumption that $W_c = W_1(r_1)$, the effective electronic energy loss S_e^* is linked to S_e by the relation $S_e^* = S_e - 2\pi L_d^2 W_c$. Knowing that the damage cross section $\sigma = S_e^*/W_c = S_e/W_c - 2\pi 2L_d^2$, with the use of the last relation W_c and L_d can be determined by fitting the track radius r assuming that $\sigma = \pi r^2$.

The damage cross sections resulting from the cluster irradiations of $Y_3Fe_5O_{12}$ are plotted versus electronic energy loss in Fig. 2.13a. The values of W_c and L_d equal to 20 keV nm^{-3} and 1.7 nm, respectively, are extracted from a fit of the damage cross sections. With these values of W_c and L_d the effective electronic energy loss S_e^* is calculated. In Fig. 2.13b the experimental values of track radii for

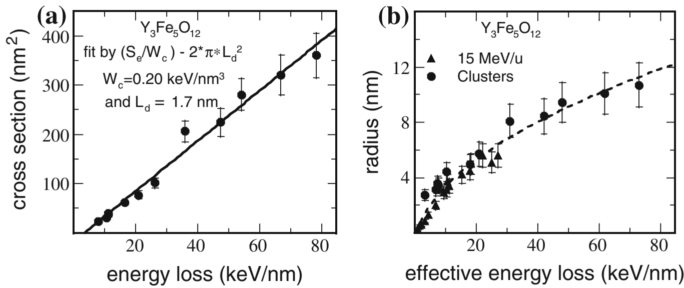

Fig. 2.13 **a** Damage cross section in $Y_3Fe_5O_{12}$, irradiated by cluster beams [109] versus electronic energy loss; **b** Track radii [18] versus effective electronic energy loss resulting from cluster beams and ions at 15 MeV/u

cluster and 15 MeV/u ion irradiations are plotted versus the effective energy loss. As can be seen the radii for both irradiation regimes are in good agreement.

2.3.5.3 The Inelastic Thermal Spike (i-TS) Model: A Complete Numerical Solution of the Heat Diffusion Equations

The common features of the i-TS model for metallic or insulating materials are the following [27, 44–51]:

a. The input energy of the spike is the known electronic energy loss described by the radial and time distribution function $A(r, t)$ obtained by Monte Carlo Calculations [26] for a specific beam energy (see Sect. 2.2.2).
b. The heat diffusion in the electron and lattice subsystems are described by coupled Fourier equations. Since the electronic energy deposition can be considered as constant along the trajectory, the heat equations are solved in a cylindrical geometry. The deposited energy and its evolution are deduced from a numerical solution of (2.6) and (2.7) allowing the calculations of the energy transfers to electronic and atomic subsystems, respectively. The initial boundary conditions of the calculations are first the temperature (T_0) of the irradiated lattice or the equivalent internal energy, $E_i(T_0)$, and the volume in which the calculations are performed. From the initial temperature of irradiation, T_0, the internal energy is calculated by an integration of the specific heat from 0 K to T_0. The distance that defines the volume in which the calculation is performed should be sufficiently large to be sure that the temperature gradient is negligible far away from the centre of the trajectory (usually a cylinder radius of ~200 nm). The evolution of the electronic and atomic temperature around the projectile trajectory is calculated as a function of time t and space r. This is illustrated in Fig. 2.14 for the case of an irradiation of pure Fe (T_0 = 80 K and $E_i(T_0)$ = 0.002 eV/at) which shows the temperatures of electronic $T_e(t,r)$

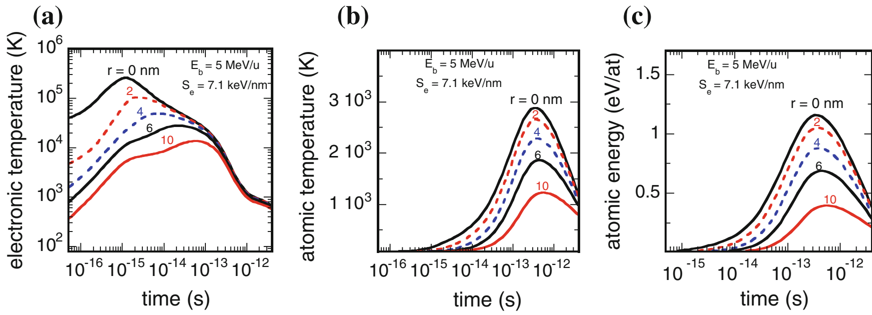

Fig. 2.14 Electronic (**a**) and atomic (**b**) temperature and energy transferred to the atoms (**c**) versus time for different radial distances in nm from the ion path. This calculation is performed for pure Fe irradiated at 80 K with an U beam of 5 MeV/u with g = 1.2 × 10^{12} W $cm^{-3}K^{-1}$ and S_e = 71 keV nm^{-1} [76]

(Fig. 2.14a) and atomic systems $T_a(t,r)$ (Fig. 2.14b) versus the time for different distances from the centre of the ion trajectory.

c. It is assumed that the relaxation of the excited electron system proceeds via electron-electron and electron-atom collisions characterized by the electron-phonon coupling strength g [55, 99]. This is connected with the electron-phonon mean free time $\tau = C_e(T_e)/g$ and with the electron-phonon mean free path $\lambda^2 = D_e\ (T_e) \times \tau = K_e(T_e)/g$ where $C_e(T_e)$ and $K_e(T_e)$ are the specific heat and the thermal conductivity, respectively, for the electronic (e) subsystem at an electronic temperature T_e [44, 48, 50].

d. Due to the short heating rate of the atoms the equilibrium melting temperature T_m is not the adequate parameter to characterize the melting process. This was experimentally observed with femtosecond laser experiments [111], i.e. the measured increase of temperature versus the input laser power does not stop at T_m but continues to increase above T_m. This was also shown by Rethfeld et al. [101]: the temperature allowing the nucleation of a molten phase is larger than T_m by a factor of ~1.3 when the heating rate is in the order of 10^{15} K s^{-1}. Such effect was also pointed out by Klaumünzer [30], and in [112] it was shown that the superheating melting temperature is in the order of 500 K larger than T_m if the heating rate is in the order of 10^{14} K s^{-1} [112]. In the case of Fe, the heating time to reach T_m (1809 K) is ~10^{-13} s, leading to a heating rate of ~10^{16} K s^{-1} (Fig. 2.14b). So the calculations were made within a superheating scenario, i.e. the increase of temperature does not stop at the melting or vaporization temperature. Such hypothesis was systematically used after 2002 [113, 114] and as an example the evolution of $T_a(r,t)$ is plotted versus time for pure Fe in Fig. 2.14b. Using the relation $E_a(r,t) \sim \int_0^{T_a(r,t)} C_a(T_a(r,t))dT_a$, the evolution of the energy $E_a(r, t)$ transferred to the atoms is plotted in Fig. 2.14c versus time t for different radii r where $C_a(T_a(r, t))$ is the specific heat of the lattice at $T_a(r, t)$. Within this superheating scenario the temperature in Fig. 2.14b

does not have the usual meaning and should be taken only as an equivalent energy transferred to the atoms.

e. Taking into account the superheating scenario, the energy E_m necessary to reach the molten phase is defined as the energy to reach the melting temperature T_m plus the latent heat of fusion [44]. Using the same criterion the track size is defined by the largest radial zone of the atoms which contains sufficient energy $E > E_m$ to induce the molten phase. In the case of pure Fe, the energy to create a track is 0.86 eV/at while the energy corresponding to the melting temperature (T_m = 1809 K [50]) is equal to 0.70 eV/at $\left(E_a(T_m) \sim \int_0^{T_m} C_a(T_a) dT_a\right)$, i.e. 0.16 eV/at smaller than the energy to reach the energy necessary for melting. The equivalent superheating temperature to create a track is then 2156 K, i.e. 347 K larger than the melting temperature as expected from the rapid heating rate.
f. For the thermophysical parameters (thermal conductivity, specific heat, melting temperature, heat of fusion, boiling temperature, heat of evaporation) the equilibrium values are used even within the transient conditions of the spike. If the latent heat of fusion is unknown, then the track radii were fitted with a unique couple of values, g or λ, with the corresponding E_m, for a metallic material a-$Fe_{85}B_{15}$ [115], a semiconductor GeS [116] and an insulator $Gd_2Ti_2O_7$ [117] as examples.

Application of the i-TS Model to Metallic Materials: Amorphous Versus Crystalline Materials

The inelastic thermal spike process was developed by Dufour et al. for Bi [48] and compared to other metallic materials by Wang et al. [50]. The first attempt to apply the model was performed for amorphous materials [29, 45] supported by the idea that the electron-phonon coupling in amorphous metallic alloys is larger than in crystalline ones.

The two coupled diffusion equations [(2.6) and (2.7)] were solved numerically [51] by taking into account the evolution of all parameters with the temperature. For the energy diffusion to the electrons, the electronic specific heat (C_e) and the electronic thermal conductivity (K_e) were calculated using the formalism of the free electron gas model [48]. Regarding the energy diffusion to the atoms the measured specific heat and the atomic thermal conductivity versus atomic temperature were introduced.

The electron-phonon coupling strength g is the key parameter governing the rate of the electron energy relaxation towards the lattice [118]. A relation for the electron-phonon coupling efficiency has been developed for metallic materials, and for a complete derivation we refer to the work of Brorson et al. [119] and Allen [120]. If the temperature of the electronic system is higher than the Debye temperature, $T_e > T_D$, then Kaganov et al. [55, 99] obtain

$$g(T_e) = \frac{\left(\frac{\pi^2}{6}\right) m_e n_e v_s^2}{\tau(T_e) T_e}. \tag{2.18}$$

n_e and m_e are the electronic density and the free electron mass, respectively, v_s is the sound velocity which writes $v_s = 2\pi k_B T_d/(h6\pi^2 n_a)$ where n_a is the atomic density, k_B is the Boltzmann constant, T_D the Debye temperature and h the Planck constant. With the Wiedemann-Franz law giving the connection between electronic and thermal conductivity, $K_e(T_e) = L^* \sigma_e(T_e) T_e$, with $L^* = (\pi^2 k_B^2)/(3e^4)$ the Lorentz number, $g(T_e)$ is expressed as

$$g(T_e) = \frac{\pi^4}{18} \frac{1}{(6\pi^2)^{2/3}} \frac{1}{n_a^{2/3}} \frac{(n_e e T_D)^2}{K_e(T_e)}. \tag{2.19}$$

It is obvious in (2.19) that $g(T_e)$ is inversely proportional to the thermal conductivity $K_e(T_e)$, which is illustrated in Fig. 2.15 for pure iron. Since in metals the thermal conductivity behaves identical with temperature as the electrical conductivity, $g(T_e)$ is also proportional to the reciprocal of the electrical conductivity. If the temperature of the electronic system becomes smaller than that of the atomic system, $T_e < T_a$, then in metallic systems the atoms are cooled by energy exchange with the electrons [48]. This leads to an atomic cooling rate of the order of the heating rate. However, the electron-phonon coupling strength is not well known and consequently it is considered as a free parameter and is determined by fitting

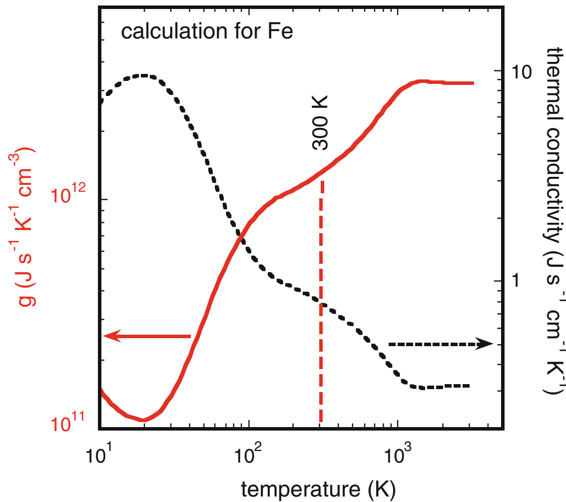

Fig. 2.15 Thermal conductivity (*dotted line* and unit on the *right*) and electron-phonon coupling strength, g (*red line*), versus atomic temperature for pure iron. At 300 K, g = 1.3 × 10^{12} J s^{-1} K^{-1} cm^{-3} [55, 99]

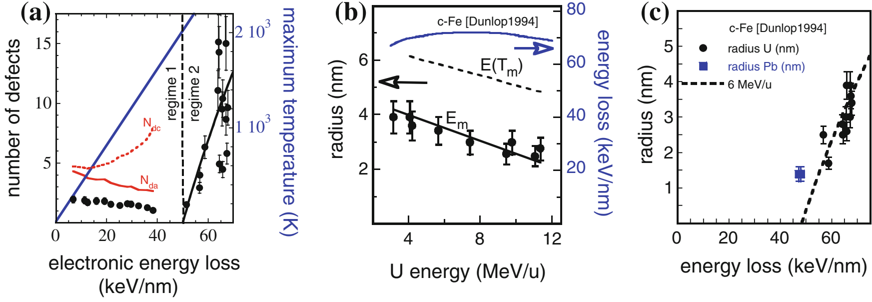

Fig. 2.16 **a** Number of defects [76] in Fe versus electronic energy loss compared to calculations with the i-TS model. *Regime 1*: defect annealing, *regime 2*: defect creation. N_{dc} is the number of defects calculated by SRIM and N_{da} is the number of stable defects calculated with the i-TS model after annealing by the electronic energy loss. **b** Radii and electronic energy loss versus the U ion energy. Calculations with the i-TS model have been performed using two different criteria: first with the energy to reach the melting temperature $E(T_m)$, and second with the energy to reach the melting phase, E_m [109]. **c** Experimental track radii for U and Pb irradiated Fe versus the electronic energy loss compared with values calculated with the i-TS model for ions of ~6 MeV/u

the track size. The *g* values determined in this way usually well agree with the predictions of (2.19) in the case of metallic materials apart for Ti [50].

A typical case for track observation in a metallic material is the irradiation of pure iron [76]. The defect creation by high electronic excitations was quantified by resistivity measurements directly correlated with the number of created defects inside the metallic material. In Fig. 2.16a, the number of defects created in Fe is plotted versus the electronic energy loss. Concerning the effect of the electronic energy deposition on structural modification in Fe, two regimes can be distinguished: first a decrease of the number of defects below 50 keV nm^{-1}, second an increase of defect creation above this energy loss.

In the first regime, below 50 keV nm^{-1}, the measured number of defects N_d (black dots in Fig. 2.16a) decreases with the electronic energy loss due to ionization induced annealing. In the same region of electronic energy deposition the defect concentration N_{dc} calculated by SRIM [14] increases (see dotted red curve in Fig. 2.16a). Assuming that the annealing of the defects is thermally activated [121], the number of residual defects N_{da} (solid red curve in Fig. 2.16a) along the ion path is calculated using the thermal spike model [122], assuming an electron-phonon coupling strength of $g = 1.3 \times 10^{12}$ J s^{-1} cm^3 K^{-1} for Fe at 300 K. This value is quite in agreement with 1.2×10^{12} J s^{-1} cm^3 K^{-1} obtained from (2.19) [50]. N_{da} decreases as also experimentally observed (compare solid red curve and black dots in Fig. 2.16a). The calculated larger values of N_{da} as compared to the experimental points are due to the fact that non thermal annealing or defect recombination in the nuclear cascade is not taken into account in the calculations. The maximum temperature of the atomic system reached along the ion track is also plotted versus the electronic energy loss in Fig. 2.16a, showing that the melting temperature (1809 K) is exceeded above 50 keV nm^{-1}.

Above 50 keV nm^{-1} an increase of the defect concentration with increasing electronic energy deposition is observed (black dots in Fig. 2.16a). This second regime can therefore be attributed to defect creation by electronic excitations. It can be assumed that melting of the material around the ion trajectory and subsequent resolidification lead to defect production in a cylinder with a radius which can be obtained from the damage cross section σ [76]. It is assumed that $\sigma = \pi R^2$ where R is the track radius. The energy to create a track was deduced by fitting the track radius measured after an irradiation of Fe by U ions. Two calculations were performed using the g value previously determined from the description of the defect annealing for $S_e < 50$ keV nm^{-1}: In a first scenario the cylinder radius calculated with the energy $E(T_m)$ necessary to reach the melting temperature T_m which is equal to 0.70 eV/at yields an overestimation of the calculated radii compared to the experimental values (Fig. 2.16b). The second calculation assumed an energy to create a track equal to $E_m = E_a(T_m) + H_m = 0.86$ eV/at where H_m is the energy to make the solid to liquid phase transition. Within this last hypothesis the calculated cylinder radii agree with the experiment (Fig. 2.16b). This supports that the equilibrium melting temperature is not an adequate criterion to describe track formation. An energy of 0.86 eV/at corresponds to an effective temperature T_{eff} equal to 2156 K which is larger than T_m as suggested [101, 112]. The track radii calculated with the same electron phonon coupling strength ($g = 1.2 \times 10^{12}$ J s^{-1} cm^{-3} K^{-1}) for an ion energy of 6 MeV/u are in good agreement with the experimental values, as it can be seen in Fig. 2.16c.

Applying this model to Bi the measured radii versus electronic energy loss can be described by using an electron-phonon coupling strength [48] equal to 4×10^{11} J s^{-1} cm^{-3} K^{-1} (see Chap. 8) with $E_m = 0.26$ eV/at. Moreover in this material a temperature effect was observed [123]: the higher the temperature the larger is the track size.

Tracks in the metallic glass a-$Fe_{85}B_{15}$ were also detected by means of SAXS (Small Angle X-ray Scattering) measurements [115]. For these investigations a-$Fe_{85}B_{15}$ was chosen because the track size had been already determined by means of ion fluence dependent resistivity measurements [124–126]. A comparison of the radii determined with different physical characterization methods in Fig. 2.17

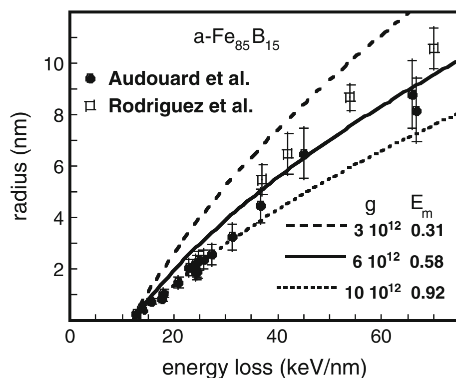

Fig. 2.17 Track radii versus electronic energy loss obtained from resistivity (*full circles* [124]) and SAXS measurements (*open squares* [115]). The lines are i-TS calculations with the parameters g (in W cm^{-3} K^{-1}) and E_m (in eV/at) given in the figure

(measurement points) shows very good agreement. For determining track radii in the framework of the i-TS model, beside other parameters the knowledge of the electron-phonon coupling strength, g, and the energy necessary to melt the material, E_m, are needed. The latter are unknown for the metallic alloys. Merely with the measured melting temperature $T_m = 1496$ K for a-$Fe_{85}B_{15}$ [127] the energy $E_m = 0.31$ eV/at could be evaluated. Therefore several calculations were performed with values of $g = 3 \times 10^{12}$, 6×10^{12} and 10×10^{12} W cm^{-3} K^{-1} in order to determine E_m by fitting the electronic energy loss threshold of ~ 13 keV nm^{-1}. The corresponding energies to melt are $E_m = 0.31$, 0.58 and 0.92 eV/at respectively. The radii calculated with these parameters are compared with the experimental results in Fig. 2.17. As can be seen, the experimental values of the evolution of the track size as function of the electronic energy deposition, S_e, are best described with $g = 6 \times 10^{12}$ W cm^{-3} K^{-1} and $E_m = (0.58 \pm 0.06)$ eV/at. In comparison to pure Fe, the electron-phonon coupling strength, g, is larger and the energy to melt, E_m, is smaller in this alloy. Such deviation of the parameters agrees with the decrease of the electrical conductivity of an amorphous metallic alloy compared to the crystalline phase and to the decrease of the energy to reach the molten phase in an amorphous material, respectively [29].

It should be mentioned that with the model developed by Trinkaus et al. [58, 59] the anisotropic growth of amorphous metals [128] and insulators [30, 129–131] under swift heavy ion irradiation can be successfully described assuming an effective temperature of melting T^*. This anisotropic growth results from the appearance of a molten track along the ion path. This phenomenon is described in more detail in Chap. 10.

Materials with Bonded Electrons: Insulators and Semiconductors

(A) *Description of track size, sputtering yield, ion velocity effect.*

The way how the high energy of the electronic system induced by swift heavy ions is transferred to the lattice atoms of an insulator is described by Baranov et al. [132]: hot electrons are excited in the conduction band and then behave like hot electrons in metals and cool down by excitations of electrons from the valence band to the conduction band and by transferring their energy to the atoms. Such concept was recently revised [133, 134] showing that crystalline SiO_2 irradiated by swift heavy ions undergoes a large enhancement of the electrical conductivity comparable to that of metals like gold, supporting the first step of this schematic description. But the values of the electron-phonon coupling strength are unknown for insulators in the case of high electronic excitations. Consequently, instead of g as the free parameter, the electron-phonon mean free path λ, which is defined as $\lambda^2 = D_e C_e / g$ (Sect. 2.3.5.3c) with $D_e = 2$ cm^2 s^{-1} and $C_e = 1$ J cm^{-3} K^{-1} corresponding in first approximation to the values for hot electrons in metals is used. Moreover, in the case of insulators the energy exchange from the atoms to electrons is inhibited and the atomic cooling rate, characterized by the thermal diffusivity of

the atoms [44], is one order of magnitude smaller than the heating rate. To illustrate the application of this model to insulators, three materials will be analysed: (1) SiO_2 quartz in its crystalline phase where track formation [46, 135] and sputtering [113] are described with the same value of λ, (2) SiO_2 in its amorphous phase illustrating the increase of the sensitivity of an amorphous material to high electronic excitation [136] and explaining the radial morphology of the track [62] and (3) track formation in $Y_3Fe_5O_{12}$ crystals to illustrate the velocity effect [18].

Taking crystalline SiO_2 quartz as typical case, λ = 3.8 nm is determined by fitting the track size (Fig. 2.18) with the i-TS model [113], assuming E_m, the energy necessary to melt the material, as the criterion to create a track. The sputtering rate Y_{tot} can be calculated within the framework of statistical thermodynamics (for details see [137]):

$$Y_{tot} = \int_0^\infty dt \int dr\, \Phi(T_a(r,t)) \text{ with } \Phi(T_a(r,t)) = N\sqrt{\frac{\mathrm{k_B\,T_a(r,t)}}{2\pi\,\mathrm{m_{sp}}}} \quad \exp\left(\frac{-\mathrm{U_s}}{\mathrm{k_B\,T_a(r,t)}}\right) \tag{2.20}$$

where $\mathrm{m_{sp}}$ is the mass of the sputtered atom and k_B the Boltzmann constant, $T_a(r,t)$ is the atomic temperature at a time t and at a distance r from the ion axis and U_s the known sublimation energy of crystalline SiO_2 [114]. In Fig. 2.18 measured and calculated track radii (filled dots and dashed line) and sputtering yields (open dots and solid line) for SiO_2 irradiated with an ion energy of 1 MeV/u are plotted versus the electronic energy loss. It is obvious that with the same value of the electron-phonon mean free path, λ = 3.6 nm, both track formation and sputtering yield can be described.

As described above for SiO_2 the electron-phonon mean free path was determined by fitting the track size in different amorphizable oxide materials [116]. It is clearly

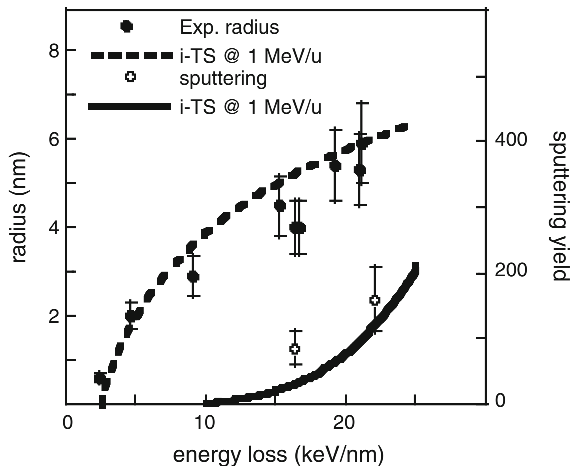

Fig. 2.18 Track radii [46] and sputtering rate [113] versus electronic energy loss for crystalline SiO_2 quartz. The lines correspond to the calculations with the i-TS model [113, 137]

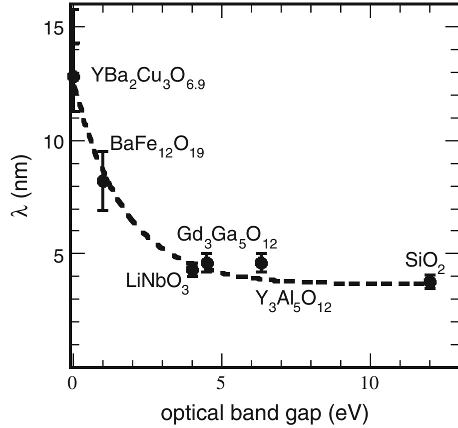

Fig. 2.19 Electron-phonon mean free path, λ, versus optical band gap energy for several amorphizable crystalline oxides [116] (figure partly extracted from [44])

to be seen in Fig. 2.19 that λ decreases monotonously with the band gap energy (E_G) of the materials investigated: the lower λ the larger the electron-phonon coupling. The decrease of λ is in agreement with the increase of the electron phonon coupling which increases with band gap energy [56]. According to Monte Carlo calculations, hot electrons in the conduction band cool down by an excitation of electrons from the valence band to the conduction band. The larger the band gap, the larger the cooling of the electrons and consequently the smaller the radial expansion of the energy to the electrons before its transfer to the atoms will be. If this correlation between the electron-phonon mean free path and the band gap energy (Fig. 2.19) is right [44] then there is no more free parameter in the i-TS model applied to crystalline insulators if E_m is known.

If E_m is not known, for materials with known gap energy at first the electron-phonon mean free path λ can be determined from its gap energy dependence as it is shown in Fig. 2.19 for the example of amorphizable oxides. Then with these values the energy necessary to melt the material, E_m, can be calculated by fitting the track radii versus the electronic energy deposition. In case of yttrium iron garnet ($Y_3Fe_5O_{12}$) with a gap energy of E_g = 2.8 eV an electron-phonon mean free path of λ = 5 nm is obtained from Fig. 2.19. For the calculation of E_m the fit of the track radii was limited to irradiations with beam energies less than 0.4 MeV/u yielding E_m = (0.55 ± 0.04) eV/at (see Fig. 2.20a) [47]. As expected this value is larger by 0.12 ± 0.04 eV/at than the energy necessary to reach the melting temperature which is equal to 0.43 eV/at. This value of 0.12 eV/at may correspond to the energy necessary to make the solid to liquid phase transition.

It is obvious in Fig. 2.20a that there is nearly no difference in the track radii in $Y_3Fe_5O_{12}$ for beam energies lower than 3.5 MeV/u while the radius is smaller for energies around 10 MeV/u. This is obviously a consequence of the different velocities in the two energy regions and the resulting different values of the mean absorption radius α. An explanation of this observation is possible by comparing the electron-phonon mean free path λ with the energy dependence of the mean

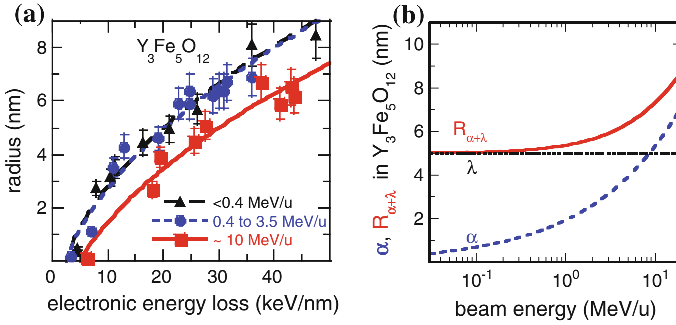

Fig. 2.20 **a** Calculation of the track radii in $Y_3Fe_5O_{12}$ measured at different beam energies (data points) for λ = 5 nm and an energy to reach the molten phase of E_m = 0.55 eV/at which takes into account the energy for the solid to liquid phase transition, (figure compiles data extracted from [47]). **b** Evolution of α (data from Fig. 2.3c) and $R_{\alpha+\lambda}$ versus beam energy for $Y_2Fe_5O_{12}$

absorption radius α for $Y_3Fe_5O_{12}$ (see Fig. 2.3c in Sect. 2.2.2). According to Fig. 2.3c the absorption radius α is equal to the electron-phonon mean free path λ at a beam energy of 10 MeV/u, $\alpha = \lambda = 5$ nm. Contrary, at smaller energies, here in the energy region between 0.04 and 3.5 MeV/u, λ is larger than α as illustrated in Fig. 2.20b. Consequently this λ value exceeds the radius in which the energy of the ions is initially deposited in the electronic system, i.e. the energy transfer to the atoms occurs in a larger radius compared to that of the initial energy deposition in the electronic system. But for energies in the order of 10 MeV/u and above the cylinder radius in which the energy is transferred to the atoms is determined by both λ and α. This radius $R_{\alpha+\lambda}$ is a convolution of both quantities and can be described by the relation $R^2_{\alpha+\lambda} = \alpha^2 + \lambda^2$. The dependence of $R_{\alpha+\lambda}$ on the ion energy is illustrated in Fig. 2.20b for $Y_3Fe_5O_{12}$ in comparison with the values of λ and α (from Fig. 2.3c) for this material. In the region of low energies, i.e. for energies <5 MeV/u, where α is smaller than λ, the deposition radius $R_{\alpha+\lambda}$ is nearly independent of the ion energy, i.e. the ion velocity does not remarkably modify the track radius in this region. In contrast, for energies >5 MeV/u, the volume in which the energy is deposited in the atomic system is mainly determined by α and remarkably influenced by the ion energy (Fig. 2.20b). Consequently, the initial energy is deposited in a larger volume leading to a smaller deposited energy density and, for a given threshold value of the electronic energy loss, S_{et}, to smaller track radii.

(B) *Amorphous versus crystalline material and radial track morphology.*

As the metallic materials, amorphous insulators are also more sensitive to electronic excitation than the same material in its crystalline phase. This will be illustrated in the following for the example of amorphous SiO_2 (a-SiO_2). The track size in a-SiO_2 was fitted by Rotaru et al. [136] and a value of λ = 3 nm was obtained for the electron-phonon mean free path, which is smaller than that of 3.6 nm for crystalline

quartz. In addition this material has a particular radial track morphology as found by SAXS measurements [62]: an under dense core is surrounded by an over dense shell. The experimental radii are plotted in Fig. 2.21 versus the Au ion energy ranging from 20 to 200 MeV. Using the electron-phonon mean free path $\lambda = 3$ nm, the track radius produced by Au ions consisting of the core+shell criterion ($\Delta E_m = 0.38$ eV/at from a temperature of irradiation = 300 K). Now if using the energy to reach the boiling phase of the material which is the sum of the melting energy plus the energy to increase the temperature from T_m to T_b, the boiling temperature, plus the energy to make the liquid-boiling phase transition, the radii of the track core can be described using the same value of λ (Fig. 2.21). The use of the melting and boiling criteria was successfully applied to analyse specific responses in LiF [138, 139] and CaF_2 [61] in order to describe damage tracks resulting from the molten phase and from the boiling phase with the same electron-phonon coupling.

(C) *New developments for semiconductors.*

In a recent revue, Klaumünzer [30] makes several propositions for a further development of the thermal spike models. These models are not only used in ion-track physics, but also to describe the behaviour of free electrons and holes (carrier pairs) generated by femtosecond lasers [140, 141] in the case of band gap materials. Though these various models deal with similar physical problems, they do not take much notice of each other. The consequence is that knowledge, which has been gained in one field, is not transferred to the others.

First the description of track formation in semiconductors should take advantage of the knowledge of the value of the electron-phonon mean free time $\tau = 0.1$ and 0.12 ps for Si and GaAs, respectively [142], as it was obtained from fs laser experiments. With these values of τ and with the relation $\lambda^2 = D_e(T_e)\ \tau$ with $D_e = 2\ \text{cm}^2\ \text{s}^{-1}$ at high electronic temperature, the electron-phonon mean free path is $\lambda \sim 5$ nm for the two semiconductors. With such λ values Si and GaAs should be

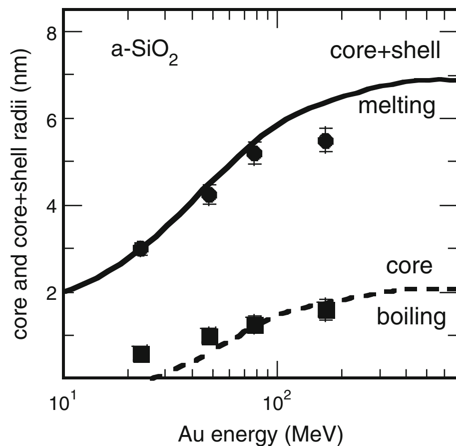

Fig. 2.21 Track radii in a-SiO_2 versus the Au ion energy. The points correspond to track radii in amorphous SiO_2 coresponding to a core (*squares*) and to core+shell (*dots*) structure as deduced from SAXS analysis [62]. The lines are the result of the calculations using the melting (*solid line*) and boiling (*dashed line*) criteria, respectively

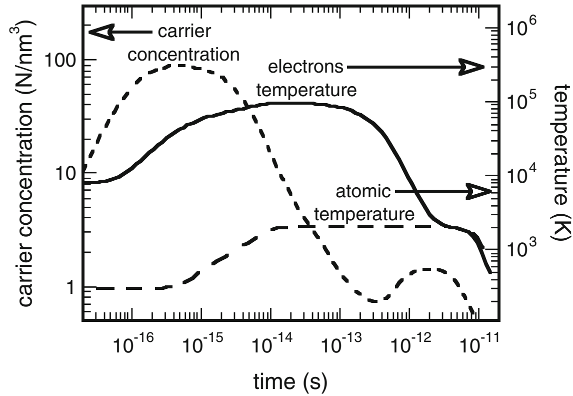

Fig. 2.22 The time evolution of the lattice temperature (*dashed line*), the electronic temperature (*solid line*) and the carrier concentration (*dotted line*) at the centre of an ion track in silicon resulting from an electronic energy deposition of 50 keV nm^{-1}(from [144])

sensitive to swift heavy ion irradiation in contrast to the results presented in Chap. 9. However, more experimental and theoretical studies are necessary in order to understand the differences between swift heavy ion and fs laser irradiation of semiconductors. For a discussion of this question the reader is referred to Sect. 2.3.2 and the paper of Sall et al. [143].

Second a severe deficiency in the currently used thermal spike models in ion track physics is the lack of taking into account the creation of electron-hole carriers. After a short time the carriers recombine, and the corresponding freed energy is transferred to the remaining electrons in the conduction band leading to an "electronic temperature". To take into account this physical phenomenon, Daraszewicz and Duffy [144] describe the creation of amorphous tracks in Si by taking into account the creation of electron-hole carriers. Instead of using the diffusion equation for the electrons [(2.6)] alone the authors try to model the fact that ionizing radiation in insulators results in a non equilibrium electron distribution, implying an excess of electrons in the conduction band connected with an increase of the number of holes in the valence band. This involves an energy confinement of the carriers. In the case of high electronic excitation carrier diffusion may be inhibited by the band gap gradient and the carriers may be confined. Such calculations have been done for Si by Daraszewicz and Duffy [144], and the time evolution of carrier concentration as well as lattice and electronic temperature are plotted versus time in Fig. 2.22. The energy given to the carriers is transferred to free electrons by carrier recombination and then transmitted to the lattice by electron-phonon coupling. If the lattice temperature exceeds the energy necessary to melt, amorphous tracks result from the quenching of the molten phase.

2.3.5.4 Combination of the Exciton with the Thermal Spike Model

The exciton decay model was recently developed for $LiNbO_3$ [145, 146] and for TiO_2 [38]. It is based on the synergy of nonradiative exciton decay and the

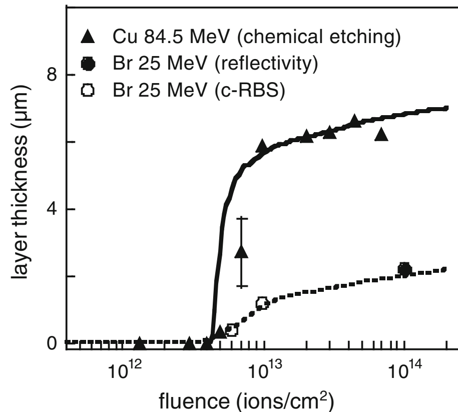

Fig. 2.23 Thickness of the amorphous layer in TiO_2 versus fluence for different irradiations [38]. The thickness of the amorphous layer was determined by chemical etching in case of the Cu irradiations, by means of reflectivity (*filled dots*) and channeling Rutherford backscattering (*open dots*) in case of Br irradiation at 25 MeV, respectively. The *solid lines* are obtained with the exciton model [38]

generated thermal spike. The non-radiative exciton decay leads to point defect-formation but it is only possible thanks to the energy provided by the thermal spike. The exciton model is described in detail in [146]. Another important point is that the model assumes that amorphization takes place when a critical defect concentration is reached, i.e., amorphization occurs as a defect driven transition whenever the stopping power of the ion exceeds the threshold value, S_{et}. Note that the model does not necessarily require melting as a process for amorphization.

The model was applied to $LiNbO_3$ and TiO_2. As example the depth evolution of the amorphous layer in TiO_2 was determined versus the ion fluence for different irradiations (see Fig. 2.23). The layer thickness values at an ion fluence of 10^{14} ions cm^{-2} for Cu and Br irradiations are 7 and 2 μm respectively. The different layer thicknesses that are amorphized are linked to the depth where the electronic energy loss threshold of track formation in TiO_2 by Cu and Br is reached. Using SRIM the corresponding electronic energy losses are then 4.7 and 5.3 keV/nm, respectively, leading to the electronic energy loss threshold of $\sim$5 keV nm^{-1} for amorphization of TiO_2.

2.4 Microscopic Models: Molecular Dynamics Approaches

Several molecular dynamics models have been developed to describe how the atoms behave after electronic excitation caused by the irradiation of matter with swift heavy ions. The following description will be separated in two parts: the first will be related to sputtering in the electronic regime and the second part will be devoted to track formation.

2.4.1 Sputtering by Electronic Excitation

The first molecular dynamics (MD) calculation was initiated by Urbassek et al. [64] to predict the emission yield of particles escaping from an argon crystal due to high electronic excitation. As a first approach it was assumed that sputtering is a consequence of a thermal spike. An idealized track is a cylinder in which the kinetic energy is deposited with a random direction of motion corresponding to thermal equilibrium. The atoms interact via a Lennard-Jones potential. The calculations show that there is a kind of two components in the angular distribution of the ejected particles: a jet perpendicular to the surface superimposed by a cosine distribution as observed in LiF [137]. As can be seen in Fig. 2.24 for the example of an Ar crystal, the sputtering yield (curve labelled as cylinder) follows a power law with $S_e^{3.3}$ for values of the electronic energy loss less than 0.6 keV nm^{-1} where the energy deposited in the atoms, E_0, is less than the sublimation energy, U_s, while it is linear with S_e for $E_0 > U_s$. In a second approach proposed by Bringa [66], a Coulomb explosion was simulated in order to study the effect of this phenomenon on the sputter rate. It was found that the energy deposited in the atoms by a Coulomb explosion is thermalized in very short time so that the distribution of the emitted particles also consists of two components similar to the approach by Urbassek et al. [64]. Consequently, it will be difficult to distinguish between the effects of Coulomb explosion and thermal spike on the sputter process when only studying the shape of the angular distribution of the emitted particles.

The approaches described above were complemented recently by Beuve et al. [147] and Mookerjee et al. [65]. In this approach the energy transfer to the atoms is obtained by a numerical solution of (2.6) in Sect. 2.3.5 which describes the energy deposition in the electrons after the electron cascade, their energy diffusion and their energy transfer to the atoms via electron-phonon coupling defined by the electron-phonon mean free path λ [65]. The sputtering yields calculated for different values of λ are plotted versus the electronic energy loss in Fig. 2.24 and compared to the result of Urbassek et al. [64]. Clearly the threshold value for onset of sputtering is larger compared to the case of direct energy transfer to the atoms as

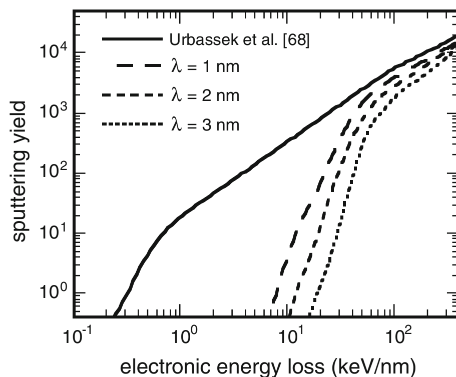

Fig. 2.24 Sputtering yield of an Ar crystal versus electronic energy loss. The *full line* is the result of MD calculations performed by Urbassek et al. [64]. The *dashed* and *dotted lines* are obtained in the framework of i-TS calculations using an electron-phonon mean free path of *1*, *2* and *3* nm (Mookerjee et al. [65])

assumed in the MD calculations (solid line in Fig. 2.24). The reason for this difference is that within the i-TS calculations the energy initially deposited in the electrons is reduced in the electronic subsystem by electron-electron interaction before it is transferred to the lattice atoms. Moreover, the threshold value increases with increasing value of the electron-phonon mean free path since the initial energy deposited in the electrons expands to the atoms in a larger volume. Near this threshold of sputtering for $S_e < 50$ keV nm^{-1}, the sputtering rate follows a power of ~ 5 with S_e independent of the λ value, reaching a power of one at larger S_e values like in the calculation of Urbassek et al. [64] for large S_e values.

In recent MD calculations by Huang et al. [148] it was tried to simulate the measured sputtering rate in UO_2 [149]. Using the approach developed by Beuve et al. [146] it was shown that the electron-phonon mean free path for UO_2, needed to reproduce the sputtering rate varies from 3 to 4 nm, depending on the value of the sublimation energy which was either obtained from the potential used for the MD calculation or from experiments, respectively. The value of 4 nm is not far from the value of 4.5 nm obtained from the systematic study of the electron-phonon mean free path as function of the band gap energy [44] in insulators (Fig. 2.19).

2.4.2 Track Formation

Several MD calculations to describe track formation have been performed following the approach by Urbassek et al. [64] where electronic excitations in the ion tracks are simulated as prompt cylindrical spikes whose energy is transferred to the atoms with a random direction of motion. Within this scheme a quantitative comparison with the experiment is difficult since in the electronic energy loss regime the energy deposition in the atoms is a complex combination of the initial energy deposition in the electrons as function of the incident ion velocity and the electron-phonon mean free path [109]. Moreover, in MD calculations the main problem consists in the development of realistic potentials that describe the main properties of the considered materials. However, the calculations follow the evolution of the energy transfer to the atoms as function of the time and give a final state of the material within the track at a time of around 10^{-10} s.

To show the strength of such MD predictions, Zhang et al. [2] analyzed the quenching states finally leading to the formation of an amorphous track in $Gd_2Ti_xZr_{2-x}O_7$, a class of pyrochlores for which it is well known that amorphization depends on the composition [150] (for details see Chap. 8). It is shown that the radial morphology of tracks in this material class can be reproduced by MD calculations, e.g. ranging from an amorphous track in $Gd_2Ti_2O_7$ to a complete defective fluorite structure in $Gd_2Zr_2O_7$. This is illustrated in Fig. 2.25 for the example of the intermediate composition with $x = 1$, i.e. for Gd_2TiZrO_7. In this case the track consists of an amorphous core surrounded by a defective fluorite shell. The difference between the real electronic energy loss of 2.2 GeV Au ions, S_e = 40 keV nm^{-1} and the value used for the MD calculation, S_e = 11 keV nm^{-1}, is due

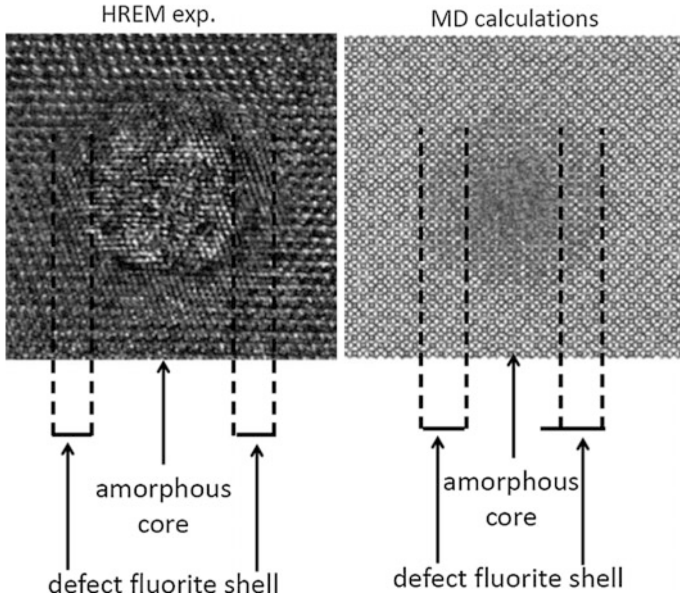

Fig. 2.25 HRTEM image of the morphology of an individual ion track produced by 2.2 GeV Au ions (S_e = 40 keV nm^{-1}) in Gd_2TiZrO_7 (*left*) that is reasonably reproduced by MD thermal spike calculations in Gd_2TiZrO_7, with an effective energy loss of 11 keV nm^{-1} (*right*) [2]

to the fact that the energy in case of the MD calculation is directly deposited in the atoms. MD calculations made by Pakarinen et al. [151] for crystalline SiO_2 and ZnO show different trends: tracks in SiO_2 become amorphous while in ZnO recrystallized tracks are observed.

In the case of graphite and diamond [66] for energy deposition within a cylinder of 3 nm radius, full amorphization of this region occurs during the first few picoseconds when the electronic energy loss is larger than (6.0 ± 0.9) keV nm^{-1} for graphite and (10.5 ± 1.5) keV nm^{-1} for diamond. These two values of electronic energy loss are "effective" since they correspond to an energy deposited in the 3 nm cylinder radius excluding any electronic energy diffusion prior to the transfer to the atoms. With another deposition model including energy diffusion to the electrons Pakarinen et al. [151] showed that the crystalline to amorphous transition in a diamond track should appear above a real electronic energy loss of 20 keV nm^{-1} if energy diffusion to the electrons is taken into consideration.

To illustrate the complexity of the description of track formation in insulators by MD calculations the core-shell structure of tracks observed in amorphous SiO_2 (a-SiO_2) [62] using small angle x-ray scattering (SAXS) [152] was calculated. The energy deposition profile was obtained from i-TS calculations [116] for Au ions with 1.1 MeV/u energy at the initial stage of the energy deposition. As previously described, such deposition profiles take into account the initial energy distribution of the electrons received from MC calculations. The energy then diffuses by

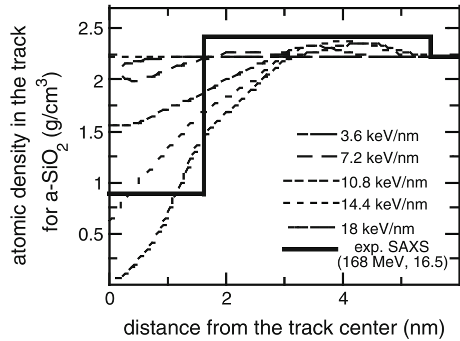

Fig. 2.26 Radial density profiles obtained from MD calculations for a-SiO_2 for different values of the electronic energy loss compared to the result of the SAXS experiment at 168 MeV irradiated a-SiO_2 [62]. The bulk density is 2.23 g/cm^3

electron-electron interactions before it is transferred to the atoms by electron-phonon coupling. The strength of this electron-phonon coupling is quantified by the electron-phonon mean free path (λ = 3 nm) which was obtained by fitting the track size in a-SiO_2 [136]. The electronic energy loss distribution was implemented in the code by an instantaneous deposition of kinetic energy in the atoms in a random direction. Now to model the anisotropic growth [129–131, 153] during track formation, MD calculations were performed for amorphous SiO_2 using the classical MD code [154–156]. The main principles of the molecular dynamics algorithms are described by Nordlund et al. [154] and Ghaly et al. [155]. The adaptive time step and electronic stopping algorithms are the same as in [154]. The atomic interactions were calculated using the Watanabe Si-O mixed system many-body potential [157, 158]. With such a model the observed permanent density changes in the track structure can be calculated by including the dynamics of the material transport. The simulations reveal a glass transition temperature of (2500 $\pm$ 500) K and a boiling temperature of (5500 $\pm$ 500) K for a-SiO_2 under superheating conditions, both in good agreement with the values used in the i-TS calculations. Figure 2.26 shows the radial density profiles achieved from the calculations for a-SiO_2 irradiated at various electronic energy depositions. All tracks consist of a low density core and a higher density shell in agreement with the SAXS measurements. The full line shows for comparison a density profile as deduced from SAXS measurements of samples irradiated with 168 MeV Au ions. The radii of the track cores obtained from the MD simulations for under-dense core and core +shell track radii, corresponding to the overall track size (under-dense core + over-dense shell), are plotted in Fig. 2.27 and agree with the SAXS measurements.

In conclusion, MD calculations are a good tool to describe the atomic rearrangement after this dense and nanometric energy deposition. However, a quantitative comparison with the experiment needs the knowledge of realistic values of the energy transfer to the atoms [62].

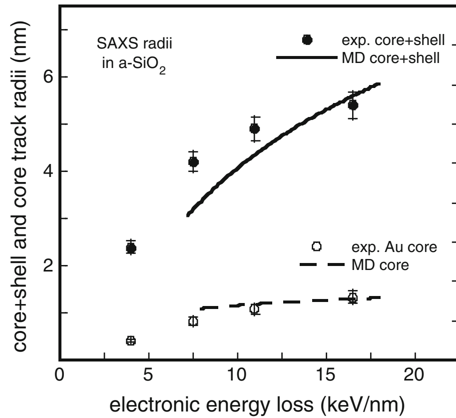

Fig. 2.27 Comparison of the calculated size of the track core (*dashed line*) and of the size of the core+shell track (*full line*) with SAXS radii for the core (*open dots*) and core +shell track (*filled dots*) measured by Kluth et al. [62]

2.4.3 Summary and Conclusions

The formation of tracks in materials irradiated in the electronic energy loss regime is the result of complex processes of energy deposition in the electrons, involving several steps on different time scales: (i) initial energy deposition in the electrons (10^{-17}–10^{-16} s), (ii) energy dissipation among the electrons (10^{-16}–10^{-14} s), leading to a radial expansion of the energy in a cylinder radius between 1 and 10 nm, and (iii) energy transfer to the atoms via the electron-phonon coupling (10^{-14}–10^{-12} s) leading to atomic motion and finally to the creation of a cylindrical damage along the ion path. The advantage to study the material transformation irradiated by swift heavy ions as compared to fs laser irradiation is given by a well-defined energy deposited in the electrons in a very short time and in a very small cylindrical volume. For most of fs laser irradiations, the electron energy excitation is created in a time of $\sim 10^{-14}$ s and the light is deposited in a volume of 0.5×0.5 μm^2 surface in a minimum depth of 10 nm. This planar geometry for the energy deposition leads to a cooling down time of the excited matter which is one order of magnitude larger than in the case of SHI.

In this chapter a review of the different models to describe the track formation are presented. There is an overall agreement on the time and on the radial distribution of energy deposition in the electrons using Monte Carlo calculations [19–25]. But several macroscopic models have been proposed to describe how this deposited energy is transferred to the atoms of the target: Coulomb explosion [32], reduced electronic energy loss [25], self-trapped exciton [36, 91], and bond weakening model [40]. The deficiency of these theoretical descriptions is the fact that they were tested on a very limited number of materials, one or two at most. Some more comparisons with numerous experimental results are needed to validate these descriptions. The only model applied to all kinds of materials, metallic materials, semiconductors and insulators, is the thermal spike model [42, 44, 48]. It was developed analytically [42] for insulators and semiconductors with two free parameters: there is a unique value of the initial radial energy deposition in the

atoms, whatever the beam energy is, using only a fraction of the energy deposited in the electrons that goes to the atoms. The numerical solution of the thermal spike model is most extensively studied [44, 48]: it takes into account (i) the initial energy deposition in the electrons obtained from Monte Carlo calculations normalized to the electronic energy loss, (ii) its evolution in the electronic system followed by (iii) its transfer to the atoms via electron-phonon coupling. The electron-phonon coupling is the only free parameter. The numerical development of the thermal spike model is powerful in describing (i) defect annealing [122], track defect creation [50], atomic mixing in metallic materials [159], (ii) track formation [116], sputtering [113] and the appearance of two thresholds of different damage creation [61, 62] in insulators, (iii) the deformation of Au nanoclusters embedded in a vitreous silica matrix [160]. However several critical examinations of the numerical solutions of the i-TS model were performed [30, 100] and the authors encourage the readers to go through these criticisms. One of the remaining questions is the description of irradiated semiconductors by this last model [63, 143] as mentioned in Chap. 9 of this book.

Aknowledgements Many thanks to S. Bouffard [25] and B. Canut [43] with whom I get deep discussions regarding their models. We would also like to thank E. Paumier who was with us when developing the numerical solutions of the inelastic thermal spike model. We would also deeply like to thank W. Wesch for critical and constructive reading of the manuscript.

References

1. M. Toulemonde, F. Studer, Phil. Mag. A **58**, 799 (1988)
2. J. Zhang, M. Lang, R.C. Ewing, R. Devanathan, W.J. Weber, M. Toulemonde, J. Mater. Res. **25**, 1345 (2010)
3. E. Balanzat, S. Bouffard, Sol. State Phenom. **30–31**, 7 (1993)
4. N. Bohr, Mat. Fys. Medd. **18**, 8 (1948)
5. J. Lindhard, M. Scharff, Phys. Rev. **124**, 128 (1961)
6. J. Lindhard, M. Scharff, H.E. Schiott, Mat Fys. Medd. **33**, 14 (1963)
7. J.P. Rozet, C. Stephan, D. Vernhet, Nucl. Instr. Meth. B **107**, 67 (1996)
8. P.L. Grande, G. Schiwietz, Nucl. Instr. Meth. B **267**, 859 (2009)
9. M. Toulemonde, Nucl. Instr. Meth. B **250**, 263 (2006)
10. J.P. Biersack, J.F. Ziegler, Nucl. Instr. Meth. **194**, 93 (1982)
11. J.F. Ziegler, Nucl. Instr. Meth. B **6**, 270 (1985)
12. P.L. Grande, G. Schiwietz, Adv. Quantum Chem. **45**, 7 (2004)
13. M. Toulemonde, F. Haas, Phys. Rev. C **15**, 49 (1977)
14. J.F. Ziegler, M.D. Ziegler, J.P. Biersack, Nucl. Instr. Meth. B **268**, 1818 (2010)
15. Y. Zhang, I.-T. Bae, K. Sun, C. Wang, M. Ishimaru, Z. Zhu, W. Jiang, W.J. Weber, J. Nucl. Mater. **389**, 303 (2009)
16. P. Sigmund, Mat. Fys. Medd. **52**, 557 (2006)
17. P. Sigmund, Eur. Phys. J. D **47**, 45 (2008)
18. A. Meftah, F. Brisard, J.M. Costantini, M. Hage-Ali, J.P. Stoquert, F. Studer, M. Toulemonde, Phys. Rev. B **48**, 920 (1993)
19. E.J. Kobetich, R. Katz, Phys. Rev. **170**, 391 (1968)
20. R. Katz, E.J. Kobetich, Phys. Rev. **186**, 344 (1969)

21. J. Fain, M. Monnin, M. Montret, Rad. Reas. **57**, 379 (1974)
22. C. Zhang, D.E. Dunn, R. Katz, Radiat. Protect. Dos. **13**, 215 (1985)
23. B. Gervais, S. Bouffard, Nucl. Instr. Meth. B **88**, 355 (1994)
24. G. Kraft, M. Krämer, Adv. Rad. Biol. **17**, 1 (1993)
25. S. Bouffard, C. Leroy, S. Della-Negra, A. Brunelle, J.M. Costantini, Phil. Mag. A **81**, 2841 (2001)
26. M.P.R. Waligorski, R.N. Hawn, R. Katz, Nucl. Track Rad. Meas. **11**, 309 (1986)
27. M. Toulemonde, W. Assmann, C. Dufour, A. Meftah, F. Studer, C. Trautmann, Mat. Fys. Medd. **52**, 263 (2006)
28. L.V. Zhigilei, D.S. Ivanov, E. Leveugle, SPIE **448**, 505 (2004)
29. M. Toulemonde, C. Dufour, E. Paumier, Phys. Rev. B **46**, 14362 (1992)
30. S. Klaumünzer, Mat. Fys. Medd. **52**, 293 (2006)
31. E. Silk, R. Barnes, Philos. Mag. **4**, 970 (1959)
32. R.L. Fleischer, P.B. Price, R.M. Walker, *Nuclear Tracks in Solids: Principles and Applications* (University of California, Berkeley, 1975)
33. D. Lesueur, A. Dunlop, Radiat. Eff. Defects Solids **126**, 163 (1993)
34. A. Iwase, N. Ishikawa, Y. Chimi, K. Tsuru, H. Wakana, O. Michikami, T. Kambara, Nucl. Instr. Meth. B **146**, 557 (1998)
35. K.S. Song, R.T. Williams, *Self Trapped Excitons* (Springer, Berlin, 1993)
36. N. Itoh, A.M. Stoneham, Nucl. Instr. Meth. B **146**, 362 (1998)
37. N. Itoh, D.M. Duffy, S. Khakshouri, A.M. Stoneham, J. Phys. Condens. Matter **21**, 474205 (2009)
38. A. Rivera, M.L. Crespillo, J. Olivares, R. Sanz, J. Jensen, F. Agulló-López, Nucl. Instr. Meth. B **268**, 3122 (2010)
39. J.A. van Vechten, R. Tsu, F.W. Saris, D. Hoonhout, Phys. Lett. A **74**(1979), 417 (1979)
40. P. Stampfli, K.H. Bennemann, Phys. Rev. B **49**(1994), 7299 (1994)
41. G. Szenes, Phys. Rev. B **51**, 8026 (1995)
42. G. Szenes, Phys. Rev. B **52**, 6154 (1995)
43. B. Canut, S.M.M. Ramos, Radiat. Eff. Defects Solids **145**, 1 (1998)
44. M. Toulemonde, Ch. Dufour, A. Meftah, E. Paumier, Nucl. Instr. Meth. B **166–167**, 903 (2000)
45. C. Trautmann, M. Toulemonde, C. Dufour, E. Paumier, Nucl. Instr. Meth. B **108**, 94 (1996)
46. A. Meftah, F. Brisard, J.M. Costantini, E. Dooryhée, M. Hage-Ali, M. Hervieu, J.P. Stoquert, F. Studer, M. Toulemonde, Phys. Rev. B **49**, 12457 (1994)
47. A. Meftah, M. Djebara, N. Khalfaoui, M. Toulemonde, Nucl. Instr. Meth. B **146**, 431 (1998)
48. Ch. Dufour, A. Audouard, F. Beuneu, J. Dural, J.P. Girard, A. Hairie, M. Levalois, E. Paumier, M. Toulemonde, J. Phys. Condens. Matter **5**, 4573, (1993)
49. Ch. Dufour, Z.G. Wang, E. Paumier, M. Toulemonde, Bull. Mater. Sci. **22**, 671 (1999)
50. Z.G. Wang, Ch. Dufour, E Paumier, M. Toulemonde, J. Phys. Condens. Matter **6**, 6733 (1994)
51. C. Dufour, B. Lesellier de Chezelles, V. Delignon, M. Toulemonde, E. Paumier, in *Proceedings of Conference on Chemical and Physical Modifications Induced by Irradiation in Glasses*, ed. by P. Mazzoldi (E-MRS, Strasbourg, 1992), p. 61
52. D.M. Duffy, S. Khakshouri, A.M. Rutherford, Nucl. Instr. Meth. **267**, 3050 (2009)
53. D.M. Duffy, S.L. Daraszewicz, J. Mulroue, Nucl. Instr. Meth. B **277**, 21 (2012)
54. C.P. Race, D.R. Mason, M.W. Finnis, W.M.C. Foulkes, A.P. Horsfield, A.P. Sutton, Rep. Prog. Phys. **73**, 116501 (2010)
55. M. Kaganov, I.M. Lifshitz, L.V. Tanatarov, Sov. Phys. JETP **4**, 173 (1957)
56. R.F. Haglund, R. Kelly, Mat. Fys. Medd. **43**, 527 (1992)
57. W. Hayes, A.M. Stoneham, in *Defects and Defect Processes in Nonmetallic Solids* (John Wiley and sons, New York, 1985)
58. H. Trinkaus, J. Nucl. Mater. **223**, 196 (1995)
59. A.L. Ryazanov, H. Trinkaus, A.E. Volkov, Phys. Rev. Lett. **84**, 919 (2000)
60. C. Trautmann, S. Klaumünzer, H. Trinkaus, Phys. Rev. Lett. **85**, 3648 (2000)

61. M. Toulemonde, A. Benyagoub, C. Trautmann, N. Khalfaoui, M. Boccanfuso, C. Dufour, F. Gourbilleau, J.J. Grob, J.P. Stoquert, J.M. Costantini, F. Haas, E. Jacquet, K.-O. Voss, A. Meftah, Phys. Rev. B **85**, 054112 (2012)
62. P. Kluth, C.S. Schnohr, O.H. Pakarinen, F. Djurabekova, D.J. Sprouster, R. Giulian, M.C. Ridgway, A.P. Byrne, C. Trautmann, D.J. Cookson, K. Nordlund, M. Toulemonde, Phys. Rev. Lett. **101**, 175503 (2008)
63. A. Kamarou, W. Wesch, E. Wendler, A. Undisz, M. Rettenmayr, Phys. Rev. **78**, 054111 (2008)
64. H.M. Urbassek, H. Kafemann, R.E. Johnson, Phys. Rev. B **49**, 786 (1994)
65. S. Mookerjee, M. Beuve, S.A. Khan, M. Toulemonde, A. Roy, Phys. Rev. B **78**, 045435 (2008)
66. E.M. Bringa, Nucl. Instr. Meth. B **209**, 1 (2003)
67. D. Schwen, E.M. Bringa, Nucl. Instr. Meth. B **256**, 187 (2007)
68. G. Schiwietz, K. Czerski, M. Roth, F. Staufenbiel, P.L. Grande, Nucl. Instr. Meth. B **226**, 6828 (2004)
69. G. Schiwietz, M. Beye, K. Czerski, A. Fohlisch, R. Konnecke, M. Roth, J. Schlappa, F. Staufenbiel, E. Suljoti, I. Kuusik, P.L. Grande, Nucl. Instr. Meth. B **317**, 48 (2013)
70. J. Rzadkiewicz, A. Gojska, O. Rosmej, M. Polasik, K. Słabkowska, Phys. Rev. A **82**, 012703 (2010)
71. A. Dunlop, D. Lesueur, Radiat. Eff. Defects Solids **126**, 123 (1993)
72. B. Canut, A. Benyagoub, G. Marest, A. Meftah, N. Moncoffre, S.M.M. Ramos, F. Studer, P. Thévenard, M. Toulemonde, Phys. Rev. B **51**, 12194 (1995)
73. N. Khalfaoui, J.P. Stoquert, F. Haas, C. Traumann, A. Meftah, M. Toulemonde, Nucl. Instr. Meth. B **286**, 247 (2012)
74. A. Dunlop, P. Legrand, D. Lesueur, N. Lorenzelli, J. Morillo, A. Barbu, S. Bouffard, Europhys. Lett. **15**, 765 (1991)
75. H. Dammak, D. Lesueur, A. Dunlop, P. Legrand, J. Morillo, Radiat. Eff. Defects Solids **126**, 111 (1993)
76. A. Dunlop, D. Lesueur, P. Legrand, H. Dammak, J. Dural, Nucl. Instr. Meth. B **90**, 330 (1994)
77. J.C. Phillips, Rev. Mod. Phys. **42**, 317 (1970)
78. M. Combescot, J. Bok, J. Benoit à la Guillaume, Phys. Rev. B **29**, 6393 (1984)
79. P. Baeri, J. de Phys. **44**, 157 (1983)
80. R.O. Bell, M. Toulemonde, P. Siffert, Appl. Phys. **19**, 313 (1979)
81. M. Toulemonde, R. Heddache, F. Nielsen, P. Siffert, J. Appl. Phys. **56**, 187 (1984)
82. M. Toulemonde, S. Unamuno, R. Heddache, M.O. Lampert, M. Hage-Ali, P. Siffert, Appl. Phys. A **36**, 31 (1985)
83. E. Fogarassy, R. Stuck, M. Toulemonde, D. Salles, P. Siffert, J. Appl. Phys. **54**, 5069 (1983)
84. F.A. Lindemann, Phys. Zeitschr. **11**, 609 (1910)
85. K. Sokolowski-Tinten, D. von der Linde, J. Phys. Condens. Matter **16**, 1517 (2004)
86. G. Sciaini, M. Harb, S.G. Kruglik, Th Payer, C.T. Hebeisen, F.J. Meyer zu Heringdorf, M. Yamaguchi, M. Horn von Hoegen, R. Ernstorfer, R.J.D. Miller, Nature **458**, 56 (2009)
87. L.D. Landau, Phys. Z. USSR **10**(1936), 154 (1936)
88. A.C. Lushchik, C.B. Lushchik, *Decay of Electronic Excitations with Defect Formation in Solids* (Nauka, Moscow, 1989)
89. N. Itoh, Adv. Phys. **31**, 49 (1982)
90. N. Itoh, D. Stoneham, Radiat. Eff. Defects Solids **155**, 277 (2001)
91. N. Itoh, Nucl. Instr. Meth. B **116**, 33 (1996)
92. A. Perez, E. Balanzat, J. Dural, Phys. Rev. B **41**, 3943 (1990)
93. K. Schwartz, C. Trautmann, A.S. El-Said, R. Neumann, M. Toulemonde, W. Knolle, Phys. Rev. B **70**, 184104 (2004)
94. R.C. Alig, S. Bloom, Phys. Rev. Lett. **35**, 1522 (1975)
95. F. Desauer, Z. Phys. **38**, 12 (1923)
96. L.T. Chadderton, H.M. Montagu-Pollock, Proc. Roy. Soc. London **A274**, 239 (1963)

97. F. Seitz, J.S. Koehler, Solid State Phys. **2**, 305 (1956)
98. P. Sigmund, C. Claussen, J. Appl. Phys. **52**, 990 (1981)
99. I.M. Lifshitz, M.I. Kaganov, L.V. Tanararov, J. Nucl. Energy A **12**, 69 (1960)
100. G. Szenes, Nucl. Instr. Meth. B **269**, 174 (2011)
101. B. Rethfeld, K. Sokolowski-Tinten, D. von der Linde, S.I. Anisimov, Phys. Rev. B **65**, 092103 (2002)
102. G. Szenes, K. Havancsak, V. Skuratov, P. Hanak, L. Zsoldos, T. Ungar, Nucl. Instr. Meth. B **166**, 933 (2000)
103. G. Szenes, Phys. Rev. B **70**, 094106 (2004)
104. G. Szenes, Radiat. Eff. Defects Solids **161**, 401 (2006)
105. J.M. Costantini, F. Brisard, J.L. Flament, A. Meftah, M. Toulemonde, M. Hage-Ali, Nucl. Instr. Meth. B **65**, 568 (1992)
106. J. Jensen, A. Dunlop, S. Della-Negra, M. Toulemonde, Nucl. Instr. Meth. B **146**, 412S (1998)
107. Ch. Houpert, F. Studer, D. Groult, M. Toulemonde, Nucl. Instr. Meth. B **39**, 720 (1989)
108. S. Moll, G. Sattonnay, L. Thomé, J. Jagielski, C. Legros, I. Monnet, Nucl. Instr. Meth. **268**, 2933 (2010)
109. M. Toulemonde, W. Assmann, C. Dufour, A. Meftah, C. Trautmann, Nucl. Instr. Meth. B **277**, 28 (2012)
110. N. Bonardi, PhD Thesis Université Claude Bernard, Lyon I, France, 1998
111. P. Hermes, B. Danielzik, N. Fabricius, D. von der Linde, J. Luhl, Y. Heppner, B. Stritzker, A. Pospieszczyk, Appl. Phys. A **39**, 9 (1986)
112. S.N. Luo, T.J. Ahrens, T. Cagin, W.A. III Goddard, D.C. Swift, A. Strachan, Phys Rev B **68**, 134206 (2003)
113. M. Toulemonde, W. Assmann, C. Trautmann, F. Grüner, Phys. Rev. Lett. **88**, 057602 (2002)
114. M. Toulemonde, W. Assmann, C. Trautmann, F. Grüner, H.D. Mieskes, H. Kucal, Z.G. Wang, Nucl. Instr. Meth. B **212**, 346 (2003)
115. M.D. Rodríguez, B. Afra, C. Trautmann, M. Toulemonde, T. Bierschenk, J. Leslie, R. Giulian, N. Kirby, P. Kluth, J. Non-Cryst. Solids **358**, 571 (2012)
116. A. Meftah, J.M. Costantini, N. Khalfaoui, S. Boudjadar, J.P. Stoquert, F. Studer, M. Toulemonde, Nucl. Instr. Meth. B **237**, 563 (2005)
117. M. Lang, M. Toulemonde, J. Zhang, F. Zhang, C.L. Tracy, J. Liang, Z. Wang, W.J. Weber, D. Severin, M. Bender, C. Trautmann, R.C. Ewing, Nucl. Instr. Meth. B **336**, 102 (2014)
118. Ch. Dufour, E. Paumier, M. Toulemonde, Nucl. Instr. Meth. B **122**, 445 (1997)
119. S.D. Brorson, A. Kazeroonian, J.S. Moodera, D.W. Face, T.K. Cheng, E.P. Ippen, M.S. Dresselhaus, G. Dresselhaus, Phys. Rev. Lett. **64**, 2172 (1990)
120. P.B. Allen, Phys. Rev. Lett. **59**, 1460 (1987)
121. G.H. Vineyard, Radiat. Eff. **29**, 245 (1976)
122. Z.G. Wang, C. Dufour, E. Paumier, M. Toulemonde, Nucl. Instr. Meth. B **115**, 577 (1996)
123. Ch. Dufour, F. Beuneu, E. Paumier, M. Toulemonde, Europhys. Lett. **45**, 585 (1999)
124. A. Audouard, E. Balanzat, J.C. Jousset, D. Lesueur, L. Thomé, J. Phys. Condens. Matter **5**, 995 (1993)
125. A. Audouard, J. Dural, M. Toulemonde, A. Lovas, G. Szenes, L. Thomé, Phys. Rev. B **54**, 15690 (1996)
126. A. Audouard, J. Dural, M. Toulemonde, A. Lovas, G. Szenes, L. Thomé, Nucl. Instr. Meth. B **107**, 185 (1996)
127. D.S. Sanditov, S.Sh. Sangadiev, B.D. Sanditov, Glass Phys. Chem. **26**, 59 (2000)
128. M.-D. Hou, S. Klaumünzer, G. Schumacher, Phys. Rev. B **41**, 1144 (1990)
129. A. Benyagoub, S. Loffler, R. Rammensee, S. Klaumunzer, Radiat. Eff. Defects Solids **110**, 217 (1989)
130. A. Benyagoub, S. Loffler, R. Rammensee, S. Klaumunzer, G. Saemann-Ischenko, Nucl. Instr. Meth. **65**, 228 (1992)
131. A. Benyagoub, S. Klaumunzer, M. Toulemonde, Nucl. Instr. Meth. B **146**, 449 (1998)

132. I.A. Baranov, YuV Martinenko, S.O. Tsepelevitch, YuN Yavlinskii, Sov. Phys. Usp. **31**, 1015 (1988)
133. O. Osmani, N. Medvedev, J.I. Juaristi, M. Schleberger, B. Rethfeld, Nucl. Instr. Meth. B **317**, 72 (2014)
134. B. Rethfeld, A. Rämer, N. Brouwer, N. Medvedev, O. Osmani, Nucl. Instr. Meth. B **327**, 78 (2014)
135. B. Afra, M.D. Rodriguez, C. Trautmann, O.H. Pakarinen, F. Djurabekova, K. Nordlund, T. Bierschenk, R. Giulian, M.C. Ridgway, G. Rizza, N. Kirby, M. Toulemonde, P. Kluth, J. Phys. Condens. Matter **25**, 045006 (2013)
136. C. Rotaru, F. Pawlak, N. Khalfaoui, C. Dufour, J. Perrière, A. Laurent, J.P. Stoquert, H. Lebius, M. Toulemonde, Nucl. Instr. Meth. B **272**, 9 (2012)
137. W. Assmann, M. Toulemonde, C. Trautmann, Top. Appl. Phys. **110**, 401 (2007)
138. C. Trautmann, M. Toulemonde, J.M. Costantini, J.J. Grob, K. Schwartz, Phys. Rev. B **62**, 13 (2000)
139. C. Trautmann, M. Toulemonde, K. Schwartz, J.M. Costantini, A. Müller, Nucl. Instr. Meth. B **164**(165), 365 (2000)
140. N.M. Bulgakova, R. Stoian, A. Rosenfeld, I.V. Hertel, E.E.B. Campbell, Phys. Rev. B **69**, 054102 (2004)
141. I.B. Bogatyrev, D. Grojo, P. Delaporte, S. Leyder, M. Sentis, W. Marine, T.E. Itina, J. Appl. Phys. **110**, 103106 (2011)
142. H.M. van Driel, Phys. Rev. B **35**, 8166 (1987)
143. M. Sall, I. Monnet, F. Moisy, C. Grygiel, S. Jublot-Leclerc, S. Della-Negra, M. Toulemonde, E. Balanzat, J. Mater. Sci. **50**, 5214 (2015)
144. S.L. Daraszewicz, D.M. Duffy, Nucl. Instr. Meth. B **269**, 1646 (2011)
145. F. Agullo-Lopez, A. Mendez, G. Garcia, J. Olivares, J.M. Cabrera, Phys. Rev. B **74**, 174106 (2006)
146. A. Rivera, A. Mendez, G. Garcia, J. Olivares, J.M. Cabrera, F. Agullo-Lopez, J. Lumin. **128**, 123 (2007)
147. M. Beuve, N. Stolterfoht, M. Toulemonde, C. Trautmann, H. Urbassek, Phys. Rev. B **68**, 125423 (2003)
148. M. Huang, D. Schwen, R.S. Averback, J. Nucl. Mat. **399**, 175 (2010)
149. S. Schlutig, Ph.D. Thesis, University of Caen, France, 2001, http://tel.archives-ouvertes.fr/tel-00002110/fr/
150. K.E. Sickafus, Science **289**, 748 (2000)
151. O.H. Pakarinen, F. Djurabekova, K. Nordlund, Nucl. Instr. Meth. B **268**, 3163 (2010)
152. A. Guinier, G. Fournet, *Small-Angle Scattering of X-rays* (John Wiley, New York, 1955)
153. A. Benyagoub, M. Toulemonde, J. Mater. Res. **30**, 1529 (2015)
154. K. Nordlund, M. Ghaly, R.S. Averback, M. Caturla, T.D. de la Rubia, J. Tarus, Phys. Rev. B **57**, 7556 (1998)
155. M. Ghaly, K. Nordlund, R.S. Averback, Phil. Mag A **79**, 795 (1999)
156. K. Nordlund, Comput. Mater. Sci. **3**, 448 (1995)
157. T. Watanabe, D. Yamasaki, K Tatsumura and I Ohdomari Appl. Surf. Sci. **234**, 207 (2004)
158. J. Samela, K. Nordlund, V.N. Popok, E.E.B. Campbell, Phys. Rev. B **77**, 075309 (2008)
159. Z.G. Wang, C. Dufour, S. Euphrasie, M. Toulemonde, Nucl. Instr. Meth. B **209**, 194 (2003)
160. C. Dufour, V. Khomenkov, G. Rizza, M. Toulemonde, J. Phys. Appl. Phys. **45**, 065302 (2012)
161. C.H. Houpert, M. Hervieu, F. Studer, D. Groult, M. Toulemonde, Nucl. Instr. Meth. B **39**, 720 (1989)
162. G. Schiwietz, G. Xiao, P.L. Grande, E. Luderer, R. Pazirandeh, U. Stettner, Europhys. Lett. **47**, 384 (1999)
163. L.E. Seiberling, C.K. Meins, B.H. Cooper, J.E. Griffith, M.H. Mendenhall, T.A. Tombrello, Nucl. Instr. Meth. **198**, 403 (1982)
164. G. Schiwietz, P.L. Grande, Phys. Rev. A **84**, 052703 (2011)

Chapter 3
Modelling Effects of Radiation Damage

William J. Weber and Elke Wendler

Abstract This chapter reviews the sources of radiation damage and models that cover irradiation-induced defect production and accumulation, as well as irradiation induced phase transitions. Various models that represent similar processes are compared with each other. Model calculations illustrate the effects of specific model parameters, and selected experimental examples are used to validate and demonstrate the applicability of the models. The roles of temperature and dose rate on damage accumulation processes are discussed and modelled. The different roles of irradiation-induced recovery processes and thermal recovery processes are identified within the models and demonstrated in experimental results.

3.1 Introduction

The implantation of energetic ions into materials is inherently connected with a disturbance in the atomic structure of the materials (radiation damage), which occurs before the ions come to rest. For a given material, the kind and concentration of radiation damage produced depend on the implantation conditions (ion fluence and ion flux, mass and energy of the ions and irradiation temperature). A comprehensive understanding of the relationship between implantation conditions and radiation damage supports the practical application of ion beams. Furthermore, ion implantation is a tool to create kinetically stable non-equilibrium (metastable) defects and phases and allows the investigation of behaviour and properties of materials far from equilibrium. A common way to understand the

W.J. Weber (✉)
Department of Materials Science and Engineering, University of Tennessee,
Knoxville, TN 37996, USA
e-mail: wjweber@utk.edu

E. Wendler
Institut für Festkörperphysik, Friedrich-Schiller-Universität Jena,
Max-Wien-Platz 1, 07743 Jena, Germany
e-mail: elke.wendler@uni-jena.de

© Springer International Publishing Switzerland 2016

W. Wesch and E. Wendler (eds.), *Ion Beam Modification of Solids*,
Springer Series in Surface Sciences 61,
DOI 10.1007/978-3-319-33561-2_3

mechanisms of damage formation due to ion irradiation is the modelling of damage evolution as a function of the implantation conditions.

In this chapter, radiation damage and the various models and concepts that describe the accumulation of radiation-induced point defects, more complex defect structures and phase transitions, such as amorphisation, are reviewed. As the most prominent parameters in these models, the roles of dose rate, ion fluence and irradiation temperature on the accumulation of radiation damage are discussed, and model calculations illustrate the dependencies on model parameters. The differing roles of radiation-induced recovery processes and thermal recovery processes are identified within the models, and selected experimental examples are used to validate and demonstrate the applicability of the models.

In the next section of this chapter, a general introduction is provided on the origin and sources of radiation damage, measurement techniques and quantitative analysis. The accumulation of radiation-induced defects is considered in the third section, and the concept of homogeneous and heterogeneous defect accumulation is introduced. The fourth section is devoted to the process of amorphisation. The results of different models or concepts are compared to each other, and similarities and differences are discussed. During ion implantation, simultaneous recovery processes can mitigate damage production and thus influence the rate of amorphisation. Therefore, the role of thermally enhanced and ion-beam induced damage recovery is especially emphasised. In a fifth section, examples of modelling of complex processes involving multiple defects of different length scales are presented. The challenges and limits of such procedures are discussed. Finally, the main aspects of the chapter are summarised in a concluding summary.

3.2 General Remarks

3.2.1 Origin of Radiation Damage

Radiation damage refers to the transfer of kinetic energy from an energetic incident particle, such as an electron, neutron or ion, to a solid and the resulting rearrangement of atoms in the solid. If the kinetic energy transferred to an atom is above some threshold, the atom can be displaced from its location in the atomic structure to become a primary knock-on atom (PKA) that can produce additional displaced atoms. The threshold displacement energy, E_d, is the minimum kinetic energy transfer to produce a permanent displacement. A series of collisions initiated by a single PKA is called a displacement cascade. A single radiation damage event results in the creation of individual displaced atoms, such as point defects, or clusters of displaced atoms, which can be point defect clusters or nanoscale amorphous domains. The accumulation of radiation damage events, migration of defects and the interaction of defects with each other and interfaces are collectively known as radiation effects.

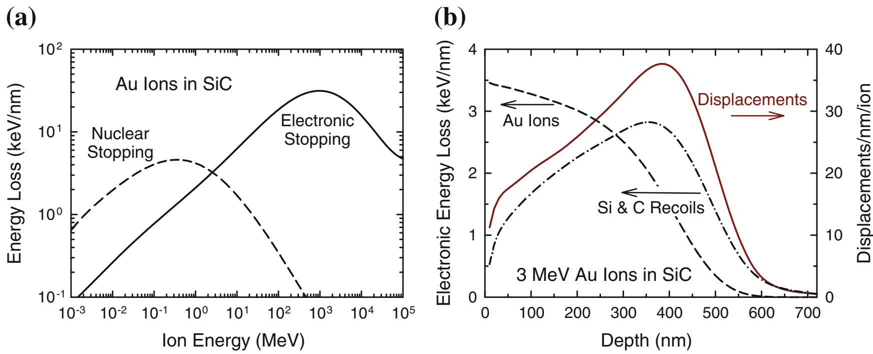

Fig. 3.1 Partitioning of incident ion energy by nuclear and electronic energy loss per ion and unit depth: **a** nuclear and electronic stopping powers, S_n and S_e, for Au ions in SiC; and **b** energy loss to electrons by both Au ions (*dashed curve*) and Si/C recoils (*dash-dot curve*) for 3 MeV Au ions incident on SiC, along with the number of displaced atoms produced per unit depth per incident ion (*solid curve*). The calculations were done with SRIM version 2008-04 [1]. The displacements are obtained using the displacement energies given in Table 3.1

Neutrons only interact with atomic nuclei in a solid; however, energetic electrons, ions and the neutron created PKAs interact with both electrons and atomic nuclei in a solid. As illustrated in Fig. 3.1a, the energy loss of ions is partitioned between energy transferred to atomic nuclei (nuclear stopping) and the energy transferred to electrons (electronic stopping), as often calculated using the Stopping and Range of Ions in Matter (SRIM) code [1]. The nuclear stopping power, S_n, (energy transferred per ion and unit path length to atomic nuclei) is dominant at low energies, while the electronic stopping power, S_e, (energy transferred per ion and unit path length to electrons) is dominant for high energy ions (see Chap. 1). High-energy heavy ions (M > 20 amu and E > 1 MeV/amu) are often referred to as swift heavy ions. For swift heavy ions (SHI), the nuclear energy loss is generally negligible, but the electronic energy loss is sufficiently high to result in the creation of damage tracks in many materials [2, 3]. The creation of such SHI tracks from the electronic energy loss is often described as due to an intense thermal spike from electron-phonon coupling that results in local melting. Nuclear energy loss at low and intermediate energies results in ballistic-like collision cascades that create a local high density of displaced atoms. The partitioning of energy between nuclear and electronic energy loss for incident ions (Fig. 3.1a) also occurs for the energetic recoils created by the ballistic-like nuclear energy transfers, as shown in Fig. 3.1b, leading to significant energy loss to electrons from both incident ions and atomic recoils, as well as to the production of displaced atoms from either the incident ions or the energetic recoils they produce. Understanding and modelling such radiation damage processes are important for the development of radiation tolerant materials and devices for nuclear and space technologies. Similarly, ion implantation doping is a critical industrial process for device fabrication, and knowledge and predictive models of the underlying defect production processes are important for successful

implementation of this technology for advanced materials and devices [4]. In the past, the electronic energy loss at these low to intermediate energies has been considered negligible; however, recent studies have demonstrated that the electronic energy loss can contribute to the overall damage production in materials like amorphous silica [5] or result in competing defect recovery processes that reduce the overall damage production [6–8]. In both cases, the additive or competitive effect of electronic energy loss on damage creation has been attributed to a thermal spike.

Scientific studies of the response of materials to irradiation with energetic ions are often driven by the need to advance the fundamental understanding and develop predictive models of radiation effects. Since irradiation with ions often drives materials far from equilibrium, there is great interest in advancing the understanding of defect structures, metastable phases, unique properties and behaviour in these far from equilibrium states. In the area of nuclear materials, applied research is often driven by a demand for more radiation tolerant materials or more accurate models of materials performance under specific radiation environments. In the area of device manufacturing, research is often driven by the need to mitigate radiation damage effects introduced by ion implantation processes, while in the area of industrial structural modification using ion beams, research and development is often driven by the need to tailor structures to specific properties or functionalities. The accumulation and recovery of radiation damage effects is an active research that is advancing the understanding and modelling of radiation damage processes over a large energy range.

3.2.2 Sources of Radiation Damage

Radiation damage can originate from the radioactive decay of radionuclides contained in natural minerals or from materials containing radionuclides, such as nuclear waste forms. In nuclear reactors, the fission of fissile isotopes in nuclear fuel, such as ^{235}U, can result in the creation of energetic fast neutrons and fission products. The high energy fission products are responsible for the majority of the radiation damage in nuclear fuels, while the fast neutrons cause radiation damage in the nuclear fuel, cladding and structural components by transferring energy to PKAs in elastic scattering events or through (n,p) and (n,α) nuclear reactions. In fusion reactors, the 14 MeV neutrons produced by fusion reactions cause radiation damage to the first wall and structural components, and the flux of energetic ions from the plasma causes radiation damage to first wall. In space, cosmic radiation and the solar wind, which are composed of high energy ions, can cause radiation damage to space craft and instruments. Finally, electron beams from electron accelerators and electron microscopes and ion beams from ion accelerators, helium ion microscopes, and focused ion beam instruments cause radiation damage by direct interaction of a charged particle (electron, ion or cluster) with materials. Such electron and ion sources of damage are used in industry to implant electrically

active dopants or to modify structure and properties, while their use in research is generally to study radiation damage processes, develop radiation tolerant materials, and create new functionalities in materials through implantation doping, creation of novel nanoscale structures, global structural modifications or phase transformations. Because of the similarities in damage production from these various damage sources and the transferability of damage accumulation models, the remainder of this chapter will focus primarily on the analysis and modelling of ion irradiation damage.

3.2.3 Measurement of Irradiation Damage

The measurement of irradiation damage is generally done indirectly by ex situ post-irradiation characterization of physical properties, such as optical absorption, luminescence, electrical resistivity, and volume swelling or contraction. Such measurements often provide a quantitative measurement that is proportional to the defect concentration or fraction of phase transformation. In some cases, such characterization can be done in situ, and there are significant advantages to this, particularly for irradiations at cryogenic temperatures. It is possible to measure or observe irradiation damage directly in situ during irradiation, for example by electrical resistivity or transmission electron microscopy; however, in some cases, the probe (e.g., electron beam) can interfere with the damage caused by an ion beam. Several examples are discussed below.

3.2.3.1 In Situ Techniques

The use of in situ techniques to characterize irradiation damage is particularly important for irradiations conducted at cryogenic temperatures; otherwise, some or all the irradiation damage of interest may recover at room temperature prior to characterization. One of the most common techniques for characterizing ion irradiation damage in single crystals is Rutherford backscattering spectrometry in channelling geometry (RBS/C) (see [9–11] and Chap. 5.2), which is an ion beam analysis method readily available, often using the same facilities employed to do the ion irradiations. This technique can determine the relative disorder from defects and amorphous materials as a function of depth. Another useful ion beam based technique is ion beam luminescence [12], which is a sensitive way to monitor changes in defect structures and phase transitions. This can be augmented by adding an electron gun or a tuneable laser to perform cathodoluminescence or photoluminescence in situ, respectively. Another technique that is more easily utilized for metallic and semiconducting materials is resistivity measurements [13], which provides one of the most sensitive measures of defect formation. Unfortunately, this technique is not readily applied to dielectric materials. It is also possible to employ other optical techniques in situ, and several laboratories are exploring the possibility

of in situ Raman spectroscopy. Finally, in situ transmission electron microscopy can be used for both electron irradiations and for ion irradiations using facilities that have an ion accelerator or ion implanter coupled to a transmission electron microscope [14, 15]. Using such a facility coupled with cooling and heating stages, phase transitions can be monitored as ion or electron damage accumulates over a range of temperatures using electron diffraction analysis. In addition, microstructural changes due to damage accumulation can be characterized.

3.2.3.2 Ex Situ Techniques

The measurement techniques discussed above are also applied to characterization of samples irradiated in one facility and analyzed at one or more other facilities. In addition to these characterization methods, X-ray scattering techniques, Raman spectroscopy, and positron annihilation are a few of the techniques employed to explore changes in structure, vibrational modes and open volume in irradiated materials.

3.2.4 Quantitative Analysis of Radiation Effects

For quantitative analysis, usually the relative defect fraction f_d or damage concentration is used and modelled as a function of ion fluence N_I (number of ions per unit area). The ion fluence, N_I, is given by $N_I = \phi t$, where ϕ is the ion flux (number of ions per unit area and time) and t is the time. The fraction f_d is either directly measured as a relative concentration of defects (number of defects per unit volume divided by the atomic density of the material) or obtained from a measured quantity M by

$$f_d(\phi t) = \frac{M(\phi t) - M_o}{M_s - M_o}, \tag{3.1}$$

where $M(\phi t)$ is the measured quantity as a function of ion fluence, M_o is the value before irradiation with $M_o = M\ (\phi t = 0)$, and M_s is the saturation value of M at very high fluences, which may be associated with a saturation in defect concentration or with a phase transformation, such as amorphisation or an order-disorder transformation.

It is often useful to convert the ion fluence, $N_I = \phi t$, into the number of displacements per atom, n_{dpa}, with $n_{dpa} = N_I N^*_{displ}/N$, where N^*_{displ} is the number of displacements per incident ion and unit depth (see example in Fig. 3.1b) and N the atomic density of the corresponding material. The displacement of target atoms results from elastic scattering of the incident ion by atomic nuclei (see Sect. 3.2.1), and N^*_{displ} exhibits a complex depth dependence (see e.g. Fig. 3.1b). Therefore, n_{dpa}

Table 3.1 Displacement energies E_d obtained from MD simulations (calc.) or from experiments (exp.) (first/second component)

Material	E_d(eV) (cal.)	E_d(eV) (exp.)
AlN	–	41
AlAs	25/20	–
GaN	45/109	41/-
GaP	–	13.7/19.2
GaAs	–	8.8/10.1
GaSb	–	6.2/(7.5–13.1)
InP	–	6.6/8.8
InAs	–	6.7/8.5
InSb	–	5.8/6.8
C	50–60	35–48
SiC	35/21	(20–35)/-
Si	15–20	13–14
Ge	–	14.5–16
ZnO	–	(40–70)/47–55)
MgO	–	55/55

The data are taken from various literature sources (see [16, 17] and references therein). The given value for AlN is estimated by comparison of damage cross sections for various materials (for details see [18])

can be used to compare, e.g., results for different ion species using the value in the maximum of the distribution, or for different depth regions. As n_{dpa} is proportional to the energy deposited in the displacement of target atoms per unit volume, it is also referred to as damage energy or dose. Often the terminology displacements per atom (dpa) is used for short. For the calculation of N^{*}_{displ}, the displacement energies E_d of the target elements have to be known. Values of E_d for some common materials [16–18] are summarized in Table 3.1. Data for additional II–VI compounds can be found in [19–22] and references therein.

3.3 Modelling of Defect/Damage Accumulation

The most intuitive and early concept in modelling the accumulation of radiation damage is to assume that during irradiation Frenkel defects (interstitial-vacancy pairs) are produced at a constant rate proportional to the ion flux. Further, the interstitials and vacancies produced by one ion can recombine with those that were produced by previous ions at a rate that is proportional to the concentration of Frenkel defects.

3.3.1 Defect Reaction Rate Theory

The accumulation of defects and the formation of defect aggregates are governed by the rate of production, concentration and reaction rates of defects. While there are some cases where the production and concentration of defects are somewhat uniform throughout the bulk, the production and concentration of defects are more often non-uniformly distributed across a sample due to changes in particle flux and energy; this is particularly true for external ion irradiations, where there is often a significant change in ion energy with depth. Thus, only the local production and concentrations at a given depth are considered here. In this case, the local concentrations of different defect types at any time are controlled by a balance between the defect production rate and the recovery or loss rate of defects, which is often described by point defect balance equations or defect reaction rate theory. Assuming for simplicity the production of a single defect type, namely a Frenkel pair, then the rate of change in the defect concentration (number of defects per unit volume), C_d, is given by the defect balance expression [23]:

$$\frac{dC_d}{dt} = P_d\left(1 - \frac{C_d}{N}\right) - L, \tag{3.2}$$

where P_d is the local rate of defect production (number of produced defects per unit volume per time), N is the atomic density, and L is the local rate of defect loss (number of lost defects per unit volume per time), such as to recombination. The term $(1 - C_d/N)$ accounts for the already displaced atoms at time t and can often be approximated by unity [24, 25]; however, it is included because of the high defect concentrations that accompany irradiation-induced amorphisation. The local production rate of defects or atomic displacements, P_d, is given by $N\sigma_d\,\phi$, where σ_d is the local atomic displacement cross section (per atom), which is determined from the integration of the product of the displacement function and scattering cross section over all recoil energies [26, 27]. Values for σ_d are usually obtained from SRIM calculations [1] by $\sigma_d = N^*_{displ}/N$ (see Sect. 3.2.4 and Fig. 3.1b). ϕ is the local ion flux. The local rate of defect loss is proportional to the local defect concentration, and if assuming defect loss is only due to recombination, then L is given by RC_d, where R is the recombination rate coefficient [28]. Thus, (3.2) can be rewritten as:

$$\frac{dC_d}{dt} = N\sigma_d\phi\left(1 - \frac{C_d}{N}\right) - RC_d. \tag{3.3}$$

Since the fraction of defects, f_d, is given by C_d/N, (3.3) can be rewritten as

$$\frac{df_d}{dt} = \sigma_d\phi(1 - f_d) - Rf_d, \tag{3.4}$$

where $\sigma_d\,\phi$ is the local dose rate in displacements per atom per second (dpa/s). If the recombination rate coefficient R is a constant (independent of t or f_d), then the solution to (3.4) is given by:

$$f_d = \frac{\sigma_d\phi}{(\sigma_d\phi + R)}[1 - \exp(-(\sigma_d\phi + R)t)]. \tag{3.5}$$

The relative defect fraction at saturation, f_s, is simply $\sigma_d\,\phi/(\sigma_d\,\phi + R)$, and (3.5) can then be expressed as:

$$f_d = f_s\left[1 - \exp\left(-\frac{\sigma_d\phi t}{f_s}\right)\right]. \tag{3.6}$$

This expression would be also derived if the terms $(1 - C_d/N)$ and $(1 - f_d)$ were approximated by unity in (3.3) and (3.4), but in this case f_s would be given by $\sigma_d\,\phi/R$.

Equation (3.6) is the exponential rise-to-saturation expression often found to describe point defect accumulation in the absence of significant defect diffusion, such as in metals at cryogenic temperatures [24, 25]. At very low ion fluences or doses, the relative defect fraction f_d increases linearly with $\sigma_d\,\phi t$, i.e. linearly with increasing ion fluence. The exponential form of (3.6) at higher fluences arises because at long times the recombination rate Rf_d becomes comparable to the production rate $\sigma_d\,\phi\,(1 - f_d)$ in (3.4). Eventually $\mathrm{d}f_d/\mathrm{d}t$ approaches zero, which means that the fraction of defects f_d reaches the saturation value f_s. This saturation can be understood as a balance between defect production and defect recombination. In other words, f_s represents the defect concentration at which every new defect created is within the recombination volume of a pre-existing defect. Independent of the approximation made (see above), the value of f_s decreases with increasing recombination rate coefficient R and increases with increasing production rate of displacements per atom $\sigma_d\,\phi$. Assuming R to be constant (e.g., at a given temperature), this implies that the value of f_s increases with increasing ion flux ϕ. Finally it should be noted that in some cases, R is not a constant, as assumed above, but can exhibit some dependence on f_d [29, 30]. This approach was developed to explain experimental data that do not show a real saturation of the defect fraction f_d, but a continuous slight increase at high fluences.

The defect accumulation model represented by (3.6) results in a broad transition region between the nearly linear increase at low ion fluences and saturation at high ion fluences. While this equation has been successfully employed to fit a lot of data [24–28, 31–34], this is not always the case. In some cases, a more rapid transition to saturation is found [35], which can require a stronger dependence on the recombination term. One approach has been to modify the basic reaction-rate equation (3.4) in a non-physical way to account for a stronger fluence dependence [35]. Another approach that leads to a faster transition to saturation is based on the more conventional defect reaction rate equations that consider interstitial, C_i, and vacancy, C_v, concentrations separately, which leads to coupled defect rate

expressions for interstitials and vacancies [26–28, 36, 37]. Under conditions where defect diffusion is negligible, these equations can be written as:

$$\frac{dC_i}{dt} = N\sigma_d\phi - RC_iC_v, \tag{3.7}$$

and

$$\frac{dC_v}{dt} = N\sigma_d\phi - RC_iC_v. \tag{3.8}$$

Under these conditions, $C_i = C_v$ is valid, so the defect rate expression for interstitials is given by:

$$\frac{dC_i}{dt} = N\sigma_d\phi - RC_i^2. \tag{3.9}$$

Notice that here the recombination parameter R has a different dimension than in (3.3) and related equations. The solution to (3.9) is given by the expression:

$$C_i(t) = \sqrt{\frac{N\sigma_d\phi}{R}}\left[\frac{1 - \exp\left(-2t\sqrt{N\sigma_d\phi R}\right)}{1 + \exp\left(-2t\sqrt{N\sigma_d\phi R}\right)}\right], \tag{3.10}$$

which can be rewritten in terms of defect fraction as:

$$f_d(t) = f_s\left[\frac{1 - \exp(-2\sigma_d\phi t/f_s)}{1 + \exp(-2\sigma_d\phi t/f_s)}\right]. \tag{3.11}$$

In this case, the defect fraction at saturation, f_s, is given by $\sqrt{\sigma_d\phi/NR}$. The two defect accumulation models represented by (3.6) and (3.11) are illustrated in Fig. 3.2 as a function of $\sigma_d\ \phi t$, or dose (dpa), assuming a value for f_s of 0.3. The more rapid rise to saturation of the model given by (3.11) is clearly evident, although both models exhibit a linear dependence on $\sigma_d\ \phi t$ at low ion fluences. Other models describing defect accumulation kinetics have been described by Clinard and Hobbs [38]. In addition, it is important to keep in mind that at high ion fluences the implanted ions themselves may contribute directly or indirectly to the defect concentration.

It should be remarked that models similar in mathematical form to (3.6) have been derived from different considerations. For example, in the case of colour centre formation by swift heavy ion irradiations [39], the defect concentration produced per ion track by electronic energy loss, $N\sigma_{def}$, where σ_{def} is an effective defect production cross section, can be a constant and unaffected by the overlapping of ion tracks. In this case, the accumulation of defects is described by (3.4), without the Rf_d term and with $(1 - f_d)$ replaced by $(1 - f_d/f_s)$ to account for the maximum defect fraction at saturation. The solution for this model is given by:

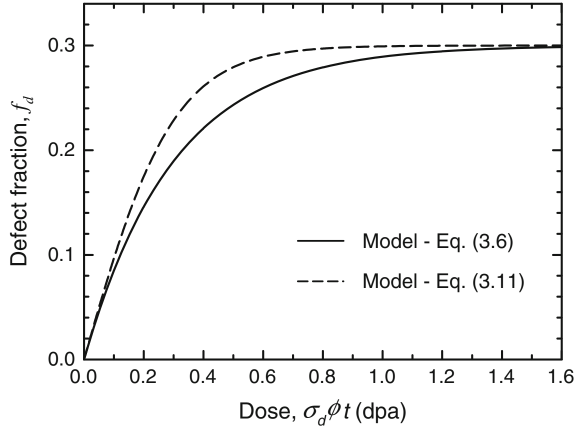

Fig. 3.2 Defect fraction f_d versus dose for two defect accumulation models with a fixed value of $f_s = 0.3$

$$f_d = f_s\left[1 - \exp\left(-\sigma_{def}\phi t/f_s\right)\right], \tag{3.12}$$

which is similar to (3.6) but now based on defect production from electronic energy loss rather than ballistic scattering processes.

So far, only the production and recombination of interstitial and vacancy point defects has been considered. The formation of interstitial and vacancy defect clusters directly in the ballistic-like collision cascades initiated by nuclear energy loss from the passage of ions through a solid is well known through molecular dynamics simulations [40–42]. Such clusters can also form from newly created interstitials (or vacancies) interacting with previously created interstitials (or vacancies). Assuming that defect cluster formation directly in a cascade is negligible, the contribution of defect cluster formation on the overall damage fraction, f_d, which is the total defect fraction (point defects plus defect clusters), can be incorporated in the damage accumulation model by an additional term in (3.4) [35]:

$$\frac{df_d}{dt} = \sigma_d\phi(1 - f_d) - Rf_d + \sigma_c\phi f_d(1 - f_d/f_c), \tag{3.13}$$

where σ_c is the cross section for cluster formation. The probability for clustering to occur is given by f_d $(1 - f_d/f_c)$, where f_d accounts for clusters forming from pre-existing defects and the term $(1 - f_d/f_c)$ takes into account that the concentration of clusters reaches a saturation value f_c at high ion fluences and clusters can only be formed in regions in which the damage fraction f_d is below the maximum value f_c. Equation (3.13) does not contain any information about the type of defect clusters, which in reality may be point defect clusters or small extended defects like dislocation loops or stacking faults. In principle, the formation of defect clusters can be taken into account also by other mathematical terms [43].

3.3.2 Effect of Temperature and Diffusion

The above models assume no temperature dependence and immobile defects. In reality, the effective displacement cross section decreases and the recombination coefficient, R, increases with temperature in (3.5) and (3.10), which results in a decrease in the defect or damage fraction at saturation with increasing temperature. The more significant effect of temperature is on the diffusivity or mobility of defects, which can significantly increase the rate of recombination and the rate of clustering. In general, interstitials are more mobile than vacancies, and Chadderton [44] included interstitial cluster formation from the migration of interstitials into the balance of defect reaction rates occurring during ion irradiation. The formation and growth of clusters from defect migration and interaction can lead to the evolution of microstructure, such as dislocation loops, dislocation tangles, stacking faults, precipitates, voids, and bubbles that serve as sinks for defects. The diffusion of defects can also result in the loss of defects to other defect sinks, such as surfaces, grain boundaries, and interfaces. In modern defect reaction rate theory, these reaction rates are included by adding sink loss terms to (3.7) and (3.8) that include the defect concentration, appropriate defect-sink reaction rate coefficients, defect concentration, and sink concentrations [26–28, 36, 37]. The defect reaction rate equations that include a sum over losses to different defect sinks are given by:

$$\frac{dC_i}{dt} = N\sigma_d\phi - RC_iC_v - \sum_s K_{is}C_sC_i, \tag{3.14}$$

and

$$\frac{dC_v}{dt} = N\sigma_d\phi - RC_iC_v - \sum_s K_{vs}C_sC_v. \tag{3.15}$$

The recombination rate and the defect-sink reaction rate coefficients, K_{is} and K_{vs}, are proportional to the interstitial and vacancy defect diffusion coefficients, D_i and D_v, which are temperature dependent. The defect-sink reaction rate coefficients also include a sink strength factor (affinity of a sink for the specific defect) for each sink type. Because of the summation over active defect sink types at any temperature, the reaction rate equations can become quite complex. In addition, (3.14) and (3.15) are coupled non-linear differential equations, which make analytical solutions difficult, and solutions generally must be derived by numerical methods. To complicate matters, these two rate equations are for simple metals and semiconductors. In the case of binary alloys, compound semiconductors and ceramics, rate equations governing interstitials and vacancies for each element or sublattice are often required, and numerical methods must be employed to obtain solutions. Further refinement of the loss term to sinks would include a bias or preference for capturing a specific defect type [27]. Neutral or unbiased sinks, such as voids and grain boundaries, have no preference for one defect type over another. Biased sinks may

show a preferential attraction for one defect type, such as dislocations for interstitials. Sinks may also be saturable, as in coherent precipitates, or unsaturable, as in dislocations. Finally, at high temperatures, a term for the thermal production of vacancies may need to be included in the rate equation for vacancies. The complexity of the defect-reaction rate equations is evident. Nonetheless, the above equations represent the framework, which can be solved numerically, for describing a range of defect loss mechanism that drive microstructural growth processes for a wide range of defect sinks. The reader is referred to more detailed descriptions and analyses of different sink types in the literature [26, 27, 36, 37].

Consider for the moment ion irradiation temperatures where only interstitials are mobile and vacancies are immobile, it is easy to see from these rate equations that once defect sinks are formed (e.g., defect clusters or dislocation loops), that the concentration of interstitials, C_i, will decrease with increasing ion fluence due to annihilation of interstitials at the defect sinks, while the concentration of immobile vacancies, C_v, will increase. In general, interstitial and vacancy concentrations will increase with ion fluence, following the behaviour given by (3.11), until the interaction of defects begins to nucleate sinks. Once defect sinks are nucleated, the interstitial concentration decreases approximately proportional to $(\sigma_d\ \phi t)^{-1/2}$, while the vacancy concentration increases proportional to $(\sigma_d\ \phi t)^{1/2}$, as described in detail elsewhere for a single sink type [26, 27, 36]. The loss of point defects to extended defects or sinks, such as dislocation loops and cavities, drives the growth and evolution of these microstructures under irradiation. Thus, for the conditions given, the decrease in interstitial concentration results in a growth of interstitial sinks (clusters or dislocation loops) that is proportional to $(\sigma_d\ \phi t)^{1/2}$. Such an increase in defect concentration proportional to $(\sigma_d\ \phi t)^{1/2}$ has been experimentally observed in Si implanted with light ions at room temperature (see [44] and references therein) and by optical absorption in GaAs [45].

3.3.3 Practical Application

When introducing (3.3) in Sect. 3.3.1, it was assumed that the production rate of defects or atomic displacements per unit volume, P_d, is determined by the local atomic displacement cross section σ_d resulting from the primary nuclear energy deposition (see Sect. 3.2.1). However, in real experiments this is not always the case. In the case of insulators, for example, it is known that not all of the primarily produced displaced lattice atoms survive the relaxation of the collision cascade [16, 46] and thus, the effective displacement cross section σ_{def} becomes smaller than the calculated local atomic displacement cross section σ_d. This effect is usually called in-cascade annealing. Therefore, the damage cross section σ_{def} is often taken as a free parameter that replaces σ_d in the models and corresponds to the local number of surviving displacements per atom from a single ion impact per unit ion fluence. The local number of surviving displaced atoms per unit pathlength of the incident ion is given by $N\sigma_{def}$, where N is the atomic density. The dependence on the ion fluence

$N_I = \phi t$ is obtained by dividing (3.4) by the ion flux ϕ, which is assumed to be constant during implantation. The solution in (3.5) remains unchanged replacing ϕt by N_I. R/ϕ has the dimension of a cross section, labelled σ_r, and is the (local) relative number of defects recombining with pre-existing defects (created by previous ions) from a single ion impact per unit ion fluence. Experimentally accessible quantities are the damage cross section σ_{def}, which is determined by the increase of damage fraction at low ion fluences, and the saturation value f_s observed at sufficiently high ion fluences or obtained by a model fit. In Fig. 3.3, it is shown how the parameters σ_{def} and f_s in (3.6) and (3.11) influence the fraction of defects, f_d, versus ion fluence N_I. In the double logarithmic plot, an increase of σ_{def} results in a clear shift of the curve towards low ion fluences (cp. curve 1 and 3 in Fig. 3.3b). From the figure, one can see that a distinct determination of the two parameters requires experimental data over a sufficiently wide range of ion fluences. Curves 1 and 4 in Fig. 3.3, calculated with (3.6) and (3.11) using the same parameters, respectively, are rather well separated. However, by increasing σ_{def} in (3.6), curve 3 is obtained that is very close to curve 4 calculated with (3.11). This demonstrates that to distinguish between the models represented by (3.6) and (3.11), experimental data with sufficient accuracy are necessary (cp. curves 3 and 4 in Fig. 3.3). From the saturation value f_s given by $\sigma_{def}/(\sigma_{def} + \sigma_r)$ (or by σ_{def}/σ_r when approximating $(1 - f_d)$ by unity (see Sect. 3.3.1)), the cross section σ_r can be extracted.

So far, only point defects like vacancies and interstitial atoms have been considered, and the recombination or annihilation of these defects with each other leads to a saturation of the damage fraction at the value f_s (see above). Including the formation of defect clusters that cannot recombine, as described in (3.13), provides in principle an explanation to the further increase or decrease of the damage fraction, with the final value of f_d given by the saturation concentration of clusters f_c (see Fig. 3.4). If $f_c > f_s$, the damage fraction exhibits a second increase with

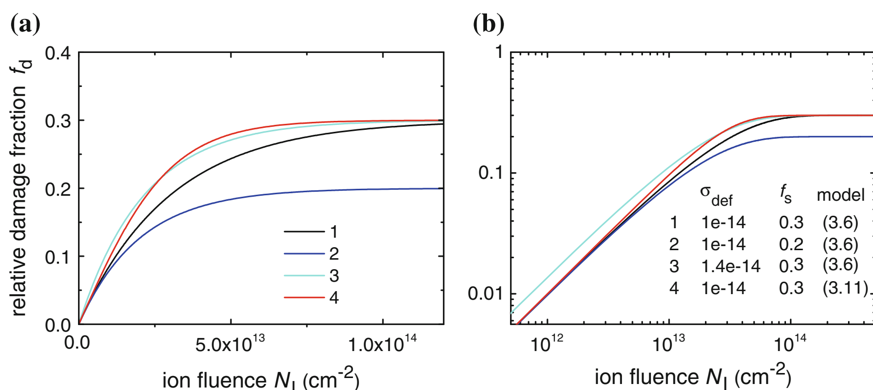

Fig. 3.3 Relative damage fraction f_d versus ion fluence N_I calculated applying (3.6) and (3.11) with the parameters indicated in the figure. The cross section σ_{def} is given in cm^2. Part **a** has a linear scale and part **b** is a double logarithmic plot

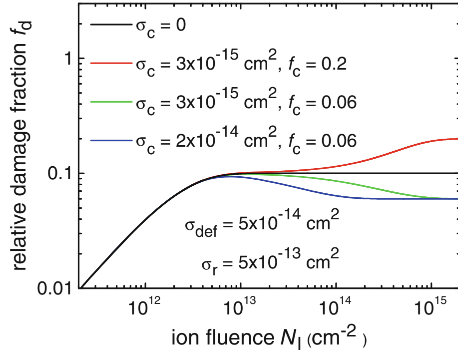

Fig. 3.4 Relative damage fraction f_d versus ion fluence N_I calculated by solving (3.13) numerically with the parameters indicated in the figure

increasing ion fluence (see red curve in Fig. 3.4), and for $f_c < f_s$, the damage fraction decreases with increasing ion fluence (see green and blue curves in Fig. 3.4). The range of ion fluences at which this change occurs is controlled by the cross section for cluster formation, σ_c (compare green and blue curve in Fig. 3.4). As discussed before, (3.13) assumes that cluster formation does not occur directly in the collision cascades. The curves in Fig. 3.4 show that only in this case (i.e. when the processes of defect and cluster formation are well separated and occur as different stages in the fluence dependence) is it at all useful to distinguish between defects and defect clusters. Only in this case can the various model parameters be explicitly determined.

In a real experiment, a physical quantity M is measured as a function of the ion fluence $N_I = \phi t$ whereby M is not necessarily the number of defects or displaced lattice atoms. When beginning a research experiment, the saturation value M_s may not be known or may appear not to be a sensible quantity. In this case, instead of f_d (3.1), relative changes in properties, such as $\Delta M = M(N_I) - M_0$ or $\Delta M/M_0 = (M(N_I) - M_0)/M_0$, will be analysed. An example for that is given in Fig. 3.5, which shows the relative lattice parameter change $\Delta a/a_0$ measured by X-ray diffraction versus ion fluence in single crystal UO_2 [31]. If one assumes that the defect fraction f_d contributes linearly to $\Delta a/a_0$ with $\Delta a/a_0 = \alpha f_d$, (3.6) can be used to fit the experimental data (see Fig. 3.5) with α being a constant giving the relative lattice parameter change per relative defect fraction. The saturation value, $(\Delta a/a_0)_s = \alpha f_s$, corresponding to very high ion fluences, can be extracted from the curve fit. Further, from the almost linear increase of lattice parameter, $\Delta a/a_0 = \alpha f_d$, at low ion fluences, the slope is approximately equal to $\alpha\sigma_{def}$, which is the relative lattice parameter change per unit ion fluence. The good agreement between measured data and calculated fit in Fig. 3.5 indicates that (3.6) is very suitable for representing the experimental results.

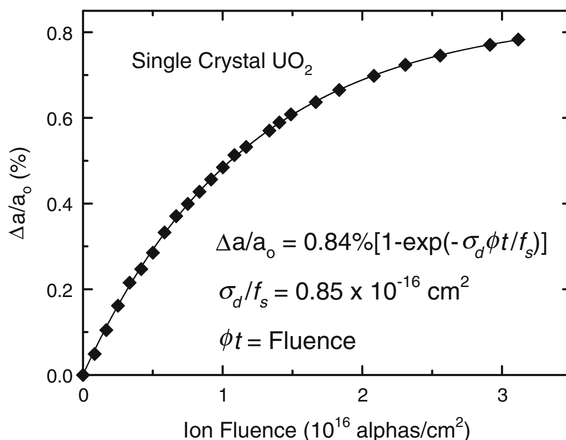

Fig. 3.5 Lattice parameter change $\Delta a/a_0$ versus ion fluence in single crystal UO_2 due to alpha particle irradiation at room temperature [31]

3.4 Modelling of Amorphisation and Order-Disorder Phase Transformations

The irradiation-induced crystalline-to-amorphous and order-disorder transformations in materials are of considerable interest, both fundamentally and technologically [26, 27, 47]. The models describing these transformations are somewhat similar and are defined in terms of the fraction of material transformed. The effects of irradiation on crystalline structures are described by competing reaction rate processes: those that drive the transformation and those that drive the recovery of the transformation. In the case of amorphisation, irradiation-induced defect accumulation and direct-impact amorphisation are the primary driving forces, while irradiation-induced and thermal defect recovery and recrystallization processes compete with the amorphisation processes. Additionally, in ordered alloys, semiconductors and many complex ceramics, irradiation-induced chemical disordering competes with irradiation-induced ordering. In general, these transformations occur homogeneously or heterogeneously, become more difficult with increasing temperature, and often occur only below a critical temperature. For the sake of simplicity, only irradiation-induced amorphisation models are described here, but the models are often directly applicable to the order-disorder transformation.

3.4.1 Irradiation-Induced Amorphisation Models

Irradiation-induced amorphisation occurs both homogeneously and heterogeneously. Homogeneous amorphisation is generally associated with a progressive process due to the accumulation of point defects or a specific defect type, as in the case of quartz [48] and coesite [49], and often occurs under electron or light ion

irradiation. Under such a progressive defect accumulation process, amorphisation may occur spontaneously after a critical concentration of defects or specific defect type is exceeded, and the progression to amorphisation is often well described by the damage accumulation model given by (3.6), except that f_s is now the defect fraction at which the damaged structure collapses to the amorphous state. Thus, the defect or damage fraction that is often measured is not a direct measurement of the amorphous fraction, which must be taken into consideration in the development of models and their application to the interpretation of experimental data. Heterogeneous amorphisation can occur directly within the collision cascade of an incident ion or within the track of a swift heavy ion, so-called direct-impact amorphisation, or can occur from single or multiple overlaps of collision cascades or ion tracks.

The definition of the damage fraction, as given in (3.1), is related to the occurrence of a saturation value of an arbitrary physical quantity at high ion fluences. Even if full amorphisation is finally achieved, it does not mean that the determined damage fraction represents the relative fraction of amorphous material at lower ion fluences. Point defects and defect clusters more often than not also contribute to a measured signature for accumulated damage or disorder, and their contribution to the measured damage, which may be represented by the defect accumulation models above, must be taken into account in the interpretation of experimental signatures of damage accumulation. With the exception of pure direct amorphisation by a single ion impact, which probably only occurs with swift heavy ion irradiation, most damage accumulation processes, including amorphisation, involves defect accumulation to some extent.

Similar to the case for defect production and accumulation above, one can assume that the local production rate of amorphous material, P_a (per unit volume), is given by $N\sigma_a\phi$, where σ_a is an effective cross section for direct-impact amorphisation that may depend on the elastic scattering cross section at low to intermediate ion energies and on the ionization cross section or electronic stopping power at high energies (e.g., for swift heavy ions). While σ_a may be proportional to the calculated displacement cross sections, σ_d, at low to intermediate ion energies, it cannot be directly calculated. In those ceramics or semiconductors that are sensitive to amorphisation, both defect production and amorphisation processes generally occur simultaneously; however, the effective displacement cross section, σ_{def}, for defect production in crystalline material is always less than the calculated displacement cross section, σ_d (see also Sect. 3.3.3). Thus, both the amorphous fraction, f_a, and the defect fraction, f_{def}, contribute to the fraction of material damaged, f_d. If the applied experimental technique is sensitive to both contributions, f_d can be analyzed as described in Sect. 3.5. In the following it is assumed that only the fraction of amorphous material f_a is measured and models are introduced that describe the transition to and the saturation of that fraction at its maximum value of unity. We have already described several models for defect accumulation above, and consider now several simple models for amorphisation. For more details and additional models for amorphisation, the reader is referred to [47].

If σ_{def} or f_{def} are negligible, then amorphisation occurs by a direct-impact process within the collision cascade or ion track, and the rate of change in the amorphous fraction can be written as:

$$\frac{df_a}{dt} = \sigma_a \phi (1 - f_a), \tag{3.16}$$

which has an analytical solution given by

$$f_a = 1 - \exp(-\sigma_a \phi t). \tag{3.17}$$

In the case of swift heavy ions where amorphous ion tracks are continuous, σ_a has physical meaning and actually corresponds to the cross sectional area of amorphous material in the track. This is similar to the model of Gibbons [50] for the condition that individual ions produce a cylindrical amorphous volume over an incremental thickness. Gibbons also considered the case for light ions where a single ion produces a cylindrical cluster of defects, and the overlap of ion-produced defect clusters is required to produce amorphisation. If A_I is defined as the cylindrical area damaged by a single ion incident on the surface, the amorphous fraction is given by the well-known Gibbons model [50]:

$$f_a = 1 - \sum_{k=0}^{m} \frac{(A_I \phi t)^k}{k!} \exp(-A_I \phi t). \tag{3.18}$$

where m is the number of overlaps required to produce amorphous material. It can be easily seen that for the case of $m = 0$ (i.e., direct impact amorphisation), (3.18) reduces to (3.17) with $A_I = \sigma_a$. The Gibbons overlap model is illustrated in Fig. 3.6.

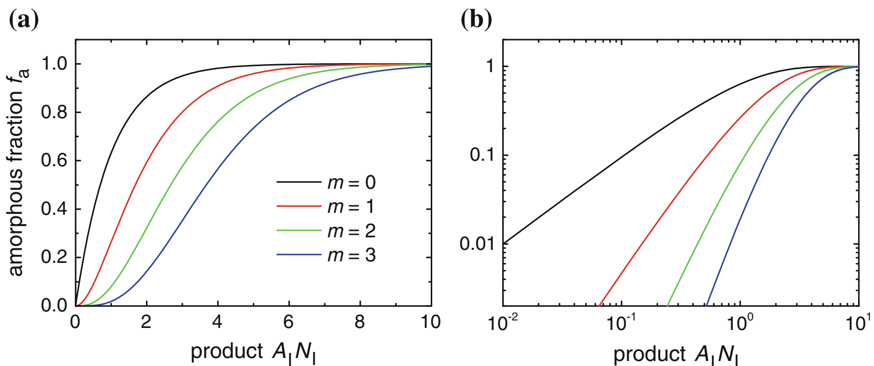

Fig. 3.6 Amorphous fraction f_a versus the product of area A_I, damaged by a single ion, and ion fluence $N_I = \phi t$ calculated with (3.18) for different numbers of overlaps m necessary to reach amorphisation. Part **a** has a linear scale and part **b** is a double logarithmic plot. $m = 0$ represents direct impact amorphisation corresponding to (3.17)

When the number of overlaps necessary for amorphisation increases, the formation of amorphous material is delayed, and a relative transition to a more rapid increase of the amorphous fraction occurs at higher ion fluences. However, this effect will be only observed if f_{def} is indeed negligible or the applied experimental technique is sensitive to amorphous regions only, but not (or much less) to defective crystalline material.

Consider now the case where the incremental cylindrical volume damaged by one ion has an inner structure consisting of an amorphous core with area A_1 surrounded by a damaged area A_2 that becomes amorphous only after being struck by $m + 1$ ions (m overlaps), (3.16) and (3.18) can be combined to

$$f_a = [1 - \exp(-A_1\phi t)] + \left[1 - \sum_{k=0}^{m} \frac{(A_2\phi t)^k}{k!} \exp(-A_2\phi t) \exp(-A_1\phi t)\right]. \quad (3.19)$$

In (3.19), the first term accounts for direct impact amorphisation from the central core of the damaged cylinder, and the second term accounts for amorphisation from the overlapping of A_2 areas from different ions, weighted by the fraction of material not amorphised by direct impact amorphisation. This process can be interpreted as a damage-stimulated amorphisation process. A very similar approach, which corresponds to (3.19) with $m = 1$, was developed to model the formation of heterogeneous tracks by swift heavy ion irradiation [51] (see also (8.4) in Chap. 8.5).

While (3.18) and (3.19) are derived from a general concept of cascade or ion track overlap, the concept of direct impact amorphisation combined with a defect or damage stimulated amorphisation process can be expressed in a rate expression given by [35, 47]:

$$\frac{df_a}{dt} = \sigma_a\phi(1 - f_a) + \sigma_s\phi f_a(1 - f_a), \quad (3.20)$$

where σ_a is the cross section for direct-impact amorphisation and σ_s is the effective cross section for defect or damage stimulated amorphisation. Direct-impact amorphisation can only occur in the remaining crystalline fraction, $1 - f_a$, while the probability for stimulated amorphisation to occur at the crystalline/amorphous interface is assumed to be $f_a\ (1 - f_a)$ [47]. An analytical solution to (3.20) is given by the expression [47]:

$$f_a = 1 - (\sigma_a + \sigma_s)/\{\sigma_s + \sigma_a \exp[(\sigma_a + \sigma_s)\phi t]\}. \quad (3.21)$$

Within this model, there must be some direct-impact amorphisation ($\sigma_a > 0$) for amorphisation to occur; otherwise, $f_a = 0$ if $\sigma_a = 0$. However, the definition of the amorphous nuclei or clusters created by direct-impact amorphisation in this model is rather ambiguous, and these amorphous nuclei may range from small defect clusters to substantial amorphous volumes within the core of a collision cascade. In the case that $\sigma_s = 0$, (3.21) reduces to the case of direct impact amorphisation given by (3.17).

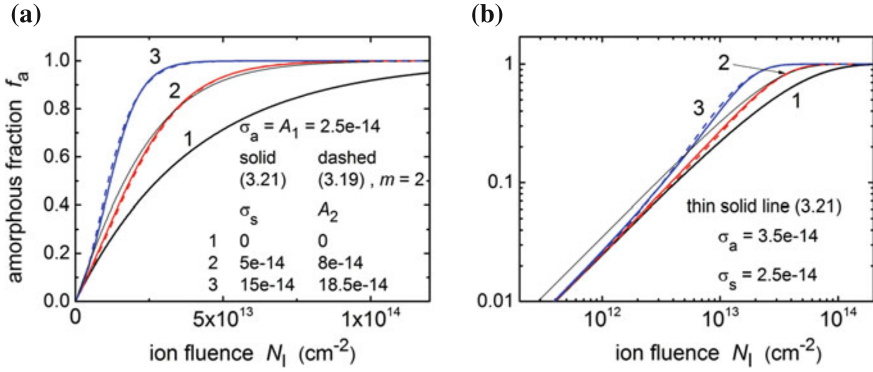

Fig. 3.7 Amorphous fraction f_a versus ion fluence N_I calculated with (3.19) and (3.21) and parameters as indicated in the figure. The cross sections and areas are given in cm^2. In parts **a**, **b** the same data are shown but in a linear and double logarithmic plot, respectively

Figure 3.7 illustrates curves that are calculated with (3.19) and (3.21). In contrast to the results of the Gibbons model (see Fig. 3.6), a linear increase of f_a with ion fluence, N_I, is always observed at sufficiently low ion fluences (see Fig. 3.7b), with the slope given by A_1 or σ_a, respectively. In the fluence range before saturation, the additional amorphisation by overlapping of the defective surrounding areas A_2 (3.19) or by stimulated growth of already existing amorphous regions (with the cross section σ_s, (3.21)) results in a stronger than linear increase of the amorphous fraction. Figure 3.7 shows that almost identical curves can be generated with (3.19) and (3.21) (cp. solid and dashed thick lines). This reflects that similar physical concepts are behind these two equations. With respect to (3.19), it should be mentioned that for a given value of A_1, different pairs of A_2 and m may give very similar curves. It is therefore often advisable to restrict m to a fixed value (as for instance to 2) and not to treat it as a free parameter. In Fig. 3.7 an additional curve is plotted as a thin solid line, which is calculated with (3.21). This curve differs from curve 2 by $\Delta f_a = 0.054$ at most. However, the direct-impact cross section, σ_a, is 40 % larger, and the cross section for stimulated amorphisation, σ_s, is 50 % smaller than the respective values used to calculate curve 2. This illustrates that the experimental uncertainty of f_a may cause huge uncertainties in the fit parameters. Equation (3.21) has been successfully utilized to fit amorphisation data for a broad range of materials [35, 47, 52–54], as illustrated in Fig. 3.8.

The Avrami nucleation and growth model [55] has also been used to describe amorphisation [56, 57]. In this case, f_a is described as a function of irradiation time, t, and given by the expression:

$$f_a = 1 - \exp\left[-RG^{m-1}t^m\right]. \tag{3.22}$$

Here, R is the irradiation-induced nucleation rate of amorphous clusters, G is the irradiation-induced growth rate of amorphous clusters, and m is a reaction order

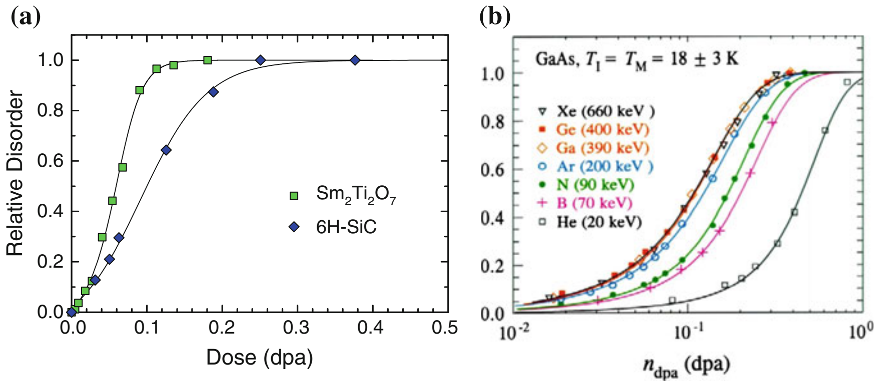

Fig. 3.8 Accumulation of disorder in **a** $SmTi_2O_7$ [53] and 6H-SiC [54] irradiated with Au ions at 300 K and in **b** GaAs [16] irradiated with various ion species at about 18 K (right part). The lines are calculated applying (3.21). Notice the different scales of the x-axes

parameter. With m of the order of 3–4, this model has been shown to provide a reasonable fit to a range of data for different materials. If one considers the nucleation rate, R, to be given by $\sigma_a\phi$ and the growth rate, G, to be dominated by $\sigma_s\phi$, then the Avrami expression given by (3.22) is conceptually similar to the direct-impact/stimulated amorphisation model in (3.21). This is also supported by the fact that (3.21) may yield similar dependences on the ion fluence as (3.22). In this case $\sigma_a \ll \sigma_s$ is valid; σ_a is unrealistically small and serves as a substitute to emulate nucleation. Likewise, in the case of $m = 1$, the growth rate becomes unity, and (3.22) reduces to the direct impact model given by (3.17).

3.4.2 Amorphisation Kinetics

The models described above represent simple descriptions of the irradiation-induced amorphisation process without any consideration for kinetics. During irradiation at temperature, simultaneous recovery processes can compete with damage production processes, and the rate of amorphisation will depend on the relative magnitude of the rate of production and recovery processes under any given irradiation conditions. Damage production processes are directly dependent on the damage rate or ion flux; thus, both damage rates and temperature affect the kinetics of amorphisation. The simultaneous damage recovery processes are associated with point defect recombination or annihilation at clusters in the crystalline state, point defect annihilation at crystalline/amorphous (c/a) interfaces, epitaxial recrystallization at c/a interfaces, or nucleation and growth recrystallization in the bulk of the amorphous state. Obviously, if the rate of amorphisation is less than the damage recovery rate at any temperature, amorphisation will not proceed.

The above amorphisation models already include damage rate through the local ion flux, ϕ; thus, in most cases, a temperature dependent rate of damage recovery is included in the rate theory expressions to derive related models for amorphisation kinetics. In the case of direct impact amorphisation, epitaxial recrystallization at c/a interfaces is the primary damage recovery process, and the amorphisation rate expression, (3.16), becomes:

$$\frac{df_a}{dt} = \sigma_a \phi (1 - f_a) - \mathrm{K}(T) f_a (1 - f_a), \tag{3.23}$$

where $K(T)$ is the epitaxial recovery rate constant at temperature T, and the term $f_a\,(1 - f_a)$ is the probability for epitaxial recrystallization at c/a interfaces. The solution of this rate expression is given by [47]:

$$f_a = \frac{1 - \exp[-\sigma_a \phi t + \mathrm{K}(T) t]}{1 - [K(T)/\sigma_a \phi] \exp[-\sigma_a \phi t + \mathrm{K}(T) t]}. \tag{3.24}$$

This expression is much more complex than that given by (3.17), and the dependence on the ratio of damage recovery rate to damage production rate, $K(T)/\sigma_a\phi$, is clearly evident. The damage recovery rate has been included in several rate theory models for amorphisation, and the solutions, which are often quite complex, are described in detail elsewhere [47].

One important point that must be noted is that the recovery rate constants can be associated with both thermal and irradiation-driven processes. Thus, the rate constant in (3.23) and (3.24) is the sum of temperature-dependent rate constants for both irradiation-driven and thermal annealing processes and is given by the expression:

$$K(T) = v_{irr} \exp(-E_{irr}/k_B T) + v_{th} \exp(-E_{th}/k_B T) \tag{3.25}$$

where v_{irr} and v_{th} are effective jump frequencies and E_{irr} and E_{th} are the activation energies for the irradiation-driven and thermal recovery processes, respectively. k_B is Boltzmann's constant. The effective thermal jump frequency, which accounts for local coordination and average number of jumps to recovery [58], generally ranges from 10^9 to 10^{14} s^{-1} [47]. On the other hand, the irradiation-driven jump frequency, ν_{irr}, is directly proportional to the ion flux and given by [59, 60]:

$$v_{irr} = \sigma_r \phi, \tag{3.26}$$

where σ_r is the recovery cross section associated with irradiation-driven defect recombination or recrystallization processes. The irradiation-driven recovery rate will always be directly proportional to the ion flux, and because $\nu_{irr} \ll \nu_{th}$, irradiation-driven recovery processes may be nearly athermal with low activation

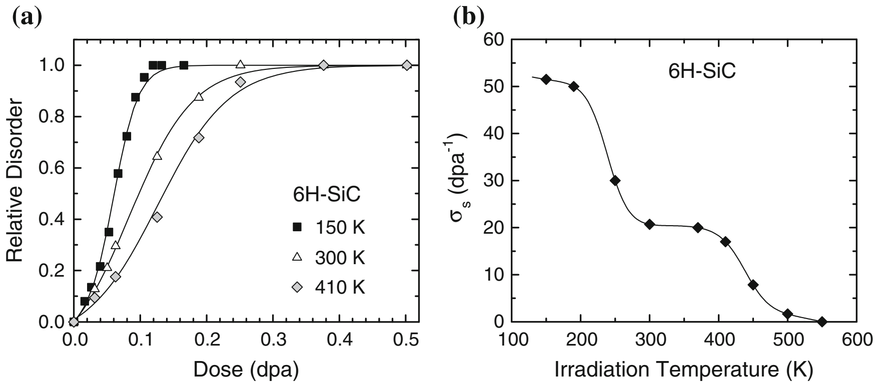

Fig. 3.9 **a** Relative disorder at the damage peak as a function of dose in 6H-SiC irradiated with 2 MeV Au ions at three different temperatures. The lines are fits to the experimental data applying (3.21). **b** The temperature dependence of the effective defect-stimulated cross section σ_s in 6H-SiC resulting from fits as plotted in (**a**) [54]. The effective amorphisation cross section, σ_a, is assumed to be constant in this temperature range, which is below the temperature for epitaxial recrystallization

energies. At high temperatures, the dominant term in (3.25) will be thermal recovery, and the recovery rate will be independent of ion flux. At lower temperatures, the irradiation-driven term in (3.25) can become large with respect to the thermal term, and irradiation-driven recovery will dominate. Under conditions where irradiation-driven processes dominate, the recovery rate constant, $K(T)$, is proportional to $\sigma_r\phi$, and the ratio of damage recovery to damage production, $K(T)/\sigma_a\phi$, in (3.24), as well as in other kinetic models of amorphisation [47], becomes a constant independent of ion flux (e.g., proportional to σ_r/σ_a for direct impact amorphisation). As a consequence, amorphisation is largely independent of ion flux when irradiation-driven recovery processes are dominant.

Because the expressions for amorphisation kinetics are complex, with recovery rates that may include both thermal and irradiation-driven processes, the kinetics of amorphisation is often investigated by applying the temperature-independent models to amorphisation data. This is illustrated in Fig. 3.9a, where (3.21) is fit to experimental ion channelling data at three different temperatures [54]. Analysis of the temperature dependence of the cross sections in such models can reveal multiple recovery mechanisms, as illustrated in Fig. 3.9b, and detailed analysis can yield activation energies [54].

One consequence of the damage recovery rate is the concept of critical temperature for amorphisation. In general, amorphisation will not occur if the damage production rate is less than the damage recovery rate. The critical temperature for amorphisation, T_c, is the temperature above which amorphisation does not occur and is defined by the condition that the production rate for amorphisation, $\sigma_a\phi$, equals the damage recovery rate, $K(T)$, (see (3.23)). When starting from (3.23),

several recovery processes can be included. If thermal recovery processes are dominant, the critical temperature is given by the expression:

$$T_c = \frac{E_{th}}{k_B \ln(v_{th}/\sigma_a \phi)}, \tag{3.27}$$

where σ_a is the cross section for amorphisation in the regime $T \to 0$, i.e. at low temperatures. The dependence of T_c on the damage production rate, $\sigma_a \phi$, is evident. Thus, increasing the damage rate will increase T_c, and decreasing the damage rate should decrease T_c. If irradiation-driven recovery processes dominate, than the critical temperature is given by:

$$T_c = \frac{E_{irr}}{k_B \ln(v_{irr}/\sigma_a \phi)}, \tag{3.28}$$

which can be rewritten, using (3.26), as:

$$T_c = \frac{E_{irr}}{k_B \ln(\sigma_r/\sigma_a)}, \tag{3.29}$$

with σ_r being the recovery cross section for damage associated with irradiation-driven recovery processes. Under these conditions, where irradiation-driven recovery is dominant, T_c is independent of ion flux and inversely dependent on the ratio σ_r/σ_a. Finally, T_c is only implicitly deduced from (3.23), if both irradiation-driven and thermal recovery processes contribute in comparable amounts. However, in this case, (3.23) has too many parameters that cannot be uniquely identified by fitting f_a versus the ion fluence $N_I = \phi t$ without additional information from other measurements.

The concept of critical temperatures also arises directly from experimental findings that show an exponential increase of the ion fluence necessary for amorphisation, N_I^{am}, with increasing temperature of irradiation, T, [61]. The temperature at which the amorphisation fluence N_I^{am} approaches infinity is called the critical temperature T_c. Early explanations were based on the direct impact amorphisation model, following from (3.18) with $m = 0$, and assumed the area A_I damaged by a single ion impact to shrink with increasing temperature [61, 62]. The radius of the amorphous region (produced by a single ion) is assumed to decrease by an amount δR due to a thermally activated vacancy-out-diffusion and defect recombination at the c/a interface. Since the amorphisation fluence is inversely proportional to the area amorphised by a single ion, the ratio of amorphisation fluence at temperature T to amorphisation fluence at $T = 0$, $N_I^{am,0}$, can be written as

$$\frac{N_I^{am}}{N_I^{am,0}} = \left[1 - C \exp\left(-\frac{E}{k_B T}\right)\right]^{-2}. \tag{3.30}$$

In this case, it follows that the critical temperature T_c, at which the amorphisation fluence approaches infinity, is given by:

$$T_c = \frac{E}{k_B \ln C}. \tag{3.31}$$

Depending on the expression used for the decrease in amorphous radius δR, E is the activation energy or only half of it [61, 62]. The parameter C was found to be inversely proportional to the damage cross section σ_a [62]. These two findings agree with (3.27) and (3.28), thus reflecting the conceptual similarity of using Arrhenius-type dependences for the decrease of relevant quantities with temperature. An expression similar to (3.30) can be also deduced from (3.23) to (3.25), which is given by

$$\frac{N_I^{am}}{N_I^{am,0}} = \left[1 - \frac{\nu_{irr}}{\sigma_a \phi} \exp\left(-\frac{E_{irr}}{k_B T}\right) - \frac{\nu_{th}}{\sigma_a \phi} \exp\left(-\frac{E_{th}}{k_B T}\right)\right]^{-1}. \tag{3.32}$$

The main difference to (3.30) is the exponent at the square bracket on the right hand side of the equation.

Finally, it should be mentioned that a critical temperature also appears when studying ion-beam induced effects at a pre-existing amorphous/crystalline interface. This temperature is usually called the reversal temperature T_R. During ion irradiation of a c/a interface, epitaxial recrystallization or interfacial amorphisation may occur [63]. In principle, both processes occur simultaneously. At the reversal temperature, T_R, crystallization and amorphisation are in balance, and the position of the c/a interface does not change. At temperatures $T > T_R$, ion-beam induced epitaxial crystallization dominates; whereas at $T < T_R$, interfacial amorphisation is the dominating process, thus shifting the position of the interface in one or the other respective direction. The reversal temperature was found to be [63]

$$T_R = \frac{E_a}{k_B \ln\left(F/\sigma_d^2 \phi\right)}, \tag{3.33}$$

where E_a is the activation energy and F is a free parameter. Despite the fact that the damage cross section σ_d appears quadratic, (3.33) resembles the dependences given in (3.27), (3.28) and (3.31). A reasonable explanation of (3.33) was given assuming the crystallization kinetics to be governed by thermal defect diffusion to the amorphous/crystalline interface [64]. That is, again, some conceptual similarity results in a similar expression for the critical (here called reversal) temperature. Equation (3.33) was also used to represent critical temperatures T_c of ion implanted III–V compound semiconductors for a wide range of ion masses and ion fluxes [45].

In the past, (3.30) and (3.32) (assuming only one recovery process) were successfully applied to represent the ion fluence necessary for amorphisation as a function of temperature (see e.g. [16, 61, 62, 65–67]). However, the model behind (3.30) is very simple and assumes formation of amorphous zones within single ion

impacts, which is often not the case. Therefore, a deeper physical interpretation of the corresponding fit parameters themselves seems not to be appropriate. Although (3.23) starts from a similar assumption, defect-stimulated amorphisation as given in (3.20) can be easily included, as shown in [47]. A further advantage of the ansatz, according to (3.23) and (3.25), is that more than one process and, in principle, even several thermal annealing processes (as for instance due to the thermal mobility of different point defects) can be easily included by adding further terms on the right hand side of (3.25). These terms correspondingly appear in the brackets of (3.32). However, irrespective of how many terms are included, the resulting dependences of $N_{\mathrm{I}}^{\mathrm{am}}/N_{\mathrm{I}}^{\mathrm{am},0}$ versus temperature T have always the same general shape. In other words, experimental results of $N_{\mathrm{I}}^{\mathrm{am}}/N_{\mathrm{I}}^{\mathrm{am},0}$ versus T do not give any hint about how many recovery processes are active. That is why in practical applications (3.30) or (3.32) (assuming only one recovery process) are generally applied to fit experimental data. Thus, the parameters obtained in that procedure are only used for calculation of the critical temperature T_{c} and usually not for determination of the activation energy. Starting from the model behind (3.30), critical temperatures were also obtained by analyzing the damage fraction for a fixed ion fluence as a function of temperature (see (5.6) and Fig. 5.6 in Chap. 5.3 and [65, 66]). This is possible with (3.24), too. It should be mentioned that when starting from one set of experimental data, (3.30) tends to yield slightly higher values of T_{c} than (3.32). Furthermore, the critical temperature can be also estimated by a visual examination of experimental data $N_{\mathrm{I}}^{\mathrm{am}}/N_{\mathrm{I}}^{\mathrm{am},0}$ versus T [68]. Therefore, some care has to be taken when comparing results obtained by different authors for a given material.

Once critical temperatures are available for different ion species implanted into a given material with various ion fluxes, one can search for dependences according to (3.27) or (3.29) in order to get some information about the cause of the occurring recovery process. Examples for that are given in Fig. 3.10. When nearly constant damage rate conditions ($\sigma_a \phi$ = constant) are realized in the experiment, then T_c should be constant if thermal recovery processes are dominant (see (3.27)).

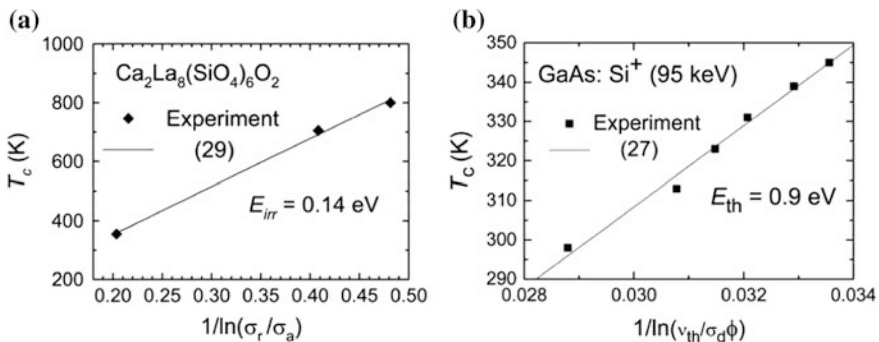

Fig. 3.10 Critical temperature, T_c, as a function of $1/\ln(\sigma_r/\sigma_a)$ for $Ca_2La_8(SiO_4)_6O_2$ [69] (**a**) and as a function of $1/\ln(\nu_{th}/\sigma_d\phi)$ for GaAs [67] (**b**) with σ_d being the calculated damage cross section

Otherwise, when the corresponding values of T_c are not constant, the temperature dependence of amorphisation is controlled by irradiation-driven recovery processes (see (3.29)). This is observed for $Ca_2La_8(SiO_4)_6O_2$, for which a linear relationship between T_c and $1/\ln(\sigma_r/\sigma_a)$ has been demonstrated (see Fig. 3.10a, [69]). In this case, based on (3.29), the critical temperature is independent of ion flux as demonstrated for $Ca_2La_8(SiO_4)_6O_2$ [70]. In the case of ion implanted GaAs, a clear dependence on the ion flux is found (see Fig. 3.10b) which indicates the importance of thermal recovery during irradiation [67]. It should be pointed out that in general it is rather difficult to distinguish between thermal and purely ion-beam induced effects, which is discussed in detail in [59].

3.5 Modelling of Complex Processes

In some materials or at certain implantation conditions, such as elevated temperatures or high ion fluxes, ion-induced damage formation becomes much more complex. Point defects may form at very low ion fluences, when each ion impinges on still pristine material. At higher ion fluences, these point defects may arrange to form extended defects like dislocation loops, stacking faults or voids but also phase changes may occur. In case amorphous seeds nucleate, eventually the implanted layers may be completely amorphised by the growth of these nuclei, which is often called ion-beam induced interfacial amorphisation [63]. In case amorphisation does not occur, a complex network of extended defects and defect clusters may form. In order to unravel such complicated processes, the application of one experimental technique is usually not sufficient. Correspondingly difficult is the modelling of such processes. It requires techniques with a more or less well-known sensitivity to the various kinds of damage. Further, such models may contain many parameters, and the distinct determination of each may not be possible.

A successful attempt of modelling more complex mechanisms of ion-induced damage formation was made in [35]. Provided the experimental technique applied is sensitive to both amorphous/heavily damaged areas and point defects, (3.13) and (3.20) can be combined and one obtains [35] the coupled differential equations:

$$\frac{df_{def}}{dt} = \sigma_d \phi (1 - f_{def}) - R f_{def} + \sigma_C \phi f_{def} \left[1 - \frac{f_{def}}{f_c(1 - f_a)} \right] - \frac{df_a}{dt} \frac{f_{def}}{1 - f_a} \tag{3.34a}$$

and

$$\frac{df_a}{dt} = \sigma_a \phi (1 - f_a) + \sigma_s \phi f_a (1 - f_a) \tag{3.34b}$$

with the total fraction f_d of damaged material given by $f_d = f_a + f_{def}$. The additional terms in (3.34a) in comparison to (3.13) take into account that clusters can only form in non-amorphous regions (third term on the right hand side) and that regions

with point defects or defect clusters can become amorphous during subsequent irradiation (last term on the right hand side of (3.34a)). Thus, these equations ensure that f_d does not exceed unity. The two coupled differential equations, (3.34a) and (3.34b), have to be solved numerically. Since (34) involves three different types of damage (point defects, defect clusters and amorphous material), a three-step process towards amorphisation can be modelled. It also means that the six free parameters in (3.34a) and (3.34b) can be determined unequivocally if and only if the measured dependence versus time t or ion fluence $N_I = \phi t$ clearly exhibits these three steps. The fraction of material damaged, f_d, can be also given as the sum of the amorphous fraction, f_a, and the defect fraction, f_{def}, in the residual crystalline material, which must be weighted by the fraction of crystalline material $(1 - f_a)$ [52],

$$f_d = f_a + f_{def}(1 - f_a). \tag{3.35}$$

When the fraction of point defects, f_{def}, is represented by (3.6) and the amorphous fraction f_a by (3.21), (3.35) yields the same results as (3.34a) provided cluster formation is ignored (i.e. $\sigma_c = 0$ in (3.34a)).

Examples for application of the coupled (3.34a) and (3.34b) are shown in Fig. 3.11. Damage analysis was performed with optical reflection (Fig. 3.11a) or with Rutherford backscattering spectrometry (Fig. 3.11b). Both methods are known to be sensitive to heavy damage as well as to point defects. In Fig. 3.11a, it is demonstrated how the continuous transition towards maximum damage occurring in ion implanted Si at low temperatures changes into a discontinuous two-step transition with increasing temperature [35]. The transition towards maximum damage in two steps is typical for semiconductors, such as Si (see [71] and references therein), GaAs, InAs, InP [16] and SiC [72], implanted with ions at temperatures close to the critical temperature, T_c. In contrast, ion implanted GaN exhibits a step-wise transition towards maximum damage that occurs even during implantation at the low temperature of 15 K (see Fig. 3.11b) [16], indicating different mechanisms of damage formation being operative in this case. The curves in Fig. 3.11 have been fitted to the experimental data using (3.34a) and (3.34b). In Fig. 3.11 a, cluster formation plays only a minor role in Si; while in Fig. 3.11b, three distinct steps are clearly visible in the experimental data for GaN, which allow the determination of all the model parameters in (3.34a) and (3.34b). It should be mentioned that in these cases σ_a is unrealistically low and mainly serves as a substitute to emulate nucleation of amorphous seeds [72].

A more detailed composite model for the production of amorphous material in semiconductors and a discussion of limits in the evaluation of experimental data are given in [73–76]. The proposed composite model considers the evolution of the undamaged fraction f_u, the amorphous fraction f_a and the fractions f_i of different types of pre-amorphous defects by combined rate equations that are of the type as given in (3.4), (3.7), (3.8), (3.14) and (3.15). The total fraction of damage is given by $f_d = f_a + \sum f_i$. For two types of point defects, i.e. $i = 2$, one obtains [73, 75, 77]

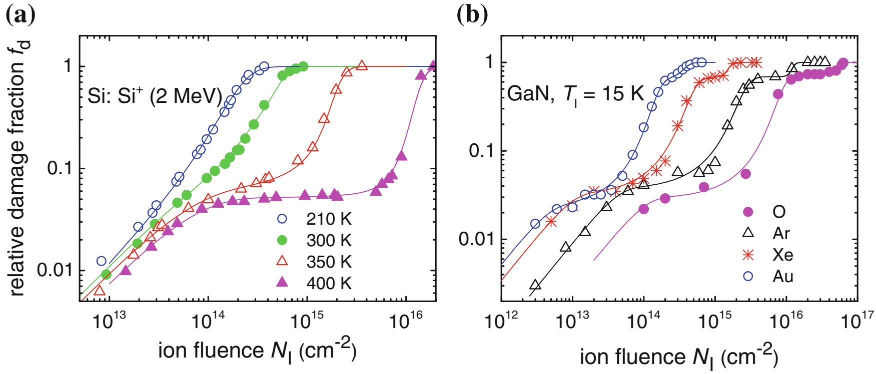

Fig. 3.11 Relative damage fraction, f_d, versus ion fluence N_I for **a** Si implanted with 2 MeV Si^+ ions at different temperatures and **b** GaN ion implanted at 15 K with different ion species. The lines are fitted to the experimental data with (3.34a) and (3.34b). The data for implanted Si are taken from [35]

$$\begin{aligned}
\frac{df_u}{dN_I} &= -(\sigma_1 + \sigma_2 + \sigma_a)f_u \\
\frac{df_1}{dN_I} &= +\sigma_1 f_u - \sigma_{12} f_1 - \sigma_{1a} f_1 f_a \\
\frac{df_2}{dN_I} &= +\sigma_2 f_u + \sigma_{12} f_1 - \sigma_{2a} f_2 f_a \\
\frac{df_2}{dN_I} &= +\sigma_a f_u + \sigma_{1a} f_1 f_a + \sigma_{2a} f_2 f_a\,.
\end{aligned} \tag{3.36}$$

σ_i and σ_a are the cross sections for formation of defect type i and of amorphous material, respectively, within a single ion impact. During further irradiation, the defect type i can be transformed to more complex defect types $i + 1$ or to fully amorphised material (a). σ_{jk} describe the cross sections for transformation between defect types i, where j and k refer to the initial and final state, respectively. The effect of stimulated amorphisation is represented by the cross sections σ_{ia}, with the probability for these processes to occur being given by $f_i f_\mathrm{a}$. For a more detailed explanation, the reader is referred to [77]. In principle, (3.36) can be extended to higher numbers of i, although one always would try to keep the number of defects i as low as possible. The presented model was successfully applied to represent both ion-induced damage formation and the evolution of damage-induced stress simultaneously in $\mathrm{LiNbO_3}$ of two different orientations [77]. In this case the high amount of information from experiment (two techniques and two crystal orientations) allowed the extraction of unique parameters. Finally, it should be mentioned that a very simple multi-step model has been introduced in which several direct-impact processes are put together at specific ion fluences [78]. This model has been applied to the accumulation of ion-induced damage in cubic zirconia and silicon carbide

[11], and it has been similarly applied to damage accumulation in in $Gd_2Ti_2O_7$ and compared to the model assuming direct-impact and damage stimulated amorphisation (see (3.20)) [79].

3.6 Summary

In this chapter, the origin of radiation damage and models that cover irradiation-induced defect production and accumulation, as well as irradiation induced phase transition, have been reviewed. A common and successful way for studying the processes of radiation damage formation is to analyse the damage evolution measured as a function of irradiation parameters on the basis of model calculations. In the past few decades, several such models have been developed in different contexts. Here, the models have been summarised, and more specifically, different models covering similar processes have been directly compared with each other. In this way, it is demonstrated that similar physical concepts result in similar dependencies, even if different mathematical formulas were obtained. In addition to general model calculations, which demonstrate the effects of the various model parameters, selected experimental examples have been presented to validate and demonstrate the applicability of the models. Substrate temperature and dose rate during irradiation are two of the most crucial parameters, the role of which on damage accumulation processes have been discussed and modelled. The different roles of irradiation-induced recovery processes and thermal recovery processes have been identified within the models and demonstrated in experimental results.

Acknowledgments One of the authors (WJW) gratefully acknowledges the support of the U.S. Department of Energy, Office of Science, Basic Energy Sciences, Materials Science and Engineering Division during the preparation of this chapter.

References

1. J.F. Ziegler, J.P. Biersack, U. Littmark, *The Stopping and Ranges of Ions in Solids* (Pergamon, New York, 2003). http://srim.org
2. M. Toulemonde, W. Assmann, C. Dufour, A. Meftah, F. Suder, C. Trautmann, Matematisk-fysiske Meddelelser **52**, 263 (2006)
3. J. Zhang, M. Lang, R.C. Ewing, R. Devanathan, W.J. Weber, M. Toulemonde, J. Mater. Res. **25**, 1344–1351 (2010)
4. G. Hobler, G. Otto, Mater. Sci. Semicond. Process. **6**, 1 (2001)
5. M. Toulemonde, W.J. Weber, G. Li, V. Shutthanandan, P. Kluth, T. Yang, Y. Wang, Y. Zhang, Phys. Rev. B **83**, 054106 (2011)
6. W.J. Weber, Y. Zhang, H.Y. Xiao, L.M. Wang, RSC Adv. **2**(2), 595–604 (2012)
7. L. Thome, A. Debelle, F. Garrido, P. Trocellier, Y. Serryus, G. Velisa, S. Miro, Appl. Phys. Lett. **102**, 141906 (2013)

8. W.J. Weber, D.M. Duffy, L. Thomé, Y. Zhang, Curr. Opin. Solid State Mater. Sci. **19**, 1 (2015)
9. M.L. Swanson, in *Handbook of Modern Ion Beam Materials Analysis*, ed. by J.R. Tesmer, M. Nastasi (Materials Research Society, Pittsburgh, PA, 1995), p. 231
10. B. Breeger, E. Wendler, W. Trippensee, Ch. Schubert, W. Wesch, Nucl. Instrum. Meth. Phys. Res. B **174**, 661 (2001)
11. L. Thomé, S. Moll, A. Debelle, F. Garrido, G. Sattonnay, J. Jagielski, Nucl. Instrum. Meth. B **290**, 6 (2012)
12. P.D. Townsend, P.J. Chandler, L. Zhang, *Optical Effects of Ion Implantation* (Cambridge University Press, Cambridge, 1994)
13. M. Schmidt, H. de Meyer, P.J. Janse van Rensburg, W.E. Meyer, F.D. Auret, Phys. Status Solidi B **251**, 211 (2014)
14. A. Taylor, J.R. Wallace, E.A. Ryan, A. Philippides, J.R. Wrobel, Nucl. Instrum. Meth. Phys. Res. **189**, 211 (1981)
15. J.A. Hinks, Nucl. Instrum. Meth. Phys. Res. B **267**, 3652 (2009)
16. E. Wendler, Nucl. Instrum. Meth. Phys. Res. B **267**, 2680 (2009)
17. S.J. Zinkle, C. Kinoshita, J. Nucl. Mater. **251**, 200–217 (1997)
18. E. Wendler, AIP Conf. Proc. **1336**, 621 (2011)
19. K. Matsuura, N. Itoh, T. Suita, J. Phys. Soc. Japan **22**, 118 (1967)
20. F.J. Bryant, A.F.J. Cox, J. Phys. C (Proc. Phys. Soc.) **1**, 1734 (1968) (Ser. 2)
21. F.J. Bryant, A.F.J. Cox, E. Webster, J. Phys. C (Proc. Phys. Soc.) **1**, 1737 (1968) (Ser. 2)
22. V.A. Panov, A.A. Khar'kov, Semiconductors **30**, 444 (1996)
23. F.L. Vook, H.J. Stein, Radiat. Eff. **2**, 23–30 (1969)
24. J.W. Marx, H.G. Cooper, J.W. Henderson, Phys. Rev. **88**, 106 (1952)
25. H.G. Cooper, J.S. Koehler, J.W. Marx, Phys. Rev. **97**, 599 (1955)
26. M. Nastasi, J.W. Mayer, J.K. Hirvonen, *Ion Solid Interactions: Fundamentals and Applications* (Cambridge University Press, Cambridge, 1996)
27. G.S. Was, *Fundamentals of Radiation Materials Science* (Springer, Berlin, 2007)
28. G.J. Dienes, A.C. Damask, J. Appl. Phys. **29**, 1713–1721 (1958)
29. G. Lück, R. Sitzmann, Phys. Stat. Sol. **5**, 683 (1964)
30. G. Lück, R. Sitzmann, Phys. Stat. Sol. **6**, 263 (1964)
31. W.J. Weber, J. Nucl. Mater. **98**, 206 (1981)
32. M.W. Thompson, *Defects and Radiation Damage in Metals* (Cambridge University Press, Cambridge, 1969)
33. W.J. Nellis, Inorg. Nucl. Chem. Lett. **13**, 393 (1977)
34. W.J. Weber, Radiat. Eff. **70**, 217 (1983)
35. N. Hecking, K.F. Heidemann, E. Te Kaat, Nucl. Instrum. Meth. B **15**, 760 (1986)
36. R. Sizmann, J. Nucl. Mater. **69** and **70**, 386–412 (1978)
37. S.I. Golubov, A.V. Barashev, R.E. Stoller, in *Comprehensive Nuclear Materials*, ed. by R.J. M. Konings (2012), pp. 357–391
38. F.W. Clinard Jr, L.W. Hobbs, in *Physics of Radiation Effects in Crystals*, ed. by R.A. Johnson, A.N. Orlov (Elsevier Science Publishers, Amsterdam, 1986), p. 387
39. P. Thevenard, G. Guiraud, C.H.S. Dupuy, B. Delaunay, Radiat. Eff. **32**, 83 (1977)
40. R.S. Averback, J. Nucl. Mater. **216**, 49 (1994)
41. F. Gao, W.J. Weber, Phys. Rev. B **63**, 214106 (2001)
42. E. Zarkadoula, R. Devanathan, W.J. Weber, M.A. Seaton, I.T. Todorov, K. Nordlund, M.T. Dove, K. Trachenko, J. Appl. Phys. **115**, 083507 (2014)
43. C.S. Schnohr, E. Wendler, K. Gartner, W. Wesch, K. Ellmer, J. Appl. Phys. **99**, 123511 (2006)
44. L.T. Chadderton, Radiat. Eff. **8**, 77 (1971)
45. E. Wendler, B. Breeger, C. Schubert, W. Wesch, Nucl. Instrum. Meth. B **147**, 155 (1999)
46. E. Wendler, K. Gärtner, W. Wesch, Nucl. Instrum. Meth. B **266**, 2872 (2008)
47. W.J. Weber, Nucl. Instrum. Meth. B **166–167**, 96–106 (2000)
48. M.R. Pascucci, J.L. Hutchison, L.W. Hobbs, Radiat. Eff. **74**, 219 (1983)
49. W.L. Gong, L.M. Wang, R.C. Ewing, J. Zhang, Phys. Rev. B **54**, 3800 (1996)

50. J.F. Gibbons, Proc. IEEE **60**, 1062 (1972)
51. G. Sattonnay, C. Grygiel, I. Monnet, C. Legros, M. Herbst-Ghysel, L. Thomé, Acta Mater. **60**, 22 (2012)
52. Y. Zhang, F. Gao, W. Jiang, D.E. McCready, W.J. Weber, Phys. Rev. B **70**, 125203 (2004)
53. Y. Zhang, W.J. Weber, V. Shutthanandan, R. Devanathan, S. Thevuthasan, G. Balakrishnan, D.M. Paul, J. Appl. Phys. **95**, 2866 (2004)
54. W. Jiang, Y. Zhang, W.J. Weber, Phys. Rev. B **70**, 165208 (2004)
55. M. Avrami, J. Chem. Phys. **9**, 177 (1941)
56. S.U. Campisano, S. Coffa, V. Rainieri, F. Priolo, E. Rimini, Nucl. Instrum. Meth. B **80**(81), 514 (1993)
57. W. Bolse, Nucl. Instrum. Meth. B **141**, 133 (1998)
58. A.C. Damask, G.J. Dienes, *Point Defects in Metals* (Gordon and Breach, New York, 1963)
59. G. Carter, Radiat. Eff. **100**, 281 (1986)
60. G. Carter, M.J. Nobes, J. Mater. Res. **6**, 2103 (1991)
61. F.F. Morehead, B.L. Crowder, Radiat. Eff. **6**, 27 (1970)
62. J.R. Dennis, E.B. Hale, J. Appl. Phys. **49**, 1119 (1978)
63. J. Linnros, R.G. Elliman, W.L. Brown, J. Mater. Res. **3**, 1208 (1988)
64. V. Heera, T. Henkel, R. Kögler, W. Skorupa, Phys. Rev. B **52**, 15776 (1995)
65. T.E. Haynes, O.W. Holland, Appl. Phys. Lett. **59**, 452 (1991)
66. R.A. Brown, J.S. Williams, Phys. Rev. B **64**, 155202 (2001)
67. E. Wendler, Th Opfermann, P.I. Gaiduk, J. Appl. Phys. **82**, 5965 (1997)
68. A. Meldrum, S.J. Zinkle, L.A. Boatner, R.C. Ewing, Phys. Rev. B **59**, 3981 (1999)
69. W.J. Weber, Y. Zhang, L. Wang, Nucl. Instrum. Meth. B **277**, 1 (2012)
70. W.J. Weber, Y. Zhang, H. Xiao, L. Wang, RSC Adv. **2**, 595 (2012)
71. J.K.N. Lindner, R. Zuschlag, E.H. te Kaat, Nucl. Instrum. Meth. Phys. Res. B **62**, 314 (1992)
72. E. Wendler, Th. Bierschenk, W. Wesch, E. Friedland, J. B. Malherbe, Nucl. Instrum. Meth. Phys. Res. B
73. R. Webb, G. Carter, Radiat. Eff. **42**, 159 (1979)
74. G. Carter, R. Webb, Radiat. Eff. **43**, 19 (1979)
75. R.P. Webb, G. Carter, Radiat. Eff. **59**, 69 (1981)
76. G. Carter, R.G. Elliman, Radiat. Eff. **68**, 155 (1983)
77. E. Schmidt, T. Steinbach, W. Wesch, J. Phys. D Appl. Phys. **47**, 265302 (2014)
78. J. Jagieski, L. Thome, Vacuum **81**, 1352 (2007)
79. S. Moll, G. Sattonnay, L. Thomé, J. Jagielski, C. Decorse, P. Simon, I. Monnet, W.J. Weber, Phys. Rev. B **84**, 064115 (2011)

Chapter 4
Synthesis of Nanostructures Using Ion-Beams: An Overview

Giancarlo Rizza and Mark C. Ridgway

Abstract The objective of this chapter is to give an overview on the basic principles underlying the synthesis of nanocomposite materials using ion-beams. In particular, those based on metallic nanoparticles embedded within a dielectric host matrix. However, this chapter is not meant as a complete literature survey and does not include all the immense existing literature. Instead, it can be taken as a practical handbook where the main ion-related strategies developed to synthesize nanocomposites are rationalized. These can be divided into two main categories: in the first one, the ion-beam is used to introduce a foreign species into a host matrix. This *bottom-up* approach is for example the domain of the ion-implantation. In the second one, the ion-beam is used to depose the energy into a host matrix already containing the foreign species. These can be in form of solute monomers, nanoparticles or thin films. This *top-down* approach is for example the domain of the ion-irradiation. Besides, the main limitations inherent to the ion-beam techniques are described and some alternative strategies are illustrated. Finally, it has recently been pointed out that the processes occurring during the ion beam synthesis are similar to those observed in driven alloys. Thus, this chapter is also an attempt to bridge the gap between the experimental and theoretical works developed so far in both the fields of driven alloys and metal-glass nanocomposites submitted to ion irradiation.

Mark C. Ridgway: Deceased December 2015

G. Rizza (✉)
Laboratoire des Solides Irradiés, Ecole Polytechnique,
CEA/DRF/IRAMIS, CNRS, Université Paris-Saclay, Palaiseau Cedex 91128, France
e-mail: giancarlo.rizza@polytechnique.edu

M.C. Ridgway
Research School of Physics and Engineering, Australian National University,
Canberra, ACT 2601, Australia

© Springer International Publishing Switzerland 2016

W. Wesch and E. Wendler (eds.), *Ion Beam Modification of Solids*,
Springer Series in Surface Sciences 61,
DOI 10.1007/978-3-319-33561-2_4

4.1 Introduction

A nanocomposite is a multi-phase solid where at least one of the phases has a nano-scale dimension, e.g. a thin film containing nanoparticles (NPs). Its properties are related to those of the embedded NPs, which in turn depend on their size, shape, concentration, spatial distribution and chemical environment. Nowadays there are paramount of techniques allowing the fabrication of nanocomposites using both bottom-up or top-down approaches [1]. However, in this chapter we only focus on the synthesis of those where a solute element A is first introduced into a solid matrix B and then allowed to evolve toward the nucleation and growth of NPs. The pathway followed by the solute, from the solid solution to the nano-phase separation, is described by the rules of both thermodynamic and kinetic processes [2–4]. Within this framework, an ion-beam can be considered as a powerful tool to widen the potentiality of the synthesis process. This can be done by artificially modifying both the thermodynamic phase diagram and the kinetic pathways. For example, to overcome the solubility limit or, by playing with the competition between thermal and ballistic effects, to modify the nucleation and growth processes. Nonetheless, irradiation adds a degree of complexity to the system. Thus, to master the synthesis process, thermodynamic, kinetic and ion-driven effects must be considered in detail.

In Sect. 4.2 the synthesis of NPs is rationalized by introducing a hierarchical description of the system: from the more simple to the more complex. At each level of complexity, new aspects or elements are introduced which participate in the evolution of the system. At the ground level, thermodynamics provides a concise description of the system at the equilibrium. A thermodynamic system is described in terms of phase stability, chemical equilibrium and graphical constructions of the equilibrium phases. Thus, in Sect. 4.2.1 basics of phase stability and construction of a phase diagram are introduced. In particular, the concept of equilibrium concentration, or solvus, is introduced. Thermodynamics is a powerful approach but it is strictly applicable to phenomena that are only achievable in an infinite amount of time. Thus, the next level of complexity is reached when kinetic effects, such as the diffusion, are taken into account. A kinetic system is described by the paths and rates adopted by a system that is out of equilibrium to return to the equilibrium state under the influence of various forces. In Sect. 4.2.2 the concept of supersaturation is introduced. When the diffusion is allowed, a supersaturated solid solution becomes instable and phase separation takes place; in our case this corresponds to the nucleation and growth of NPs. The highest level of complexity is reached when irradiation effects are also introduced. Indeed, an ion-beam can be considered as an external perturbation allowing the system to explore novel configurations, e.g. the dynamic stabilization of non-equilibrium phases [5]. A system evolving under the effect of both ballistic and thermal processes is defined as a *driven system*. In Sect. 4.2.3, basics concepts of driven systems are introduced. In particular, an historical overview of the models developed so far is given. Besides, the concepts

of direct and inverse coarsening, or inverse Ostwald ripening, are also introduced and commented.

In Sect. 4.3 some of the ion-beam strategies developed so far for the synthesis of NPs are reviewed. Depending on the role played by the ions delivered by the accelerator, these can be divided into two main categories. In the domain of ion-implantation, charged particles are used to introduce one or more atomic species into a host matrix. In the domain of ion-irradiation, charged particles are used to depose their energy into the sample. This can be the matrix, the solute atoms or the confined NPs. Finally, in Sect. 4.3.4 we show how a driven system can be studied using a *model system*.

To conclude this introduction it is worth mentioning that in this chapter we mainly focus on the processes that occur within the nuclear stopping regime. Some examples of the evolution of a nanophase in the electronic stopping regime will be described in detail in *Part IV,* Chap. 11.

4.2 From Thermodynamic to Driven System

In material science a phase is defined as an homogenous, physically distinct and mechanically separable portion of the material with a given chemical composition and structure. A phase is characterized by its temperature, pressure and chemical composition. Within a phase, these values are constant. Each phase is characterized by its atomic structure (vapor, liquid or solid), its crystalline structure (e.g. body centered, face centered, …) and its chemical composition. If two or more phases coexist, they are separated by a phase boundary, or an interface. The ensemble of the phases present in the material is called *system*. If a material possesses more than one phase, it is called a multi-component system. If at least one of the phases has a sub-micrometer dimension, the system is named *nanocomposite*.

4.2.1 Thermodynamic System

The key issue in thermodynamics is the determination of the most stable phase [2]. A convenient way is to use the Gibbs free energy:

$$G = H - TS \tag{4.1}$$

where H is the enthalpy, T the temperature and S the entropy. This is schematically represented in Fig. 4.1a. When the Gibbs free energy is at a local, or relative, minimum, the system is said to be in a metastable state (point A). Conversely, when the Gibbs free energy is at a maximum, the system is instable (point B). Finally, if

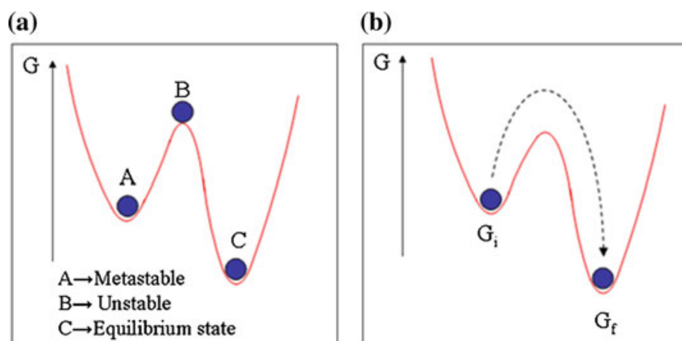

Fig. 4.1 **a** Sketch for a metastable (*A*), an instable (*B*) and a stable (*C*) equilibrium condition. **b** A phase transition is only possible if the Gibbs free energy for the final state, G_f, is lower than the Gibbs free energy for the initial state, G_i, such that $\Delta G = G_f - G_i < 0$.

the Gibbs free energy is at an absolute minimum, the system lies in an equilibrium state (point C). In general, a phase transformation takes place only if the Gibbs energy of the final state, G_f, is lower than that of the initial one, G_i (Fig. 4.1b), such that:

$$\Delta G = G_f - G_i < 0 \tag{4.2}$$

Besides these basic concepts, the widespread use of the Gibbs energy lies on the fact that it allows a graphical construction of a diagram representing the ensemble of the equilibrium phases, whose relative extension is function of the thermodynamic parameters, such as the temperature, the pressure or the solute concentration. As it is beyond the scope of this review to explain how a phase diagram is obtained, in the following we focus on a system whose characteristics are handy in describing a metal-glass nanocomposite. The latter can be approximated to a binary system, $A - B$, where the solid host matrix *A* shows a limited miscibility with a solute element *B*.

Within these very crude simplifications, a nanocomposite can be described as an *eutectic phase diagram*, Fig. 4.2a. A graphical interpretation can be done by considering that for a given solute concentration, for instance *c*, the stable phase is a function of the temperature. If the temperature, e.g. T_1, is larger than the melting temperature of both *A* and *B*, the two elements are in a liquid phase. When the temperature is reduced to T_2, a mixture of solid (*A*) and liquid (*A* + *B*) phases is observed. A further reduction of the temperature, T_3, results in the formation of a solid solution, where the element *B* is dissolved into the host matrix *A*. Finally, at T_4, the solid solution becomes instable and a phase separation between the two elements occurs. This region is called *coexistence region* and represents the phase domain where the nucleation and growth processes take place.

When the coexistence region does not intercept the minimum of the solid + liquid region, the system has a *miscibility gap*, Fig. 4.2b. The miscibility

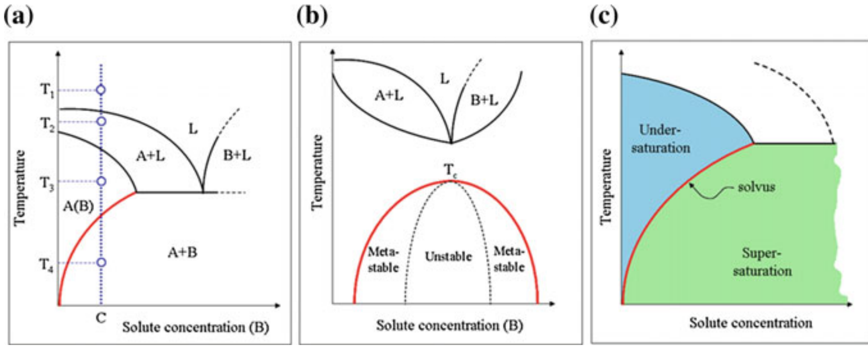

Fig. 4.2 **a** Eutectic phase diagram, and **b** phase diagram with a miscibility gap. **c** the solvus, or solubility limit, represents the equilibrium concentration at the interface between the elements A and B both in a solid phase

gap is characterized by a critical temperature T_c. Depending on how the solid solution, $A(B)$, decomposes into separate phases, $A + B$, the miscibility gap region can be further divided into two sub-regions: (i) if an energy barrier exists, the system is metastable and a phase separation occurs through the nucleation and growth processes. (ii) if there is not such energy barrier, the system is unstable and the phase transformation takes place through a *spinodal decomposition*.

The region separating the solid solution to the coexistence region is called *solvus*, or the *solubility limit*, and it is represented by the red curve in Figs. 4.2a–c and 4.3a, b. It refers to the maximum amount of solute that can be added to the solid solution before the system becomes metastable and eventually a phase separation occurs. Thus, the solubility gives the equilibrium concentration at the interface between the elements A and B. In particular, the higher the temperature, the larger the concentration of solute B that can be dissolved into the matrix A. Besides, at a given temperature, when the solute concentration is lower than the solubility, the system is said to be *under-saturated* and the phase separation (precipitation) does not occur, Fig. 4.2c. On the other hand, when the solute concentration is larger than the solubility limit, the system is said to be *super-saturated* and the precipitation of a novel phase is possible upon solute diffusion, Fig. 4.2c.

For a planar interface separating two solid phases, e.g. *A/B*, the solubility curve scales as:

$$C_\infty(T) = C_0 \exp\left(-\frac{H_{vf}}{k_B T}\right) \tag{4.3}$$

where C_0 is a pre-factor, H_{vf} the enthalpy for vacancy formation, k_B the Boltzman constant and T the temperature. As C_0 is always larger than zero, two elements are never completely immiscible [2].

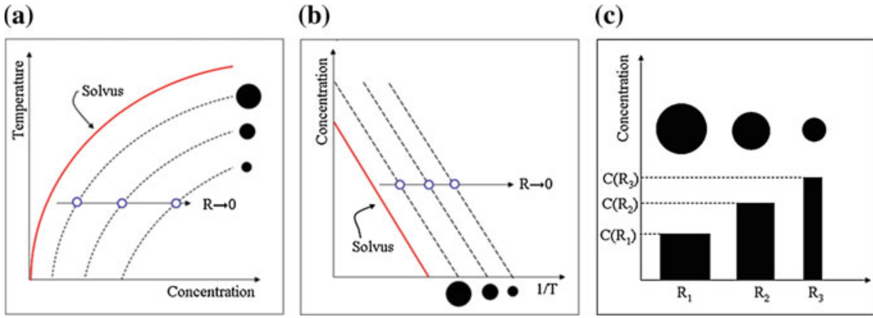

Fig. 4.3 Dependence of the solubility limit on the nanoparticle size as a function of **a** the solute concentration and **b** the inverse of the temperature (Arrhenius plot). **c** Relationship between the size of the nanoparticle, R, and its equilibrium concentration, C(R). In the figure, the width of the bar is proportional to R, while its hight is proportional to C(R). Equation (4.4) states that larger nanoparticles are thermodynamically more stable as they have a lower equilibrium concentration

However, when the plane interface is replaced by a nanoparticle of finite size, the curvature of the surface modifies the pressure between the two phases and the new equilibrium condition is given by the Gibbs-Thomson equation:

$$C(R) = C_{\infty}\exp\left(\frac{2\sigma\Omega}{k_B RT}\right) = C_{\infty}\exp\left(\frac{L_c}{R}\right) \tag{4.4}$$

C_{∞} is the solubility for a plane interface and $L_c = 2\sigma\Omega/k_B T$ the capillarity length, where σ is the surface tension and Ω the atomic volume. The importance of the Gibbs-Thomson equation relies on the fact that the equilibrium concentration at the nanoparticle/matrix interface scales with both the size of the nanoparticle and the temperature. In Fig. 4.3a the evolution of C(R) is represented as a function of both the temperature and the solute concentration for different particle radii. To facilitate its physical interpretation, in Fig. 4.3b C(R) has also been represented in an Arrhenius plot as a function of the inverse of the temperature. In this case (4.4) reads:

$$\ln\left(\frac{C(R)}{C_{\infty}}\right) \propto \frac{1}{TR} \tag{4.5}$$

In Fig. 4.3a–b the red solid curve corresponds to the *solvus* for the flat interface, C_{∞}, whereas the dashed black curves represent the evolution of C(R) for decreasing values of the nanoparticle size, e.g. $R \rightarrow 0$. Equation (4.4) indicates that larger nanoparticles have a lower concentration than smaller ones. This is graphically represented in Fig. 4.3c where the width of the bar represents the dimension of the nanoparticle and its height the equilibrium concentration. Figure 4.3a shows that the solubility at the matrix/nanoparticle interface increases when the nanoparticle radius is reduced. It states that smaller nanoparticles are less stable than larger ones.

Figure 4.3b shows that to maintain the same equilibrium concentration, the solvus curve is shifted toward lower temperatures and smaller sizes. This is, a small nanoparticle has the same equilibrium concentration as a larger one but at lower temperature.

However, thermodynamics provides no information on the rate of the transformation, only whether or not the transformation can take place. The main process controlling the rate at which the transformation occurs is the diffusion of atoms, cf. Sect. 4.5. The evolution of a system with time is the domain of the kinetics as we will describe in the next section.

4.2.2 Kinetic System

A kinetic system describes the rates and the pathways adopted by the system to reach the equilibrium condition [3, 4]. So far, we have introduced the concept of solubility to discriminate between an under- and a super-saturated system. In this section, the concept of supersaturation is used to describe the kinetic evolution of the solute toward the nucleation and growth of a nanophase. An operative definition for the supersaturation is given by considering the ratio between the amount of solute at a given time to the solubility limit for a flat interface:

$$s(t) = \frac{C(t)}{C_\infty} \tag{4.6}$$

Depending the on the value of $s(t)$, the kinetic evolution of the solute can be divided into four distinct regimes as shown in Fig. 4.4a–c.

4.2.2.1 Supersaturation Regime

Initially, the solute concentration, $s(t)$, increases proportionally to the amount of deposited monomers, e.g. the implantation fluence, Fig. 4.4a, b. The solute accumulation goes on up to a time t_1 till it reaches the solubility limit, i.e. $s_c = 1$.

4.2.2.2 Nucleation Regime

When $s(t)$ becomes larger than one stable embryos start to form, Fig. 4.4. Their stability depends on the competition between volume and surface energy terms. In particular, Fig. 4.4d shows that the critical energy barrier, ΔG^*, index critical energy barrier (ΔG^*) and the critical radius, R^*, necessary to form a stable particle

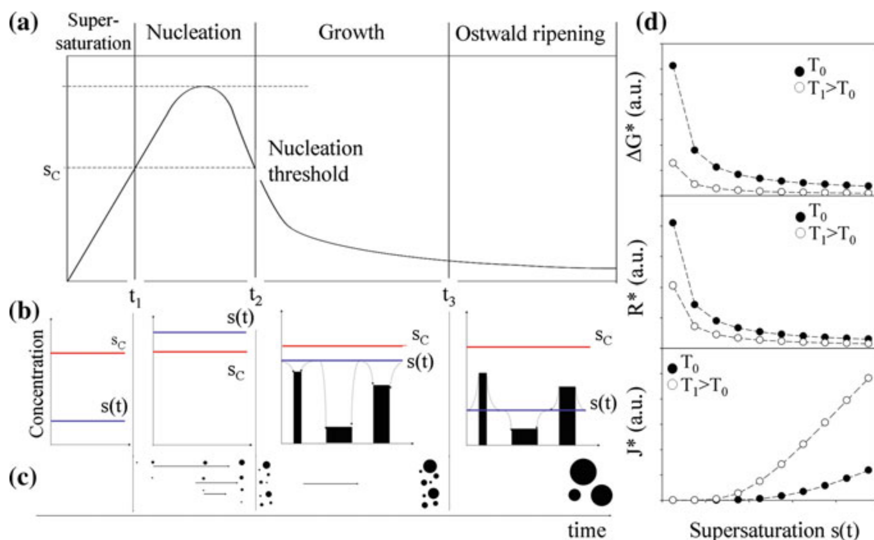

Fig. 4.4 **a** Evolution of the supersaturation as a function of time, s(t). The solubility limit, s_C, can be used to characterize the different kinetic regimes, i.e. supersaturation, nucleation, growth and Ostwald ripening. **b** Snapshots representing the value of s(t) with respect to the solubility, s_C, in the different regimes. The nanoparticles are represented by the back bars, where the width is the nanoparticle size and the hight its equilibrium concentration. **c** Time-line evolution of the nanoparticle population. **d** Evolution of several thermodynamic parameters with the supersaturation s(t): energy barrier (ΔG^*) critical radius (R^*) and nucleation rate (J^*). These variables are represented for two different temperatures, T_0 and $T_1 > T_0$

upon solute fluctuations scale with both the temperature, T, and the supersaturation, $s(t)$:

$$\Delta G^* \propto \frac{1}{T^2 \times \ln\left(s(t)^2\right)}, \tag{4.7}$$

$$R^* \propto \frac{1}{T \times \ln(s(t))}, \tag{4.8}$$

On the other hand, the nucleation rate, J^*, is function of ΔG^* and writes:

$$J^* \propto \exp\left(\frac{\Delta G^*}{k_B T}\right), \tag{4.9}$$

Owing to their inverse dependence on $s(t)$, both ΔG^* and R^* decreases when the supersaturation is increased. Conversely, J^* increases with the monomer concentration. This has a consequence on the nucleation process. At the beginning of the nucleation regime the solute concentration is generally important, thus ΔG^* and R^*

are small and J^* high enough such that the formation of small stable nuclei is an explosive process. Besides, as ΔG^* and R^* inversely scale with T, the nucleation process is further enhanced when the temperature is increased.

Once formed, each precipitate acts as a sink for the diffusing solute. Thus, s(t) starts to decrease despite the ongoing monomer deposition, Fig. 4.4a. The dropping of $s(t)$ results in an increasing of both ΔG^* and R^*, and thus in a reduction of the nucleation rate, J^*, Fig. 4.4d. Whenever $s(t)$ falls below the nucleation threshold, e.g. at time t_2, the nucleation of new stable nanoparticles is hindered. The temporal window between t_1 and t_2 is usually referred to as the *nucleation window*.

Within the nucleation window, stable embryos nucleate and grow at different times, Fig. 4.4c. As the precipitates that have been formed close to t_1 have had much more time to grow than those formed close to t_2, the nucleation process ends up with a broad size distribution. We will see in Sect. 4.3.2 that this is one of the main drawbacks of the ion-beam synthesis techniques.

4.2.2.3 Growth Regime

Below s_c the nucleation of new particles is not allowed. However, $s(t)$ is sufficiently high such that all the existing nanoparticles can grow by incorporating the incoming monomers. Otherwise stated, $s(t)$ is larger than the interface concentration of all the growing nanoparticles. The latter is given by the Gibbs-Thomson equation, see (4.4), and shown in Fig. 4.4b. The kinetic evolution of the second phase is completely characterized by knowing the time-evolution of:

- the size distribution function, $f(R(t))$
- the nanoparticle size, $R(t)$
- the nanoparticle density, $n(t)$.

However, de Lamaëstre et al. [6] have shown that when ion-implantation is involved, the nucleation and growth history of the nanoparticles is no longer revealed by the distribution function, $f(R(t))$. Conversely, the two other quantities, $R(t)$ and $n(t)$, are experimentally accessible. In the growth regime the nucleation of new nanoparticles is not allowed, thus their density remains constant upon time, i.e. $n(t)$ = constant. Conversely, as their solubility is lower than the solute concentration, i.e. $C(R) < s(t)$, they can grow incorporating the diffusing monomers, Fig. 4.4b. In this case the growth will depend on the absorption mechanism.

If the monomer absorption is the faster process, the growth is *limited by the diffusion*. In this case, the number of particles and their radius scale as:

$$n(t) = const. \tag{4.10}$$

$$R(t) \propto t^{0.5} \tag{4.11}$$

If the monomer diffusion is the faster process, the growth is *limited by the interface reaction*. In this case, the number of particles and their radius scale as:

$$n(t) = const. \tag{4.12}$$

$$R(t) \propto t \tag{4.13}$$

4.2.2.4 Ostwald Ripening Regime

The growth of the precipitates further reduces the concentration of the dissolved monomers which, in turn, affects their stability. Indeed, the critical nanoparticle radius, R^*, scales as the inverse of the supersaturation level, i.e. $R^* \propto 1/s(t)$, Fig. 4.4d. Thus, when $s(t)$ is sufficiently low, the smallest particles become instable and eventually dissolve, Fig. 4.4c. This regime is called *Ostwald ripening* (*OR*). The evolution of a precipitate phase in the OR regime is different for closed and open systems

In *closed systems* the mass is conserved. As the supersaturation cannot remain constant indefinitely soon or less it starts to decrease and the system minimizes its energy through a mass redistribution, i.e. larger precipitates grow at the expense of the smaller ones. *This situation occurs, for instance, during a post-implantation thermal annealing experiment, cf.* Sect. 4.3.1.3. The description of the evolution of the particles in an OR regime was originally developed by Lifshitz and Slyozov [7] and Wagner [8], and is nowadays known as the LSW theory. For surface absorption limited by the diffusion of the monomers, the precipitates size and density evolve as:

$$n(t) = \propto t^{0.33} \tag{4.14}$$

$$R(t) \propto t^{-1} \tag{4.15}$$

On the other hand, if the monomer assimilation is limited by the interface reaction one has:

$$n(t) = \propto t^{0.5} \tag{4.16}$$

$$R(t) \propto t^{-1.5} \tag{4.17}$$

In an *open system*, the continuous monomer supply allows the particle dissolution to be reduced, or eventually stopped. This mechanism has been named Ostwald ripening in an open system or second independent growth (SIG) [9]. *This situation occurs, for instance, during the implantation and/or the ion-beam mixing processes, where solute monomers are continually injected into the system, cf.* Sect. 4.3 In an open system the kinetic laws are the same as for the particles evolving under mass conservation. However, the scaling law for the number of

particles is different and depends on the absorption mechanism [10]. In the diffusion-limited regime, the particle size and number evolve as:

$$n(t) = \propto t^{0.33} \tag{4.18}$$

$$R(t) = const \tag{4.19}$$

On the other hand, if the monomer absorption is limited by the surface reaction, they evolve as:

$$n(t) = \propto t^{0.5} \tag{4.20}$$

$$R(t) \propto t^{-0.5} \tag{4.21}$$

4.2.3 Driven System

So far we have seen that a supersaturated solid solution is metastable. The restoration of the equilibrium state is associated to the minimization of its Gibbs free energy and it is accompanied by the nucleation, growth and coarsening of the embedded NPs. The pathway followed by the system toward a stable phase depends on the transformation rate and it is described by the laws of kinetics.

The situation is completely different when the system is subjected to a sustained irradiation. Here, the main effect is the continuous production of damage within the irradiated material. This damage can be either in the form of elementary processes, such as the formation of point defects or ballistic displacements, or in the form of collective processes, such as displacement cascades or the formation of latent tracks. These dynamic effects force the system to explore configurations that are non accessible by merely thermodynamic or kinetic processes. A system evolving under the effects of both ballistic (destructive) and thermal (restoring) processes is defined as a *driven system*—see for instance [5] and references therein. As ballistic and thermal processes occur in parallel, either in synergy or in competition, the system evolves within a phase diagram that can be different from the equilibrium one. By analogy with the latter it has been named *dynamical phase diagram*. Within a dynamical phase diagram, the equilibrium is called a *steady-state* and it is reached when thermal and ballistic fluxes compensate one another, i.e. they attain a stationary condition. It is worth noticing that equilibrium and steady-state conditions are generally different.

As a general rule of thumb, the evolution of a driven system can be rationalized using the temperature as key parameter. In this case, two regimes can be distinguished:

- at high temperature, thermal effects dominate over ballistic ones and the system evolves toward a thermodynamic equilibrium, i.e. the classical Ostwald ripening.

- at low temperature, ballistic effects dominate over thermal ones and the system evolves either toward a complete dissolution or toward a steady-state.

Historically, probably the first experimental observation of the role played by the irradiation in modifying the thermodynamic phase diagram is the dissolution and stabilization of Ni_3Al precipitates in a Ni–Al alloy irradiated at 550 °C with 100 keV Ni ions [11]. Precipitates of 5 nm in diameter formed prior to the irradiation by heat treatment were reduced to 2 nm after irradiation. Clearly, this dynamic stabilization of the precipitates toward a finite size represents a non-equilibrium process, where smaller particles are more stable than larger ones. Again, by analogy with the Ostwald ripening regime, where lager nanoparticles are more stable than smaller ones, the latter has been named *inverse coarsening* or *inverse Ostwald ripening*. Recently the same behavior has been reported in metal-dielectric nanocomposites, indicating that this phenomenon is not limited to only driven-alloys but it has a more general validity [12]. This will be discussed in more detail in Sect. 4.3.4.

4.2.3.1 An Overview on the Existing Models for a Driven System

The evolution of a driven system has been mainly studied for materials evolving in extreme environments, such as high temperature, irradiation, or severe plastic deformation, and the fundamental question on how to predict their evolution toward a steady-state occupied researchers for decades, see for instance [5] and references therein. The models developed so far can be classified into two main categories: (i) unidirectional ballistic mixing models and (ii) full account of forced mixing models. These will be briefly described hereafter.

- **Unidirectional ballistic mixing**

The first category is associated with the so called *unidirectional ballistic mixing models* [11, 13, 14, 15, 16, 17]. Here, the irradiation-induced atomic relocation is restricted to the displacement of solute atoms from the precipitate to the matrix. This is, the ballistic relocation of the solute atoms from the matrix into the particle in not taken into account. These models are based on the solution of a diffusion equation with a ballistic *source term*, G(r), where the coarsening effects are included into the boundary conditions:

$$\frac{\partial c(r)}{\partial t} = D\nabla c(r) + G(r) \tag{4.22}$$

where D is the solute diffusion coefficient.

The solution of (4.22) necessitates the correct estimation of the source term, G(r), which in turn requires the evaluation of both of the relocation distance and the spatial profile of the displaced atoms. For a sake of clarity, this is sketched in

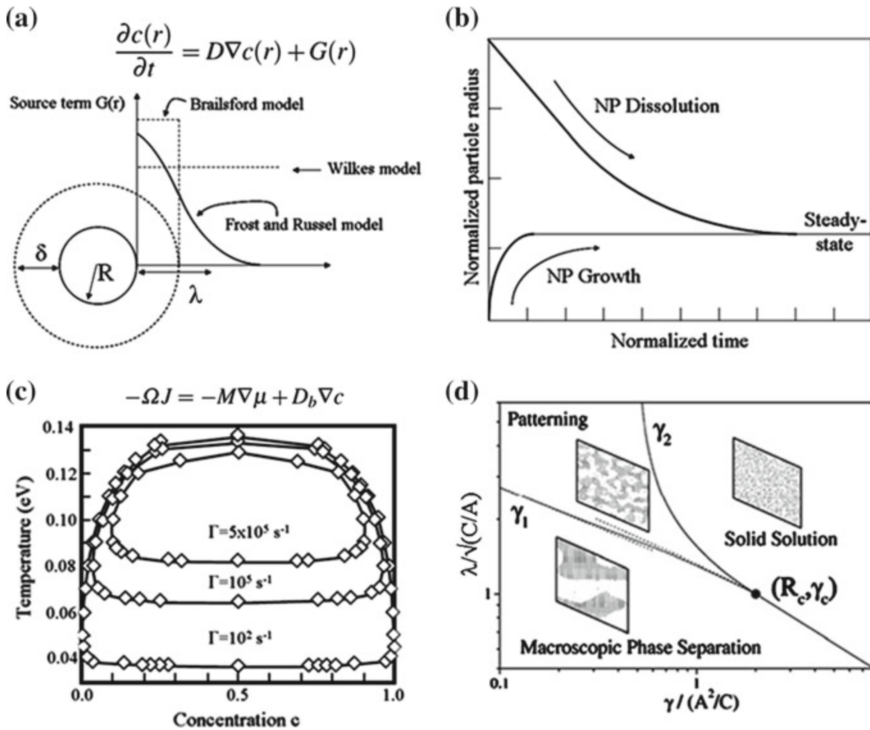

Fig. 4.5 Models for a driven system. Unidirectional mixing models: **a** Source terms, G(r), according to various models, describing the profile of the solute atoms ballistically displaced from the precipitate into the host matrix, and **b** size evolution of a nanoparticle submitted to a sustained irradiation given by the Frost and Russell's model [15, 16]. Full account of forced mixing models: **c** Dynamic phase diagrams obtained for several values of the displacement rates, Γ, calculated using the Martin's effective temperature criterion. Reproduced with permission from [18]. Copyright 1999 American Physical Society. **d** The steady-state dynamic phase diagram calculated using the Bellon's model for a A-B alloy under irradiation with ballistic exchanges as a function of the reduced rate of ballistic mixing, γ, and the average relocation distance, λ. Typical steady-state microstructures obtained in kinetic Monte Carlo simulations are shown in the inset. Reproduced with permission from [19]. Copyright 2000 American Physical Society

Fig. 4.5a. In early models [11, 13], the source term was simply set to be proportional to the displacement rate, Γ (dpa s^{-1})), and the relocation distance taken infinitely large. A first development is due to Brailsford [14] who introduced a finite relocation distance and assumed the inter-particle distance sufficiently large such that the ballistic effects at one particle are unaffected by other particles. Moreover, the model states that atomic displacements occur at a uniform rate in a shell of thickness δ around a particle of radius R. However, the main improvement is due to

Frost and Russell (FR) [15, 16]. Assuming that all recoils are randomly displaced at the same constant distance, λ, they described the source term as:

$$G(r) = \frac{S}{4r\lambda}\left[R^2 - (r-\lambda)^2\right], \tag{4.23}$$

where S is the constant recoil generation rate, r the distance from the particle center and R the particle radius. Besides, they introduced the concept of *critical flux* to describe the transition from classical-to-inverse Ostwald ripening, and derived an equation describing the dissolution rate of the irradiated nanoparticles. The numerical solution of Fig. 4.5b shows that the nanoparticle is partially dissolved if its initial size is larger than the steady-state size. Otherwise, its growth will be observed. The FR model has been implemented by Heinig and Strobel (HS) using a better description of the source term [17]. The solubility under irradiation, $C^I(R)$, is obtained by solving (4.22) and its linearized solution reads:

$$C^I(R) = C^I_\infty\left(1 + L^I_c/R\right) \tag{4.24}$$

where C^I_∞ is the solubility under irradiation for a flat interface, L^I_c (the key parameter of the model) is the capillarity length under irradiation and R the NP radius. Depending on the sign of L^I_c the existence of two regimes is predicted: (i) Ostwald Ripening (OR) regime when $L^I_c > 0$ and (ii) a coarsening resistent regime when $L^I_c < 0$. The latter regime is supposed to take place without precipitation. Finally, kinetic Monte Carlo (KMC) simulations predict the existence of a second coarsening resistant regime where the precipitation process is allowed [20]. This has been named *precipitation and inverse Ostwald ripening* (*PRIOR*).

- **Full account of forced mixing**

In full account of forced mixing models, the ballistic transport of solute atoms is explicitly calculated not only from the precipitate to the matrix, but also from the matrix toward the precipitate. This approach was first developed by Martin by introducing the ballistic mixing as an additional diffusion term into a flux equation [21–23]:

$$-\Omega J = -M\nabla\mu + D_b\nabla_c \tag{4.25}$$

where Ω is the atomic volume, M is the mobility, μ is the chemical potential of the diffusing species, D_b is the diffusion coefficient and c the solute concentration. This approach neglects both medium- and long-range relocation distances, and assumes that ballistic exchanges are random and take place only between nearest neighbor atoms, i.e. $D_b = \Gamma a^2/6$, where Γ is the displacement rate and a the nearest neighbor distance. The main result of the model is the definition of a criterion describing the stability of a driven system, i.e. the *effective temperature* criterion [22]. It states that

the steady-state dynamical phase diagram under irradiation is precisely the same as in absence of irradiation, but at an effectively higher temperature, T_{eff}:

$$T_{eff} = T\left(1 + \frac{D_b}{D'_{th}}\right) \tag{4.26}$$

where D_b is the ballistic diffusion coefficient and D'_{th} is the radiation-enhanced diffusion coefficient. As an illustration, Fig. 4.5c shows steady-state dynamical phase diagrams for three values of Γ with nearest-neighbor mixing a, calculated using kinetic Monte Carlo simulations. At low temperatures, increasing the value of Γ from $10^2\ s^{-1}$ to $5 \times 10^5\ s^{-1}$ shrinks the coexistence region—cf. Fig. 4.2. Thus, the system becomes a solid solution. At high temperatures, the dynamic phase diagram approaches the thermodynamic one. Similar to the FR's model [15, 16], Martin's model predicts the existence of a critical flux. In particular, above this threshold flux the dissolution of the precipitates must occur.

The main limitation of Martin's model relies on the fact that irradiation processes operating at different length scales—larger than the nearest neighbor distance—are not taken into account. For instance, within a displacement cascade the average relocation distance can range between 0.1 nm up to 1 nm where the cascade itself can range between 1 up to 10 nm. Recent developments in this direction are due to Bellon and collaborators [19, 24, 25, 26, 27]. They show that a driven system evolving under processes competing at different length scales has the tendency to create compositional patterning if the average relocation distance is larger than a critical distance, Fig. 4.5c or chemical patterning if the average size for a cascade is larger than a critical dimension.

4.3 On the Strategies to Synthesize Nanostructures Using Ion-Beams: The Case of Metal-Glass Nanocomposites

As almost all materials can be doped or irradiated, these approaches are routinely used to fabricate nanocomposite materials [28]. It is thus nearly impossible, and beyond the scope of this short review, to give an exhaustive description of all the ion-beam techniques applied to all possible materials. Besides, in literature several excellent review articles and book chapters already exist describing the potential applications of these nanocomposites—see for example [29, 28, 30, 31, 32, 33, 34]. In our opinion, what is lacking is an attempt to rationalize, if not all, at least the main strategies to synthesize nanocomposites using ion-beams. Thus, in the following these are classified and rationalized into a unique and possible coherent framework. With this objective in mind, these strategies can be divided in two main categories as schematically represented in Fig. 4.6. The first one consists in using the ion-beam to introduce a foreign species into a host matrix, Fig. 4.6a, b. This is

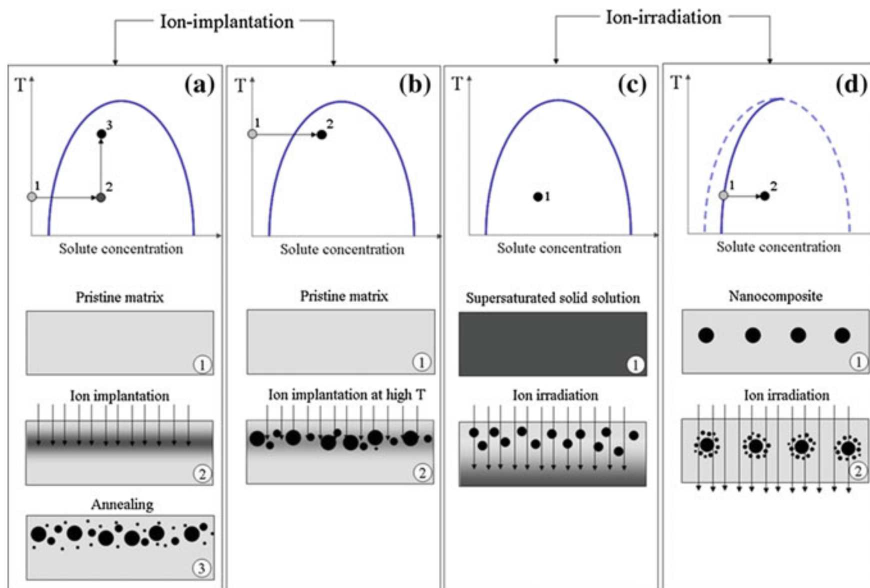

Fig. 4.6 The strategies to fabricated nanocomposites using ion-beams can be divided in two main categories: **a**, **b** the ion-beam is used as a way to introduce a foreign species into an host matrix. This is the domain of the ion-implantation, or **c**, **d** the ion-beam is used to assist the nucleation and growth of the nanoparticles promoting the solute diffusion and relocation within the host matrix. This is the domain of the ion-irradiation

the field of the ion implantation. Depending on the solute mobility, the ion-implantation process can be further divided into two sub-categories:

- If the implantation is done at sufficiently low temperature, such that the solute mobility is low or negligible, a post-implantation thermal treatment is necessary to induce the precipitation. This two steps process is named *ion-beam synthesis*, Fig. 4.6a.
- If the implantation is done at sufficiently high temperature, such that solute atoms can diffuse within the host matrix, the precipitation occurs during the implantation stage. In this case the process is named *ion-beam direct synthesis*, Fig. 4.6b.

In the second strategy the ion-beam is used to assist/favor the nucleation and growth of the NPs promoting the solute diffusion and relocation within the host matrix, Fig. 4.6c, d. This is the field of the *ion-irradiation*. Here, charged particles are used to depose their energy—both through elastic and inelastic processes—into the matrix, whereas they are stopped far inside the matrix substrate and do not directly contribute to the precipitation process. Depending on the configuration of the sample, the irradiation process can be further divided into two sub-categories:

- the pristine sample only contains solute atoms dispersed within the matrix but not precipitate NPs, Fig. 4.6c.
- the pristine sample already contains either thin films or NPs embedded within the matrix but a low or negligible concentration of solute atoms, Fig. 4.6d.

In this chapter, we have decided to focus only on metal-glass nanocomposites with a particular attention to the case of noble metal NPs embedded within a silica matrix. In particular, our description will be limited to the basic physico-chemical processes associated with the nucleation and growth of NPs taking place during the implantation and irradiation steps. Finally, for argument's sake, only a couple of experimental results will be reported for each topic.

4.3.1 Ion Implantation

During the implantation process a foreign element *A* is forced into a host matrix *B* in a region close to the sample surface. This is schematically represented in Fig. 4.6a, b. Here, the solute concentration is increased from zero (point 1) to a given value above the solubility limit (1 → 2). Depending on the temperature, and thus on the atomic mobility, the evolution of the solute toward the nucleation and growth of NPs occurs either during a post-implantation heat treatment (2 → 3) (Fig. 4.6a) or directly during the implantation process (Fig. 4.6b). It is worth noticing that as the overall process occurs during the continuous monomer supply, the mass is not conserved and the system can be considered an open system as described in Sect. 4.2.2.

The probability that the precipitation process takes place depends on the competition between the deposition rate and the atomic mobility. Indeed, if the injection of solute monomers increases the supersaturation level, its diffusion toward the existing sinks, e.g. free surfaces, defective regions or nucleating nanoparticle, reduces the amount of available monomers. In particular, near the absorbing sinks the solute concentration is generally low and the precipitation is highly unlike.

For a given ion-substrate system, the primary nucleation stage can be roughly rationalized by comparing the diffusion length of the implanted impurities, L_{Diff}, to the nucleation volume, $V_{nucleation}$. L_{Diff} is related to the diffusion coefficient of the solute atoms, i.e. $L_{Diff} \propto (Dt)^{0.5}$, whereas the nucleation volume represents the minimum portion of solid containing sufficient solute atoms to form a stable embryo, i.e. a sphere of radius $R_{nucleation}$. Thus, the following phenomenological characterization has been proposed [20]:

- $L_{Diff} \ll R_{nucleation}$. The mobility of the implanted monomers is so small such that the formed embryos cannot reach the critical size. Thus, they are unstable upon thermal fluctuation or ballistic events and their growth is not favored. In this case, implanted monomers remain in solution even for high implantation fluences.

- $L_{Diff} \geq R_{nucleation}$. Here the mobility of the implanted monomers is sufficient to create stable embryos. Owing to the implantation fluence, the precipitation can occur either at low temperature, for large enough implantation fluences, or directly at higher temperature, at a lower fluence. Due to the Gaussian-like implantation profile, the largest supersaturation is reached at the implantation depth, R_p. As the critical size for stable embryos scales as the inverse of the supersaturation, e.g. $R^* \propto 1/\ln(s)$, the first stable nanoparticles will appear close to R_p.
- $L_{Diff} \gg R_{nucleation}$. During high temperature experiments, the nucleation and growth of stable embryos take place directly during the implantation stage. The precipitation of the nanoparticles starts close to R_p, i.e. at the highest concentration of implanted impurities. However, due to large solute mobility, these processes are biased by the diffusional effects associated to both the presence of an ion-damaged region and the free surfaces.

4.3.1.1 Key Parameters in Ion-Implantation Experiments

When setting up an actual ion implantation experiment, after choosing the species to be implanted and the host matrix, the most important parameters to be optimized are:

- ion energy (E)
- ion fluence (N_I)
- ion flux (j)
- implantation temperature (T).

The influence of these parameters on the final nanocomposite is described hereafter.

(a) **Ion Energy**

The ion energy determines the penetration depth of the implanted impurities into the host matrix. Typical values range from few keV up to several MeV, corresponding to implantation depths ranging from few dozen of nanometers up to few microns. Owing to the stochastic interaction processes taking place between the impinging ion and the target atoms, the implanted impurities are statistically dist ributed over an average implantation depth. The latter can be roughly approximated by a Gaussian function centered at an average projected range R_p and defined by a straggling ΔRp. Implantation profiles are usually simulated using the SRIM code [35, 36], Fig. 4.7.

In general, the higher the ion energy, the deeper the implantation depth. However, as the energy straggling increases with the implantation depth, the deeper the implantation depth, the broader the final depth distribution of the implanted species. This is detrimental if the final objective is to obtain a nanocomposite containing nanoparticles with a narrow size dispersion. Figure 4.7e shows the

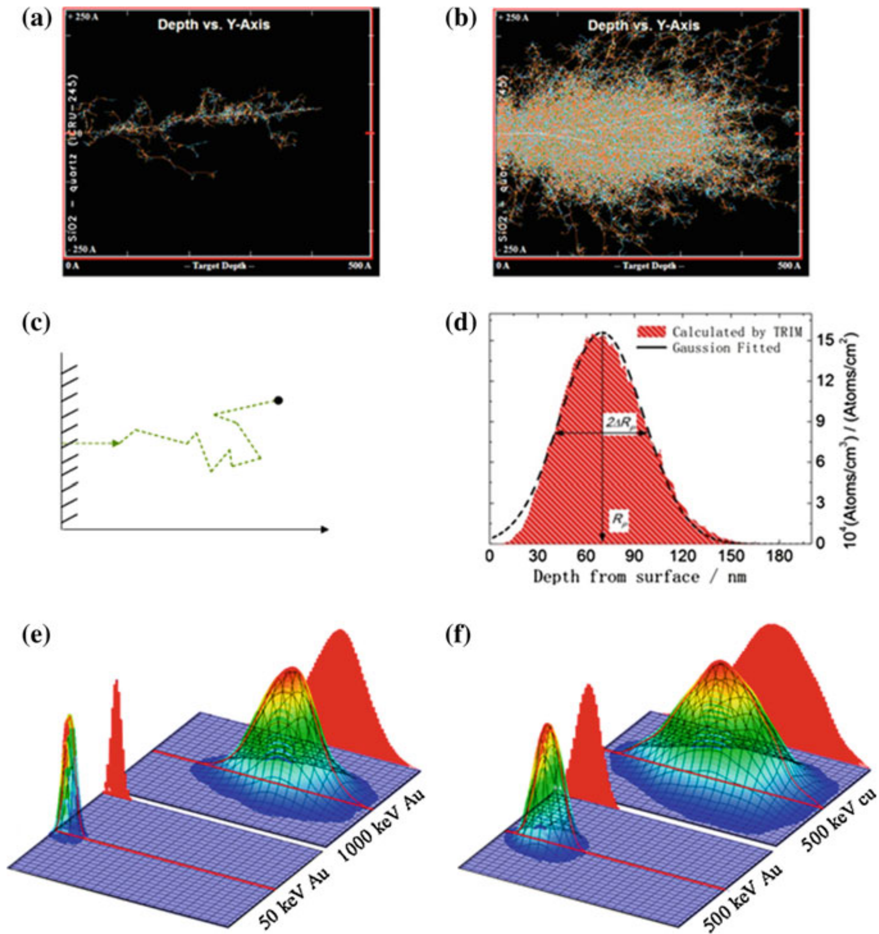

Fig. 4.7 SRIM simulations showing the implantation of **a** a single Au ion and **b** of 10^4 Au ions into a SiO_2 matrix. The initial energy of the impinging Au ions is E = 4 MeV. **c** Snapshot representing the path followed by a single Au ion. **d** Owing to the stochastic ion-matter interactions, the implantation profile has a Gaussian-like shaped centered at the implantation depth, R_p, and characterized by the implantation width, or straggling, ΔR_p. SRIM simulations indicate that R_p and ΔR_p depend on both the atomic number of the projectile and its energy: **e** implantation profile for 10^4 Au ions implanted into a silica matrix at different energies (50 and 1000 keV) and for **f** two different ions (Au and Cu) having the same initial energy (500 keV)

spatial distribution of Au ions implanted into a silica matrix at two different energies: 50 and 1000 keV. In Fig. 4.7f the implantation profiles are compared for two different ions (Au and Cu) at the same initial energy of 500 keV. These plots clearly show that the implanted profile becomes broader when the ion energy is increased and/or the ion mass reduced.

(b) **Ion fluence**

The ion fluence, N_I, is related to the amount of solute monomers that is injected into the host matrix. It is measured in ions cm^{-2}, or cm^{-2}, and represents the integral over the implantation profile. In typical implantation experiments, the ion fluence ranges from few 10^{14} cm^{-2} up to several 10^{17} cm^{-2}. The implantation fluence defines to what extent the matrix is modified by the foreign species such that three main domains can be defined [20]:

(i) For fluences $N_I < 10^{14}$ cm^{-2} the implanted ions are assumed to remain isolated within the substrate. This is the domain of the doping of materials. For example, when implanted into a crystalline matrix these impurities may reside on regular lattice sites and change the physico-chemical properties of the host material, Fig. 4.8a.
(ii) For fluences in the range 10^{14}–10^{16} cm^{-2}, the deposited impurities start to exceed the solubility limit and the formation of new phases takes place within the host matrix, Fig. 4.8b. When the implantation is performed at low temperature and in a crystalline material the amorphization of the sample can be observed.
(iii) For fluences larger than 10^{17} cm^{-2} precipitates start to coalesce, which might result in the formation of a continuous layer below the sample surface at the implantation depth, Fig. 4.8c.

(c) **Ion flux**

Ion flux or current density, Φ, characterizes the implantation time, e.g. $t = N_I/\Phi$. It is defined as the number of ions introduced into the host matrix per unit time and unit surface area of the target. It is measured in μA cm^{-2} or in ions cm^{-2} s^{-1}. The larger the ion flux, the shorter the implantation time. Whenever charge states larger than one are considered the use of the *power density* is more appropriate, e.g. it is expressed in W cm^{-2}.

Ion flux affects the time rate at which the energy is transferred to the target and in turn the sample heating. Thus, the ion flux controls both the mobility of the solute atoms and the stability of the irradiation-induced defects, cf. Sect. 4.5.2. The determination of the irradiation flux is often a subtle compromise between the

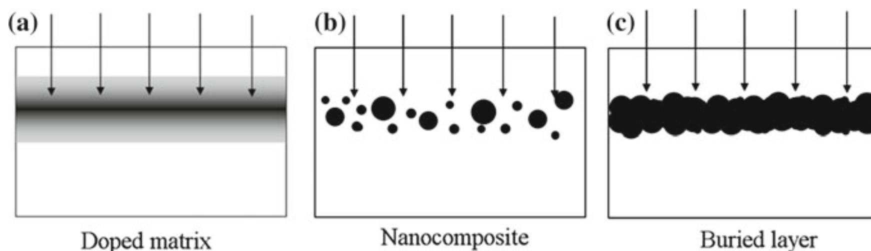

Fig. 4.8 Depending on the fluence, N_I, the implanted materials can be roughly grouped into three main categories: **a** doped materials, **b** nanocomposites and **c** materials containing a continuous buried layer

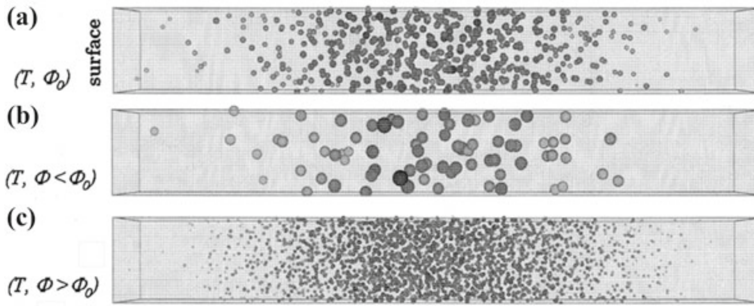

Fig. 4.9 3D lattice Monte Carlo simulations showing the effect of the ion flux on the precipitation process. **a** Implantation at temperature T and flux Φ_0. **b**, **c** the temperature is kept constant while the ion flux is changed. **b** Decreasing the ion flux ($\Phi<\Phi_0$) results in the formation of smaller number of larger precipitates. **c** Increasing of the ion flux ($\Phi>\Phi_0$) results in the formation of a larger number of smaller precipitates. Reproduced with permission from [37]

reduction of the irradiation time and the minimization of detrimental effects associated to it. In general, the ion flux should not exceed 20–25 μA cm^{-2}. However, when dealing with insulating targets typical fluxes used in high fluence implantations are 0.1–10 μA cm^{-2}, taking into account that above 2–5 μA cm^{-2} thermal heating in the insulator should be considered. Correspondingly, to avoid heating effects, a power density lower than about 1 W cm^{-2} should be used.

The effect of the ion flux has been studied by Strobel et al. [37] using 3D lattice Monte Carlo simulations, Fig. 4.9. The initial configuration is shown in Fig. 4.9a where simulations have been performed at temperature, T, and ion flux, Φ_0. In a second step, injection rate is changed while the temperature is kept constant at T, Fig. 4.9a, c. When the ion flux is reduced ($\Phi<\Phi_0$) the supersaturation level is maintained low as the existing precipitates act as sinks for the diffusing solute. Thus, the nucleation of new precipitates becomes unlikely, whereas the growth of the existing NPs is favored. In this case, the formation of larger NPs with a lower density is observed, Fig. 4.9b. When the deposition rate is increased ($\Phi>\Phi_0$), the reduction of the solute concentration around each NP is compensated by the massive arrival of new monomers. In this case, the nucleation and growth of new precipitates is favored. This results in the formation of a larger number of smaller precipitates, Fig. 4.9c.

(d) **Temperature**

Temperature controls the atomic mobility of the implanted monomers as well as the stability of the irradiation-induced defects, cf. Sect. 4.5.2. Thus, it controls the evolution of the solid solution toward the nucleation and growth of the precipitates, cf. Sect. 4.2.2.

Low temperature implantations

At low temperature, e.g. at cryogen temperature, the implanted species are nearly immobile and the irradiation defects can be frozen in. Under these conditions, the

implantation stage can be completed avoiding the nucleation of NPs. However, if the host matrix is crystalline, sufficiently large implantation fluence may result in its amorphisation.

High temperature implantation

At sufficiently high temperature implanted monomers are mobile and the recovery of the defects is favored. In this case NPs can directly nucleate and grow during the implantation stage. For insulating matrices the implantation at high temperature can range from 400 to 900 °C.

The influence of the implantation temperature is shown in Fig. 4.10 [37]. In this experiment, a silica matrix is implanted with 2.75 MeV Au ions at a fluence of 1.5×10^{17} cm^{-2} under a constant ion flux of 1 μA cm^{-2}. Implants have been done at increasing temperatures: 30, 400 and 600 °C. At room temperature, as the dopant concentration overcomes the nucleation threshold, precipitation occurs directly during the implantation stage, Fig. 4.10a. As the atomic mobility is low, the supersaturation is locally high. Thus, following the discussion of Sect. 4.2.2 critical energy, ΔG^*, and critical radius, R^*, are low and the explosive precipitation of a large number of small NPs is favored, Fig. 4.6d. When the temperature is increased two competing effects are active. This is shown in Fig. 4.10b, c. On one hand, increasing the temperature reduces both ΔG^*, and R^*. This enhances the nucleation probability. On the other hand, increasing the temperature enhances the solute mobility. As solute atoms diffuse faster, the supersaturation, s(t), is reduced. This decreases the probability for stable embryos to be formed. Otherwise stated, a larger nucleation volume is necessary for the nucleation and growth of a stable second

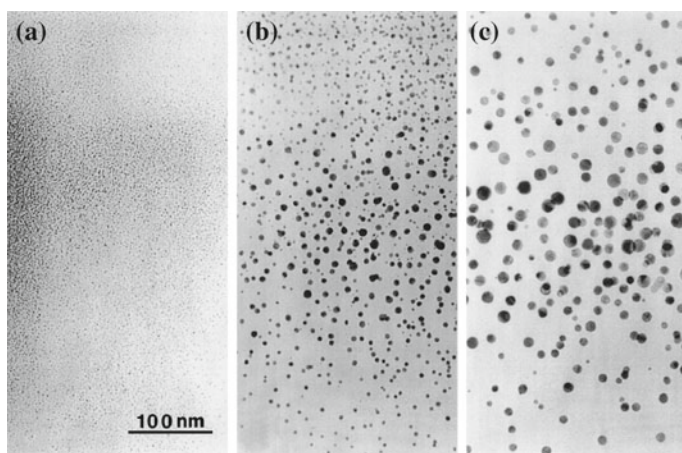

Fig. 4.10 Cross-section TEM micrographs of 2.75 MeV Au implantation into fused silica for a fluence of 1.5×10^{17} cm^{-2}. The implantation temperatures are **a** 30 °C, **b** 400 °C, and **c** 600 °C. Reproduced with permission from [37]

phase. The outcome is the formation of larger NPs but with a reduced density. Finally, this effect is enhanced when the temperature is increased.

4.3.1.2 Ion-Beam Synthesis

When a thermal treatment is applied after the implantation stage the mass is conserved (close system) and the overall process is a two step process commonly named as *ion-beam synthesis*. There are two main reasons for the post-implantation thermal treatment to be performed. The first one is that implant creates defects within the silica matrix which are detrimental for the properties of the nanocomposite, cf. Sect. 4.5.2.3. Thus, their recovery is essential. For instance, in silica E′ defects start to recover from about 500 °C, whereas B_2 centers above 900 °C [38]. The second reason is that thermal treatment triggers the diffusion-driven nucleation, growth and ripening of the NPs. As the annealing stage is a kinetic process, the evolution of the supersaturated solid solution follows the classical nucleation-growth-ripening process as exemplified in Sect. 4.2.2.

4.3.1.3 Annealing Treatment

Thermal treatments can be divided into two sub-categories: *isochronal and isothermal*:

- During an *isochronal annealing*, the time is fixed and the temperature is varied.
- During an *isothermal annealing*, the temperature is fixed and the annealing time is varied.

During an annealing treatment, the annealing atmosphere must be chosen to control the chemical reactivity of the implanted species. Three possible atmospheres can be used: reducing, inert and oxidizing:

- *Reducing atmosphere*. In this case oxidation of the sample is avoided by removal of oxygen and other oxidizing gases or vapor. This is for example the case of annealing in H_2–Ar atmosphere.
- *Inert atmosphere*. An inert gas is a gas which does not undergo chemical reactions under a set of given conditions. The noble gases like argon (Ar) and nitrogen (N) often do not react with many substances.
- *Oxidizing atmosphere*. This is a gaseous atmosphere in which oxidation reactions are favored. This is for example the case for annealing in air atmosphere.

(a) Isothermal annealing in oxidizing atmosphere

Figures 4.11a–d show the result of an *isothermal* post-implantation annealing treatment in an oxidizing atmosphere [30]. First, fused silica was implanted at room

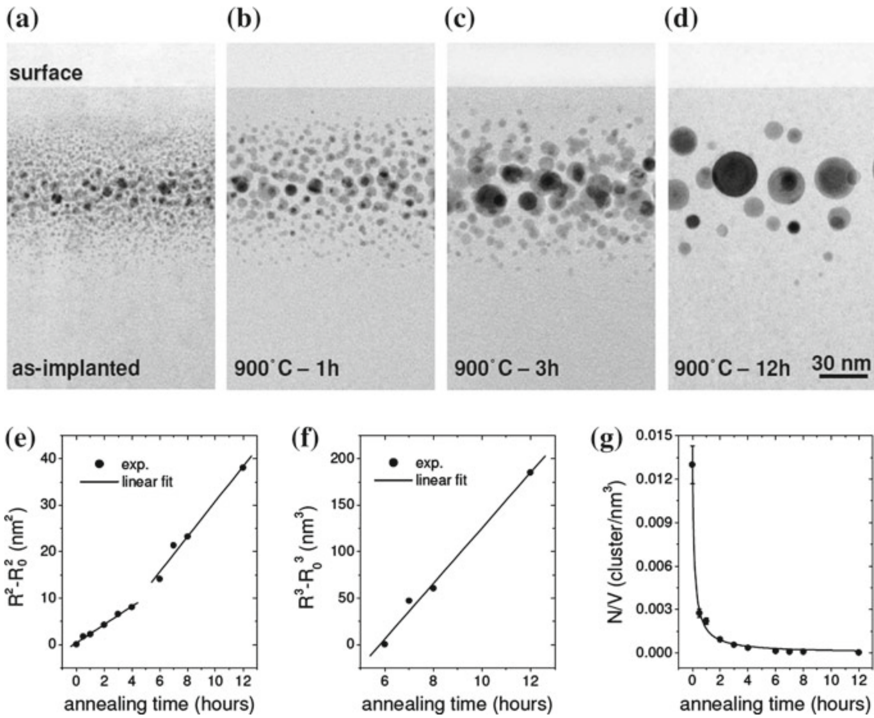

Fig. 4.11 Isothermal annealing in oxidizing atmosphere. **a** as implanted sample (90 keV Au ions in silica at a fluence of 4×10^{16} cm^{-2}). **b–d** annealing in air at 900 °C for different time intervals. Time evolution of **e** $R^2 - R_0^2$ and **f** $R_3 - R_0^3$, where R_0 is the initial cluster radius and R its mean value at time t. **g** Time evolution of the nanoparticle density. Reproduced with permission from [39]

temperature with 190 keV Au ions at a fluence of 4×10^{16} cm^{-2}, Fig. 4.11a. Here, the precipitation already occurs during the implantation step as the dopant concentration at the implantation peak is above the nucleation threshold (about 1 %). In a second step, the sample was annealed in air at 900 °C for increasing time up to 12 h, Fig. 4.11b–d. The temperature was chosen to be above the recovering temperature of the implantation defects [38]. This experiment proves the occurrence of a transition from a diffusion-limited growth regime to an Ostwald ripening regime, Fig. 4.11e–g. Indeed, at the beginning of the thermal treatment, NPs grow as $R \sim t^{0.5}$. In this regime, the supersaturation is sufficiently elevated such that the growth of all the NPs is favored. However, for annealing times longer than 6 h, the time-dependence of the scaling law changes to $R \sim t^{0.33}$ while NPs density is observed to decrease. As the available solute is continuously consumed by the growing NPs, the supersaturation level is progressively reduced. When it becomes sufficiently low, the system minimizes its energy through a mass redistribution. In this coarsening regime, the growth of larger nanoparticles is favored at the expense of the smaller ones. Besides, an accurate exploitation of the kinetic laws allows both

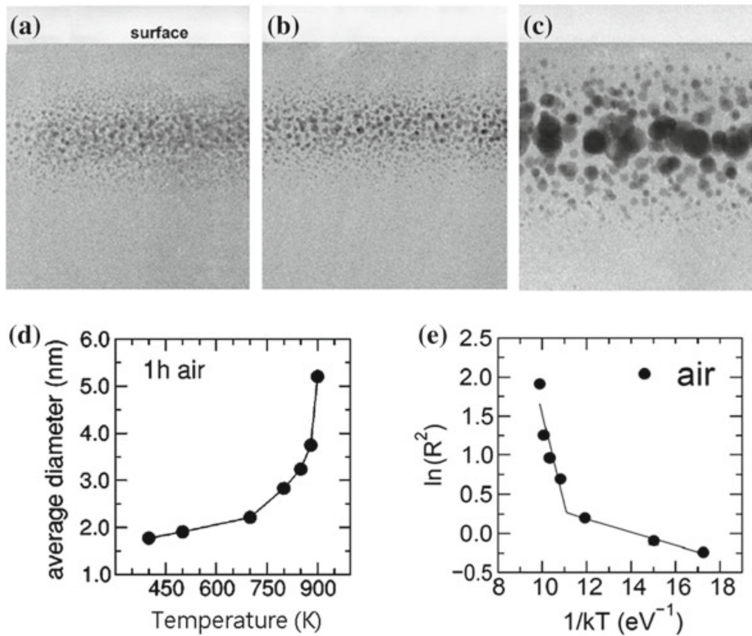

Fig. 4.12 Isochronal annealing in oxidizing atmosphere. **a**–**c** Cross-sectional bright field TEM micrographs of a silica matrix implanted with Au ions at 3 × 10^{16} cm^{-2} and after 1 h annealing in air at **a** 400 °C, **b** 700 °C, and **c** 900 °C. Evolution with the annealing temperature of **d** the mean cluster diameter and **e** Arrhenius plot of the squared mean cluster radius. Reproduced with permission from [40]. Copyright 2001 American Physical Society

the diffusion coefficient of gold (D ~ 2 × 10^{-17} cm^2 s^{-1}) and the surface tension of the embedded NPs (σ ~ 4 × 10^{-4} J cm^{-2}) to be estimated.

(b) **Isochronal annealing in oxidizing atmosphere**

Figure 4.12 shows the result of an *isochronal* post-implantation annealing treatment in oxidizing atmosphere [40]. Fused silica is first implanted at room temperature with 190 keV Au ions at a fluence of 4 × 10^{16} cm^{-2}. Second, the annealing time is fixed to one hour, whereas the temperature is increased from 30 °C up to 900 °C, Fig. 4.12a–c. The evolution of the NP size with the temperature is shown in Fig. 4.12d. However, much more information is obtained if an Arrhenius-like plot is drawn. In this case, the square of the NP radius is represented as a function of the inverse of the temperature, Fig. 4.12e. The very slow variation of the nanoparticle size for temperatures lower than about 800 °C suggests a diffusion mechanism driven by the irradiation defects, e.g. the E′ centers. Besides, the abrupt change observed at about 800 °C indicates that a change of the regime has occurred. Finally, using the Arrhenius plot the activation energy for gold diffusion in silica is estimated to be 1.17 eV $atom^{-1}$.

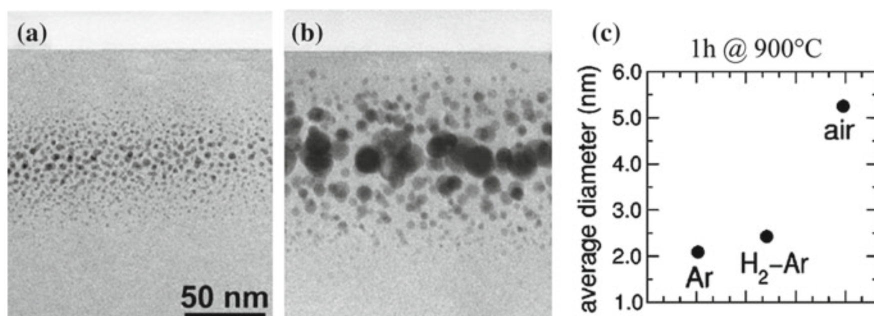

Fig. 4.13 Isochronal annealing in different atmospheres. **a**, **b** Cross-sectional bright field TEM micrographs after 1 h annealing in **a** argon, and **b** air. The silica matrix was implanted with Au ions at a fluence of 3×10^{16} cm^{-2}. **c** Mean cluster diameter after 1 h annealing in different atmospheres. Reproduced with permission from [40]. Copyright 2001 American Physical Society

(c) **Isochronal annealing in different atmospheres**

The third example concerns a set of isochronal annealing experiments in different atmospheres [40]. First, fused silica is implanted at room temperature with 190 keV Au ions at a fluence of 4×10^{16} cm^{-2}. Second, isochronal annealing (1 h) is done in oxidizing (air), inert (Ar) and reducing (H_2–Ar) atmospheres, Fig. 4.13a, b. The sample annealed in air exhibits a much larger NP size and a broader size dispersion than samples annealed in Ar and H_2–Ar atmospheres, Fig. 4.13c. Thus, annealing in air is more effective in promoting cluster aggregation. This is ascribed to diffusion of the gold monomers interacting with excess of oxygen coming from the external ambient.

4.3.1.4 Ion-Solid Chemistry

Ion implantation is not solely driven by irradiation and temperature processes. Indeed, also chemical reactivity and charge state of the implanted monomers play a relevant role in establishing the pathway followed by the solid solution toward the precipitation of a second phase. Although the overall mechanism explaining the role of the chemistry during the implantation process is still lacking, some models, or criteria, have been proposed so far.

(a) **Free energy of formation** [41]

The free energy formation criterion has been developed by Hosono [41] and it is based on the fact that in implanted silica mainly oxygen-deficient centers are produced, e.g. Si–Si homobonds and neutral oxygen vacancies. The underlying idea is that there is a competition between implanted monomers and silicon defects to create bonds with oxygen vacancies [41]. When implanted ions (M) form bonds with oxygen, a high concentration of Si–Si bonds is observed. Conversely, if the implanted ions do not react with the oxygen, a low concentration of Si–Si bonds is observed. In this case, the formation of mono-elemental precipitates is favored.

As the probability to precipitate a NP depends on the dominating bonding mechanism, the key parameter is the free energy for the formation of an oxide, ΔG_f. A metallic NP is formed whenever the free energy of formation for the metal-oxide, $\Delta G_f(M_xO_2)$, is larger than that of the silicon-dioxide such that $\Delta G_f(M_xO_2) > \Delta G_f(SiO_2)$. Free energies are estimated considering a fictive implantation temperature of $T \sim 3000$ K. The latter is defined from thermal spike considerations. Although in a first approximation the validity of this criterion is good, it fails in describing the formation of oxides in the case of Cu, W and Cr monomers implanted into silica [42].

(b) **Electronegativity criterion** [43, 44]

A more general approach has been developed by Hosono, Matsunami and Imagawa [43, 44]. They suggest that it is the electronegative nature of the implanted monomer that determines the type of predominant defects created within the silica matrix. Using this criterion, the implanted species can be divided into three groups:

- The elements belonging to the first group are characterized by an electronegativity value larger than 3.5, e.g. fluorine. During the implantation stage, implanted monomers replace oxygen atoms in the substrate structure producing O_2 molecules and peroxy radicals (POR). In this case, the formation of Si–M bonds and the precipitation of silicate NPs is favored.
- The elements belonging to the second group are characterized by an electronegativity value smaller than 2.5, e.g. Ti, Cr, B, C and P. These implants react chemically with the oxygen atoms leaving Si–Si bonds with a concentration comparable to that of the implant. In this case the formation of M–O bonds and thus the precipitation of metal-oxide NPs is favored.
- The last group is formed by the elements presenting a weak or negligible chemical interactions with the matrix, e.g. Au, Ag or Cu. Here, the implantation creates comparable concentrations of the E' center and peroxy radicals. The neutral states of the monomers favor the precipitation of pure metal NPs.

(c) **Two-step approach** [45]

Basing on the works of Kelly [46] on the role played by the chemistry during ion-beam mixing, the model distinguishes two different energy steps in the implantation process [45]. In the first stage, high energy ballistic effects create a damaged region within the host matrix. In a second stage, low energy, chemically guided processes drive the formation of compounds on the basis of thermodynamic considerations. The latter are determined by calculating the Gibbs energy variation for a chemical reaction between the implanted element (in the gaseous form) and the silica molecule at a given temperature. The allowed compound is determined by calculating the value of ΔG for the reaction M(gas) + SiO_2. The more negative this value, the more likely is the formation of the particular compound. The two step model correctly predicts the formation of various compounds, including silicides for Cr, Mn, Pd, Pt and Ti in silica and the formation of metallic NPs at room temperature.

However, it fails in predicting the silicide formation in the case of Fe, Co and Ni. The model is only applicable to stoichiometric silica and calculations are limited by the precise estimation of thermodynamic quantities such as the local temperature and the chemical interactions between the implanted monomer and the substrate compound.

(d) **Redox potential criterion** [47]

The basic idea of this criterion is that in a radiative environment the primary mechanisms driving the precipitation of a NP are similar to those occurring during the conventional photographic process [48]. This is, when a photon is absorbed by an AgBr crystal, electron-hole pairs are produced. They can migrate and eventually be trapped by defect centers or metal ions in different charge states. Thus, it is the charge state that drives the evolution of the metallic species toward clustering or dissolution.

The criterion states that in glasses the formation of NPs requires the medium to be sufficiently reducing to favor the growth over the dissolution. Thus, the standard phase diagram is drawn as a function of temperature, *T*, and redox potential of the host matrix, *Red*. Under irradiation, the precipitation mechanism can be described by adding a third variable: the ion-irradiation deposited energy (DED) [47, 49]. It accounts for the initial charge density (holes and electrons) injected into the glass by irradiation. The DED influences nucleation and growth through primary charges injection and defects creation. A sketch of a T-Red-DED phase diagram is shown in Fig. 4.14. In (T, Red) plane the effects of standard chemical redox (Red) properties

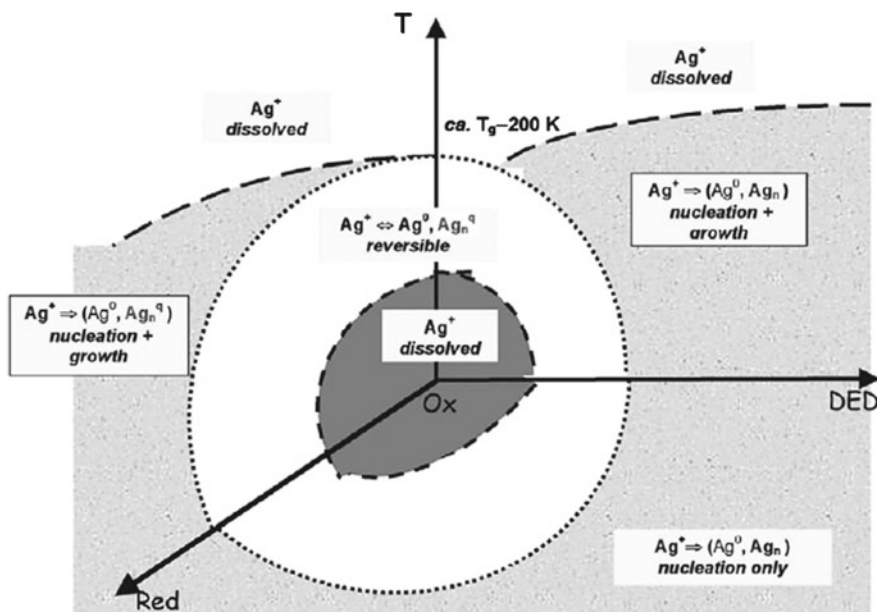

Fig. 4.14 Phase diagram in terms of temperature, *T*, redox potential, *Red*, and ion-irradiation deposited energy, *DED*. Reproduced with permission from [47]. Copyright 2007 American Physical Society

leading to Ag NP clustering in glass are shown. In (T, DED) plane, the effect of the deposited energy density is evidenced. The possibility of combining redox and DED effects creates novel conditions for NPs formation.

4.3.1.5 Single Versus Sequential Implantation

So far we have briefly reported how implantation parameters and ion-matter chemistry influence the nucleation and growth of NPs when only one atomic species is implanted. However, the possibility to form more complex nanostructures can be largely improved if the first implantation stage is followed by a second one. In general, three well distinguished classes of NPs can be obtained:

- isolated monelemental A and B NPs
- A_xB_{1-x} alloys
- A @ B core-shell NPs.

Conversely to single implantation, there is no general criterion for predicting which one of the three classes of NPs will be favored during sequential implantation. Nevertheless, heuristic trial-and-error approach allows to assess some basic rules allowing to drive the solid solution toward one of these three classes.

- To optimize the interaction between the implanted species, the superposition of the implanted profiles must be maximized. This is, the implantation depths of the different atomic species must be nearly the same.
- Implantation order does matter. In general, the result is different if the element A is implanted before or after the element B.
- Relative concentration of the two elements, i.e. the implantation fluence, determines the final composition of the NPs.
- Thermodynamic factors, such as the miscibility between the two implanted species, play a crucial role. The fact that at the nanoscale the rules of thermodynamic are not as rigorous as for bulk materials, leads to the formation of novel phases—see for example [30] and references therein. As a general rule of thumb perfectly miscible elements like noble metals (Au, Ag, Pd, Cu) exhibit a direct alloying during sequential implantation at room temperature. On the contrary, immiscible bulk phases, such as Co–Cu or Au–Fe necessitate a thermal treatment for the alloy to be formed. This effect points out the role of the temperature on the evolution of the implanted species.
- Post-implantation annealing, most of the time in a controlled atmosphere, influences the diffusivity of the implanted species, the evolution of the irradiation-induced defects, and the chemical reactivity of the matrix, see for example [30] and references therein. Thus, their proper combination can be used to tune the stability of the precipitate NPs. Annealing in oxidizing atmosphere is more effective in the alloy decomposition in comparison to an annealing treatment performed in reducing or inert atmospheres.

- A possible protocol to obtain core-shell nanoparticles is as follows: first, the precipitation of the first implanted species is obtained by a post-implantation annealing. Afterward, a second implantation is done at high temperature to favor the diffusion of the implanted species toward the already formed precipitates. Following this idea, Kluth et al. were able to synthesize Au @ Co core-shell nanoparticles [50].
- Finally, kinetic Monte Carlo (KMC) simulations have been used to study the interaction kinetics of the sequentially implanted atom types A and B in a chemically neutral matrix [51]. Since ion implantation is inevitably accompanied by a specific level of collisional mixing, for sequential implantation there is a competition between the coating of the pre-implanted nanoparticles and the random arrangement of A and B impurities. As a rule of thumb core@shell formation is favored if: (i) the solubility of B exceeds the solubility of A in the matrix, (ii) the atomic mass of B is small, i.e. the efficiency of the collisional mixing is reduced, and (iii) the ion flux is low and/or the second implantation temperature is high, which favors a compensation of displacements by thermodynamically driven atomic movements.

4.3.2 Limits and Drawbacks of the Implantation Technique and Some Alternative Approaches

Ion implantation is routinely used to fabricate nanocomposite materials. Probably its main advantage is that almost any foreign species can be forced into almost any host matrix at a concentration that can be larger than the solubility limit. However, these advantages are partially counterbalanced by a certain number of disadvantages. Some of them are mentioned hereafter:

- For practical applications it is important to have the narrowest possible NPs size distribution. However, in ion-implanted systems the latter is generally quite large, e.g. 20–50 %.
- A high temperature thermal processing is necessary either to recover the ion-beam damage or to tune the final NPs size. However, this treatment favors their coarsening (Ostwald ripening) and thus the broadening of the corresponding size distribution.
- The homogeneous spatial distribution of the NPs is restricted to only the first micrometers of the host matrix.
- The control over the lateral distribution of the NPs is generally poor.

Roughly speaking, three factors mainly affect the final size distribution of the NPs, Fig. 4.15:

- The critical size for stable embryos scales as the inverse of the supersaturation, e.g. $R^* \propto 1/\ln(s)$. Thus, precipitation first takes place at the maximum of the

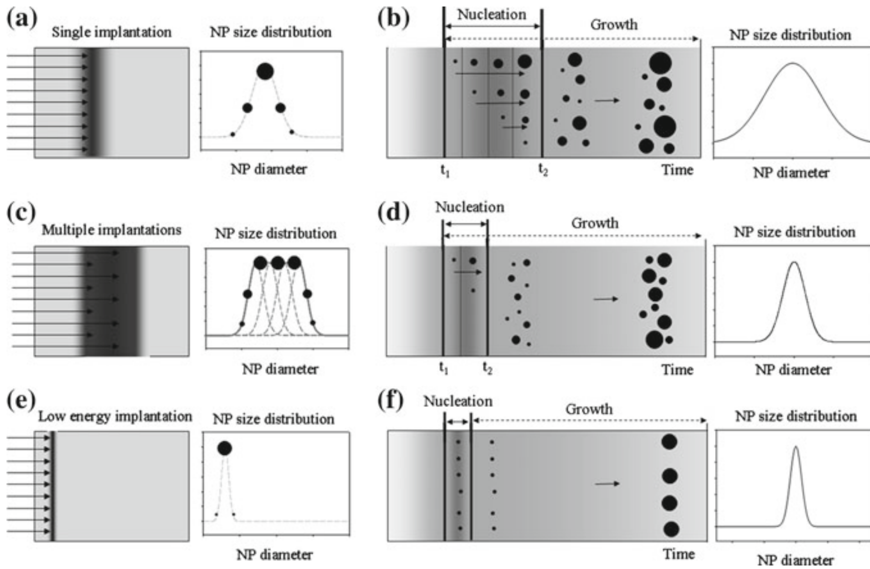

Fig. 4.15 Limits and drawbacks of the ion-beam synthesis: **a** the broader the concentration profile and **b** the longer the nucleation regime, the larger the final size distribution of the precipitates. See also Fig. 4.4. Strategies to obtain a narrow nanoparticle size distribution: **c**, **e** optimization of the implantation profile. **d**, **f** control of the nucleation and growth regimes

implant distribution, i.e. at the implantation depth R_p. Subsequently, the nucleation of new stable embryos develops toward the tails of the distribution. NPs are thus formed across the whole deposition range with a size roughly scaling with the impurity profile, Fig. 4.15a.

- Nucleation and growth regimes are temporally superimposed during the implant, Fig. 4.15b. Thus new NPs nucleate at different times while the exiting ones are growing. The consequence is that at the end of the nucleation regime, i.e. for $s(t) \leq 1$, NPs of different sizes are present.
- Implanted impurities preferentially diffuse toward either free surfaces or defective regions. This may result in the formation of additional layers of NPs either close to the sample surface or at the depth where the amount of defects is maximum [52].

So far, several strategies have been developed to overcome these drawbacks and to reduce the broadening of the NPs size distribution. Depending on the experimental approach these can be divided into two main categories:

- Approaches based on the optimization of the implantation profile, Fig. 4.15c, e.
- Approaches based on the control of the nucleation and growth regimes, Fig. 4.15d, f.

Multiple implantations A commonly employed method to narrow the size distribution is to get a more homogeneous profile for the implanted monomers, e.g. a box-like profile. This can be obtained using multiple implantations at slightly different energies, Fig. 4.15c. Although this approach allows to obtain a *plateau* with an homogeneous concentration of the solid solution, it does not solve the problems associated with the edges of the distribution, where the profile remains Gaussian-like.

Low energy implantation The width of the implantation profile, ΔR_p, roughly scales with the energy of the impinging ion, see e.g. Fig. 4.7e. Thus, implantation at low energy results in a narrower distribution of the implanted solute, Fig. 4.15e. Whenever the nucleation is allowed, this results in the formation of a δ-like size distribution. However, given the vicinity of the sample surface, sputtering effects, and eventually the built-in of an electric field, the final impurity profile is generally different from the theoretical Gaussian distribution. For example for Ag solute this implies that in general larger precipitates are observed close to the implanted glass surface, whereas smaller particles are found below the implant zone [52, 53].

Separation of nucleation and growth regimes The shorter the nucleation regime, the narrower the final particle dispersion, as all the particles nucleate at almost the same time, Fig. 4.15f. Thus, the way one must follow to improve the final particle monodispersity is to separate the nucleation from the growth stages. The underlying idea is schematically shown in Fig. 4.16a. Novel ion-based methodologies operate within this direction.

The objective of the first strategy is to minimize the nucleation window by alternating implantation and annealing steps [54], Fig. 4.16b. First, solute monomers are implanted at room temperature and with a low fluence. This step is followed by a short, high temperature, *spike* annealing to bring nucleation to completion. Subsequently, an additional implantation is done at elevated temperature (lower than the spike anneal temperature). In particular, the annealing temperature must be sufficiently high to efficiently drain the background supersaturation toward the existing NPs but low enough to inhibit nucleation of novel NPs.

A second strategy is to apply a photographic-like process in glasses containing dispersed metal oxides [49], Fig. 4.16c. In this case, the electronic stopping power, S_e, is used to created stable embryos of pure metal. Using this approach the duration of the nucleation window is reduced to the passage of the ion through the matrix. Subsequently, NPs are grown under thermal annealing. This process allows total control over the cluster density, average size, and size distribution.

Laser annealing Long range diffusion associated with thermal annealing can be avoided if pulsed laser annealing is performed. In this case, rapid heating and cooling inhibit mass redistribution associated with the Ostwald ripening process

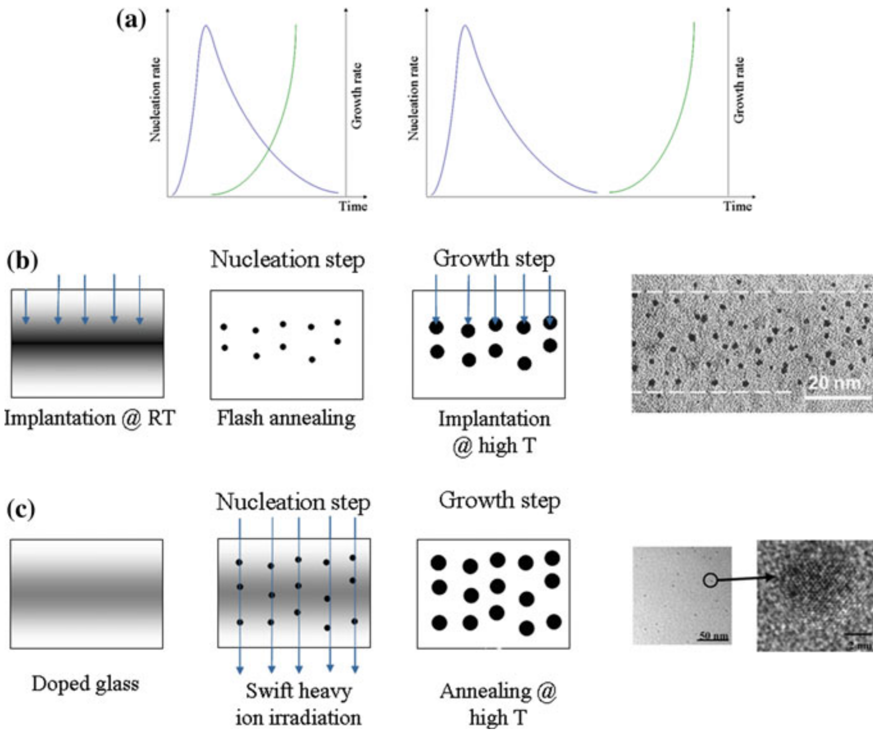

Fig. 4.16 **a** Snapshots showing both the superposition and the separation of the the nucleation and the growth regimes. See also Fig. 4.4. The separation of the two regimes can be obtained either **b** by alternating implantation and annealing steps. Adapted with permission from [54]. Copyright 2005 American Chemical Society, or **c** by using a photographic-like process. Reproduced with permission from [49]. Copyright 2001 American Physical Society

[55–58]. Depending on the pulse power density, laser annealing can be used to either reduce the average particle size, or to allow the clustering process [56, 57].

4.3.3 *Ion Irradiation*

In previous sections, ion beams have been used to introduce a foreign species into a host matrix. In this section, an alternative way to fabricate nanocomposites is described. Here, the host matrix already contains the metallic species to be precipitated and irradiation is used to promote the diffusion and the relocation of the solute monomers, Fig. 4.6c, d. As for the implantation case, the synthesis of the NPs can be divided into two sub-categories.

- The system is a solid solution, i.e. the matrix does not contain a second solid phase, neither in the form of NPs nor in the form of thin films, Fig. 4.6c.

- Nanostructures are already embedded within the host matrix in the form of either thin films or NPs. Moreover, solute concentration is negligible, Fig. 4.6d.

4.3.3.1 Irradiation of a Doped Matrix

A first strategy is to apply a two-step approach. First, the host matrix is doped above the solubility limit (avoiding the precipitation) with the selected solute impurity. Successively, the energy released by the impinging ions is used to promote the diffusion and precipitation of the solute monomers. Although somehow arbitrary, this process can be categorized by considering the method used to dope the host matrix. In this way, three sub-categories can be defined:

- Samples doped by ion-implantation.
- Samples doped by ion-exchange.
- Samples doped during the glass synthesis.

Samples doped by ion-implantation Historically, early attempts to fabricate metal-glass nanocomposites were based on an implantation step followed by an irradiation with light mass ions (H, He or Ar)—see for example [59–62]. In this case, the precipitation is driven by the complex radiolytic processes following the passage of the ions, which, in turn, are governed by the energy deposited into the electronic sub-system.

Samples doped by ion-exchange process The ion-exchange process is usually performed by immersing the glass substrate, generally soda-lime or borosilicate glasses, in a molten eutectic salt bath containing the required metallic ion—see for example [63–67]. In glasses, the ion-exchange is typically carried out by replacing monovalent alkali ions, e.g. Li^+, K^+, with the metallic ions of the molten salt, e.g. Ag^+, Cu^+. Diffusion starts from a metallic film deposited onto the glass surface. Migration is promoted using an external voltage which is applied between the two faces of the glass layer. Depending on both the exchange time and the temperature, metal concentrations of several at.%, extending to a depth of several microns can be achieved. In some cases, an external electric field is applied to better control the profile of the doping species.

Samples doped during the glass synthesis Glasses doped during the synthesis contain metal oxides with a concentration level ranging from 1 to 10 %. Irradiations with light ions, H or He, at energies between 0.1 and 1.5 MeV favor the precipitation of a second phase—see for example [68, 44, 69]. More recently, heavy-ion irradiations (Br, Si, O) in the MeV region have also been performed [47, 49]. In both cases, precipitation process occurs during the irradiation step. It is driven by the electronic stopping power and it is ascribed to the interaction between metal monomers and irradiation-induced defects.

4.3.3.2 Irradiation of Embedded Nanostructures

Starting from late nineteens, a novel approach based on the ion-beam mixing technique has been developed. It exploits the ballistic displacements of the atomic species to be precipitated. Indeed, if two systems of different chemical composition, e.g. A/B, are separated by an interface, irradiation-induced cascade mixing allows high solute concentrations of the element B (respectively A) to be introduced into the matrix A (respectively B) at relatively low irradiation fluences, e.g. in the range of few 10^{16} cm^{-2}. Depending on whether or not the two elements are miscible, the process ends up with either an alloyed layer if $\Delta H_{mix} < 0$ or a phase separation if $\Delta H_{mix} > 0$, where ΔH_{mix} is the enthalpy of mixing. If one of the two systems has a sub-micron dimension, e.g. if it is a thin layer or a NP, the latter condition can be exploited to create a supersaturated solid solution that evolves toward the formation of precipitates whose size and composition can be tuned by the energy (electronic and/or nuclear) released by the impinging ions.

Depending on the preparation protocol, three different configurations of samples have been used:

- Metal-glass multilayered samples.
- Ion-beam synthesized NPs.
- Embedded colloidal NPs.

Irradiation of metal-glass multilayered samples

In early experiments, pristine samples were fabricated by alternating dielectric and metallic layers [70–76]. The thickness of the former was in the range of hundred of nanometers whereas that of the latter never exceeded few tens of nanometers. Irradiation with heavy-ions in the MeV region was used to induce the complete dissolution of the metallic layer and its successive precipitation throughout the sample thickness. The first experimental result reported on the formation of Ag clusters within a silica matrix after irradiation of a Ag/SiO_2 multilayered sample with 4 MeV Au ions [70]. Successively, this approach has been extended to other metallic species (Cu, Au, Pd, Pt) confined within various oxide matrices (SiO_2, Al_2O_3, TiO_2, ZrO_2) [71–76].

The ensemble of these experimental results allows to separate the evolution of the metal layer into two sub-processes:

- At the beginning of the irradiation surface tension plays a major role. In particular, the poor wettability between metal and dielectric layers favors the lateral segregation of the former one. This balling up is somehow equivalent to the Rayleigh instability of a thin liquid film deposited onto a hydrophobic substrate: the rupture of the liquid film results in the formation of droplets. Besides, the balling up is controlled by the degree of wetting between metal and dielectric surfaces, for instance in silica the process is faster for a gold layer than for a palladium layer.

- At the same time, ion-beam mixing allows the injection of the metallic species into the host matrix. This process favors the nucleation and growth of a halo of smaller precipitates around these large inclusions. Because of their peculiar spatial distribution, these NPs have been named *satellites* or *nanoplanets* [12, 77].

The main drawback of this approach is that, even for large irradiation fluences, the complete dissolution of the metallic layer is hardly achieved. Thus, irradiated sample is often composed of a bimodal size distribution of NPs formed of large inclusions (20–40 nm) and smaller satellites (5–10 nm).

Although the ion-mixing of multilayered samples was not completely successful in obtaining a homogeneous distribution of monodispersed precipitates, it probably represents the first attempt where nanotechnology and irradiation have been coupled to explore a *top-down* approach to manipulate the matter at the nanoscale. Indeed, in the following years these studies have generated an abundant literature on how the ion-irradiation could be used to modify in a convenient way nano-objects already confined within a host matrix, cf. Part IV Chap. 11. In the following sections, we summarize some of the principal results in this research field.

Irradiation of ion-beam synthesized nanoparticles

Collisional mixing in embedded metal NPs leads to two effects: on one hand, it favors the dissolution of the NP. Ejected monomers increase the solute concentration in the surrounding matrix such that the nucleation probability overcompensates the probability of dissolution, e.g. $R^* \propto 1/\ln(s)$. On the other hand, interstitials are produced by replacement collision sequences and are further separated from vacancies when the liquid core of the cascade collapses and drags vacancies to the center of the cascade [78]. Thus, two correlated effects are generally observed: The first is formation of a halo of satellites around it. An embedded NP can thus be seen as an internal source of solute whose emission strength is controlled by the irradiation parameters [79]. The second is nucleation and growth of cavities within the NP. These two effects are discussed hereafter:

- *Formation of a halo of satellites around the nanoparticle*

The first observation was published in 2001 [12], where a thin Au layer (7 nm) buried in SiO_2 was irradiated with 4 MeV Au ions, Fig. 4.17. As aforementioned irradiation produces the balling up of the metallic film and the formation of a halo of satellite clusters around large inclusions. Using TEM analysis it is found that both size and density of the satellites increases for low irradiation fluences and then saturate for larger fluences, indicating that a steady-state condition has been reached, Fig. 4.17d. These observations give a strong indication that in a driven system and under appropriate irradiation and temperature conditions, the steady-state solute concentrations dependence on precipitate size may be opposite to that expected from the equilibrium Gibbs-Thomson relation. For this reason the article was titled: *Experimental evidence for inverse Ostwald ripening*.

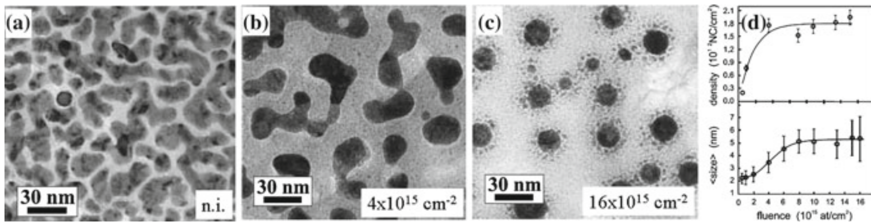

Fig. 4.17 TEM plan view micrographs showing the fluence dependent evolution of a SiO_2(70 nm)/Au(7 nm)/SiO_2(70 nm) sample. **a** The unirradiated sample shows a percolative structure. **b** The balling-up of the pristine metallic film is observed after 4.5 MeV ion irradiation at a fluence of 3×10^{15} cm^{-2}. **c** Satellite nanoparticles are visible after irradiation to a fluence of 1.5×10^{16} cm^{-2}. **d** Size and density evolutions of satellites with irradiation fluence. Saturation occurs at high irradiation fluences, showing that a steady-state regime is reached. Reproduced with permission from [12]

A further development of this approach is due to Mazzoldi's group [77]. Here, the multilayered sample was replaced by a silica matrix containing ion-beam synthesized NPs. Considering Au–Cu and Ag–Cu alloy NPs an element-selective dealloying is observed whose pathway can be controlled by a post-synthesis treatment. On one hand, annealing treatment in oxidizing atmosphere (T = 900 °C in air for t = 15 min to 5 h) favors the extraction of the less noble element, i.e. the copper atoms. This process has been associated with a corrosion-like process where the more reactive element (or the less noble metal) is dissolved from the alloy. On the other hand, post-irradiation favors the preferential extraction of the more noble element, i.e. the gold atoms. In this case the de-alloying is triggered by the energy released to the NP by the impinging ions.

- *Formation of hollow nanoparticles*

Ion-beam mixing is not limited to the ballistic ejection of atoms from the NP into the matrix. Indeed, vacancies are also generated within the NP, whose clustering leads to the formation of cavities in its core [33, 80]. Although this phenomenon has been known for a long time—see for example [81–86]—the first systematic investigation was done by Feng Ren and collaborators [87–90].

Formation of Cu, Ag and Au hollow NPs has been studied under different implantation conditions: 180 keV Cu, 200 keV Ag and, 250 keV Au at room temperature and under an ion flux of about 2 μA cm^{-2}. Evolution of the cavities has been observed to depend on both the implantation fluence and the metallic species. In particular, at low fluences (5×10^{16} cm^{-2}) solid NPs, i.e. without cavities, are formed for all three samples (Cu, Ag and Au) Fig. 4.18a. When the fluence is increased to 1×10^{17} cm^{-2}, the presence of cavities is only observed in Cu and Ag NPs, Fig. 4.18b. At last, at a fluence of 2×10^{17} cm^{-2}, core@shell nanostructures appear in Ag samples. These are composed by a solid Ag core surrounded by a cavity and a solid Ag shell—see arrow in Fig. 4.18c. Finally, both cavities and core@shell features are observed to be instable upon both thermal annealing and electron-beam irradiation.

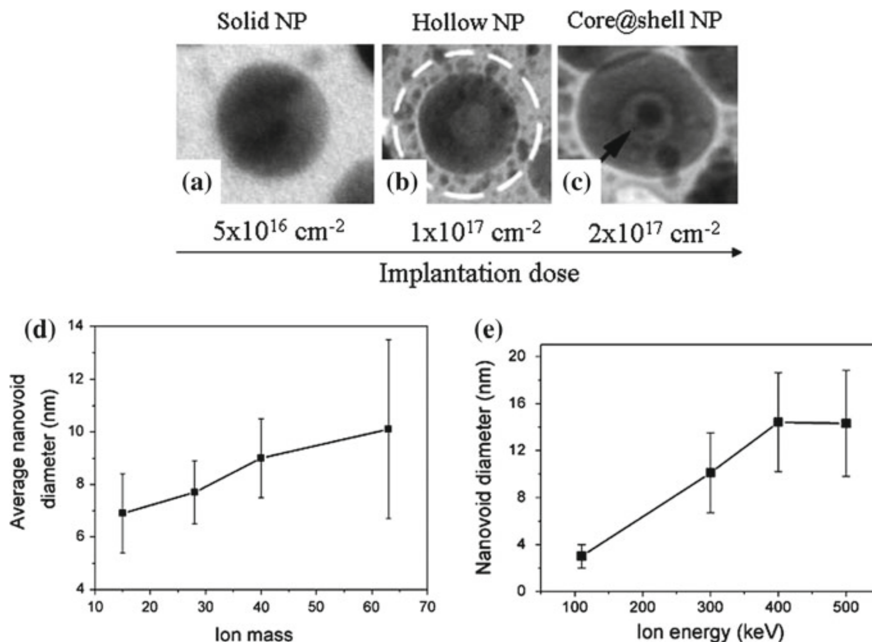

Fig. 4.18 Fluence dependent evolution of **a** a solid nanoparticle into **b** a hollow nanoparticle and **c** a core@shell nanoparticle. Reproduced with permission from [90]. Evolution of hollow nanoparticles with **d** the mass and **e** the energy of the impinging ion. Reproduced with permission from [89]

A more quantitative investigation has been performed on Ag NPs, where the formation, evolution and stability of the cavities has been observed to depend on both mass and energy of the implanted ions. For instance, the average diameter of the cavities increases with the mass of the impinging ion, Fig. 4.18d. Similarly, for a given ion species, e.g. Cu^+, it increases with the ion energy reaching a plateau for energies larger than 400 keV, Fig. 4.18e.

Irradiation of embedded nanoparticles prepared either by colloidal chemistry or by electron beam lithography

In the field of nanocomposites fabricated using ion-beams the synthesis process is mainly based on trial-and-error strategies. This empirical approach necessitates a great experimental effort, in tailoring the implantation/irradiation parameters, to achieve the required level of reproducibility and control on the NP properties. An alternative would be to develop a complete theoretical framework. However, so far this approach has been only scarcely followed where only phenomenological models exist, cf. Sect. 4.3.1.4. A possible issue comes from the observation that compositional patterning in implanted and irradiated nanocomposites follow the same pathways as those observed in driven alloys, e.g. in oxide dispersion strengthened (ODS) ferritic steels [5]. This indicates that the underlying physics has a common

background. In particular, both these systems can be defined as dissipative. This is, an open system that evolves under far from thermodynamical equilibrium conditions, and exchanges energy (or matter) with an external environment. A nanocomposite under sustained irradiation behaves as a dissipative system as the energy is transferred from the impinging ion, which fulfills the role of the external environment, to the atoms of the target matrix, which fulfills the role of the system. Most of the work to bring the gap between these two research fields has been done by Heinig et al. [17], and by Rizza and collaborators [79, 91, 92, 93, 94]. The latter is based on the development of a model system and it will be described in the next section.

4.3.4 A Model System to Investigate the Behavior of Nanoparticles Under Irradiation

From an operative point of view, an ensemble of NPs is completely characterized once the time evolution of the (i) size (ii) density, and (iii) size distribution are known, cf. Sect. 4.2.2.3. However, in usual irradiation experiments these quantities are barely accessible. The reason is twofold:

First, the energy delivered by the impinging ions—either in the nuclear or electronic stopping regimes—scales with the ion path. Thus, NPs at different depth receive different amounts of energy. The same is true for the defects created within the host matrix whose role is to mediate the diffusion of the solute atoms. Second, irradiation effects are function of the NP size. In particular, in the nuclear regime, the number of atoms that are ballistically injected into the host matrix, i.e. the emission strength, scales with the NP size [91].

As NPs of different sizes and embedded at different depths within the matrix behave differently, it is nearly impossible to separate the kinetic evolution of a single precipitate from the statistical noise due to the other NPs composing the system. Consequently, the control of the irradiation parameters (ion energy, ion flux and temperature) is not alone a sufficient condition to fully characterize the evolution of a nanophase.

A possible issue for this long-standing and puzzling problem is to prepare a sample where not only the irradiation conditions but also the properties of the as-prepared NPs are mastered [79]. This model system is composed of nearly monodispersed NPs placed at unique plane below the sample surface, Fig. 4.19. This experimental configuration allows to overcome the aforementioned drawbacks inherent to the irradiation process. First, as all the NPs lie on the same plane, they receive the same amount of energy. Second, as their size dispersion is narrow, their strength in emitting solute atoms is the nearly same. Third, the irradiation-induced defects are homogeneously distributed around the NPs.

In practice, this model system can be conveniently fabricated by sandwiching monodispersed metallic NPs between two dielectric layers, Fig. 4.19a. The protocol is as follows. First a layer is deposited onto a substrate. Then NPs are prepared and

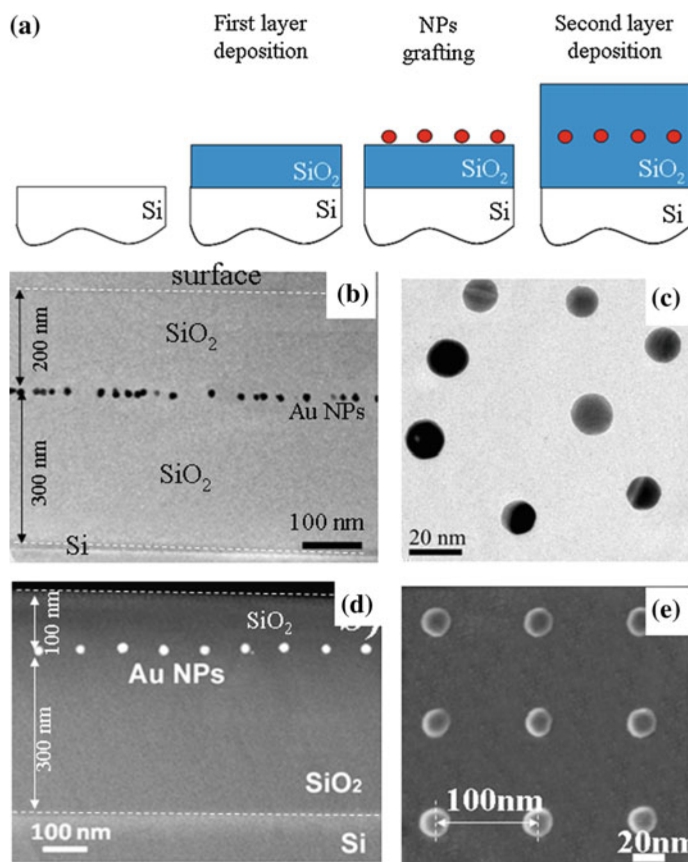

Fig. 4.19 **a** Fabrication of a model system**b**, **c** Model system composed of chemically synthesized and grafted Au NPs. **d**, **e** Model system composed of a regular array of Au NPs prepared by electron beam lithography

grafted at the surface of the film. They can either be chemically synthesized, Fig. 4.19b, c, or prepared using electron beam lithography (EBL), Fig. 4.19d, e. This step allows to set the initial size and density of NPs. In particular, if EBL is used arrays of NPs with a controlled pitch distance can be obtained. Finally the particles are embedded by achieving the deposition of a second layer under the same conditions as the first one. In this case, the thickness of the second layer defines the depth at which the NPs are confined within the host matrix.

The strength of this approach is that the average evolution of an ensemble of NPs is equivalent to that of a single NP. This is shown, for instance, in Fig. 4.20 where the irradiation-induced dissolution toward the steady-state size is followed step-by-step for 15 nm Au NPs in SiO_2 irradiated with 4 MeV Au ions at different temperatures [79]. Figure 4.20a–e show the evolution of a single nanoparticle. TEM micrographs indicate that, at low irradiation fluences, a first generation of satellites nucleates close

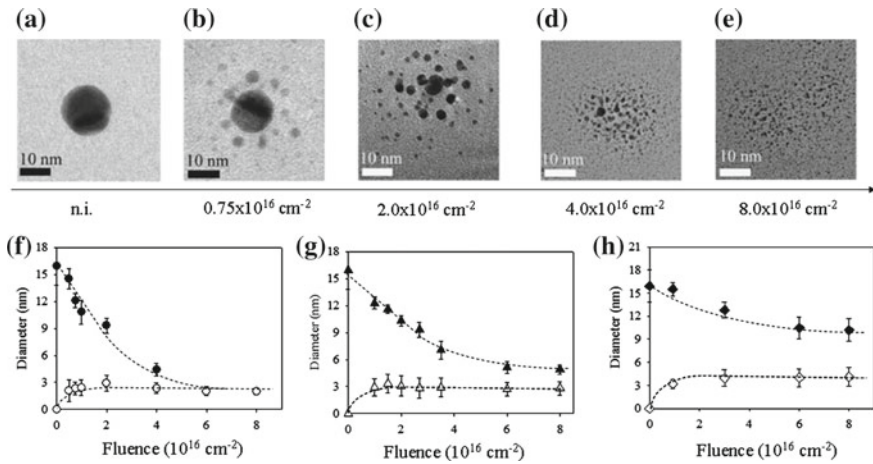

Fig. 4.20 **a–e** Evolution of 15 nm Au nanoparticles under 4 MeV Au irradiation at room temperature (30 °C). The fluence is increased from 0 to 8×10^{16} cm^{-2}). Reproduced with permission from [79]. Size evolution of both the nanoparticles (*triangles*) and precipitates (*circles*) at different temperatures: **f** 30 °C, **g** 500 °C, and **h** 800 °C. Reproduced with permission from [79]

to the NP surface, where the latter is considered a solute reservoir, Fig. 4.20b. Increasing the irradiation fluence, the satellites are observed to grow, while *mother* NP is consumed. At the same time, new precipitates nucleate at larger distances, Fig. 4.20c. Finally, Fig. 4.20e shows that for the largest fluence, all the populations, NP and satellites, converge toward a unique steady-state size of about 2 nm.

The average evolution of the NPs (full symbols) and of the satellites (open symbols) is graphically represented in Fig. 4.20f–h for three different irradiation temperatures, i.e. T = 30, 500, and 800 °C. It is worth noting that this behavior is similar to that theoretically predicted by Frost and Russell for the inverse Ostwald ripening regime [15, 16], see for instance Fig. 4.5b. Temperature modifies the kinetics of dissolution [93]. Indeed, when the temperature is increased to 600 °C the dissolution rate is reduced, such that the system takes longer time to reach the steady-state, Fig. 4.20g. The slowing of the dissolution process is further enhanced when the temperature is increased at 800 °C, Fig. 4.20h.

The model system can also be used to study the kinetic evolution of a precipitate phase (nucleation, growth, and coarsening) during the implantation process [92]. The underlying idea is that the ballistic injection of solute atoms from the embedded NPs into the surrounding matrix is equivalent to the implantation of impinging ions into the solid target. Thus the former process has been named *nanoimplantation* [79, 91, 92]—Thus, the evolution of the satellite clusters under irradiation is equivalent to the nucleation growth, and coarsening taking place during the implantation process.

Following this approach, it has been shown that:

- The evolution of the satellites obeys to a two step mechanism [79]. For low irradiation fluences, the original inclusion acts as an infinite source of solute

allowing to keep a high supersaturation level in its surrounding. Here, the growth of the satellites is sustained by the dissolution of the NP. In this first regime, the dimension of the satellites can be larger than their steady-state value. However, once the size of the inclusion becomes comparable to that of the surrounding satellites, it looses its capability to sustain their growth. For longer times, larger satellites start to dissolve and the whole system evolves toward a steady-state.

- Both the dimension and the density of the satellites are function of the nanoparticle size [91]. This explains, for instance, why starting with a broad size distribution is detrimental for an optimum control of the properties of the corresponding nanocomposite.
- The precipitates evolve in an open system under an Ostwald ripening regime where the monomer supply is limited by the diffusion of the solute [92].
- For a model system composed of 15 nm Au NPs embedded in SiO_2 and irradiated with 4 MeV Au ions at room temperature, several thermodynamical parameters have been experimentally determined [92]: the diffusion coefficient under irradiation ($D_{irr} \sim 3.8 \times 10^{-16}$ cm^2 s^{-1}), the concentration threshold for nucleation ($c_{nucl} \sim 2.8 \times 10^{21}$ cm^{-3}), and the surface tension under irradiation ($\sigma \sim$ 1–2.2 $\times 10^{-5}$ J cm^{-2}).

4.4 Conclusion

In the last decades, the use of ion-beams has demonstrated to be a versatile and flexible approach for synthesizing nanocomposite materials. However, despite a large variety of potential applications has been identified and are being actively explored, there are currently no commercial devices based on the ion-beam technology. Indeed, most of them are critically limited by both the broad size distribution and the poor spatial control of the NPs. Current forefront researches focus on the development of novel strategies to overcome these drawbacks; some of them have been illustrated in this chapter. For instance, the temporal separation of the nucleation and growth stages or the use of the inverse Ostwald ripening offer promise for improving size distributions. A more recent approach based on the combination of colloidal chemistry (or electron beam lithography) and ion-irradiation allows to improve the control of the spatial distribution of the NPs. Besides, new technical approaches going in this direction are the use of focused ion-beams or the use of stencil masks.

However hitherto the development of ion-based techniques for the synthesis of nanocomposites has been mainly based on trial-and-error strategies. This empirical approach necessitates a great experimental effort, in tailoring the implantation/ irradiation parameters, to achieve the required level of reproducibility and control on the NP properties. An alternative issue is to improve the description of the synthesis processes within a more complete theoretical framework. A possible starting point is to make use of the theoretical work that has already been developed so far in the field of driven alloys [5]. Indeed, recently similar behaviors have been

reported in driven alloys and nanocomposites, indicating that underlying physics has a common basis. The evolution and stability of a driven alloy is described in the framework of non-equilibrium thermodynamics, where the energy continuously flows from the impinging ions, i.e. the external environment, to the atoms of the target matrix, i.e. the system or the thermostat [95, 96]. As both ion implantation and ion irradiation processes are inevitably accompanied by the continuous production of damage within the irradiated material, a nanocomposite evolving in a radiative environment can also be described in the same theoretical framework.

4.5 Appendix: Elementary Processes in Irradiated Solids

Under irradiation the continuous production of damage modifies the evolution of the NPs toward the steady-state configuration. In particular, a fundamental role is played by the synergy between several effects occurring in parallel: ballistic displacements, irradiation-induced defects, radiation-enhanced diffusion, and temperature. Their knowledge allows to control both the stability and the final features of the NPs. Thus, in this section the fundamentals of radiation effects in solids are briefly reviewed. A more complete description of the basics of the ion-matter interaction is given in *Part I*, Chap. 1 of this book.

4.5.1 Principles of Ion-Matter Interaction

A charged particle penetrating into a solid progressively looses its energy through a complex interaction with the atoms of the host matrix. Neglecting nuclear reactions, basically two processes are at the origin of the slowing-down of the impinging ion: (i) the elastic interactions with the target atoms, also named nuclear interactions, and (ii) the inelastic interactions with the electrons, e.g. excitation and ionization processes, also named electronic interactions. Owing to the Born-Oppenheimer approximation, these two mechanisms can be separated allowing the total energy loss per unit length (stopping power) to be written as the sum of an elastic and an inelastic process:

$$\left(\frac{\partial E}{\partial x}\right)_{total} = \left(\frac{\partial E}{\partial x}\right)_{nuclear} + \left(\frac{\partial E}{\partial x}\right)_{electronic} \tag{4.27}$$

However, the stopping cross section can also be used:

$$S_{total} = \frac{1}{N}\left(\frac{\partial E}{\partial x}\right)_{total} = S_{nuclear} + S_{electronic} \tag{4.28}$$

where N is the density of the target.

The probability for an elastic collision to take place is determined by the scattering cross-section, dσ, which in turn depends on both the interaction potential, V(r), and the energy of the impinging ion, E, and the energy transferred to the target ion, T:

$$S_n = \int_0^{T_{MAX}} T d\sigma(E, V) \tag{4.29}$$

In general, elastic collisions dominate for low ion energies [97].

Inelastic interactions are mainly the result of excitation and ionization processes and dominate for medium-high ion energies [98]. The slowing down of the impinging ions in the inelastic regime is treated by considering a charged particle moving in a viscous background formed by the electrons of the matrix. If the ion energy is large enough, the energy density deposited along the ion path results in the formation of a cylindrical defective region, named ion-track (see for example *Part I*, Chap. 2 and *Part III*, Chap. 2 of this book).

Irradiation processes favor to the formation of defects. For instance, ballistic collisions and displacement cascades lead to interstitial-vacancy, or Frenkel pair, defects, whenever the energy received by the target atom is larger than a displacement threshold value, E_d [97]. These directly affect the mobility of the solute species and, in turn, control the kinetics of the nucleation and growth processes. This is described in the next section.

4.5.2 Defects and Diffusion

In this section, diffusion mechanisms are briefly described. First, diffusion under thermodynamic conditions is introduced. Afterward, we show how the mobility of solute monomers is modified when a radiative environment is considered. This will be done for both metal and silica matrices.

4.5.2.1 Diffusion Under Thermodynamic Conditions, D_{th}

Roughly speaking, the diffusion in a solid can be described as the jump of an atom from one stable position to another one in the lattice. Although a diffusion process can follow several pathways, in most of the cases it occurs through a vacancy mechanism. This is, an atom on a normal site jumps into an adjacent unoccupied lattice site (vacancy). Thus, the mobility of a diffusing species is triggered by both the concentration and diffusivity of the vacancies where the diffusion coefficient is described by an Arrhenius equation with an activation energy E_a, e.g. $D_{th} \sim \exp(-E_a/k_B T)$, Fig. 4.21.

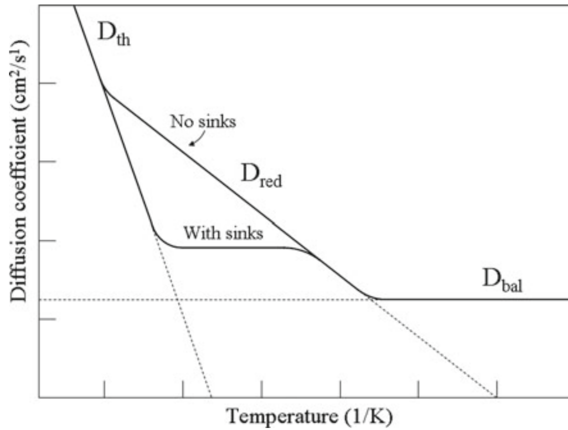

Fig. 4.21 The diffusion coefficient is modified by the irradiation. Depending on the temperature three regimes can be defined: (i) at low temperature the diffusivity is controlled by ballistic displacements, D_{bal}. (ii) At intermediate temperatures, it becomes function of the generation and annihilation rates of vacancies and interstitials that are continuously created by the irradiation, D_{RED}. Thus, it depends on whether or nor sinks are presents as well as on their capability to absorb defects, e.g. their strength. (iii) At sufficiently high temperatures the thermal diffusivity dominates, D_{th}

4.5.2.2 Diffusion Under Irradiation in Metals, D_{bal} and D_{RED}

In a metal the energy required to displace a substrate atom is about 25 eV [97]. When the energy deposited by the impinging ion overcomes this threshold value, point defects and defect clusters are created. Thus, irradiation produces a supersaturation of point defects which increases the solid state diffusion coefficient. For example, if diffusion occurs by a vacancy mechanism, the diffusion coefficient under irradiation, D_{irr}, is enhanced relative to the purely thermal value, D_{th}, by

$$D_{irr} = \frac{C_{irr} + C_{th}}{C_{th}} D_{th} \tag{4.30}$$

where C_{irr} is the concentration of vacancies under irradiation, and C_{th} is the equilibrium concentration of vacancies under purely thermal conditions.

Owing to (4.30) several regimes exist for the diffusion coefficients of the moving species, Fig. 4.21:

- at low temperature, the migration of the point defects is negligible and the diffusion is mainly controlled by the temperature independent ballistic processes, [97]. In this case, the ballistic diffusion coefficient writes:

$$D_{bal} = \frac{1}{6} \Gamma a^2 \tag{4.31}$$

where Γ is the displacement rate, and a the average displacement distance.

- as the temperature is increased, defects become mobile and the diffusion coefficient becomes temperature dependent. In this regime, the diffusion coefficient is controlled by the production and the annihilation/recombination rates, and the mobility is characterized by the radiation-enhanced diffusion coefficient, D_{RED}. In particular, the concentration of radiation-induced vacancies and interstitials is a balance between the production rate of point defects, and their loss rate to sinks which is adequately described by the point defect balance equations [80]. As the concentration of vacancies and interstitials produced under irradiation are in general much greater than the thermal ones, the diffusion coefficient D_{RED} is much larger than both thermal and mixing ones, $D_{RED} \gg D_{th} \gg D_{bal}$.
- for sufficiently high temperatures, the thermal diffusivity dominates over the two previous mechanisms, e.g. $D_{th} \gg D_{RED} \gg D_{bal}$.

4.5.2.3 Irradiation-Induced Defects in a Silica Matrix

For metal-glass nanocomposites the diffusion of the metal solute is triggered by the defects within the silica matrix [99, 100, 101, 38, 102, 103, 104, 105]. Here, two kinds of defects are mainly created during the implantation/irradiation processes. Both are associated to the irradiation-induced oxygen vacancies. Depending on their charge state they can be either E' or B_2 centers. An E' center has an unpaired electron which can be monitored by electron paramagnetic resonance (EPR). A B_2 center is a diamagnetic defect formed by an oxygen vacancy which has trapped two electrons. This defect is generally studied with optical absorption and photoluminescence techniques.

Oliver et al. show that B_2 defects preexist in virgin samples and that their density increases with irradiation fluence [106]. On the other hand, the creation of E' centers is due to the irradiation with both Si and Au ions. In particular, both defects are mainly generated through the electronic excitations. Valentin et al. [107] studied the correlation between the density of E' defects and those of the precipitates in glasses doped with copper atoms and irradiated at room temperature with 7 MeV Si ions. A similar study was done by Oliver et al. [106], for silica irradiated with 3 and 10 MeV Au ions. Finally, these defects become instable when the temperature is increased above a threshold value [103–105]. In particular, E' defects start to recover from about 500 °C, whereas B_2 defects are stable up to about 900 °C [38].

References

1. P.M. Ajayan, L.S. Schadler, P.V. Braun, *Nanocomposite Science and Technology*. (Wiley, New York, 2003)
2. D.A. Porter, K.E. Easterling, M. Sherif, *Phase Transformations in Metals and Alloys*, 3rd Edn. (CRC Press, Boca Raton, 2009)
3. L. Ratke, P.W. Voorhees (eds.), *Growth and Coarsening*. (Springer, New York, 2002)

4. R.W. Balluffi, S.M. Allen, W.C. Carter (eds.), *Kinetics of Materials*. (Wiley, New York, 2005)
5. P. Bellon, in *Precipitate and Microstructural Stability in Alloys Subjected to Sustained Irradiation in Materials Science with Ion Beams, Series: Topics in Applied Physics*, vol. 116, ed. by H. Bernas (Springer, Berlin, 2010)
6. R.E. de Lamaëstre, H. Bernas, Phys. Rev. B **73**, 125317 (2006)
7. I.M. Lifshitz, V.V. Slyozov, J. Phys. Chem. Solids **19**, 35 (1961)
8. V.C. Wagner, Z. Elektrochem. **65**, 581 (1961)
9. E. Brosh, A. Kiv, J. Nucl. Mater. **306**, 173 (2002)
10. K. Nozawa, M.-H. Delville, H. Ushiki, P. Panizza, J.-P. Delville, Phys. Rev. E **72**, 011404 (2005)
11. R.S. Nelson, J.A. Hudson, D.J. Mazey, J. Nucl. Mater. **44**, 318 (1972)
12. G.C. Rizza, M. Strobel, K.H. Heinig, H. Bernas, Nucl. Instrum. Methods Phys. Res. B **178**, 78 (2001)
13. P. Wilkes, J. Nucl. Mater. **83**, 166 (1979)
14. A.D. Brailsford, J. Nucl. Mater. **91**, 221 (1980)
15. H.J. Frost, K.C. Russell, J. Nucl. Mater. **103–104**, 1427 (1981)
16. H.J. Frost, K.C. Russell, Acta Metal. **30**, 953 (1982)
17. K.H. Heinig, T. Müller, M. Strobel, B. Schmidt, W. Möller, Appl. Phys. A Mater. Sci. Process. **77**, 17 (2003)
18. R. Enrique, P. Bellon, Phys. Rev. B **60**, 14649 (1999)
19. R. Enrique, P. Bellon, Phys. Rev. Lett. **84**, 2885 (2000)
20. M. Strobel, *Modeling and Computer Simulation of Ion Beam Synthesis of Nanostructures*. PhD Thesis FZR-277, (1999). ISSN 1437-322X
21. G. Martin, Phys. Rev. B **30**, 1424 (1984)
22. G. Martin, P. Bellon, Solid State Phys. **50**, 189 (1997)
23. P. Bellon, G. Martin, in *Alloy Physics*, ed. by W. Pfeiler (Wiley VCH, Weinheim, 2007), p. 423
24. R.A. Enrique, P. Bellon, Phys. Rev. B **63**, 134111 (2001)
25. J. Ye, P. Bellon, Phys. Rev. B **70**, 094104 (2004)
26. J. Ye, P. Bellon, Phys. Rev. B **73**, 224121 (2006)
27. D. Schwen, M. Wang, R.S. Averback, P. Bellon, J. Mater. Res. **28**, 2687 (2013)
28. H. Bernas (ed.), *Materials Science with Ion Beams, Series: Topics in Applied Physics*. (Springer, Berlin, 2010), vol. 116
29. G. W. Arnold, P. Mazzoldi, in *Ion Beam Modification of Insulators*, ed. by P. Mazzoldi, G. W. Arnold (Elsevier, Amsterdam, 1987)
30. P. Mazzoldi, G. Mattei, Riv. Nuovo Cimento **28**, 1 (2005)
31. R.F. Haglund Jr., in *Optics of Small Particles, Surfaces and Interfaces*, ed. by R.E. Hummel, P. Wißmuth (CRC Press, Boca Raton, 1997)
32. A.V. Krasheninnikov, K. Nordlund, J. Appl. Phys. **107**, 071301 (2010)
33. M. Nastasi, J. Mayer, *Ion Implantation and Synthesis of Materials*. (Springer, Berlin, 2006)
34. F. Gonella, P. Mazzoldi, in *Handbook of Nanostructured Materials and Nanotechnology*, ed. by H.S. Nalwa (Academic Press, San Diego, 2000), vol. 4, pp. 81–158
35. J.F. Ziegler, J.P. Biersack, U. Littmark, *The Stopping Ranges and Ranges of Ions in Solids*. (Pergamon Press, New York, 1985)
36. http://www.srim.org
37. M. Strobel, K.-H. Heinig, W. Möller, A. Meldrum, D.S. Zhou, C.W. White, R.A. Zuhr, Nucl. Instr. Meth. B **147**, 343 (1999)
38. D.L. Griscom, Nucl. Instrum. Methods Phys. Res. B **1**, 481 (1984)
39. G. De Marchi, G. Mattei, P. Mazzoldi, C. Sada, A. Miotello, J. Appl. Phys. **92**, 4249 (2002)
40. A. Miotello, G. De Marchi, G. Mattei, P. Mazzoldi, C. Sada, Phys. Rev. B **63**, 075409 (2001)
41. H. Hosono, Jpn. J. Appl. Phys. **32**, 3892 (1993)
42. G. Battaglin, Nucl. Instr. Meth. B **116**, 102 (1996)
43. H. Hosono, N. Matsunami, Phys. Rev. B **48**, 13469 (1993)

44. H. Hosono, N. Matsunami, A. Kudo, T. Ohtsuka, Appl. Phys. Lett. **65**, 1632 (1994)
45. E. Cattaruzza, Nucl. Instr. Meth. B **169**, 141 (2000)
46. R. Kelly, Mater. Sci. Eng., A **115**, 11 (1989)
47. R. Espiau de Lamaestre, H. Béa, H. Bernas, J. Belloni, J.L. Marignier, Phys. Rev. B **76**, 205431 (2007)
48. J. Belloni, M. Treguer, H. Remita, R. De Keyzer, Nature **402**, 0865 (1999)
49. E. Valentin, H. Bernas, C. Ricolleau, F. Creuzet, Phys. Rev. Lett. **86**, 99 (2001)
50. P. Kluth, B. Hoy, B. Johannessen, S.G. Dunn, G.J. Foran et al., Appl. Phys. Lett. **89**, 153118 (2006)
51. M Strobel, K.-H Heinig, W Möller, Nucl. Instr. Meth. B **104** (1999)
52. A.L. Stepanov, Rev. Adv. Mater. Sci. **26**, 1 (2010)
53. P. Benzo, L. Cattaneo, C. Farcau, A. Andreozzi, M. Perego et al., J. Appl. Phys. **109**, 103524 (2011)
54. V. Ramaswamy, T.E. Haynes, C.W. White, W.J. MoberlyChan, S. Roorda, M.J. Aziz, Nanoletters **5**, 373 (2005)
55. P.D. Townsend, Vacuum **51**, 301 (1998)
56. A.L. Stepanov, D.E. Hole, A.A. Bukharaev, Vacuum **64**, 169 (2001)
57. A.L. Stepanov, D.E. Hole, P.D. Townsend, Nucl. Instr. Meth. B **191**, 468 (2002)
58. N. Okubo, N. Umeda, Y. Takeda, N. Kishimoto, Nucl. Instr. Meth. B **206**, 610 (2003)
59. P. Mazzoldi, *Modifications Induced by Irradiation in Glasses* (Elsevier, North Holland, 1992)
60. D. Ila, Z. Wu, C.C. Smith, D.B. Poker, D.K. Hensley, C. Klatt, S. Kalbitze, Nucl. Instr. Meth. B **127**, 570 (1996)
61. D. Ila, E.K. Williams, C.C. Smith, D.B. Poker, D.K. Hensley, C. Klatt, S. Kalbitzer, Nucl. Instr. Meth. B **148**, 1012 (1999)
62. D. Ila, R.L. Zimmerman, C.I. Muntele, P. Thevenard, F. Orucevic et al., Nucl. Instr. Meth. B **191**, 416 (2002)
63. F. Caccavale, G. De Marchi, F. Gonella, P. Mazzoldi, C. Meneghini et al., Nucl. Instr. Meth. B **96**, 382 (1995)
64. G. De Marchi, F. Gonella, P. Mazzoldi, G. Battaglin, E.J. Knystautas, C. Meneghini, J. Non-Crys. Sol. **106**, 79 (1996)
65. D.P. Peters, C. Strohhöfer, M.L. Brongersma, J. van der Elsken, A. Polman, Nucl. Instr. Meth. B **168**, 237 (2000)
66. G. Battaglin, E. Cattaruzza, F. Gonella, R. Polloni, F. D'Acapito et al., Nucl. Instr. Meth. B **200**, 185 (2003)
67. H.-E. Mahnke, B. Schattat, P. Schubert-Bischoff, N. Novakovic, Nucl. Instr. Meth. B **245**, 222 (2000)
68. R.F. Haglund Jr., L. Yang, R.H. Magruder III, C.W. White, R.A. Zuhr et al., Nucl. Instrum. Methods B **91**, 493 (1994)
69. H. Hosono et al., J. Appl. Phys. **82**, 4232 (1997). (and references therein)
70. F. Garrido, J.-C. Dran, L. Thomé, C. Meneghini, F. Gonella, A. Quaranta, Nucl. Instr. Meth. B **115**, 561 (1996)
71. L. Thomé, F. Garrido, Nucl. Instr. Meth. B **121**, 237 (1997)
72. G. Rizza, F. Garrido, J.C. Pivin, J.C. Dran, L. Thomé, M. Gusso, L. Tapfer, A. Quaranta, P. Colombo, Nucl. Instr. Meth. B **127/128**, 574 (1997)
73. L. Thomé, J. Jagielski, G. Rizza, F. Garrido, J.C. Pivin, Appl. Phys. A **66**, 327 (1998)
74. L. Thomé, G. Rizza, F. Garrido, M. Gusso, L. Tapfer, A. Quaranta, Appl. Phys. A **67**, 241 (1998)
75. J.C. Pivin, G. Rizza, Thin Solid Films **366**, 284 (2000)
76. J.C. Pivin, G. Rizza, Nucl. Instr. Meth. B **166/167**, 115 (2000)
77. G. Mattei, G. Marchi, C. Maurizio, P. Mazzoldi, C. Sada, V. Bello, G. Battaglin, Phys. Rev. Lett. **90**, 085502 (2003)
78. K. Nordlund, M. Ghaly, R.S. Averback, M. Caturla, T. Diaz de la Rubia, J. Tarus, Phys. Rev. B **57**, 7556 (1998)

79. G. Rizza, H. Cheverry, T. Gacoin, A. Lamasson, S. Henry, J. Appl. Phys. **101**, 014321 (2007)
80. G.S. Was, *Fundamentals of Radiation Materials Science: Metals and Alloys*. (Springer, Berlin, 2007)
81. A. Meldrum et al., Nucl. Instrum. Methods Phys. Res. B **178**, 7 (2001)
82. C. de Julián, Fernández. Nucl. Instrum. Methods Phys. Res. B **175–177**, 479 (2001)
83. G. Battaglin et al., Nucl. Instrum. Methods Phys. Res. B **191**, 392 (2002)
84. C. de Julián Fernández, Nucl. Instrum. Methods Phys. Res. B **216**, 245 (2004)
85. K.S. Buchanan, Nano Lett. **5**, 383 (2005)
86. C.M. Wang, Appl. Phys. Lett. **87**, 153104 (2005)
87. F. Ren, C.Z. Jiang, C. Liu, J.B. Wang, App. Phys. Lett. **88**, 183114 (2006)
88. F. Ren, C. Jiang, C. Liu, J. Wang, T. Oku, Phys. Rev. Lett. **97**, 165501 (2006)
89. F. Ren, G. X. Cai, X.H. Xiao, L.X. Fan, C. Liu, D.J. Fu, J.B. Wang, C.Z. Jiang, J. App. Phys. **103**, 084308 (2008)
90. F. Ren, X.H. Xiao, G.X. Cai, J. Wang, C.Z. Jiang, Appl. Phys. A **96**, 317 (2009)
91. G. Rizza, Y. Ramjauny, T. Gacoin, S. Henry, Nucl. Instrum. Methods Phys. Res. B **257**, 15 (2007)
92. G. Rizza, Y. Ramjauny, T. Gacoin, L. Vieille, S. Henry, Phys. Rev. B **76**, 245414 (2007)
93. Y. Ramjauny, G. Rizza, S. Perruchas, T. Gacoin, R. Botha, J. Appl. Phys. **107**, 104303 (2010)
94. T.H.Y. Vu, Y. Ramjauny, M. Hayoun, G. Rizza, S. Perruchas, J. Appl. Phys. **117**, 174305 (2015)
95. I. Prigogine, G. Nicolis, *Self-Organization in Non-Equilibrium Systems*. (Wiley, New York, 1977)
96. K.C. Russell, J. Nucl. Mater. **83**, 176 (1979)
97. M. Nastasi, J. Mayer, J.K. Hirvonen, *Ion-Solid Interactions: Fundamentals and Applications, Cambridge Solid State Science Series* (Cambridge University Press, Cambridge, 1996)
98. P. Sigmund, *Stopping of Heavy Ions: A Theoretical Approach, Series: Springer Tracts in Modern Physics (Book 204)*. (Springer, Berlin, 2004)
99. E. Friebele, D. Griscom, *Radiation Effects in Glass* (Academic Press, New York, 1979)
100. R.A.B. Devine, J. Appl. Phys. **56**, 563 (1984)
101. J. Robertson, J. Phys. C **17**, L221 (1984)
102. D.L. Griscom, Radiation effects in optical materials SPIE **541**, 38 (1985)
103. R.A.B. Devine, C. Fiori, J. Appl. Phys. **58**, 3368 (1985)
104. R.A.B. Devine, Phys. Rev. B **35**, 9783 (1987)
105. R.A.B. Devine, Nucl. Instrum. Meth. B **91**, 378 (1994)
106. A. Oliver, J.C. Cheang-Wong, A. Crespo, L. Rodriguez-Fernandez, J.M. Hernandez, E. Munoz, R. Espejel-Morales, Mater. Sci. Eng. B **78**, 32 (2000)
107. E. Valentin, Ph.D. thesis, Ecole Centrale, 1999

Part II
Damage Formation and Amorphization by Nuclear Energy Deposition

Chapter 5
Primary Processes of Damage Formation in Semiconductors

Elke Wendler and Werner Wesch

Abstract In this chapter damage formation and amorphisation in various semiconductors are reviewed with special focus on primary processes. Trends are shown how the parameters during ion implantation influence damage formation and to what extend the results for the various semiconductors can be generalised. It is shown that three groups of semiconductors can be identified. One group of materials exhibits a continuous transition towards amorphisation at sufficiently low temperatures. In these materials comparable mechanisms of defect formation are observed provided the implantation temperature is similarly close to or below the corresponding critical temperature of amorphisation, T_c, the concept of which is discussed in this chapter. In a second group, amorphisation can be achieved at low temperatures only and only by secondary processes resulting in a discontinuous transition to amorphisation. And in a third group of materials amorphisation by ion implantation is not observed even not at low temperatures for moderate ion fluences which do not significantly alter the stoichiometry of the material. Various models are applied for describing the damage evolution. This represents a further step towards a prediction of damage to be expected for certain irradiation conditions in the corresponding materials.

5.1 Introduction

Ion-beam induced effects in semiconductors have been studied since more than 60 years. The first papers on radiation damage and ion-beam induced changes of the electrical properties of semiconductors appeared in the middle of the 20th century (see [1, 2] and references therein). But it took another twenty years to

E. Wendler (✉) · W. Wesch
Institut für Festkörperphysik, Friedrich-Schiller-Universität Jena,
Max-Wien-Platz 1, 07743 Jena, Germany
e-mail: elke.wendler@uni-jena.de

W. Wesch
e-mail: werner.wesch@uni-jena.de

© Springer International Publishing Switzerland 2016

W. Wesch and E. Wendler (eds.), *Ion Beam Modification of Solids*,
Springer Series in Surface Sciences 61,
DOI 10.1007/978-3-319-33561-2_5

collect sufficient understanding—especially to distinguish between doping and radiation effects—for making ion implantation applicable to semiconductor device production [2]. Since then, demands from industry regarding size and quality of structures to be produced promoted the research in that field, which continues up today.

Ion implantation has become a powerful technique for the precise modification of the properties of semiconductors and other materials. Besides the introduction of foreign atoms the implantation process is inherently connected with the formation of radiation damage which is often undesired for practical applications. The efficiency of subsequent treatments for damage removal such as thermal annealing or irradiation with intense light may strongly depend on kind and concentration of the damage produced. Therefore, a successful technological application of ion implantation requires knowledge about the relationship between implantation conditions and damage formation. Laterally and vertically selected electrical doping is the most common application of ion implantation in semiconductors. In this process radiation damage plays an important role as it may cause transient enhanced diffusion and influences the activation of dopants. In the case of Si for example, assiduous efforts are made to model the as-implanted damage as input for simulation of interaction of damage with dopant atoms during annealing (see [3] and references therein).

In recent years a wide range of semiconductors has become available for fabrication of electronic and optical devices with improved properties or new functionalities. In this process ion implantation is always a matter of choice which stimulates damage studies in these materials. And of course, these studies are also driven by a considerable scientific interest in understanding the fundamentals of ion-solid interaction in these materials. For example, much work has been done for comparison of the susceptibility of various semiconductors to ion-beam induced damage formation and amorphisation which reveals differences in the bonding properties of these materials (see e.g. [4, 5] and references therein).

As to the time span of research and the importance of the field, countless scientific papers appeared dealing with ion implantation of semiconductors. Therefore, it is neither possible nor is it the aim here to summarise all that research. In this chapter trends are shown, how the various implantation parameters influence the formation of radiation damage and to what extend the results for the various semiconductors can be generalised and related to the properties of the corresponding materials. This does not exclude that different microscopic processes occur during ion implantation in the various materials, which is beyond controversy. The results presented here refer especially to the work of the Jena group. According to that, the main focus is directed to binary compound semiconductors with results for silicon (Si) and germanium (Ge) being mentioned for comparison. For ion-beam induced effects in Si and Ge the reader is referred to Chap. 6. Ion beam induced effects in Si are also summarised in [3, 6, 7]. Furthermore, there are many studies on ternary or quaternary compounds which are not included in this chapter. Some information on that can be found in Chap. 6 and [8] and references therein. It should be also mentioned that some semiconductors

(especially Ge and the group III antimonides) become porous under ion irradiation. This effect is not reviewed here and the reader is referred to Chap. 6 and the recent papers [9, 10] with references therein. Finally, a broad overview on the use of ion beams in materials processing and analysis—with special emphasis on ion beam technique—can be found in [11].

Rutherford backscattering spectrometry (RBS) is a technique which is widely used for studying radiation effects in materials. This is true in this chapter for semiconductors as well as in other parts of this book. Therefore, Sect. 5.2 gives a brief introduction to this method. Mechanisms of damage formation are presented for groups of materials which show a certain similarity in their behaviour under ion irradiation. As this part of the book is devoted to effects of nuclear energy deposition, damage formation is investigated which is caused by the displacement of lattice atoms within the collision cascades produced by the implanted ions. The majority of semiconductors can be amorphised in this process and exhibit a continuous damage evolution up to complete amorphisation (see Sect. 5.3). In this section an attempt is made to correlate the cross-section of low temperature damage formation with the primary energies deposited in the displacement of lattice atoms and in electronic interactions. Examples for a discontinuous transition towards amorphisation are given in Sect. 5.4. A few semiconductors cannot be amorphised by ion irradiation, examples for which are presented in Sect. 5.5. And finally, Sect. 5.6 gives a summarising discussion.

5.2 Rutherford Backscattering Spectrometry for Damage Analysis

5.2.1 General Considerations

Rutherford backscattering (RBS) spectrometry is a common method for investigation of composition and structure of crystalline films. There are several books on that topic, which are suggested for further reading [11–14]. Here only a brief introduction will be given.

The geometrical arrangement for RBS measurements is depicted in Fig. 5.1. A well collimated mono-energetic beam of light ions with mass m_1 and energy E_0 (usually helium (He) ions or protons with $E_0 \approx 1$–5 MeV) impinges on a target. Part of the ions are scattered into the half-space above the target (backscattering). The energy of the backscattered ions is registered by a detector the position of which determines the backscattering angle θ (see Fig. 5.1). The signal of the detector is electronically processed (shaped and amplified) and the number of ions is counted as a function of their energy. Thus, the result of the RBS measurement is the number of ions scattered into the detector as a function of the ion energy, which is called RBS spectrum. For given conditions (see Fig. 5.1), the energy of detected

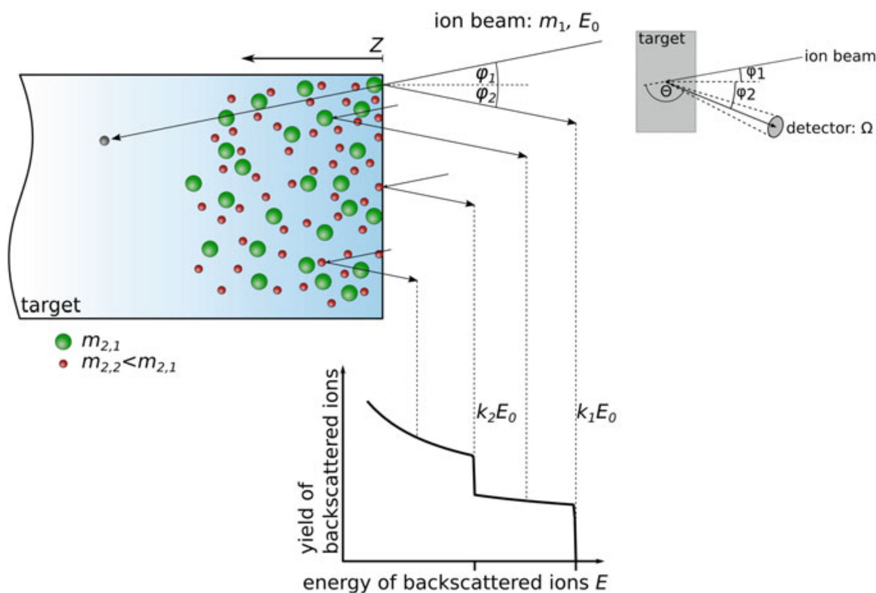

Fig. 5.1 Schematic representation of the geometry in RBS experiments and origin of RBS spectrum for a material composed of two atomic species with masses $m_{2,1} > m_{2,2}$

ions depends on the depth at which and on the mass of the target atom on which the scattering event took place.

After collision (ac) with a target atom of mass $m_{2,\mathrm{i}}$, the energy of the ion is reduced to E_{ac} which can be described by the kinematic factor k according to

$$E_{\mathrm{ac}} = kE_{\mathrm{bc}} \tag{5.1}$$

with k given by

$$k = \left[\frac{\cos\theta + \sqrt{\left(\frac{m_{2,\mathrm{i}}}{m_1}\right)^2 - \sin^2\theta}}{1 + \frac{m_{2,\mathrm{i}}}{m_1}}\right]^2 \tag{5.2}$$

and E_{bc} being the ion energy before collision. When the collision takes place at a certain depth z, the ion additionally undergoes an energy loss dE per unit depth dz on the way in and on the way out. The energy $E_{m_{2,\mathrm{i}}}$ of an ion backscattered on a target atom with mass $m_{2,\mathrm{i}}$ at the depth z—as registered by the detector—is then given by

$$E_{m_{2,i}}(z) = k\left[E_0 - \int\limits_0^{z/\cos\varphi_1}\left(\frac{\mathrm{d}E}{\mathrm{d}z}\right)_{\mathrm{in}}\mathrm{d}z\right] - \int\limits_0^{z/\cos\varphi_2}\left(\frac{\mathrm{d}E}{\mathrm{d}z}\right)_{\mathrm{out}}\mathrm{d}z \tag{5.3}$$

with the angles $\varphi_{1,2}$ being defined as shown in Fig. 5.1. For each atomic species i of the target a separate energy-depth conversion is obtained which is calculated numerically with (5.1)–(5.3). For that, data of the stopping power dE/dz are needed and Bragg's rule is applied for targets consisting of more than one atomic species (see Chap. 1). The stopping powers of Ziegler and Biersack are most commonly used [15].

The yield Y_{ij} of ions backscattered on atoms of kind i within a thin depth interval Δz_{j} at depth z_{j} into the detector with solid angle Ω (see Fig. 5.1) is given by

$$Y_{\mathrm{ij}} = n\left(\frac{\mathrm{d}\sigma}{\mathrm{d}\Omega}\right)_i \Omega \frac{N_{0i}\Delta z_j}{\cos\varphi_1} \tag{5.4}$$

for amorphous materials or random incidence of ions in crystalline materials. Herein $(\mathrm{d}\sigma/\mathrm{d}\Omega)_{\mathrm{i}}$ is the differential Rutherford scattering cross-section for atoms of kind i (see Chap. 1), n the number of incident ions and $N_{0\mathrm{i}}$ the atomic density (number of atoms per unit volume) of component i of the target. The Rutherford scattering cross-section dσ/dΩ is proportional to the atomic number of the corresponding atom squared and to one over the ion energy squared. This means that the yield of backscattered ions increases significantly with increasing atomic number of the target atoms and with decreasing ion energy. The yield of ions backscattered from the different atoms of the target adds up and finally forms the RBS spectrum which is called random spectrum in this case. The chemical composition of the target versus depth z can be determined from the RBS spectrum by using (5.1)–(5.4). The accessible depth usually ranges from few ten nanometers up to few micrometers. A typical random spectrum of a binary material is shown in Fig. 5.2a with the depth scales for the two components being marked (see spectrum 1).

5.2.2 *Analysis of RBS Aligned Spectra*

When the ions enter a monocrystalline solid in direction of a low-index axis, the yield of backscattered ions decreases significantly in comparison to the value given in (5.4). Along the axis, the atoms of the crystal are arranged in rows which form channels. Within these channels the ions perform a guided movement due to the periodic atomic potentials. This is called channelling effect (see Chap. 1). It occurs if the angle Ψ between the ion velocity and the atomic rows is below a critical value Ψ_{c}. The consequence of channelling is the reduction of the probability for the occurrence of backscattering events and thus, the significant decrease of the yield of backscattered ions. The RBS spectra measured in channelling configuration (i.e.

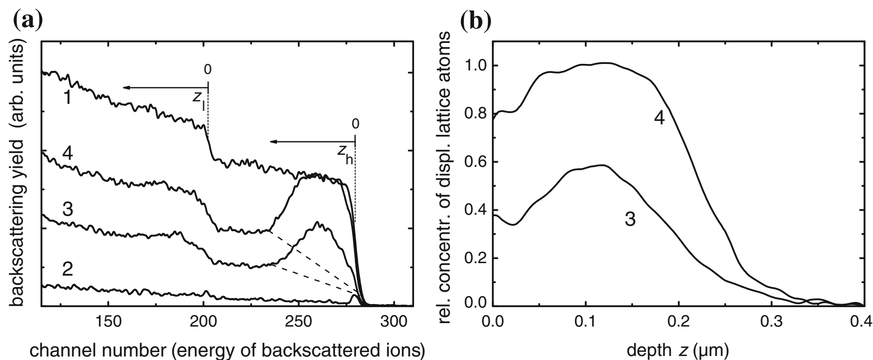

Fig. 5.2 Typical RBS spectra of backscattered He ions for a binary material (**a**). A random spectrum (*1*) and aligned spectra of a perfect (*2*) and two differently damaged (*3*, *4*) crystals are shown. The depth scales for the heavier (h) and lighter (l) component are marked. For the aligned spectra 3 and 4, the dechannelling background is schematically indicated by the *dashed lines*. The depth distributions of randomly displaced lattice atoms calculated from the spectra in part (**a**) are depicted in part (**b**)

with the analysing ions entering the solid along a low-index axis) are called channelling or aligned spectra. An example for that is shown in Fig. 5.2a (see spectrum 2). It can be seen that the height of the aligned spectrum of a perfect crystal is of the order of few percent of that of the corresponding random spectrum. The exact value depends on the ion energy, the crystal under investigation (structure, mass of atoms and quality) and on the temperature of the target. The ratio between RBS yield in aligned (Y_{al}) and random direction (Y_{ra}) is called minimum yield χ_{min} with $\chi_{min} = Y_{al}/Y_{ra}$.

Defects in crystals appear as atoms being displaced from their original lattice sites. Direct backscattering takes place when an ion gets backscattered in a single collision with a lattice atom. Additionally, displaced lattice atoms disturb the movement of the ions within the channels, resulting in an increase of Ψ. When Ψ exceeds the critical angle Ψ_c (see Chap. 1), the guided movement of the ions is ceased and eventually backscattering takes place in a further scattering event. This process is called dechannelling. Both processes occur simultaneously. In case of direct backscattering, backscattering of the ions takes place at the depth at which the displaced lattice atom is located. Backscattering of ions due to dechannelling is the consequence of all defects within the layer the ions traversed up to the depth where the backscattering event takes place. This contribution to the aligned backscattering spectra is usually called dechannelling background. As an example, Fig. 5.2a depicts two aligned RBS spectra of the binary crystal with a damaged surface layer (see spectrum 3 and 4). The dechannelling background is schematically indicated in the figure by the dashed lines. For both untreated (perfect) and damaged (implanted) crystals the minimum yield can be calculated (see above). If the implanted layer is

close to the surface, the difference in minimum yield of implanted and unimplanted (perfect) crystalline sample, $\Delta\chi_{\min} = \chi_{\min}^{\text{impl}} - \chi_{\min}^{\text{perf}}$, can be used as a first estimate to quantify the amount of damage. In case of spectrum 4, the backscattering yield in channelling direction reaches the random level over a certain depth range. This is commonly taken as an indication of amorphisation as visible by RBS.

In case of damaged layers, height and energy dependence of the dechannelling background (see dashed lines in Fig. 5.2a) strongly depend on kind and concentration of defects. Therefore, by means of backscattering spectrometry utilizing the effect of dechannelling, both qualitative and quantitative analysis of various kinds of lattice defects in single-crystalline solids can be performed [12, 13, 16–19]. Ion dechannelling can be caused by uncorrelated multiple scattering processes due to point defects, defect clusters or amorphous regions. And it can be caused by bent channels (within the strain field around dislocations) or by displaced strings or planes (in layers containing stacking faults and twin lamellae), which are both characterized by correlated displaced lattice atoms. To identify the special kind(s) of defects, RBS measurements with different ion energies represent a decisive tool in combination with further methods of analysis as for instance electron diffraction [18]. In case of point defects, i.e. uncorrelated displaced lattice atoms, further information can be obtained by temperature-dependent RBS channelling measurements [13, 19].

In the following text, damage analysis by RBS measurements is restricted to point defects, defect clusters and amorphous regions, which are characterized by uncorrelated displaced lattice atoms. For this type of defects aligned spectra exhibit clear damage peaks as shown in Fig. 5.2a. To extract the concentration of displaced lattice atoms versus depth z from the corresponding aligned and random RBS spectra requires a procedure to calculate and subtract the dechannelling background. This is usually done in an iterative way starting from the surface and taking into account that the dechannelling probability increases with depth, i.e. with increasing area density of defects the ions traversed before becoming backscattered. The dechannelling probability is usually calculated analytically for the type of defects under consideration here. An early two-beam-model was developed by Bøgh [20] and also used by Schmid [21]. A more sophisticated description is given by [22, 23] which is based on the discontinuous model of dechannelling. This model is exploited in the computer code DICADA (**D**echannelling of **I**ons in **C**rystals **A**nd **D**efect **A**nalysis) [16, 22] which was used to obtain most of the data presented here (see examples in Fig. 5.2b). Another more time consuming method for the determination of damage profiles is the simulation of channelling spectra using a Monte Carlo code (see [17, 23, 24] and references therein). If the existing defects are characterized by uncorrelated displaced lattice atoms, within experimental uncertainty all methods yield similar defect profiles [23].

5.3 Continuous Damage Evolution up to Amorphisation

5.3.1 Typical RBS Channelling Spectra of Ion Implanted Semiconductors

Figure 5.3a–c show energy spectra of He ions backscattered on various semiconductors implanted with Ar ions to different ion fluences N_I (number of ions per unit area). The spectra were measured with the He ion beam aligned along the low-index axis parallel to the surface normal of the samples. Random spectra and corresponding aligned spectra of the unimplanted substrates are included for comparison. With increasing ion fluence defects are produced which result in an increasing yield of backscattered ions. At a certain ion fluence, aligned spectra may reach the random level (see Fig. 5.3a) which—as mentioned before—is commonly taken as an indication of amorphisation. Here it should be mentioned that definition of amorphousness is a crucial point. Within a given experimental technique the

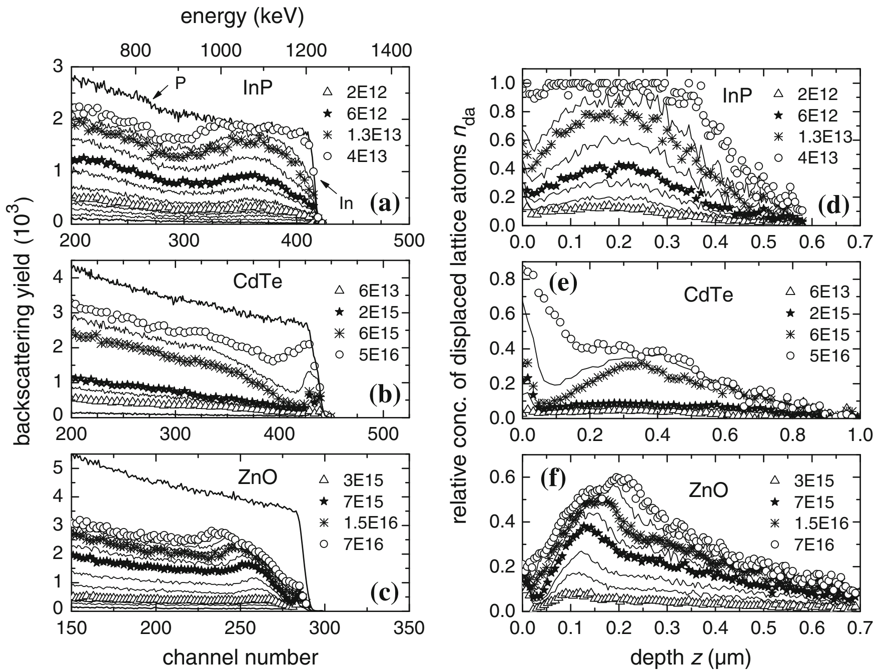

Fig. 5.3 Energy spectra are depicted of 1.4 MeV He ions backscattered on InP (**a**), CdTe (**b**) and ZnO (**c**) which were implanted with Ar ions and analysed at the implantation temperature of 15 K. In each part, the random spectrum is the upper thick solid line and the aligned spectrum of the unimplanted substrate is the lower thick solid line. The corresponding relative concentration of displaced lattice atoms versus depth, $n_{da}(z)$, is given in parts (**d**) to (**f**). The energy of Ar ions was 350 keV for InP [25], 270 keV for CdTe [26] and 200 keV for ZnO [27]. The ion fluences are given in cm^{-2}. For clarity only selected ion fluences are given

saturation of the measured quantity is usually attributed to amorphisation. But different techniques may have a different sensitivity (see also discussion in Sects. 3.2.4 and 3.4.1). This has to be taken into account when comparing results obtained with different experimental methods. For the case of RBS for example it is known that reaching the random level within a small depth interval only, does not necessarily mean that a closed amorphous layer as visible by transmission electron microscopy (TEM) has formed. But this is not or less relevant when results of one and the same experimental method are compared.

The yield in Fig. 5.3a–c is given versus the channel number with each channel representing an ion energy width $E \ldots E + \Delta E$. For the case of InP (Fig. 5.3a) the ion energy E is given in the upper scale for comparison. The on-set of backscattering for the two components at $z = 0$ is indicated in the figure. It occurs at $E = 1219$ keV for In and 836 keV for P (see Fig. 5.3a). That is, for ion energies below 836 keV, i.e. below channel number 271, the yield of ions backscattered on P atoms is superimposed to that backscattered on In atoms at larger depths. Therefore, the evaluation of RBS spectra as explained in Sect. 5.2.2 is usually performed for the high-energy part of the spectra only which results from the heavier component of the material.

Figure 5.3d–f show the relative concentration of displaced lattice atoms n_{da} versus depth z calculated from the backscattering spectra given in Fig. 5.3a–c with DICADA assuming the existence of uncorrelated displaced lattice atoms. n_{da} is often called defect or damage concentration and $n_{da}(z)$ defect or damage profile for short. From Fig. 5.3d, e it can be seen that the defect concentration reaches zero at the end of the implanted layers. This suggests that the assumption of uncorrelated displaced lattice atoms existing within the implanted layers describes well what is observed. This indicates that the occurring defects are mainly point defects, defect clusters and amorphous zones. It should be mentioned that for ion implanted CdTe the aligned spectra do not show a pronounced damage peak (except the one at the surface) but a knee-like shape around channel number 370 (see Fig. 5.3b). The peak in the damage profile around $z \approx 0.35$ µm (see Fig. 5.3e) follows from that knee. This result demonstrates that the relatively high dechannelling background—which causes the knee-like structure of the spectrum—is strongly related to the high mass of the target atoms in this case [26]. A more sophisticated analysis of RBS measurements performed with different ion energies reveals that the layers contain also a small amount of correlated displaced atoms, i.e. some extended defects [28]. This example demonstrates that care has to be taken when interpreting the results of channelling RBS measurements. In the case of ion implanted ZnO the damage profiles do not reach zero even at large depths (see Fig. 5.3f). In such a case additional experimental techniques as for instance TEM have to be applied to check up to which depths defects really exist. With respect to the RBS analysis, it can be shown that artificial tails in the damage profile occur if the assumption of randomly displaced lattice atoms made to extract the profiles from the spectra is not correct [27]. Thus the occurrence of these tails indicates the existence of correlated displaced lattice atoms which occur in case of extended defects within the defective layer. For ion implanted ZnO it was shown that similar profiles are obtained for

implantation at room temperature (RT) and at 15 K [29]. The existence of extended defects in ZnO after implantation at RT was proven by TEM (see [30] and references therein) which is in agreement with the conclusions drawn from the RBS channelling measurements. From the examples shown in Fig. 5.3 only InP represents an example of the group of amorphisable materials exhibiting a continuous transition towards amorphisation, which are under consideration in the following subsections. A more detailed discussion of ion implantation induced effects in CdTe and ZnO will be given in Sect. 5.5.

5.3.2 Introduction of Critical Temperatures and Effect of Ion Flux

At sufficiently low temperatures (what this means will be specified below) many semiconductors can be amorphised by ion implantation with the damage concentration increasing continuously up to the final value representative for amorphisation. This is the case for SiC, Si, Ge, InSb, InAs, InP, GaSb, GaAs, GaP and some ternary compounds as $Al_xGa_{1-x}As$, $In_xGa_{1-x}As$ and $In_xGa_{1-x}P$. In the latter materials the damage evolution and amorphisation kinetics are remarkably influenced by the stoichiometry of the compounds. For more details the reader is referred to [8] and references therein. Examples for the evolution of damage profiles are shown in Fig. 5.4 which presents results for InP implanted with 300 keV Si ions and 600 keV Se ions to different ion fluences at different temperatures [31]. The corresponding RBS measurements were carried out at RT. For all temperatures applied here, a damage peak evolves which increases with increasing ion fluence until $n_{da} = 1$ is reached which is commonly taken as an indication of amorphisation (see Sect. 5.2.2). A further increase of the ion fluence results in a broadening of the amorphous layer towards the surface and into the depth. For a given ion fluence, the damage concentration remaining after implantation decreases with increasing temperature (cp. results for 1×10^{14} cm^{-2} in Fig. 5.4a–c). This can be attributed to dynamic defect annealing during the irradiation, which becomes more prominent with rising temperature and is a typical effect occurring in all semiconductors. The ion fluence at which the damage concentration $n_{da}(z)$ reaches unity in the maximum of the distribution is referred to as amorphisation fluence N_I^{am}. From Fig. 5.4 it is obvious that—for a given ion species—N_I^{am} increases with increasing temperature during implantation.

Figure 5.5a plots the amorphisation fluence as a function of the implantation temperature for various ion species implanted into InP. The curves shown in the figure are fitted to the experimental data applying the vacancy-out-diffusion model [32] which is explained in detail in Chap. 3. This model assumes that cylindrical amorphous clusters produced by individual ions shrink with increasing temperature due to a thermally activated vacancy out-diffusion and defect recombination at the

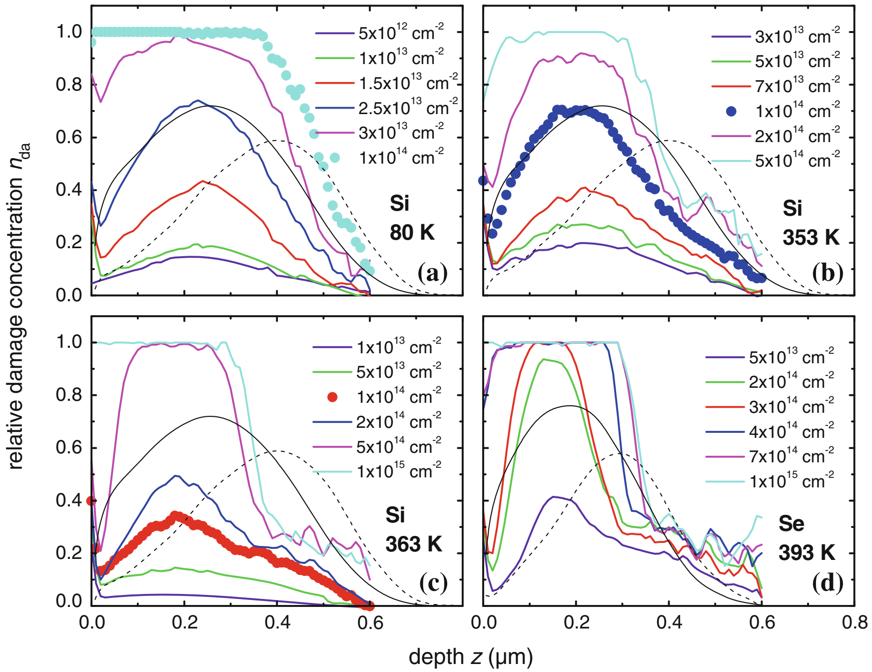

Fig. 5.4 Damage profiles $n_{da}(z)$ for InP implanted with 300 keV Si or 600 keV Se ions at different temperatures to various ion fluences [31]. The distribution of primary displacements (*solid lines*) and the ion distributions (*dashed lines*) are given for comparison in arbitrary units. They were calculated with SRIM [15] using the displacement energies given in Chap. 3

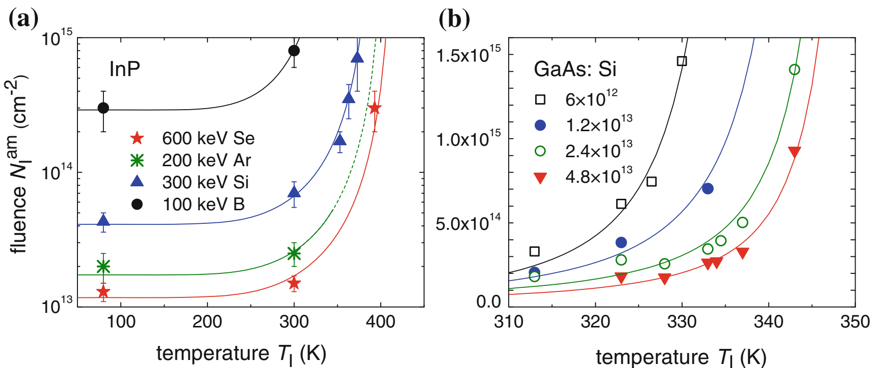

Fig. 5.5 Amorphisation fluence N_I^{am} versus temperature of implantation T_I (**a**) for different ion species implanted into InP and (**b**) for GaAs implanted with 95 keV Si ions applying different ion fluxes (given in cm^{-2} s^{-1}). The *lines* are fitted to the experimental data using (5.5) (for details see [31, 40]). Notice the different ordinate scales used in part (**a**) and (**b**)

amorphous/crystalline interface. Within this model the ratio of amorphization fluence at temperature T_I to amorphization fluence at T_I = 0 K, $N_\mathrm{I}^{\mathrm{am},0}$, follows to

$$\frac{N_\mathrm{I}^{\mathrm{am}}}{N_\mathrm{I}^{\mathrm{am},0}} = \left[1 - C\,\exp\left(-\frac{E}{2k_B T_\mathrm{I}}\right)\right]^{-2}. \tag{5.5}$$

The parameters $N_\mathrm{I}^{\mathrm{am},0}$, C and E were adjusted to represent the experimental data and k_B is Boltzmann's constant. As can be seen, a good fit is obtained for all ion species used. The curves in Fig. 5.5a reveal that for each ion species the amorphisation fluence $N_\mathrm{I}^{\mathrm{am}}$ becomes infinity at a certain temperature. These temperatures are called critical temperatures T_c. Similar results with respect to the temperature dependence of the critical ion fluence necessary for amorphisation, $N_\mathrm{I}^{\mathrm{am}}$, are also found for other semiconductors like SiC [33, 34], Si [32, 35, 36], Ge [32], InAs [37] and GaAs [38–40], with the experimental data being represented by (5.5).

Besides (5.5) further models exist to represent the temperature dependence of ion-induced damage formation (see Chap. 3). In the case of ion implanted SiC a successful representation of experimental data succeeded by incorporating temperature effects in a damage rate theory which yields a similar result as given in (5.5) (see Chap. 3 and references therein). Although the various concepts are slightly different, they all take into account Arrhenius-like temperature dependencies of relevant quantities. Correspondingly, the parameter E in (5.5) has the meaning of an activation energy. However, the physical interpretation is very crucial. First, the assumption of amorphisation within single ion impacts is often not fulfilled and second, more than one thermally activated process may be active (see Chap. 3.4). The latter would result in further terms in the brackets of (5.5) and correspondingly more free parameters which cannot be deduced from dependencies as shown in Fig. 5.5. Therefore, the fit parameters C and E are commonly used to calculate the critical temperatures T_c only (see Chap. 3). Finally it should be mentioned that the vacancy out-diffusion model can be also applied to model the damage concentration n_da for a given ion fluence at a fixed depth as a function of the temperature of implantation T_I. It is given by [39]

$$n_\mathrm{da} = \frac{N_\mathrm{I}^{\mathrm{am}}}{N_\mathrm{I}^{\mathrm{am},0}}\left[1 - C\,\exp\left(-\frac{E}{2k_B T_\mathrm{I}}\right)\right]^{2}. \tag{5.6}$$

An example for that is depicted in Fig. 5.6 for Si ion implanted InP with the data taken from Fig. 5.4. However, it was shown that this calculation overestimates the damage concentration in GaAs implanted with Si ions to low ion fluences, i.e. low damage concentrations [39]. This indicates that the assumption of direct-impact amorphisation does not apply. Another reason for the observed behaviour may be that some samples had to be warmed to RT before analysis. Figure 5.7 shows that this warming of the samples causes significant damage annealing in GaAs (and also in InP) especially for low damage concentrations [38, 41]. Contrary, close to maximum damage with $n_\mathrm{da}^{\max} \approx 1$ almost no annealing is observed which often

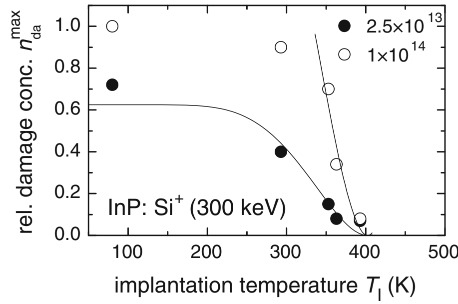

Fig. 5.6 Relative damage concentration in the maximum of the measured distribution, n_{da}^{max}, versus temperature T_I for 300 keV Si ion implantation of InP. Results from Fig. 5.4 are plotted as symbols for two different ion fluences (given in cm^{-2}). The *lines* are fitted to the data using (5.6)

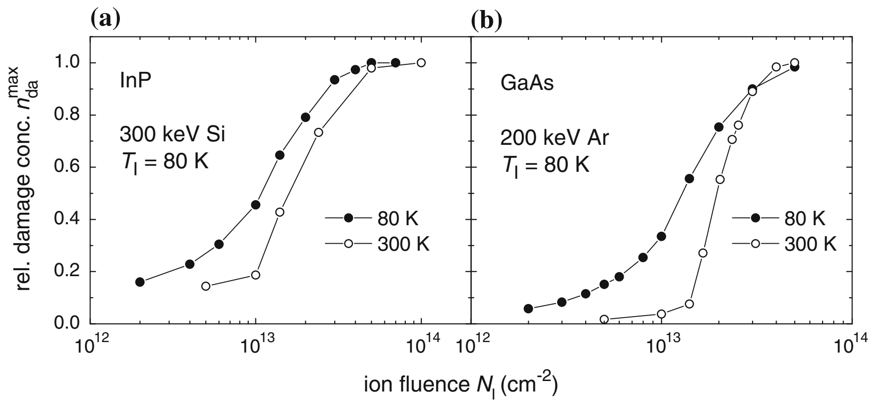

Fig. 5.7 Relative damage concentration in the maximum of the measured distribution, n_{da}^{max}, versus ion fluence N_I for InP implanted with 300 keV Si ions (**a**) and GaAs implanted with 200 keV Ar ions (**b**) [38]. Damage analysis by RBS was performed immediately after implantion at 80 K and after warming the samples to RT

favours the application of (5.5) for the determination of critical temperatures. Similar curves as shown in Fig. 5.6 were successfully used for extracting critical temperatures in Si ion implanted SiC [42] in which the damage produced was found to be rather stable.

From the curves in Fig. 5.5a it becomes obvious that the critical temperature T_c for InP is not a fixed value but varies over a certain range. It is further found that T_c varies with the ion flux ϕ for a given ion-energy/target combination. This is shown in Fig. 5.5b which plots the amorphisation fluence versus temperature for 95 keV Si ions implanted into GaAs with different ion fluxes [40]. The variation of the critical temperature with ion mass and ion flux is observed in other semiconductors as well. But the range and in particular the lower limit of T_c is different for the

Table 5.1 Estimates of lower limits of critical temperatures T_c of ion implanted semiconductors, which follow from implantation of B ions in most cases

Material	Lower limit of T_c (K)	Annealing stage T_a (K)	Reference suggested mechanism
SiC	290	300 330–390	Recombination of close Frenkel pairs [43] annealing stage [44]
Si	300		
Ge	350		
GaP	330[a]	300–500	Annealing stage [45]
GaAs	230	250–350	Mobility of Ga interstitials [46] Annealing stage [45]
InP	340	330–420	Mobility of P interstitials [47] Annealing stage [45]
InAs	<300		

The temperature ranges of known annealing stages and the corresponding references are given for comparison. References for T_c are given in the text
[a]See [38]

various materials. Estimates of the lower limits of the critical temperatures are summarised in Table 5.1. They are compared with known annealing stages of intrinsic defects in the corresponding materials. Table 5.1 shows that some correspondence between the lower limit of T_c and annealing stages of intrinsic defects occurs, at least in the case of III–V compounds. Of course, the processes within the collision cascade of an implanted ion are very complex and various types of point defects may occur and interact with each other. But never the less, a thermally activated mobility of defects is the main concept for introducing the critical temperatures. Therefore, it is assuring to observe some correspondence with the mobility of intrinsic defects.

Figure 5.5 shows that the critical temperature T_c increases with increasing ion mass and with increasing ion flux. An increase of T_c means a lower amorphisation fluence N_I^{am} for a fixed implantation temperature with $T_I < T_c$ (see Fig. 5.5). When N_I^{am} decreases, then the damage to be expected for a given ion fluence N_I increases (provided the regarded fluence is below N_I^{am}). This means, the statement that T_c increases with increasing ion flux ϕ is equivalent to the statement that the damage remaining after implantation increases with increasing ion flux for a given ion fluence and fixed temperature. And this is what usually is observed for the semiconductors under consideration here (see e.g. [39, 48, 49]). Figure 5.8 shows an example for 100 keV Si ions implanted into Ge and GaAs [39] which clearly reveals the increase of integral damage concentration (which follows from the absolute concentration of displaced lattice atoms integrated over the depth) with rising ion flux ϕ. It is found that the integral damage concentration increases proportional to ϕ^n with $n \approx (0.1 \ldots 0.8)$. The strength of the flux dependence is represented by the exponent n which increases with rising temperature during implantation. From Fig. 5.8 it is obvious that at RT the ion flux dependence is weak

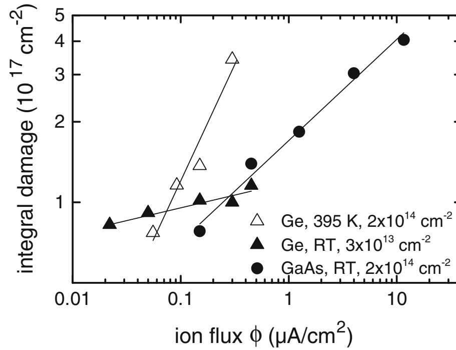

Fig. 5.8 Integral damage concentration versus ion flux ϕ for 100 keV Si ions implanted into Ge and GaAs at different temperatures [39]

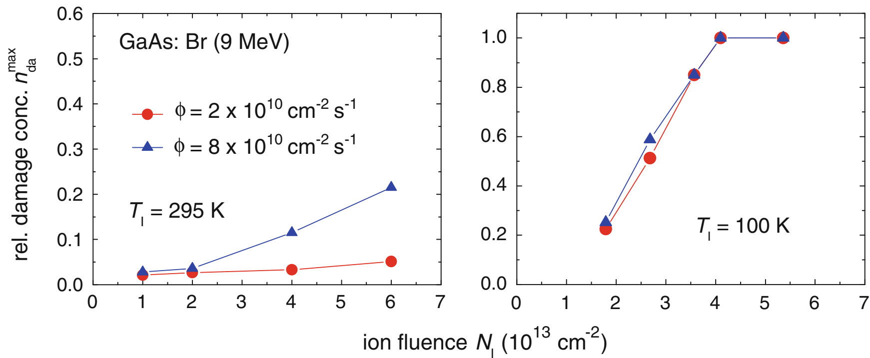

Fig. 5.9 Relative damage concentration in the maximum of the measured distribution, n_{da}^{max}, versus ion fluence N_I for Br ions implanted into GaAs at two different ion fluxes and two different temperatures [50]

in Ge and strong in GaAs. When ion implantation of Ge is performed at 395 K, a similarly strong flux dependence is found in Ge as in GaAs at RT. That is both materials exhibit a similar behaviour but at temperatures which are different by about 100 K. This difference corresponds to that of the lower limit of the critical temperatures T_c for the two materials (see Table 5.1). Another example for the effect of implantation temperature and ion flux on damage formation is given in Fig. 5.9 for Br implanted GaAs [50]. This figure again demonstrates that the flux dependence is stronger at higher temperatures (for corresponding results in InP see [51]). This means the flux dependence becomes more pronounced the closer the implantation temperature is to the critical temperature T_c (see also Fig. 5.5b) or better to the lower limit of it because the ion flux itself influences T_c.

As already mentioned above, the critical temperature T_c depends on ion flux and ion mass (see Fig. 5.5). The effect of the ion mass is better represented by that of

the number of primary displacements per ion and unit depth, N^*_{displ}. This quantity can be converted to the primary damage cross-section σ_d by $\sigma_d = N^*_{\text{displ}}/N_0$ with N_0 being the atomic density of the corresponding material (see Chap. 3). It was shown by a damage rate theory that an ion-flux dependence of T_c indicates that thermal recovery processes are dominant during the implantation (see Chap. 3 and references therein). In this case T_c is given by

$$T_c = \frac{E_{\text{th}}}{k_B \ln(\nu_{\text{th}}/\sigma_a\phi)}. \tag{5.7}$$

Herein ν_{th} is the effective jump frequency and E_{th} the activation energy. σ_a is the cross-section of amorphisation at zero temperature. Equation (5.7) can be changed to

$$\sigma_a\phi = \nu_{\text{th}} \exp\left(\frac{E_{\text{th}}}{k_B T_c}\right). \tag{5.8}$$

Such a relation between ion flux ϕ and critical temperature T_c was found for GaAs implanted with various ion species [40]. Because σ_a is often not known, the primary damage cross-section σ_d calculated by SRIM as described above, is usually taken for replacing σ_a in (5.8). For ion implanted GaAs $\sigma_d\phi$ was plotted versus T_c (see Fig. 3.10 of Chap. 3 and Fig. 6.16 of Chap. 6). From this plot for all ion species implanted into GaAs an activation energy E_{th} of 0.9 eV was obtained. In the case of ion implanted SiC E_{th} = 0.6 eV was obtained [34]. An activation energy of E_{th} = 1.1 eV was found for ion implanted InP and InAs [37]. In the latter cases $\sigma_d^2\phi$ instead of $\sigma_d\phi$ followed the dependence given in (5.8). The dependence on ${\sigma_d}^2\phi \propto \exp[E_{\text{th}}/(kT_c)]$ was experimentally found and theoretically motivated for ion-beam induced effects at amorphous/crystalline interfaces (see [52, 53] and Chap. 3) but could be successfully applied also for ion implantation in pristine III-V compounds [38].

From the discussion above two conclusions can be drawn. (i) The semiconductors under consideration here exhibit a similar damage evolution if the temperatures at which the experiments are carried out are similarly close or similarly far away from the critical temperature for the corresponding conditions of implantation. This statement will be further verified in the following subsections. At temperatures well below the corresponding critical temperature T_c the ion flux becomes less important and the transition towards amorphisation proceeds continuously (see Sect. 5.3.4). That is sufficiently low temperatures—as mentioned at the beginning of this section—means temperatures being well below T_c. (ii) It can be suspected that damage formation in semiconductors is subject to a complicated interplay of target temperature T_I and ion flux ϕ when $T_I \ll T_c$ is not valid. This will be discussed in more detail in Chap. 6.

5.3.3 Depth Distribution of Damage and Effect of Ion Energy

For the ion energies under consideration here, damage formation is mainly caused by the nuclear interaction of the incoming ions and the lattice atoms. In case no secondary processes occur, one would therefore expect that the measured damage concentration versus depth agrees with the calculated depth distribution of displaced lattice atoms—at least with respect to the position of the maximum and the shape. When implantation and measurement are done at a temperature well below the critical temperature, this is indeed the case (see e.g. [5, 27]). This is also visible in Fig. 5.4a for InP implanted with Si ions at 80 K for which a reasonable agreement between the measured and the calculated distribution is observed. A very good agreement between measured and calculated profiles may occur also for higher ion energies as shown for example for 10 MeV Au ions in GaAs and implantation and measurement at very low temperature [54]. For certain ion-energy/target combinations, however, deviations with respect to the position of the maximum may occur which can be caused by uncertainties in the energy loss data [55]. When the temperature during implantation increases towards the critical temperature, the measured heavily damaged layers become thinner compared to those implanted at very low temperatures. This can be seen in Fig. 5.4 for InP implanted with Si ions at 80, 353 and 363 K. The reduction in layer thickness is obviously caused by an enhanced defect recombination and annealing at the interface to the unirradiated substrate. Furthermore, Fig. 5.4 shows that the strength of this effect is similar for Si implantation at 363 K and Se implantation at 393 K. In both cases the implantation temperature is about 30 K below the corresponding critical temperature. As already mentioned above, similar effects are to be expected for different ion masses provided that the difference between target temperature and corresponding critical temperature is similar for the given material. A significant reduction of the thickness of the heavily damaged layer was also found in GaAs implanted with 280 keV N ions at RT with a rather high ion flux of 1.25×10^{13} cm^{-2} s^{-1} (see Fig. 5.10). Since RT is very close to the critical temperature of N implanted GaAs, this finding is clearly a combined effect of temperature and ion flux. In Fig. 5.10 depth profiles of damage are depicted which were obtained by optical sub-gap spectroscopy in combination with successive chemical etching of the implanted layer. In GaAs this method allows to quantify the contribution of heavily damaged/amorphous regions and of defective crystalline regions containing point defects and point defect complexes (see [56, 57]). By this method it is observed that the total thickness of the damaged layer is still as expected from the primary nuclear energy deposition, but it consists of a heavily damaged part close to the surface and a defective crystalline part at the interface to the un-irradiated substrate. The latter may be interpreted as point defects or small dislocation loops left after damage annealing in this depth range. This finding is consistent with the RBS results shown in Fig. 5.4 for InP. At the elevated temperatures (see Fig. 5.4c, d) the damage concentration measured by RBS tends not to

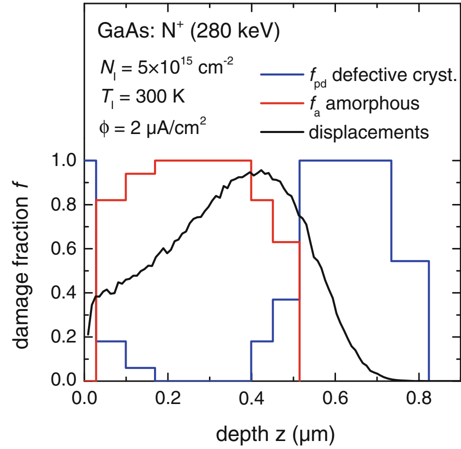

Fig. 5.10 Fraction of heavily damaged/amorphous material f_a and defective crystalline material f_{pd} as obtained by optical absorption measurements versus depth z for GaAs implanted with 280 keV N ions (for details see text; [49]). The distribution of primary displacements is included in arbitrary units for comparison. The applied beam current of 2 µA/cm^2 corresponds to an ion flux of 1.25×10^{13} cm^{-2} s^{-1}

reach zero behind the heavily damaged layers as it is the case for implantation at 80 K. This observation may have two origins: (i) there are still defects at that particular depth and (ii) the surface layer contains a mixture of heavily damaged material and extended defects. In the case under consideration here it is to be expected that both effects influence the measured depth distribution of damage. An even stronger defect diffusion into the underlying crystalline substrate may occur if the implantation temperature is even closer to the corresponding critical temperature and the ion flux is sufficiently small which results in longer implantation times [31].

The nuclear energy loss of the implanted ions occurs at the end of their range when the current energy is falling below a certain value. Before that, the electronic energy loss is dominating which has no detectable effect in semiconductors for the ion energies under consideration in this part (for influence of electronic energy loss in semiconductors see Chap. 9). The consequence is that with increasing ion energy the position of maximum primary displacements and correspondingly the position of maximum damage shift into larger depth. This is demonstrated in Fig. 5.11 for Br ions in GaAs for different ion energies. This figure also shows that the longer path of ions at high ion energies is connected with a stronger straggling resulting in a broadening of the distribution and a reduction of the maximum value with increasing ion energy. Since the mass of the ions does not change, the density of the collision cascades at the end of range of the individual ions is always the same. Considering a certain voxel within the sample close to the maximum of the distribution, the low straggling at lower ion energies means that this voxel is much more often struck by ions than a corresponding voxel for a high ion energy. In other words, the enhanced straggling of the ions over the depth results in a reduction of the local ion flux at a fixed depth. This so-called local ion flux decreases with increasing ion energy even if the real macroscopic ion flux is the same for all ion energies. From that it can be suspected that the damage concentration measured in the maximum of the distribution depends on the ion energy if for the given implantation conditions the material is susceptible to the macroscopic ion flux. This

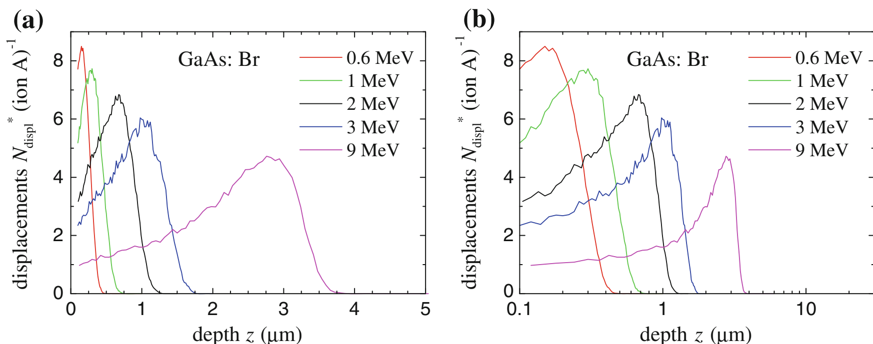

Fig. 5.11 Number of displacements per ion and unit depth, N^*_{displ}, versus depth z for Br ions implanted into GaAs with different ion energies calculated with SRIM. Part (**a**) has a linear depth scale for demonstrating the increasing broadness of the distribution with increasing ion energy. For better visibility of all distributions in following figures a logarithmic depth scale is used as demonstrated in part (**b**)

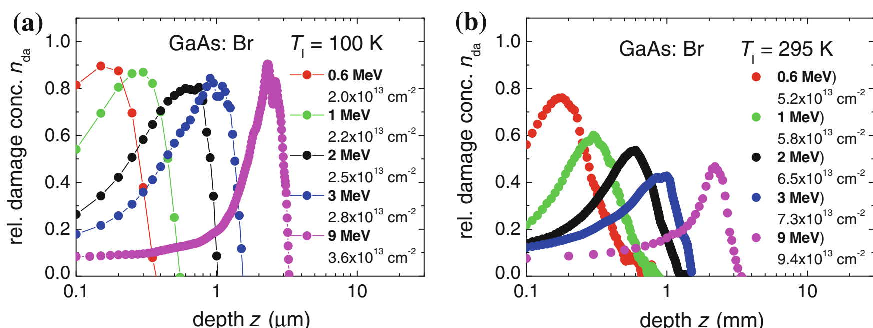

Fig. 5.12 Damage profiles $n_{da}(z)$ for Br ions of different energy implanted into GaAs at 100 K (**a**) and at RT (**b**) [50]. Notice the logarithmic depth scale. Combinations of ion fluence and ion energy are chosen for obtaining the same number of displacements per unit volume within the maximum of the distribution at each temperature. For details see text

effect was studied in detail in Br implanted GaAs for ion energies between 0.6 MeV and 9 MeV [50]. Figure 5.12 shows corresponding damage profiles for implantation of Br ions at 100 K (a) and at 295 K (b). The ion fluence was chosen to reach an equal number of primary displacements in the maximum of the distribution, i.e. an equal energy deposition in the displacement of lattice atoms for all ion energies. For quantifying this, the normalised ion fluence n_{dpa} is used which is given by $n_{dpa} = N_I N^*_{displ}/N_0$ using N^*_{displ} in the maximum of the distribution calculated with the displacement energies given in Chap. 3. The ion fluences were chosen to obtain n_{dpa} = 1 dpa at 295 K and n_{dpa} = 0.4 dpa at 100 K in the maximum of the distribution. Figure 5.12a shows that for implantation at 100 K for all ion energies

applied, almost the same maximum damage concentration is found. This means that the ion energy does not cause any special effects. In contrast, for implantation at RT the maximum damage concentration decreases with increasing ion energy, although the ion fluence was adjusted to obtain equal n_{dpa} values. This means that the local flux is not important at 100 K, whereas it is important at RT. This finding is in very good agreement with the results obtained when varying the (real macroscopic) ion flux (see Fig. 5.9). It is also consistent within the concept of critical temperatures as 295 K is close to but 100 K is well below the critical temperatures of GaAs (see Table 5.1). A similar effect was observed for ion implanted Si for which the critical ion fluence necessary for amorphisation increases with increasing ion energy [35].

5.3.4 *Fluence Dependence and Effect of Ion Mass*

As already mentioned above, the semiconductors under consideration here exhibit a continuous transition towards amorphisation for temperatures well below the critical temperature, i.e. for $T_{\mathrm{I}} \ll T_{\mathrm{c}}$. An example for that is shown in Fig. 5.13 which plots the damage concentration in the maximum of the measured distribution versus ion fluence for various ion species implanted into 4H-SiC at 15 K [58]. Similar results were found for GaAs, InP, Ge and Si ion implanted at low temperatures. Various models exist for explanation of such a transition to amorphisation (see Chap. 3). In general, the concepts behind are similar: A certain amount of damage is produced within each ion impact and additionally ion-beam induced effects are assumed, which occur when the ion fluence increases and the ion impacts start to overlap. The similarity of the concepts is expressed in the similarity of the fluence

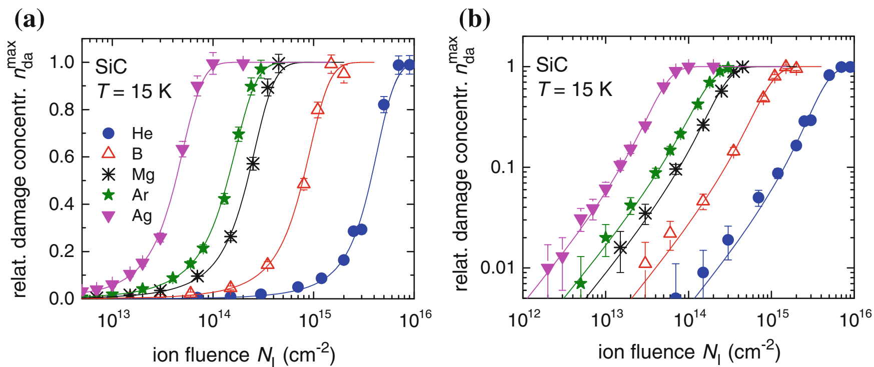

Fig. 5.13 Relative damage concentration in the maximum of the measured distribution, $n_{da}^{\max}$, versus ion fluence N_{I} for various ions species implanted into SiC at 15 K [58]. The *lines* are fitted to the experimental data applying (5.9). For better visibility of all data, part (**a**) has a linear and (**b**) a logarithmic ordinate scale. Both ion implantation and subsequent damage analysis by RBS were made at T = 15 K

dependencies which can be generated by the various models (see Chap. 3). In recent time it became common to apply rate equations that take into account damage formation within the direct ion impacts with the cross-section σ_{dam} and stimulated growth of damage with the cross-section σ_s. This results in (see Chap. 3 and references therein)

$$\frac{dn_{da}}{dN_I} = (\sigma_{dam} + \sigma_s n_{da})(1 - n_{da}). \tag{5.9}$$

For this equation an analytical solution exists (see Chap. 3) which makes it comfortable to use common fitting procedures for the determination of σ_{dam} and σ_s (see e.g. [58]). The curves in Fig. 5.13 are fitted to the experimental data applying (5.9). It can be seen that a satisfactory fit is obtained which means that (5.9) gives a good description of what is experimentally observed. This holds well in many other cases, too. In [59] a detailed analysis is given how thermal and ion-beam induced effects could be distinguished. Following the discussion of this paper, the stimulated growth of damage—when observed at $T_I \ll T_c$—can be regarded as a purely ion-beam induced effect. In a simple picture a collision cascade can be thought to consist of regions which are heavily damaged contributing significantly to the backscattering of analysing He ions, and of those which are only weakly damaged containing point defects or small clusters of them which contribute only weakly to the backscattering of He ions. Within such a picture, the heavily damaged regions mainly contribute to what is called direct-impact-damage and the weakly damaged regions are relevant for the stimulated growth of damage. The latter can be interpreted in two main ways. (i) The weakly damaged regions need to overlap for the point defects to agglomerate into larger complexes which are then more visible to the ion beam. Such a process may be driven by the strain introduced by the point defects. A possible mechanism of amorphisation is the transformation of material into the amorphous state when the strain introduced by point defects exceeds some critical value (see [60] and references therein). (ii) When the point defects are close to a heavily damaged cluster produced by previous ions, the latter clusters can grow by a process which is known as ion beam induced interfacial amorphisation (IBIIA) [52, 61]. It is interesting to note that in most cases the cross-section of stimulated growth σ_s is by a factor of 10…20 larger than the cross-section of direct impact damage formation σ_{dam} [25, 58, 62]. However, one needs to keep in mind that all data behind were determined from RBS studies. Thus the observed relation σ_s/σ_{dam} may be related to the sensitivity of this particular method. Therefore, it would be desirable to have similar data measured with other techniques for comparison.

The cross-section σ_{dam} is the area integral over the relative damage concentration produced per ion at the depth at which the corresponding data are taken. If one assumes a homogeneous damage distribution across the area, σ_{dam} is given by the product of the area and the relative damage concentration produced per individual ion. If one further assumes that each ion produces an amorphous cluster corresponding to a relative damage concentration per ion equal to unity, then σ_{dam} is the area damaged by one ion at the corresponding depth. Then the cross-section σ_{dam}

can be used for estimating the diameter of such a cluster. In doing so it may happen that the diameter of the amorphous clusters is of the order of the distance between nearest neighbours in the corresponding crystal only. This means the cluster would consist of very few atoms only for which an amorphous state cannot be defined. Such a finding suggests that the assumption of complete amorphisation within a single ion impact is not correct. This in turn may lead to the conclusion that within the primary collision cascades mainly point defects or clusters of point defects are produced. Such a behaviour is often observed for implantation of light ions such as He ions (see e.g. [62]). In these cases one may suspect that amorphisation does not occur heterogeneously by direct ion impacts but homogeneously on a finer scale by the coalescence of point defects and point defect complexes as suggested for ion implanted SiC [63]. The predominant formation of point defects after implantation of light ions such as H and He in crystalline semiconductors (i.e. at low ion fluences) was also concluded from the evolution of strain and microhardness as a function of damage detected by RBS [64, 65].

For studying the effect of ion mass, the ion fluence N_I is usually converted to the number of displacements per lattice atom, n_{dpa}, by using the number of displacements per ion and unit depth, N^*_{displ}, in the maximum of the calculated distribution. Examples for damage production curves n^{max}_{da} versus n_{dpa} are shown in Fig. 5.14. Corresponding results for GaAs are given in Fig. 3.8 of Chap. 3. If the damage formation would only depend on the total amount of energy per unit volume deposited in the displacement of lattice atoms, for all ion species a uniform dependence should be observed. From Figs. 5.14 and 3.8 of Chap. 3 it can be seen that this is obviously not the case even though implantation and analysis were performed at a rather low temperature at which thermal effects can be assumed to be negligible. Especially in the case of light ions much more energy has to be deposited per unit volume for obtaining a certain amount of damage than for heavier ions. Only for ion masses above a certain value mass-independent, uniform dependencies are found. The deviation for light ions is in coincidence with the discussion given above regarding the radii of the damage clusters, from which a different mechanism of amorpisation could be concluded in these cases. Further, from Fig. 5.14 it can be seen that the fit with (5.9) succeeds better for InP than for SiC which is another hint to the somewhat different mechanisms occurring in this material as mentioned above. In agreement with that it was found that a nucleation and growth model (see Chap. 3) allows a slightly better representation of the damage evolution in SiC [66]. Furthermore, the results in Figs. 5.14 and 3.8 of Chap. 3 indicate non-linear effects to occur within the primary collisions cascades (see Sect. 5.6).

For the examples in Figs. 5.14 and 3.8 (Chap. 3) the ion energies were chosen such as to obtain similar thicknesses of the implanted layers for all ion species. In this case the decrease of the maximum value of N^*_{displ} with decreasing ion mass reflects the decreasing density of the primary collision cascades. It should be noted that this situation is different compared with that for which the ion energy is varied for a given ion species (see Fig. 5.11). As discussed in Sect. 5.3.3, in the latter case

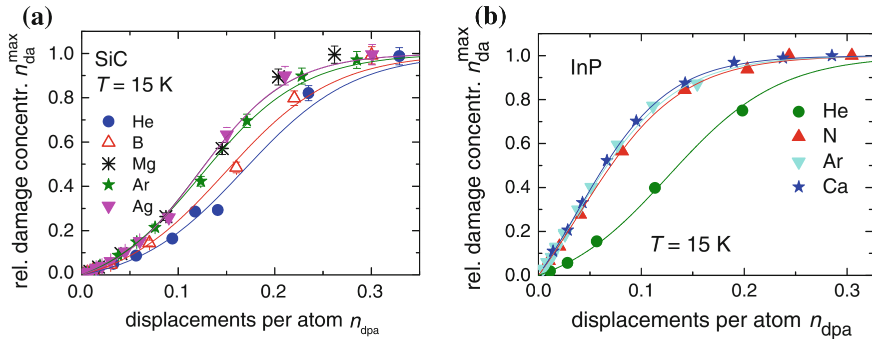

Fig. 5.14 Relative damage concentration at the maximum of the distribution, n_{da}^{max}, versus the number of displacements per lattice atom, n_{dpa}, (**a**) for ion implanted SiC (data are taken from Fig. 5.13) and (**b**) for 30 keV He, 150 keV N, 350 keV Ca and 350 keV Ar ions implanted into InP [62]. In both cases ion implantation and subsequent damage analysis by RBS were made at $T = 15$ K

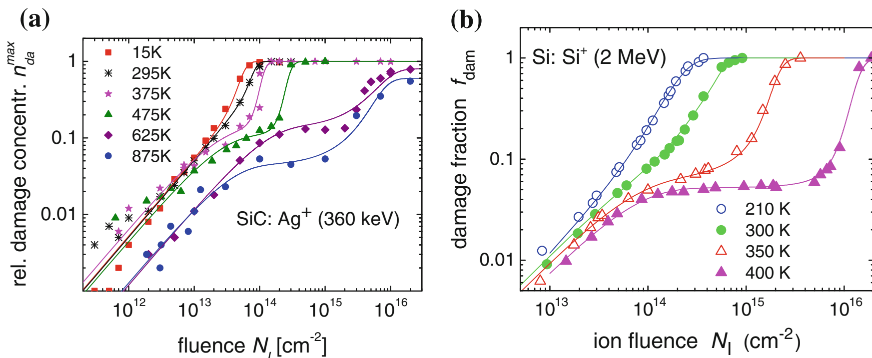

Fig. 5.15 Relative damage concentration in the maximum of the measured distribution versus ion fluence N_I (**a**) for Ag ions implanted into SiC [67] and (**b**) for Si ions implanted into Si [68] at various temperatures. The data in part (**a**) are from RBS and that in part (**b**) from optical reflection measurements

the decrease of maximum N^*_{displ} with increasing ion energy has to be interpreted in terms of a decreasing local ion flux whereas the density of the individual collision cascades is always the same.

So far only temperatures with $T_I \ll T_c$ were regarded. In Fig. 5.15 examples for damage production curves $n_{da}^{max}(N_I)$ and $f_{dam}(N_I)$ (fraction of damage obtained from optical reflection measurements) are shown for Ag ion implanted SiC and Si ion implanted Si, respectively, for a wide range of temperatures during implantation. As T_I increases towards T_c, dynamic annealing during the implantation due to thermally enhanced processes becomes more and more important. As long as the temperatures are not too high, this results in a shift of the curves to higher ion

fluences and correspondingly to an increase of the critical ion fluence necessary for amorphisation. As the temperature T_I further increases, the continuous transition towards amorphisation gradually changes into a discontinuous one, i.e. complete amorphisation of the implanted layers proceeds in two steps. This is observed in Ag ion implanted SiC for temperatures of 375 and 475 K and in Si for 350 and 400 K (see Fig. 5.15). In these cases amorphisation is still achieved but the mechanisms are different in comparison with those occurring at $T_I \ll T_c$. Most notably, the amorphisation in two steps cannot be understood by assuming one type of damage only. A possible interpretation of the experimental results can be given as follows. It is assumed that only point defects remain from a single ion impact due to dynamical annealing during relaxation of the primary collision cascade. At low ion fluences this results in an almost linear increase of the damage concentration with increasing ion fluence. The slope of this linear increase is given by the cross-section σ_{def} of that process at the particular depth which is usually the depth of maximum damage concentration. When the impacts of individual ions start to overlap the produced point defects can recombine with those already existing from previous ions. Such a process results in a plateau of the damage concentration versus ion fluence due to a balance between defect formation and annihilation. The rather low saturation value of 0.05….0.15 observed in experiments (see results for $T_I > 400$ K for SiC and $T_I > 300$ K for Si in Fig. 5.15) indicates a significant defect recombination. This in turn supports the assumption that mainly point defects remain from a single collision cascade in these cases. As the implantation proceeds and the ion fluence increases, a second increase of the damage concentration is observed, which finally leads to complete amorphisation indicated by $n_{da}^{max} = 1$ or $f_{dam} = 1$, respectively. This transition towards amorphisation can be best described by nucleation and growth of amorphous seeds. Small precipitates of implanted ions and/or extended defects may act as nucleation sites. The latter implies that at lower ion fluences corresponding to the first plateau, the processes are more complicated than just being formation and recombination of point defects. It is to be expected that already within this range of ion fluences small clusters of point defects start to form, which may be non-ordered aggregates of point defects or ordered aggregates of point defects such as small dislocation loops and stacking faults. Furthermore, Fig. 5.15 shows that the transition towards amorphisation occurs within a very narrow range of ion fluences. This demonstrates that the amorphous nuclei—once they have formed—grow rapidly during further irradiation by IBIIA (see above). The same effect also occurs in other semiconductors for temperatures close to the corresponding critical temperatures as shown in Fig. 5.16. For GaAs [19] and InP [31] the transition to the first plateau is discussed in more detail based on temperature dependent RBS channelling measurements. The lines in Figs. 5.15 and 5.16 are fitted to the experimental data applying the defect-interaction and amorphisation model introduced by Hecking et al. [68]. In this model the occurrence of point defects, non-recombinable point defect clusters and of amorphous material is considered. The relative concentration of point defects and point defect clusters, n_{def}, is given by

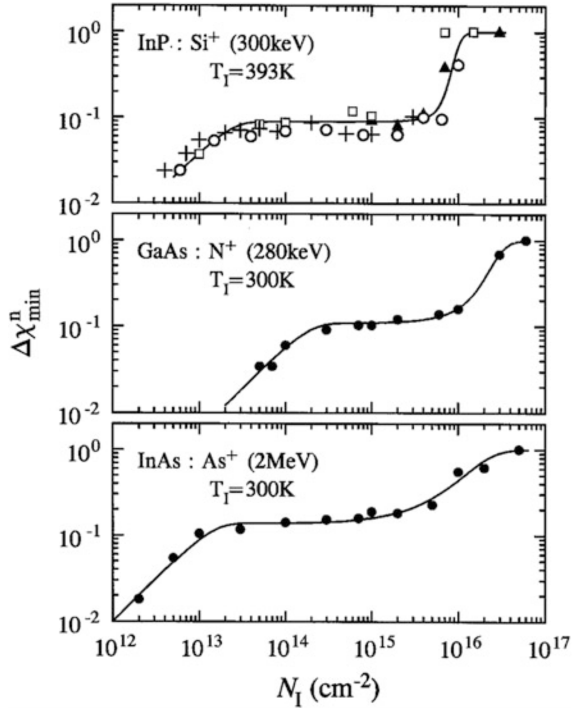

Fig. 5.16 Difference in minimum yield (see Sect. 2.2) normalised to its maximum value, $\Delta\chi^{n}_{min}$, representing the relative damage concentration versus ion fluence N_{I} for different implantation conditions. In each case the temperature of implantation is close to the corresponding critical temperature [38]

$$\frac{\mathrm{d}n_{\mathrm{def}}}{\mathrm{d}N_I} = [\sigma_{\mathrm{def}} - Rn_{\mathrm{def}}](1 - n_{\mathrm{a}}) + \sigma_c n_{\mathrm{def}}\left[1 - \frac{n_{\mathrm{def}}}{n_c(1 - n_{\mathrm{a}})}\right] - \frac{\mathrm{d}n_{\mathrm{a}}}{\mathrm{d}N_I}\frac{n_{\mathrm{def}}}{1 - n_{\mathrm{a}}}. \tag{5.10}$$

Herein σ_{def} is the cross-section for point defect production within a single ion impact, σ_c the cross-section for cluster formation, R the recombination parameter and n_{c} the saturation concentration of non-recombinable point defect clusters. The formation of amorphous material is assumed to occur within single ion impacts and by stimulated growth of amorphous material already existing from previous ions. The relative concentration of amorphous material, n_{a}, can be represented by (5.9) with σ_{dam} being replaced by the cross-section for direct-impact amorphisation, σ_a. It is assumed that the measured relative damage concentration or damage fraction, respectively, is the sum of n_{def} and n_{a} (for further explanations see Chapt. 3). In the case of elevated temperatures, the formation of amorphous zones within single ion impacts is not to be expected. In these cases σ_a serves to emulate the nucleation of amorphous seeds. This interpretation is supported by the fact that the corresponding cross-sections σ_a needed to represent the experimental data are rather small. For example, for SiC implanted with Ag ions at 375 K $\sigma_a = 1.5 \times 10^{-17}$ cm^2 is obtained [67]. Assuming a circular shape of the damage cluster projected to the sample surface as discussed above, a diameter of 0.04 nm is obtained. This is less than the bond length of the SiC crystal and hence, σ_a cannot be interpreted as a

cross-section of amorphisation in a single ion impact. The same argument holds well for Si implanted with Si ions at $T_I = 350$ K (see Fig. 5.15b) for which $\sigma_a \approx 1 \times 10^{-17}$ cm^2 is obtained [68]. At even higher temperatures for which $T_I \approx T_c$ or $T_I > T_c$ is valid (see results for 625 and 875 K in Fig. 5.15a), amorphisation is no more reached and the relative damage concentration saturates at a value well below unity. By TEM it is shown that the produced structures consist of a dense network of extended defects and point defect clusters [69].

5.3.5 Correlation of Damage Cross-Section with Primary Energy Deposition

For sufficiently low ion fluences each ion impinges on still crystalline, undamaged material. If one assumes that no further annealing takes place after relaxation of the primary collision cascades, the damage produced by each ion adds up and a linear increase of the damage concentration with increasing ion fluence will be observed. The slope of this increase yields the cross-section of defect production per individual ion, σ_{dam}. However, often this purely linear range of the damage evolution occurs at rather low concentrations which might be below the detection limit of the applied method. Then, the amount of damage measured in an experiment is already determined by various interaction processes which can be represented by damage rate equations (see Chap. 3). Fitting model curves to the experimental data allows for extracting corresponding cross-sections. For the materials discussed here, (5.9) often provides a very good fit to the experimental data yielding σ_{dam} and the cross-section of stimulated growth of damage, σ_s.

The damage annealing during implantation can be minimized by doing experiments at low temperatures and in situ defect analysis. In this section only low-temperature experiments are regarded. Ion implantation and subsequent RBS channelling analysis were performed at (15…20) K without changing the temperature or the environment of the samples. In this case the influence of thermal effects on damage formation can be assumed to be negligible. This in turn means that damage formation should be only determined by the energy of the implanted ions deposited into the solid and by the properties of the solid itself. This stimulated the attempt to represent the cross-sections of damage formation σ_{dam} as a function of quantities representing the primary energy deposition. For doing so two quantities were used (i) the cross-section for formation of primary displacements σ_d and (ii) the energy loss in electronic interactions per ion and unit depth, S_e. These two quantities were calculated with the code SRIM using the displacement energies given in Table 3.1 of Chap. 3. For clarity the cross-section σ_d is called σ_{SRIM}.

In Fig. 5.17 the cross-section of stimulated growth of damage, σ_s, is plotted versus σ_{SRIM} for various ion species implanted into III-V semiconductors. A linear dependence $\sigma_s = \alpha\, \sigma_{SRIM}$ is found with $\alpha = 15 \pm 5$. It is remarkable to note that one and the same factor accounts for all ion species and materials investigated.

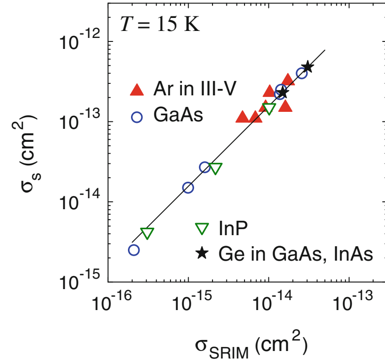

Fig. 5.17 Cross-section of stimulated growth of damage, σ_s, versus the cross-section for formation of primary displacements, σ_{SRIM}, as calculated by SRIM for implantation of various ion species into different III–V compound semiconductors (for details see [25])

A few data points deviate by a factor of about two which may be related to the fact that the data were collected over many years. Figure 5.18 shows σ_s versus σ_{SRIM} for SiC ion implanted with different ion species, which were obtained in one series of experiments. Again, a linear dependence of $\sigma_s(\sigma_{SRIM})$ is observed and with $\alpha = 17.9 \pm 0.8$ even the absolute value of the pre-factor is very close to that obtained for the III-V materials. In the case of SiC a more sophisticated analysis of the uncertainties of the determined cross-sections was performed (for details see [58]). The increase of σ_s with increasing σ_{SRIM} as seen in Fig. 5.17 is in good agreement with the two scenarios presented in Sect. 5.3.4 for explaining mechanisms of stimulated growth of damage. In both scenarios a higher concentration of primary displacements would lead to a stronger growth of damage.

If one assumes that the damage production is solely determined by the energy deposited in the displacement of lattice atoms and no defect recombination or other effects occur within the primary collision cascades, one would expect that σ_{dam} is directly proportional or even equal to σ_{SRIM}. However, in experiments it is found that the increase of σ_{dam} with σ_{SRIM} is stronger than linear. The general trend was found to be $\sigma_{dam} \propto (\sigma_{SRIM})^2$ [5, 25] which is a clear hint to non-linear processes occurring within the primary collision cascades. For the case of SiC the non-linearity is demonstrated in Fig. 5.18. To account for the non-linear dependence of $\sigma_{dam}(\sigma_{SRIM})$ the ansatz $\sigma_{dam} = \sigma_{SRIM}\, f_{\mathrm{enh}}/f_{\mathrm{red}}$ is used with f_{enh} being a function of enhancement and f_{red} a function of reduction of damage formation within the primary collision cascades of individual ions impinging on crystalline material (for details see [25]). In analogy to the macroscopic dependence $\sigma_s \propto \sigma_{SRIM}$ (see Figs. 5.17 and 5.18) the function of enhancement is taken to be $f_{\mathrm{enh}} \propto \sigma_{SRIM}$. For the function of reduction of damage formation f_{red} a useful dependence was found to be $f_{\mathrm{red}} \propto \sigma_{\mathrm{SRIM}}^{0.2} S_{\mathrm{e}}$. This considers that both nuclear and electronic energy deposition contribute to in-cascade annealing (for details see [25] and references therein). Finally these assumptions yield

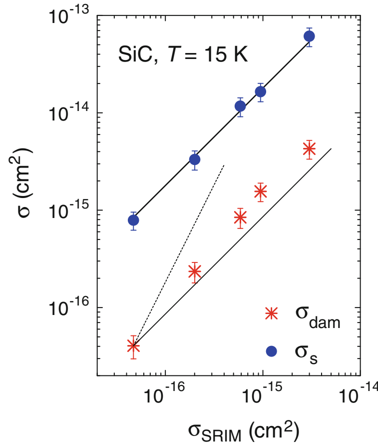

Fig. 5.18 Cross-section σ_{dam} of direct-impact-damage formation and σ_s of stimulated growth of damage versus the cross-section σ_{SRIM} of formation of primary displacements for SiC implanted at 15 K. The thick solid line is a linear fit to the experimental data of σ_s through the origin using the errors as weighting factors (for details see [58]). The *thin solid* and *dashed lines* represent a linear and quadratic dependence on σ_{SRIM}, respectively

$$\sigma_{dam} = \xi \frac{\sigma_{SRIM}^{1.8}}{S_e}. \tag{5.11}$$

The pre-factor is obtained to be $\xi = (4.68 \pm 0.4) \times 10^{21}$eVcm$^{-13/5}$ for the III–V compounds and $\xi = (1.08 \pm 0.08) \times 10^{22}$ eVcm$^{-13/5}$ for SiC [58]. For the latter $\sigma_{dam} S_e$ versus σ_{SRIM} is plotted in Fig. 5.19. The nearly quadratic dependence of $\sigma_{dam} S_e$ on σ_{SRIM} is clearly to be seen in this figure.

The experimental data available up to now suggest that empirical dependences of the cross-sections $\sigma_{dam}(\sigma_{SRIM}, S_e)$ and $\sigma_s(\sigma_{SRIM})$ occur. The advantage is that empirical formulas allow the prediction of damage formation at very low temperatures. Furthermore, this result can be taken as input for the modelling of damage formation as a function of temperature and ion flux (see Chap. 3). So far the empirical dependences are not verified by theoretical considerations and thus may stimulate further work. In some cases deviations exist which cannot solely be explained by the statistics of the measurement and the uncertainty of the ion fluence. Another aspect which has to be considered for the quasi in situ measurements, results of which are presented here, is the effect of analysing He ions. In some materials beam annealing occurs which results in an underestimation of the damage cross-section (an extreme example for that (Al_2O_3) and how one can cope with beam annealing is given in [70]). Therefore, further investigations are necessary to collect data with higher precision and to improve the empirical formula. Finally it should be mentioned that also for ion implanted $LiNbO_3$ an empirical model was created for describing ion-induced damage formation as a function of primary energy deposition [71].

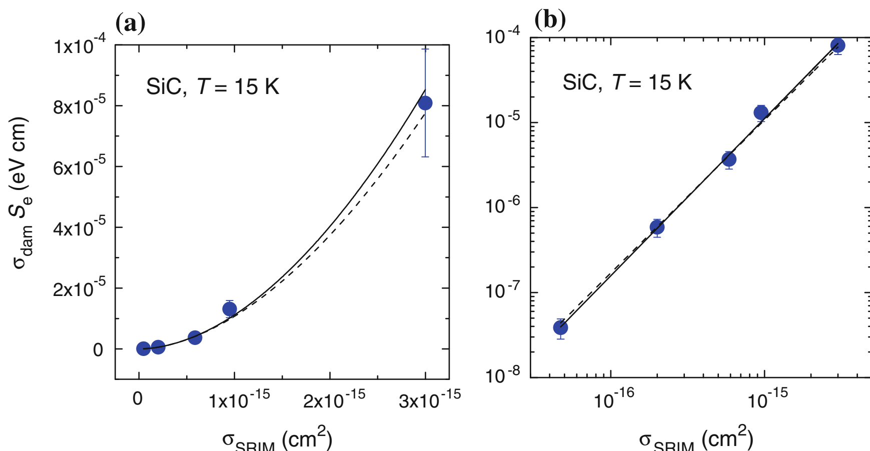

Fig. 5.19 Product $\sigma_{dam}S_e$ of damage cross-section σ_{dam} and electronic energy loss per ion and unit depth, S_e, versus the cross-section σ_{SRIM} of formation of primary displacements for SiC implanted at 15 K. For better visibility of all data, part (**a**) has linear and (**b**) logarithmic scales. The function $y = \xi\ x^B$ is fitted to the experimental data using the errors of σ_{dam} as weighting factors. The solid line is the result of a free fit and the dashed line is a fit with the exponent B set fixed to 1.8. For details see [58]

5.4 Discontinuous Damage Evolution up to Amorphisation

In difference to the semiconductors discussed in Sect. 5.3, AlAs and GaN are very resistant against ion-beam induced damage formation. Both materials cannot be amorphised at RT. And even at temperatures as low as 15–20 K the results presented below indicate that only point defects remain from a single collision cascade, which recombine when the collision cascades start to overlap, thus resulting in a saturation of the defect concentration at a rather low value of $n_{da} = 0.05 \ldots 0.15$. Amorphisation of the implanted AlAs and GaN is finally achieved at such low temperatures due to secondary effects at rather high ion fluences. In these materials the concept of critical temperatures does not apply. The processes being relevant during ion irradiation are not dominated by thermal effects. With other words, the way how these crystals cope with ion-beam induced defects is much less influenced by thermal processes than it is the case for the materials discussed in Sect. 5.3.

5.4.1 Damage Formation in AlAs

Ion implanted AlAs was found to be very resistant to damage formation with particular effects occurring at the interface to GaAs which is often adjacent to AlAs at least at the surface for protecting AlAs from ambient oxygen (see [60, 72–77]

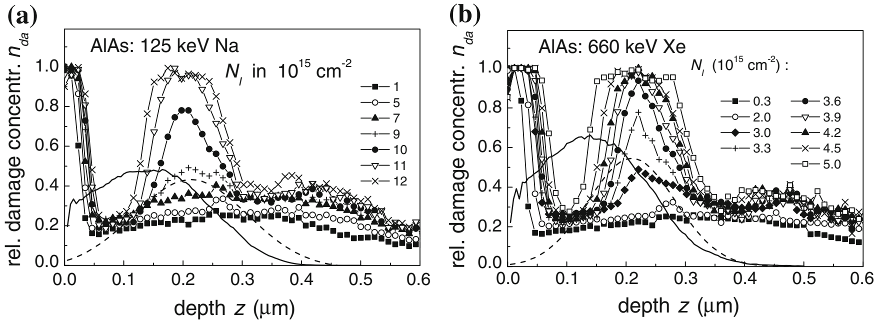

Fig. 5.20 Damage profiles $n_{da}(z)$ for AlAs implanted with 125 keV N (**a**) or 660 keV Xe ions (**b**) at 15–20 K to various ion fluences [76]. The distribution of primary displacements (*solid lines*) and the ion distributions (*dashed lines*) are given for comparison in arbitrary units

and references therein). Further it is worth mentioning that with RBS no defect annealing was detected in AlAs in the temperature range between 77 K and RT [78]. Typical damage profiles in AlAs ion implanted and measured at a rather low temperature of (15…20) K are shown in Fig. 5.20 for two different ion species. The high damage concentration close to the surface results from amorphisation of the GaAs cap layer. For ion fluences up to 7×10^{15} Na cm^{-2} or 2×10^{15} Xe cm^{-2} the defect distributions are rather broad and flat with maximum values below 0.3. For higher ion fluences a clear damage peak evolves. The maximum value of the damage peak increases until unity is reached, which is commonly taken as an indication of amorphisation. A further increase of the ion fluence results in a broadening of the amorphous layer towards the surface and into the depth (see Fig. 5.20b).

It is important to note that the depth of peak maximum occurs at the depth of maximum ion concentration and not at the depth at which the maximum of lattice displacements is produced. The same effect is found for other ion species, too. Figure 5.21 summarises the damage concentration in the maximum of the measured distribution, n_{da}^{max}, versus ion fluence for AlAs ion implanted and analysed at 15–20 K. In part (a) the fluence dependence of n_{da}^{max} is depicted for a wide range of ion fluences for the case of Ar ions. The fluence range in part (b) covers the transition towards amorphisation for various ion species. Figure 5.21a shows that amorphisation occurs in two steps. After a first increase of the defect concentration at very low ion fluences a broad plateau is observed within which the defect concentration amounts to about 0.15 and increases only slightly during proceeding implantation. Then within a relatively narrow ion fluence interval, amorphisation indicated by $n_{da}^{max} = 1$ is finally achieved. The curve $n_{da}^{max}(N_I)$ in Fig. 5.21a was calculated applying (5.9) and (5.10). For representing the experimental data of Ar ion implanted AlAs all mechanisms included in the model were taken into account (point defect formation and recombination, formation of non-recombinable point defect clusters, nucleation and growth of amorphous material).

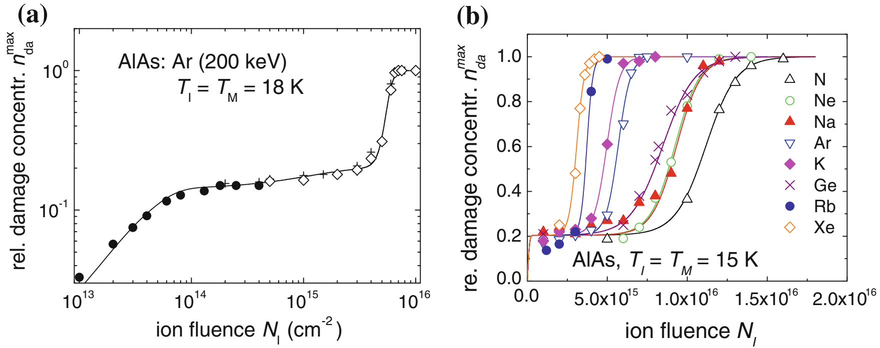

Fig. 5.21 Relative damage concentration in the maximum of the measured distribution versus ion fluence N_I (**a**) for Ar ions [79] and (**b**) for various ion species implanted into AlAs [80] at 15–18 K. In part (**a**) different symbols represent repeated implants and the line is fitted to the experimental data (for details see text). The results in part (**b**) for Na and Xe ions follow from the profiles shown in Fig. 5.20. For the other ion species the ion energies are adjusted for obtaining almost the same thicknesses of the implanted layer as seen in Fig. 5.20. Notice the different scales in parts (**a**) and (**b**)

At very low ion fluences the defect concentration increases almost linearly until it saturates at the low level of 0.15 for ion fluences around 1×10^{14} cm^{-2} (see Fig. 5.21a). This saturation implies a balance between defect production and recombination. Both the small cross-section following from the first increase of the defect concentration of $\sigma_{def} = 3.5 \times 10^{-15}$ cm^2 and the low saturation value indicate that only point defects remain from the primary collision cascades even though ion implantation and defect analysis were performed at 18 K. Low-temperature irradiations of AlAs were also performed with electrons [81]. In this case the change of lattice constant was measured at the temperature of irradiation and it was concluded that Frenkel pairs in AlAs can be frozen in at low temperatures in large quantities. A similar effect seems to occur during ion irradiation at very low ion fluences for which the impacts of individual ions do not overlap (i.e. for fluences below 3×10^{13} cm^{-2} in Fig. 5.21a). The saturation of the defect concentration at fluences between 1×10^{14} and 4×10^{14} cm^{-2} can be explained, for example, by assuming that newly produced interstitials and vacancies recombine with their opposite defects produced by previous ions [60].

The slight increase of the defect concentration within the plateau at ion fluences between 4×10^{14} and 4×10^{15} cm^{-2} (see Fig. 5.21a) can be attributed to the formation of non-recombinable point defect clusters. Most probably these are small extended defects like dislocations or stacking faults. The existence of some extended defects at ion fluences before the onset of amorphisation is also indicated by the broad and flat defect distributions which tend not to reach zero at the end of the implanted layer (see Fig. 5.20 and [75]) for Ar ions, and Sect. 5.2.2 for comments on the RBS analysis). From TEM studies on AlAs implanted with 2.4 MeV Au ions it was concluded that damage in the AlAs must be in the form of point defects, small clusters of defects or very small dislocation loops which cannot be resolved

by TEM [60]. In the case of $Al_{0.95}Ga_{0.05}As$ implanted with Si ions at 77 K and analysed by transmission electron microscopy, the existence of extended defects was demonstrated [73].

For implantation of 200 keV Ar ions (see Fig. 5.21a) amorphisation occurs at fluences above 5×10^{15} cm^{-2} within a rather small ion fluence increment. A similarly steep transition is also seen for the other ion species (see Fig. 5.21b). Such a steep transition towards amorphisation, which is typical for AlAs and AlGaAs with high Al content [73, 75], is usually attributed to nucleation and growth of the amorphous phase. It is found that the critical ion fluence necessary for amorphisation by using different ion species does not exhibit a systematic dependence on the energy density deposited in the displacement of lattice atoms. The results rather indicate a correlation with the total volume introduced by the implanted ions. To quantify this effect of ion species, a critical ion concentration (per unit volume) $N_{\mathrm{ion}}^{\mathrm{c}}$ is determined at which the maximum damage concentration reaches a value of $n_{\mathrm{da}}^{\mathrm{max}} = 0.6$. This value was chosen because the corresponding ion fluence $N_{\mathrm{I}}^{\mathrm{c}}$ can be more precisely determined than $N_{\mathrm{I}}^{\mathrm{am}}$ (see Fig. 5.21b). $N_{\mathrm{ion}}^{\mathrm{c}}$ is given by $N_{\mathrm{ion}}^{\mathrm{c}} = N_{\mathrm{ion}}^{*} N_{\mathrm{I}}^{\mathrm{c}}$ with N_{ion}^{*} being the number of introduced atoms per ion and per unit depth calculated with SRIM and taken in the maximum of the distribution. In Fig. 5.22 the critical ion concentration N_{ion}^{c} necessary to reach a relative defect concentration of 0.6 is plotted versus the atomic volume V_{ion} of the corresponding ion species. Here a clear correlation is observed. With increasing volume V_{ion} less ions per unit volume are needed for reaching 60 % damage. This finding coincides with the fact that the onset of amorphisation occurs at the depth of maximum ion concentration as shown in Fig. 5.20. From these results we conclude that nucleation of amorphous seeds in AlAs is triggered by the implanted ions. Once amorphous seeds exist, they grow rapidly during further implantation by IBIIA thus causing the steep increase of the damage concentration versus ion fluence up to complete amorphisation and the broadening of the amorphous layers (see Fig. 5.20).

Amorphisation of AlAs was also registered by RBS and TEM after implantation with 90 keV Si ions at 77 K and analysis at RT [73]. The transition occurred at ion fluences between 7×10^{15} and 8×10^{15} cm^{-2}. That is, the ion fluence $N_{\mathrm{I}}^{\mathrm{c}}$ for

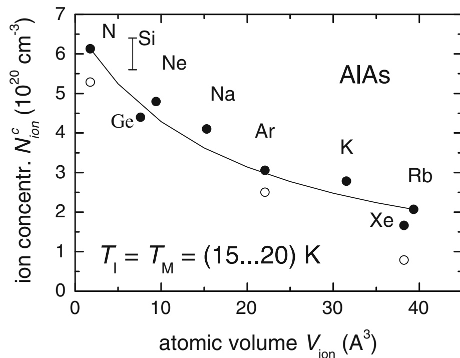

Fig. 5.22 Critical ion concentration $N_{\mathrm{ion}}^{\mathrm{c}}$ necessary for reaching a damage fraction of 0.6 versus the atomic volume V_{ion} of the implanted ion species [79, 80]. The open symbols follow from the results given in Fig. 5.25. The interval given for Si ions follows for T_{I} = 77 K and T_{M} = 300 K [73] (for details see text)

reaching 60 % damage must be between these two values. Using results of SRIM calculations for the experimental conditions applied in [73], a critical Si ion concentration necessary for reaching 60 % damage can be estimated. The range of $N_{\mathrm{ion}}^{\mathrm{c}}$ corresponding to the two Si ion fluences given above is indicated in Fig. 5.22. It reasonably falls into line with the results for the other ion species. The slightly higher value may be related to the higher temperature of implantation and analysis. Contrary, a 90 nm thick AlAs layer embedded between GaAs layers did not get amorphous after implantation of 150 keV Si ions at 80 K up to 6×10^{15} cm^{-2}, the highest fluence employed [72]. An SRIM calculation made for the corresponding experimental conditions shows that the Si concentration within the AlAs layer did not exceed 3.5×10^{20} cm^{-3}, which is below the critical value which can be deduced from Fig. 5.22. That is also this result is consistent with the statement given above that the onset of amorphisation requires a certain volume introduced by the implanted ions.

Damage formation in ion irradiated AlAs at 80 K or 25 K and its effect on lattice strain was studied by measuring the lattice parameter using X-ray diffraction [60]. The in-plane lattice parameter did not change, whereas the out-of-plane lattice parameter increased with ion fluence at low fluences, saturated and then decreased to its original value. A uniform dependence was found when scaling the ion fluences for the different ion species applied with the energy deposited in the displacement of lattice atoms per ion and unit depth. This means that the results are independent of the ion species [60]. As an example, the resulting lattice strain measured after 1.7 MeV Ar ion irradiation of AlAs at 80 K is shown in Fig. 5.23. The strain increases and saturates in a similar way as seen for the defect concentration measured by RBS as shown in Fig. 5.21a. However, for the conditions applied in [60] at very high ion fluences the strain decreases to its original value (see Fig. 5.23). Applying RBS and TEM no amorphisation could be detected in any of these samples. It is concluded that the strain reduction results from partial cancelation of opposing strain elements comprising the evolving damage structure, e.g., vacancy (negative) and interstitial (positive) clusters or loops. Regarding the non-amorphisation, the authors argue in the following way. If the viewpoint is

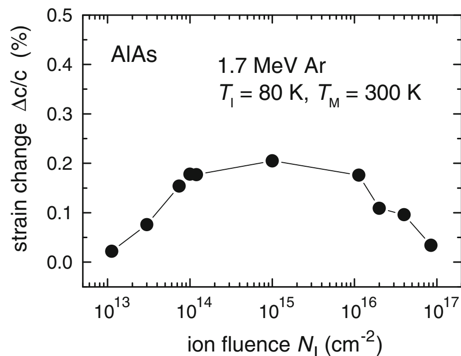

Fig. 5.23 Percent strain $\Delta c/c$ resulting from the lattice parameter change normal to the surface versus ion fluence N_{I} for AlAs ion implanted with 1.7 MeV Ar ions at 80 K and analysed at RT [60]

accepted that amorphisation is due to a mechanical instability, triggered by a critical strain energy in the material, it can be concluded that AlAs did not amorphise simply because the strain saturated below the critical strain [60]. When comparing this result with those given above one has to take into account the structure of the samples and the irradiation conditions. Here a 180 nm thick AlAs layer was studied being surrounded by GaAs and more importantly, much higher ion energies of few MeV were used [60]. The consequence is that in these experiments (see Fig. 5.23) no ions did come to rest within the AlAs layer. This is different to the experiments the results of which are shown in Figs. 5.20, 5.21, 5.22 and to the conditions used in [72, 73]. In these cases the ions came to rest within the AlAs layer and amorphisation started at the depth of maximum ion concentration. The comparison of these results implies that the high-energy ion implanted AlAs did not get amorphous because the implanted ions did not come to rest within the AlAs layer. This in turn suggests that the volume introduced by the implanted ions in case of low ion energies results in an increase of strain above the critical value necessary for the nucleation of amorphous seeds.

In the case of $Al_{0.95}Ga_{0.05}As$ it was shown that besides the implanted ions also extended defects play an important role in the nucleation of amorphous seeds (see Chap. 6). The material was implanted with Si ions at 77 K and analysed by TEM at RT [73]. In this case, after implantation of 5×10^{15} cm^{-2} a thin band of mixed amorphous and heavily damaged material of about 40 nm thickness formed, which is surrounded by regions with extensive stacking faults. Interestingly also here, the position of this band around 100 nm is very close to the depth of maximum ion concentration as calculated by SRIM. Therefore it may be suspected that formation and growth of extended defects are also influenced by the implanted ions. Thus, nucleation of amorphous seeds in ion implanted AlAs or $Al_{0.95}Ga_{0.05}As$ is a complicated process involving implanted ions and formation of extended defects.

As already mentioned above, particular effects occur at the interface between AlAs and GaAs [72, 74, 77]. At low ion fluences, damage formation of GaAs at the boundary to AlAs is delayed within a thin layer of about 12-15 nm. This effect seems to be caused by point defect interactions involving, for example, Al-related species [72]. At high ion fluences when the GaAs adjacent to AlAs is completely amorphised, amorphisation proceeds into the AlAs layer. An example for that is

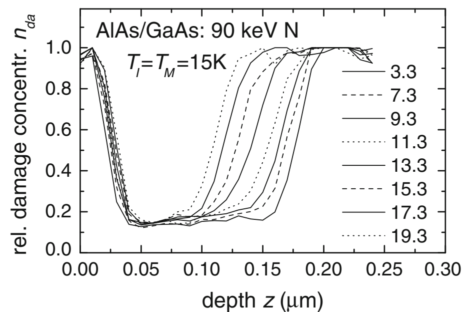

Fig. 5.24 Damage profiles $n_{da}(z)$ for the system 20 nm GaAs/160 nm AlAs/GaAs implanted with 90 keV N at 15 K to various ion fluences given in 10^{15} cm^{-2} [77]. For details see text

shown in Fig. 5.24 in which N ion implantation-induced damage profiles are depicted for a 160 nm thick AlAs layer embedded between a 20 nm thick GaAs surface layer and bulk GaAs. Amorphisation of AlAs proceeds from both interfaces. The amorphisation rate of AlAs from the front amorphous GaAs layer amounts to about 1 nm per 10^{23} displacements per cm^3 and was found to be independent of ion species [76, 77]. Consequently this process is governed by the primary displacements. The position of the deeper lying amorphous/crystalline interface of AlAs is shown in Fig. 5.25. It is found that amorphisation of AlAs is first initiated by the displacement of lattice atoms. The rate of AlAs amorphisation amounts to 1.7 nm per 10^{23} displacements per cm^3 independent of the ion species (see solid line in Fig. 5.25a). But during proceeding irradiation when the interface moves below a depth of $z \approx 160$ nm, changes occur. The position of the interface is no more controlled by the number of displacements deposited at the respective depth (see Fig. 5.25a). Instead, it is determined by a certain local concentration of implanted ions (see Fig. 5.25b). This means that the position of the interface, i.e. the growth of the amorphous AlAs layer, is now governed by a critical concentration of implanted ions. The critical concentrations of N, Ar or Xe ions which can be deduced from Fig. 5.25b) are included in Fig. 5.22. A good agreement with those given in Fig. 5.22 is found with the latter resulting from different experiments. This again supports the crucial role of implanted ions in damage formation and amorphisation of AlAs.

Finally it should be mentioned that in case of high ion energies of few MeV, the interfacial amorphisation of AlAs is also affected by the energy deposited in electronic interactions. It was shown that primary displacements due to nuclear interaction promote the growth of amorphous AlAs layers as shown above, and that the electronic energy deposition leads to epitaxial regrowth of amorphous AlAs layers [74].

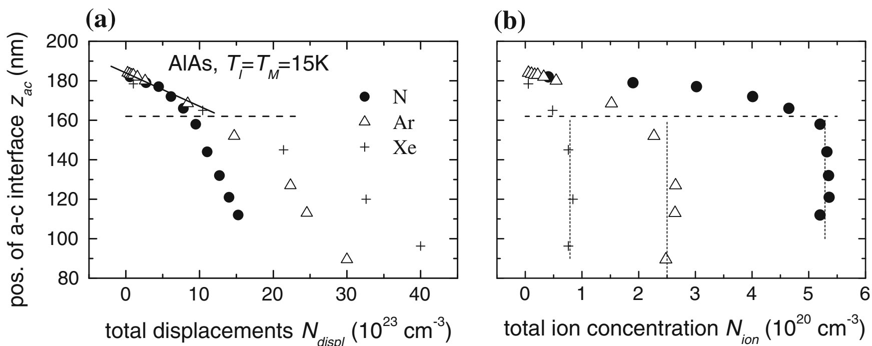

Fig. 5.25 Position of the amorphous/crystalline interface, z_{ac}, for amorphisation of AlAs beginning at the buried GaAs (see Fig. 5.24) versus (**a**) the total number of displacements per unit volume N_{displ} and (**b**) the total ion concentration per unit volume N_{ion} at the depth $z = z_{ac}$. The *dashed line* marks the change of amorphisation due to lattice displacements into an ion-controlled process. The *dotted lines* serve to guide the eye

5.4.2 Damage Formation in GaN

Damage formation in GaN by ion implantation has been studied since the late 1990's (see e.g. [82–85]). The experimental data collected since then yield a comprehensive picture of what occurs even though the physical processes behind are not yet fully understood. Typical sets of RBS channelling spectra of GaN are shown in Fig. 5.26 which plots the difference in minimum yield $\Delta\chi_{min}$ (see Sect. 5.2.2) versus depth for 300 keV Ar ions implanted at 15 K (a) and at RT (b) [29]. At the low temperature, amorphisation as seen by RBS is observed at depth (close to maximum energy deposition in lattice displacements, as will be discussed below) and at the surface, whereas at RT amorphisation only starts at the surface.

Figure 5.27 summarises $\Delta\chi_{min}$ from Fig. 5.26 at a fixed depth of 0.13 μm (corresponding to the depth of maximum energy deposited in lattice displacements) versus ion fluence. It becomes obvious that amorphisation of GaN at 15 K proceeds in three steps [86]. At RT a saturation of damage (below amorphisation) is reached in two steps. It is interesting to note that the first two steps of damage formation are very similar for the two different temperatures. Within the first step the values are only slightly lower and the transition to the second plateau is slightly broader for the higher temperature. The general similarity of the effects at 15 K and at RT also exhibits in the similar shape of the RBS channelling spectra (see Fig. 5.26). All spectra are characterized by a high dechannelling background, i.e. a high level of $\Delta\chi_{min}$ at depths behind the damaged layers. As discussed in Sect. 5.2.2 this indicates the existence of extended defects. Therefore, it can be already concluded that (i) extended defects play an important role in damaging of GaN by ion implantation and (ii) this is independent of the substrate temperature during implantation at least for temperatures between 15 K and RT.

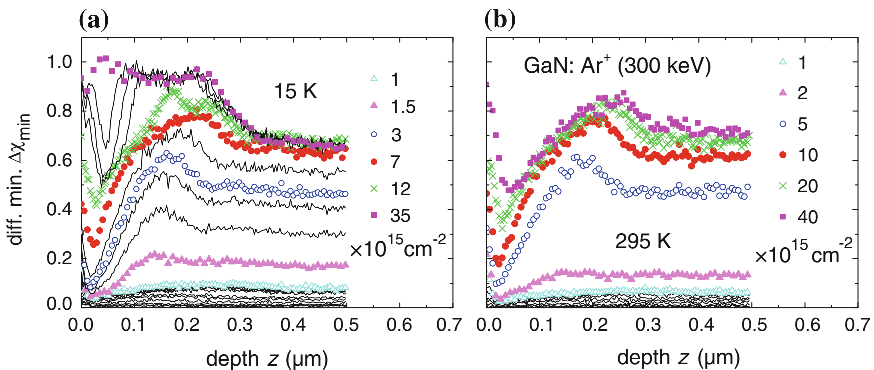

Fig. 5.26 Difference in minimum yield $\Delta\chi_{min}$ versus depth z for 300 keV Ar ion implanted GaN with implantation and subsequent measurement being performed at 15 K (**a**) and at 295 K (**b**) [29]. *Solid lines* are results for intermediate fluences which are not included in the legend for clarity

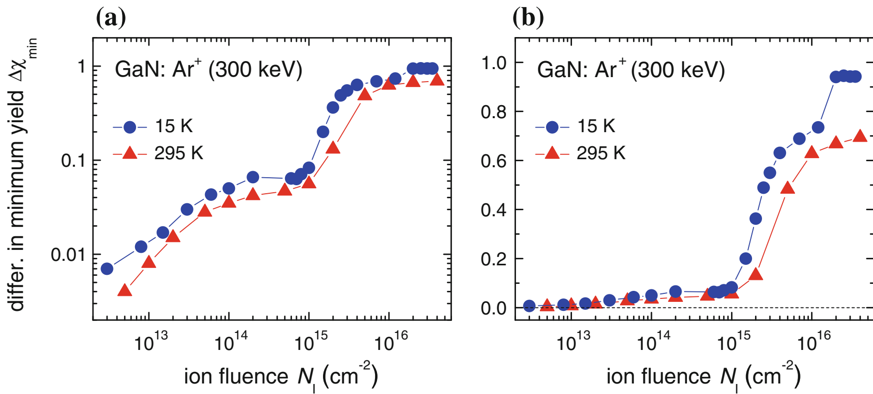

Fig. 5.27 Difference in minimum yield $\Delta\chi_{min}$ versus ion fluence N_I for Ar ion implanted GaN. Data are average values over a depth of 30 nm taken at the depth of maximum energy deposition in the displacement of lattice atoms [86]. For better visibility of the steps of damage formation the data are given in double logarithmic (**a**) and half logarithmic scale (**b**)

The strong damage at the surface of the implanted samples is one of the most striking effects in GaN during ion implantation [84]. It is not very pronounced for the examples shown in Fig. 5.26 but was found to be tremendous for heavy ions such as 200 keV Ag and 300 keV Au or in case of cluster ions (see [87] and references therein). Once a heavily damaged surface layer has formed, it grows into depth with rates of 0.5–5 nm/dpa. Experiments done for one and the same ion-energy combination reveal that at a lower temperature for a given ion fluence more surface damage is produced [29] and a higher damage rate is measured [87] than at a higher temperature. By increasing the angle of incidence of 300 keV Xe ions the distance between surface and depth of maximum nuclear energy deposition could be decreased from about 70 nm to about 10 nm, but this did not affect the thickness of the surface layer versus the normalised ion fluence [88]. These experimental findings cannot be explained by simple thermal diffusion of primarily produced point defects. The growth of the damaged surface layer is also not influenced by pre-existing defects at the surface [89]. That is already existing surface damage does not enhance the growth rate. In [87] the growth rate was correlated with an average depth-dependent cluster density which was deduced from SRIM calculations. It was shown that the growth rate is almost constant below a critical value of this cluster density and increases above. However, so far no obvious correlation between the growth of the heavily damaged surface layers and the energy deposition of the implanted ions was found. It might be that the reason for that lies within the process itself, i.e. how these heavily damaged surface layers are produced and what a structure they have. The data for determining the growth rates given above were collected by RBS. For sufficiently thick surface layers the RBS aligned spectra reach the random level. Therefore it was assumed that amorphous layers are formed. And amorphous layers are known to grow by ion-beam induced interfacial amorphisation

(IBIIA) already mentioned in Sect. 3.3. However, the mechanisms behind IBIIA seem not to be able for explaining the experimental findings regarding the surface damage of GaN. This suggests that a different mechanism must be active. And indeed more recent sophisticated high-resolution TEM measurements reveal that the damaged GaN surface layers are not amorphous but consist of randomly oriented nanocrystals [90]. With RBS such a nanocrystalline layer cannot be distinguished from an amorphous one. In [90, 91] it is shown that the crystalline (wurtzite) structure of GaN collapses into a nanocrystalline state starting from a rough surface and a surface layer saturated with stacking faults. Basal stacking faults were found to be the dominant extended defects that appear first and propagate to the layer surface through an easy formation of prismatic stacking faults (for details see [91]). This means that most probably the mobile species are not individual vacancies or interstitials which are created within the primary collision cascades but small clusters in form of certain types of stacking faults. This in turn may explain why the increase in layer thickness as visible by RBS cannot easily be related to the number of primary displacements as explained above.

The damage profiles $n_{da}(z)$ in GaN after Ar ion implantation and subsequent analysis at 15 K are given in Fig. 5.28. They result from the $\Delta\chi_{min}$ spectra in Fig. 5.26a and were calculated with DICADA assuming the existence of uncorrelated displaced lattice atoms (see Sect. 5.2.2). The distribution of primary displacements N^*_{displ} and implanted ions N^*_{ion} per ion and unit depth as calculated with

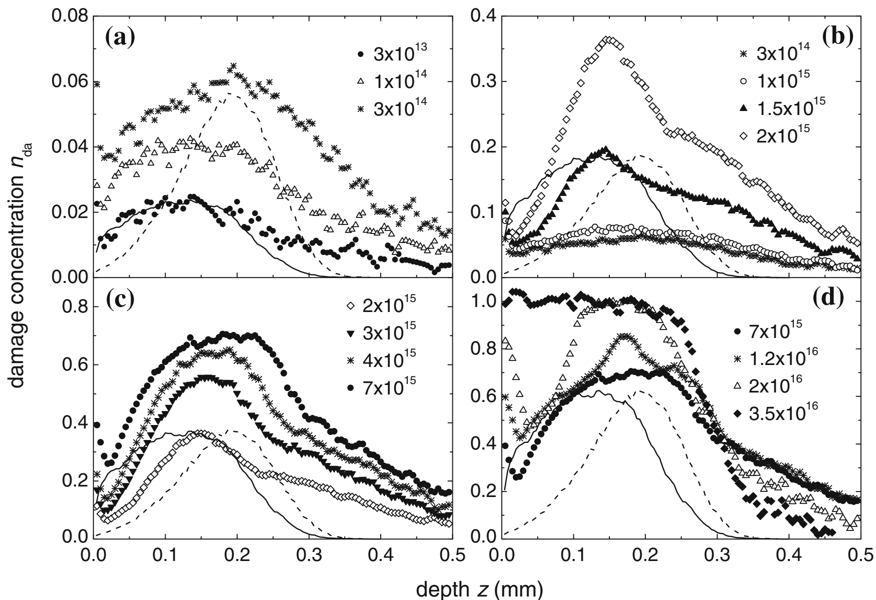

Fig. 5.28 Damage profiles $n_{da}(z)$ for GaN implanted with 300 keV Ar ions at 15 K to various ion fluences given in cm^{-2} [86]. The distribution of primary displacements (*solid lines*) and the ion distributions (*dashed lines*) are given for comparison in arbitrary units

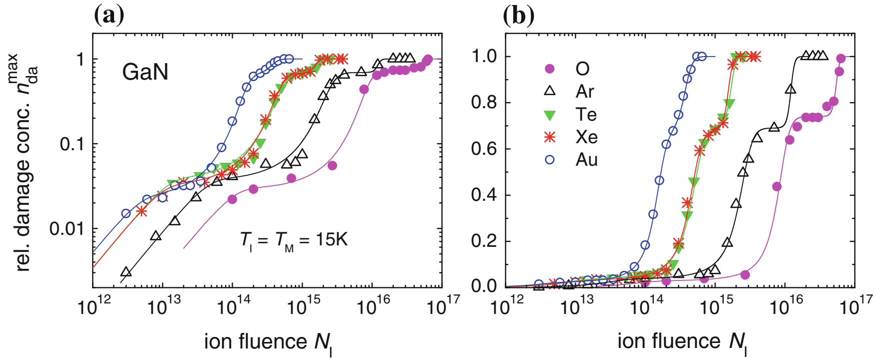

Fig. 5.29 Relative damage concentration in the maximum of the measured distribution, n_{da}^{max}, versus ion fluence N_I for different ion species implanted into GaN at 15 K. For better visibility of the steps of damage formation the data are given in double logarithmic (**a**) and half logarithmic scale (**b**)

SRIM are included for comparison (see Fig. 5.28). For illustration of the damage evolution versus ion fluence Fig. 5.29 presents the damage concentration in the maximum of the measured distribution n_{da}^{max} for 300 keV Ar ions (see Fig. 5.28) as well as for other ion species implanted at 15 K in GaN. At this temperature for all ion species investigated, amorphisation proceeds in three steps with each step being characterized by an increase and a plateau-like saturation of the damage concentration. The lines in Fig. 5.29 are fitted to the experimental data applying (5.9) and (5.10) which allows a very good representation of the experimental data. A similarly good fit of the data succeeds also with other concepts which also assume different types of defects to exist (see Chap. 3, [92]).

The first step visible in Fig. 5.29 can be interpreted by production and recombination of point defects as explained for AlAs (see Sect. 5.4.1). By X-ray spectroscopy the formation of nitrogen split interstitials could be identified at this early stage of damage formation [93]. For the low ion fluences defect formation is dominated by the nuclear energy deposition [86]. This becomes also obvious from the good agreement between the shape of $n_{da}(z)$ and $N_{ion}^{*}(z)$ (see result for $N_I = 3 \times 10^{13}$ cm^{-2} in Fig. 5.28a). Once the collision cascades start to overlap at higher ion fluences, defect formation and recombination result in the first plateau with a relative defect concentration of ≈0.04. However, the defect concentration is not completely constant and, more importantly, the defect distributions extend into depth far behind the depths in which primary displacements are produced (see Fig. 5.28b). That is, the processes within the first plateau are more complicated than just being a balance between production and recombination of defects. It has to be assumed that already in this range of ion fluences extended defects start to grow. For GaN ion implanted at RT this is indeed shown by TEM [94]. And because of the low influence of the temperature, it can be assumed that extended defects also

start to grow during implantation at low temperature at this stage of damage formation (see discussion above). Within this first step of damage formation the normal lattice strain as measured by X-ray diffraction (XRD) increases progressively [94, 95]. This is accompanied by a slight increase of the nano-hardness and the reduced elastic modulus of the GaN layers whereas the characteristics of defect-induced effects in the Raman spectra do not change [96].

The second step starts at $N_I > 1 \times 10^{15}$ cm^{-2} for 300 keV Ar ion implantation (see Figs. 5.28b and 5.29). This value is almost independent of the target temperature during implantation (see Fig. 5.27, [95]). The given Ar ion fluence of 1×10^{15} cm^{-2} corresponds to a normalised ion fluence of $n_{dpa} = 0.7$ dpa. A similar value can be estimated for the other ion species (except Au) from the data given in Fig. 5.29 [30] and from data of RT implants in GaN measured by other authors (see e.g. [87, 94]). For the 350 keV Au ion implantation the data of which are shown in Fig. 5.29, the second step starts at 0.3–0.4 dpa. The difference to the other examples shown in Fig. 5.29 is the thickness of the Au ion implanted layer which amounts to 0.1 µm only compared to 0.35 µm as seen for Ar ions in Fig. 5.25; 0.35 µm are also realised for the other ion species the results of which are shown in Fig. 5.29. From the existing data this effect cannot be explained satisfactorily. A more detailed analysis of the profile for $N_I = 1.5 \times 10^{15}$ cm^{-2} in Fig. 5.28b (subtracting the background of damage from previous ions) shows that the damage peak evolves at the depth of maximum energy deposited in the displacement of lattice atoms. These findings suggest that in ion implanted GaN more heavy damage resulting in the second step of damage formation (as far as visible by RBS, see Figs. 5.27 and 5.29) is produced when the energy deposition in the displacement of lattice atoms exceeds a critical value. This strong increase of defect concentration exhibits also in an abrupt enhancement of the phonon confinement in disorder-activated Raman lines [96]. Furthermore, it could be shown that at this stage of damage formation nitrogen molecules start to form [93]. The critical displacement density mentioned before is almost independent of the temperature, which allows the conclusion that the processes behind are not thermally driven. And indeed, from studies of GaN implanted with 300 keV Ar ions at RT with XRD and RBS, it was concluded that the mechanism of this transition can be directly related to mechanical properties of GaN (for details see [95]). For ion fluences within the second plateau-like range as seen by RBS (see Fig. 5.29), the strain saturates and a tangle of dislocations, stacking faults and point defect complexes forms as shown by TEM [94, 95]. The formation of these complex defect structures results in an abrupt decrease of the nano-hardness and the reduced elastic modulus of the GaN layers [96]. It is argued that densification resulting from compression and shear and plastic (viscous) flow due to shear strain, that in some cases may invoke breaking of bonds, can lead to easier plastic deformation, which explains satisfactorily the observed softening of the layers (for details see [96]).

As already mentioned, final amorphisation as seen by RBS at depth is observed at 15 K [86] as well as for implantation at 80 K and subsequent analysis at RT [84]. From the profiles for 300 keV Ar ion implanted GaN (see Fig. 5.28d) it can be seen that amorphous material is formed within a very narrow depth interval. This

suggests the nucleation of amorphous seeds which grow rapidly during proceeding implantation. Obviously this process is related to defect-impurity interactions and requires both a high number of primary displacements and a high ion concentration [86, 95]. Using TEM it was shown that such RBS-amorphous layers implanted at low temperatures to high ion fluences consist of amorphous and nanocrystalline phases [97]. Additionally nitrogen bubbles are indentified (see [97] and references therein) which obviously developed from nitrogen molecules identified at the earlier stage of damage formation as mentioned above [93].

5.5 Non-amorphisable Materials

No amorphisation by ion implantation was observed in case of the III-V compound AlN [92, 98, 99]. So far only for Ar ion implantation fluence dependencies of damage formation were measured [92, 99]. The results indicate a two-step behaviour similar to the first two steps discussed for GaN in Sect. 5.4.2 with a saturation value of $n_{da}^{max} \approx 0.6$ [92]. Also no amorphisation by ion implantation could be found in II-VI compounds, although it has to be mentioned that the number of papers dealing with ion implantation in this group of materials is rather limited. More systematic studies exist only for CdTe and ZnO. As an example, Fig. 5.30 shows a mean defect concentration for ZnO (a) and CdTe (b) ion implanted with Ar ions at 15 K and at RT. Independent of temperature, ion fluences up to about several 10^{16} cm^{-2} do not render these materials amorphous. This is true also for heavier ion species implanted into ZnO [30, 100] and into CdTe [26].

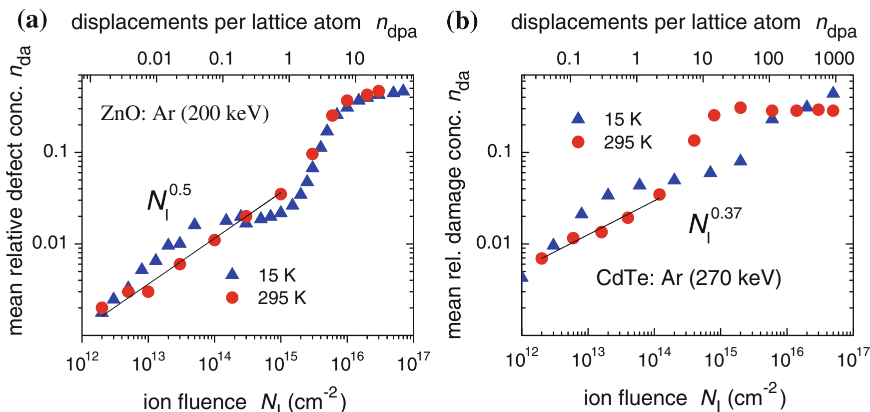

Fig. 5.30 Mean relative damage concentration n_{da} versus ion fluence N_I (*lower scale*) and displacements per lattice atoms n_{dpa} (*upper scale*) for (**a**) ZnO [29] and (**b**) CdTe [26] implanted with Ar ions at two different temperatures. The *thin solid lines* are fits through the low-fluence data with the dependence on N_I being indicated in the figure

The dependence on ion fluence (Fig. 5.30) shows two steps of damage formation at 15 K which in general are similar to the first two steps discussed in Sect. 4.2 for GaN. At RT the first step is more vague and can be also interpreted as a sub-linear increase of the mean defect concentration with ion fluence (see black lines in Fig. 5.30 and discussion below). For ZnO the second step occurring at ion fluences above 2×10^{15} cm^{-2} does not show an effect of temperature. In contrast to that for CdTe a clear effect of temperature is seen. Furthermore, it is worth mentioning that for both materials there is a certain range of ion fluences for which more damage is produced at RT than at 15 K (see Fig. 5.30) with the effect being stronger in CdTe than in ZnO (for details see [26] and [101]). More damage at a higher temperature is opposite to what one usually would expect (see Sect. 5.3.1). From this finding it can be suspected that secondary defects are formed by a process which is enhanced at RT.

5.5.1 ZnO

In Fig. 5.31a defect profiles of ZnO implanted with Ar ions at 15 K are shown for very low ion fluences corresponding to the first step of damage formation (see Fig. 5.30a). In this case the shape of the measured profiles is in reasonable agreement with that calculated by SRIM using the displacement energies given in Chap. 3. This suggests that damage formation at 15 K is determined by the primary displacements. In Fig. 5.31b the defect concentration is plotted versus the number of displacements per lattice atom, n_{dpa}, for different ion fluences and various depths with n_{dpa} being calculated for the respective depth. The unique curve obtained

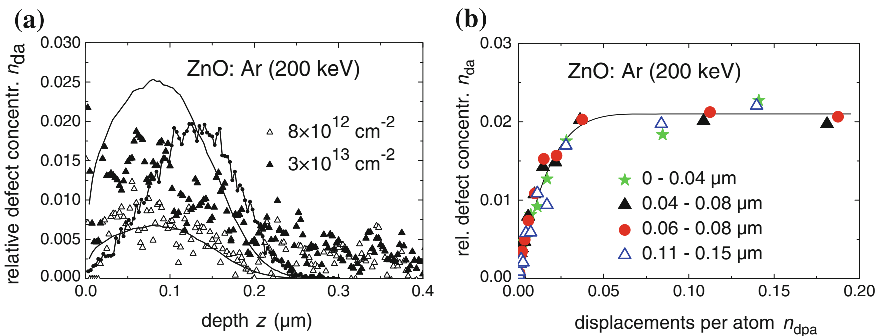

Fig. 5.31 Defect profiles $n_{da}(z)$ for ZnO implanted with 200 keV Ar ions at 15 K to two ion fluences (**a**). The distribution of primary displacements per atom (*thin solid lines*) and the ion distribution (*thick dashed line*; in arbitrary units) are given for comparison. In part (**b**) the relative defect concentration n_{da} is plotted versus the number of displacements per atom, n_{dpa}, for different ion fluences and different depths. The n_{dpa} values here are taken at the particular depths indicated in the figure (for details see [27])

confirms the suggestion made above. The correlation of damage formation at this early stage with the number of primary displacements is also obvious when comparing the results for different ion species implanted at 15 K [30, 100]. The curve in Fig. 5.31b shows the typical increase-and-saturation behaviour of the first step of damage formation as already discussed in Sects. 5.4.1 and 5.4.2. For this early stage of damage formation a slight effect of temperature is seen (see Fig. 5.30 (a)). At RT no clear step occurs but the defect concentration increases continuously but sub-linear with ion fluence (see Fig. 5.30a). The RT data are well represented by $n_{\mathrm{da}} \propto N_{\mathrm{I}}^{0.5}$ (see black line in Fig. 5.30a). Such a fluence dependence was deduced for describing damage formation in B ion implanted Si at RT (see Sect. 3.3.2). For that, homogeneous nucleation of defects was assumed with unsaturable traps being dominant that can accept migrating interstitials without limit and without change of probability of this process to occur [102]. Dislocation loops may be such traps. The suggested mechanism implies that defects are mobile which is consistent with the fact that it is found at RT but not at 15 K. However, more experimental data would be necessary to confirm this conclusion.

For higher ion fluences corresponding to the second step of damage formation (see Fig. 5.30a), typical RBS channelling spectra of ZnO Ar ion implanted at 15 K are shown in Fig. 5.3c). Damage profiles were calculated from these spectra with DICADA assuming the existence of uncorrelated displaced lattice atoms (see Fig. 5.3f). As already discussed in Sect. 5.2.2, the shape of these profiles indicates that this assumption is not correct. The high dechannelling background of the spectra points to the existence of extended defects even though implantation and analysis were performed at 15 K. For implantation at RT the RBS channelling spectra exhibit the same appearance (see Fig. 5.32) which suggests that similar defect structures are produced at both temperatures. TEM investigations were performed for ZnO implanted with N ions at RT to an ion fluence corresponding to about 0.1 dpa which is close to the start of the second step of damage formation

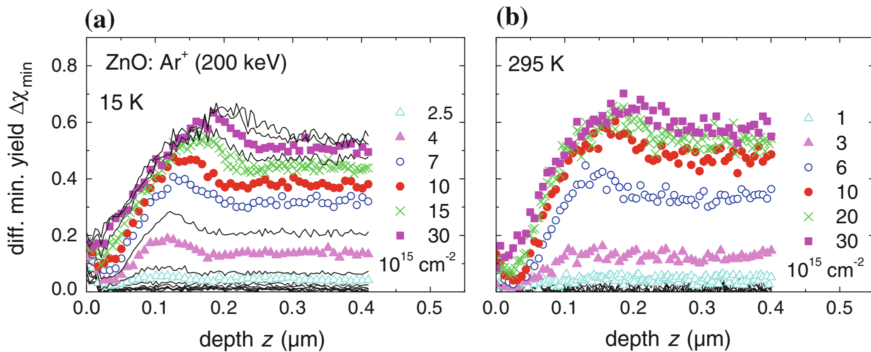

Fig. 5.32 Difference in minimum yield $\Delta\chi_{\mathrm{min}}$ versus depth z for 200 keV Ar ion implanted ZnO with implantation and subsequent measurement being performed at 15 K (**a**) and at 295 K (**b**) [86]. *Solid lines* are results for intermediate fluences which are not included in the legend for clarity

(see Fig. 5.30a) [103]. The formation of interstitial loops was observed in agreement with theoretical calculations that predict a high mobility of interstitials in ZnO at RT (see [103] and references therein). Obviously this process continues during further implantation and results in a dense network or tangle of dislocation loops and stacking faults which results in an increase of the yield of backscattered He ions as shown in Figs. 5.3c and 5.32. The similarity in the shape of the RBS spectra at RT and at 15 K suggests that extended defects form already at temperatures as low as 15 K. Taking further into account the low effect of temperature at this stage of damage formation (see Fig. 5.30a) it can be concluded that thermal diffusion of point defects is less important for the process of formation of extended defects. One may suspect that the formation of ordered clusters of interstitials (i.e. interstitial loops) is energetically favoured against random agglomerates. This may yield a driving force being almost independent of temperature. Furthermore, the second step of damage formation was found to be almost independent of ion species. The defect concentration measured at RT scales with n_{dpa}, the number of displacement per lattice atom [104]. Results measured at 15 K indicate a weak effect of ion mass but there are not enough data for a clear statement [30]. The low effect of ion mass means that there is no influence of the density of the collision cascades. Only the total number of displacements is important for the amount of damage measured after implantation. However, there are also few exceptional elements for which chemical effects become important in the process of damage formation. For RT ion implantation in ZnO B ions were found to stabilise defects in ZnO [101]. And by implantation of 60 keV Si ions in ZnO at 77 K even partial amorphisation was found for an ion fluence of 8×10^{16} cm^{-2} [105]. This ion fluence corresponds to a Si concentration of 10–15 at.%. Obviously the high Si concentration allows for nucleation and stabilisation of the amorphous phase. In summary, the mechanisms of damage production in ZnO are not yet fully understood, and more experimental work is necessary in order to clarify the influence of ion mass and of chemical effects on damage formation in this material.

5.5.2 CdTe

In case of CdTe ion implanted and analysed at 15 K, two steps of damage formation are clearly visible (see Fig. 5.30b. The corresponding defect profiles are depicted in Fig. 5.33b for low and in Fig. 5.3e for high ion fluences. It can be seen that only for fluences below 1×10^{13} cm^{-2} the defects as visible by RBS are located at the depth of nuclear energy deposition. In combination with the low defect concentration of $n_{da} < 0.04$ this suggests that the damage accumulation in this stage can be ascribed to isolated point defects the formation of which is based on nuclear energy deposition. The defect concentration remains below 0.1 over a wide range of ion fluences up to about 2×10^{15} cm^{-2} (see Figs. 5.3e, 5.30b, 5.33b)

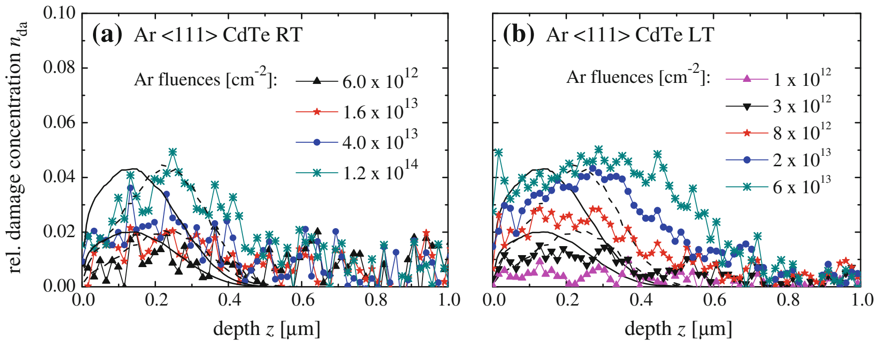

Fig. 5.33 Damage profiles $n_{da}(z)$ for CdTe implanted with 270 keV Ar (**a**) at RT and (**b**) at 15 K (LT) to various ion fluences [28]. The distribution of primary displacements (*solid lines*) and the ion distributions (*dashed lines*) are given for comparison in arbitrary units. They were calculated with SRIM

which indicates an equilibrium between defect production and recombination. However, already from $N_I = 2 \times 10^{13}$ cm^{-2}—when the first plateau is about reached—a significant deviation between measured and calculated defect distribution occurs and the thickness of the implanted layers equals at least twice of the projected range of the implanted ions. However, secondary ion mass spectrometry measurements on CdTe implanted with 150 keV Mg ions show a good agreement of the measured dopant profiles with the calculated distributions although the corresponding RBS spectra clearly indicate post-range defects [106]. This indicates that the deviation between calculated and measured defect profiles as seen in Fig. 5.33b is not a problem of calculation but points to a diffusivity of defects even at 15 K. The second step of damage formation starts for $N_I > 2 \times 10^{15}$ cm^{-2} (see Fig. 5.30b) and the mean defect concentration saturates at $n_{da} \approx 0.3$. A more detailed RBS study with different energies of the analysing He ions performed at the temperature of implantation of 15 K suggests that the defects produced are predominantly characterised by uncorrelated displaced lattice atoms. The contribution of correlated displaced lattice atoms pointing to extended defects was found to be low [28]. Therefore it is assumed that at high ion fluences non-recombinable random clusters of point defects and only very few extended defects are produced. These defects start to form at a depth of about 0.35 μm (see Fig. 5.3e) which is rather deep at the end of the range of the implanted ions (see Figs. 5.3e and 5.33b). Finally it should be mentioned that at very high ion fluences additional damage formation starts at the surface (see Fig. 5.3e and [26]).

When the Ar ions are implanted at RT, the damage evolution with ion fluence is clearly different to what is observed at 15 K (see Fig. 5.30b). At low ion fluences $N_I < 2 \times 10^{14}$ cm^{-2} the mean defect concentration n_{da} increases proportional to N_I^m with $m \approx 0.37$. A linear relationship of $n_{da}(N_I)$ is not observed but may occur at

even lower ion fluences and correspondingly smaller defect concentrations which cannot be detected by RBS. The exponent m is even smaller than the one of 0.5 discussed for the case of ZnO (see Sect. 5.5.1). A possible explanation for this could be complicated interaction processes of defects from different ion impacts involving annihilation and conglomeration of certain defect clusters. Further defect studies would be necessary for understanding the defect formation in CdTe ion implanted at RT with low ion fluences. For fluences $N_I > 2 \times 10^{14}$ cm^{-2} a steeper increase of the defect concentration is found, which finally saturates at a value of $n_{da} \approx 0.3$ which is similar to what is observed for implantation at 15 K (see Fig. 5.30b). But the onset of this second increase of n_{da} is at an ion fluence being about one order of magnitude lower than that at 15 K. Finding more damage after implantation at a higher temperature is a quite unusual behaviour. The most obvious explanation is the formation of extended defects the growth of which is supported by a thermal mobility of point defects. And indeed the existence of extended defects in CdTe after implantation at RT is experimentally confirmed both by energy-dependent RBS analysis and by TEM (see [26, 107] and references therein) for sufficiently high ion fluences.

Similar experiments as presented here for Ar ion implantation in CdTe were performed with Sb ions. In general the same results were found [26]. Besides the lack of amorphisation, the most intriguing feature in CdTe is that the defects extend deeply into the crystal. In previous studies at RT this observation was attributed to thermal effects. In CdTe, for instance, the high mobility of irradiation induced Te interstitials may result in an enhanced defect recombination as well as defect diffusion both towards the surface and into the depth. This has been suggested to be responsible for the behaviour observed at RT (see [106] and references therein). And indeed comparing damage formation at RT and at 15 K reveals significant differences which—in difference to the behaviour in GaN and ZnO—indicate the importance of thermal mobility of defects. However, efficient non-thermal defect diffusion and recombination seems to occur also at the low temperature. One explanation for the low damage concentration remaining from single ion impacts is related to the high ionicity of the material which may allow for efficient defect recombination during relaxation of the collision cascades by mechanisms as described in [4]. A possible explanation for non-thermal defect diffusion is based on the electronic energy loss of the implanted ions by an effect known as recombination-enhanced diffusion [108, 109]. Electron–hole pairs produced by electronic energy loss recombine and release energy in the form of photons, secondary electronic excitations (Auger effect), or phonons. Whereas the former two processes do not enhance defect diffusion, the recombination energy deposited locally at the recombination center, i.e., the defect, in form of vibrational energy (phonons) can result in recombination-enhanced diffusion. This mechanism was successfully used for explaining the observations for low-temperature ion implanted CdTe (see [26] for a more detailed discussion). Also for ion implanted ZnSe, the long range of defects has been attributed to this process [110].

5.6 Summarising Discussion

It is without debate that the microscopic processes during ion implantation are different for every single semiconductor. However, three groups of semiconductors can be identified which show a similar behaviour on a macroscopic scale. Materials of group I exhibit a continuous transition towards amorphisation at temperatures T being sufficiently lower than a critical temperature T_c. In case of group II, amorphisation can be achieved at low temperatures but only by secondary processes resulting in a discontinuous transition to amorphisation. And finally, materials of group III could not be amorphised by implantation of moderate ion fluences (which do not alter the stoichiometry significantly) nor yet at low temperatures.

When the implantation starts, i.e. for very low ion fluences, each ion impinges on still crystalline material. In this range a linear increase of the damage concentration as a function of the ion fluence is often found experimentally and is used for determining damage cross-sections σ_{dam} of individual ions as explained in Sect. 5.3.5. The σ_{dam} values presented above result from RBS measurements. In a rough approximation one could say that with this technique a weighted counting of displaced lattice atoms is performed. Assuming all atoms being displaced within a single ion impact (relative concentration of displaced lattice atoms of unity), the cross-section σ_{dam} turns into an area of the damaged region (projected to the surface). The latter yields an estimate of the diameter of the damage cluster produced per ion assuming a circular shape as a first approximation.

If the diameter of the damage cluster is much larger than the interatomic spacing, it is reasonable to conclude that within a single ion impact heavily damaged and/or amorphous material is produced. This is the case for materials of group I at $T \ll T_c$ for sufficiently heavy ion species (see Sect. 5.3.4). Under such conditions complete amorphisation of the ion implanted layers is obtained by accumulation and stimulated growth of these clusters.

In many other cases the diameter of the damage cluster is of the order of the interatomic spacing only. In this case an amorphous or heavily damaged cluster cannot be defined. This in turn means that the assumption that all atoms within the damage cluster are displaced is not correct. From that it may be suspected that only point defects or point defect clusters survive the relaxation of the collision cascades of a single ion in perfect material, which often was supported by other experimental techniques such as TEM. There are several scenarios for which only point defects remain from single ion impacts in crystalline semiconductors: (i) It is observed for materials of group I at $T \ll T_c$ for light ions such as He or B which produce more dilute collision cascades (see Fig. 5.14 and corresponding text in Sect. 5.3.4). (ii) It is further found for materials of group I at temperatures close T_c (see Figs. 5.15 and 5.16) at which intrinsic defects become thermally mobile, which promotes defect recombination during relaxation of the collision cascades. (iii) Independent of temperature it is the case for materials, in which more dilute collision cascades are to be expected due to high displacement energies (see Table 3.1 in Chap. 3) as for instance for ZnO, GaN and to some extent also for SiC. (iv) There is a group of

materials with moderate displacement energies but exhibiting a high intrinsic in-cascade recombination efficiency. This is the case for AlAs, CdTe and probably other II-IV semiconductors of this type. A high recombination efficiency due to some fundamental properties may also play a role in case of ZnO and GaN. Extensive Molecular Dynamics (MD) calculations were performed for ion implanted $Al_xGa_{1-x}As$ and compared with experimental results [111]. For reproducing the experimentally measured damage evolution as a function of ion fluence, for AlAs (x = 1) the temperature of the material in the MD calculations had to be artificially increased. This can be understood as emulating non-thermal recombination processes, i.e. a non-thermal mobility of defects. In case of CdTe the low damage cross-section even at low temperatures was attributed to the high ionicity of the material as well as to effects of the electronic energy loss of the ions [26].

As the implantation proceeds and the ion fluences increases, the ion impacts start to overlap. That is the ions do no more impinge on crystalline but on material which is already damaged by previous ions. In case of scenario (i) this results in the agglomeration of point defects to larger clusters and finally to amorphisation (see Sect. 5.3.3) as there is almost no defect mobility at the respective temperatures. Contrary, for all other scenarios the either thermal or non-thermal mobility of intrinsic defects results in recombination of newly produced defects with those from previous ions. The balance between defect production and defect recombination explains the almost constant defect concentration over a wide range of ion fluences (i.e. the first plateau in the damage evolution versus ion fluence) observed in corresponding cases of (ii) to (iv) as seen in Figs. 5.15, 5.16, 5.21a, 5.27, 5.29 and 5.30. In several cases it could be shown by TEM that besides point defect recombination also small extended defects such as stacking faults and dislocation loops start to form in this range of ion fluences (see e.g. Sects. 5.4.2 and 5.5.1).

In all cases investigated with scenarios (ii)–(iv), the first plateau gets interrupted as ion implantation continues and the damage concentration again starts to increase significantly. The processes being responsible for this behaviour depend very much on the particular material (see sections above). At this stage of rather high ion fluences the following aspects or secondary processes are of importance: the high concentration of implanted ions which introduce additional volume into the implanted layer or may cause chemical effects, the increase of ion flux for reaching the correspondingly high ion fluences and the further formation of tangles of extended defects. For the latter also mechanical properties may come into play. Especially in materials with wurtzite structure such as GaN and ZnO even at low temperatures the ordered aggregation of vacancies or interstitial atoms into extended defects seems to be favoured against the formation of random damage clusters (see Sects. 5.4.2 and 5.5.1).

The secondary processes mentioned above may finally result in the nucleation of amorphous seeds which—once they have formed—grow rapidly during further implantation. This mechanism may explain the transition towards complete amorphisation of the implanted layers within a narrow ion fluence interval often observed in these cases (see e.g. Figs. 5.15, 5.21 and 5.29). However, so far no amorphisation by ion implantation was observed in ZnO and CdTe (for moderate

ion fluences which do not alter the stoichiometry significantly). They are composed of elements from group 12 and 16 of the periodic table. Although there are much less papers on ion-beam induced damage formation in other than the two mentioned compounds of group 12 and 16, resistance to amorphisation seems to be a common characteristic of all of them (see [26] and references therein). Except for ZnO, for most of these compounds displacement energies below 10 eV were found (see [112] and references therein). This suggests very efficient recombination processes to occur during ion implantation even in pre-damaged material.

Finally, it is interesting going back to the damage cross-section σ_{dam} measured at low temperature for ions impinging on still undamaged materials. This quantity is determined from the increase of the defect concentration measured by RBS at sufficiently low ion fluences (see (5.9) and σ_{def} in (5.10)). As already mentioned above, the susceptibility of materials to ion-beam induced damage formation—and consequently σ_{dam}—should be related to some fundamental properties characterising the chemical bonds and the bond strength of the materials. In this context one of the most commonly used ordering parameters is the ionicity. We found the quantity $\tilde{R}_\sigma$ to be useful which is quoted as to be an effective orbital iconicity. $\tilde{R}_\sigma$ is calculated from the orbital radii of the atoms of the respective material and was used for investigating the ability of binary semiconductors for wurtzite formation [113]. In Fig. 5.34 the cross-section σ_{dam} is plotted as a function of $\tilde{R}_\sigma$ for Ar ion implantation into various materials. It is found that anion series form for the cations of one period. Within each anion series the cross-section decreases with rising ionicity. Exceptions are SiC and CdTe. In case of SiC the value of σ_{dam} is higher than one would expect. The measured value for CdTe one would expect close to the values of In containing compounds. However, it is significantly lower. So far no satisfactory explanation can be given for the observed deviations. The general relation of σ_{dam} to the ionicity of the materials coincides with the well-known picture regarding the amorphisability of materials under ion irradiation. Already in a very early paper it was observed that the resistance to ion beam induced amorphisation increases with the bond ionicity [114]. In a more recent review about

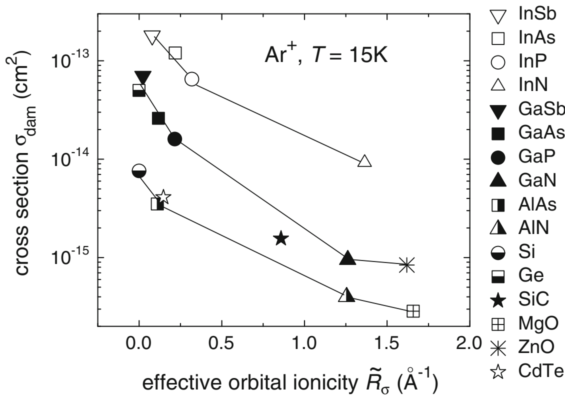

Fig. 5.34 Cross-section of damage formation σ_{dam} for Ar ion implantation in various materials versus $\tilde{R}_\sigma$ representing an effective orbital ionicity. The *lines* indicate the anion series for the cations of one period (for details see text)

understanding the resistance to amorphisation by ion irradiation it is stated that a material is amorphisable by radiation damage if its chemistry allows it to form a covalent network [115]. Contrary, nondirectional ionic bonds are assumed to enable a more easy recovery of ion-induced damage during relaxation of the collision cascades. Here we do not regard the amorphisability of materials but try to understand the trend of the cross-section of damage formation per individual ion in the virgin (undamaged) materials. However, it is obvious that the mechanisms discussed above are also important for this subject, because they pertain to the effects within the primary collision cascades. The occurrence of anion series being different for the various cations was found in other contexts too (see e.g. [116]).

In this chapter ion beam induced effects in semiconductors are reviewed with special attention to primary effects and binary materials. The influence of the various parameters during implantation on the process of damage formation is demonstrated. Simple models allow for a systematisation of the results over a wide range of parameters. This is a further step on the way for predicting of damage to be expected for certain implantation conditions. Empirical relations seem to exist between the low-temperature cross-section of damage formation and the nuclear and electronic energy loss of the implanted ions. The low-temperature damage cross-section also reveals bonding properties of the materials. However, the microscopic processes are different in the various materials and still not completely understood. This makes modelling beyond empirical knowledge difficult. More experimental data and more defect-specific techniques are needed. This together with new demands from industry and new materials will keep ion implantation in semiconductors a vivid field of research.

References

1. J.A. Davies, Mater. Chem. Phys. **46**, 111 (1996)
2. C.B. Yarling, J. Vac. Sci. Technol. **A18**, 1746 (2000)
3. G. Hobler, G. Otto, Mater. Sci. Semicond. Process. **6**, 1 (2003)
4. K. Trachenko, J.M. Pruneda, E. Artacho, M.T. Dove, Phys. Rev. B **71**, 184104 (2005)
5. E. Wendler, in *AIP Conference Proceedings 1336*, 2011, p. 621
6. H. Bernas (ed.), *Material Science with Ion Beams* (Springer, Berlin, 2010)
7. L. Pelaz, L.A. Marqués, J. Barbolla, J. Appl. Phys. **96**, 5947 (2004)
8. W. Wesch, E. Wendler, C.S. Schnohr, Nucl. Instrum. Methods Phys. Res. B **277**, 58 (2012)
9. T. Steinbach, J. Wernecke, P. Kluth, M.C. Ridgway, W. Wesch, Phys. Rev. B **84**, 104108 (2011)
10. T. Steinbach, W. Wesch, Nucl. Instrum. Methods Phys. Res. **B319**, 112 (2014)
11. B. Schmidt, W. Wetzig (eds.), *Ion Beams in Materials Processing and Analysis* (Springer, Wien, 2013)
12. W.-K. Chu, J.W. Mayer, M.-A. Nicolet, *Backscattering Spectrometry* (Academic Press, New York, 1978)
13. G. Götz, K. Gärtner (eds.), *High Energy Ion Beam Analysis of Solids* (Akademie-Verlag, Berlin, 1988)
14. M. Nastasi, J.W. Mayer, Y. Wang, *Ion Beam Analysis: Fundamentals and Applications* (CRC Press, New York, 2014)

15. J.P. Biersack, J.F. Ziegler, *The Stopping and Ranges of Ions in Matter*, vol. 1 (Pergamon Press, Oxford, 1985)
16. K. Gärtner, Nucl. Instrum. Methods B **132**, 147 (1997). and references therein
17. A. Turos, P. Jozwik, L. Nowicki, N. Sathish, Nucl. Instrum. Methods Phys. Res. **332**, 50 (2014). and references therein
18. G. Götz, B. Gruska, Nucl. Instrum. Methods **194**, 199 (1982)
19. W. Wesch, K. Gärtner, A. Jordanov, G. Götz, Nucl. Instrum. Methods Phys. Res. B **45**, 446 (1990)
20. E. Bøgh, Can. J. Phys. **46**, 653 (1968)
21. K. Schmid, Rad. Eff. **17**, 201 (1973)
22. K. Gärtner, Nucl. Instrum. Methods Phys. Res. B **227**, 522 (2005)
23. E. Albertazzi, M. Bianconi, G. Lulli, R. Nipoti, M. Cantino, Nucl. Instrum. Methods Phys. Res. B **118**, 128 (1996)
24. A. Mazzone, Nucl. Instrum. Methods Phys. Res. B **34**, 22 (1988)
25. E. Wendler, L. Wendler, Appl. Phys. Lett. **100**, 192108 (2012)
26. C.W. Rischau, C.S. Schnohr, E. Wendler, W. Wesch, J. Appl. Phys. **109**, 113531 (2011)
27. E. Wendler, O. Bilani, K. Gärtner, W. Wesch, F.D. Auret, K. Lorenz, E. Alves, Nucl. Instrum. Methods Phys. Res. B **267**, 2708 (2009)
28. C.W. Rischau, C.S. Schnohr, E. Wendler, W. Wesch, Nucl. Instrum. Methods Phys. Res. B **272**, 338 (2012)
29. E. Wendler, W. Wesch, AYu. Azarov, N. Catarino, A. Redondo-Cubero, E. Alves, K. Lorenz, Nucl. Instrum. Methods Phys. Res. B **307**, 394 (2013)
30. K. Lorenz, E. Wendler, in *Ion Implantation*, ed. by M.S. Goorsky (InTech, Rijeka, 2012)
31. E. Wendler, T. Opfermann, P.I. Gaiduk, J. Appl. Phys. **82**, 5965 (1997)
32. F.F. Morehead Jr, B.L. Crowder, Rad. Eff. **6**, 27 (1970)
33. E. Wendler, A. Heft, W. Wesch, Nucl. Instrum. Methods Phys. Res. B **141**, 105 (1998)
34. W.J. Weber, Y. Zhang, L. Wang, Nucl. Instr. Meth. B **277**, 1 (2012)
35. J.R. Dennis, E.B. Hale, J. Appl. Phys. **49**, 1119 (1978)
36. R.D. Goldberg, J.S. Williams, R.G. Elliman, Nucl. Instrum. Methods Phys. Res. B **106**, 242 (1995)
37. E. Wendler, N. Dharmarasu, E. Glaser, Nucl. Instrum. Methods Phys. Res. B **160**, 257 (2000)
38. E. Wendler, B. Breeger, C. Schubert, W. Wesch, Nucl. Instrum. Methods Phys. Res. B **147**, 155 (1999)
39. T.E. Hayes, O.W. Holland, Appl. Phys. Lett. **59**, 452 (1991)
40. R.A. Brown, J.S. Williams, Phys. Rev. B **64**, 155202 (2001)
41. A. Turos, A. Stonert, B. Breeger, E. Wendler, W. Wesch, R. Fromknecht, Nucl. Instrum. Methods Phys. Res. B **148**, 401 (1999)
42. AYu. Kuznetsov, J. Wong-Leung, A. Hallén, C. Jagadish, B.G. Svenson, J. Appl. Phys. **94**, 7112 (2003)
43. F. Gao, W.J. Weber, J. Appl. Phys. **94**, 4348 (2003)
44. G. Litrico, G. Izzo, L. Calcagno, F. La Via, G. Voti, Diam. Relat. Mater. **19**, 39 (2009)
45. H. Hofsäss, S. Winter, S.G. Jahn, U. Wahl, E. Recknagel, ISOLDE Collaboration, Nucl. Instrum. Methods Phys. Res. **B63,** 83 (1992)
46. A. Pillukat, K. Karsten, P. Ehrhart, Phys. Rev. **B53**, 7823 (1996)
47. H. Hausmann, P. Ehrhart, Phys. Rev. B**51**, 17542 (1995)
48. U.G. Akano, I.V. Mitchell, F.R. Shepherd, Appl. Phys. Lett. **62**, 1670 (1993)
49. E. Wendler, W. Wesch, G. Götz, Nucl. Instrum. Methods Phys. Res. B **52**, 57 (1990)
50. W. Wesch, E. Wendler, N. Dharmarasu, Nucl. Instrum. Methods Phys. Res. B **175–177**, 257 (2001)
51. U.G. Akano, I.V. Mitchell, F.R. Shepherd, C.J. Miner, Can. J. Phys. **70**, 789 (1992)
52. J. Linnros, R.G. Elliman, W.L. Brown, J. Mater. Res. **3**, 1208 (1988)
53. V. Heera, T. Henkel, R. Kögler, W. Skorupa, Phys. Rev. B **52**, 15776 (1995)
54. R. Lauck, E. Wendler, W. Wesch, Nucl. Instrum. Methods Phys. Res. B **242**, 484 (2006)

55. K. Jin, Y. Zhang, H. Xue, Z. Zhu, W.J. Weber, Nucl. Instrum. Methods Phys. Res. B **307**, 65 (2013)
56. W. Wesch, E. Wendler, G. Götz, Nucl. Instrum. Methods Phys. Res. B **22**, 532 (1987)
57. E. Wendler, G. Peiter, J. Appl. Phys. **87**, 7679 (2000)
58. E. Wendler, M. Schilling, L. Wendler, Vacuum **105**, 102 (2014)
59. G. Carter, Rad. Eff. **100**, 281 (1986)
60. P. Partyka, R.S. Averback, D.V. Frobes, J.J. Coleman, P. Ehrhart, W. Jäger, Appl. Phys. Lett. **65**, 421 (1994)
61. E. Glaser, T. Fehlhaber, B. Breeger, Nucl. Instrum. Methods Phys. Res. B **148**, 426 (1999)
62. E. Wendler, A. Stonert, A. Turos, W. Wesch, Nucl. Instrum. Methods Phys. Res. B **307**, 377 (2013)
63. W.J. Weber, L.M. Wang, N. Yu, N.J. Hess, Mater. Sci. Eng. A **253**, 62 (1998)
64. C. Ascheron, H. Neumann, Cryst. Res. Technol. **22**, 1493 (1987)
65. C. Ascheron, A. Schindler, R. Flagmeyer, G. Otto, Nucl. Instrum. Methods Phys. Res. B **36**, 163 (1989)
66. W. Bolse, Nucl. Instrum. Methods Phys. Res. B **148**, 83 (1999)
67. E. Wendler, Th Bierschenk, W. Wesch, E. Friedland, J.B. Malherbe, Nucl. Instrum. Methods Phys. Res. B **268**, 2996 (2010)
68. N. Hecking, K.F. Heidemann, E. TeKaat, Nucl. Instrum. Methods Phys. Res. B **15**, 760 (1986)
69. E. Wendler, P. Schoeppe, T. Bierschenk, S. Milz, W. Wesch, N.G. van der Berg, E. Friedland, J.B. Malherbe, Nucl. Instrum. Methods Phys. Res. B **286**, 93 (2012)
70. C.S. Schnohr, E. Wendler, K. Gärtner, W. Wesch, K. Ellmer, J. Appl. Phys. **99**, 123511 (2006)
71. M. Bianconi, G.G. Bentini, M. Chiarini, P. De Nicola, G.B. Montanari, A. Menin, A. Nubile, S. Sugliani, Nucl. Instrum. Methods Phys. Res. B **268**, 3451 (2010)
72. A.G. Cullis, P.W. Smith, D.C. Jacobson, J.M. Poate, J. Appl. Phys. **69**, 1279 (1991)
73. H.H. Tan, C. Jagadish, J.S. Williams, J. Zou, D.J.H. Cockayne, A. Sikorski, J. Appl. Phys. **77**, 87 (1995)
74. J.L. Klatt, R.S. Averback, D.V. Forbes, J.J. Coleman, Phys. Rev. B **48**, 17629 (1993)
75. B. Breeger, E. Wendler, Ch. Schubert, W. Wesch, Nucl. Instrum. Methods Phys. Res. B **148**, 468 (1999)
76. E. Wendler, B. Breeger, W. Wesch, Nucl. Instrum. Methods Phys. Res. B **175–177**, 78 (2001)
77. E. Wendler, B. Breeger, W. Wesch, Nucl. Instrum. Methods Phys. Res. B **175–177**, 83 (2001)
78. A. Stonert, A. Turos, L. Novicki, B. Breeger, E. Wendler, W, Wesch, Mod. Phys, Lett. **B15**, 1437 (2001)
79. E. Wendler, in *AIP Conference Proceedings 680*, Melville, New York, 2003, p. 670
80. B. Breeger, E. Wendler, unpublished
81. A. Gaber, H. Zillgen, P. Ehrhart, P. Partyka, R.S. Averback, J. Appl. Phys. **82**, 5348 (1997)
82. C. Liu, B. Mensching, M. Zeitler, K. Volz, B. Rauschenbach, Phys. Rev. B **57**, 2530 (1998)
83. E. Alves, M.F. da Silva, J.C. Soares, R. Vianden, J. Bartels, A. Kozanecki, Nucl. Instrum. Methods Phys. Res. B **147**, 383 (1999)
84. S.O. Kucheyev, J.S. Williams, C. Jagadish, J. Zou, G. Li, Phys. Rev. B **62**, 7510 (2000)
85. W. Jiang, W.J. Weber, S. Thevuthasan, J. Appl. Phys. **87**, 7671 (2000)
86. E. Wendler, A. Kamarou, E. Alves, K. Gärtner, W. Wesch, Nucl. Instrum. Methods Phys. Res. B **206**, 1028 (2003)
87. S.O. Kucheyev, A. Yu. Azarov, A. Titov, P.A. Karaseov, T.M. Kuchumova, J. Phys. D: Appl. Phys., 085309 (2009)
88. S. Charnvanichborikarn, M.T. Myers, L. Shao, S.O. Kucheyev, Scripta Mater. **67**, 205 (2012)
89. AYu. Azarov, A.I. Titov, S.O. Kucheyev, J. Appl. Phys. **108**, 033505 (2010)

90. F. Gloux, T. Wojtowicz, P. Ruterana, K. Lorenz, E. Alves, J. Appl. Phys. **100**, 073520 (2006)
91. P. Ruterana, B. Lacroix, K. Lorenz, J. Appl. Phys. **109**, 013506 (2011)
92. K. Pagowska, R. Ratajczak, A. Stonert, L. Nowicki, A. Turos, vacuum **83**, S145 (2009)
93. M. Katsikini, F. Pinakidou, E.C. Paloura, E. Wendler, W. Wesch, R. Manzke, J. Phys. **190**, 012065 (2009). (Conference series)
94. B. Lacroix, S. Leclerc, A. Declémy, K. Lorenz, E. Alves, P. Ruterana, Europhys. Lett. **96**, 46002 (2011)
95. A. Turos, Rad. Eff. Defects Solids **168**, 431 (2013)
96. K. Filintoglou, P. Kavouras, M. Katsikini, J. Arvanitidis, D. Christofilos, S. Ves, E. Wendler, W. Wesch, Thin Solid Films **531**, 152 (2013)
97. M. Ishimaru, Y. Zhang, W.J. Weber, J. Appl. Phys. **106**, 053513 (2009)
98. C. Ronning, M. Dalmer, M. Uhrmacher, M. Restle, U. Vetter, L. Ziegeler, H. Hofsäss, T. Gehrke, K. Järrendahl, R.F. Davies, ISOLDE Collaboration, J. Appl. Phys. **87**, 2149 (2000)
99. E. Wendler, W. Wesch, Nucl. Instrum. Methods Phys. Res. B **242**, 562 (2006)
100. K. Lorenz, E. Alves, E. Wendler, O. Bilani, W. Wesch, M. Hayes, Appl. Phys. Lett. **87**, 191904 (2005)
101. AYu. Azarov, E. Wendler, AYu. Kuznetsov, B.G. Svenson, Appl. Phys. Lett. **104**, 052101 (2014)
102. L.T. Chadderton, Radiat. Eff. **8**, 77 (1971)
103. G. Perillat-Marceroz, P. Gergaud, P. Marotel, St. Brochen, P.H. Jouneau, G. Feuillet, J. Appl. Phys. **109**, 023513 (2011)
104. AYu. Azarov, S.O. Kucheev, A.I. Titov, P.A. Karaseov, J. Appl. Phys. **102**, 083547 (2007)
105. S.O. Kucheyev, J.S. Williams, C. Jagadish, J. Zou, C. Evans, A.J. Nelson, A.V. Hamza, Phys. Rev. B **67**, 094115 (2003)
106. G. Leo, A.V. Drigo, A. Traverse, Mater. Sci. Eng., B **16**, 123 (1993)
107. G. Leo, M.O. Ruault, J. Appl. Phys. **73**, 2234 (1993)
108. J.C. Bourgoin, J.W. Corbett, Radiat. Eff. **36**, 157 (1978)
109. L.C. Kimerling, Solid-State Electron. **21**, 1391 (1978)
110. H. Kerkow, V.X. Quang, B. Selle, J. Cryst. Growth **117**, 677 (1992)
111. K. Gärtner, T. Clauß, Nucl. Instrum. Methods Phys. Res. B **268**, 155 (2010)
112. V.I. Panov, A.A. Kharkov, Semiconductors **30**, 444 (1996)
113. C.-Y. Yeh, Z.L. Lu, S. Froyen, A. Zunger, Phys. Rev. B **46**, 10086 (1992)
114. H.M. Naguib, R. Kelly, Radiat. Eff. **25**, 1 (1975)
115. K. Trachenko, J. Phys. Condens. Matter **16**, R1491 (2004)
116. J.J. Gilman, J. Phys. D Appl. Phys. **41**, 074020 (2008)

Chapter 6
Damage Formation, Amorphization and Crystallization in Semiconductors at Elevated Temperatures

James S. Williams

Abstract This chapter focusses on damage build up, amorphization and crystallization processes in a range of semiconductors under irradiation conditions close to the critical temperature for amorphization where small changes in ion fluence, ion flux, ion mass and irradiation temperature have a strong effect on the damage level and nature of the residual disorder. Layer-by-layer amorphization (IBIIA) and ion-beam-induced epitaxial crystallization (IBIEC) phenomena are also highlighted as well as anomalous processes such as ion-induced swelling, porosity and surface erosion.

6.1 Introduction

This chapter reviews ion irradiation in semiconductors at elevated temperatures and builds on the content of the previous chapter (Chap. 5) which treated primary damage formation processes and focussed on damage accumulation and amorphization under a wide range of ion irradiation conditions. A key feature of this current chapter is that it focusses on irradiation conditions in which the damage produced within collision cascades is not stable at irradiation temperatures close to or above room temperature. In this case, as indicated in Chaps. 3 and 5, point defects can annihilate and can suppress amorphization but can also lead to the formation of a range of complex defect structures within the semiconductor, depending on the irradiation conditions used. Following the terminology used in previous chapters, this chapter specifically addresses the regime close to the critical temperature for amorphization, T_c, a situation where the disorder build up and amorphization processes are particularly difficult to model. Furthermore, to compliment the disorder build up data in previous chapters, this chapter highlights the

J.S. Williams (✉)
Research School of Physics and Engineering, Australian National University, Canberra ACT 2601, Australia
e-mail: jim.williams@anu.edu.au

© Springer International Publishing Switzerland 2016

W. Wesch and E. Wendler (eds.), *Ion Beam Modification of Solids*,
Springer Series in Surface Sciences 61,
DOI 10.1007/978-3-319-33561-2_6

nature of ion-induced disorder through presentation of transmission electron micrographs which directly show the disorder and amorphization microstructures.

For applications of ion implantation, the nature and location of amorphous layers and defect microstructures need to be known (and ideally to be able to be modelled) since ion-induced disorder usually needs to be effectively removed to restore the pristine semiconductor crystal. In this chapter, ion disordering, amorphization and ion-induced crystallization processes in silicon (Si) are treated first in some detail in Sect. 6.2. At irradiation temperatures where ion-induced defects are relatively stable, normally close to room temperature, disorder builds up in Si with ion fluence until complete amorphization occurs. However, at elevated temperatures efficient dynamic defect annealing can occur and the nature of residual disorder and the onset of amorphization with ion fluence change completely, a regime close to T_c that is treated in Sect. 6.2.1. Damage build up often follows a two stage process in this regime: the first stage usually involving an increase in the level of residual crystalline defects with fluence to a saturation level and a second stage in which an amorphous phase is spontaneously nucleated at a critical high fluence. Such nucleation-limited amorphization (treated in Sect. 6.2.2) is more difficult to model, particularly as the critical fluence for amorphization depends in a complex way on irradiation temperature, ion mass, ion energy and ion flux. Once an amorphous layer forms in this regime, it can grow with increasing fluence in a layer-by-layer manner, by so called ion beam induced interfacial amorphization (IBIIA) and the modelling of this process is treated in Sect. 6.2.3. At higher irradiation temperatures, defect-mediated crystallisation of pre-existing amorphous layers can be induced in Si. This latter ion beam induced epitaxial crystallisation (IBIEC) process, treated in Sect. 6.2.4, occurs at temperatures well below those at which normal thermal epitaxial crystallisation takes place. Although it is now possible to establish that ion-induced defect generation precisely at the amorphous-crystalline interface is responsible for IBIEC, modelling of the process (covered in Sect. 6.2.5) has again proven to be difficult.

In germanium (Ge), treated in Sect. 6.3, dynamic annealing is also important in suppressing amorphization at elevated temperatures but the defect interactions, stable defect formation and amorphization in Ge are all somewhat different to the behaviour in Si. For example, it is easier to amorphize Ge at lower critical fluences and higher temperatures than Si, and disorder build up, amorphization and IBIEC processes in Ge are treated in Sect. 6.3.1. Vacancy-related defects appear to be more stable in Ge than in Si and, when formed, amorphous Ge develops distinct porosity for irradiation at and above room temperature. The formation of porous amorphous Ge at and above room temperature is covered in Sect. 6.3.2.

In terms of compound semiconductors, Chap. 5 illustrated that they can exhibit very different damage build up processes since the mobility of irradiation-induced defects is widely different across these materials. For example, like Si and Ge, gallium arsenide (GaAs), silicon carbide (SiC) and indium phosphide (InP) are easily amorphized at room temperature under ion irradiation although, as might be expected, the details of disorder build up, dynamic annealing and amorphization in these materials are material-specific, exhibiting differences in both T_c and the

critical fluence for amorphization, as illustrated in the previous chapter. Of this class of compound binary semiconductors, GaAs is treated in Sect. 6.4 in the temperature region close to T_c. Section 6.4.1 covers the disordering and amorphization mechanisms and Sect. 6.4.2 the layer-by-layer growth processes such as IBIIA and IBIEC. In Sect. 6.5 there is a further focus on disordering close to T_c in SiC (Sect. 6.5.1) and InP (Sect. 6.5.2), especially on IBIIA and IBIEC processes and the activation kinetics associated with them.

Another class of binary III-V semiconductors that are not as readily amorphized includes aluminium arsenide (AlAs) and gallium nitride (GaN) that are discussed in detail in Chap. 5. These materials require low irradiation temperatures and/or the trapping of irradiation-induced defects at implanted impurities (that is, chemical effects) in order to amorphize them. This indicates that irradiation-induced defects are not stable in these materials and readily annihilate during irradiation (within or immediately following collision cascades), thus suppressing amorphization. Yet another class of binary compound materials consists of those that appear to be not amorphizable under any moderate-fluence irradiation conditions, such as II-VI materials cadmium telluride (CdTe) and zinc oxide (ZnO) that are also discussed in some detail in Chap. 5. Extremely high defect annihilation rates and ionic bonding in these materials, as well as the inability to nucleate amorphous layers at defects and surfaces are factors which characterize such materials. The disorder build-up processes in the binary semiconductors AlAs, GaN, CdTe and ZnO are not further discussed in this chapter. However, III-V ternary compound semiconductors and binary multilayers are briefly covered in Sect. 6.5.3 since they exhibit some interesting disordering behaviour as a result of varying one or more of the group III species in ternary alloys or, in the case of multilayers, placing a difficult to amorphize binary material (such as AlAs) adjacent to a material easy to amorphize (such as GaAs). Finally, some unusual features in GaN irradiated at and above room temperature, related to swelling and anomalous erosion, are treated in Sect. 6.5.4. Brief illustrations of irradiation-induced microstructures and species-specific amorphization in ZnO are given in Sect. 6.5.5. The final section (Sect. 6.6) in this chapter gives a summary of irradiation-induced amorphization and crystallization behaviour in a range of semiconductors, as well as providing some overall conclusions related to elevated temperature irradiation.

6.2 Si Disordering, Amorphization and Crystallisation Processes at Elevated Temperature

6.2.1 Dynamic Annealing and Defect Formation During Irradiation

As was outlined previously in Sect. 3.4 of Chap. 3 and Sect. 5.3.2 of Chap. 5, implantation temperature can determine whether point defects and clusters generated within collision cascades are stable or whether they can annihilate and/or

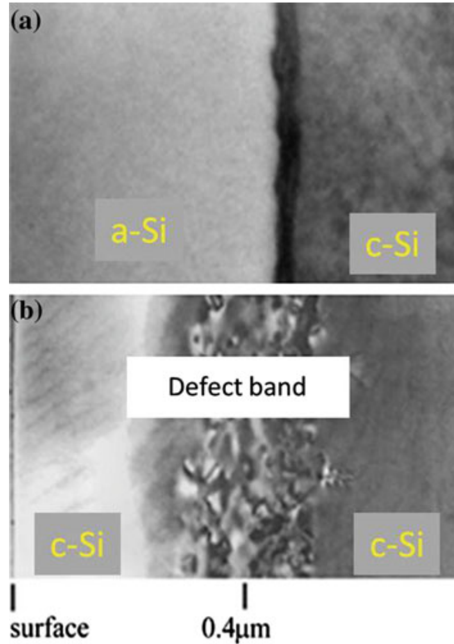

Fig. 6.1 XTEM images corresponding to 230 keV Si ion irradiation of Si (100) to a fluence of 5×10^{15} cm^{-2} at **a** 50 °C, and **b** 350 °C. Adapted from Williams [1]

migrate through dynamic annealing. Hence, the rate of build-up of residual disorder with fluence is reduced as the irradiation temperature is increased and subsequent amorphization, if indeed it occurs at all, will occur at increasingly higher ion fluence. An example of temperature-dependent effects in Si is shown by the cross-sectional transmission electron micrograph (XTEM) images in Fig. 6.1 [1]. Figure 6.1a depicts a continuous amorphous layer in Si, produced by 230 keV Si ions at a fluence of 5×10^{15} cm^{-2} at an implantation temperature of around 50 °C. The ion range is ~350 nm but, under these irradiation conditions, the amorphous layer is ~460 nm thick. Note that the boundary between the amorphous layer and the underlying Si substrate is quite sharp, indicating that defects produced in the tail of the Si implant distribution can annihilate quite effectively and perfectly at this implant temperature. However, if the implant temperature is raised to 350 °C, irradiation-produced defects are considerably more mobile and annihilate or cluster to effectively suppress amorphization [2], as shown in the XTEM micrograph in Fig. 6.1b. In this case there is a clearly observed band of defects consisting of interstitial clusters that evolve into well-defined line defects such as {311} defects and dislocation loops [3] on subsequent annealing. Note also that the defect band is centred considerably beyond the Si ion range, which is a feature of elevated temperature irradiation that we will discuss more fully below.

The build-up of ion damage as a function of fluence at various temperatures is conveniently obtained from the disorder peak area of Rutherford backscattering and

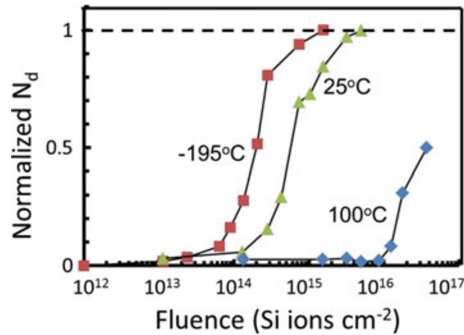

Fig. 6.2 Normalized number of displaced atoms (N_d) calculated from RBS and channelling spectra as a function of Si ion fluence for implant temperatures of −195 (*squares*), 25 (*triangles*) and 100 °C (*diamonds*) in Si. The disorder is normalised to that required to just form an amorphous layer (1.0). Adapted from Johnson and McCallum [4]

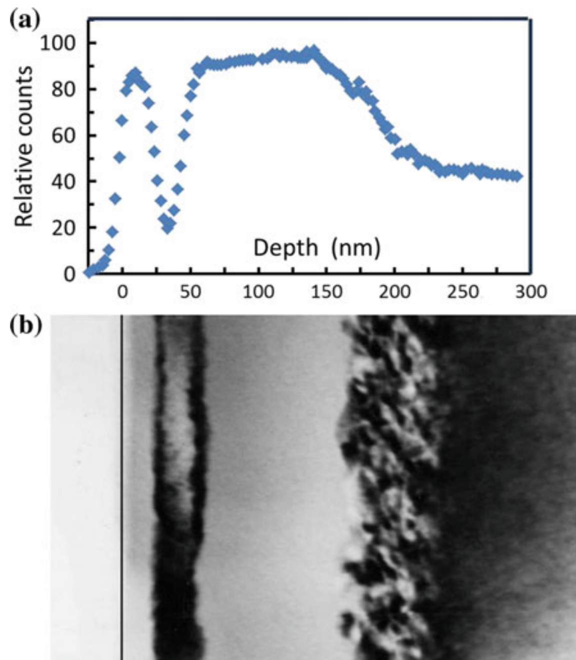

Fig. 6.3 **a** An RBS and channelling spectrum for an 80 keV Si implant into Si at 160 °C to a fluence of 10^{16} cm^{-2} at a beam flux of 2.7×10^{13} ions cm^{-2} s^{-1}. Adapted from Goldberg et al. [7]. **b** XTEM image of the sample in (**a**). Adapted from Goldberg [8]

channelling (RBS-C) spectra, as was illustrated in the previous chapter (Chap. 5) by Figs. 6.2, 6.3 and 6.4. This enables the relative disorder to be plotted as a function of irradiation temperature as shown in Fig. 6.6 of the previous chapter, where a critical temperature T_c and critical fluence N_{Ic} for the formation of continuous amorphous layers can be found. We show a further example of such disorder build-up for 245 keV Si ion bombardment of Si in Fig. 6.2, following the work of Johnson and McCallum [4]. Here, the integrated disorder is plotted as a function of Si ion fluence

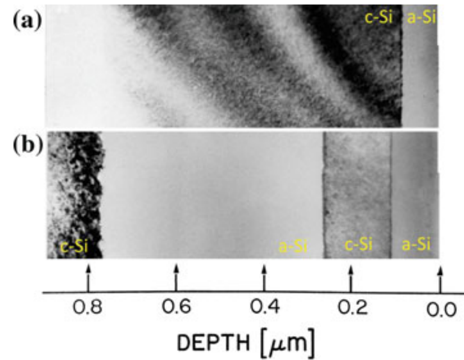

Fig. 6.4 XTEM images illustrating layer-by-layer amorphization of Si by 1.5 MeV Xe ion irradiation to a fluence of 5×10^{15} cm^{-2}: **a** a pre-existing amorphous layer on Si prior to Xe irradiation; and **b** following Xe irradiation at 208 °C. Adapted from Elliman et al. [9]

for 3 irradiation temperatures using a constant Si ion flux. The disorder builds up slowly at low fluences and then increases rapidly before saturation, giving rise to the well-known superlinear shape of the damage accumulation curve. However, the curves at −195 and 25 °C are displaced in fluence indicating that some defect annihilation is occurring under the irradiation conditions used even at room temperature. Raising the temperature to 100 °C causes this offset in fluence to shift by around two orders of magnitude compared with the −195 °C data, indicating quite efficient annihilation of irradiation-induced disorder at this temperature. These curves can be used to extract the N_{Ic} for amorphization from the half height. Thus, in order to form a buried amorphous layer the N_{Ic} are 2×10^{14}, 7×10^{14} and 2×10^{16} Si ions cm^{-2} for the irradiation temperatures of −195, 25 and 100 °C, respectively.

Between the two extreme disordering regimes illustrated in Fig. 6.1, namely near-stable damage leading to easy amorphization as opposed to strong annihilation and clustering of defects, the close balance between the rate of damage production within collision cascades and the rate of dynamic defect annealing and clustering can give rise to interesting defect-mediated phenomena. In this intermediate regime close to T_c, the disorder exhibits strong dependencies on implantation temperature, ion fluence and ion flux. Small changes in any of these parameters can result in dramatic differences in residual disorder from almost damage-free structures, as a result of efficient defect annihilation, to continuous amorphous layers. In this regime, amorphization can occur in an entirely different way, as a result of nucleation-limited or preferential amorphization processes [5]. For example, as the irradiation fluence increases and the density of defects increases, amorphous layers can spontaneously nucleate at the depth of maximum disorder. Such amorphous pockets and layers can then grow with increasing fluence to encompass the entire defective region [6]. We illustrate this behaviour in the next section.

6.2.2 *Amorphisation Processes at Elevated Temperature*

In the intermediate temperature regime referred to above, amorphous layers can be observed to nucleate preferentially at depths significantly away from the maximum

in the ion's nuclear energy distribution, at, for example, surfaces [7], interfaces and pre-existing defects [6, 7]. Figure 6.3 illustrates the case of preferential amorphization at a Si surface or, more precisely, at a SiO_2-Si interface. Figure 6.3a shows an RBS/channelling spectrum for an 80 keV Si implant into Si at 160 °C for a fluence of 10^{16} cm^{-2} at a flux of 2.7×10^{13} ions cm^{-2} s^{-1} [7].

This spectrum shows a strong disorder peak at the surface and a buried peak centred around the end-of-ion-range at about 120 nm. (The end-of-ion-range refers to the region in the tail of the ion range distribution about two standard deviations deeper than the projected ion range.) The corresponding XTEM micrograph in Fig. 6.3b [8] indicates that there are two amorphous layers present, one extending 25 nm from the surface and a buried layer from 60 to 160 nm. Between these layers is a crystalline Si region containing few defects but below the buried layer there is Si crystal rich in (interstitial-type) defect clusters. This result shows not only the nucleation of an amorphous region around the maximum in the nuclear energy distribution at about 80 nm but nucleation of an amorphous layer well away from the maximum disorder depth, at the surface. When the evolution of this defect structure was examined as a function of ion fluence [8], it was found that the deep disorder first accumulated as defect clusters of interstitial character at lower fluences. This defective region then appeared to collapse into an amorphous layer as the fluence increased. In addition, the surface amorphous layer was found to thicken with increasing fluence. This behaviour suggests that, in a regime where substantial dynamic annealing occurs during ion irradiation, defects not only annihilate and locally form defect clusters, but can also migrate and accumulate at SiO_2-Si interfaces. Collapse of such disorder to an amorphous phase, or nucleation of an amorphous phase at a defect band, can occur at a sufficiently high implantation fluences. Indeed, it has also been shown that a pre-existing dislocation band can act as a nucleation site for amorphization, even when it is situated well away from the disorder peak [5]. Furthermore, such dislocation bands were found to 'getter' interstitial-based defects from deeper in the material during irradiation [5]. Thus, it would appear that dislocation bands, surfaces (actually SiO_2-Si interfaces) and amorphous layers themselves are all good trapping sites or sinks for mobile defects in Si that may otherwise annihilate or form stable clusters close to where they come to rest.

With regard to existing amorphous layers acting as nucleation sites for preferential amorphization at elevated temperatures, the particular case of layer-by-layer amorphization or IBIIA is especially intriguing. An example of such behaviour is illustrated by the XTEM micrographs in Fig. 6.4 [9], where a pre-existing amorphous layer has been re-irradiated at elevated temperatures with MeV Xe ions. Clearly, the near-surface amorphous layer in Fig. 6.4a has increased in thickness when irradiated with 1.5 MeV Xe ions at 208 °C (Fig. 6.4b). Note that a buried amorphous layer has also formed at the Xe end-of-ion-range and the crystalline Si between the two amorphous layers is essentially defect-free, which suggests near-perfect defect annihilation in this region. Furthermore, both amorphous layers are observed to extend layer-by-layer via IBIIA with increasing ion fluence, presumably by the preferential trapping of mobile defects at the respective amorphous-crystalline interfaces.

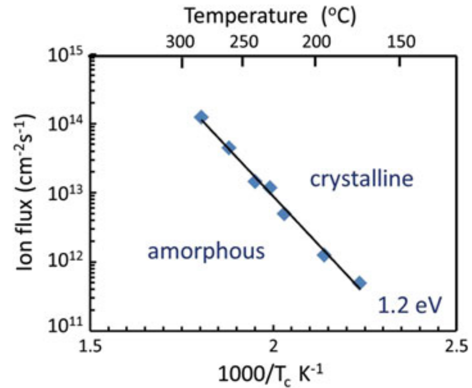

Fig. 6.5 Ion flux as a function of $1/T_c$ for ion irradiation conditions (1.5 MeV Xe ions at a fluence of 5×10^{15} cm^{-2}) under which a buried amorphous layer is just formed in Si. Adapted from Elliman et al. [10]

In cases where there are no pre-existing nucleation sites, amorphization at elevated temperatures usually ‘nucleates’ at the end-of-ion-range, where interstitial clusters (and often extended defects) agglomerate. In this regime, the ion flux can control the critical amorphization temperature T_c [10], as illustrated in Fig. 6.5. In this example, a fixed fluence of 5×10^{15} cm^{-2}, 1.5 MeV Xe ions caused amorphization only below 200 °C if the average beam flux is kept below 10^{12} ions cm^{-2} s^{-1}, but up to 300 °C if the ion flux is raised above 10^{14} ions cm^{-2} s^{-1}. This demonstrates the critical dependence of amorphization on the balance between disorder production rate (controlled by ion flux in the case of Fig. 6.5) and the degree of dynamic annealing (controlled by irradiation temperature). For implant conditions on the left hand side of the solid line in Fig. 6.5, no amorphous Si was formed (only defect clusters in crystalline Si), whereas buried amorphous layers are generated under conditions on the right. Note that the onset of amorphization in Fig. 6.5 fits well to an ‘apparent’ activation energy of 1.2 eV. The activation energy from the plot in Fig. 6.5 arises from the amorphization kinetics treatment in Chap. 3. Such amorphization kinetics are governed by (3.28) in that chapter, where plotting the ion flux as a function of $1/T_c$ provides the defining activation energy (E_{th}) for amorphization. This treatment is discussed further below.

6.2.3 *Modelling of Ion-Induced Amorphization at Elevated Temperature*

In Chap. 3 on modelling of radiation damage, various models for damage accumulation and direct amorphization are given. However, as indicated in Sect. 3.5 of that chapter, modelling of amorphization at elevated temperatures is very complex, involving a number of stages from damage production, through defect migration, clustering and annihilation, to trapping of specific defects at favourable sites for nucleating an amorphous phase. Although there has been some success at modelling

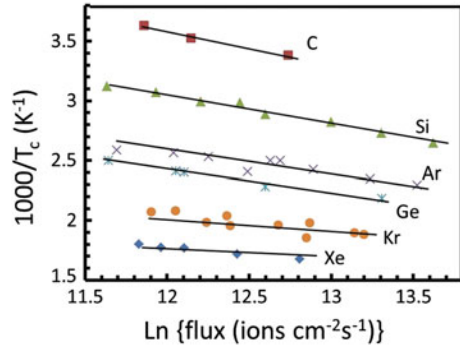

Fig. 6.6 Ion flux as a function of $1/T_c$ for ion irradiation conditions under which a buried amorphous layer is just formed in Si for a number of ions at a fluence of 10^{15} cm^{-2} (except C where the fluence was 2×10^{15} cm^{-2}). Adapted from Goldberg et al. [12]

the build-up of disorder with increasing fluence at different irradiation temperatures using analytical models, the situation with Si under irradiation conditions where dynamic annealing is very efficient (but amorphization still occurs at high fluence) adds further levels of difficulty. For example, following the first observations of layer-by-layer amorphization via IBIIA, there was considerable speculation in the literature [2, 5, 10, 11] as to the specific defects that might be mobile under irradiation and trapped at existing amorphous layers, hence being directly responsible for the growth of these amorphous layers under continued irradiation. Based on the observed 1.2 eV activation energy in Fig. 6.5 (which is close to the dissociation energy of Si divacancies), it was suggested that divacancies [10] may be the main defects preferentially trapped at amorphous layers. In contrast, the nucleation of amorphous layers at interstitial-based defect clusters or dislocation networks that were well removed from the depth of maximum nuclear energy deposition [5] suggested that the continued trapping of interstitials may have a role to play. Indeed, in more recent studies that use ion beams of widely varying mass and energy to examine the dependence of the onset of amorphization on ion flux and temperature, a range of 'activation energies' between 0.5 and 1.7 eV have been observed [7, 12], as illustrated in Fig. 6.6. The conclusion is that more complex defects and defect interaction processes may control amorphization, depending on the implant conditions used, particularly the implantation temperature.

Nevertheless, regardless of the specific defects that accumulate prior to amorphization, it was considered likely that an increase in the local free energy that accompanies the build-up of defects ultimately results in a collapse of the defective volume to the amorphous state when the free energy of the former exceeds that of the latter [13]. Thus, it can then be energetically favourable for the defective crystalline lattice to collapse to the amorphous phase, thus giving a local minimum in free energy. Such behaviour suggests that, in cases where irradiation-induced defects are mobile, defect agglomeration can occur at specific depths and the amorphous phase can preferentially nucleate at such sites to minimise the local free energy. Under such situations amorphization can be considered as nucleation-limited. As reviewed by Pelaz et al. [14], this behaviour for the formation of amorphous layers in Si at elevated temperature is somewhat consistent with previous critical energy density

[15–17] or nucleation-limited [7, 18] models of amorphization. These models address the accumulation of defects at particular sites within the disordered Si, and treat either the subsequent collapse of the lattice or nucleation of an amorphous phase above a critical defect density. While these mostly phenomenological models can account for amorphization behaviour under particular conditions such as for light ions at low irradiation temperatures (critical energy density models) or for growth of amorphous layers under elevated temperature irradiation (nucleation-limited models as briefly covered in Chap. 3), Pelaz et al. [14] argue that they do not treat the fundamental atomistic processes, such as the specific defects that are involved or the atomic bonding rearrangements that may ultimately control amorphization. Indeed, the observation of a range of activation energies associated with amorphization for different ion masses, as indicated in Fig. 6.6, strongly suggests that atomistic processes and different defect types and interactions play crucial roles in elevated temperature amorphization where certain defects are mobile and can accumulate at specific sites. Several types of defects formed by ion bombardment and dynamic annealing that are likely to play a role in amorphization at elevated temperatures have been reviewed in [14]. Single vacancies [19] and divacancies [20] migrating to an amorphous-crystalline interface during elevated temperature irradiation have been suggested to control annealing (crystallisation) behaviour and, when Elliman and co-workers [10, 21, 22] decreased the irradiation temperature, layer-by-layer amorphization via IBIIA was observed as shown in Figs. 6.4 and 6.5. As indicated above, the activation energy of 1.2 eV associated with IBIIA also suggested a crucial role for divacancies. Hence, these authors suggested that, at irradiation temperatures where divacancies were 'stable', amorphization could occur but at higher temperatures their dissociation would lead to crystallisation. However, as outlined above and shown in Fig. 6.6, single vacancies and divacancies cannot explain all of the observed behaviour nor the bonding configurations in amorphous Si that give rise to high densities of 5 and 7 membered Si rings [14] rather than the 6-fold rings of perfect crystalline Si. For similar reasons self-interstitial clusters by themselves, as has been proposed by Takeda and co-workers [23, 24], can only account well for light ion- or electron-induced amorphization at low temperatures. Atomistic models based on incomplete annihilation of vacancy-interstitial pairs, the so-called IV or bond defect [25], or divacancy and di-interstitial pairs or D-D defects [26], have shown more promise. As shown by [14] these defects can introduce 5 and 7 membered rings into the Si lattice which are the signatures of an amorphous structure. Moreover, molecular dynamics (MD) simulations of irradiation-induced ballistic processes have revealed IV defects [27] and these defects have been shown to be quite stable [28].

Pelaz et al. [14, 29] have proposed that vacancies, interstitials and IV or bond defects control amorphization over a wide range of implantation conditions, particularly for elevated temperature irradiations. They have undertaken non-lattice kinetic Monte Carlo (kMC) simulations [30] under a range of irradiation conditions to generate ion damage and assume that Si interstitials and vacancies generated in each collision cascade do not annihilate but interact to form the metastable IV defect. The stability of IV pairs (that is, annihilation rate) decreases as the number

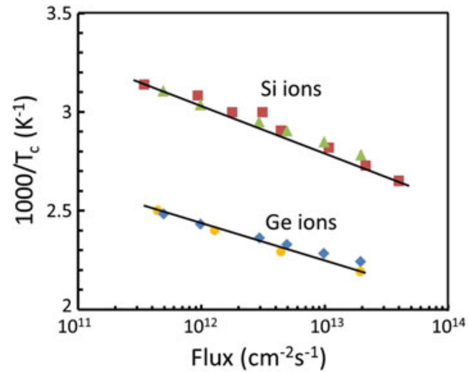

Fig. 6.7 Critical crystalline-to-amorphous transition temperatures as a function of flux for 80 keV Si and Ge implants into (100) Si to a fluence of 10^{15} cm^{-2}. *Triangle* and *diamond* symbols correspond to the simulations from (6.1) (from Pelaz et al. [29]) and *square* and *circle* symbols to experimental data from Goldberg et al. [7]. *Solid lines* are to guide the eye

of neighbouring pairs increases, consistent with MD simulations. The activation energy (for dissociation) of an isolated IV is taken as 0.43 eV and an IV pair imbedded in amorphous Si as 5 eV, both values again taken from MD simulations. Damage accumulation of IV pairs is assumed to lead to amorphization. They showed that damage accumulation can be parameterized by a simple reverse exponential:

$$IV(\text{peak concentration}) = a + b(1/[1 + \exp\{c(T - T_c)\}]), \tag{6.1}$$

where T_c is the crystal-to-amorphous transition temperature, c describes the width of the transition, and a and $a + b$ set the limits for temperatures $T > T_c$ and $T < T_c$, respectively. Equation (6.1) has been used to generate curves for peak IV concentration versus temperature, fluence and flux. Excellent fits to the shape of experimental disorder curves as a function of these parameters are found. For example, Fig. 6.7 shows the experimental transition temperature for 80 keV Si and Ge ions implanted into Si as a function of flux from [7] and compared with simulations using (6.1). The denser cascades with the heavier Ge ions leads to a higher density of IV pairs, thus increasing their stability and hence raising T_c. Furthermore, the model also accurately captures the shape of the superlinear build-up of damage with fluence (see Fig. 6.2).

There have been other attempts to model the amorphization process at elevated temperatures with the help of kMC and MD simulations, such as that of Mok et al. [31]. These authors focussed on highly disordered amorphous pockets of varying size (number of disordered atoms) that comprise isolated vacancies and interstitials (or divacancies and di-interstitials) that have not annihilated nor have formed IV defects. They assume that these ‘amorphous-like’ pockets collapse to fully amorphous regions when the defective/displaced atom concentration in a small volume exceeds 30 % of the Si atom concentration. As temperature increases, the vacancy and interstitial defects can annihilate and contribute to crystallization. Given the activation energy for a given set of implant conditions (such as those from Fig. 6.6) good fits to the experimental data can also be obtained using this model. However,

despite the success of various models of disorder build up and amorphization under different ion irradiation conditions of temperature, energy, flux, fluence and ion mass, no overarching amorphization model exists that is valid in all regimes even for a much studied elemental semiconductor such as Si. Maybe this is too much to ask, given the complexity of irradiation-induced defects in semiconductors and their migration, trapping and dissociation processes that depend on temperature, defect density and other parameters.

6.2.4 Ion Beam Induced Epitaxial Crystallisation (IBIEC)

The previous section illustrated implantation conditions where disorder production by ion irradiation at elevated temperatures can give rise to preferential amorphization at pre-existing defect sites and IBIIA phenomena. If the implantation conditions are changed to further favour the rate of dynamic annealing over defect production, by raising the temperature for example, pre-existing amorphous layers can be observed to crystallize epitaxially by the IBIEC process. IBIEC is illustrated for the particular case of MeV Xe irradiation in Fig. 6.8 [9]. At an irradiation temperature of 227 °C, the pre-existing surface amorphous layer is observed to shrink. Note that there is no observable disorder in the single crystal substrate immediately below the recrystallized layer but there is considerable disorder at the end-of-ion-range of the 1.5 MeV Xe ions centred at around 0.6 µm. Increasing the fluence causes further epitaxial growth of the amorphous layer.

It is interesting to note that a slight reduction in irradiation temperature to 208 °C, keeping the other irradiation conditions the same, induces IBIIA, as previously shown in Fig. 6.4. However, if the temperature is increased above that corresponding to the data in Fig. 6.8, the IBIEC rate (per unit of fluence) speeds up and Elliman et al. [9] found an activation energy for IBIEC of around 0.3 eV for 1.5 MeV Xe irradiation of Si, by plotting the epitaxial growth thickness per unit fluence against 1/T. This activation energy for IBIEC is much smaller than that

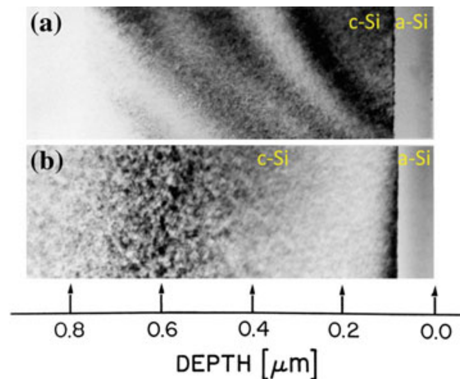

Fig. 6.8 XTEM images illustrating IBIEC of a pre-existing amorphous layer in Si (shown in **a**) using 1.5 MeV Xe ions to a fluence of 5×10^{15} cm^{-2} at 227 °C (shown in **b**). Adapted from Elliman et al. [9]

typically observed for ion-induced amorphization as illustrated in the previous section but, like the amorphisation regime, the IBIEC activation energy is not a single value for all ion irradiation conditions, as is illustrated below.

More generally, the temperature dependence of IBIEC over the temperature range 250–400 °C for intermediate mass ions in the 0.3–1 MeV range was initially found to exhibit an activation energy of around 0.24–0.3 eV and consistent with that found for 1.5 MeV Xe ions as in Fig. 6.8 [32–34]. In early IBIEC studies [9, 33], this low IBIEC activation energy suggested defect-mediated processes, possibly vacancies, and it was proposed that IBIEC arose as a result of athermally generated, ion-induced displacements at or close to the amorphous-crystalline interface. These displacements provide the stimulus for bonding rearrangements at the interface and hence epitaxial crystallization. It is important to understand the origin of the activation energy for crystallization in order to understand the defect processes that may be mediating it. In the thermal case, the recrystallization velocity, v, can be written as a function of temperature T as an Arrhenius relationship [35]:

$$v = v_o \exp(-E_a/k_B T), \tag{6.2}$$

where v_o is a constant, E_a is the thermal activation energy and k_B is the Boltzmann constant. Thermal epitaxy has a high activation energy (E_a = 2.7 eV) [35] and this has been attributed [33] to the sum of two activation terms: nucleation of the defects that influence epitaxial crystallization, E_n, and a second term involving migration and bond rearrangement at the interface, E_i. In IBIEC, the first activation term is eliminated by athermal defect generation and only the second activation term E_i is operative. Thus, it is possible to represent the IBIEC process by an Arrhenius relationship linking the regrown thickness normalized to ion fluence, r_N, as a function of temperature:

$$r_N = r_o \exp(-E_i/k_B T), \tag{6.3}$$

where r_o is a constant and E_i is now the activation energy related to IBIEC where E_i was measured to be around 0.3 eV in early studies [32–34]. Indeed, early studies [9, 19, 22, 33, 36] indicated that the IBIEC rate was proportional to ion fluence and was controlled by nuclear energy deposition. This rather simple view of a single activation energy for IBIEC was shown to be considerably more complex in the work of Kinomura et al. [37], who found a range of apparent activation energies depending on ion mass and energy deposition density. These data are illustrated in Fig. 6.9, where the growth rate, normalised to the displacements per ion (dpa) for each ion mass studied (rather than r_N in (6.3)), is plotted against 1/T. For each ion mass the ion flux was kept constant at 2×10^{12} cm^{-2} s^{-1}. It is clear that the apparent activation energy can vary from 0.18 to 0.4 eV, depending on ion mass, with carbon ions apparently exhibiting two different activation energies in different temperature regimes.

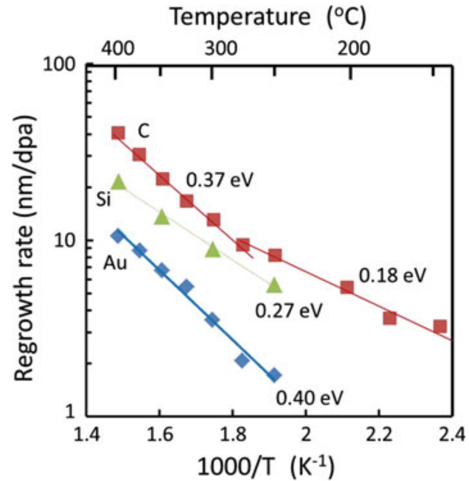

Fig. 6.9 Temperature dependence of IBIEC regrowth rates for Si normalized to the number of displacements per ion for 3.0 MeV C, Si and Au with a flux of 2×10^{12} cm^{-2} s^{-1}. Adapted from the data of Kinomura et al. [37]

A further illustration of the complexity of the IBIEC process is that the IBIEC growth rate does not scale with nuclear energy deposition across widely different ion masses. In fact, Kinomura et al. [37] quantified the mass dependence of IBIEC in terms of an influence of cascade density and ion flux on IBIEC rate. Such ion mass effects, which illustrate the role of cascade density are illustrated in Fig. 6.10 [37]. Here 3 MeV Au, Ag, Ge, Si and C ions were used to irradiate an amorphous Si layer of about 200 nm in thickness on a Si <100> substrate. Different fluences were chosen to provide the same total nuclear energy deposition at the amorphous-crystalline interface and MeV ions were chosen to provide a near constant energy deposition at the interface during IBIEC growth. Figure 6.10 plots the IBIEC regrowth rate (normalized to constant nuclear energy deposition at the interface) as a function of defect (vacancy) generation rate at the interface for five ion masses, four ion energies and two fluxes at 350 °C. The defect generation was calculated using TRIM [38]. Note that the defect generation rate varies over more than 4 orders of magnitude from C to Au and

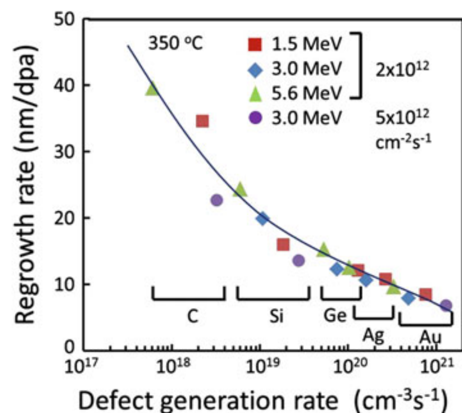

Fig. 6.10 Normalised regrowth rates for Si as a function of defect generation rate for five ion species (C, Si, Ge, Ag, and Au) at three energies (1.5, 3.0, and 5.6 MeV) with two fluxes (2×10^{12} and 5×10^{12} cm^{-2} s^{-1}). Adapted from data of Kinomura et al. [37]

the normalized growth rate for C is about 4 times that of Au under these conditions. A similar flux dependence for 300 keV ions has also been demonstrated [34, 39].

Furthermore, Heera et al. [40] proposed a diffusion-limited model to explain IBIEC, where the regrowth thickness, normalized to fluence, was proportional to ion flux to the −1/4 power. Kinomura et al. [37] have extended this treatment and the solid curve in Fig. 6.10 has been fitted to the equation:

$$r_d = cg^{-1/4}, \tag{6.4}$$

where r_d is the regrowth thickness normalized to the number of displacements, c is a constant and g is the defect generation rate. The curve is a good fit to the data points for the conditions employed in Fig. 6.10 but it does not fit particularly well to more extended ion flux data. Indeed, when the ion flux for Au and Ag ions was varied over a much wider range than that in Fig. 6.10, to cover defect generation rates extending down to the 10^{18} cm^{-3} s^{-1} region, a more linear dependence than the proposed fit in Fig. 6.10 was observed. This suggests that the two parameters that change the defect generation rate, namely the ion mass (cascade size) and ion flux, do not have a common influence on the IBIEC rate that the fit in Fig. 6.10 might otherwise indicate. This is further discussed in [37] and more fully in a review paper [41].

In attempts to determine the origin of the defects that mediate IBIEC, channelling of the incident ion beam in the crystalline Si above or below the amorphous layer was employed to reduce the nuclear energy deposition in the crystal. However, early measurements [33, 34, 42] were inconclusive, despite the fact that channelling caused an observed reduction in IBIEC rate in some cases, because it was difficult to estimate the exact number of point defects generated in the crystalline region, particularly after an ion beam had traversed an amorphous layer before entering the underlying crystal. This led to some authors claiming that defects migrating short distances to the interface from the crystalline side of the interface played a role in the IBIEC process [34] whereas other studies [33, 42] suggested that the defects contributing to IBIEC were generated at or very near the amorphous-crystalline interface. More recent experiments of the channelling effect on IBIEC for buried amorphous layers [43] have been somewhat more conclusive, with accurate measurements of the regrowth differences between channelled and random irradiations for the front and back interfaces of a buried amorphous layer strongly suggesting that defects at or extremely close to both amorphous-crystalline interfaces were controlling IBIEC. However, it was also argued that more detailed simulations would be necessary before a more precise determination of the origin of defects responsible for IBIEC could be made and such data are discussed in the following section.

6.2.5 IBIEC Models

Priolo and Rimini [44] have given an overview of various models to explain IBIEC observations up to about 1990. In early studies, the similarity of the activation

energy of IBIEC (around 0.3 eV) to that of vacancy migration led Linnros et al. [21] to propose that migrating vacancies, produced athermally by the ion beam, mediated IBIEC, whereas, if the temperature was lowered, then the increased stability of divacancies, with a dissociation energy of 1.2 eV, may cause amorphization at the interface and control the amorphization kinetics. This two-defect model qualitatively explains both the IBIIA and IBIEC processes but presupposes the migration of such defects in crystalline Si to the interface. Other defects proposed to mediate IBIEC are (charged) kinks [33, 44] and dangling bonds [45] that are formed athermally by the ion beam directly at the interface. A difficulty with a single defect model is the fact that the apparent activation energy of IBIEC has been shown to vary from about 0.18 to 0.4 eV (Fig. 6.9), which led Kinomura et al. [37] to suggest that the rate limiting effect in IBIEC may involve several different defect-mediated processes, depending on the cascade density at the interface and the temperature. This proposal does not necessarily preclude kinks or other specific interface defects as the final step in the IBIEC process, but rather suggests that more complex defect interaction processes may be involved in the annealing of dense cascades before discrete kinks are formed. A particular concern of vacancy models is that the channelling studies outlined in the previous section provide considerable weight to arguments suggesting that defects produced right at the interface dominate IBIEC. Another explanation for both IBIIA and IBIEC is due to Jackson [11], who developed an intra-cascade model in which each ion penetrating through the interface creates a disordered zone. Subsequent local interaction between defects in this zone can either lead to amorphization or crystallization, in which the net rate of interface movement is controlled by a rate equation. The simplicity of the Jackson model is attractive but it does not adequately account for ion mass and flux effects. Indeed, no single model appears to adequately explain all observations. We now briefly discuss more recent channelling measurements and simulations that address more directly the origin of defects that influence IBIEC.

Azevedo et al. [46] have studied IBIEC rates for both channelling and random irradiations of buried amorphous layers in Si with a MeV Au ion beam and compared the results with simulations obtained from the MARLOWE code [47]. Unlike previous measurements of IBIEC induced by a channelled ion beam [32, 33, 43] where no channelling effect was observed at the deep amorphous-crystalline interface of a buried amorphous layer, Azevedo et al. [46] observed a small but reproducible difference in IBIEC rate, with the rate for channelling being around 20 % smaller than the rate for random implants. For the same MeV Au ion irradiations, the front interface of the buried layer was observed to crystallize around 60 % slower in a channelling irradiation compared with a random case. These data were then compared with simulations to obtain the number of vacancies produced per unit length along the ion trajectories for random and channelled beams. Details of the simulation parameters and results are given in [46, 41] but it is the comparison between experimental IBIEC rates and simulated vacancy distributions between channelled and random irradiations that is most illuminating. The experimentally observed $\sim$20 % lower IBIEC rate for channelling beam alignment for the deep interface of an amorphous layer is consistent with the difference in

magnitude of vacancy generation exactly at the amorphous-crystalline interface that is obtained from the simulations. Hence, the observed IBIEC rates are most consistent with vacancies produced precisely at the interface than with vacancies produced in the amorphous or crystalline regions. Considering the front interface of a buried amorphous layer, MARLOWE predicts a large channelling effect, consistent with the experimental data. To better determine the origin of the defects that control IBIEC, the ratio between the channelling and random IBIEC rates can be compared with the ratio between the corresponding simulated defect profiles in different parts of the structure (that is, in the amorphous material, in the crystal near the interface or precisely at the interface). It turns out that the ratio of the IBIEC rates is a much closer match to the ratio of vacancies (or displaced atoms) produced precisely at the interface. The role of defects coming from the amorphous region can be ruled out since this should only give a ∼5–10 % effect, whereas the observed rate difference is close to 60 %. On the other hand, if vacancies in the crystal close to the interface were contributing to IBIEC, the simulations would predict a 90 % reduction for a channelled case. Indeed, the 60 % observed reduction matches well for simulation of displaced atoms at the interface for the channelled case compared to the random case. Hence, although the precise interface defect controlling IBIEC is not revealed by these results, the data is consistent with any crystallisation-enabling defect, such as a kink, produced directly at the interface by the ion beam.

6.3 Irradiation of Ge at Elevated Temperatures

6.3.1 Disorder Formation, Amorphization and Ion-Induced Crystallization

Prior to the 1980s there were several studies of ion implantation into Ge that focussed on disorder and amorphization, including solid phase crystallization of amorphous Ge layers and the behaviour of potential dopants during annealing [48, 49]. However, once Si became the dominant semiconductor for integrated circuits, Ge was less studied, which accounts for the fact that there are fewer studies of ion-induced disorder and amorphization in Ge and the understanding of such processes is not as developed as for Si. However, in terms of damage production, amorphization and IBIEC at temperatures above room temperature, Ge is qualitatively similar to the behaviour for Si that was extensively reviewed in the previous section. Nevertheless, there are also significant differences between Si and Ge, such as in the defect production rate (that is illustrated below), in point defect mobilities, their stability and clustering behaviour, and the fact that a porous structure can develop in ion amorphized Ge (outlined in the following section), whereas such behaviour has never been observed in Si, with the exception of high fluence swift heavy ion irradiation in the electronic excitation regime (see Chap. 10).

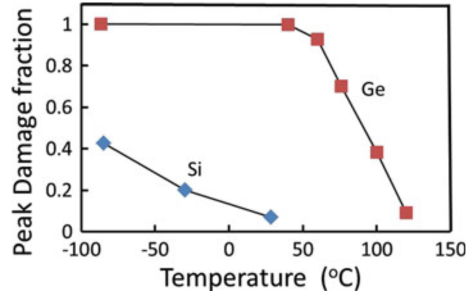

Fig. 6.11 Temperature dependence of peak damage fraction measured from RBS and channelling spectra for Si and Ge irradiated at a Si ion fluence of 1×10^{14} cm^{-2} at 70 and 100 keV, respectively. Data extracted from Haynes and Holland [50]

The differences in disorder production and amorphization at elevated temperature between Si and Ge have been appreciated for several decades and typical behaviour is illustrated in Fig. 6.11, taken from the data of Haynes and Holland [50]. Here, the peak damage fraction, obtained from the height of the damage peak relative to the random height (from RBS and channelling measurements), is plotted as a function of temperature for Si and Ge irradiated with a fluence of 1×10^{14} Si ions cm^{-2} at 70 and 100 keV Si, respectively. The different energies were chosen to normalise the ion range and the nuclear energy deposition per unit depth. In terms of damage production, it can be seen from Fig. 6.11 that, at and below room temperature, the Ge peak damage coincides with the random level for a Si ion fluence of 1×10^{14} cm^{-2}, indicating a completely amorphous layer has formed, whereas in Si the residual damage is only of the order of 0.05 of the random yield at room temperature. This clearly shows that damage production at roughly the same nuclear energy deposition per unit depth is much more efficient in Ge around room temperature than in Si. Furthermore, as shown in Fig. 6.11, the temperature dependence is very different. For Si the measured damage drops off slowly with increasing temperature and approaches zero at around 30 °C, which was defined [50] as a critical damage temperature T_o. For Ge, the fall-off in damage with increasing temperature is much sharper and the T_o is much higher, at 125–130 °C. A significant flux effect on the rate of damage build up was also observed in this study around the critical damage temperature T_o [50]. Such damage build up differences between Si and Ge were explained not only in terms of the greater damage production rate in Ge but also vastly superior dynamic annealing in Si compared with Ge at and above room temperature.

The latter effect was attributed to a much reduced point defect migration in Ge [50]. In this same study, unstrained SiGe alloys were investigated and it was found that the observed damage at a given temperature scaled with the Ge content in the alloy. Furthermore, Vos et al. [51] examined disordering of strained SiGe alloys and found a similar scaling of damage level with Ge content to that of Haynes and Holland [50]. Indeed, these last authors found that MeV Si ion irradiation of Si/SiGe superlattices at room temperature caused complete amorphization of the Ge-rich layers while leaving the adjacent Si layers relatively damage free. This behaviour is symptomatic of the much more efficient disordering in Ge compared with Si under similar irradiation conditions. Indeed, it is also clear from the above

studies that the threshold fluence for amorphization in Ge is lower than that for Si as a result of higher nuclear stopping, the reduced defect mobility and hence the efficiency for producing atomic displacements.

There have been fewer studies of IBIIA and IBIEC in Ge but again the behaviour is qualitatively similar to that in Si. For example, in very early studies [52, 53] it was found that irradiating Ge with Ge ions at 40 keV formed an amorphous layer at a fluence of 2×10^{15} cm^{-2} at 228 °C if a high flux of 6×10^{13} cm^{-2} s^{-1} was employed and this layer appeared to extend in a layer-by-layer manner at higher fluences, characteristic of IBIIA behaviour. However, if a lower flux of 6×10^{11} cm^{-2} s^{-1} was used, amorphization was not induced under the same implantation conditions. Furthermore, if the original amorphous layer created at the high flux was re-irradiated under the same conditions at the lower flux then complete epitaxial crystallization (later termed IBIEC) occurred. These studies were clearly the first demonstrations of IBIIA and IBIEC in Ge that pre-dated similar studies in Si. More recently, a study by Bachmann et al. [54] of high energy ion irradiation of amorphous Ge layers at elevated temperatures observed both ion-induced amorphization and crystallization effects, depending on the temperature and other irradiation conditions. In particular, they found that the amorphous layer increased in thickness with ion fluence below a critical temperature (T_R) at which the amorphous thickness did not change with fluence. Above T_R epitaxial crystallisation was observed and the IBIEC rate was found to scale roughly with the nuclear energy deposition at the interface and also increase with increasing temperature. Like Si, TEM micrographs revealed a sharp amorphous-crystalline interface in both the IBIIA and IBIEC regimes. An activation energy of 1.16 eV was found for the amorphization regime and 0.82 eV for IBIEC in Ge under the particular irradiation conditions carried out by Bachmann et al. [54]. They also found that the T_R value was considerably higher (by about 100 °C) for Ge compared with Si under similar irradiation conditions. This observation is consistent with the much more efficient disordering behaviour with Ge.

6.3.2 Formation of Porous Amorphous Layers

It has been known since the early 1980s that ion-amorphized Ge turned porous under irradiation at room temperature above a critical fluence [55, 56]. In these early studies it was realised that the agglomeration of vacancies in amorphous Ge was in some way responsible for the development of a porous structure during irradiation. Despite a resurgence of interest in this structure over the past 15 years, as a result of the importance of Ge in modern integrated circuit technology, it is only recently that a reasonably comprehensive understanding of the mechanism of its formation has emerged. Two general models have been proposed: a vacancy clustering and agglomeration model [57] that was suggested in early studies and a ‘microexplosion’ model [58] that involves void formation through pressure waves and thermal spikes caused by cascade overlap. Various recent studies have

attempted to design experiments to clarify which model is appropriate in porous development. For example, Romano et al. [59] studied the formation and evolution of porous structures in Ge during bombardment at room temperature with 300 keV Ge ions as a function of ion fluence in the range up to 4×10^{16} cm^{-2}. They suggested that microexplosions characterize the morphology of the porous material which is subject to enormous swelling during bombardment but that agglomeration of vacancy clusters and voids also plays an important role. The morphology consists of a random cellular structure composed of cells surrounded by amorphous Ge ripples. This evolving structure and swelling is illustrated in the XTEM images in Fig. 6.12. The porous structure overlays 'normal' amorphous Ge: indeed, annealing of such a structure can cause the underlying amorphous Ge to recrystallise epitaxially until the porous region is reached, suggesting little porosity in this underlying material. In another study, it has been shown that vacancies initially form into clusters in the near-surface of ion implanted Ge [60]. However, the evolving void formation does not occur uniformly across the surface: rather, voids exist in random clusters, which can be explained via a combination of both the vacancy clustering and microexplosion theories of void formation. This behaviour and other features of porous evolution at low irradiation fluences indicate that the mechanism involves vacancy trapping in amorphous Ge close to the surface, followed by gettering of subsequent irradiation-induced vacancies to this region to grow voids, and, when the voids intersect the surface, the subsequent evolution of the honeycomb porous structure occurs.

The ability to form voids is a result of nuclear collisions that produce mobile vacancies in amorphous Ge and this process can occur for any heavy ions, although

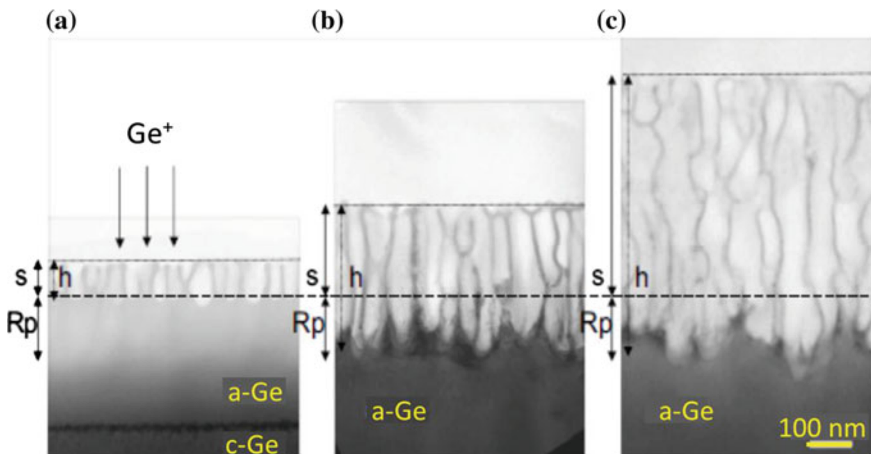

Fig. 6.12 XTEM micrograph of Ge irradiated samples with **a** 1×10^{16} cm^{-2}, **b** 2×10^{16} cm^{-2}, and **c** 4×10^{16} cm^{-2} 300 keV Ge^+ ions at room temperature. The *dotted line* is the position of the new surface after ion implantation; the lower *dashed line* is the position of the original surface for the unimplanted sample; s is the mean step height measured by AFM; h is the mean porous layer thickness; and R_p is the projected range of Ge ions. Adapted from Romano et al. [59]

the threshold fluence is dependent on ion mass and energy as might be expected. Romano and coworkers [60, 61] have also shown that irradiation of deposited a-Ge can be rendered porous although the microstructure in this case depends on the original structure (that is, density) and impurity content of the deposited film.

Of more particular relevance to this chapter is the effect of elevated temperature bombardment on the development of porous Ge. The study of Stritzker et al. [62] has addressed this issue. As might be expected, the ability to develop a porous structure at elevated temperature first depends on the ability to amorphize Ge and the amorphization process is temperature-dependent as was shown in Fig. 6.11. The step height of irradiated Ge and hence the degree of swelling (and porosity) was measured during elevated temperature bombardment of Ge [62]. Some of the results in [62] are shown in Fig. 6.13, where the step height is plotted as a function of temperature for 1 MeV Ge ion irradiation of Ge at two fluences, 3×10^{16} cm^{-2} and 1×10^{17} cm^{-2}. For the lowest fluence the swelling is small but noticeable: below room temperature there is no observable swelling since the amorphous layer that is formed is presumably not porous. However, at room temperature and up to 200 °C a clear increase in step height is observed but above 200 °C the step height drops, suggesting that the Ge remains crystalline at these elevated temperatures (under the irradiation conditions employed) and is not porous. Similar trends are obtained for the high fluence case, where the step height is now very large at around 300–400 nm in the temperature range between −50 and 200 °C. This again suggests that a porous layer is only formed in this latter temperature range. These conclusions on the temperature range for obtaining a porous structure were confirmed by XTEM [62]. It is interesting that the dramatic drop in swelling at 200 °C is consistent with the data shown in the previous section, that is, the expected transition from an amorphization regime in Ge into a regime where dynamic annealing prevents the formation of amorphous Ge. Stritzker et al. [62] also noted that the porous amorphous Ge structure was stable to more than 500 °C or until the amorphous Ge within the porous structure crystallised.

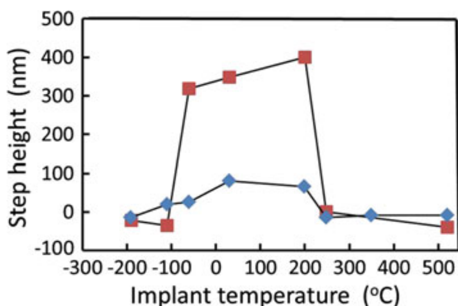

Fig. 6.13 Measured step height versus irradiation temperature for 1 MeV Ge ion bombardment of Ge at two fluences, 3×10^{16} cm^{-2} (*diamonds*) and 1×10^{17} cm^{-2} (*squares*). Data adapted from Stritzker et al. [62]

6.4 Irradiation of GaAs at Elevated Temperatures

6.4.1 Disordering and Amorphization

Like Si and Ge, dynamic annealing at elevated temperatures inhibits amorphization of GaAs, with T_c strongly dependent on both ion mass and flux. It was illustrated in previous chapters, using the data of Haynes and Holland [63–65] and Brown and Williams [66], that the observed flux effects on GaAs amorphization exhibited an activation energy of 0.9 eV and could be effectively modelled using the vacancy release model of Morehead and Crowder [67]. In this section, more detail is given of such dynamic annealing processes in GaAs at elevated temperatures [66, 68, 69]. In a first example, Fig. 6.14 illustrates the effect of ion mass on the critical temperature for amorphization [66].

In Fig. 6.14, the number of displaced atoms, obtained from the damage peak area of RBS and channelling spectra, has been plotted against irradiation temperature for 6 different ion masses at the same ion energy of 95 keV and fluence of 1×10^{15} cm^{-2}, with fluxes in the range 2–6 $\times$ 10^{12} ions cm^{-2} s^{-1} [66]. It can be noticed that, under these conditions, the critical temperature for amorphization T_c, which roughly coincides with the half height of the disorder curves, can vary by over 40 °C across the different ion masses. For light ions such as boron (B), where the ion cascades are dilute, the defect annihilation rate can exceed the defect production rate even at temperatures below room temperature. On the other hand, heavier ions with dense cascades require significantly higher temperatures before defect annihilation can compete favourably with defect production. Using the data in Fig. 6.14, it has been shown that T_c does not scale linearly with the rate of energy deposition, behaviour which is similar to observations for Si and Ge. Such behaviour makes it difficult to model damage build up and amorphization close to T_c in GaAs since the defect-mediated processes are quite complex.

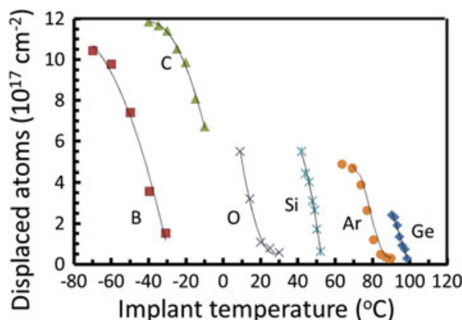

Fig. 6.14 The areal density of displaced atoms in GaAs as a function of substrate temperature for irradiation of GaAs with 1×10^{15} ions cm^{-2} of 95 keV: B (flux 2.2×10^{12} cm^{-2} s^{-1}), C (flux 6×10^{12} cm^{-2} s^{-})^{1}, O (flux 4.8×10^{12} cm^{-2} s^{-1}), Si (flux 4.8×10^{12} cm^{-2} s^{-1}), Ar (flux 2.6×10^{12} cm^{-2} s^{-1}), and Ge (flux 6×10^{12} cm^{-2} s^{-1}). *Solid lines* are a guide to the eye. Adapted from the data of [66]

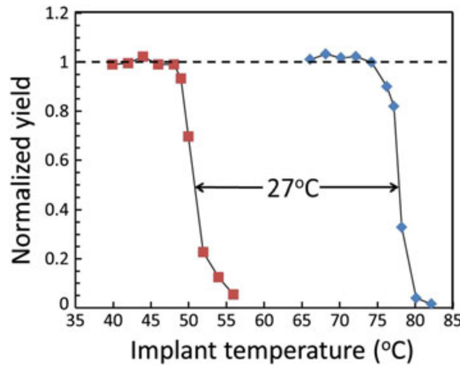

Fig. 6.15 The normalised peak damage taken from RBS and channelling measurements for GaAs plotted as a function of substrate temperature for implantation of 95 keV Si to a fluence of 1×10^{15} Si cm^{-2} at fluxes of 4.8×10^{12} (*squares*) and 4.8×10^{13} Si cm^{-2} s^{-1} (*diamonds*). The rapid decrease in residual damage defines a critical temperature T_c for amorphization, as confirmed by XTEM [69]. The order of magnitude change in ion flux has produced a shift of T_c by 27 °C. Adapted from the data of [66, 68]

Close to T_c there is a very strong flux effect on both the nature and magnitude of disorder in GaAs [68]. This is illustrated in Fig. 6.15 for a fluence of 1×10^{15} Si ions cm^{-2} at 95 keV. In this case an order of magnitude change in ion flux causes a 27 °C change in T_c, whereby T_c increases as the flux increases [68]. Note also that the transition from a continuous amorphous layer to very little detected disorder (as measured by the RBS and channelling normalized yield and confirmed by XTEM [69]) is very sharp in temperature, occurring over only a few degrees about T_c. This indicates that changing the temperature or flux in GaAs by a small amount can change the balance between the rates of defect annihilation and defect production quite dramatically. Indeed, GaAs would appear to exhibit considerably sharper changes in disorder type and magnitude than either of the elemental semiconductors Si and Ge.

Initially, the amorphization kinetics for (Si) ion irradiation of GaAs at elevated temperatures were characterized by an activation energy of 0.9 eV. More extensive activation energy data for several ion masses is given in Fig. 6.16 [66]. Although different mass ions for the same fluence induce amorphization over a 150 °C

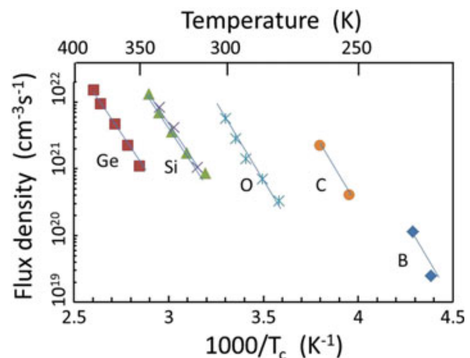

Fig. 6.16 Displacement flux density as a function of inverse critical temperature for irradiation of GaAs with 1×10^{15} cm^{-2} B, C, O, Si, and Ge ions. The lines connecting the data points for each species all correspond to the same activation energy of 0.9 eV. Adapted from the data of [66]

temperature range, the measured activation energy (0.9 eV) is independent of ion mass. Furthermore, the data in Fig. 6.16 includes two Si ion energies, 95 keV and 1.5 MeV, which again exhibit the same activation energy for amorphization. This is quite different to the behaviour in Si, where the activation energy for amorphization was found to vary from 0.5 to 1.7 eV when the ion mass was changed from B to Xe, as illustrated in Fig. 6.6 of Sect. 6.2.3. Thus, unlike Si this suggests that the same defect interaction processes may control amorphization in GaAs regardless of the ion mass, flux and implant temperature. However, despite the independence of the measured activation energy on ion species, T_c does not scale linearly with the rate of energy deposition or displacement density in GaAs, indicating that the processes occurring in the collision cascades which influence defect quenching, trapping, clustering and annihilation determine the pathway to amorphization. This suggests that there is difficulty in nucleating or stabilizing the amorphous phase in GaAs at temperatures where defects are highly mobile, and that nucleation occurs locally at stable defect complexes which are formed more readily in the dense collision cascades created by heavier ions. Nevertheless, based on the data shown above it is not possible to identify the specific defect-related process which characterizes amorphization and leads to the measured 0.9 eV activation energy [69].

There are few detailed studies of disorder production in GaAs at elevated temperatures since the mid to late 1990s that add to the details given above. However, a high resolution XTEM study of Zn implantation at 110 °C into GaAs [70] found that the distribution of stable defect clusters following implantation better matched the Zn ion distribution than the shallower nuclear energy deposition distribution. This is somewhat similar to the behaviour in Si outlined in Sect. 6.2.2, where the build-up of defect clusters at elevated temperatures (and the ultimate amorphization at higher fluences) occurs preferentially close to the end-of-ion-range. This was explained for the Si case in terms of excess interstitials at the end-of-ion-range generated by ion collisions that act as gettering sites for mobile defects which agglomerate into well-defined clusters. It would appear that similar behaviour is occurring in GaAs under elevated temperature irradiation and hence it would be expected that such defect clusters also act as nucleation sites for amorphization [69]. In the section below it is additionally shown that, like Si and Ge, pre-existing amorphous layers in GaAs provide nucleation sites for defect trapping and ultimate extension of the amorphous layers.

6.4.2 IBIIA and IBIEC Processes in GaAs

Initial attempts to induce IBIIA in GaAs by ion irradiation were not successful as a result of excessive crystalline disorder adjacent to amorphous layers and hence the difficulty in identifying their thickness by RBS [71, 72]. However, Wesch et al. [73] and Brown [69] were able to demonstrate that, like Si and Ge, it was possible to extend the thickness of an amorphous layer in GaAs by subsequent higher energy irradiation at elevated temperatures under appropriate conditions. This indicated

that the amorphous-crystalline interfaces were acting as preferential trapping sites for defects, thus mediating the extension of the amorphous layer. However, more significant accumulation of extended defects was also observed close to the amorphous layers than is found for Si and Ge. It was further shown that the increase in thickness of an amorphous layer with fluence was initially linear [69] but then appeared to exhibit a super-linear dependence as a result of the disorder build up close to the amorphous-crystalline interface and its subsequent collapse to an amorphous phase with increasing fluence.

IBIEC of amorphous layers at temperatures well below those at which thermal-only epitaxy occurred was also demonstrated in early studies [71, 72], where it was shown that a buried amorphous layer in GaAs could be induced to regrow epitaxially from both near-surface and deep interfaces under subsequent MeV Ne ion irradiation at 100 °C [72]. However, good epitaxy was found to break down in a somewhat similar manner to thermal epitaxy of GaAs [74] beyond a critical thickness. In the case of thermal crystallization of GaAs, amorphous layers can crystallise epitaxially at around 300 °C but good quality epitaxial growth only occurs for the first 40 nm, thereafter becoming very defective [74].

It was suggested that the breakdown in good quality epitaxial growth is related to local stoichiometry imbalances in irradiated GaAs (that is, a departure from the 1:1 Ga:As ratio within volumes of the order of a couple of unit cells) and this imbalance leads to extended defect formation during epitaxial growth. This behaviour was also found for IBIEC, where 1.5 MeV Ne ion irradiation at 75 °C can induce epitaxy for thin amorphous layers but good quality epitaxy breaks down after only about 15 nm of growth [72] as a result of a competing damaging process under irradiation at 75 °C. In these early studies there was no TEM examination to study the microstructure of the recrystallizing layers.

In Fig. 6.17 more recent work is shown [69] which compares RBS and channelling data with XTEM images for a pre-existing buried amorphous GaAs layer re-irradiated with 600 keV Si ions (fluence 2.8×10^{16} cm^{-2}) at 110 °C. The buried amorphous layer was generated with 95 keV Si ion implantation to a fluence of 4.5×10^{16} cm^{-2} at 110 °C. The RBS and channelling spectra in (a) show that the re-irradiation has caused the front edge of the amorphous layer to crystallize epitaxially whereas the back edge has extended in depth suggesting layer-by-layer amorphization via IBIIA. The XTEM image in (b), when compared with an image of the original amorphous layer in (c), confirms IBIEC at the front interface and IBIIA at the back interface. It is interesting that the channelling spectrum for the 600 keV Si irradiation alone indicates quite a low damage level in GaAs. The interpretation of this behaviour is that: (i) the energy deposition density for the 95 keV irradiation at 110 °C has resulted in the nucleation and growth of a buried amorphous layer centred about the end-of-ion-range by a fluence of 4.5×10^{16} cm^{-2}; (ii) for the 600 keV irradiation alone, the irradiation-induced defects at 110 °C are highly mobile and annihilation is efficient, with little stable disorder generated; (iii) when the buried layer is re-irradiated with 600 keV ions the lower energy deposition density at the front interface fosters IBIEC rather than defect accumulation at this interface, whereas at the back interface the energy deposition density (defect generation rate) is high enough for defects to

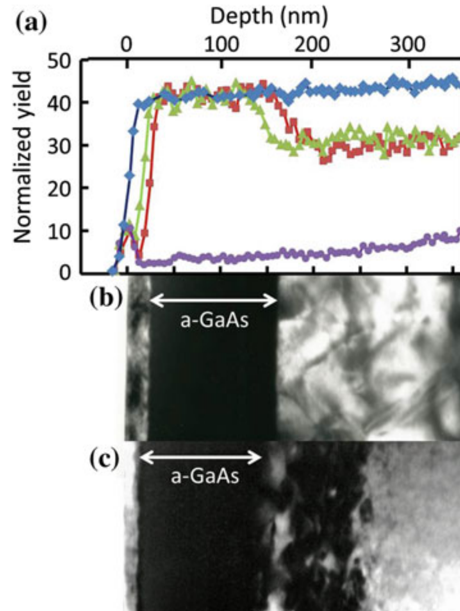

Fig. 6.17 **a** RBS and channelling spectra showing both layer-by-layer amorphization and IBIEC in GaAs; an initial buried amorphous layer (*triangles*), following a subsequent 600 keV Si ion irradiation (*squares*), and the 600 keV only irradiation (*circles*) at 110 °C, with a random spectrum (*diamonds*). The XTEM image in **b** shows the original buried amorphous layer after the subsequent 600 keV irradiation; and the image in **c** is the original buried amorphous layer only. Adapted from [69]

accumulate at this interface and lead to IBIIA. This overall behaviour confirms the fact that small changes in energy deposition density close to T_c can change the behaviour from amorphization to crystallization as was illustrated by the data in Fig. 6.15 of the previous section.

6.5 Other Compound Semiconductors

6.5.1 SiC Near and Above T_c

In previous sections, it was shown that for semiconductors such as Si, Ge and GaAs, there is a strong flux effect on accumulated damage and eventual amorphization as the irradiation temperature approaches T_c. This effect is also observed for SiC, which was shown in Chaps. 3 and 5 to be readily amorphized at room temperature. The flux effect for 100 keV Si ion implantation of SiC at temperatures between 25 and 220 °C is illustrated in Fig. 6.18 [75]. Here, the relative damage, as obtained from the normalized damage peak height from RBS and channelling data, is plotted as a function of temperature for several ion fluxes in the range 1.9×10^{10} to 4.9×10^{13} cm^{-2} s^{-1}. As expected, the damage curves shift to higher temperatures with increasing flux in a similar manner to the GaAs data shown previously in Fig. 6.15. Indeed, the displacement of the half height of the curves with flux (around 25 °C for an order of magnitude flux increase) is similar in both GaAs and SiC cases. The half height of the curves in Fig. 6.18 is a measure of T_c which can be extracted and used to plot the ion

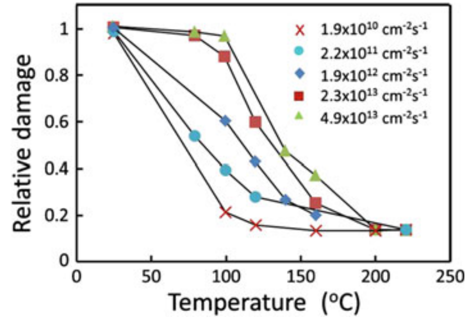

Fig. 6.18 Relative damage from RBS and channelling as a function of temperature for a range of fluxes for 100 keV Si ions to a constant fluence of 5×10^{14} cm^{-2} into SiC. Adapted from [75]

flux as a function of inverse temperature ($1/T_c$) to obtain an activation energy (c.f. (3.28) in Chap. 3) for the crystalline-to-amorphous transition as for other semiconductors in previous sections of this chapter. Such data is shown in Fig. 6.19 from which an activation energy of 1.3 eV is obtained.

It is interesting to ponder the significance of this activation energy, that is, which defect interaction processes might lead to it. However, there has been considerable discrepancy in the subsequent literature as to the activation energy related to the amorphization kinetics in SiC. For example, for 1.1 MeV Al ion irradiation of SiC, a study of the flux and temperature dependence of amorphization [76] found an activation energy of 0.9 eV. These authors used (3.28) in Chap. 3 to obtain the activation energy (E_{th}) from a single experimental T_c value and ion flux (Φ) combination. They suggested that this procedure is not as rigorous as E_{th} obtained by plotting a family of fluxes against $1/T_c$ as was the case in Fig. 6.19. Nevertheless, the difference in measured activation energies for Si and Al ion irradiation could suggest that there is an ion mass effect on activation energy for SiC as was found for Si (see Sect. 6.2.3). Indeed, in a more recent paper [77], an activation energy of 0.6 eV was found for amorphization of SiC using a range of different ions (Ne, Ar, Xe and Au) at various energies. In this case, a specific T_c was found for each ion species as the temperature at which the amorphization fluence converged to infinity by plotting the critical fluence for amorphization as a function

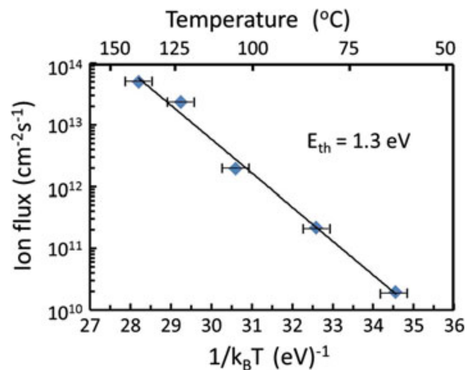

Fig. 6.19 Plot of ion flux as a function of inverse critical temperature T_c for SiC which is found from the half height of the flux curves in Fig. 6.18. Adapted from [75]

of temperature, similar to the plot for InP in Fig. 5.5a of Chap. 5. Again, (3.28) of Chap. 3 was used to obtain the activation energy from a plot of damage rate as a function of $1/T_c$. The different activation energy obtained by this method strongly suggests that there is not a single activation energy that describes the defect interaction processes leading to amorphization in SiC, where different ion masses, and hence the defect density within ion cascades, can strongly influence defect stability and ultimate amorphization.

In terms of ion irradiation of SiC above T_c, as expected it is not possible to render the material amorphous since the defect annihilation rate exceeds the defect production rate. However, imperfect defect annihilation occurs and visible defect clusters can be formed. An example of this situation is shown in Fig. 6.20 [78] for dual irradiation with Si and C ions at 625 K. In this study Si ions were implanted at 105 keV and C ions at 45 keV to give the same depth ($\sim$75 nm) for the respective peaks of the nuclear energy deposition distributions and a similar ion range of $\sim$110 nm in both cases. The damage build-up and microstructure of the residual disorder was examined as a function of dual ion fluence and Fig. 6.20a shows RBS and channelling data. The disorder initially builds up with increasing fluence, reaching a low saturation damage level in the range 10^{14}–10^{16} cm^{-2}. Thereafter, a clear damage peak builds up rapidly with increasing fluence but does not reach the random level, indicating that the formation of an amorphous layer is unlikely. Thus, at this temperature range there is a two-stage damage build up: an initial region where defect annihilation is efficient and a low saturation damage level results (<0.1 of the random level) that is stable up to a fluence of 10^{16} cm^{-2}. Thereafter, disorder increases rapidly with increasing fluence. The second stage disorder peak is close in depth to the projected range of the ions, suggesting that it may be the excess Si and C atoms in this region that trap and stabilize irradiation-induced defects.

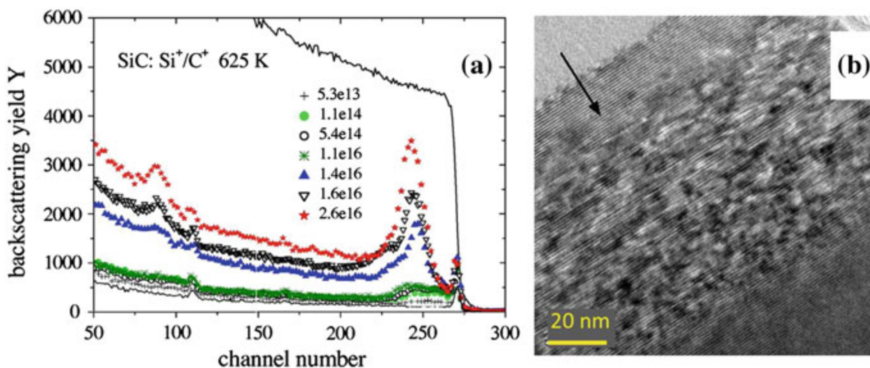

Fig. 6.20 **a** RBS and channelling spectra showing the build-up of disorder with fluence (cm^{-2}) for dual Si and C irradiation at 625 K and at ion energies of 105 and 45 keV, respectively; the random spectrum is the *solid curve*. **b** XTEM image of the damage band in SiC implanted with Si/C ions to a total fluence of 2.6×10^{16} cm^{-2}. The *arrow* indicates the ion beam direction. Adapted from [78]

Figure 6.20b shows the damage microstructure associated with the highest Si/C fluence in Fig. 6.20a. This consists of a band of defect clusters around 65 nm wide, consistent with the second stage disorder peak in the RBS spectra. Note that there is near-damage-free material above and below the damage band. This damaging behaviour in SiC at irradiation temperatures above T_c is very similar to behaviour observed for Si in Fig. 6.1, where the residual disorder in terms of defect clusters in otherwise good crystal is observed to build up around the end-of-ion-range.

6.5.2 IBIIA and IBIEC Behaviour in InP

Like binary compound semiconductors GaAs and SiC, InP is also easily amorphized by ion irradiation at room temperature and exhibits significant dynamic annealing above room temperature, as indicated in Chap. 5. As a result of the latter behaviour, both IBIIA and IBIEC have been observed with respect to pre-existing amorphous layers in InP. This is illustrated in Fig. 6.21a where the RBS and channelling spectra show both layer-by-layer extension (IBIIA) and epitaxial crystallization (IBIEC) of a 195 nm amorphous InP layer following re-irradiation with 1.7 MeV Si ions at temperatures below and above T_c, respectively [79]. At a temperature of 377 K the amorphous layer is observed to thicken by about 20–25 nm, whereas at 396 K the layer epitaxially regrows by around 40 nm. This behaviour is similar to that previously illustrated for Si in Sects. 6.2.2 and 6.2.3. Furthermore, it is possible to establish the temperature (transition temperature, T_R) at which the amorphous layer neither grows nor shrinks under irradiation as a function of ion flux, from which an

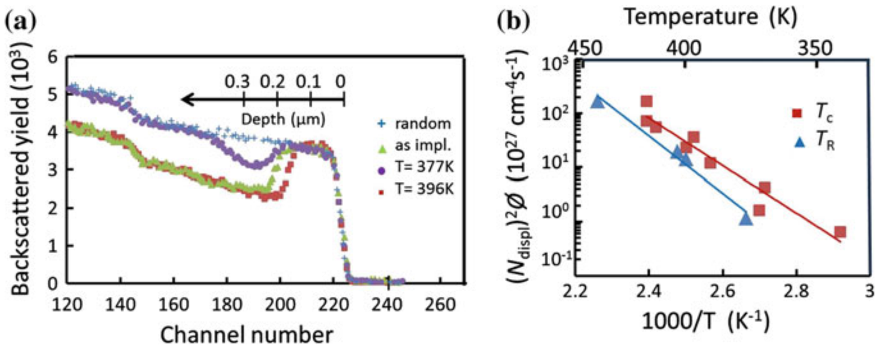

Fig. 6.21 **a** RBS and channelling spectra showing IBIIA and IBIEC behaviour in InP. The as-implanted spectrum shows an amorphous layer ~200 nm formed by 300 keV Se ions to a fluence of 1×10^{15} cm^{-2} at liquid nitrogen temperature. This layer was re-irradiated with 1.7 MeV Si ions (fluence, $N_I = 5 \times 10^{15}$ cm^{-2}; flux, $j = 6 \times 10^{11}$ cm^{-2} s^{-1}) at temperatures of 377 and 396 K to induce IBIIA and IBIEC, respectively. **b** Activation energies obtained by plotting the product of the square of the number of displaced atoms and flux ($(N_{displ})^2 j$) against 1/T for two cases, one where $T = T_c$, the critical temperature for amorphization (*squares*), and another where $T = T_R$, the transition temperature between IBIIA and IBIEC (*triangles*). Adapted from [79]

activation energy can be found for the process. This is done in Fig. 6.21b where the ion flux j (or actually j multiplied by the square of the number of displaced atoms per ion) is plotted against $1/T_R$ [79]. This yields an activation energy of 1.05 eV for the processes that control the transition kinetics for InP. This plot and the extracted activation energy are analogous to the plot for Si shown previously in Fig. 6.5, where the region (or irradiation conditions) above the T_R line relate to amorphization and those below the line to crystallization under 1.7 MeV Si ion irradiation. It is also possible to plot the disorder curves in InP for different ion masses and energies as a function of ion fluence and flux at a range of temperatures, similar to Fig. 6.18 for SiC or, more specifically Fig. 5.5 in Chap. 5 for InP. From such data a set of T_c values can be extracted, along with the ion flux used in each case. This has been done for InP for various ion masses in [80, 81] and the resultant T_c values and other parameters have been used to plot $(N_{displ})^2 j$ against $1/T_c$ in Fig. 6.21b [79]. The activation energy for amorphization obtained by this method is around 0.9 eV for InP, which differs significantly from the activation energy of 1.05 eV that describes T_R for 1.7 MeV Si irradiation. Again this difference may indicate that, like Si and SiC, there is no single activation energy for InP that describes amorphization and IBIIA under a range of ion masses at elevated temperatures.

In light of the amorphization kinetics for binary semiconductors GaAs, SiC and InP illustrated in this chapter, it is relevant to ask whether such data exists for other binary semiconductors. In fact there is little extensive data that can be used to ascertain whether a single activation energy or a range of activation energies exists for amorphization kinetics in other compound semiconductors. For example, in InAs, a plot like that in Fig. 6.21b has been constructed [79] but the authors are careful to indicate that an activation energy of 0.85 eV extracted from T_R values obtained from several sources may not be representative of a single activation energy for amorphization in InAs.

6.5.3 *Ternary Semiconductors and Multilayers*

In both this chapter and in Chap. 5, a comparison of GaAs and AlAs in terms of ease of amorphization indicates that GaAs is easily amorphized at room temperature whereas AlAs is subject to efficient dynamic annealing and resists amorphization even at liquid helium temperatures. Indeed, it is clear that III-V compounds with Ga and In as the group III element are easily amorphized but Al-based materials strongly resist amorphization [82]. Thus, it is interesting to examine the amorphization behaviour of ternary compounds of varying composition such as $Al_xGa_{1-x}As$ materials. Typical behaviour is illustrated in Fig. 6.22, where the threshold fluence for amorphization (T_c) for 90 keV Si ions is shown across the entire Al composition range for various $Al_xGa_{1-x}As$ materials [83]. The implantations were carried out at liquid nitrogen temperature and the amorphization threshold fluences were obtained from RBS and channelling data. As expected, the critical fluence is low ($\sim 3 \times 10^{13}$ cm^{-2}) for GaAs and rises steadily with Al content in the alloy to a

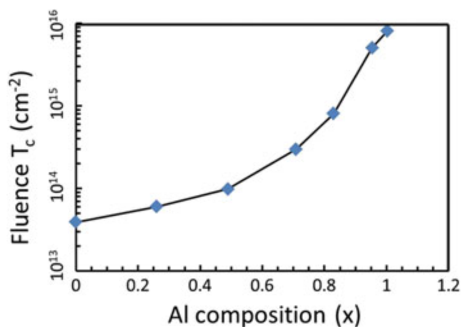

Fig. 6.22 Critical threshold for amorphization (T_c) for 90 keV Si implantation of $Al_xGa_{1-x}As$ alloys of various composition at liquid nitrogen temperatures. Adapted from [83]

critical fluence of close to 10^{16} cm^{-2} for AlAs. This indicates that the defect annihilation efficiency is very sensitive to the Al concentration in the alloy. It was also shown in this study [83] that, in the intermediate composition range, disorder builds up in the form of defect clusters that act to nucleate the amorphous phase at higher fluences, whereas for the highest Al content materials, well defined dislocations are observed for fluences of the order of 1×10^{15} cm^{-2} and above. It is unclear whether these extended defects then act as nucleation sites for the amorphous phase or whether the high concentration of the implanted species (Si) plays the major role in seeding amorphization. Furthermore, it was found that the threshold fluence for amorphization was very sensitive to the implantation flux for the mid to high Al concentrations, suggesting that, for these alloys, there is a close balance between the rates of defect production and defect annihilation for liquid nitrogen temperature bombardment. It is interesting that this threshold fluence for amorphization with keV ions as a function of alloy composition is qualitatively similar to the case for MeV ion irradiation [84].

Since AlAs and GaAs are subject to very different defect interaction and annihilation processes under ion bombardment, it is interesting to examine disordering of multilayer GaAs/$Al_xGa_{1-x}As$ materials. Typical ion disordering behaviour is illustrated by the RBS and channelling spectra in Fig. 6.23 for two different multilayer arrangements [85] irradiated with 1 MeV Si ions at liquid nitrogen temperature. Figure 6.23a shows the case for a GaAs layer sandwiched between two $Al_{0.5}Ga_{0.5}As$ layers and Fig. 6.23b shows the opposite case of $Al_{0.5}Ga_{0.5}As$ between two GaAs layers. As might be expected, GaAs is readily amorphized but amorphization is considerably suppressed in the $Al_{0.5}Ga_{0.5}As$ layers. Indeed, the proximity of one layer can affect the disorder build up near the interface in the other. For example, a fluence of 3×10^{14} cm^{-2} causes almost complete amorphization in the thicker buried GaAs layer in panel (a) but the thin surface GaAs layer in panel (b) is far from amorphous at the same fluence, noting that a fluence of 1×10^{14} cm^{-2} is sufficient to totally amorphize a bulk GaAs substrate. It has been suggested [83–87] that this behaviour results from mobile defects in the $Al_{0.5}Ga_{0.5}As$ layers suppressing amorphization close to the interface in adjacent GaAs layers. Note also that the back edge of the buried GaAs layer (arrowed in

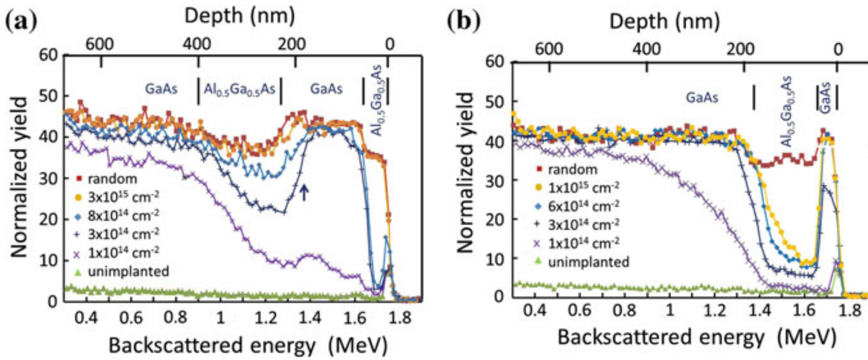

Fig. 6.23 RBS and channelling spectra showing the ion damage for 1 MeV Si irradiation at 77 K of: **a** an $Al_{0.5}Ga_{0.5}As/GaAs/Al_{0.5}Ga_{0.5}As/GaAs$ multilayer for various fluences as indicated; and **b** a $GaAs/Al_{0.5}Ga_{0.5}As/GaAs$ multilayer for various fluences as indicated. Adapted from [85]

Fig. 6.23a) is not completely amorphous, again caused by the proximity of the underlying $Al_{0.5}Ga_{0.5}As$ layer.

In addition, close to the interface in $Al_{0.5}Ga_{0.5}As$, disorder builds up rapidly with fluence once the adjacent GaAs layer becomes amorphous (note the disorder near the back $Al_{0.5}Ga_{0.5}As$ interface in panel (b) for the highest fluence).

A further example of disordering in a ternary III-V semiconductor is shown in Fig. 6.24 for an $Al_xGa_{1-x}N$ material, again with varying Al content [88]. In this case the various alloy compositions were implanted with 300 keV Au ions at 20 °C. It is interesting to note from Chap. 5 that GaN is difficult to amorphize as a result of efficient dynamic annealing even at significantly below room temperature. Despite this strong dynamic annealing, GaN can be rendered amorphous at room temperature by Au ion implantation [82] but amorphization is nucleated from the surface in this case rather than at the peak of the nuclear energy deposition distribution at a fluence of around 1×10^{15} cm^{-2}. AlN is even more difficult to amorphize than GaN [82] and, as the alloy becomes more Al rich, this would be expected to suppress amorphization. Indeed, the data in Fig. 6.24 supports this assertion. It turns out that even

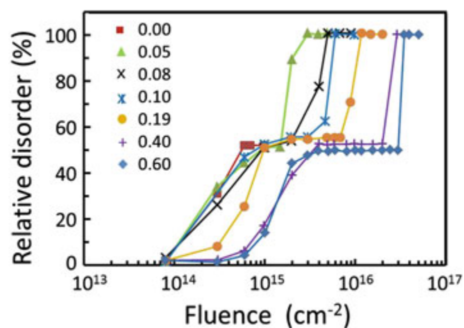

Fig. 6.24 The fluence dependence of maximum relative disorder extracted from RBS and channelling spectra in the bulk defect peak region for $Al_xGa_{1-x}N$ samples bombarded with 300 keV Au ions at 20 °C. The Al content (x) in different samples is given in the figure. Adapted from [88]

as little as 5 % Al in the alloy has a dramatic effect on disorder build up and ultimate amorphization. The peak disorder at the depth of maximum nuclear energy deposition for GaN in Fig. 6.24 increases to a 50 % saturation level by a fluence of 6×10^{14} cm^{-2} and thereafter amorphization from the surface takes over. However, for a 5 % Al alloy this surface amorphization is completely suppressed and amorphization in the bulk occurs via a two stage process as has been illustrated for GaN. For this 5 % Al composition, full amorphization occurs at around 3×10^{15} cm^{-2}, catalysed by seeding at dislocations and/or the implanted Au [82]. At higher Al contents, dynamic annealing is more efficient in both suppressing the initial disorder build up to saturation and the eventual amorphization at higher fluences. For example, compositions of 40 and 50 % Al do not reach the 50 % damage saturation level until a fluence of around 3×10^{15} cm^{-2} and full amorphization does not occur until fluences above 2×10^{16} cm^{-2} at which the implanted Au almost certainly has a major role in seeding amorphization.

6.5.4 Unusual Swelling and Erosion Behaviour in Ion Implanted GaN

Although GaN exhibits strong dynamic annealing even at temperatures as low as 15 K (see Chap. 5), it is still possible to form amorphous layers at high fluences. However, the nature of damage build up is very much dependent on temperature, ion mass and ion flux even at temperatures at and below room temperature [82]. Typically, whereas amorphous layers formed at 15 K are nucleated close to the maximum in the nuclear energy deposition density with sufficiently high fluence, at liquid nitrogen and room temperatures strong nucleation of amorphous layers directly at the surface occurs. In these higher temperature irradiations the surface amorphous layer is observed to extend layer-by-layer with increasing fluence before a buried amorphous layer is nucleated at the depth of maximum nuclear energy deposition at higher fluences. The temperature, ion flux and ion mass dependence of the nucleation and growth of these surface and deeper amorphous layers in GaN has been reviewed in Chap. 5 and in [82]. This aspect will not be discussed further here but some anomalies associated with swelling and erosion of GaN under bombardment at elevated temperatures will be treated.

Figure 6.25 illustrates the surface swelling of GaN that can be observed at liquid nitrogen temperatures under high fluences of heavy ions [89]. In this case, 2 MeV Au implantation leads to substantial swelling of the surface shown in Fig. 6.25a beyond a fluence of 10^{15} cm^{-2} (measured by the step height between unimplanted and implanted surface regions from AFM). It was found that the swelling began following the formation of an amorphous layer continuous to the GaN surface. Figure 6.24b shows a XTEM image of a sample following a fluence of 10^{16} cm^{-2} that clearly indicates pronounced porosity in an amorphous GaN surface layer, with

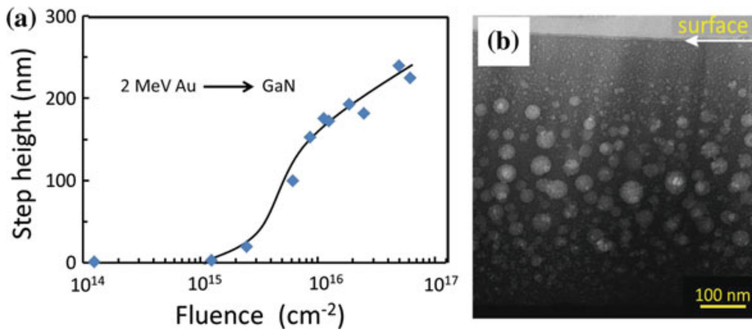

Fig. 6.25 **a** Swelling as measured by surface step height for 2 MeV Au irradiation of GaN at liquid nitrogen temperature as a function of fluence. **b** XTEM image of a sample bombarded as in **a** to a fluence of 1×10^{16} cm^{-2}. Adapted from [89]

the presence of voids or gas bubbles within this layer. Indeed, it has been proposed [82, 89, 90] that the porosity arises as follows: (i) an amorphous layer is first formed under heavy ion irradiation; (ii) beam-induced dissociation of amorphous GaN occurs at higher fluences leading to the formation of N_2-rich gas bubbles; and (iii) continued bombardment leads to surface craters as the bubbles intersect the surface and a highly porous structure evolves with a decidedly rough surface. It has been proposed [82] that swelling and porosity only occur in amorphous GaN layers and is a general phenomenon for ion irradiation of amorphous layers to high fluences at and above liquid nitrogen temperatures. However, the phenomenon is difficult to observe under keV ion irradiation cases since fluences well above 10^{16} cm^{-2} are required and the scale of the swelling is small, requiring AFM and XTEM examination to verify the presence of porosity.

It is further interesting to examine the behaviour of GaN under irradiation above room temperature where amorphization may be expected to be suppressed. Indeed, at elevated irradiation temperatures, amorphization is inhibited and the build-up of ion-induced disorder is very much suppressed as a result of extremely efficient dynamic annealing and defect annihilation [82, 91]. For example, a study of the disordering of GaN at 550 °C with 300 keV Au ions [91] found that the disorder built up with fluence, as measured by RBS and channelling, reached a saturation level of about 50 % of the random level at a fluence of around 6×10^{14} cm^{-2}. The microstructure of such residual damage is shown by the XTEM images in Fig. 6.26 under two diffracting conditions to highlight different defects [91]. The images in Fig. 6.26a, c illustrate point defect clusters in the near surface region that grow and coarsen with increasing fluence. In Fig. 6.26b, d the XTEM images indicate the presence of a band of planar defects parallel to the basal plane of the GaN substrate. Again the concentration of these defects is observed to increase with increasing fluence. This type of defect structure for elevated temperature irradiation of GaN is typical for a wide range of ions and implantation conditions [82]. In fact, it is somewhat surprising that this type of defect structure is also observed at much

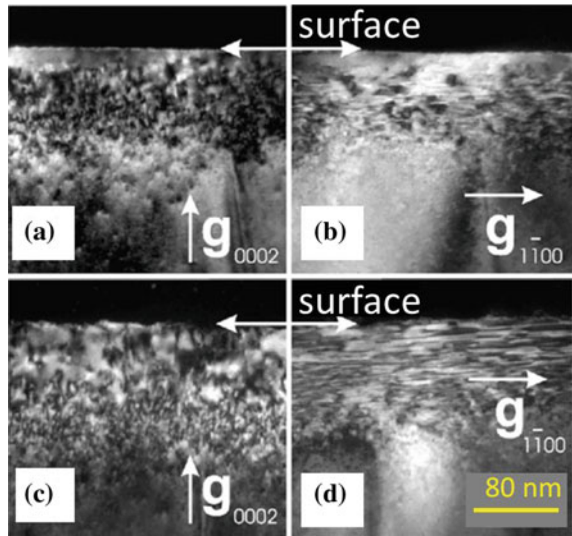

Fig. 6.26 Dark-field XTEM images [**a**, **c** **g** = 0002* and **b**, **d** **g** = 1100*] of GaN irradiated at 550 °C with 300 keV Au ions at fluences of 6×10^{14} cm^{-2} [**a** and **b**] and 4×10^{15} cm^{-2} [**c** and **d**]. Adapted from [91]

lower temperatures, even at liquid nitrogen temperature prior to eventual amorphization [82]. Indeed, it would seem that the strong dynamic annealing in GaN leads to substantial but not perfect defect annihilation and some defect clustering into point defects and planar defects occurs at all temperatures. However, defect clustering is more prominent at low temperatures and such defects act as nucleation centres for amorphous layer formation at and below room temperature. At elevated temperatures, disorder builds up to a saturation defect level that decreases with increasing irradiation temperature, with no amorphous layer formation in this case.

Despite the fact that amorphization does not occur for irradiation at sufficiently high temperatures, a related phenomenon to ion-induced porosity in amorphous GaN, namely that of efficient ion-induced surface erosion, does occur. This phenomenon is illustrated in Fig. 6.27, again for 300 keV Au irradiation at 550 °C [91]. In this case the step height between implanted and unimplanted regions of the GaN substrate

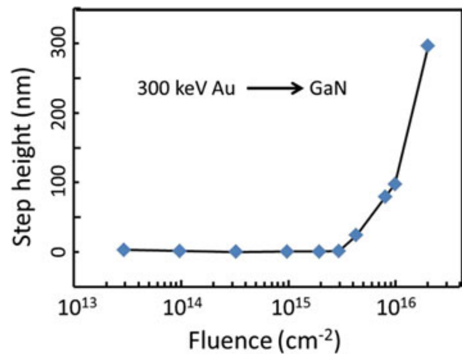

Fig. 6.27 Fluence dependence of the step height between implanted and unimplanted regions of GaN irradiated with 300 keV Au ions at 550 °C. Adapted from [91]

measured by AFM showed an anomalously high etching rate beyond fluences of 3×10^{15} cm^{-2} [91]. For example, it is observed that a fluence of 1×10^{16} Au cm^{-2} results in the erosion of a 100 nm thick GaN surface layer (sputtering yield around 100). It is clear that ballistic sputtering mechanisms alone cannot account for such a large sputtering yield and it has been proposed that this anomalous surface erosion can be attributed to a three-step process of: (i) the build-up of disorder with increasing ion fluence; (ii) thermally and ion-beam-induced decomposition of a heavily damaged GaN near-surface layer at high fluences; and (iii) ion-beam-induced erosion or evaporation of such a dissociated, N-deficient and Ga-rich surface layer [91]. Comparing the elevated temperature anomalous erosion process with the swelling phenomenon in amorphous GaN under irradiation at lower temperatures, both processes appear to originate with ion-induced dissociation of GaN but swelling occurs if the temperature is sufficiently low such that N-rich regions form gas bubbles, whereas anomalous erosion occurs at sufficiently high temperatures where N is lost and evaporation of a Ga-rich surface occurs.

In light of the anomalous erosion behaviour shown above, it is interesting to examine the behaviour of pre-existing amorphous GaN layers under elevated temperature bombardment. For example, in many other semiconductors, it has been shown in previous sections of this chapter that IBIEC occurs if the temperature is sufficiently high during subsequent ion bombardment. In Fig. 6.28, it is shown that such re-irradiation of amorphous GaN layers leads to a reduction in the amorphous layer thickness, a process that is accelerated with increasing temperature. However, this process is not IBIEC behaviour but rather anomalous surface erosion [92]. In this particular case, an amorphous layer of around 200 nm thickness was first formed by 900 keV Au ions at liquid nitrogen temperature to a fluence of 4×10^{15} cm^{-2}. Under such conditions the amorphous layer was not porous, such behaviour requiring appreciably higher fluences. This sample was subsequently re-irradiated with 2 MeV Cu ions at temperatures above room temperature to a range of fluences up to 3×10^{16} cm^{-2}. RBS and channelling data showed that the thickness of the amorphous layer decreased with increasing Cu ion fluence at all temperatures above room temperature, suggesting IBIEC behaviour as shown in Fig. 6.28. However,

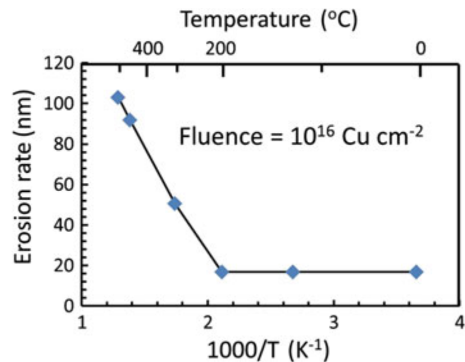

Fig. 6.28 Arrhenius plot of the rate of surface erosion (corresponding to the reduction in amorphous layer thickness) for 2 MeV Cu ion irradiation of a pre-existing amorphous layer in GaN to a fluence of 10^{16} cm^{-2}. Adapted from [92]

AFM measurements of the step height between Cu irradiated and unirradiated regions on the sample indicated that the effect was totally a result of anomalous surface erosion rather than IBIEC. Furthermore, XTEM measurements confirmed a porous-like structure and a very rough surface after elevated temperature Cu irradiation [92]. The erosion rate at 500 °C was around 100 nm corresponding to a sputtering yield of around 100 atoms per ion, again far exceeding that from ballistic sputtering, and similar in magnitude to that for irradiation of crystalline GaN shown in Fig. 6.27. It turns out that the amorphous GaN layer partly recrystallizes thermally to a polycrystalline layer at 500 °C [92], whereas at the lower temperatures it remains essentially amorphous during heating. For extraction of sputtering rates at lower temperatures, the Arrhenius plot is a little misleading, with the sputtering yield rising from around 30 at 200 °C, still well beyond ballistic sputtering values, to around 80 by 400 °C where the original Au-implanted layer that remains after the Cu irradiation is still amorphous. Thus, both crystalline and amorphous GaN are subject to anomalous erosion during elevated temperature bombardment, a process that is likely to arise from ion-induced near-surface dissociation and evaporation of a resulting Ga-rich surface.

6.5.5 ZnO Microstructure Following Irradiation

In Chap. 5, it was stated that, as a II-VI semiconductor, ZnO is almost impossible to amorphize at any irradiation temperature. This is true except for cases with specific ion species at very high fluences in which there can be a chemical effect that acts to stabilize the formation of an amorphous phase. One such ion species is Si, where it has been found that greater than about 10 atomic % of implanted Si in the ZnO lattice can foster the nucleation of an amorphous layer during liquid nitrogen temperature implantation [93]. However, normally the dynamic annealing and defect annihilation rates of irradiation-induced damage are so efficient in ZnO that amorphization is completely suppressed even at very high fluence implantation at liquid helium temperatures. Indeed, the stable defects that form in ZnO build up via a two stage process as measured by RBS and channelling (see Fig. 5.27a in Chap. 5) but the saturation damage is well below the random (or amorphization) level. Such residual damage is in the form of defect clusters and eventually planar defects [93] similar to the case of GaN. This microstructure is illustrated by XTEM in Fig. 6.29a, b [93] for 60 keV Si ions implanted into ZnO at liquid nitrogen temperature.

In this case, Fig. 6.29a, b illustrate the typical defects at low to medium fluences (specifically 7×10^{15} cm^{-2}), where a dense band of point defect clusters and planar defects are observed. The particular diffracting conditions in Fig. 6.29b indicate that the planar defects are concentrated in a band between 30 and 70 nm from the surface, with the surface region free of such defects but containing a high density of clusters. Similar to the GaN case in Fig. 6.26, the planar defects are parallel to the ZnO basal plane. However, when the Si implantation fluence is

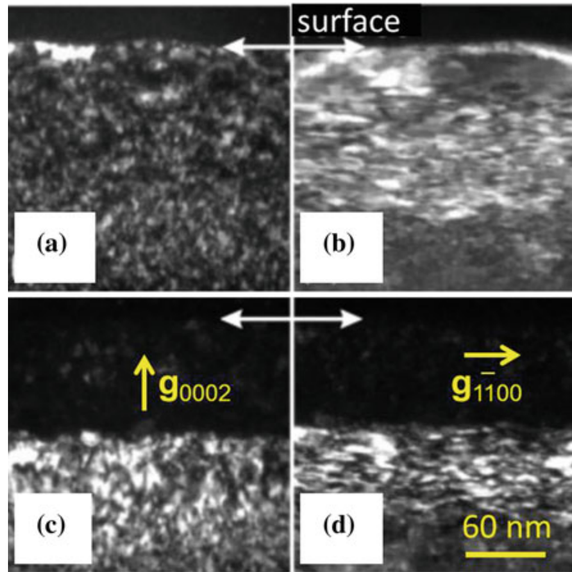

Fig. 6.29 Dark-field XTEM images under two different diffracting conditions for ZnO bombarded with 60 keV Si ions (beam flux 1.2×10^{13} cm^{-2} s^{-1}) to fluences of 7×10^{15} cm^{-2} [**a** and **b**] and 8×10^{16} cm^{-2} [**c** and **d**] at liquid nitrogen temperatures. Adapted from [93]

increased to 8×10^{16} cm^{-2} the formation of an amorphous ZnO(Si) layer is obtained, as shown in Fig. 6.29c, d. In this case the Si concentration peak in ZnO is around 15 atomic % and an amorphous layer of around 70 nm thick is obtained, confirmed by selected area diffraction analysis. The amorphous layer is somewhat continuous up to the surface but detailed analysis [93] shows that there are very small pockets of crystalline material within this essentially amorphous layer. Comparison of the XTEM and RBS and channelling results from this study [93] has shown that the disorder builds up beyond the end-of-ion-range where an excess of implant-generated interstitials and/or a high concentration of the implanted species may be expected. This region appears to stabilize the build-up of further defects with increasing fluence. At a critical fluence, associated with the Si concentration exceeding a particular concentration, an amorphous layer is seeded as a result of chemical effects associated with a high Si concentration in the ZnO lattice, as previously discussed in detail for such chemical effects in GaN [94]. It is interesting that the amorphous layer is not totally continuous in ZnO and this may suggest a locally non-uniform Si concentration and/or Si precipitation.

6.6 Summary and Conclusions

This chapter has focussed on ion-induced disordering, amorphization and crystallization behaviour in a range of semiconductors at elevated temperatures close to the critical temperature T_c for amorphization. The class of semiconductors which are easily amorphized at room temperature, such as Si, Ge, GaAs, InP and SiC are

Table 6.1 Summary of amorphization and crystallization behaviour below and above T_c in a range of semiconductors that can be amorphized under ion irradiation

Semiconductor	T_c range (K)	Amorphous nucleation	IBIIA E_{th} (eV)	IBIEC range	IBIEC E_i (eV)
Si	260–590 [12]	End-of-range defects, defect bands, surfaces [8]	0.5–0.7 [12]	400–680 K [37]	0.2–0.4 [37]
Ge	300–450 [52, 54]	Probably end-of-range defects, surfaces	1.16 but only one case [54]	Occurs but not determined	0.82 [54]
GaAs	230–400 [66]	End-of-range defects, defect bands, surfaces [69]	0.9 [66]	Occurs but not determined	Not determined
InP	330–460 [79]	Probably end-of-range defects and surfaces [81]	0.9–1.5 [79]	Occurs but not determined	Not determined
SiC	220–420 [75, 77]	End-of-range defects, clusters, surfaces [75, 78]	0.6–1.3 [75, 77]	Not measured	Not determined
GaN	–	End-of-range defects (low temps), impurities, surfaces; but often porous	Not determined	Does not occur: surface erosion	–
ZnO	–	At high Si impurity concentrations >10 % only	Not determined	Probably does not occur	–

treated in some detail to illustrate the nature of amorphization when the rate of dynamic annealing closely balances the defect production rate, as well as IBIIA and IBIEC processes. In addition, other semiconductors have been treated in less detail to illustrate disorder microstructures in materials such as: (i) GaN, which is a class of semiconductors that is subject to strong dynamic annealing during ion irradiation even at sub-liquid nitrogen temperatures but still can be amorphized; and (ii) a II-VI material, ZnO, which cannot normally be amorphized under any moderate-fluence irradiation conditions. Finally, some interesting cross-layer defect interactions are illustrated for multilayers. Table 6.1 summarizes the various behaviours highlighted in this chapter for a range of elemental and binary compound semiconductors.

It can be seen in Table 6.1 that the easily amorphizable semiconductors exhibit a range of T_c values that are all close to and above room temperature. However, under the same irradiation conditions (temperature, ion flux and ion mass) they do not amorphize at the same ion fluence, with Ge being the easiest to amorphize, then InP, SiC, and GaAs, followed by Si.

This behaviour does not only indicate that dynamic annealing is stronger in semiconductors which need higher fluences to amorphize them but that the density of collision cascades also plays a role in determining the critical fluence for amorphization. For all of these semiconductors, disorder is found to build up via a two stage process close to T_c, first the build-up of defect clusters to saturation, with

amorphization occurring in the second stage. In such cases amorphization is nucleation-limited and is seeded from either end-of-range defects, defect bands, surfaces and interfaces, or at regions of high impurity concentration, as outlined in the Table. This is the regime where ion flux and temperature can subtly change defect generation rate and defect annihilation rate, respectively. Tipping this balance between these processes can enhance or inhibit amorphization very sensitively. In this regime the defect interaction processes are very complex and it is impossible to model damage build up and amorphization using the treatments in previous chapters, such as Chaps. 3 and 5. Once an amorphous phase is nucleated close to T_c, essentially all semiconductors exhibit layer-by-layer amorphization via IBIIA with increasing fluence, as also shown in Table 6.1. The amorphization kinetics associated with this process is characterized by a single or mostly multiple activation energies (E_{th}). For Si, multiple activation energies for different ion mass and temperature regimes suggest that a range of defect interaction processes are operative. Such is probably the case for Ge, InP and SiC but there is insufficient data to be conclusive. It is only GaAs that appears to exhibit a single activation energy of 0.9 eV but this has not as yet been correlated with a particular defect interaction process that controls amorphization. At temperatures above T_c, IBIEC has been demonstrated in Si, Ge, GaAs and InP but only studied in detail for Si, where again there are multiple activation energies (E_i) characterizing this process in different ion mass and temperature regimes. In this case it is possible to say that it is defects generated precisely at the amorphous-crystalline interface under ion irradiation that are responsible for IBIEC but it is not possible to isolate the specific defect interactions controlling IBIEC. The situation is less clear for the other semiconductors where less data are available.

For GaN, although amorphous layers can be nucleated at relatively high ion fluences at end-of-range defects, impurities and surfaces, there have been no measurements of T_c. Indeed, the amorphous layer so produced can develop a decidedly porous structure and excessive surface swelling with extended bombardment. This process has been shown to relate to ion-induced dissociation and the formation of N-rich gas bubbles in amorphous GaN. Furthermore, at temperatures above room temperature, GaN (in both crystalline and amorphous form) exhibits anomalous erosion that is related to ion-induced dissociation and evaporative loss of a Ga-rich surface. Such effects prohibit any measurements of IBIEC in GaN. For ZnO, ion-induced amorphization is normally not possible under any ion irradiation conditions except very high impurity concentrations of some species such as Si.

It was also shown in this chapter that ternary compounds such as $Al_xGa_{1-x}As$ and $Al_xGa_{1-x}N$ are more resistant to disordering and amorphization at the high Al concentration side of the composition range than for high Ga concentrations. Furthermore, it was shown that only 5 % of Al added to GaN is sufficient to completely suppress surface nucleation of an amorphous phase for liquid nitrogen temperature irradiation. For $GaAs/Al_xGa_{1-x}As$ multilayers, in addition to much easier amorphization of Ga-rich layers, it is more difficult to amorphize GaAs layers adjacent to high Al content layers as a result of mobile defect interactions across the

interface. However, when the Ga-rich layer is ultimately amorphized, disorder builds up at the interface in an adjacent Al-rich layer.

References

1. J.S. Williams, (1998) unpublished
2. J.S. Williams, MRS Bull. **17**, 47 (1992)
3. S. Takeda, M. Kohyama, K. Ibe, Phil. Mag. **A70**, 287 (1994)
4. B.C. Johnson, J.C. McCallum, J. Appl. Phys. **95**, 1096 (2004)
5. R.D. Goldberg, J.S. Williams, R.G. Elliman, Phys. Rev. Lett. **82**, 771 (1999)
6. R.D. Goldberg, J.S. Williams, R.G. Elliman, Nucl. Instr. Meth. Phys. Res. B **106**, 242 (1995)
7. J.S. Williams, H.H. Tan, R.D. Goldberg, R.A. Brown, C. Jagadish, Mat. Res. Soc. Symp. Proc. **316**, 15 (1994)
8. R.D. Goldberg, Ion-induced disordering processes in silicon, Ph.D. thesis, University of Melbourne, 1995
9. R.G. Elliman, J.S. Williams, W.L. Brown, A. Leiberich, D.A. Maher, R.V. Knoell, Nucl. Instr. Meth. Phys. Res. B **19**(20), 435 (1987)
10. R.G. Elliman, J. Linnros, W.L. Brown, Mat. Res. Soc. Symp. Proc. **100**, 363 (1988)
11. K.A. Jackson, J. Mater. Res. **3**, 1218 (1988)
12. R.D. Goldberg, R.G. Elliman, J.S. Williams, Nucl. Instr. Meth. Phys. Res. B **80**(81), 596 (1993)
13. J.S. Williams, Trans. Mat. Res. Soc. Jpn. **17**, 417 (1994)
14. L. Pelaz, L.A. Marquez, J. Barbolla, J. Appl. Phys. **96**, 5947 (2004)
15. M.L. Swanson, J.R. Parsons, C.W. Hoelk, Rad. Eff. **9**, 249 (1971)
16. F.L. Vook, H.J. Stein, Rad. Eff. **2**, 23 (1969)
17. J.R. Dennis, E.B. Hale, J. Appl. Phys. **49**, 1119 (1978)
18. S.U. Campisano, S. Coffa, V. Raineri, F. Priolo, E. Rimini, Nouv. J. Chim. **80–81**, 514 (1993)
19. J. Linnros, G. Holmén, B. Svensson, Phys. Rev. B **32**, 2770 (1985)
20. D.A. Thompson, A. Golanski, H. Haugen, L. M. Howe, J.A. Davies, Radiat. Eff. **50**, 125 (1980)
21. J. Linnros, W.L. Brown, R.G. Elliman, Mat. Res. Soc. Symp. Proc. **100**, 369 (1988)
22. J. Linnros, R.G. Elliman, W.L. Brown, J. Mater. Res. **3**, 1208 (1988)
23. S. Takeda, J. Yamasaki, Phys. Rev. Lett. **83**, 320 (1999)
24. J. Yamasaki, S. Takeda, K. Tsuda, Phys. Rev. B **65**, 115213 (2002)
25. M. Tang, L. Colombo, J. Zhu, T.D. de la Rubia, Phys. Rev. B **55**, 14279 (1997)
26. T. Motooka, Phys. Rev. B **49**, 16367 (1994)
27. D.M. Stock, B. Weber, K. Gärtner, Phys. Rev. B **61**, 8150 (2000)
28. L.A. Marqués, L. Pelaz, J. Hernández, J. Barbolla, G.H. Gilmer, Phys. Rev. B **64**, 45214 (2001)
29. L. Pelaz, L.A. Marques, M. Aboy, J. Barbolla, G.H. Gilmer, Appl.Phys. Lett. **82**, 2038 (2003)
30. M. Jaraiz, P. Castrillo, R. Pinacho, I. Martin-Bragado, J. Barbolla, in *Simulation of Semiconductor Processes and Devices*, ed. by D. Tsoukalas, C. Tsamis (Springer, Vienna, 2001), pp. 10–17
31. K.R.C. Mok, M. Jaraiz, I. Martin-Bragado, J.E. Rubio, P. Castrillo, R. Pinacho, J. Barbolla, M. P. Srinivasan, J. Appl. Phys. **98**, 046104 (2005)
32. J.S. Williams, R.G. Elliman, W.L. Brown, T.E. Seidel, Mat. Res. Soc. Symp. Proc. **37**, 127 (1985)
33. J.S. Williams, R.G. Elliman, W.L. Brown, T.E. Seidel, Phys. Rev. Lett. **55**, 1482 (1985)
34. J. Linnros, G. Hólmen, J. Appl. Phys. **59**, 1513 (1986)
35. G.L. Olson, J.A. Roth, Mat. Sci. Rep. **3**, 1 (1988)
36. F. Priolo, C. Spinella, A. La Ferla, E. Rimini, G. La Ferla, Appl. Surf. Sci. **43**, 178 (1989)
37. A. Kinomura, J.S. Williams, K. Fuji, Phys. Rev. B **59**, 15214 (1999)

38. J.F. Ziegler, J.P. Biersack, U. Littmark, *The Stopping and Range of Ions in Solids* (Pergamon, New York, 1985)
39. V. Heera, R. Kögler, W. Skorupa, R. Grötzschel, Nucl. Instr. Meth. Phys. Res. B **80–81**, 538 (1993)
40. V. Heera, T. Henkel, R. Kögler, W. Skorupa, Phys. Rev. B **52**, 15776 (1995)
41. J.S. Williams, G.M. de Azeveda, H. Bernas, F. Fortuna, in *Materials Science with Ion Beams*, ed. by H. Bernas. Topics in Applied Physics, vol 116 (Springer, Heidelberg, 2009), p. 73
42. R.G. Elliman, J.S. Williams, D.M. Mayer, W.L. Brown, Mat. Res. Soc. Symp. Proc. **51**, 319 (1986)
43. J.S. Williams, I.M. Young, M.J. Conway, Nucl. Instr. Meth. Phys. Res. B **161–163**, 505 (2000)
44. F. Priolo, E. Rimini, Mat. Sci. Rep. **5**, 319 (1990)
45. L.E. Mosley, M.A. Paesler, Appl. Phys. Lett. **45**, 86 (1984)
46. G.M. de Azevedo, J.S. Williams, I.M. Young, M.J. Conway, A. Kinomura, Nucl. Instr. and Meth. Phys. Res. B **190**, 772 (2002)
47. M.T. Robinson, Nucl. Instr. and Meth. Phys. Res. B **48**, 408 (1990)
48. J.W. Mayer, L. Eriksson, J.A. Davies, *Ion Implantation in Semiconductors* (Academic Press, New York, 1970)
49. L. Csepregi, R.P. Küllen, J.W. Mayer, T.W. Sigmon, Solid State Commun. **21**, 1019 (1977)
50. T.E. Haynes, O.W. Holland, Appl. Phys. Lett. **61**, 61 (1992)
51. M. Vos, C. Wu, I.V. Mitchell, T.E. Jackman, J.-M. Baribeau, J. McCaffrey, Appl. Phys. Lett. **58**, 951 (1991)
52. G. Holmen, S. Peterstom, A. Buren, Rad. Eff. **24**, 45 (1975)
53. G. Holmen, A. Buren, P. Horberg, Rad. Eff. **24**, 51 (1975)
54. T. Bachmann, R. Schulz, E. Glaser, U. Richter, S. Schippel, Nucl. Instr. Meth. Phys. Res. B **106**, 350 (1995)
55. B.R. Appleton, O.W. Holland, J. Narayan, O.E. Schow, J.S. Williams, K.T. Short, E. Lawson, Appl. Phys. Lett. **41**, 711 (1982)
56. I.H. Wilson, J. Appl. Phys. **53**, 1698 (1982)
57. R. Kogler, A. Mucklich, W. Skorupa, A. Peeva, A.Y. Kuznetsov, J.S. Christensen, B.G. Svensson, J. Appl. Phys. **101**, 033508 (2007)
58. M. Ghaly, K. Nordlund, R.S. Averback, Philos. Mag. A **79**, 795 (1999)
59. L. Romano, G. Impellizzeri, M.V. Tomasello, F. Giannazzo, C. Spinella, M.G. Grimaldi, J. Appl. Phys. **107**, 084314 (2010)
60. B.L. Darby, B.R. Yates, N.G. Rudawski, K.S. Jones, A. Kontos, R.G. Elliman, Thin Solid Films **519**, 5962 (2011)
61. L. Romano, G. Impellizzeri, L. Bosco, F. Ruffino, M. Miritello, M.G. Grimaldi, J. Appl. Phys. **111**, 113515 (2012)
62. B. Stritzker, R.G. Elliman, J. Zou, Nucl. Instr. Meth. Phys. Res. B **175–177**, 193 (2001)
63. T.E. Haynes, O.W. Holland, Appl. Phys. Lett. **58**, 62 (1991)
64. T.E. Haynes, O.W. Holland, Nucl. Instr. Meth. Phys. Res. **59–60**, 1028 (1991)
65. T.E. Haynes, O.W. Holland, Appl. Phys. Lett. **59**, 452 (1991)
66. R.A. Brown, J.S. Williams, Phys. Rev. B **64**, 155202 (2001)
67. F. Morehead, B.L. Crowder, Rad. Eff. **6**, 27 (1970)
68. R.A. Brown, J.S. Williams, J. Appl. Phys. **81**, 7681 (1997)
69. R.A. Brown, Ion beam damage in GaAs, Ph.D. thesis, University of Melbourne, 1995
70. G. Zollo, C. Pizzuto, G. Vitali, M. Kalitzova, D. Manno, J. Appl. Phys. **88**, 1806 (2000)
71. R.G. Elliman, J.S. Williams, D.M. Maher, W.L. Brown, Mat. Res. Soc. Symp. Proc. **51**, 319 (1986)
72. R.G. Elliman, J.S. Williams, S.T. Johnson, E. Nygren, Mat. Res. Soc. Symp. Proc. **74**, 471 (1987)
73. W. Wesch, E. Wendler, T. Bachmann, O. Herre, Nucl. Instr. Meth. Phys. Res. B **96**, 290 (1995)
74. M.G. Grimaldi, B.M. Payne, M.A. Nicolet, D.K. Sadana, J. Appl. Phys. **52**, 4038 (1981)
75. A.Y. Kuznetsov, J. Wong-Leung, A. Hallén, C. Jagadish, B.G. Svensson, J. Appl. Phys. **94**, 7112 (2003)

76. Y. Zhang, W.J. Weber, W. Jiang, C.M. Wang, A. Hallén, G. Possnert, J. Appl. Phys. **93**, 1954 (2003)
77. W. Weber, Y. Zhang, L. Wang, Nucl. Instr. Meth. Phys. Res. B **277**, 1 (2012)
78. E. Wendler, P. Schoppe, T. Bierschenk, S. Milz, W. Wesch, N.G. van der Berg, E. Friedland, J.B. Malherbe, Nucl. Instr. Meth. Phys. Res. B **286**, 93 (2012)
79. E. Wendler, N. Dharmarasu, E. Glaser, Nucl. Instr. Meth. Phys. Res. B **160**, 257 (2000)
80. E. Wendler, B. Breeger, Ch. Schubert, W. Wesch, Nucl. Instr. Meth. Phys. Res. B **147**, 155 (1999)
81. E. Glaser, T. Bachmann, R. Schulz, S. Schippel, U. Richter, Nucl. Instr. Meth. Phys. Res. B **106**, 281 (1995)
82. S.O. Kucheyev, J.S. Williams, S.J. Pearton, Mat. Sci. Eng. **33**, 51 (2001)
83. H.H. Tan, C. Jagadish, J.S. Williams, J. Zou, D.J.H. Cockayne, A. Sikorski, J. Appl. Phys. **77**, 87 (1995)
84. A.G. Cullis, A. Polman, P.W. Smith, D.C. Jacobson, J.M. Poate, C.R. Whitehouse, Nucl. Instr. Meth. Phys. Res. B **62**, 463 (1992)
85. H.H. Tan, C. Jagadish, J.S. Williams, J. Zou, D.J.H. Cockayne, J. Appl. Phys. **80**, 2691 (1996)
86. A.G. Cullis, N.G. Chew, C.R. Whitehouse, D.C. Jacobson, J.M. Poate, S.J. Pearton, Appl. Phys. Lett. **55**, 1211 (1989)
87. A.G. Cullis, P.W. Smith, D.C. Jacobson, J.M. Poate, J. Appl. Phys. **69**, 1279 (1991)
88. S.O. Kucheyev, J.S. Williams, J. Zou, G. Li, C. Jagadish, M.O. Manasreh, M. Pophristic, S. Guo, I.T. Ferguson, Appl. Phys. Lett. **80**, 787 (2002)
89. S.O. Kucheyev, J.S. Williams, C. Jagadish, J. Zou, V.S.J. Craig, G. Li, Appl. Phys. Lett. **77**, 1455 (2000)
90. S.O. Kucheyev, J.S. Williams, C. Jagadish, J. Zou, G. Li, Nucl. Instr. Meth. Phys. Res. B **175–177**, 230 (2001)
91. S.O. Kucheyev, J.S. Williams, J. Zou, C. Jagadish, G. Li, Appl. Phys. Lett. **78**, 1373 (2001)
92. S.O. Kucheyev, J.S. Williams, C. Jagadish, J. Zou, G. Li, J. Appl. Phys. **88**, 5493 (2000)
93. S.O. Kucheyev, J.S. Williams, C. Jagadish, J. Zou, C. Evans, A.J. Nelson, A.V. Hamza, Phys. Rev. B **67**, 094115 (2003)
94. S.O. Kucheyev, J.S. Williams, C. Jagadish, J. Zou, G. Li, A. Titov, Phys. Rev. B **64**, 035202 (2001)

Chapter 7
Defect Accumulation, Amorphization and Nanostructure Modification of Ceramics

Yanwen Zhang and William J. Weber

Abstract A long-standing objective in materials research is to understand and control the dynamic response of ceramic structures to energy deposition from irradiation. The design of radiation tolerant materials and creation of new functional materials by ion beam modification demand a comprehensive understanding and predictive models of energy deposition, transfer and exchange processes within and between the electronic and atomic subsystems. The exchange of energy between electrons and ions can act to dampen the ionic motion, to inhibit or enhance defect production, or to reduce damage accumulation. Understanding the materials response to both electronic and nuclear energy deposition is a challenge of materials science in diverse fields.

7.1 Introduction

The response of ceramics, such as carbides, nitrides and oxides, to energy deposition from energetic ions is inherently connected with a disturbance of the atomic structure of the materials (radiation damage). Such energy deposition initiates rich sets of interactions and dynamic processes that are possible on the energy landscape. Ion implantation is a tool to create kinetically stable non-equilibrium defects and metastable phases, which allows the investigation of behaviors and properties of materials far from equilibrium. Understanding of damage accumulation, phase transformation and structural modification processes in ceramics using ion beams has evolved over the past several decades, and ion beam methods are well

Y. Zhang (✉)
Materials Science and Technology Division, Oak Ridge National Laboratory,
Oak Ridge, TN 37831, USA
e-mail: zhangy1@ornl.gov

W.J. Weber
Department of Materials Science and Engineering, University of Tennessee,
Knoxville, TN 37996, USA
e-mail: wjweber@utk.edu

© Springer International Publishing Switzerland 2016

W. Wesch and E. Wendler (eds.), *Ion Beam Modification of Solids*,
Springer Series in Surface Sciences 61,
DOI 10.1007/978-3-319-33561-2_7

established as a quantifiable tool to synthesize and modify materials for a wide range of research and applications. A comprehensive understanding of the relationship between irradiation conditions and the corresponding damage is essential to the application of ion beams, to ion-beam processing and modification of materials, as well as in mimicking the effects of radiation in natural radioactive minerals and in ceramics for a broad range of nuclear applications and space exploration.

The irradiation of ceramics with ion beams can lead to defect accumulation, phase transformations and structural modifications that can dramatically alter the physical and chemical properties of the materials. The irradiation-induced crystalline-to-amorphous transformation, or amorphization, is the most significant phase transformation in ceramics. For a given material, the kind and concentration of irradiation damage produced, the nature of the structural modifications and phase transformations depend on the irradiation conditions (ion mass, energy, fluence, flux, and irradiation temperature), as well as any post-irradiation treatment.

In this chapter, damage accumulation, phase changes and structural modification in ceramics due to low and intermediate energy ions (from a few hundred keV to tens of MeV) are reviewed (swift heavy ion effects are the subject of Chap. 8). In this energy range, the study of irradiation effects has been primarily focused on elastic collisions between atoms initiated by energy transfer from incident ions to target atoms through nuclear energy loss (stopping power), while less attention has been given to the effects of electronic energy loss. The first part of the chapter (in this Sect. 7.1) provides a general introduction to irradiation effects in ceramics. The nature of defect structures produced directly in a single ion event and the unique nature of collision cascades in ceramics, due to separate and distinct sublattices, are discussed in part two (Sect. 7.2). This section also includes the results of molecular dynamics simulations. While many ceramic structures, such as the fluorite structure, are relatively resistant to amorphization, other ceramic structures, including perovskites, pyrochlores, apatite, are highly susceptible to irradiation-induced amorphization or order-disorder transformations. The application of models to describe damage formation, how the structural modifications are driven to phase transformations, as well as the analysis and interpretation of experimental data (beyond that shown in Chap. 3) are illustrated in several examples in the third part (Sect. 7.3) of the chapter. Ionization-induced damage annealing or ionization-enhanced amorphization, including examples of such effects observed in carbides and oxides, will be discussed in part four (Sect. 7.4) of this chapter. A fifth section on *Structural Modifications in Nanostructured Ceramic Matrices* (Sect. 7.5) is devoted to structural modifications that include evolution of nanostructures and microstructures, grain growth, ion-beam annealing, and structural phase transformations. Finally, the main aspects of the chapter are reviewed in the concluding summary (Sect. 7.6).

7.2 Energy Deposition Processes in Crystalline Ceramics

Irradiation of materials by energetic ions has been under intensive investigation for many decades, due to the unique possibility of controllable modification of material properties. It is well established experimentally and through the development of theoretical models that ions incident on target materials transfer their energy to two subsystems, namely the atomic and electronic subsystems, through the nuclear and electronic stopping powers. Many dedicated experiments have evaluated electronic stopping power. The resulting values as functions of the velocity of a moving atom inside the matrix were summarized in a vast data set by Ziegler et al. [1] for all commonly studied monoatomic materials along with a significant number of compounds. For many device and industrial applications, ion range and doping concentration are commonly estimated using the widely accepted Stopping and Range of Ions in Matter (SRIM) [1] code. This code provides a general description of the energy transfer paths from the ion to electrons and atomic nuclei in irradiated materials. For example, SRIM calculations are often used to relate ion fluence (number of ions per unit area given by the product of ion flux ϕ and time t) to a damage profile (dose as a function of depth) resulting from energetic ions. Such damage profiles are given in terms of the local displacements per atom (dpa) as a function of depth using the SRIM code, as explained in Chap. 3. Depending on the material systems or individual research groups, the irradiation-induced damage profiles are calculated with the Kinchin-Pease damage calculation model or under full-cascade simulations. While ion fluence is defined as the total number of ions that intersect a unit area in a specific time interval of interest and has units of cm^{-2}, the ion dose is essentially a local energy deposition density to the electrons and atomic nuclei, which are each expressed separately. The total energy transferred to electrons from both the incident ions and the resulting atomic recoils is described as the ionization dose, while the total energy that only goes into displacing atoms is described as the damage energy and is often converted to the unit of dpa. Studying the dose dependence of irradiation response provides insights into the nature of ion-solid interaction processes and reveals mechanisms of disordering. The electronic and nuclear energy losses of the incident high-energy ions as a function of depth can be calculated using SRIM under a quick calculation of energy deposition. The assumed sample density in the calculations can be based on either experimentally determined values or the theoretical density. The threshold displacement energy for a monoatomic substrate or the respective threshold displacement energies for the different sublattices of a compound target are a few tens eV, which may be calculated or measured. In the case of complex materials, the values commonly suggested by the SRIM code may be used, but only with extreme caution, since these are primarily based on elemental targets. For complex materials, bonding types often change the threshold displacement energies, as compared to elemental

values. Accurate values of threshold displacement energies, particularly for complex materials, are critical for reliable prediction of damage on different sublattices.

Accurate information on energy transfer from energetic ions to materials is essential for fundamental research, electronic and optical device fabrication, and prediction of the performance of materials subject to high radiation environments. While the electronic stopping powers for light ions have been extensively measured and validated in elemental targets and simple compounds, the measurement of electronic stopping powers for heavy ions, especially for very heavy ions (such as Pt and Au), at low to medium energy ranges has been a long-standing challenge. Recent experimental results have shown considerable errors in the SRIM predictions for the stopping of heavy ions in compounds containing light elements. For example, the SRIM predictions on both the damage profile and the Au implantation profile in SiC irradiated with Au ions are much shallower than the experimental results [2–4]. The disagreement between the SRIM predictions and experimental results has also been observed in GaN [5]. Sigmund [6] has suggested that the electronic stopping cross section may be determined from the inverted ion-target system by applying the concept of reciprocity. The principle of reciprocity is based on the invariance of the inelastic excitation in ion-atom collisions against interchange of the projectile and target. Reciprocity is applicable in the low velocity regime, where the projectiles are neutral and the probability for electron loss is small. Good agreement between the reciprocity prediction and experimental stopping results has been reported [4]. Comparison of the electronic stopping cross section predicted by the SRIM code and with the reciprocity approach suggests that the SRIM predicted electronic stopping power can be overestimated by a factor of ~ 2 in the energy ranging up to ~ 20 keV/u (energy per nucleon) [2, 3]. Refinement in theory and models will demand accurate stopping data over a wide range of ion masses and energies.

The deposition of energy by external energetic particles (e.g., ions, electrons, neutrons, and cosmic rays) to crystalline ceramics may cause the formation of defects in both the atomic and electronic structures. When energetic particles, such as ions, penetrate a material, energy and momentum are transferred from the energetic particles to the target electrons and atomic nuclei (energy deposition to the electronic and atomic sublattices). Kinetic energy transfers to the atomic nuclei can result in displacement of atoms from their original sites. As the energy transferred from single collision is often many times greater than the binding energy, the target atoms can be displaced from their lattice site. Moreover, the lattice atoms displaced by incident ions become primary knock-on atoms (PKAs) that may have sufficient energy to displace other additional target atoms, creating a cascade of atomic collisions that result in a locally high concentration of atomic-scale defects in the structure. Energy transfers to the target electrons produces electron-hole pairs that can result in the formation of charged defects, localized electronic excitations, rupture of covalent and ionic bonds, enhanced defect and atomic diffusion, increased free energy, changes in phase transformation dynamics, as well as formation of atomic-scale defects.

Much of the work on radiation effects in ceramics has focused on atomic collision processes [7–11], in terms of defect formation, migration, recombination, and

microstructure evolution. The effects of ionization (electronic excitations) [12–16] and the coupled effects of ionization and atomic dynamics on material behavior are not well understood and have become an important area of research [17]. In this section, we will describe the damage production, including primary damage state, unique nature of separate and distinct sublattices, effects of electronic energy loss, and coupled effects of ionization and atomic dynamics on material behavior.

7.2.1 Damage Production from Atomic Collision Processes

While damage production in the intermediate ion regime includes energy transfer to both electrons and atomic nuclei, many irradiation effects are the result of defects produced primarily from atomic collision processes, and the loss of energy to electrons has been considered to have a negligible effect. When an energetic ion passes through material, the energy deposited to atomic recoils can be just sufficient to produce simple interstitial-vacancy (Frenkel) pairs or large enough to result in a cascade of elastic collisions producing a locally high concentration of defects. In some ceramics, the energy of the recoil is sufficient to cause ballistic melting, resulting in the formation of an amorphous core in the cascade [18]. The basic processes of defect and damage production by ballistic collisions on the atomic structure are fairly well understood. Energy transfer processes between atoms due to nuclear energy loss are reasonably well described by a screened interatomic potential, and the entire energy cascade (temporal and spatial characteristics) can be simulated by computational approaches, such as empirical potential molecular dynamics (MD).

The existence of two or more distinct sublattices in ceramics leads to a greater number of defects than in elemental semiconductors, such as Si and Ge. In simple binary carbide and nitride ceramics, such as SiC or AlN, there are two types of interstitials (in various defect configurations), two types of vacancies and two types of anti-site defects. In simple binary oxides, such as ZrO_2, there are cation (Zr) and anion (O) interstitials and vacancies on both the Zr and O sublattices; however, antisite defects are generally unstable due to Coulomb repulsion. In more complex oxides with multiple cations and cation sublattices, the number of interstitial and vacancy types increases, and in structures with ordered cation sublattices, cation anti-site defects result in cation disorder. In both simple and complex oxide ceramics, electro-neutrality is often a constraint on defect complexes. More discussion on chemical effects can be found in Sect. 7.3.2.

7.2.2 Effects of Electronic Energy Loss

While understanding irradiation damage from elastic collision events is much better understood, some recent research has emphasized the effects of electronic energy loss on both damage production and damage accumulation processes [19–27]. In

most ion irradiation events, target electrons absorb a significant portion of the energy from the incoming ions (from a few percent up to a dominant amount). In the case of intermediate energy ions, from approximately 1 to 100 keV/u, this electronic energy loss has essentially been ignored in the past because of the common assumption that this energy is largely dissipated locally as a thermal spike, which is transported away without noticeable effects on the atomic structure. In the case of swift heavy ions (>1 MeV/u), however, the energy dissipation is sufficient to cause a thermal spike that results in the formation of amorphous tracks in many ceramic oxides. Recent studies have shown that in the intermediate energy regime, the thermal spike from electronic energy deposition is sufficient to induce damage production or damage annealing. Electronic excitations induced by ionization energy losses in materials can also cause trapping of electrons or holes at defects, as well as local changes in bonding and free energy. These effects can lead to permanent bond breakage and accompanying defect production in the atomic structure (solid-state radiolysis), local changes in barriers to atomic diffusion, and phase instabilities. Under extreme ion fluxes available in the laboratory today, some electronic excitations from ionization can have lifetimes in the order of the time between events. As a result, a steady-state concentration of electronic excitations can exist, which has a significant effect on the evolution of microstructure, phase changes, and thermodynamic properties in materials. In addition, such localized excitation can influence the complex interaction of materials with the environment.

7.2.3 Coupled Effects of Ionization and Atomic Dynamics

With a few exceptions, interpretations of irradiation effects in ceramics have often focused on collision cascade processes at low and intermediate energies and on electronic energy loss processes at high energies typical of swift heavy ions. This generally means that nuclear and electronic damage effects are investigated separately, and the response of materials to energy deposition is assumed through independent and non-correlated defect dynamic processes. Commonly, material response to kinetic energy transfer to atomic nuclei has been investigated at keV to MeV ion energies, where the density of defect production increases as the ion loses energy in penetrating the target material. However, except at very low energies, the electronic energy loss of intermediate energy ions can be much larger than the nuclear energy loss (or more specifically the local damage energy). This means that the electronic energy loss can affect defect production and damage accumulation processes. The coupling of nuclear and electronic energy deposition processes can lead to additive, competitive (recovery) and synergistic effects on defect production and evolution.

Currently, simulation and modeling of radiation effects in materials primarily focus only on processes occurring in the atomic structure. There is little understanding of how ionization creates defects directly or affects the kinetics of atomic processes through enhanced defect diffusion or atomic mobility. Consequently, there is a great need for revolutionary advances in understanding and modeling of

radiation effects that address the consequences of ionization and the coupled dynamics of electronic and atomic processes from charged-particle irradiation. New computational and experimental approaches are needed to develop predictive models to correctly describe the separate and coupled effects of electronic and nuclear energy loss.

7.3 Damage Accumulation

7.3.1 Defect Accumulation

The accumulation of defects produced by collision cascades represents the earliest stages of damage accumulation. If the defects are immobile and the structure is stable, irradiation damage results in a steady state concentration of defects that is maintained by simple interstitial-vacancy recombination processes, as discussed in Chap. 3. An example of such defect accumulation process is illustrated in Fig. 7.1, where the relative lattice parameter change, $\Delta a/a_0$, measured by X-ray diffraction is plotted as a function of ion fluence for polycrystalline CeO_2, UO_2 and PuO_2 with the stable fluorite structure [28]. The change in lattice parameter is proportional to the defect concentration and follows the simple exponential ingrowth model given by the expression:

$$\Delta a/a_0 = \mathrm{A}[1 - \exp(-\mathrm{B}\phi t)], \tag{7.1}$$

where A is the saturation value for the change in lattice parameter, B is related to the cross section for defect production and the recombination rate, and ϕt is the ion fluence (see (3.6) and accompanying text in Chap. 3). Even if defect accumulation leads to phase changes or evolution of microstructure, such as dislocation loops, the early state of defect accumulation often follows this exponential ingrowth model, which is used in deconvolution of more complex damage accumulation behavior, where both defect accumulation and amorphization are occurring simultaneously.

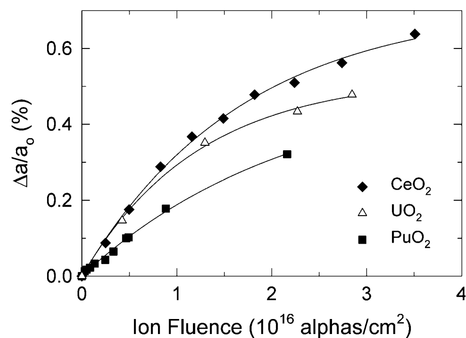

Fig. 7.1 Lattice parameter change $\Delta a/a_0$ versus ion fluence in polycrystalline CeO_2, UO_2 and PuO_2 due to alpha particle irradiation at room temperature [28]

It is worth noting that the saturation levels are different for the polycrystalline oxides, which may reflect the intrinsically greater radiation resistance in PuO_2 versus CeO_2 in terms of less volume swelling in PuO_2. Moreover, a lower saturation level is observed in the polycrystalline UO_2 than in the case of single crystalline UO_2 (Fig. 3.5 Chap. 3). One of the contributing factors to these differences may be the additional grain boundaries that can act as defect sinks to enhance defect annihilation. Ion beam modification of nanocrystalline, polycrystalline, single crystal, and thin film ceramics is one of the frontiers of material research. It can be used to control and tailor defect dynamics, structural stability, and exceptional size-dependent electronic, optical and magnetic properties of functional materials.

7.3.2 *Irradiation-Induced Phase Transformations*

Irradiation-induced phase transformations in ceramics are of considerable interest, both fundamentally and technologically [29–34]. As discussed in Chap. 3, the models describing these transformations are somewhat similar and are generally defined in terms of the fraction of material transformed, comparable to what is generally measured experimentally. The dynamics of phase transformation in crystalline ceramics are defined by competing reaction rate processes: those that drive the transformation and those that drive the recovery of the transformation. In the case of the irradiation-induced crystalline-to-amorphous transformation, irradiation-induced defect accumulation and direct in-cascade amorphization are the primary driving forces. Irradiation- and thermal-induced defect recovery and recrystallization processes, however, compete with the amorphization processes. In ordered semiconductors and oxide ceramics, irradiation-induced chemical disordering from anti-site defect formation competes with irradiation-induced ordering. These irradiation-induced phase transformations occur homogeneously or heterogeneously, and often occur only below a critical temperature that is dependent on the irradiation conditions.

7.3.2.1 Chemical Effects on Resistance to Amorphization

Materials can have identical or similar structure, but are different chemically, hence in bonding type. These chemical effects may lead to remarkable differences in resistance to amorphization. Oxides with similar structure can exhibit different damage and amorphization behavior [9, 35–37].

In the study of radiation tolerance of complex oxides, pyrochlore compositions display distinctive responses to ion beam-induced amorphization, depending on the chemical composition [35, 38]. Pyrochlore materials, in the $A_2B_2O_7$ crystal structure, have remarkable elemental versatility. Considerable self-radiation damage from alpha decay in actinide-bearing phases can result in amorphization, macroscopic swelling and order-of-magnitude increases in dissolution rates [39, 40]. These changes in

structure and chemical durability affect long-term performance of actinide waste forms. Radiation studies of actinide-doped, synthesized or natural pyrochlores indicate that pyrochlores with Ti, Nb, and Ta as the major B-site cations become amorphous as a result of the gradual accumulation of cascade damage. For example, all of the titanate pyrochlores are readily amorphized by ion beam irradiation at a relatively low fluence. $Gd_2Ti_2O_7$ can be amorphized at ~ 0.2 dpa under room temperature 600 keV Ar^+ irradiation [41], which is consistent with the result from ^{244}Cm-doped (3 wt%) $Gd_2Ti_2O_7$ with an amorphization dose of ~ 0.16 dpa [42] and swift heavy ion irradiations [43, 44]. Damage evolution on the Sm and O sublattices in $Sm_2Ti_2O_7$ single crystals irradiated with 1 MeV Au^{2+} ions at 170, 300, and 700 K have been studied using Rutherford backscattering spectroscopy and $^{16}O(d,p)^{17}O$ nuclear reaction analysis [10]. The critical dose for amorphization at 170 and 300 K is ~ 0.14 dpa. The rate of damage accumulation at 700 K decreases dramatically due to significant dynamic recovery, and a higher amorphization dose of ~ 0.22 dpa is observed under irradiation at 700 K. The results from the ion irradiation studies are in agreement with the in situ TEM results for polycrystalline $Sm_2Ti_2O_7$ irradiated with 600 keV Bi^+ ions [39]. Damage evolution at room temperature in $Ho_2Ti_2O_7$ single crystals has also been studied under 1 MeV Au^{2+} ion irradiation [45]. The relative disorder at the damage peak on the Ho sublattice increases nonlinearly with the dose, approaching a fully amorphous state at a dose of ~ 0.12 dpa. While the critical dose for amorphization under 1 MeV Au^{2+} irradiation at room temperature is similar for both $Ho_2Ti_2O_7$ and $Sm_2Ti_2O_7$ [10, 39], a slower damage accumulation rate for $Ho_2Ti_2O_7$, as compared with damage evolution in $Sm_2Ti_2O_7$, is mainly attributed to a lower effective cross section for defect-stimulated amorphization [39]. With increasing ionic radius of the A-site cation, from Lu^{3+} (0.098 nm) to Gd^{3+} (0.106 nm), the critical temperature for amorphization, above which the material will not be amorphized, increases from 480 K (for $Lu_2Ti_2O_7$) to 1120 K (for $Gd_2Ti_2O_7$) [46, 47] under Kr^+ ion irradiation; however, the critical temperature for these materials is nearly constant (1000 K) under heavy ion irradiation [7]. Zirconate pyrochlores are generally resistant to radiation-induced amorphization, and both $Gd_2Zr_2O_7$ and $Er_2Zr_2O_7$ remain crystalline at doses as high as 100 dpa at cryogenic temperatures [9, 41]. Sickafus et al. [9] point out that fluorite crystal structure should accept radiation-induced defects into their lattices far more readily than a structurally similar pyrochlore crystal structure; therefore, fluorites are inherently more radiation resistant than pyrochlores. Sickafus et al. [9] have, however, proposed that complex oxides, which possess both complex chemistry and structure that provide an inherent propensity to accommodate lattice disorder, should be able to resist lattice instability in the presence of a displacive radiation environment.

In contrast to Sickafus' hypothesis, Trachenko et al. [36] suggests that the type of interatomic force may hold the key to radiation performance. He proposes that the ability to form a short-range covalent network leads to damage stabilization and makes a material more readily amorphizable by radiation damage. Long-range high ionicity, on the other hand, results in higher resistance. Examples supporting his argument include SiO_2, TiO_2, and GeO_2. Crystalline SiO_2 is easily amorphizable,

and TiO_2 is more resistant than SiO_2 and GeO_2, which is attributed to the larger ionicity of the bonding in TiO_2 than in the classical network formers SiO_2 and GeO_2. Trachenko has further demonstrated that complex titanates (such as perovskites $CaTiO_3$, $SrTiO_3$, $BaTiO_3$, pyrochlores $Gd_2Ti_2O_7$, $Sm_2Ti_2O_7$, $Eu_2Ti_2O_7$, $Y_2Ti_2O_7$, zirconolite $CaZrTi_2O_7$) are readily amorphizable by radiation damage, due to disordering of the covalent Ti-O-Ti bonds. On the other hand, binary oxides MgO, ZrO_2 and Al_2O_3 are known to be highly resistant to amorphization by radiation damage, which Trachenko attributes to the high ionicity of these binary oxides [36]. The same argument, high ionicity of Zr–O bond, is used to explain the extreme resistance of zirconate oxides $Gd_2Zr_2O_7$, $Sm_2Zr_2O_7$, $Nd_2Zr_2O_7$, $Ce_2Zr_2O_7$ and $Er_2Zr_2O_7$. Trachenko further proposes that the resistance to amorphization of a complex (non-metallic) material is defined by the competition between the short-range covalent and long-range ionic forces.

Chemical effects on resistance to amorphization are still an open research topic. While Sickafus and his co-workers [9] focus on the role of atoms on the cation sublattice, Trachenko et al. [36] call attention to the bonding types. The two concepts are related to each other, and some consistencies are observed. As discussed above, Ti is able to form disordered covalent Ti–O–Ti bonds, which is taken by Trachenko et al. [36] as the underlying mechanism for the radiation-sensitivity of complex oxides containing Ti. For the same amount of energy deposited by ions, the materials dissipate the energy differently due to the bonding types (chemical effects). This is consistent with the suggestion of Sickafus et al. [9] that the Ti-containing pyrochlores have the highest cation antisite defect energy, which is responsible for the low probability of the natural transition from the ordered pyrochlore structure to the disordered defect-fluorite structure in $A_2B_2O_7$ materials. Results show that if this phase transition does not occur naturally, the material more readily forms radiation-induced defects and can be more easily amorphized.

7.3.2.2 Amorphization in Complex Oxides

In crystalline ceramics, as the number of incident ions (ion fluence) increases, the individual damaged regions begin to overlap, and damage accumulation in single crystals can be readily followed by Rutherford backscattering spectrometry (RBS) (see Sect. 5.2) and nuclear reaction analysis (NRA) along a major crystal direction over a wide range of ion fluences and temperatures. Irradiation-induced damage in crystalline samples can be quantified utilizing the channeling technique. If a crystal contains displaced lattice atoms, the backscatter yield resulting from direct backscattering and dechanneling of the probing ions due to the interaction with the displaced atoms will increase with increasing concentration of displaced atoms. For example, the damage accumulation in $Sm_2Ti_2O_7$ single crystals irradiated with 1.0 MeV Au^{2+} ions [48], as measured by RBS channeling along the <001> direction, is shown in Fig. 7.2. Because the backscattering yield due to the ion-implantation-induced disordering is much more evident from the Sm sublattice, all analyses of cation disordering were performed on that part of the RBS

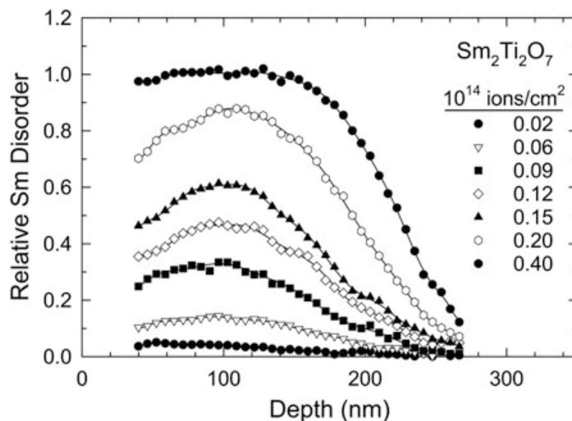

Fig. 7.2 Damage profiles on the Sm sublattice in $Sm_2Ti_2O_7$ single crystal following 1 MeV Au ion irradiation at 300 K to ion fluences from 2.0×10^{12} to 4×10^{13} ions/cm^2 [48]

spectrum. The depth profiles of the relative Sm disorder were determined from the RBS spectra using an iterative procedure [49–51], which provided a more reliable determination than the linear dechanneling approximation often employed. The emergence of the damage peak at a low ion fluence of 2.0×10^{12} cm^{-2} indicates the presence of disorder due to locally displaced atoms. The relative Sm disorder increases with ion fluence at each depth, and the amorphous state is defined as achieving a relative disorder of 1.0, where the crystalline structure is so highly disordered that the resulting aligned backscattering yield overlaps with the random spectrum. The implantation-induced disorder profile has a peak located at about 100 nm, and full amorphization at the damage peak is observed for a fluence of 4×10^{13} cm^{-2}. For most irradiation damage, especially at early stages [52], the damage peak is located at the maximum in the damage profile, as shown in Fig. 7.2. As discussed earlier in Sect. 7.2 of this chapter, one should also note the large error predicted by the SRIM predictions in damage and implanted ion profiles. This error is the direct result of the inaccurate prediction of electronic stopping powers of heavy ions in targets containing light elements, such as C, N or O [2–6]. SRIM results can underestimate the depth of the damage region, due to the overestimation of the electronic stopping powers, in ion irradiation studies where heavy ions with energies up to a few MeVs are utilized to create a damage layer for ion beam analysis and microstructural characterization.

Under the right conditions, relative disorder on both cation and anion sublattices can be determined using a combination of RBS and NRA along channeling directions. The relative O disorder is generally provided from NRA, using the ^{16}O (d,p)^{17}O reaction along a channeling direction, and determined from the ratio of aligned spectra to random spectra and correcting for the background-dechanneling fraction. In the case of $Sm_2Ti_2O_7$ single crystals irradiated at room temperature, the relative disorder induced by Au ion irradiation has been determined on both the Sm and O sublattices [10]. The relative disorder on both the Sm and O sublattices at the damage peak are shown in Fig. 7.3 as a function of the local dose at the damage peak. In other words, the relative disorder values in Fig. 7.3 are taken from the

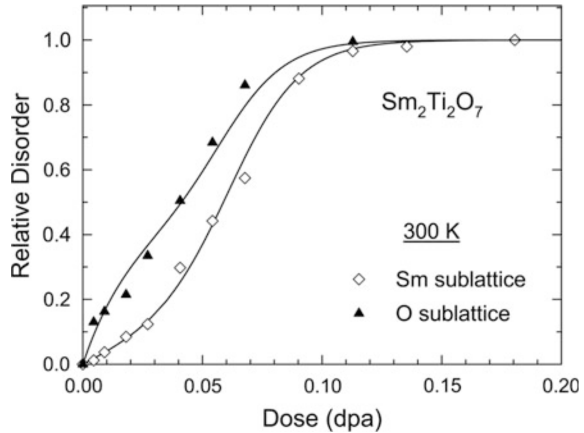

Fig. 7.3 Relative disorder at the damage peak on both the Sm and O sublattices as a function of local dose for $Sm_2Ti_2O_7$ single crystals irradiated with 1.0 MeV Au^+ ions at 300 K [10]. *Solid lines* are fits of (7.2) to the data, using (7.3) and (7.4)

profiles in Fig. 7.2 at ~100 nm, where the maximum disordering rate occurs. For each ion fluence, the local dose at the damage peak, in dpa, can be determined using the Stopping and Range of Ions in Matter (SRIM) 2003 code [1] under full-cascade mode, assuming a theoretical density of 6.305 g cm^{-3} and threshold displacement energies of 50 eV for Sm, Ti, and O atoms, respectively. The conversion factor at the damage peak from ion fluence (10^{14} Au^+ cm^{-2}) to dose (in dpa) is 0.45 [10]. The results in Fig. 7.3 indicate that the atomic disorder on both the Sm and O sublattices increases nonlinearly with dose, eventually achieving a fully amorphous state. Significantly more O disorder, as compared with the Sm disorder, is primarily attributed to a lower displacement energy for the O sublattice.

7.3.3 Modelling Amorphization

Various approaches exist for modeling disorder accumulation (see Chap. 3). Disorder accumulation is usually studied at the depth of the damage peak, where displacement damage is dominant due to the maximum in nuclear energy deposition and where amorphization will generally first appear, unaffected by the lower damage accumulation at other depths. Ion-induced damage accumulation can be described by a disorder accumulation model [53, 54]. In this model, amorphous nuclei are directly produced within a cascade, and the irradiation-induced point defects accumulate and stimulate further amorphization at the crystalline-amorphous interfaces. As discussed in Sect. 3.5, the total irradiation-induced damage fraction, f_d, generally consists of two contributions at relatively low irradiation temperatures: the irradiation-induced amorphous fraction, f_a, and the relative defect fraction, f_{def}. In the case of disorder accumulation, these contributions are from irradiation-induced interstitials and small interstitial clusters in the residual crystalline regions [11], which must be weighted by the fraction of residual crystalline volume $(1 - f_a)$. The expression for f_d is given by:

$$f_d = f_a + f_{def}(1 - f_a), \tag{7.2}$$

(similar to (3.35) in Sect. 3.5). While the amorphous fraction f_a is well described using a direct-impact, defect-stimulated (DI/DS) model for amorphization [55], the formation and accumulation of point defects or defect clusters, f_{def}, depend on defect properties in the residual crystalline material [56, 57]. The two contributions to the damage fraction, f_a and f_{def}, are given by the expressions:

$$f_a = 1 - (\sigma_a + \sigma_s) / \{\sigma_s + \sigma_a \exp[(\sigma_a + \sigma_s)\phi t]\}, \tag{7.3}$$

which was derived in Sect. 3.5 (3.21), and

$$f_{def} = f_s[1 - \exp(-B\phi t)], \tag{7.4}$$

which is similar to (7.1) described earlier, where σ_a is the amorphization cross section, σ_s is the effective cross section for defect-stimulated amorphization, and f_s is the relative defect fraction at saturation. Because the local damage production rate generally varies with depth, as well as with ion mass and energy, the analysis of experimental data is often carried out in terms of the local atomic displacement dose, $\sigma_d\phi t$, in unit of dpa, as discussed in Chap. 3, where σ_d is the local atomic displacement cross section (per atom). As discussed earlier, RBS along a channeling direction of single crystals is often used, and f_d is the measured relative disorder at the damage peak for one or more major compositional elements. For example, the disorder accumulation on the Si sublattice at the damage peak as a function of local dose is shown in Fig. 7.4 for SiC irradiated at room temperature with 550 keV Si ions [58]. The solid line is a fit of the disorder accumulation model (7.2) to the data using (7.3) and (7.4). These results show that the contribution of defects to disordering is dominant at low doses, while the contribution of the amorphous material dominates at higher doses due to the decrease in crystalline fraction.

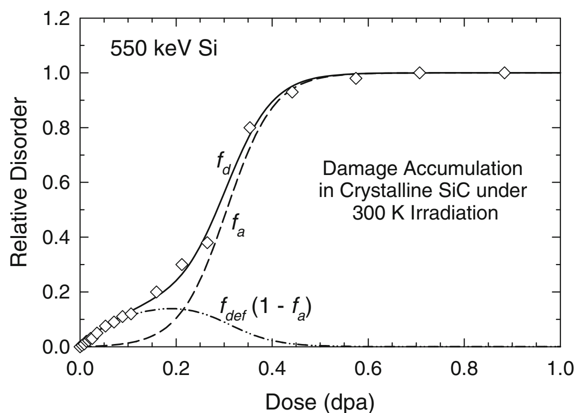

Fig. 7.4 Relative disorder on the Si sublattice as a function of the local dose at the damage peak in single crystal 4H-SiC irradiated with 550 keV Si ions at room temperature [58]. The *solid line* is a fit of the disorder accumulation model, (7.2), based on using (7.3) for the amorphous fraction, f_a, and (7.4) for the defect fraction, f_{def}, in the residual crystalline material

At elevated irradiation temperatures, instantaneous recombination of interstitials and vacancies is enhanced, and irradiation-induced defects become more mobile. At temperatures close to the critical temperature for amorphization, mobile defects can precipitate to form two-dimensional extended defect clusters that contribute to both damage accumulation and measured disorder, as well as to reducing the local strain. Under these conditions, an additional term should be added to (7.2) that is proportional to the relative cluster fraction, f_c, to account for the effect of extended defect clusters on measured damage fraction. Such cluster formation depends on the mobile defect concentration and a steady-state saturation value that is closely related to the irradiation temperature. Unlike point defects and amorphous domains, the contribution of extended defect clusters to a measured property change, such as disorder, varies considerably with size, orientation and cluster fraction. In the case of relative disorder, as measured by RBS, the contribution of extended defect clusters to disorder can be considered to follow behavior similar to (7.4) and also weighted by the fraction of residual crystalline volume, $(1 - f_a)$. Under these assumptions, the contribution from extended clusters to relative disorder is proportional to f_c and given by Sf_c, where S is a proportionality constant, and the relative contribution to measured disorder from accumulation of extended defects can be expressed as:

$$Sf_c = Sf_c{}^*[1 - \exp(-R\sigma_d \phi t)](1 - f_a), \quad (7.5)$$

where $Sf_c{}^*$ is the saturation value for relative cluster disorder, and R is proportional to a probability for clustering.

7.3.4 *Effect of Temperature*

The models portrayed above represent simple descriptions of the irradiation-induced amorphization process without any consideration for kinetics. During irradiation at elevated temperatures, simultaneous recovery processes can compete with damage production processes, and the rate of amorphization will depend on the relative magnitude of the rates of production and recovery processes under any given irradiation conditions. Damage production processes directly depend on the damage rate or ion flux; thus, both damage rates and temperature affect the kinetics of amorphization. The simultaneous damage recovery processes are associated with point defect recombination or annihilation at defect clusters in the crystalline state, point defect annihilation at crystalline/amorphous (c/a) interfaces or at grain boundaries (GBs), epitaxial recrystallization at c/a interfaces, or nucleation and growth recrystallization in the bulk of the amorphous state. Obviously, if the rate of amorphization is less than the damage recovery rate at any temperature, amorphization will not proceed.

An example of the disorder accumulation on both the Si and C sublattices in 4H-SiC at the damage peak as a function of dose is shown in Fig. 7.5 over the

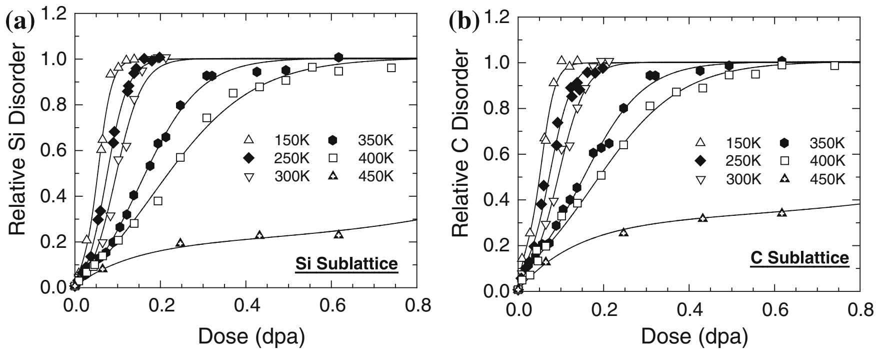

Fig. 7.5 Relative disorder at the damage peak as a function of local dose for 4H-SiC irradiated with 1.1 MeV Al_2^{2+} molecular ions at temperatures from 150 K to 450 K [53]. Solid lines are fits of (7.2) to the data, using (7.3)–(7.5)

temperature range from 150 to 450 K [53]. The solid lines are fits of the disorder accumulation model, (7.2) to the data, using (7.3)–(7.5). The model fit parameters [53] change dramatically with increasing temperature due to defect recombination, defect diffusion to sinks, and formation of defect clusters. The results in Fig. 7.5 illustrate a general behavior for damage accumulation that the relative rate of disorder decreases with temperature. Under these irradiation conditions, the disordering behavior of the Si and C sublattices is similar; however, a slightly higher level of disorder is observed on the C sublattice at low doses, which may be due to the lower threshold displacement energy for C in SiC that is predicted by MD simulations [59–61].

The temperature dependence of the irradiation dose to achieve a relative disorder level of 0.92 for both the Si and C sublattices, as determined from the data shown in Fig. 7.5, is used to reflect the critical dose for amorphization as a function of temperature. The value of 0.92 was chosen because the exponential dependence of the disorder on dose increases the error in defining a dose for complete amorphization as the disorder approaches 1.0. Varying the disorder level from 0.90 to 0.95, the shape of the curve as a function of temperature stays largely unchanged. The temperature-dependence of the critical dose for amorphization in 4H-SiC under 1.1 MeV Al_2^{2+} irradiation is shown in Fig. 7.6, which clearly shows the increase in dose with irradiation temperature. The significant increase at 450 K indicates that this temperature is just below the critical temperature for amorphization in 4H-SiC under the Al irradiation conditions. At 450 K, the dynamic damage recovery processes (e.g., recombination of interstitials and vacancies) nearly balance the irradiation-induced damage production processes, which lead to a slower rate of damage accumulation [62]. As a result, a much higher dose is needed to achieve an equivalent level of damage. As the irradiation temperature approaches the critical temperature for amorphization, cluster formation has a major influence on disorder accumulation, and ion flux plays an important role in dislocation loop formation.

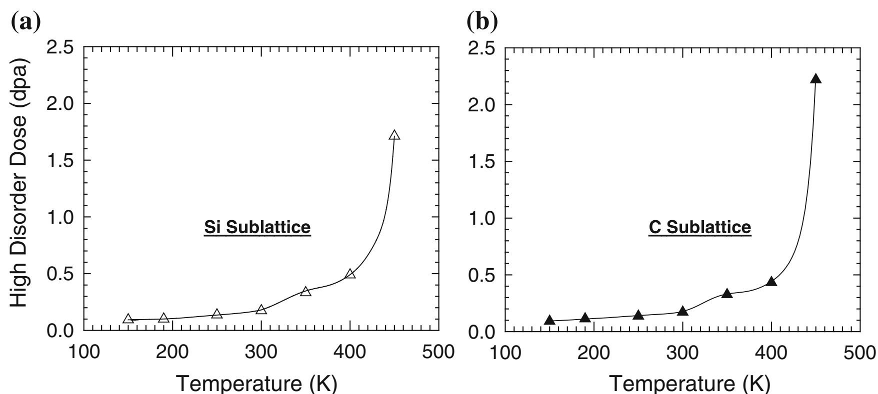

Fig. 7.6 Temperature dependence of dose to achieve a relative disorder level of 0.92 in 4H-SiC under 1.1 MeV Al_2^{2+} irradiation [53]

Dislocation loops, which are formed under high ion flux irradiations, act as sinks for point defects that reduce the disorder accumulation rate.

In situ transmission electron microscopy (TEM) has been extensively used to investigate the temperature dependence of amorphization in single crystal and polycrystalline ceramics for nearly 25 years [63, 64]. In this method, a transmission electron microscope is coupled to an ion accelerator, and the ion beam passes through the electron-transparent specimens. The dependence of the critical amorphization dose on temperature, as measured by in situ TEM, is shown in Fig. 7.7 for several $ATiO_3$ perovskite-type structures (A = Sr, Ca and Ba) irradiated with 800 keV Kr ions [65]. Under these irradiation conditions, the critical temperature for amorphization changes with the A site cation. Such compositional dependence of the critical temperature for amorphization is commonly observed in complex oxide ceramics. With the in situ TEM technique, it is also possible to vary the ion species to increase or decrease the ion mass, which can affect the recoil spectra along the ion path, thereby changing the local displacement density per ion, as well

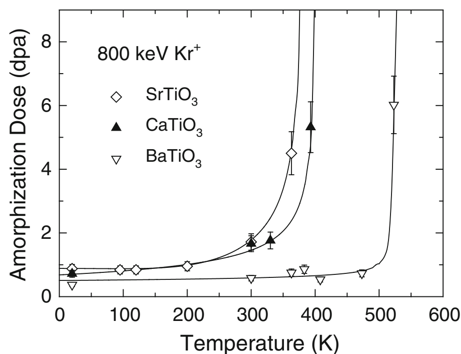

Fig. 7.7 Dependence of critical amorphization dose on temperature for several titanate perovskite structures (adapted from [65])

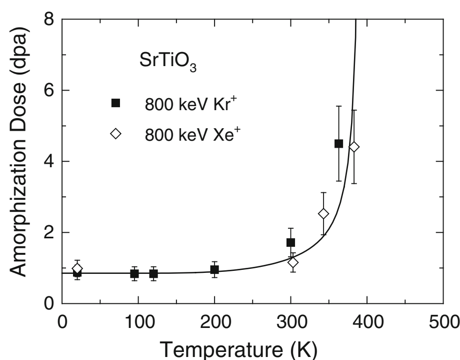

Fig. 7.8 Dependence of critical amorphization dose on temperature for $SrTiO_3$ irradiated with 800 keV Kr or 800 keV Xe ions (adapted from [65])

as the local electronic energy loss. In the case of $SrTiO_3$ irradiated with either 800 keV Kr or 800 keV Xe ions, as shown in Fig. 7.8, a higher dose for amorphization may be suggested for Kr than for Xe at room temperature and higher; however, the temperature dependence of amorphization, within experimental error, is independent of the ion mass used. While the in situ TEM technique is very convenient, the use of high-energy ions to pass through the specimens can result in significant electronic energy loss that may affect the kinetics of amorphization, as discussed further in the next section.

7.3.5 Effect of Electronic Energy Loss on Amorphization

In situ TEM is a very powerful technique to monitor damage accumulation and amorphization processes during irradiation. Many of these studies are carried out using a single ion species at intermediate energies, such as Kr ions, that produce a relatively flat damage profile and pass completely through the TEM specimen. Under such irradiation conditions, the ion species and energy are often invariant in many studies, and while the ratio of electronic to nuclear energy loss can be quite high, any effect of the high electronic energy loss may be overlooked. Surprisingly, there have been only a few studies in which different ions and energies have been used to vary the ratio of energy loss to electrons and atomic nuclei.

One example of these studies is shown in Fig. 7.8, where the temperature dependence of amorphization in $SrTiO_3$ is relatively insensitive to the change in the ratio of electronic to nuclear energy loss, estimated at $\sim$30 nm below the surface using the SRIM code, in going from 800 keV Kr ions ($\sim$0.6) to 800 keV Xe ions (0.3). Another material that exhibits similar insensitivity to the ratio of electronic to nuclear energy loss is $Gd_2Ti_2O_7$ [7]. However, other in situ TEM studies have demonstrated that the dynamic irradiation response of some materials is sensitive to variations in the ratio of electronic to nuclear energy loss [23]. These include SiC [24], $Ca_2La_8(SiO_4)_6O_2$ [24, 66], and Gd_2ZrTiO_7 [7]. In these cases, it is commonly observed that the increase in dose for complete amorphization with temperature is

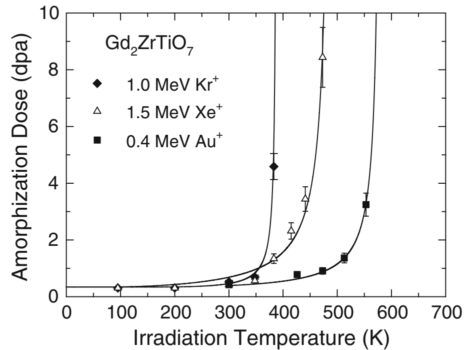

Fig. 7.9 Critical dose for amorphization in Gd_2ZrTiO_7 as a function of temperature and ion species [23]

dependent of the ratio of electronic to nuclear stopping, which enhances dynamic recovery processes at elevated temperatures. Figure 7.9 illustrates that, for the case of Gd_2ZrTiO_7 with the pyrochlore structure, there is an increase in the dose for amorphization and a significant decrease in the critical temperature with decreasing ion mass, which has been attributed to the increasing ratio of electronic to nuclear energy loss. This behavior is in marked contrast to that shown in Fig. 7.8 for $SrTiO_3$ or reported for $Gd_2Ti_2O_7$ pyrochlore [7], which suggests that this sensitivity to electronic energy loss is very dependent on composition.

7.4 Ionization-Induced Annealing and Ionization-Enhanced Amorphization

7.4.1 Ionization-Induced Annealing: Single Beam Experiments

A long-standing objective in materials research is to find innovative ways to remove pre-existing damage and heal fabrication-induced defects or environmentally-induced defects in materials. Ion beams provide several approaches to induce annealing processes. Epitaxial crystallization of damaged or amorphous layers can be induced by irradiation at elevated temperatures using low-energy ions in the nuclear dominated regime. This epitaxial crystallization process, referred to as ion-induced epitaxial crystallization (IBIEC), is driven by the diffusion of point defects created by elastic collision processes. The advantage of this technique is that it generally occurs at temperatures that are lower than those necessary for crystallization by thermally-activated solid phase epitaxy [67], although elevated temperatures are still required. For example, IBIEC of an amorphous $SrTiO_3$ layer, 110 nm thick, on single crystal $SrTiO_3$ can be readily induced by irradiation with Ne^+ or Ar^+ ions with energies from 200 keV to 2 MeV at 473 K [68]. The crystallization rate increased with ion mass and energy, and the quality of the layers

recrystallized by IBIEC at 473 K were comparable to those thermally recrystallized by solid phase epitaxy at 623 K.

At high energies where electronic energy loss is dominant, swift heavy ion induced epitaxial crystallization (SHIBIEC) at room temperature has been observed for damaged and amorphous layers in 6H-SiC [20] and 3C-SiC [21, 69], using 827 MeV Pb^+ ions and 870 MeV Pb^+ ions, respectively. Molecular dynamics simulations, based on the thermal spike model, have been successfully used to model the crystallization process for both a fully amorphous layer and a partially disordered layer in 3C-SiC due to 870 MeV Pb^+ ions [21, 69, 70]. The high electronic energy loss (33 keV/nm) from the 870 MeV Pb ions is largely transferred to the atomic structure via electron-phonon coupling, which results in a local thermal spike that can exceed the melting temperature for several picoseconds (see Chap. 2). This thermal spike results in incremental epitaxial crystallization from neighboring crystalline regions. At high ion fluences, complete recrystallization of partially disordered layers in 6H-SiC are observed experimentally [20].

The ionization-induced crystallization observed at high energies for the SHIBIEC process has also been observed at much lower intermediate energies in SiC and some oxide ceramics. In 4H-SiC, ionization-induced annealing of pre-existing damage has been recently observed at room temperature using 21 MeV Si^+ or Ni^+ ions, with a relatively low electronic energy loss of 5 or 8 keV/nm, respectively [26]. This is clearly demonstrated in the ion channeling spectra along the <0001> direction of the pre-damaged samples before and after 21 MeV Ni irradiation, as shown in Fig. 7.10. In these ion-channeling measurements, 3.5 MeV He with a scattering angle of 155° was chosen, so that the interaction between He ions and the C atoms is above the Coulomb barrier and non-Rutherford backscattering spectrometry (NRBS) analysis with much higher scattering cross section becomes possible. As a consequence, the backscattering yield from C atoms is significantly enhanced. This combination of RBS and NRBS analysis enables

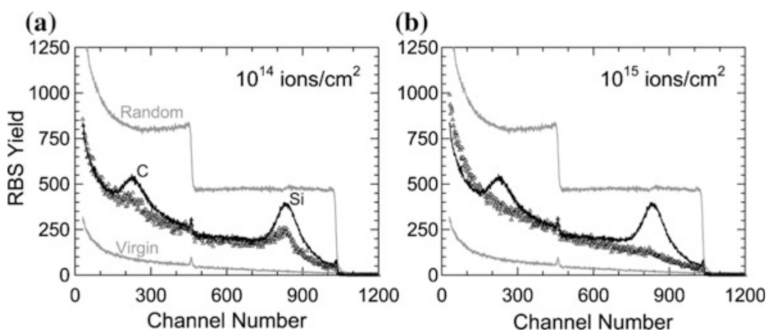

Fig. 7.10 RBS spectra along the <0001> direction in SiC for the pre-damaged sample (*solid black line*) and after ion annealing (*triangles*) with 21 MeV Ni ions at room temperature to ion fluences of **a** 10^{14} and **b** 10^{15} ions/cm^2. The virgin (defect free) and random spectra (*solid gray lines*) are included. The initial damage state and Ni-induced recovery on both Si and C sublattices are evident by the RBS yield changes around channel 220 and 830 for the C and Si damage peak region, respectively

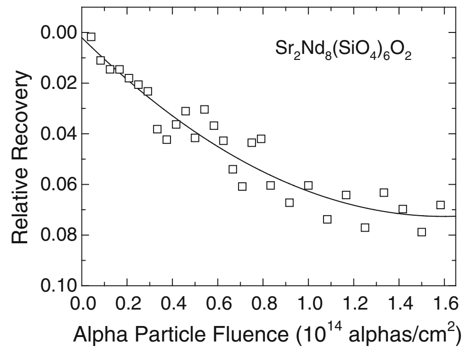

Fig. 7.11 Relative recovery in the thickness of a buried amorphous layer in $Sr_2Nd_8(SiO_4)_6O_2$ under irradiation with 2.0 MeV alpha particles at 300 K [66]

quantification of the disorder on both the Si and C sublattices from a single channeling backscattering measurement. As observed in Fig. 7.10, nearly full recovery of the buried damage layer occurs following irradiation to 10^{15} ions/cm^2. This ion annealing process in SiC may have implications for annealing ion-implantation defects or defects from thin film processing in SiC-based devices.

Ionization-induced epitaxial crystallization of an amorphous layer in fluorapatite, $Ca_{10}(PO_4)_6F_2$, occurs at room temperature using 0.3–3.2 MeV alpha particles, and the recovery rate per ion increased with increasing electronic energy loss, i.e. increasing ion energy [71]. Similar epitaxial crystallization of a buried amorphous layer has been observed in a silicate apatite, $Sr_2Nd_8(SiO_4)_6O_2$, when irradiated with 2 MeV alpha particles at room temperature [66], as shown in Fig. 7.11, which is consistent with the observed sensitivity of silicate apatite compositions to ionization-induced annealing [24, 66]. In both these studies on apatite structures, the electronic energy loss of the alpha particles is less than 0.5 keV/nm, which is unusually low for such a dramatic effect. It is unclear whether the epitaxial crystallization induced by the alpha particles in these two studies is due to a thermal spike or enhanced defect mobility due to localized excitations or charged defects. This ionization-induced annealing from alpha particles has potential implications for reducing the accumulation of radiation damage in nuclear waste forms.

7.4.2 Ion-Induced Annealing: Dual Beam Irradiations

Dual and triple beam irradiation capabilities were initially developed in the 1970s for investigating the response of materials to fusion radiation environments, where the 14 MeV fusion neutron spectra would produce energetic PKAs, as well as hydrogen and helium from nuclear reactions [72]. In these studies, irradiations were carried out using a metal self-ion beam, along with simultaneous implantation of hydrogen and helium. While such studies continue today in the development of radiation tolerant materials for nuclear environments, the use of dual ion beams also

has advantages in maintaining stoichiometry in ceramics by co-implantation of metal and oxygen (or carbon/nitrogen) ions.

Recently, irradiation studies have been conducted using dual ion beams simultaneously, where one ion (700 keV I^+) is in the high nuclear dominant energy loss regime, and the other ion (36 MeV W^+) is in the high electronic energy loss regime, in order to investigate the dynamics between nuclear and electronic energy loss processes [25, 73]. Single beam irradiations, sequential beam irradiations, and simultaneous beam irradiations have been conducted to quantify the separate and combined effects of the dual beams. In yttria-stabilized zirconia (YSZ), the disorder produced under simultaneous dual beam irradiation is simply an additive sum of the disorder produced by the separate ions, which is consistent with recent observations on irradiation-induced grain growth [22]. In $Gd_2Ti_2O_7$, the combined effect of simultaneous dual beam irradiation is unclear, since this material is very sensitive to both nuclear and electronic damage processes. In the case of SiC and MgO, simultaneous dual beam irradiation decreases the disordering rate below that induced by only I^+ ions.

7.4.3 Ionization-Enhanced Amorphization

Ionization-induced annealing or ionization-enhanced amorphization is strongly material dependent. Such ionization-enhanced effects have been reported for semiconductors and ceramics, as in the case of InP, GaAs, Si_3N_4, SiC and $SrTiO_3$ [25, 27, 74–76], and some examples are discussed in Chaps. 8 and 9.

To highlight the magnitude of such effects, a colossal synergistic effect observed in $SrTiO_3$ is described here. In a separate effects study to quantify the interaction of ionization energy loss with pre-existing atomic defects created by low-energy ions [77], single crystals of $SrTiO_3$ have been pre-damaged with 900 keV Au ions at 7° off the ⟨100⟩ direction at 300 K to produce a range of damage states from elastic energy loss. As shown in Fig. 7.12a, a fractional disorder of ~ 0.29 at the damage peak region has been produced as the pre-damage state. Both undamaged and the pre-damaged single crystals have been subsequently irradiated to different ion fluences with 21 MeV Ni ions, which have a high electron energy loss of 9.5–10 keV/nm and a very low nuclear energy loss of 0.09 keV/nm across the pre-damaged thickness. The RBS results in Fig. 7.12a show that the electronic energy deposition from 21 MeV Ni ions leads to rapid amorphization due to the formation of nanometer-sized amorphous tracks only in the narrow region where pre-existing defects exist; whereas tracks are not produced under similar irradiation conditions in the absence of pre-existing defects. Large scale molecular dynamics (MD) simulations (7 million atoms) of ion track formation in $SrTiO_3$, as illustrated in Fig. 7.12b, have been performed using a simulation cell with and without any defects [77]. Scanning transmission electron microscopy (STEM) with high angle annular dark field (HAADF) imaging has also been used to characterize the irradiated samples (with a pre-damage level of ~ 0.07), and a circular ion track with an

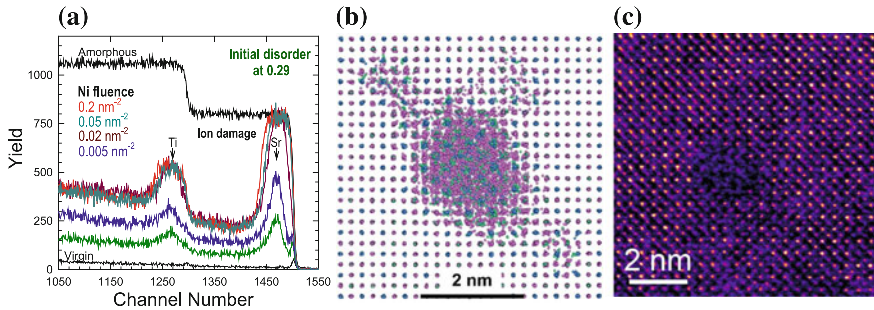

Fig. 7.12 **a** RBS/C spectra along [100] direction of a pre-damaged $SrTiO_3$ irradiated with 21 MeV Ni ions. The pre-damaged sample has a relative disorder level of 0.29 and the fluence of the Ni ion irradiation ranges from 0.005 to 0.2 ions/nm^2. **b** MD simulation of 21 MeV Ni ion track formed in $SrTiO_3$ using a simulation cell containing 1 % Frenkel pairs. **c** A scanning transmission electron microscopy (STEM) image. The high angular annular dark field image of ion track in pre-damaged $SrTiO_3$ (a relative disorder level of 0.07) is taken with 200 keV electrons showing an amorphous core of ion track produced by irradiation with 21 MeV Ni ions to a fluence of 0.02 ions/nm^2 [77]

amorphous core of ~2 nm is clearly visible in Fig. 7.12c [77]. Track size, structure, and interfacial strain from the MD simulations can be directly compared to the STEM image, as illustrated in Fig. 7.12. This synergistic effect significantly decreases the electronic energy loss threshold for amorphous track formation to much lower values (below 10 keV/nm) than previously suggested by swift heavy ion irradiations with electronic energy loss values from 20 to 50 keV/nm (92 MeV Xe to 2.0 GeV U ions) [78, 79]. Due to differences in thermal stabilities of the defects and the amorphous tracks, thermal annealing may lead to isolated amorphous tracks or pillars embedded in a highly crystalline matrix.

Such observation necessitates the reinterpretation of data on irradiation induced amorphization in $SrTiO_3$ and other materials at intermediate energies. Since amorphous tracks can be produced using intermediate energy ions, which are widely available in research and industry, this effect of ionization-enhanced amorphization provides a new pathway for the exploitation of such tracks in $SrTiO_3$ substrates and thin films.

7.5 Structural Modifications in Nanostructured Ceramic Matrices

Due to the remarkable variations in electrical, optical and magnetic properties, nanoscale science and engineering have attracted increasing academic and industrial interest. Nanostructured materials with building blocks in the 1–100 nm size are one of the new classes of materials that have attracted increasing attention over the past two decades [80–86]. The properties of materials can be engineered as

systems of confined low dimensionality, such as embedded nanoparticles (metallic, semiconducting or dielectric) in a crystalline or amorphous matrix, nanocrytalline materials, and nanolayered materials based on multi-component layers or single component materials with intrinsic nanolayers (for example, stacking faults or twins with nanoscale separation). The ability of altering the physical, electronic, optical and magnetic properties by merely changing the size of the embedded nanoparticles makes them very flexible for tailoring the properties or functionality of nanocomposites to a broad range of applications. Nanocrystalline oxides, with nanoscale grain sizes compared to their microcrystalline counterparts, are of great interest due to the stability of metastable or high-temperature phases on the nanoscale, the high density of grain boundaries, exceptional size-dependent properties and technological implications. Nanostructured materials have attracted interest for a wide range of applications, including novel catalytic, sensor, membrane, structural, electric, magnetic, and biomaterial applications. While more research and applications of energetic ions are discussed in other chapters, here we discuss irradiation effects in nanostructured ceramics with a high ratio of grain boundaries or planar interfaces.

7.5.1 Intrinsically Nanolayered Structures

Engineered 3C-SiC with a high-density of stacking faults (SFs) is representative of nanostructured ceramic matrices with a high concentration of planar interfaces. SiC, as one of the most investigated wide-band gap semiconductors, is a key functional material in high-power, high-frequency, and high-temperature electronic and space applications. SiC materials and composites are also being considered as key engineering materials in nuclear applications for operations in extreme environments. As the world increases its reliance on energy, there is an ever-increasing demand for high performance materials. SiC can be fabricated in bulk or thin film forms with high densities of SFs. In the case of thin films, there are potential applications in sensors and nanomechanical devices, where ion irradiation can be used to modify properties or functionalize the films.

For nanostructured materials with a high density of grain boundaries (GBs), interfaces and SFs, high self-healing power is expected due to enhanced interstitial and vacancy annihilation at these defect sinks. Interfaces generally considered to contribute to radiation resistance are GBs and interfaces between dissimilar phases; however, the contribution of stacking faults (SFs) to radiation resistance has recently been demonstrated. While single crystal SiC readily undergoes an irradiation-induced crystalline to amorphous transformation at room temperature, a nano-engineered SiC with a high-density of SFs exhibits significantly enhanced resistance to amorphization [58, 87, 88]. The structural evolution of a nanosize grain under electron irradiation is shown in Fig. 7.13 as an example [88]. The high density of SFs are observed as (111) planar defects. There are four equivalent {111} planes in 3C-SiC. While most of the SFs are (111) planar defects, other equivalent planar defects along the $(1\bar{1}1)$ and $(\bar{1}11)$ are also visible in the images and are

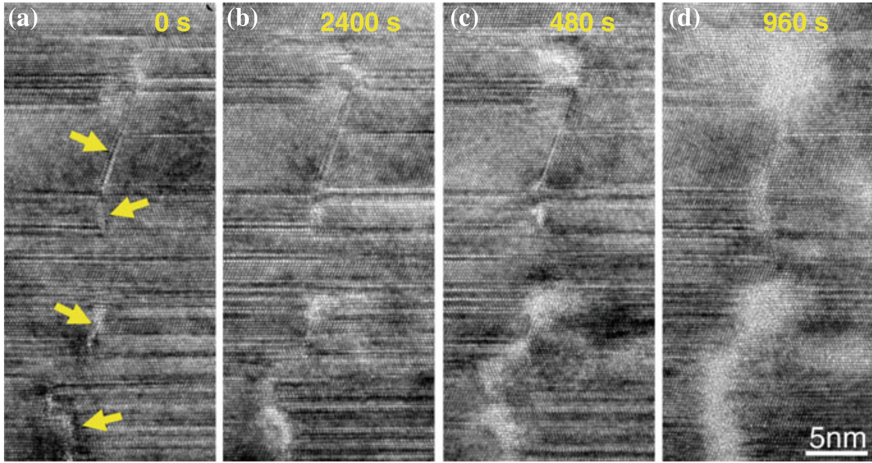

Fig. 7.13 Structural evolution of a nano-engineered 3C-SiC under irradiation at 300 K with 300 keV electrons at a flux of 2.2×10^{20} e cm^{-2} s^{-1} [88]

marked with arrows. Under electron beam irradiation, the small planar defects along the $(1\bar{1}1)$ and $(\bar{1}11)$ directions are amorphized first, and the amorphous regions extend along the planar defect with increasing electron fluence. This suggests that radiation-induced point defects are preferentially trapped at the grain boundaries, and damage accumulates at the planar defects existing on different planes. Complete amorphization occurs at the $(1\bar{1}1)$ and $(\bar{1}11)$ planar defects, while the crystallinity is maintained at the (111) SFs.

Based on DFT calculations, the presence of SFs makes interstitial defects more mobile parallel to the SFs and decreases the binding energy of interstitial-antisite defects [87], both of which suppress or delay defect accumulation. In addition, Si interstitial annihilation at grain boundaries and Si antisite removal are enhanced due to the presence of SFs in the nano-engineered 3C-SiC. Stacking fault enhanced defect recombination and annihilation are proposed to account for the extraordinary self-healing behavior of the nano-engineered SiC. The SFs, as self-layered interfaces, effectively modify dissipation of energy, defect survivability and migration pathways of interstitials. As added energy barriers, the SFs prevent large separation of interstitials and vacancies, and confine diffusion to 2-dimensional (2D) interlayers. With the normal 3-dimensional random diffusion process becoming a 2D-like interlayer diffusion between SFs, the possibility of interstitials finding nearby vacancies in a less dispersed defect region is significantly increased. As a result, significantly enhanced recombination of interstitials and vacancies will lead to suppressed accumulation of irradiation-induced defects and more than an order of magnitude improvement of radiation resistance. Microstructural observations also reveal that the nano-layered SF structure in the nano-engineered SiC is highly radiation tolerant and stable under irradiation to a dose of 30 dpa at 973 K.

As long as the high density of SFs is retained, the enhanced self-healing behavior observed should remain active.

It is known that in nanocrystalline materials, properties can be engineered as systems of confined low dimensionality, with unique interfaces and grain boundaries, as demonstrated by many studies over the past 20 years [80–87]. The work on nano-engineered SiC clearly demonstrates that, in addition to interfaces and grain boundaries, a high density of SFs may be highly effective for promoting efficient point defect recombination. Understanding the response of nanostructured materials to irradiation effects may hold the key to unlock the design of new materials for advanced nuclear energy systems. The significant self-healing promoted by the engineered stacking faults may have significant implication to the design, discovery and development of novel materials that may not be limited to SiC.

7.5.2 Nanocrystalline Materials

Nanocrystalline materials, while often resistant to the formation of dislocations, are inherently prone to grain growth. Grain growth of nanocrystalline materials is generally thermally activated, but can also be driven by irradiation at much lower temperatures. Understanding and controlling stoichiometry and grain size through thermal and irradiation processes are essential to tailoring the properties of nanocrystalline materials. Energetic ions can be used to effectively tailor the grain size and properties of nanocrystalline ceramics.

In nanocrystalline 3C-SiC with average grain sizes from 2.0 to 3.8 nm, the dose for full amorphization under irradiation at 300, 400 and 500 K is reduced relative to the amorphization dose for single crystal 3C-SiC under the same irradiation conditions [89, 90]. The amorphization dose in nanocrystalline 3C-SiC irradiated at 400 and 500 K increases with temperature, but at each temperature, the dose for amorphization decreases with decreasing grain size. It is worth noting that, in these studies, the grain boundaries are amorphous in nature. In other words, the nanocrystalline 3C-SiC samples may be better described as nanometer size crystalline particles embedded in an amorphous SiC matrix. This amorphization behavior in nanocrystalline SiC is attributed to an irradiation-induced interface-driven amorphization process at the amorphous grain boundaries. The large fraction of amorphous grain boundary material in the nanocrystalline material eliminates the nucleation stage required for amorphization in SiC. In addition, the fraction of initial crystalline phase available for amorphization decreases with decreasing grain size, which accounts for the significant decrease in the dose for amorphization with decreasing grain size. In contrast, above the critical temperature for amorphization, irradiation of nanocrystalline 3C-SiC at 550 K leads to irradiation-induced epitaxial crystallization of the amorphous grain boundary network, and the average grain size tends to saturate at about 15 nm at high fluences [90].

A substantial enhancement in radiation-induced amorphization resistance has been reported in single-phased nanocrystalline $MgGa_2O_4$, with grain sizes ranging

from 4 to 12 nm, versus large-grained polycrystalline ceramic, with an average grain size of 10 μm [91]. This resistance demonstrates that the large fraction of interfacial regions plays an important role as sinks for point defects and their clusters produced under irradiation.

Energetic ion irradiation has been shown to be effective in tailoring the grain size in nanocrystalline ceria and zirconia, from a few nm up to several tens of nm, which is the critical region for controlling size-dependent material properties. Irradiation-induced grain growth in nanocrystalline ceria [22, 92, 93] and nanocrystalline cubic (stabilizer-free) zirconia [94, 95] has been studied using nanocrystalline thin films (a few hundreds of nanometers in thickness) grown on Si wafers. The grain growth in ceria results in an increase in symmetric grain boundaries [93]. In the nanocrystalline zirconia, the cubic structure is stable at high irradiation doses (>30 dpa); however, faster grain growth is observed at 160 K, as compared to 400 K [22], which is speculated to be due to stable localized electronic excitations or charged defects that enhance mobility.

To evaluate the grain growth mechanisms, irradiation-induced growth is plotted as a function of displacement damage (average ion dose in the film in dpa), as shown in Fig. 7.14. As Au ions are more efficient in producing displacement damage, one would expect faster grain growth under Au irradiation. The more rapid and larger grain growth under the Si irradiation versus the Au case is somewhat surprising. Moreover, in the case of ZrO_2, different grain growth under Au irradiation (3 vs. 12 MeV) also suggests that cascade damages resulting from nuclear energy deposition cannot be the only contributing factor for the grain growth, electronic energy deposition should also play an important role in grain growth.

In both nanocrystalline ceria and zirconia films, recent experimental results [22] have demonstrated that irradiation-induced grain growth is dependent on the total energy deposited, where an additive effect from both electronic energy loss (inelastic thermal spike) and atomic collision cascades (elastic thermal spike)

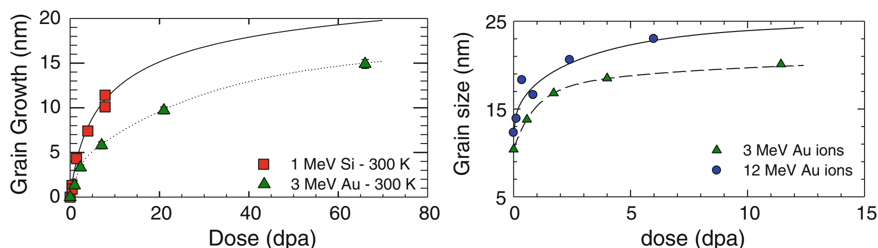

Fig. 7.14 Grain growth of nanocrystalline CeO_2 and ZrO_2 films: (*left*) average growth of the grain in the CeO_2 films under Si and Au irradiation at room temperature, and (*right*) average grain size in the ZrO_2 films under 3 and 12 MeV Au irradiation at room temperature. The grain growth is determined using grazing-incidence X-ray diffraction, representing an average size increase of the coherently diffracting crystallites. The experimental uncertainty is equivalent to the size of the symbols. The results clearly show that grain growth is not solely dependent on displacement damage

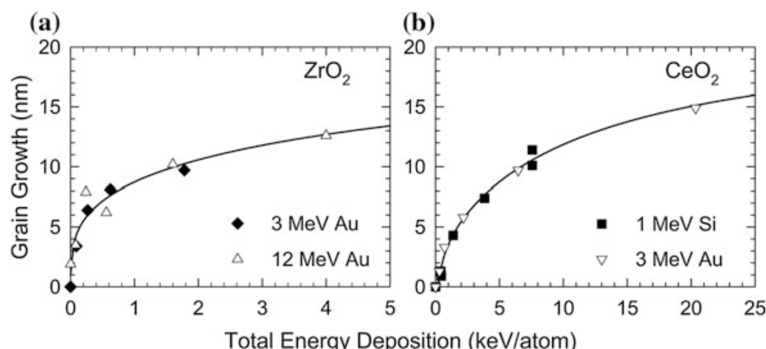

Fig. 7.15 Irradiation-induced grain growth as a function of total energy deposition [22]: **a** nanocrystalline ZrO_2 films under 3 and 12 MeV Au irradiation; **b** nanocrystalline CeO_2 films under 1 MeV Si and 3 MeV Au irradiation

contribute to the production of disorder and grain growth, as shown in Fig. 7.15. By varying the amount of energy deposition into the electronic and atomic structures, an additive effect from both displacement and ionization is observed, where irradiation-induced grain growth is a function of total energy deposited, as shown in Fig. 7.15. The experimental results have shown that both high electronic energy loss and nuclear energy loss lead to additional disorder. Molecular dynamics (MD) simulations indicate that a high density of disorder near the grain boundaries leads to rapid local grain motion [96]. This disorder-driven mechanism leads to much faster grain growth kinetics, as compared to processes based on curvature-driven or grain-rotation mechanisms. This is illustrated in Fig. 7.16, where irradiation is simulated by the introduction of a large amount of local disorder, and grain movement is complete after 40 ps. As the grain size increases, the introduction of irradiation-induced disorder from single ion events becomes less likely to interact with the grain boundaries, leading to the eventual saturation of the grain size, as illustrated experimentally in Fig. 7.15.

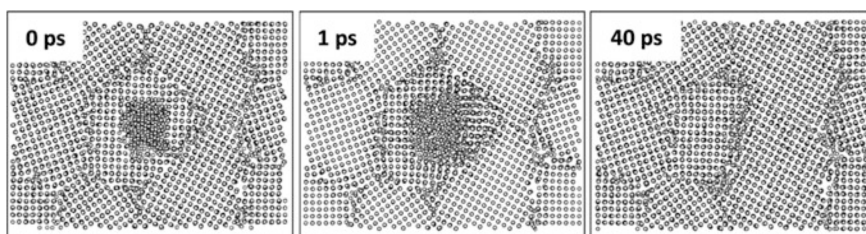

Fig. 7.16 Molecular dynamics simulation of disorder-driven grain growth in nanocrystalline CeO_2 with an initial grain size of 4.5 nm (only Ce atoms shown). Disorder introduced in the central grain at time 0. After 1 ps, the disorder and atomic motion have spread to an adjacent grain boundary, which moves inward after 40 ps. This MD simulation was performed at T = 2500 K to enhance the kinetics for observable grain growth on MD time scales

While materials containing high concentrations of nanoscale interfaces and second-phase features may offer high resistance to radiation damage accumulation, they are not inherently resistant to radiation damage, and irradiation-enhanced amorphization in nanocrystalline solids is strongly materials dependent. Defect absorption alters interface structures, interfaces can become saturated with defects, and damaged interfaces can act as sources of defects instead of defect sinks. Radiation can also atomically mix interfaces and layers or destroy the geometrical arrangement of layered morphologies, because the flow of radiation-induced point defects into an interface changes its atomic configuration. Interface degradation may ultimately determine material response under irradiation. It has been shown that small ZrO_2 crystallites, with an average particle size less than ~ 3 nm embedded in a nanostructured ZrO_2/SiO_2 composite, amorphize at a low ion irradiation dose (0.9 dpa); whereas much larger ZrO_2 crystallites do not amorphize following very high ion exposures (680 dpa) [97–99]. A model [100] suggests that the competition between irradiation-induced formation of point defects and the absorption of point defects by grain boundaries defines the radiation resistance of nanocrystalline materials.

Although nanotechnology is now well-known, it is just emerging from fundamental research to industrial applications. Despite being in an exploration stage, further research in nanotechnology promises breakthroughs. The ability to control interface volume in thin films by ion irradiation may open new pathways to unique manufacturing, nanostructures and properties, as well as contribute to research areas for new clean energy sources, sensors, and high energy density batteries. In addition, there is considerable interest within the nuclear field on the role of nanostructures on improving radiation tolerance, and some pioneering work [22, 96] provides results on the irradiation stability of nanostructured inert matrix fuels. The observation of ionization effects and the unraveling of fast disorder-driven grain growth mechanisms may present new possibilities to better control grain sizes and tailor the functionality of nanocrystalline materials.

7.6 Summary

In this chapter, ion-irradiation-induced defect accumulation, amorphization and modification of nanostructures in crystalline ceramics have been reviewed. While many processes are primarily due to the displacement of atoms resulting from the elastic collision cascade initiated through nuclear energy loss by incident ions, it has also been demonstrated that the electronic energy loss by incident ions can contribute additively to damage production from nuclear energy loss, or it may lead to competive recovery of displacement damage. These processes occur in single crystals, polycrystalline ceramics, and nanostructures. Understanding the coupling

of electronic and nuclear energy loss processes in ceramics can lead to the development of radiation tolerant materials, improved predictive models on the response of ceramics to ion beams and extreme radiation environments, and new approaches to functionalizing ceramic films and structures.

Acknowledgements The authors gratefully acknowledge the support of the U.S. Department of Energy, Office of Science, Basic Energy Sciences, Materials Science and Engineering Division during the preparation of this chapter.

References

1. J.F. Ziegler, J.P. Biersack, U. Littmark, *The Stopping and Range of Ions in Solids* (Pergamon, New York, 1985), http://www.srim.org/
2. K. Jin, Y. Zhang, Z. Zhu, D.A. Grove, H. Xue, J. Xue, W.J. Weber, J. Appl. Phys. **115**(4), 044903 (2014)
3. K. Jin, Y. Zhang, H. Xue, Z. Zhu, W.J. Weber, Nucl. Instrum. Methods Phys. Res. B **307**, 65–70 (2013)
4. Y. Zhang, I.-T. Bae, K. Sun, C. Wang, M. Ishimaru, Z. Zhu, W. Jiang, W.J. Weber, J. Appl. Phys. **105**(104901), 1–12 (2009)
5. Y. Zhang, M. Ishimaru, J. Jagielski, W. Zhang, Z. Zhu, L.V. Saraf, W. Jiang, L. Thome, W.J. Weber, J. Phys. D: Appl. Phys. **43**, 085303 (2010)
6. P. Sigmund, Eur. Phys. J. D **47**, 45 (2008)
7. R.C. Ewing, W.J. Weber, J. Lian, J. Appl. Phys. **95**, 5049 (2004)
8. W.J. Weber, R.C. Ewing, C.R.A. Catlow, T. Diaz, L.W. de la Rubia, C.Kinoshita Hobbs, A.T. Hj Matzke, M.Nastasi Motta, E.K.H. Salje, E.R. Vance, S.J. Zinkle, J. Mater. Res. **13**, 1434 (1998)
9. K.E. Sickafus, L. Minervini, R.W. Grimes, J.A. Valdez, M. Ishimaru, F. Li, K.J. McClellan, T. Hartmann, Science **289**, 748 (2000)
10. Y. Zhang, W.J. Weber, V. Shutthanandan, R. Devanathan, S. Thevuthasan, G. Balakrishnan, D.M. Paul, J. Appl. Phys. **95**, 2866 (2004)
11. Y. Zhang, W.J. Weber, W. Jiang, A. Hallén, G. Possnert, J. Appl. Phys. **91**, 6388 (2002)
12. Y. Zhang, J. Lian, C.M. Wang, W. Jiang, R.C. Ewing, W.J. Weber, Phys. Rev. B **72**, 094112 (2005)
13. I.-T. Bae, Y. Zhang, W.J. Weber, M. Higuchi, L.A. Giannuzzi, Appl. Phys. Lett. **90**, 021912 (2007)
14. H. Inui, H. Mori, T. Sakata, H. Fujita, J. Non-Cryst. Solids **116**, 1 (1990)
15. L.W. Hobbs, M.R. Pascucci, J. Phys. **41**, C6–C237 (1980)
16. W.L. Gong, L.M. Wang, R.C. Ewing, J. Zhang, Phys. Rev. B **54**, 3800 (1996)
17. Y. Zhang, I.-T. Bae, W.J. Weber, Nucl. Instrum. Methods Phys. Res. B **266**, 2828 (2008)
18. R. Devanathan, L.R. Corrales, W.J. Weber, A. Chartier, C. Meis, Mol. Simul. **32**, 1069 (2006)
19. M. Toulemonde, W.J. Weber, G. Li, V. Shutthanandan, P. Kluth, T. Yang, Y. Wang, Y. Zhang, Phys. Rev. B **83**, 054106 (2011)
20. A. Benyagoub, A. Audren, L. Thomé, F. Garrido, Appl. Phys. Lett. **89**, 241914 (2006)
21. A. Debelle, M. Backman, L. Thomé, W.J. Weber, M. Toulemonde, S. Mylonas, A. Boulle, O.H. Pakarinen, N. Juslin, F. Djurabekova, K. Nordlund, F. Garrido, D. Chaussende, Phys. Rev. B **86**, 00102 (2012)
22. Y. Zhang, D.S. Aidhy, T. Varga, S. Moll, P.D. Edmondson, F. Namavar, K. Jin, C.N. Ostrouchov, W.J. Weber, Phys. Chem. Chem. Phys. **16**, 8051 (2014)

23. W.J. Weber, D.M. Duffy, L. Thomé, Y. Zhang, Curr. Opin. Solid State Mater. Sci. **19**(1), 1–11 (2015)
24. W.J. Weber, Y. Zhang, L.M. Wang, Nucl. Instrum. Methods Phys. Res. B **277**, 1 (2012)
25. L. Thomé, A. Debelle, F. Garrido, P. Trocellier, Y. Serruys, G. Velisa, S. Miro, Appl. Phys. Lett. **102**, 141906 (2013)
26. Y. Zhang, T. Varga, M. Ishimaru, P.D. Edmondson, H. Xue, P. Liu, S. Moll, F. Namavar, C. Hardiman, S. Shannon, W.J. Weber, Nucl. Instrum. Methods Phys. Res. B **327**, 33 (2014)
27. Y. Zhang, R. Sachan, O.H. Pakarinen, M.F. Chisholm, P. Liu, H. Xue, W.J. Weber, Nat. Commun. **6**, 8049 (2015). doi:10.1038/ncomms9049
28. W.J. Weber, Radiat. Eff. **83**, 145 (1984)
29. R. Hristu, S.G. Stanciu, D.E. Tranca, A. Matei, G.A. Stanciu, Sci. Rep. **4**, 5258 (2014)
30. T. Shinada et al., Nanotechnology **19**, 345202 (2008)
31. W.F. Koehl, B.B. Buckley, F.J. Heremans, G. Calusine, D.D. Awschalom, Nature **479**, 84–87 (2011)
32. B.E. Fischer, M. Heiss, Nucl. Instrum. Methods Phys. Res. B **260**, 442–444 (2007)
33. A.G. Smart, Phys. Today **65**, 10–11 (2012)
34. S. Castelletto et al., Nat. Mater. **13**, 151–156 (2014)
35. J. Lian, L.M. Wang, K. Sun, R.C. Ewing, Microsc. Res. Tech. **72**, 165–181 (2009)
36. K. Trachenko, J. Phys. Condens. Matter **16**, R1491–R1515 (2004)
37. R. Devanathan, W.J. Weber, J.D. Gale, Energy Environ. Sci. **3**, 1551–1559 (2010)
38. M. Lang, M. Toulemonde, J.M. Zhang, F.X. Zhang, C.L. Tracy, J. Lian, Z.W. Wang, W.J. Weber, D. Severin, M. Bender, C. Trautmann, R.C. Ewing, Nucl. Instrum. Methods Phys. Res. B **336**, 102–115 (2014)
39. B.D. Begg, N.J. Hess, W.J. Weber, R. Devanathan, J.P. Icenhower, S. Thevuthasan, B.P. McGrail, J. Nucl. Mater. **288**, 208 (2001)
40. W.J. Weber, J.W. Wald, H.J. Matzke, J. Nucl. Mater. **138**, 196 (1986)
41. S.X. Wang, L.M. Wang, R.C. Ewing, G.S. Was, G.R. Lumpkin, Nucl. Instrum. Methods Phys. Res. B **148**, 704–709 (1999)
42. W.J. Weber, J.W. Wald, H.J. Matzke, Mater. Lett. **3**, 173–180 (1985)
43. G. Sattonnay, S. Moll, L. Thomé, C. Legros, A. Calvo, M. Herbst-Ghysel, C. Decorse, I. Monnet, Nucl. Instrum. Methods Phys. Res. B **272**, 261–265 (2012)
44. S. Moll, G. Sattonnay, L. Thomé, J. Jagielski, C. Decorse, P. Simon, I. Monnet, W.J. Weber, Phys. Rev. B **84**, 064115 (2011)
45. Y. Zhang, J. Jagielski, I.-T. Bae, X. Xiang, L. Thomé, G. Balakrishnan, D.M. Paul, W.J. Weber, Nucl. Instrum. Methods Phys. Res. B **268**, 3009 (2010)
46. J. Lian, J. Chen, L.M. Wang, R.C. Ewing, J.M. Farmer, L.A. Boatner, K.B. Helean, Phys. Rev. B **68**, 134107 (2003)
47. J. Lian, K.B. Helean, B.J. Kennedy, L.M. Wang, A. Navrotsky, R.C. Ewing, J. Phys. Chem. B **110**, 2343–2350 (2006)
48. Y. Zhang, V. Shutthanandan, R. Devanathan, S. Thevuthasan, D.E. McCready, J. Young, G. Balakrishnan, D.M. Paul, W.J. Weber, Nucl. Instrum. Methods Phys. Res. B **218**, 89 (2004)
49. L.C. Feldman, J.W. Mayer, S.T. Picraux, *Materials Analysis by Ion Channeling* (Academic Press, New York, 1982), p. 117
50. M.L. Swanson, in *Handbook of Modern Ion Beam Materials Analysis*, ed. by J.R. Tesmer, M. Nastasi (Materials Research Society, Pittsburgh, 1995), p. 263
51. J.S. Williams, R.G. Elliman, in *Ion Beams for Materials Analysis*, ed. by J.R. Bird, J.S. Williams (Academic Press, Australia, 1989), p. 286
52. Y. Zhang, C.M. Wang, M.H. Engelhard, W.J. Weber, J. Appl. Phys. **100**, 113533 (2006)
53. Y. Zhang, W.J. Weber, W. Jiang, C.M. Wang, V. Shutthanandan, A. Hallén, J. Appl. Phys. **95**, 4012 (2004)
54. W. Jiang, Y. Zhang, W.J. Weber, Phys. Rev. B **70**, 165208 (2004)
55. W.J. Weber, Nucl. Instrum. Methods Phys. Res. B **166–167**, 98 (2000)
56. F.L. Vook, H.J. Stein, Radiat. Eff. **2**, 23 (1969)

57. W.J. Weber, J. Nucl. Mater. **98**, 206 (1981)
58. Y. Zhang, M. Ishimaru, T. Varga, T. Oda, C. Hardiman, H. Xue, Y. Katoh, S. Shannon, W.J. Weber, Phys. Chem. Chem. Phys. **14**, 13429 (2012)
59. F. Gao, W.J. Weber, Phys. Rev. B **63**, 054101 (2001)
60. R. Devanathan, W.J. Weber, F. Gao, J. Appl. Phys. **90**, 2303 (2001)
61. F. Gao, W.J. Weber, Phys. Rev. B **66**, 024106 (2002)
62. Y. Zhang, W.J. Weber, W. Jiang, C.M. Wang, A. Hallén, G. Possnert, J. Appl. Phys. **93**, 1954 (2002)
63. J.A. Hinks, J.A. van den Berg, S.E. Donnelly, J. Vac. Sci. Technol. **A29**, 021003 (2011)
64. K. Hattar, D.C. Bufford, D.L. Buller, Nucl. Instrum. Methods Phys. Res. B **338**, 56–65 (2014)
65. A. Meldrum, L.A. Boatner, W.J. Weber, R.C. Ewing, J. Nucl. Mater. **300**, 242 (2002)
66. W.J. Weber, Y. Zhang, H.Y. Xiao, L.M. Wang, RSC Adv. **2**, 595 (2012)
67. A. Kinomura, A. Chayahara, Y. Mokuno, N. Tsubouchi, Y. Horino, J. Appl. Phys. **97**, 103538 (2005)
68. K. Oyoshi, S. Hishita, H. Haneda, J. Appl. Phys. **87**, 3450 (2000)
69. A. Debelle, M. Backman, L. Thomé, K. Nordlund, F. Djurabekova, W.J. Weber, I. Monnet, O.H. Pakarinen, F. Garrido, F. Paumier, Nucl. Instrum. Methods Phys. Res. B **326**, 326 (2014)
70. M. Backman, M. Toulemonde, O.H. Pakarinen, N. Juslin, F. Djurabekova, K. Nordlund, A. Debelle, W.J. Weber, Comp. Mater. Sci. **67**, 261 (2013)
71. S. Ouchani, J.-C. Dran, J. Chaumont, Nucl. Instrum. Methods Phys. Res. B **132**, 447 (1997)
72. S.J. Zinkle, A. Möslang, Fusion Eng. Des. **88**, 472 (2013)
73. L. Thomé, G. Velisa, A. Debelle, S. Miro, F. Garrido, P. Trocellier et al., Nucl. Instrum. Methods Phys. Res. B **326**, 219–222 (2014)
74. W. Wesch, O. Herre, P.I. Gaiduk, E. Wendler, S. Klaumünzer, P. Meier, Nucl. Instrum. Methods Phys. Res. B **146**, 341–349 (1998)
75. A. Kamarou, W. Wesch, E. Wendler, S. Klaumünzer, Nucl. Instrum. Methods Phys. Res. B **225**, 329–335 (2004)
76. W. Wesch, A. Kamarou, E. Wendler, K. Gärtner, P.I. Gaiduk, S. Klaumünzer, Nucl. Instrum. Methods Phys. Res. B **206**, 1018–1023 (2003)
77. W.J. Weber, E. Zarkadoula, O.H. Pakarinen, R. Sachan, M.F. Chisholm, P. Liu, H. Xue, K. Jin, Y. Zhang, Sci. Rep. **5**, 7726 (2015)
78. C. Grygiel et al., Rev. Sci. Instrum. **83**, 013902 (2012)
79. W. Li, Nucl. Instrum. Methods Phys. Res. B **302**, 40–47 (2013)
80. R.W. Grimes, R.J.M. Konings, L. Edwards, Nat. Mater. **7**, 683 (2008)
81. A. Misra, M.J. Demkowicz, X. Zhang, R.G. Hoagland, JOM **59**(9), 62 (2007)
82. X.-M. Bai, A.F. Voter, R.G. Hoagland, M. Nastasi, B.P. Uberuaga, Science **327**, 1631 (2010)
83. G. Ackland, Science **327**, 1587 (2010)
84. Y. Chimi, A. Iwase, N. Ishikawa, M. Kobiyama, T. Inami, S. Okuda, J. Nucl. Mater. **297**, 355 (2001)
85. N. Nita, R. Schaeublin, M. Victoria, J. Nucl. Mater. **329–333**, 953 (2004)
86. T.D. Shen, S. Feng, M. Tang, J.A. Valdez, Y.-Q. Wang, K.E. Sickafus, Appl. Phys. Lett. **90**, 263115 (2007)
87. L. Jamison, M.-J. Zheng, S. Shannon, T. Allen, D. Morgan, I. Szlufarska, J. Nucl. Mater. **445**, 181 (2014)
88. M. Ishimaru, Y. Zhang, S. Shannon, W.J. Weber, Appl. Phys. Lett. **103**, 033104 (2013)
89. W. Jiang, Y. Zhang, W.J. Weber, J. Mater. Res. **25**, 2341 (2010)
90. W. Jiang, L. Jiao, H. Wang, J. Am. Ceram. Soc. **94**, 4127 (2011)
91. T.D. Shen, S. Feng, M. Tang, J.A. Valdez, Y. Wang, K.E. Sickafus, Appl. Phys. Lett. **90**, 263115 (2007)
92. Y. Zhang, P.D. Edmondson, T. Varga, S. Moll, F. Namavar, C. Lan, W.J. Weber, Phys. Chem. Chem. Phys. **13**, 11946 (2011)

93. P.D. Edmondson, Y. Zhang, S. Moll, T. Varga, F. Namavar, W.J. Weber, Acta Mater. **60**, 5408 (2012)
94. Y. Zhang, W. Jiang, C. Wang, F. Namavar, P.D. Edmondson, Z. Zhu, F. Gao, J. Lian, W.J. Weber, Phys. Rev. B **82**, 184105 (2010)
95. P.D. Edmondson, W.J. Weber, F. Namavar, Y. Zhang, Scripta Mater. **65**, 675 (2011)
96. D.S. Aidhy, Y. Zhang, W.J. Weber, Scripta Mater. **83**, 9–12 (2014)
97. A. Meldrum, L.A. Boatner, R.C. Ewing, Phys. Rev. Lett. **88**, 025503 (2002)
98. A. Meldrum, L.A. Boatner, R.C. Ewing, Nucl. Instrum. Methods in Phys. Res. B **207**, 28–35 (2003)
99. K.E. Sickafus, H. Matzke, T. Hartmann, K. Yasuda, J.A. Valdez, P. Chodak, M. Nastasi, R.A. Verrall, J. Nucl. Mater. **274**, 66 (1999)
100. I.A. Ovid'Ko, A.G. Sheinerman, Appl. Phys. A **81** 1083, (2005)

Part III
Damage Formation and Amorphisation by High Electronic Energy Deposition

Chapter 8
Swift Heavy Ion Irradiation of Crystalline Insulators and Metals

Lionel Thomé

Abstract This chapter presents a review of the structural modifications induced by electronic excitation in crystalline insulators and metals irradiated with swift heavy ions. After some generalities about electronic energy loss in insulators and the presentation of the main experimental techniques used to observe electronic energy loss effects, results on the formation of ion tracks are presented in metals and metallic alloys and in various classes of insulating materials. Structural transformations occurring when tracks overlap at high ion fluences are then discussed in the framework of existing theoretical descriptions.

8.1 Introduction

As it is discussed in Part I of this book, the interaction of swift heavy ions (energy higher than ~ 1 MeV/u) with solid targets mainly leads to electronic excitation and ionization processes (electronic energy loss—S_e) occurring in a cylinder along the ion path. The amount of electronic energy loss varies from a few eV nm^{-1} to a few keV nm^{-1} (maximum value on the order of 50 keV nm^{-1} for very heavy ions moving at a velocity comparable to the Bohr velocity of electrons).

The nature of the modifications induced by swift ions depends on the electrical, thermal and structural properties of the target materials, the mass of the projectile and irradiation parameters such as the target temperature. In most insulators, due to their low electrical conductivity, electronic energy loss results in the creation of cylindrical damaged regions generally referred to as "ion tracks" at low irradiation fluences (generally below $\sim 10^{12}$ cm^{-2}). When the ion fluence is increased, individual tracks overlap and a specific microstructure is formed in the material. Thus, strong electronic excitations may lead to extended disorder creation, swelling, polygonization, phase transformations or amorphization of ion-irradiated solids. Ion

L. Thomé (✉)
Centre de Sciences Nucléaires et de Sciences de la Matière (CSNSM),
Université Paris-Sud, CNRS-IN2P3, 91405 Orsay, France
e-mail: Lionel.Thome@csnsm.in2p3.fr

© Springer International Publishing Switzerland 2016

W. Wesch and E. Wendler (eds.), *Ion Beam Modification of Solids*,
Springer Series in Surface Sciences 61,
DOI 10.1007/978-3-319-33561-2_8

tracks are hardly observed in metals and metallic alloys, due to the fact that the excitation is rapidly screened by mobile free electrons. Nevertheless, intense electronic excitation may be responsible for damage production and phase transformations even in pure metals.

This chapter is organized in the following way. Section 8.2 provides general considerations about electronic energy loss and the creation of tracks. Section 8.3 discusses how electronic energy loss effects may be experimentally evidenced. Results concerning the observation of ion tracks at low fluences in metals and insulators are described and discussed in Sect. 8.4. The structural transformations resulting from the overlapping of individual ion tracks at high fluences are described and discussed in the framework of theoretical descriptions in Sect. 8.5.

8.2 General Considerations About Electronic Energy Loss in Insulators

Figure 8.1 presents Monte Carlo calculations, performed with the widely used SRIM Monte-Carlo code [1], that illustrate the slowing-down of swift heavy ions (1-GeV Xe) penetrating a solid target (zirconia). The figure clearly shows that swift ions present quite straight trajectories with a very few direct encounters with the atoms of the target during the major part of their path (from the sample surface down to ~20 μm). In this depth range, the ion slowing down process is dominated by interactions with the target electrons (S_e). At the end of the ion trajectory, i.e. before having reached the resting position (around 25 μm in the example of Fig. 8.1), nuclear collisions at low energy overwhelm the ion slowing down process (see Part II of this book).

The basic processes that lead to the creation of lattice defects by electronic energy loss are not as well understood as those responsible for the damage created by elastic collisions described in Part II of this book. The high electronic energy deposition due to the passage of swift ions induces the formation of electrostatically unstable cylinders of ionized atoms (latent tracks) and the emission of electrons (see a schematic representation in Fig. 8.2). Different approaches were considered to account for the resulting atomic rearrangements, depending on whether the

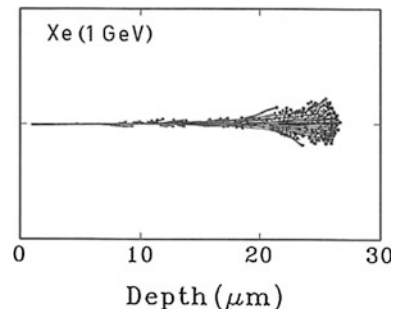

Fig. 8.1 Calculations of the trajectories of 1-GeV Xe ions in a zirconia target with the SRIM code [1]

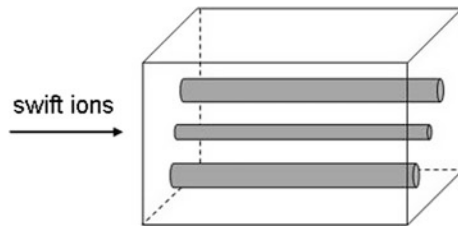

Fig. 8.2 Schematic representation of cylindrical ion tracks formed in solids irradiated with swift ions

attention is focused on the process by which the energy of electrons is dissipated in the lattice or on the response of ionized atoms. The thermal spike models use the former approach [2–5], whereas the Coulomb-explosion models use the latter one [6–8] (see Chap. 2).

Particle tracks were discovered in the late 50s of the last century [9, 10]. The understanding of track formation was then improved by irradiations performed on large-scale accelerators developed in the 80s (GANIL-Caen, UNILAC-Darmstadt, ISL Berlin).

The morphology of ion tracks is known to strongly depend on the value of S_e. Spherical defects generally appear at low S_e, whereas discontinuous or continuous cylinders are formed at high S_e. In a given solid, the track radius was shown to increase with increasing S_e. The structure of the material inside each individual track essentially depends on the energy density deposited by irradiating ions, on the investigated material, and on the temperature at which irradiation is performed.

Figure 8.3 presents the electronic energy loss of swift monoatomic ions and C clusters in CaF_2 as a function of the beam energy [11]. For each ion, there is a clear maximum of S_e (the "Bragg peak") which is obtained at a given energy. It is also worth noting that the electronic energy loss is higher for C clusters than for single elements since S_e for a cluster is approximately equal to the sum of S_e of the constituents. Figure 8.3 shows that a given value of S_e can be reached either below or above the Bragg peak, for example $S_e \sim 3$ keV nm^{-1} both at 0.1 and 10 MeV/u for Ca ions. However, it was demonstrated that, although S_e is the same, there is

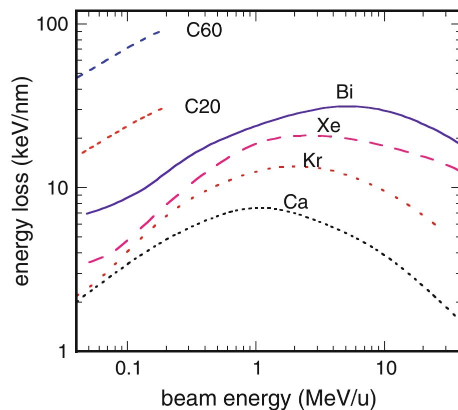

Fig. 8.3 Electronic energy loss (S_e) versus ion energy per nucleon for different monoatomic ions and for C clusters in a CaF_2 target [11]. Calculations were performed with the SRIM code [1]

generally a significant difference in the efficiency to create damage which is due to different deposited energy densities. This important feature (referred to as the "velocity effect") is due to the fact that the target volume in which S_e is deposited depends on the maximum energy transfer to electrons which increases with the beam velocity. This effect has to be considered for the interpretation of the experimental results presented in the following sections.

8.3 Experimental Observation of Electronic Energy Loss Effects

8.3.1 Direct Observation of Ion Tracks

The most powerful experimental technique for the observation of ion tracks in solids undoubtedly is transmission electron microscopy in normal (TEM) or high-resolution (HRTEM) modes. These experiments, initiated in the 80s [12–16], present the great advantage to allow direct measurement of track diameters. An example is provided in Fig. 8.4a which shows a HRTEM image of an ion track formed in Gd_2TiO_5 irradiated with swift heavy ions [17]. The image exhibits three

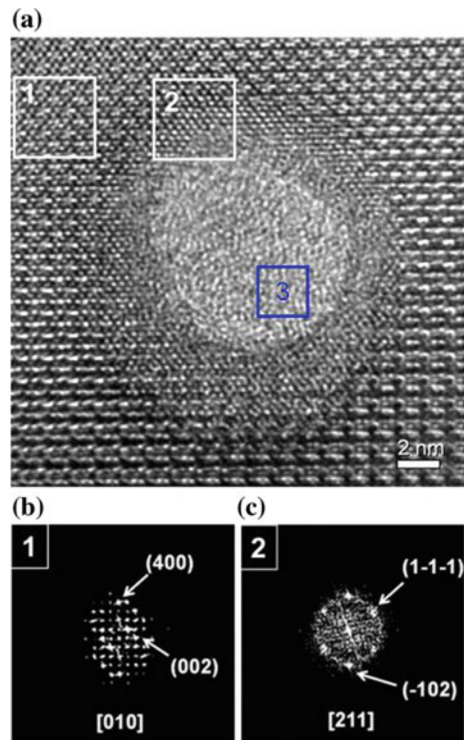

Fig. 8.4 **a** HRTEM image of the track structure in Gd_2TiO_5 irradiated with 2.2-GeV Au ions; **b** FFT analysis of the structure outside the track core/shell (area 1); **c** FFT analysis of the track shell (area 2) [17]

typical zones: an amorphous core (with a diameter of ~8 nm) which represents a quenched molten phase (3); an outer concentric shell (~3 nm wide) with a hexagonal structure which is due to epitaxial recrystallization from the melt (2); the pristine orthorhombic structure outside the track region (1). Fast Fourier transform (FFT) analyses of the HRTEM image of the track in Fig. 8.4b, c clearly demonstrate an epitaxial relation between the ordered orthorhombic matrix and the disordered hexagonal track shell.

A methodology based on the use of the focused ion beam (FIB) technique to prepare high-quality TEM specimens for high resolution imaging of ion tracks was recently employed for a titanate pyrochlore ($Gd_2Ti_2O_7$) irradiated with swift U ions [18]. Thus, the track morphology and structure have been clearly identified and analyzed from the surface of the sample down to the ion resting position (~10 μm). The results provide several salient outcomes such as the distinctive effects of nuclear and electronic processes as well as their combination, the direct measurement of threshold energies for (continuous and discontinuous) track formation and crucial information on the size and morphology of ion tracks. They are briefly summarized in Fig. 8.5 which compares the variation of the ion track section

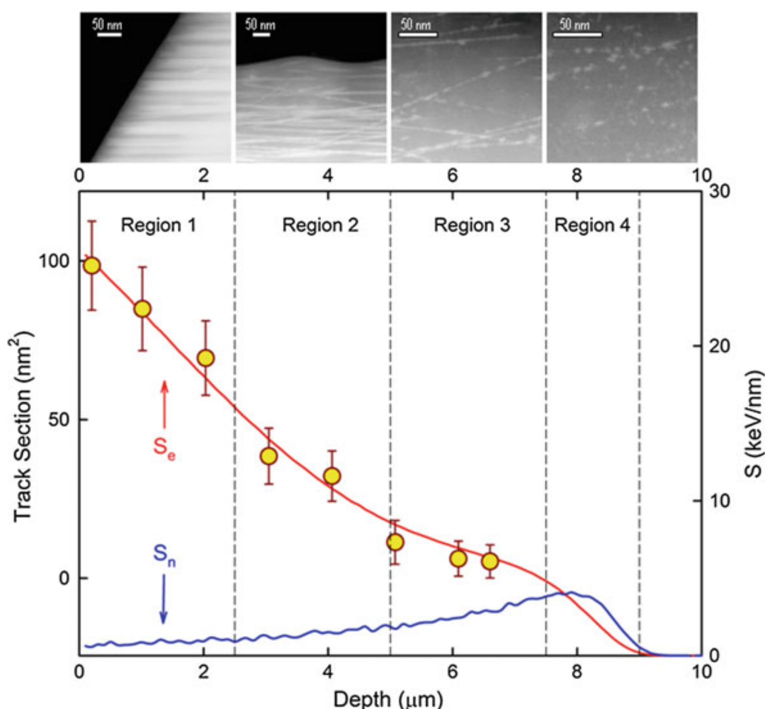

Fig. 8.5 Track sections (*circles*) as a function of depth for a $Gd_2Ti_2O_7$ pellet irradiated with 120-MeV U ions [18]. *Lines* represent the inelastic (*red*) and elastic (*blue*) energy losses. HRTEM images, showing characteristic features of ion tracks, are inserted at the *top* of the figure (Color figure online)

to the elastic and inelastic energy losses, as a function of the ion penetration depth, and provides selected TEM images depicting the track morphology at different depths. The data indicate that the section of ion tracks follows remarkably S_e down to a depth of 6–7 μm, in agreement with calculations based on the thermal spike model (see Chap. 2). Moreover, the TEM micrographs show that: (i) at low depth, ion tracks are continuous, parallel and uniform (Region 1); (ii) between ~2.5 and ~5 μm, tracks lose their parallelism and sharp, local increases of their diameter are observed (formation of nodules), due to the increased probability of elastic collisions between incoming ions and matrix atoms (Region 2); (iii) at ~5 μm, tracks become clearly discontinuous and have a heavily defective structure (Region 3); (iv) beyond ~7.5 μm, tracks fade away and only small damaged areas, due to collision cascades induced by elastic collisions, are observed (Region 4).

Tracks created in the volume of solids irradiated with swift ions may also be visualized at the surface of samples by means of scanning force microscopy (SFM). Under suitable imaging conditions, each ion impact produces a nanometric hillock [19–29]. Figure 8.6a shows a typical atomic force microscopy (AFM) micrograph

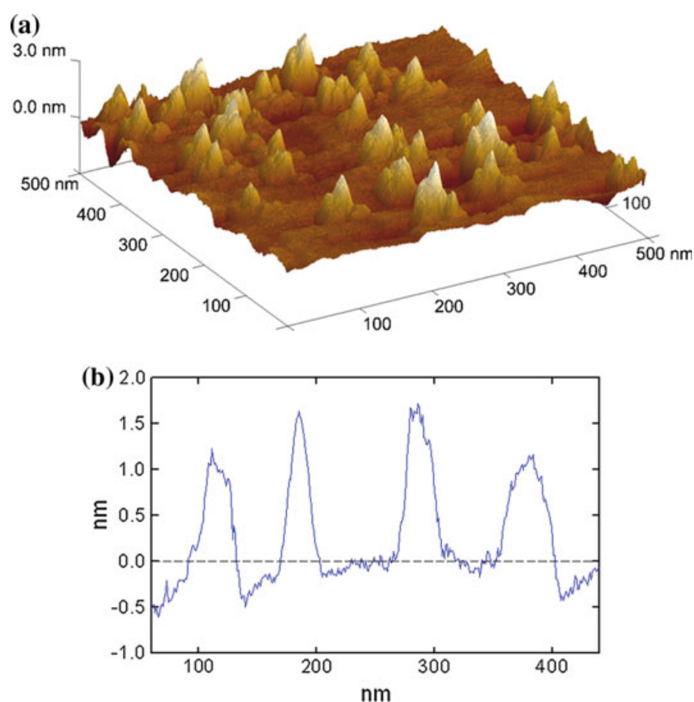

Fig. 8.6 **a** AFM micrograph obtained from a cubic zirconia single crystal irradiated with 940-MeV Pb ions at a fluence of 10^{10} cm^{-2} showing the formation of nanometer-sized hillocks on the crystal surface; **b** Profilometry of the crystal surface across hillocks [28]

obtained on a cubic zirconia crystal irradiated with swift heavy ions exhibiting randomly-distributed hillocks over the whole sample surface [28]. Actually, a good agreement is found between the density of hillocks and the irradiation fluence (10^{10} cm^{-2}). A surface profile, presented in Fig. 8.6b, shows that the height of hillocks is ~2 nm and their diameter ~30 nm. This latter value is much larger than the track diameter measured by TEM (4–5 nm). Such a discrepancy between the results obtained by techniques probing the sample surface (AFM) and techniques probing the sample bulk (TEM) was already observed in a previous work [29]. It may be explained by using an image arising from the observation of volcanoes. The inner ion track (measured by TEM) is similar to the volcano chimney and is due to the melting of the solid in the wake of an incident ion. The surface track (measured by AFM) would then result from a mechanism similar to the expulsion of lava and the formation of a cone of ejected matter with a larger diameter.

Recent classical molecular dynamics simulations were carried out to investigate the development of surface topographies following irradiation with swift ions, using either a thermal spike or an electron stripping model [30]. Both models give qualitatively similar results and show the formation of hillocks on the surface above the ion track and a less dense track core near the surface.

Small angle X-ray scattering (SAXS) is also a powerful tool for the observation of ion tracks [31–34], since this technique is sensitive to small density changes at the nanometer scale (see an example in Sect. 8.4). SAXS requires only low ion fluences that yield well-separated tracks, and it presents the great advantage to avoid difficult sample preparation such as TEM.

8.3.2 Indirect Observation of Ion Tracks

Direct observations of ion tracks by using the techniques discussed in the previous section provide rather straightforward access to track diameters but present numerous limitations due to sample preparation or spatial resolution problems. Actually, in many materials, the determination of track formation thresholds is a difficult task since track diameters are very small (often less than 1–2 nm) for low S_e values and tracks often fragment into discontinuous sections. Thus, in addition to direct track observation, a large variety of other techniques may be used in order to identify and quantify the modifications of the structure of materials due to swift ion irradiation. Damage profiles are easily determined by channeling Rutherford backscattering spectrometry (RBS/C) provided that single crystals may be used for the study [35, 36]. X-ray diffraction (XRD) [37, 38] gives access to structural modifications, phase transformations and radiation-induced strains via modifications of lattice parameters. The creation of defects may be studied by electrical resistivity measurements (ER) [39, 40], UV, IR or Raman spectroscopy [41–43]. In magnetic materials, the appearance of a paramagnetic phase can be detected by

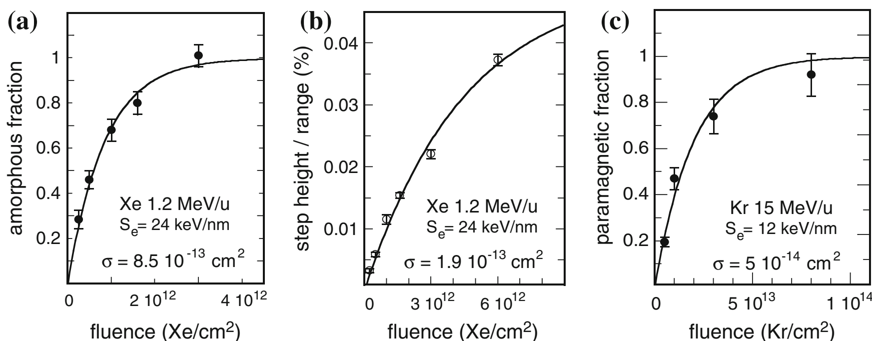

Fig. 8.7 Variation with ion fluence of specific properties of $Y_3Fe_5O_{12}$ irradiated with swift ions. **a** Fraction of amorphized matter quantified by RBS/C; **b** step height of out-of-plane swelling, normalized to the ion range, measured by profilometry; **c** fraction of paramagnetic regions deduced from Mössbauer spectrometry [46]

Mössbauer spectrometry (MS) [44]. Finally, volume changes induced by irradiation (swelling) are quantified by surface profilometry [45].

Ion irradiation-induced materials modifications are generally studied as a function of the ion fluence. Figure 8.7 shows typical variations of specific properties of $Y_3Fe_5O_{12}$ irradiated with swift heavy ions [46]. In this work, the amorphous fraction was quantified by RBS/C (Fig. 8.7a), the step height of out-of-plane swelling (normalized to the ion range) was measured by profilometry (Fig. 8.7b) and the fraction of paramagnetic regions was deduced from MS (Fig. 8.7c). Data show that the measured parameters usually follow a linear variation in the regime where ion tracks are well separated (typically below few 10^{11} cm^{-2}). When tracks become overlapping (typically above 10^{12} cm^{-2}), values of parameters evolve towards saturation.

The analysis of damage build-ups similar to those shown in Fig. 8.7 with pertinent phenomenological models (see Chap. 3 of this book) provides values of track diameters (d_i) via the determination of damage cross-sections σ_i, according to the equation:

$$d_i = 2\,(\sigma_i/\pi)^{1/2} \tag{8.1}$$

It is worth mentioning that (8.1) may be used to evaluate the diameter of ion tracks provided that the damage induced by swift ions is continuous and of cylindrical geometry. Moreover; the absolute value of σ_i may depend on the chatacterization technique and on the nature of the ion beam-induced modifications.

8.4 Formation of Ion Tracks at Low Fluences

8.4.1 Track Formation in Metals and Metallic Compounds

Before the 90s it was believed that electronic excitation processes were inefficient to create tracks in metallic targets, due to the possibility given to conduction electrons to easily smear out the perturbation caused by the passage of swift ions. Shortly after the evidence of partial amorphization of Ni_3B ribbons due to electronic excitation [47], the first observation of (more or less continuous) amorphous tracks was done in crystalline Ni-Zr alloys irradiated at low temperature (80 K) with GeV heavy ions (Fig. 8.8) [48]. These intermetallic compounds were chosen owing to their high ordering energies and their capability to be amorphized by nuclear elastic collisions at low energy. It was shown that the number of tracks is equal to the number of incident ions and that the track diameter varies along the ion path (starting from $\sim$8 nm). Moreover, it was demonstrated that the S_e threshold for track formation is rather high (30–50 keV nm^{-1}) in this type of solids.

In pure metals, ion tracks were first observed in titanium, either in bulk material or in thin films [49–53]. TEM experiments (see Fig. 8.9) [51] show that discontinuous tracks (3–5 nm diameter) are formed upon GeV monoatomic heavy ion irradiation at 80 or 300 K, whereas continuous tracks with a much larger diameter ($\sim$20 nm) are formed upon 30-MeV cluster (C_{60}) irradiation at low temperature (below 80 K). These tracks remain crystalline and an alpha-omega phase transformation is observed when tracks overlap (see Sect. 8.5).

Ion tracks were also observed in bismuth irradiated at very low temperature (20 K) with heavy ions of energy in the GeV range, above a S_e threshold of 30 keV nm^{-1} [54]. The largest track diameter observed for S_e = 51 keV nm^{-1} in

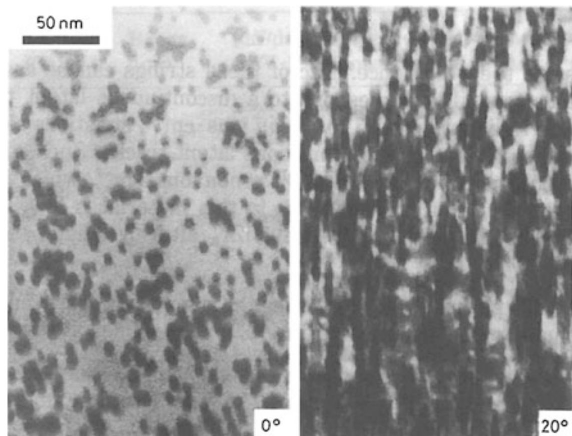

Fig. 8.8 TEM micrographs recorded on $NiZr_2$ irradiated with 700-MeV Pb ions at 7×10^{11} cm^{-2} [48]. The samples were tilted by angles of 0° (*left*) and 20° (*right*) with respect to the beam direction in order to see ion tracks with various incidences

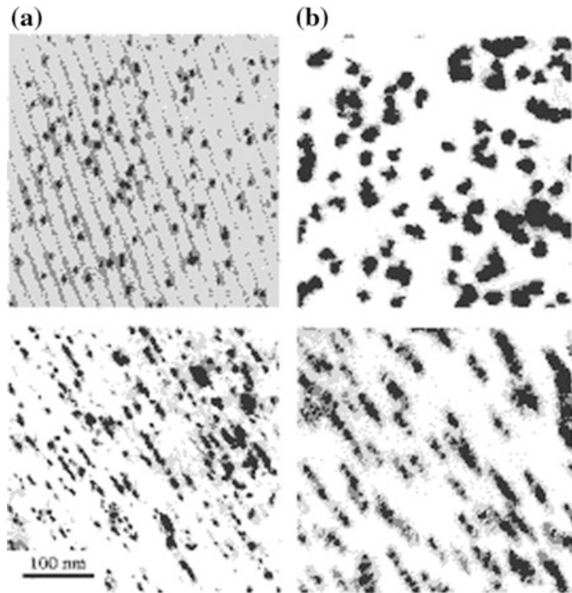

Fig. 8.9 TEM bright field images of Ti irradiated with swift projectiles. **a** 845-MeV Pb ions (fluence: 10^{11} cm^{-2}); **b** 18-MeV C_{60} (fluence: 6×10^{10} cm^{-2}). *Top* images are recorded with the electron beam parallel to the ion beam, whereas *bottom* images are recorded with the sample tilted by 25° [51]

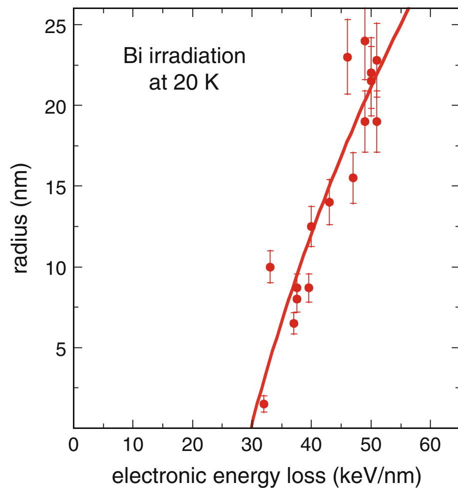

Fig. 8.10 Latent track radii versus S_e for Bi irradiated at 20 K with swift heavy ions [55]. The *line* is a fit of data using the thermal spike model (see Chap. 2)

this material is about 22 nm. Figure 8.10 presents the variation of the radius of ion tracks as a function of S_e for different ion energies [55]. The results may be interpreted in the framework of a theoretical description involving the formation of thermal spikes (see Chap. 2 of this book). Different S_e thresholds for track formation, depending on the ion velocity, were also evidenced.

8.4.2 *Track Formation in Insulators*

8.4.2.1 Mineral Analogs

Tracks created by fission fragments were observed in mineral analogs. Visualization of the effects of swift ions by AFM was made in muscovite mica [19]. In this material tracks were imaged as hollows which may be associated with softer areas in the mica surface. The diameter of hollows was seen to increase with S_e above a track formation threshold of ~ 20 keV nm^{-1}. Later on, the formation of tracks in mica was investigated by STM, TEM, X-ray and neutron scattering [20, 37, 56]. STM shows the formation of conical-shaped hillocks having nearly circular bases with a mean width of ~ 20 nm and a mean height of ~ 0.5 nm [20]. The presence of craters beneath hillocks was observed after hillocks were erased due to the strong interaction between the STM probe tip and the sample surface. Amorphous tracks with a maximum diameter of 2 nm, surrounded by a distorted crystalline region with an increased inter-planar distance, were indirectly observed by wide-angle X-ray diffraction [37]. The large discrepancies obtained for the track diameters measured with different techniques reflect the structural complexity of latent tracks in mica. An interesting effect of both the velocity of swift ions and the use of high-energy cluster beams was also evidenced [56]. Figure 8.11a shows that the track diameter measured by STM for the same value of S_e is smaller when the velocity of irradiating ions increases. Furthermore, Fig. 8.11b clearly demonstrates the cluster effect since the diameter of ion tracks is larger for C and Al cluster irradiations than for monoatomic ion irradiations.

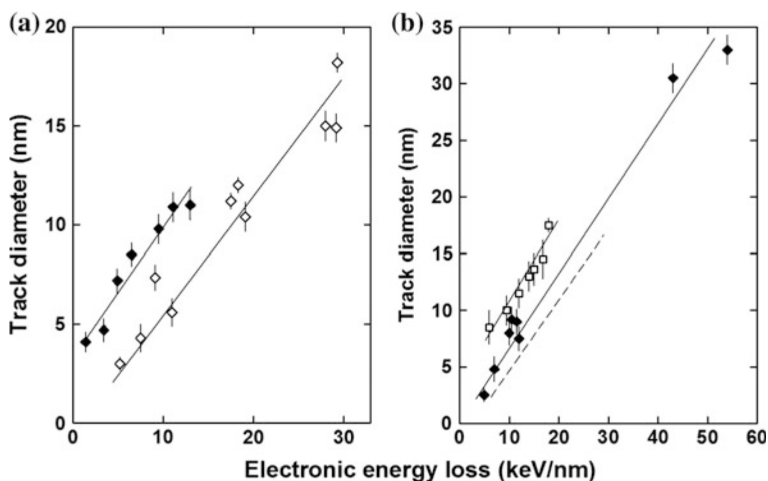

Fig. 8.11 Diameters of ion tracks as a function of S_e in mica irradiated with monoatomic ions and clusters. **a** Comparison of low and high velocity monoatomic ions; **b** Comparison of monoatomic ions (*dashed line*), C clusters (*filled diamonds*) and Al clusters (*open squares*) [56]

Apatites constitute another class of mineral analogs where track formation was much investigated [57–61]. Amorphous tracks with a diameter of ~4 nm were observed by TEM in fluoroapatite irradiated with swift Kr and I ions [58]. For I irradiation amorphization occurs via a single-impact process, whereas for Kr irradiation amorphization follows a double-impact mechanism. An expansion of the lattice parameter was also observed, that is likely generated by the stress due to the volume increase of the track core. Fluoroapatite irradiated with 30-MeV C_{60} clusters exhibits the formation of tracks with diameter ~10 nm showing different shapes: circular, drop-like, hexagonal [57]. Recently, the effect of both swift ion irradiation and high pressure (up to 12 GPa) was investigated on Durango apatite [59, 61]. Confocal Raman spectroscopy indicates the formation of amorphous tracks, but the application of pressure has a stabilizing effect leading to decrease the rate of amorphization in comparison with samples irradiated without pressure. Similar irradiations were performed on fluoroapatite single crystals which exhibit anisotropic lattice expansion due to the formation of strain [60]. X-ray diffraction patterns indicate that the long-range strain distribution within the host lattice is reduced when pressure is applied during irradiation. This result can be attributed to the different compressibilities of amorphous tracks and host lattice.

8.4.2.2 Ionic Crystals

Ionic crystals, and more particularly alkali halides, are appropriate materials to investigate track formation by swift ion irradiation, since they are among the most sensitive solids to electronic excitation [62–67]. This extreme sensitivity results from the rather large amount of ionic relaxation that follows any electronic change inducing a directed ionic motion of halide ions. The use of a micro-spectrophotometric technique to explore the coloration of LiF crystals along the penetration depth of incident ions allowed for the first time a direct comparison between point defect creation and the energy deposition in individual ion tracks [62]. Results show that tracks are saturated with primary defects (mainly F centers) with a constant concentration all along the ion tracks. The damage microstructure in an individual ion track is very complex due to the presence of a large variety of aggregate centers (F_2) in anionic and cationic sublattices. The irradiation-induced structural and optical modifications were also studied using glancing angle X-ray diffraction, optical absorption and photoluminescence spectroscopy on thermally-deposited polycrystalline LiF films irradiated with swift Ag ions [65]. A fragmentation of LiF grains (from ~50 nm down to ~20 nm) is observed upon irradiation, which may be attributed to the formation of large strains. The optical absorption curves show the dominant formation of F_2 and F_3 colour centers with a concentration which increases with increasing ion fluence and saturates at high fluence. The formation of hillocks with a diameter of ~20 nm was observed by STM in LiF single crystals irradiated at different temperatures with swift Pb ions [66]. The stability and the size of hillocks are not influenced by the elimination of F and F_2 centers when the temperature is increased.

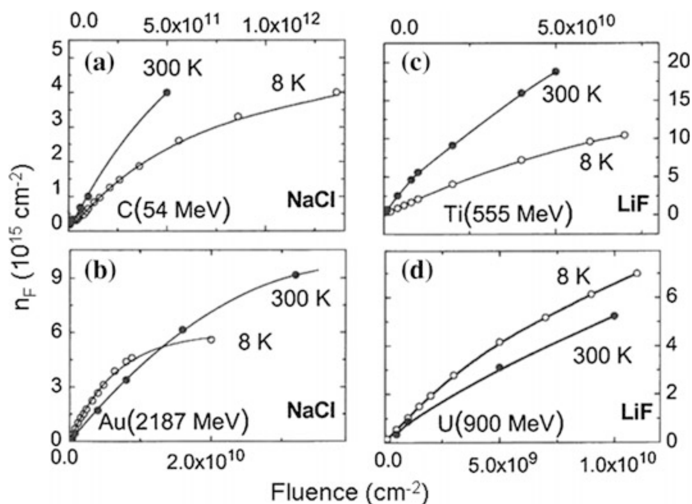

Fig. 8.12 Concentration of F centers (n_F) versus ion fluence in NaCl and LiF crystals irradiated at 8 K and 300 K. **a**, **b** NaCl irradiated with 54-MeV C and 2.2-GeV Au ions; **c**, **d** LiF irradiated with 550-MeV Ti and 900-MeV U ions [67]

A comparison of the effects of electronic energy loss and irradiation temperature in LiF and NaCl crystals irradiated with swift ions was performed using STM measurements, optical absorption and thermostimulated luminescence spectroscopy [67]. Anion interstitials (I and H centers) were only observed in crystals irradiated at very low temperature (8 K). These defects are unstable and disappear in the temperature range 10–100 K. Upon irradiation with heavy ions (Au or U), the F-center accumulation efficiency at low fluence is larger at 8 K than at RT. The opposite behavior is observed for irradiation with light ions (C, Ti, Ni). This effect, shown in Fig. 8.12, can be explained by a local transient temperature spike, which directly influences the separation of primary H and F centers. Based on thermal spike estimations, the average temperature increase in an ion track is low for light ions but can reach several hundreds Kelvin for heavy ions. In contrast to color centers, the diameter and height of hillocks created at each ion impact site is independent of the irradiation temperature. The mechanism of hillock formation should be linked to a mechanism of stress relaxation close to the crystal surface that is driven by the modifications produced in the core region of tracks.

8.4.2.3 Simple Oxides

Simple oxides present a large variety of behaviour upon swift ion irradiation, depending on their composition and structure. The most stable oxides are those possessing the fluorite structure (UO_2, ZrO_2, ThO_2, CeO_2). Tracks with a diameter ~ 10 nm, exhibiting a hexagonal shape, were first observed in the surface region of

UO_2 single crystals and pellets irradiated at RT with heavy ions in the GeV range [68, 69]. In this work the threshold value of S_e for track formation was found to lie between 22 and 29 keV nm^{-1}. This high value explains why no visible tracks are formed due to fission in UO_2. Hillocks with a diameter of ~30 nm (i.e. much larger than the track diameter measured in previous studies) and a height of ~5 nm were also observed by AFM at the surface of UO_2 single crystals irradiated at RT with GeV Pb ions [70]. A comparison of the diameter of ion tracks observed in UO_2 and CeO_2 leads to the conclusion that CeO_2 is more sensitive to electronic excitation than UO_2 [71].

The study of ion track formation in fluorite-type ceramics has been mainly performed on cubic-stabilized ZrO_2 single crystals [28, 38, 72, 73]. Stabilization of the cubic structure of zirconia is generally achieved by incorporating a small (~10 %) atomic fraction of yttria (Y_2O_3). Figure 8.13 shows TEM micrographs recorded on a cross-sectional specimen prepared from a crystal irradiated with 940-MeV Pb ions at 5×10^{11} cm^{-2} [28]. This micrograph displays the trajectories of incident Pb ions that present the aspect of tracks. It shows the presence of two regions in depth with different microstructures: the subsurface region (extending up to ~70 nm) exhibits a lack of matter inside ion tracks (Fig. 8.13 left); a deeper region where dark rows reveal filled tracks with dislocation loops in their vicinity (Fig. 8.13 right). The AFM micrograph presented in Fig. 8.6a of Sect. 8.3.1 shows that the formation of ion tracks also led to the formation of hillocks over the sample surface.

The formation of tracks was investigated in other simple oxides submitted to swift ion irradiation. Zircon crystals irradiated at RT with 2.9-GeV Pb ions exhibit linear latent tracks of 8 nm diameter and 140 μm length [15]. Direct observation of the track core, by HRTEM at atomic resolution, shows a core having roughly circular cross-section with some facetting of the core/matrix interface on the {101} planes of zircon. The core diameter appears quite uniform. Conventional TEM

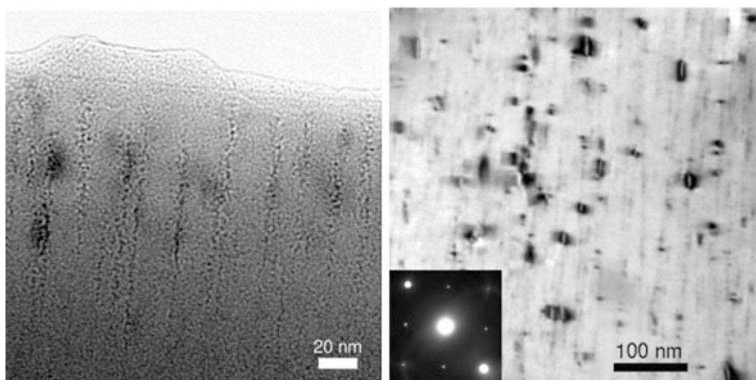

Fig. 8.13 TEM micrographs obtained from a c-ZrO_2 single crystal irradiated with 940-MeV Pb ions at 5×10^{11} cm^{-2}. (*Left*) Near-surface ion tracks, obtained using overfocused condition; (*right*) bulk region showing isolated dislocation loops along Pb ion trajectories [28]

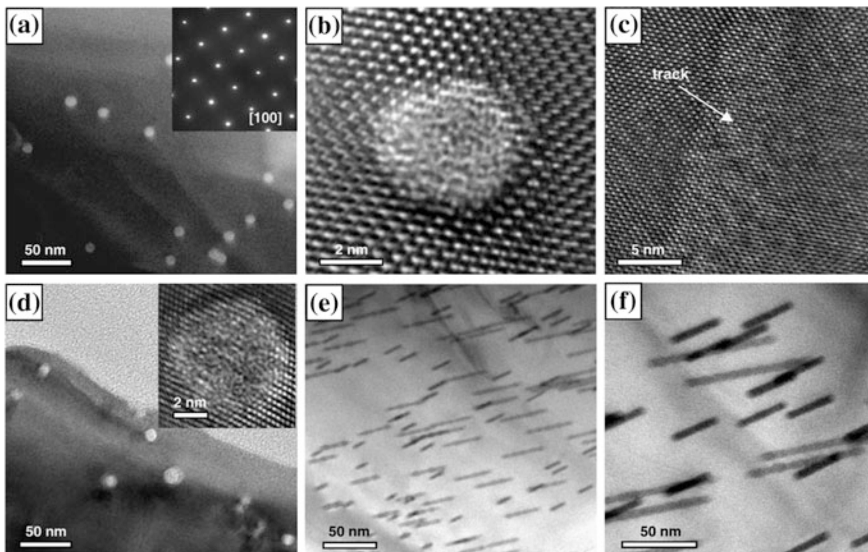

Fig. 8.14 TEM images of zircon irradiated with 10-GeV Pb ions at 5×10^{10} cm^{-2}. **a**–**c** Sample irradiated at RT and ambient pressure; **d**, **f** Sample pressurized at 7.5 kbar and heated at 250 °C [74]. Bright-field micrographs **a**, **d**–**f**, high-resolution images (**b**, *inset* of **d**) and electron diffraction pattern (*inset* of **a**)

(bright- and dark-field imaging) reveals an elastic strain field extending over a short distance into the zircon matrix. Analysis of the various contrast mechanisms indicates that the core is essentially amorphous. Using a new experimental approach, fission-track formation has been simulated for the first time under crustal conditions by exposing natural zircon, at a pressure of 7.5 kbar and a temperature of 250 °C, to a beam of relativistic heavy ions [74]. The latent tracks were investigated using HRTEM, and the mean values of the track diameters were found to be 5.2 and 5.4 nm for zircon at ambient and elevated pressure-temperature, respectively (Fig. 8.14). The slightly larger size of the tracks at elevated pressure can be understood in terms of the increased efficiency of the damage process in a strained crystal lattice. This slight variation in track diameter ($\sim$0.2 nm) at high pressure probably does not affect the dimensions of etched tracks.

Swift ion irradiation of SiO_2 [34, 75–78], TiO_2 [79, 80], SnO_2 [81], Al_2O_3 [82–89], Y_2O_3 [90] and MgO [84–86] was shown to induce tracks in the bulk of these materials as well as hillocks at the surface. Their behaviour upon electronic excitation depends on the type of oxide. Tracks were found to be amorphous above a S_e threshold in SiO_2 and TiO_2, whereas the track core remains crystalline in SnO_2 and MgO. In Al_2O_3 a controversy still exists and different disordering processes were observed in the Al and O sublattices in experiments using the RBS/C technique [29]. In a more recent work, RBS/C experiments indicate the existence of two processes: partially disordered tracks are created in a first step, an amorphous layer

grows linearly with fluence from the sample surface in a second step [88]. In SiO_2 the analysis of the amorphization build-up is well reproduced with a cumulative model assuming that the track is composed of an amorphous core and a surrounding defective halo [77].

Figure 8.15 provides an example of SAXS experiments recorded on a quartz sample at the SAXS/WAXS beamline of the Australian Synchrotron in transmission geometry with an X-ray energy of 12 keV [34]. Figure 8.15 (left-a) shows the isotropic scattering in collinear geometry for tracks produced by 1.6-GeV Au ions at a fluence of 5×10^{10} cm^{-2}. Due to the parallel orientation of the ion tracks, the radial symmetry is consistent with a circular cross section of the track cylinders or a random rotation of tracks with a non-circular cross section along the track axis. By tilting the sample from this position, the scattering changes to two slightly curved streaks, as apparent from Fig. 8.15 (left-b). This anisotropy results from the high aspect ratio of the tracks being only a few nanometers wide, and tens of micrometers long. Figure 8.15 (right) shows SAXS spectra of ion tracks as a function of the scattering vector $\boldsymbol{q}$ [34]. The presence of strong oscillations is consistent with monodisperse track radii and a sharp density change between the tracks and the matrix material. The scattering intensity scales almost linearly with the ion fluence, or equivalently with the number of tracks. This proportionality indicates that, at low fluences, tracks are still well separated so that track overlap is negligible. Fits of the data with a model which considers tracks as cylinders with constant density, different from that of the surrounding matrix, yield track radii on the order of 4 nm for the three fluences used in this study, in good agreement with independent TEM measurements. A density change of $\sim$2 % in the amorphous core of tracks with respect to the matrix is consistent with observations from macroscopic swelling measurements, but is significantly lower than the $\sim$15 % difference between bulk silica and quartz.

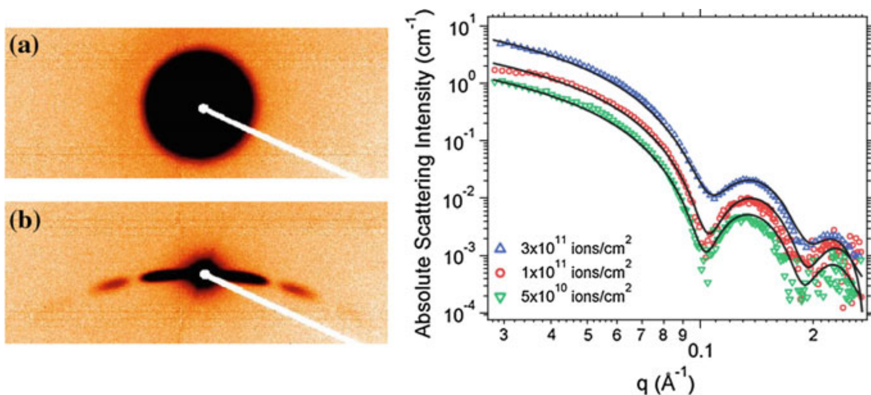

Fig. 8.15 (*Left*) SAXS images of a quartz sample irradiated with 1.6-GeV Au ions at 5×10^{10} cm^{-2}. **a** The X-ray beam is parallel to the ion tracks, **b** The ion tracks are tilted by 5° with respect to the X-ray beam. (*Right*) SAXS spectra from ion tracks in quartz as a function of the scattering vector q. Samples were irradiated with 1.4-GeV Au ions at the indicated fluences [34]

8.4.2.4 Complex Oxides

The effects of swift heavy ion irradiation, and more particularly the possibility to form ion tracks, were also studied in various complex oxides, such as spinel (AB_2O_4), δ-phase ($A_4B_3O_{12}$ and $A_6B_1O_{12}$), perovskite (ABO_3), A_2BO_5 and pyrochlore ($A_2B_2O_7$) compounds. The study of these systems is particularly interesting since their radiation behaviour generally depends on A and B cations.

Extensive work has been performed in the case of spinel [91–103]. Figure 8.16 shows a cross-sectional TEM micrograph and high angular resolution electron channeling spectroscopy (HARECXS) spectra taken on $MgAl_2O_4$ (the most investigated composition) irradiated at RT with swift Au ions [101]. In HARECXS experiments, the normalized X-ray intensity is plotted as a function of incident electron-beam direction (in k/g_{400}), where k refers to the intersection of the Ewald sphere with the [001] zone axis along the (400) reflection. The bright-field image of the cross sectional specimen (Fig. 8.16a) indicates that continuous ion tracks are seen as diffraction contrasts up to a depth of ~10 μm. The HARECXS analysis, which provides quantitative information about the number of ions existing at tetrahedral sites in the spinel structure, reveals that significant disordering occurs along the ion tracks (Fig. 8.16b). Changes in the HARECXS profiles are more important at 2 μm (corresponding to $S_e \sim 33$ keV nm^{-1}) than at 8 μm

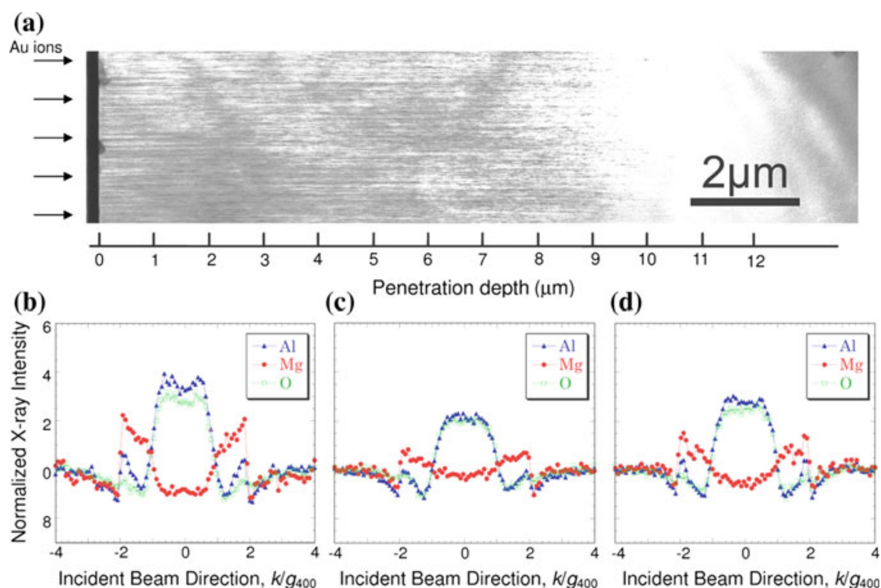

Fig. 8.16 **a** Bright-field cross section of $MgAl_2O_4$ irradiated at RT with 350-MeV Au ions at 5×10^{11} cm^{-2}, illustrating the formation of continuous ion tracks along the trajectory of incident ions; **b** HARECXS profiles taken from virgin $MgAl_2O_4$; **c**, **d** HARECXS profiles taken from depths of 2 μm (**c**) and 8 μm (**d**) in $MgAl_2O_4$ irradiated at RT with 350-MeV Au ions [101]

(corresponding to $S_e \sim 23$ keV nm^{-1}), indicating greater disordering with higher values of S_e. Moreover, it was shown that ion tracks in $MgAl_2O_4$ consist of three concentric circle structures: the structurally defective regions are formed at the core of ion tracks with a size of $\sim$2 nm, surrounded by a strained region with a size of $\sim$5 nm and then by a cation disordered region with a size of $\sim$10 nm. No amorphization is detected in $MgAl_2O_4$ for values of S_e lower than $\sim$40 keV nm^{-1}. In $ZnAl_2O_4$ irradiated with a large variety of swift ions, X-ray diffraction and TEM experiments have shown that individual ion tracks are crystalline, whereas amorphization occurs at very high fluence by a defect accumulation process above a S_e value of $\sim$10 keV nm^{-1} [102].

The creation of either crystalline or amorphous ion tracks was revealed by HRTEM in, respectively, $Sc_4Zr_3O_{12}$, $Lu_4Zr_3O_{12}$ [104] and $Y_6W_1O_{12}$, $Yb_6W_1O_{12}$ [105] delta phase compounds irradiated with swift heavy ions. Amorphous tracks were also observed in $CaZrO_3$ perovskite [106] and A_2TiO_5 compounds [107]. In these latter materials, it was found that the size of tracks decreases as smaller cations (higher Z) occupy the A site.

The formation of ion tracks in pyrochlores was rather recently investigated [108–113]. Figure 8.17b shows a HRTEM image of an amorphous track created in $Gd_2Ti_2O_7$ upon irradiation with swift heavy ions, and Fig. 8.17a presents the variation of the track diameter in $Gd_2Zr_{2-x}Ti_xO_7$ with the Ti content, determined by TEM, Raman or XRD [108, 110]. The figure clearly shows that all diameters increase systematically with increasing Ti-content. However, for a given composition, the various analytical techniques provide different track diameters because they

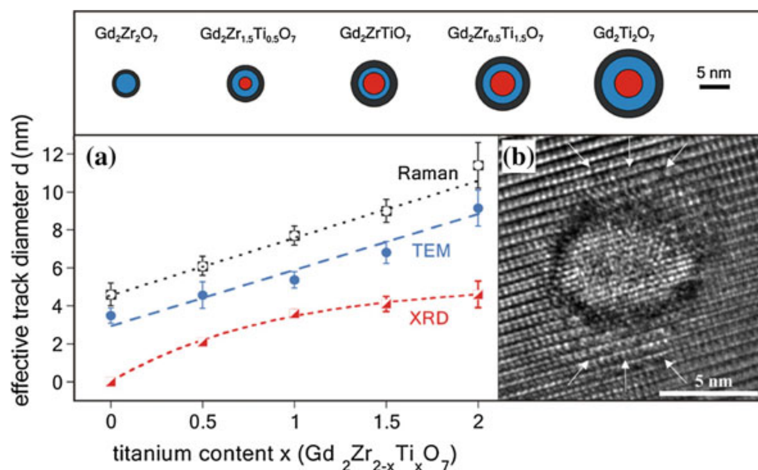

Fig. 8.17 **a** Track diameter obtained from XRD, Raman and TEM as a function of pyrochlore composition (Ti-content x); **b** HRTEM image of $Gd_2Ti_2O_7$ irradiated at RT with 1.4-GeV Xe ions. The *inset* illustrates schematically the concentric track cylinders, composed of amorphous core, disordered defect-fluorite structured shell and strained defect-rich pyrochlore halo, for all pyrochlore compositions, as revealed by the three analytical techniques [108]

probe different length-scales of the structure. Raman data reflect the total contribution from all the radiation damage states (amorphous + defect-fluorite + defects and strain), which results in the largest diameter values. The mean track diameters measured by TEM are the widths of the cylinders according to contrast variations along the ion trajectory. In particular, for Ti-rich compositions both the amorphous material and the disordered defect-fluorite structure contribute to this contrast change. Therefore, the diameter associated with a bright-field TEM image represents a track size that includes two types of radiation damage states (amorphous + defect-fluorite). This explains the smaller diameters, as compared with the results from the Raman measurements. The track diameters obtained by synchrotron XRD are the smallest among the three techniques. The damage cross-sections and diameters were determined by the increasing amorphous background in the XRD patterns and represent the effective diameter of the amorphous core within the track. In summary, the various results lead to a semi quantitative track description consisting of concentric cylindrical zones. Except for $Gd_2Zr_2O_7$ (which is not amorphizable), the track of a swift heavy ion in $Gd_2Zr_{2-x}Ti_xO_7$ has an amorphous core, surrounded by a disordered defect fluorite structured shell and a strained defect-rich pyrochlore halo (schematically illustrated by concentric circles in the inset of Fig. 8.17). For the Ti-endmember ($Gd_2Ti_2O_7$), the damage morphology and size of individual damage zones are in general agreement with the actual track structure as imaged by HRTEM (Fig. 8.17b). Both the amorphous core and the surrounding disordered defect-fluorite shell are clearly seen in a single ion track. Fast Fourier transform analysis of the HRTEM image reveals the details of the local atomic structure within the track shell and confirms the disordering of the defect-fluorite structure. Individual point defects in the defect-rich pyrochlore halo are not revealed by TEM. However, some contrast modifications (see arrows) are shown in the pyrochlore matrix that surrounds the defect-fluorite structure.

Figure 8.18 shows TEM images of ion tracks in several pyrochlores ($Gd_2Ti_2O_7$, Gd_2ZrTiO_7 and $Nd_2Zr_2O_7$) irradiated with swift heavy ions [113]. Tracks in $Gd_2Ti_2O_7$ (Fig. 8.18a, b) consist of totally amorphous cylinders with a diameter of 10–12 nm. A very thin shell (containing few atoms), located between the amorphous and pyrochlore regions, exhibits a different contrast which is characteristic of the fluorite phase. On the contrary, tracks in Gd_2ZrTiO_7 and $Nd_2Zr_2O_7$ clearly exhibit both amorphous and fluorite phases with different spatial distributions: in Gd_2ZrTiO_7 an amorphous core (diameter 7–9 nm) is surrounded by a shell of fluorite structure (Fig. 8.18c, d), whereas in $Nd_2Zr_2O_7$ the fluorite phase is predominantly observed (diameter 8–10 nm) with the presence of small areas of amorphous phase distributed inside the fluorite region (Fig. 8.18e, f). Fast Fourier transform analyses performed on Gd_2ZrTiO_7 and $Nd_2Zr_2O_7$ micrographs supply the internal structure of tracks for these compounds [113]. For Gd_2ZrTiO_7, the disappearance of superlattice diffraction reflections reveals the presence of a defect fluorite structure in the shell, whereas the track core shows diffuse scattering corresponding to the amorphous phase. In the case of $Nd_2Zr_2O_7$, the track core exhibits both fluorite structure spots and diffuse scattering, indicating a mixture of disordered crystalline and amorphous phases (the latter one having a smaller fraction).

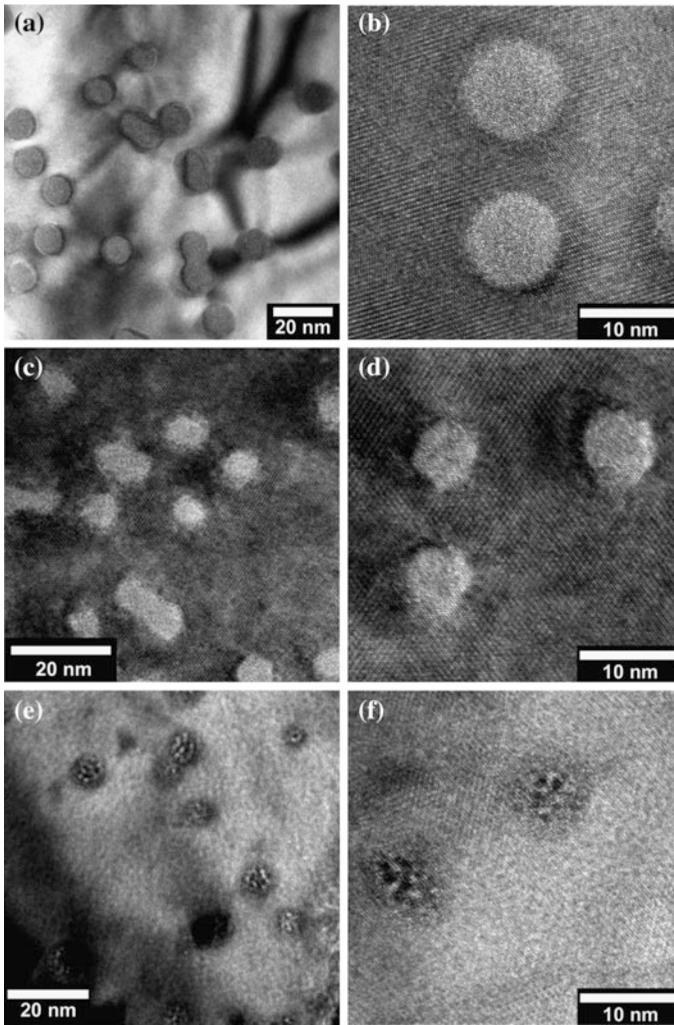

Fig. 8.18 HRTEM micrograph of $Gd_2Ti_2O_7$ (**a**, **b**), Gd_2ZrTiO_7 (**c**, **d**) and $Nd_2Zr_2O_7$ (**e**, **f**) irradiated at RT with 120-MeV U ions at 2×10^{11} cm^{-2}, showing tracks with structures strongly depending on the irradiated material [113]

8.4.2.5 High-Tc Superconductors

Irradiation of high-T_c superconductors with swift heavy ions has long been known to produce linear damage tracks that consist of (continuous or discontinuous) amorphized columns depending on both the value of S_e and the irradiation temperature [114–135]. The diameters of ion tracks are most often ideally suited to enhance flux pinning by inducing vortex entanglement and reducing the

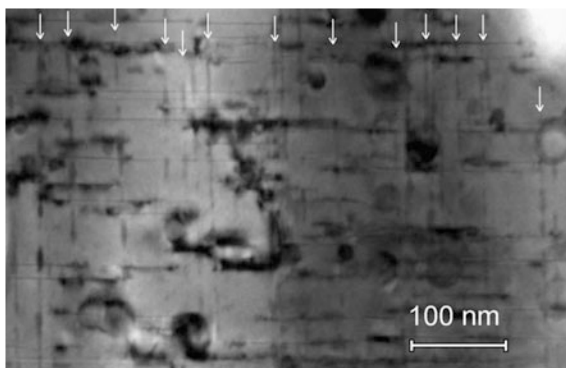

Fig. 8.19 TEM micrograph of discontinuous ion tracks (indicated by *arrows*) in $YBa_2Cu_3O_7$ irradiated at RT with 74-MeV Ag ions at 10^{11} cm^{-2} [133]

propagation of double-kink formations. A typical result is presented in Fig. 8.19 which shows discontinuous damage tracks in $YBa_2Cu_3O_7$ irradiated at RT with 74-MeV Ag ions at low fluence (10^{11} cm^{-2}) [133]. In this experiment, the irradiation direction is parallel to the $YBa_2Cu_3O_7$ c-axis and the value of S_e ($\sim$19 keV nm^{-1}) is below the threshold for the formation of continuous columns in this material (S_{et} $\sim$ 35 keV nm^{-1}). The track diameter is 2–4 nm, i.e. close to the superconducting coherence length, which is therefore expected to give a strong flux pinning enhancement. Basically, the formation of tracks leads to a continuous reduction of the transition temperature (T_c), as it is shown in Fig. 8.20 [133]. Similarly, irradiation also reduces the zero-field relatively to the virgin value by a factor depending on the ion fluence.

An interesting study dealt with the determination of the morphology of an ion track all along the ion path in $Bi_2Sr_2CaCuO_X$ single crystals irradiated with swift ions [128, 129]. Columnar defects are clearly formed in a depth region ranging from the sample surface to a depth of about 7.5 μm, and defect cascades appear between 5 and 11 μm. From a series of HRTEM images zooming the irradiation-induced columnar defects, it is also shown that the diameter of the damaged amorphous

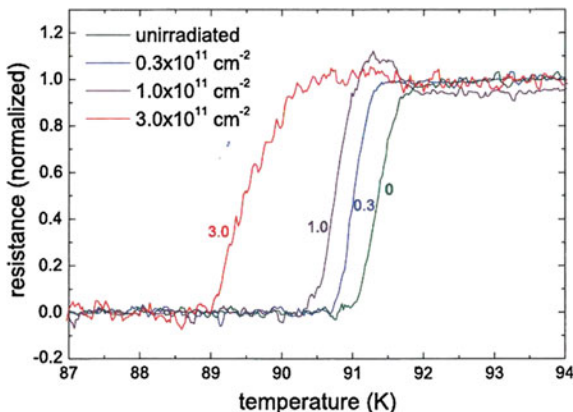

Fig. 8.20 Superconducting transition, measured by the 4-probe transport method, in $YBa_2Cu_3O_7$ irradiated at RT with 74-MeV Ag ions at the indicated fluences [133]

cylinders gradually decreases from 13.5 to 3 nm when the penetration depth of incident Au ions changes from 1 to 7.5 μm.

Recent detailed XRD studies [134] suggest that the ion tracks created by swift ion irradiation in high-T_c superconductors (namely $YBa_2Cu_3O_7$) are composed of three main regions: (i) narrow amorphous cylinders (diameter of a few nanometers) provided $S_e > S_{et}$, (ii) strained zones around ion tracks which cause contraction of a- and b-axes and extension of c-axis (parallel to incoming ions), and (iii) oxygen disorder (point defects) in the CuO basal plane.

8.4.2.6 Garnets

The production of radiation damage by electronic excitation in garnets was investigated early in the eighties by using a panoply of experimental techniques [136–146]. Figure 8.21 shows the variation of the radius of ion tracks (extracted from cross-section measurements arising from RBS/C data) as a function of the electronic energy loss for $Gd_3Ga_5O_{12}$ single crystals irradiated at RT with various swift heavy ions [144]. An interesting issue of this study is the observation of a velocity effect: for the same S_e value, measured radii are higher for low ion velocities (beam energy ~1.5 MeV/u) than for high ion velocities (beam energy ~6 MeV/u). Similarly, the S_e threshold for track formation is lower in the former case (7.2 keV nm^{-1} for ~1.5 MeV/u) than in the latter one (9.3 keV nm^{-1} for ~6 MeV/u). Lines in the figure are fits to data by using the inelastic thermal spike model described in Chap. 2.

Another aim for studies involving electronic excitation effects in garnets was to tailor the magnetic and magneto-optical properties of this interesting class of materials via swift ion irradiation. For that purpose the amorphous phase produced by irradiation via the formation of tracks was studied by using ^{57}Fe Mössbauer spectroscopy. Figure 8.22 (left) shows Mössbauer spectra recorded using the standard absorption method with a source of ^{57}Co placed on a constant-acceleration spectrometer [140]. Quantitative information on the hyperfine magnetic field (B_{hf})

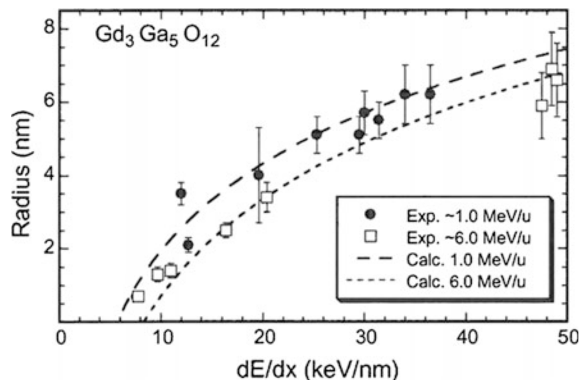

Fig. 8.21 Radius of ion track versus electronic energy loss for $Gd_3Ga_5O_{12}$ irradiated at RT with swift heavy ions. *Open squares* and *filled circles* correspond to beam energies of ~6 and ~1.5 MeV/u, respectively. *Lines* are calculations using the thermal spike model (with λ = 4.6 nm) [120]

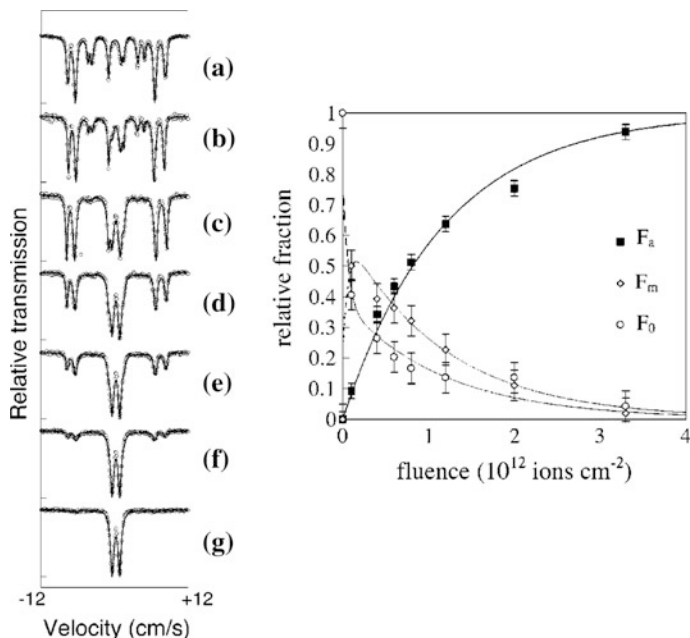

Fig. 8.22 (*Left*) Mössbauer spectra of $Y_3Fe_5O_{12}$ irradiated at RT with 6-GeV Pb ions. The labels correspond to the virgin sample (**a**) and to samples irradiated at fluences of 10^{11} cm^{-2} (**b**), 4×10^{11} cm^{-2} (**c**), 8×10^{11} cm^{-2} (**d**), 1.2×10^{12} cm^{-2} (**e**), 2×10^{12} cm^{-2} (**f**) and 3.3×10^{12} cm^{-2} (**g**). (*Right*) Variation of the amorphous fraction F_a, oriented magnetic fraction F_m, and virgin fraction F_0 as a function of the Pb ion fluence [140]

at the iron nuclei can be deduced from the intensity ratio of the Mössbauer peaks. The spectrum recorded on a virgin sample may be reproduced using two octahedral and one tetrahedral contributions (with proportions of ~40 and ~60 %, respectively), which lead to the peaks shown in Fig. 8.22 (left-a). The radiation damage due to irradiation results in an amorphous paramagnetic fraction (F_a) which appears in the form of a doublet in the middle part of the spectra (Fig. 8.22 left-c–g). At the final fluence of 3.3×10^{12} cm^{-2}, the fraction of amorphous paramagnetic material is 100 %. Moreover, whatever the irradiation fluence, the remaining magnetic part of the samples shows no change in B_{hf} nor in the distribution of Fe^{3+} ions in both octahedral and tetrahedral sites. Figure 8.22 (right) presents the variation of F_0 (virgin fraction), F_m and F_a with the ion fluence, arising from spectra of Fig. 8.22 (left) [140]. Fits to the data of Fig. 8.22 (right) provide the radii of the amorphous track cores (~5 nm) and of the stressed magnetic-oriented cylinders surrounding the track cores (~20 nm). These radii are strongly depending on both S_e and the ion velocity.

8.5 Structural Transformations at High Fluences

The previous section dealt with the formation of individual ion tracks observed in solids irradiated with swift ions at low ion fluences (<10^{12} cm^{-2}). This section reports the large variety of structural transformations occurring in metals and insulators irradiated at high fluences where individual tracks begin to overlap. Experimental evidences of typical structural transformations are first examined in different types of solids. Materials modifications are then interpreted in the framework of the phenomenological models described in Chap. 3 of this book.

8.5.1 Experimental Observations of Structural Transformations

When individual ion tracks overlap, crystalline solids experience a large variety of structural transformations depending on their physico-chemical properties. Irradiation may lead to the formation of damaged layers with a given density of (more or less) complex damage, such as defect clusters, dislocation loops, network of dislocations, may induce the formation of amorphous layers over the whole ion paths or may even cause partial or total phase modifications occurring in one or several steps.

A rather broad panoply of advanced techniques, which sense the investigated materials at various spatial scales and with different sensitivities, can be implemented to investigate the structural transformations occurring in solids irradiated with swift ions. Among them, Rutherford backscattering spectrometry in channeling conditions (RBS/C), X-ray diffraction (XRD), transmission electron microscopy (TEM), and Raman spectroscopy were most often implemented in order to: (i) monitor the damage build-up, (ii) quantify the strain/stress level as a function of ion fluence, (iii) characterize radiation defects, (iv) determine the formation of new structures or phases, (v) specify the parameters which trigger the micro- and macro-structural changes, (vi) understand the mechanisms involved in the structural transformations. Experimental results may then feed databases, be compared to computational works, using for instance ab initio calculations or molecular dynamics simulations, and finally help the development of theoretical models or at least of phenomenological descriptions.

The first materials to be examined are pure metals which are known to be very weakly sensitive to electronic excitation [48, 147]. The first radiation-induced phase transformation in metals was observed in Ti [50, 51]. In this material, a TEM study demonstrated the occurrence of a α-ω phase transition (i.e. from a compact hexagonal phase to a distorted hexagonal phase generally obtained under pressure), which takes place only at low temperature (below 80 K), at high fluence (above 10^{12} cm^{-2}) and for an electronic stopping power higher than $\sim$30 keV nm^{-1}.

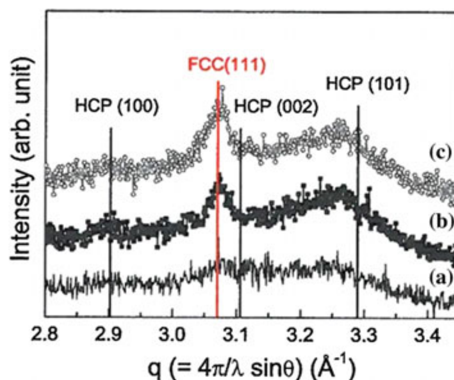

Fig. 8.23 XRD pattern of Co films before (**a**) and after irradiation with 120-MeV Au ions at 5×10^{12} cm^{-2} (**b**) and 5×10^{13} cm^{-2} (**c**) [148]

A high saturation resistivity increase and a significant volume change were also observed since the ω phase is denser than the α phase.

Another example of phase transformation induced in metals by electronic excitation is provided by the case of the hcp-fcc transition observed in Co thin films deposited on a Si substrate upon irradiation with swift heavy ions [148]. Figure 8.23 presents XRD patterns which show the progressive occurrence of the fcc phase as the irradiation fluence increases. This result is confirmed by the study of the magnetic properties of Co films. The as-deposited films show the uniaxial magnetic anisotropy with an in-plane coercive field characteristic of the hcp-Co phase, whereas a fourfold anisotropic pattern is exhibited on swift ion irradiated films which indicates the formation of the fcc-Co phase. Actually, earlier studies showed that phase transformations mainly occur in metals exhibiting high-pressure phases in the pressure-temperature diagram.

Several phase transformations upon swift ion irradiation were also observed in metallic alloys. Amorphization was obtained in Ni_3B [149] and $NiZr_2$ [48] in particular conditions (high fluences, low irradiation temperature). In the austenite phase of Cu-Zn-Al, particles with close-packed structures were formed on the irradiated surface [150], but similar microstructural changes have also been noticed following low-energy ion irradiation. In vacuum deposited FeNiCr multilayers, swift ion irradiation led to the observation of metastable highly-disordered ferromagnetic and paramagnetic phases with a relative amount increasing with increasing ion fluence [151].

An interesting case is the behavior of quasicrystals upon irradiation with swift ions. The stability of this particular phase was examined on AlCuFe and ZrTiNiCu [152]. The results seem to strongly depend on the materials considered. Whereas one might have expected irradiation to induce a phase transition from the icosahedral to a rhombohedral phase in AlCuFe, only minor structural modifications were observed in this compound. Conversely, amorphization was observed for irradiation to a fluence of 10^{13} cm^{-2} above an electronic energy loss threshold of $\sim$20 keV nm^{-1} in ZrTiNiCu, as demonstrated by the XRD data presented in Fig. 8.24d where the sharp peaks vanish and a broad bump appears at $2\theta \sim 36°$.

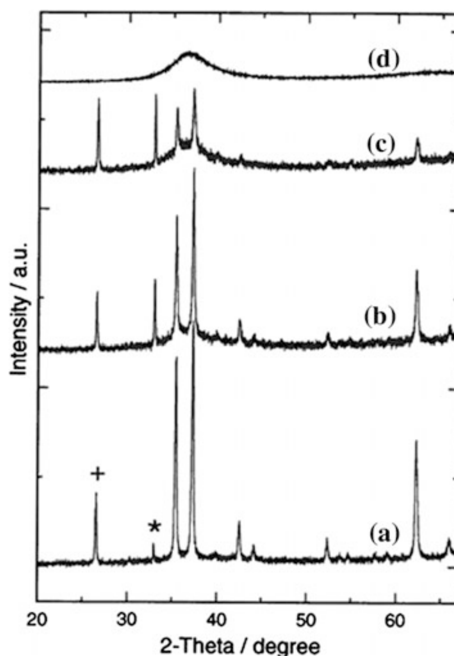

Fig. 8.24 XRD patterns of quasicrystalline $Zr_{64.5}Ti_{11.4}Ni_{13.8}Cu_{10.3}$ before (**a**) and after irradiation with 593-MeV Au ions at 5×10^{11} cm^{-2} (**b**), 1.3×10^{12} cm^{-2} (**c**) and 10^{13} cm^{-2} (**d**) [152]

In the case of insulators, ceramics with the fluorite structure (yttria-stabilized cubic zirconia (c-ZrO_2), ceria (CeO_2), thoria (ThO_2) and urania (UO_2)) are particularly resistant to electronic excitation [28, 38, 68–73, 153–155]. Irradiation of this kind of materials with swift heavy ions does not induce any phase transformation but is generally responsible for the formation of a network of tangled dislocations at high fluences (above 10^{12} cm^{-2}) (Fig. 8.25 [28]). The formation of nanodomains, that are slightly disoriented from the main crystallographic direction, and the production of a large amount of fission gases could be an explanation of the high burn-up structure (known as RIM effect) observed in the nuclear fuel. An increase of the irradiation temperature generally leads to a decrease of the global disorder with an enhancement of the formation rate of dislocation loops.

Another category of materials to be considered concerns unstable solids for which swift ion irradiation leads to amorphization of the irradiated layer. This is the case for many insulating compounds in which swift ion irradiation creates amorphous ion tracks (see Sect. 8.4.2) and thus leads to total amorphization of the irradiated layer when ion tracks overlap. A typical example is provided by titanate pyrochlores [108–112, 156–159] and is illustrated in Fig. 8.26 [111]. Irradiation of $Gd_2Ti_2O_7$ with swift heavy ions induces the formation of an amorphous layer clearly evidenced by the Raman mapping of Fig. 8.26 (left) where the narrow peaks at 305 and 510 cm^{-1} are characteristic of the crystalline phase (they disappear at the surface of the sample) and the vibrational mode at 767 cm^{-1} may be attributed to the amorphous phase (it vanishes above 20 μm where the crystal is not affected by

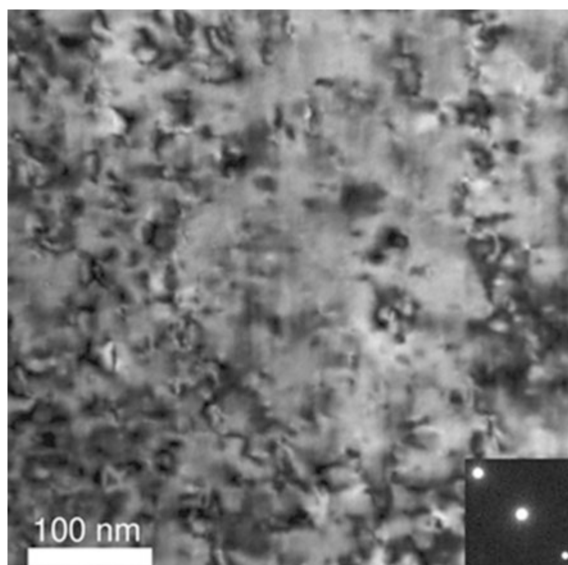

Fig. 8.25 TEM micrograph from a cubic zirconia crystal irradiated with 940-MeV Pb ions at 2×10^{12} cm^{-2} showing the formation of a network of dislocations [28]

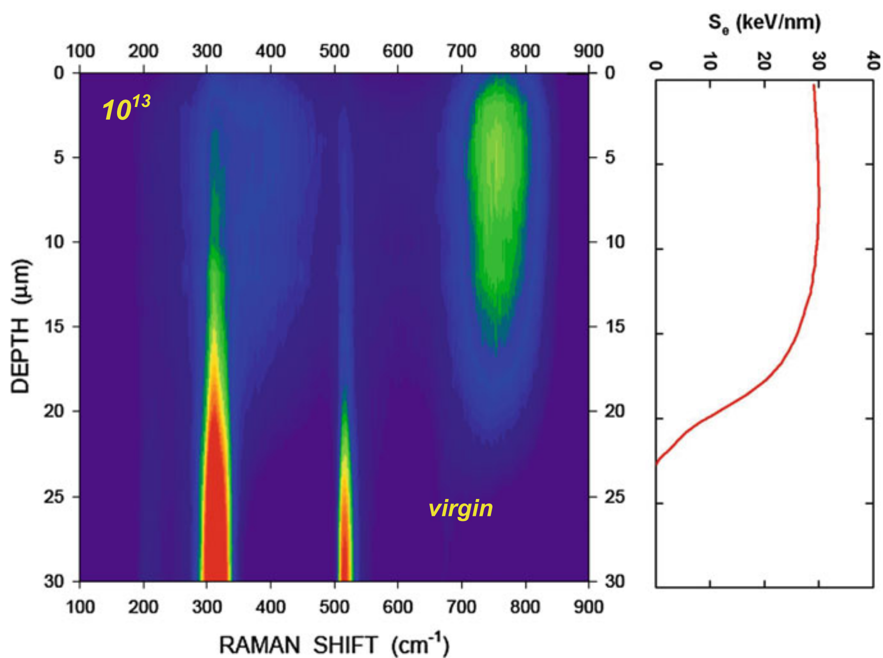

Fig. 8.26 (*Left*) Raman cartography made of spectra recorded at different depths on a $Gd_2Ti_2O_7$ crystal irradiated with 870-MeV Xe ions at 10^{13} cm^{-2}; (*Right*) Variation of the electronic energy loss (S_e) with depth for 870-MeV Xe ions in $Gd_2Ti_2O_7$ [111]

irradiation). These experiments show that the thickness of the amorphous layer (~ 15 μm) fits remarkably well the electronic energy deposition represented in Fig. 8.26 (right). Other examples of amorphization by swift ions are provided by SiO_2 [75], TiO_2 [79, 80], $ThGeO_4$ in both zircon (Z) and scheelite (S) phases [160], fluoroapatite ($Ca_{10}(PO_4)_6F_2$) [58–61], and $A_3B_5O_{12}$ garnets where A is Y, Ba, Gd and B is Al, Fe, Ga [13, 35, 44, 139–144].

A large variety of phase transformations may also occur in different classes of solids irradiated with swift ions. The first crystalline phase transition driven by swift ions in oxides was observed in yttria (Y_2O_3) [90, 160–162]. This cubic-monoclinic transition was also obtained at high pressure, under shock compression, and by the creation of oxygen vacancies. The most extensive work certainly concerns monoclinic zirconia (m-ZrO_2) and hafnia (HfO_2) [163–168]. Figure 8.27 shows XRD patterns recorded on m-ZrO_2 irradiated with swift ions, where it is observed that the peaks at 28.2° and 31.5° due to the monoclinic phase are highly reduced after irradiation, whereas a new peak located at 30.4° which may be attributed to the tetragonal phase appears [167]. After irradiation to the highest fluence (3.5×10^{12} cm^{-2}), only the new peak is plainly visible, while the peaks of the monoclinic phase vanish. Thus, contrarily to the case of its cubic counterpart, monoclinic zirconia experiences a clear transformation from the monoclinic towards the tetragonal phase upon irradiation with swift ions. It should be noticed that this monoclinic-tetragonal phase transition was also observed upon irradiation with low-energy ions and by simple thermal annealing [169, 170]. It was thus assumed that the thermal spike temperature created by swift ions may exceed the phase transition temperature (1170 °C). Nanocrystalline m-ZrO_2 (with a grain size

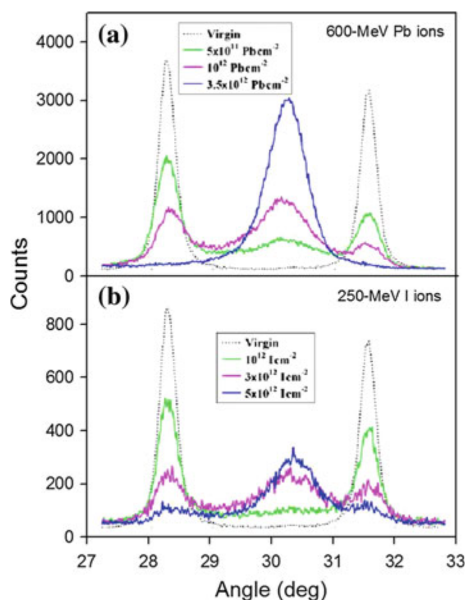

Fig. 8.27 Evolution of XRD patterns recorded on monoclinic zirconia irradiated with swift heavy ions at various fluences [167]

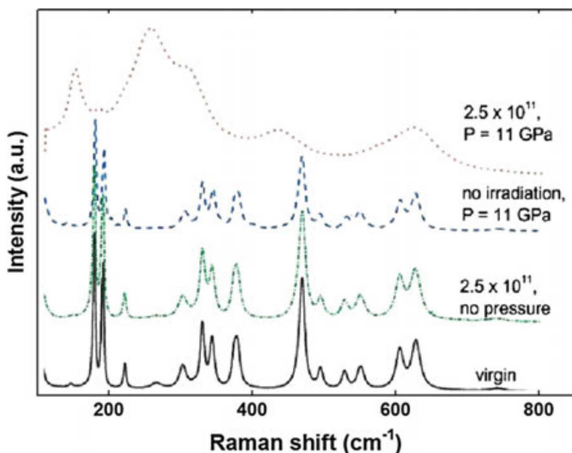

Fig. 8.28 Raman spectra recorded on monoclinic zirconia submitted to swift ion irradiation (*dash-dotted line*), high pressure (*dashed line*) and both irradiation and pressure (*dotted line*) [171]

of 40–50 nm) was amorphized upon irradiation with GeV Au and U ions [168]. This result indicates that materials which are highly radiation tolerant in bulk forms may well be radiation sensitive with a reduced length scale.

The combination of irradiation and pressure plays a crucial role in the monoclinic-tetragonal phase transformation mechanism [171, 172]. Raman spectra of Fig. 8.28 show that neither pressure nor irradiation alone can provoke such a phase transition. The pressure must exceed a value of 11 GPa in order to initiate the transformation and further pressure increase enhances the process.

Swift ion irradiation of calcite ($CaCO_3$) single crystals led to the observation of a calcite-vaterite phase transformation using Raman and infrared spectroscopy [173]. The anatase structure of annealed TiO_2 thin films was shown to be almost totally converted to a rutile phase upon irradiation at RT with 200-MeV Ag ions [174]. Copper oxides also present an interesting behavior, since they exist in two stoichiometric forms: cuprous oxide (Cu_2O) and cupric oxide (CuO) having cubic and monoclinic structures, respectively. Swift ion irradiation has been shown to convert the monoclinic CuO phase to the cubic Cu_2O phase [175], revealing interesting applications for solar cells.

Phase transformations were also observed in δ-phase oxides. A striking example is provided by $Sc_4Zr_3O_{12}$ and $Lu_4Zr_3O_{12}$ [104]. Figure 8.29 shows XRD patterns obtained from $Sc_4Zr_3O_{12}$ (a) and $Lu_4Zr_3O_{12}$ (b) samples irradiated with 185-MeV Au ions. The structure of $Sc_4Zr_3O_{12}$ can be described as an ordered rhombohedral δ-phase, which is represented by the peaks labeled R in Fig. 8.29. Upon ion irradiation, the δ-phase R peaks decrease in intensity with increasing ion fluence and almost completely vanish at 10^{13} cm^{-2}. The four major diffraction peaks (labeled F) are associated with the parent fluorite structure. Moreover, the absence of the weaker δ-phase (R) reflections with increasing ion fluence suggests that $Sc_4Zr_3O_{12}$ and $Lu_4Zr_3O_{12}$ gradually undergo an O-D transformation from an ordered δ-phase structure to a disordered fluorite structure. One difference between the structural

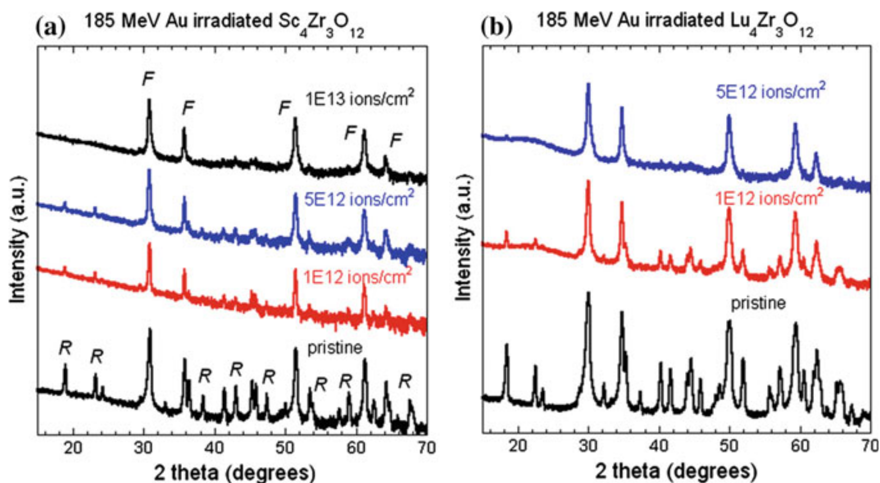

Fig. 8.29 XRD patterns obtained from $Sc_4Zr_3O_{12}$ (**a**) and $Lu_4Zr_3O_{12}$ (**b**) before and after irradiation with 185-MeV Au ions [104]

evolution of $Sc_4Zr_3O_{12}$ and $Lu_4Zr_3O_{12}$ is that for $Lu_4Zr_3O_{12}$ all R peaks associated with the δ-phase disappear, leaving only F peaks at a fluence of 5×10^{12} cm^{-2}. This effect occurs at lower ion fluence for $Lu_4Zr_3O_{12}$ as compared to $Sc_4Zr_3O_{12}$. No irradiation-induced amorphization was observed in these compounds.

Pyrochlores with the $A_2B_2O_7$ stoichiometry are fascinating materials to study phase transformations induced by irradiation with swift ions. The variety of the pyrochlore chemistry leads to a remarkable versatility of the physico-chemical properties of these compounds, and their stability seems to be essentially governed by the ratio of the ionic radii of A and B cations (r_A/r_B). For instance, in the $Gd_2(Zr_xTi_{1-x})_2O_7$ series, the susceptibility to radiation-induced disordering (amorphization) exhibits a systematic decrease with increasing Zr content: whereas $Gd_2Ti_2O_7$ is readily amorphized, the end member $Gd_2Zr_2O_7$ is transformed into a radiation resistant anion-deficient fluorite structure upon irradiation at room temperature [17, 108–112, 156–159]. Irradiation with swift heavy ions of many pyrochlores has shown a great variety of behaviors [113] which are represented in Fig. 8.30. In the case of $Gd_2Ti_2O_7$ and Gd_2ZrTiO_7, a gradual vanishing of all diffraction peaks and the observation of additional diffuse scattering indicate progressive amorphization of samples, with a rate which is decreased for Gd_2ZrTiO_7. Conversely, for the zirconate pyrochlores the diffraction peaks related to the supercell of the pyrochlore structure (stars) disappear and only the peaks corresponding to the fluorite structure are observed at 5×10^{12} cm^{-2}, indicating the occurrence of an order-disorder phase transition. Moreover, the intensity of the broad amorphous peak, which appears around 30° above 5×10^{12} cm^{-2}, depends on the nature of the A cation: $Nd_2Zr_2O_7$ is totally amorphized, while the peaks related to the fluorite phase are always visible in other zirconate pyrochlores.

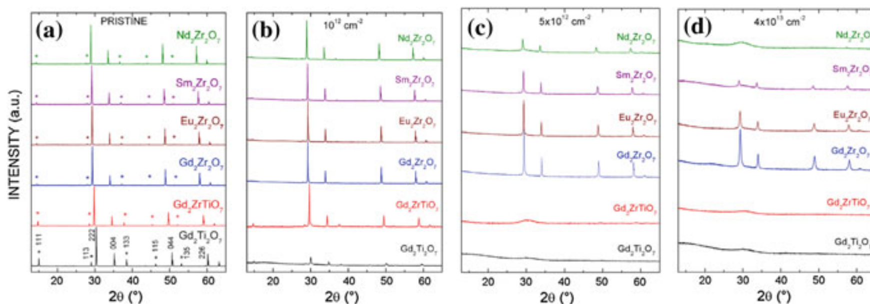

Fig. 8.30 XRD patterns recorded on pyrochlores before (**a**) and after irradiation with 120-MeV U ions at the indicated fluences (**b–d**). The peaks corresponding to the supercell of the pyrochlore structure are indicated by stars [113]

As mentioned previously, an interesting topic is the comparison of results obtained by performing irradiation or by applying pressure, or even by combining both solicitations for a given material. Pyrochlores have been the subject of such an investigation [110, 176]. Figure 8.31 shows XRD patterns recorded on $Gd_2Zr_2O_7$ as a function of releasing pressure in unirradiated or swift-ion irradiated samples [110]. The pyrochlore structure of $Gd_2Zr_2O_7$ is only stable below $\sim$20 GPa and, above this pressure, a cotunnite-like structure is formed (see the peaks at 9° and 12° in Fig. 8.31a—43.2 GPa). During decompression, the cotunnite high-pressure

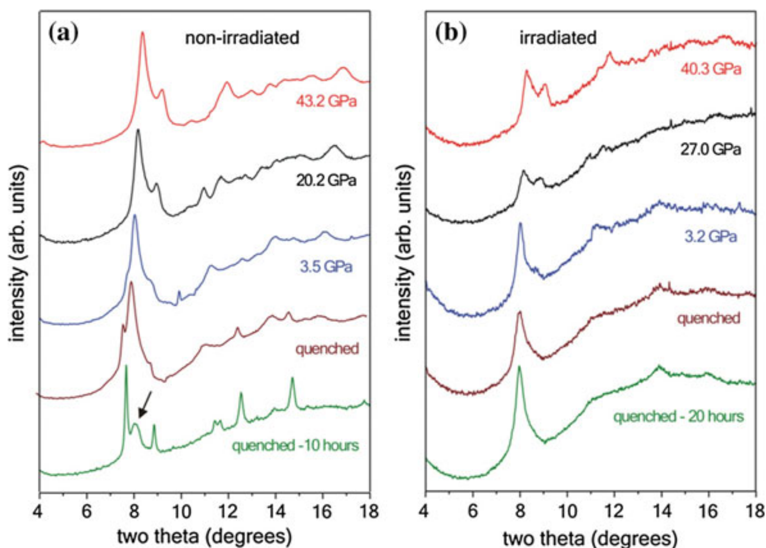

Fig. 8.31 Synchrotron XRD patterns recorded on $Gd_2Zr_2O_7$ as a function of releasing pressure in an unirradiated sample (**a**), or in a sample irradiated with 4-GeV Xe ions at 3×10^{12} cm^{-2} (**b**) [110]

phase gradually transforms to a disordered defect-fluorite structure. This defect-fluorite structure is also the stable phase occurring in swift-ion irradiated $Gd_2Zr_2O_7$. When both pressure and irradiation are combined, the cotunnite phase is also formed (Fig. 8.31b—40.3 GPa). However, when pressure is released, a new phase of unknown structure is observed in the irradiated sample (Fig. 8.31b—3.2 GPa). Thus, the ion-matter interactions in the cotunnite-like structure have obviously accelerated the transformation to the new phase during pressure release and, more importantly, have triggered a remarkable stabilization of this novel structure. Finally, the substitution of Ti for Zr at the B-site significantly increases the pressure required for the transformation to the high-pressure phase [110].

8.5.2 Analysis of the Build-Up of Radiation-Induced Structural Transformations with Phenomenological Models

In amorphizable materials, the structural transformation build-up due to swift ion irradiation may be described in the framework of the direct impact model (see Chap. 3 of this book), since one ion impact is most often sufficient to totally transform the matter inside an ion track, the overall microstructure observed at high fluences resulting from the overlapping of a large number of tracks. Therefore, the amorphization build-up follows the following equation:

$$f = f_{sat}[1 - \exp(-\sigma\,\phi t)] \tag{8.2}$$

where f_{sat} is the amorphized fraction at saturation (i.e. $f_{sat} = 1$ for total amorphization), σ is the amorphization cross section and ϕt is the ion fluence.

An example of direct amorphization is provided by titanate pyrochlores (e.g. $Gd_2Ti_2O_7$) for which f_{sat} reaches unity at high fluences whatever the experimental technique used to monitor amorphization (see Fig. 8.32) [112]. In this case, the value obtained for σ (46 nm^2) gives the diameter of amorphous ion tracks according to (8.1) in Sect. 8.3.2.

Irradiation of oxides with the fluorite structure (e.g. yttria-stabilized cubic zirconia) generally leads to accumulated disorder build-ups that are reasonably fitted by using the model of direct-ion impact represented by (8.2) (see Fig. 8.33) [28]. However, the fact that f_{sat} is often lower than 1 for these materials indicates that either the transformation is not total, or the technique used to obtain the transformation build-up is sensitive to a particular atomic configuration. In the case of cubic zirconia, the formation of a network of dislocations sensed by channeling leads to a saturation value of the transformed fraction which measures the sensitivity of the channeling technique to this particular type of damage. Nevertheless, the value obtained for σ provides a value of the diameter of cylinders from which matter is ejected towards the surface of crystals and around which dislocation loops are

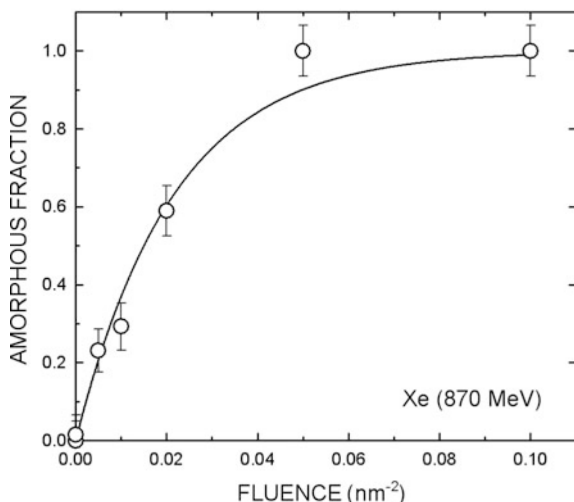

Fig. 8.32 Variation of the amorphous fraction versus the ion fluence for $Gd_2Ti_2O_7$ crystals irradiated with 870-MeV Xe ions [112]. The *line* is a fit to the data with (8.2)

formed at low fluence. This diameter is very close to that measured directly by TEM. As it is shown in Fig. 8.33, the values of f_{sat} and σ strongly depend on both the mass and the energy of incoming ions via the electronic energy deposition. Moreover, very week damage is created below a S_e threshold which generally depends on the investigated material.

The situation is often more complex when swift ion irradiation leads to the formation of new phases. An example is provided by the monoclinic-tetragonal phase transformation obtained upon swift ion irradiation of monoclinic zirconia [167]. The rate of monoclinic-tetragonal phase transformation obtained using XRD (see Fig. 8.34) is poorly accounted for by using (8.2) (dashed line). A reliable fit of XRD data requires the use of the general Gibbons overlap model (see Chap. 3):

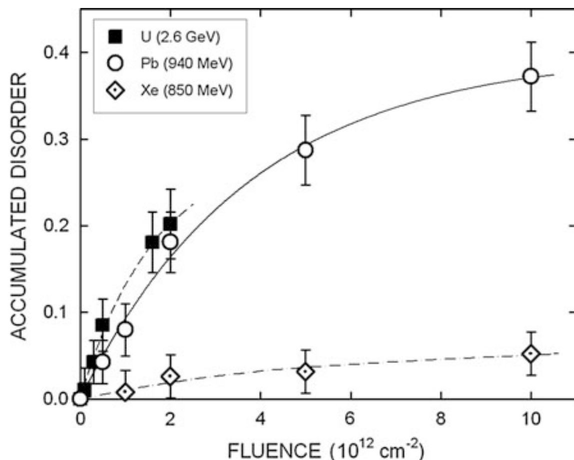

Fig. 8.33 Variation of the accumulated disorder versus the ion fluence for cubic zirconia crystals irradiated with various swift heavy ions [28]. *Lines* are fits to the data with (8.2)

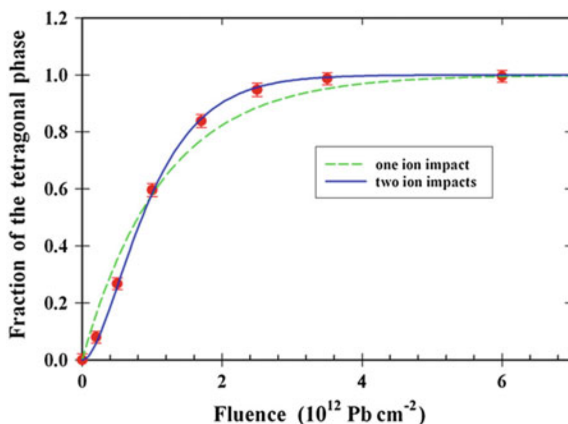

Fig. 8.34 Variation of the fraction of tetragonal phase versus the ion fluence for monoclinic zirconia irradiated with 600-MeV Pb ions [167]. *Dashed* and *solid lines* are fits to the data with (8.2) and (8.3), respectively

$$f = 1 - \sum_{k=0}^{m-1} \frac{(\sigma\,\phi t)^k}{k!} \exp(-\sigma\,\phi t) \tag{8.3}$$

where m is the number of ion impacts required to transform a given volume of the sample, σ is the transformation cross section, and ϕt is the ion fluence.

The phase transformation build-up shown in Fig. 8.34 may accurately be reproduced using (8.3) with two ion impacts (and not only one) for completing the phase transformation process (solid line). In this description, the first ion is assumed to create defects, mainly oxygen vacancies, which generate a large strain field and might be responsible for lowering the transition temperature. These local strain fields are necessary to trigger the phase transformation by the second ion impact.

When pressure is applied during irradiation of the same material, the phase transformation follows a single ion impact process [108, 110]. The role of pressure is to induce a strain that otherwise has to be created by the first ion impact. In this case, the first ion takes over the role of the second ion in triggering the phase transition and a double impact is no longer necessary. This feature could also explain why the transformation appears only locally within the sample.

Complex oxides may exhibit rather complicated behaviors upon irradiation. Figure 8.35 compares the phase transformation build-ups of a given phase (pyrochlore, fluorite or amorphous) obtained for typical pyrochlores [113]. These data were extracted from the analysis of the X-ray diffraction patterns shown in Fig. 8.30, and have been confirmed by TEM experiments (see tracks in Fig. 8.18). The results indicate that only a pyrochlore (P) → amorphous (A) transformation is observed for $Gd_2Ti_2O_7$ and only a pyrochlore (P) → anion-deficient fluorite (F) transformation occurs in $Gd_2Zr_2O_7$. For the other compositions (e.g. $Nd_2Zr_2O_7$), P → A and P → F phase transformations are observed simultaneously at low fluence, whereas a F → A phase transformation occurs at higher fluences.

The direct ion impact model, formalized by (8.2), and even the general Gibbons overlap model, formalized by (8.3), fail to interpret intricate phase transformation

build-ups similar to those exhibited in Fig. 8.35. A new model (heterogeneous track overlap model—HTOM), which considers that phase transformations result from the overlapping of heterogeneous tracks, was thus derived to account for these complex results [113]. This model assumes that an ion impinging into a virgin region of a sample (labelled V) creates a track composed of two regions with either a stable (labelled S) or a metastable (labelled M) structure, and that a second ion impact does not influence the stable region but transforms the metastable region into the stable one. Thus the variation of the fractions (f_V, f_M and f_S) of virgin, metastable and stable regions with the ion fluence may be written:

$$f_V = \exp[-(\sigma_S + \sigma_M)\phi t] \tag{8.4a}$$

$$f_M = \sigma_M \phi t \, \exp[-(\sigma_S + \sigma_M)\phi t] \tag{8.4b}$$

$$f_S = 1 - \exp[-(\sigma_S + \sigma_M)\phi t](1 + \sigma_M \phi t) \tag{8.4c}$$

where σ_S and σ_M are the cross sections related to the virgin-stable and virgin-metastable transitions, respectively.

The complex phase transformation build-ups represented in Fig. 8.35 may be interpreted in the framework of the HTOM model using (8.4a)–(8.4c). In these equations, since the virgin, metastable and stable regions have pyrochlore, fluorite and amorphous structures, respectively, the fractions f_V, f_M and f_S may be relabelled f_P, f_F and f_A, and the cross sections σ_S and σ_M may be relabelled σ_A and σ_F, respectively.

The values of σ_i obtained from the fits to the phase transformation build-ups of Fig. 8.35 with (8.4a)–(8.4c) depend on the chemical composition of pyrochlores, i.e. on the cation radius ratio, r_A/r_B (see Fig. 8.36 [113]). It is shown that σ_A clearly increases with increasing r_A/r_B, whereas σ_F globally decreases as r_A/r_B increases with a stable value around 50 nm^2 for r_A/r_B between 1.5 and 1.6. The former result indicates that the susceptibility to amorphization by electronic excitation of the pyrochlore phase increases with increasing r_A/r_B; the latter result suggests that,

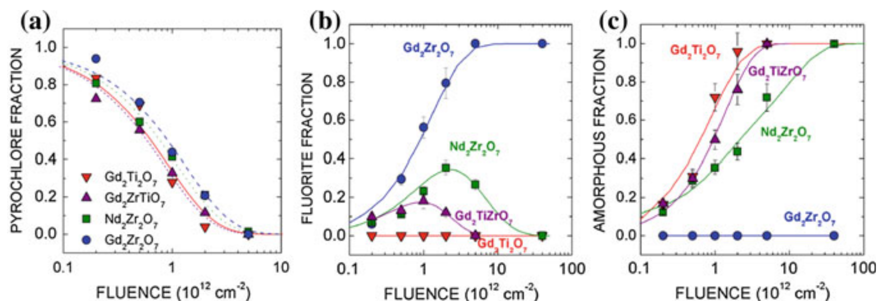

Fig. 8.35 Fraction of pyrochlore (**a**), fluorite (**b**) and amorphous (**c**) phases versus ion fluence for pyrochlores irradiated with 120-MeV U ions [113]. *Solid lines* are fits to the data with (8.4a)–(8.4c)

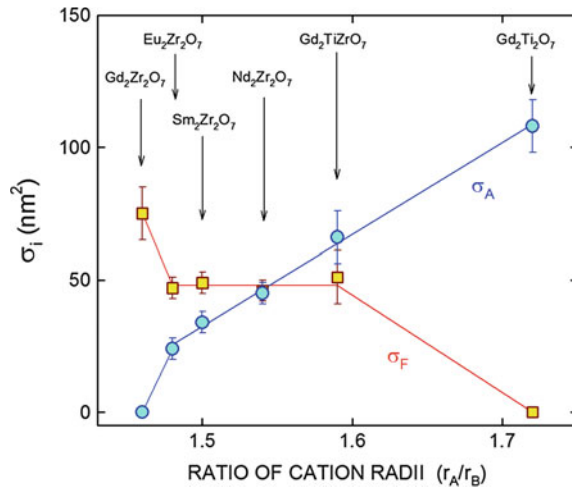

Fig. 8.36 Variation of σ_A and σ_F, calculated from the fits to XRD data of Fig. 8.35 with (8.4a)–(8.4c), versus the ratio of the ionic radii of A and B cations (r_A/r_B) [113]

except for the extreme compositions ($Gd_2Zr_2O_7$ and $Gd_2Ti_2O_7$), the rate of formation of the fluorite phase is almost independent of the sample composition. Moreover, these data demonstrate that the radiation resistance of pyrochlores depends more on the cation radius ratio (both B and A cations play a significant role in the amorphization process) than on the B cation itself (e.g. whether the sample contains Ti or Zr elements).

8.6 Summary

Electronic excitation and ionization processes occurring in solids irradiated with swift heavy ions lead to the creation of cylindrical damaged regions (tracks) at low ion fluences which overlap to form a specific microstructure when the ion fluence is increased above typically $\sim 10^{12}$ cm^{-2}. Ion tracks and structural modifications may be detected using either local microscopic observation by TEM, AFM or SAXS, or global techniques such as RBS/C, XRD, UV, IR or Raman spectroscopy (Sect. 8.3).

The possibility to form ion tracks depends on the energy density deposited by the irradiating ions, on the investigated material and on the temperature at which irradiation is performed. Thus, tracks were rarely detected in metals and metallic alloys (Sect. 8.4.1) since conduction electrons easily smear out the perturbation caused by the passage of swift ions. Exceptions to this rule are provided by Ti, Bi or Ni-Zr alloys: in these solids discontinuous tracks were observed when irradiations were performed at cryogenic temperatures and for high values of S_e (generally above 30–40 keV nm^{-1}). On the contrary, tracks with a large variety of inner structures, often accompanied by hillocks at the surface of samples, are generally easily formed in insulators (Sect. 8.4.2). Complex oxides (spinel, δ-phase

perovskite and pyrochlore compounds) offer ideal systems to study the mechanisms of track formation since their radiation behaviour generally depends on the atomic radius of their cations. An example is provided by the $Gd_2Zr_{2-x}Ti_xO_7$ pyrochlore family where it was shown that the diameter and the morphology of ion tracks are directly linked to the cationic Ti/Zr ratio.

When individual ion tracks overlap, irradiated solids exhibit a large panoply of structural modifications: formation of damage clusters and/or dislocations, partial or total phase transformations, polygonization, amorphization, which depend on the physico-chemical properties of targets and occur in one or several steps (Sect. 8.5.1). Insulators with the fluorite structure (cubic ZrO_2, CeO_2, ThO_2 and UO_2) were demonstrated to be particularly resistant to electronic excitation, whereas some simple oxides or compounds (SiO_2, TiO_2, zircon, garnets, apatites, titanate pyrochlores) are much more unstable since swift heavy ion irradiation leads to amorphization of the irradiated layer. Other insulators (Y_2O_3, $CaCO_3$, monoclinic ZrO_2, HfO_2, δ-phase oxides, zirconate pyrochores) experience specific phase tranformations. This chapter also reports a few results obtained for pyrochlores in the aim of comparing the structural modifications observed by performing swift ion irradiation, by applying pressure or by combining both solicitations.

More or less sophisticated phenomenological models were developed to account for the structural transformation build-ups occurring in both amorphizable and non-amorphizable solids irradiated with swift ions (Sect. 8.5.2). The interpretation of experimental data using those models allow the determination of interesting parameters, such as the fraction of new phases and the transformation cross-sections, for the different phase transitions induced all along the irradiation process.

References

1. J.F. Ziegler, J.P. Biersack, U. Littmark, The stopping and range of ions, in *Solids*, vol. 1, ed. by J.F. Ziegler (Pergamon, New York, 1985)
2. F. Seitz, J.S. Koehler, Solid state physics: advances in research and applications, ed. F. Seitz, D. Turnbull (Academic, NY, 1956), p. 305
3. M. Toulemonde, C. Dufour, E. Paumier, Phys. Rev. B **46**, 14362 (1992)
4. G. Szenes, Phys. Rev. B **51**, 8026 (1995)
5. H. Trinkaus, A.I. Ryazanov, Phys. Rev. Lett. **74**, 5072 (1995)
6. R.L. Fleischer, P.B. Price, R.M. Walker, J. Appl. Phys. **36**, 3645 (1965)
7. L.E. Seiberling, J.E. Griffith, T.A. Tombrello, Rad. Eff. **52**, 201 (1980)
8. D. Lesueur, A. Dunlop, Radiat. Eff. Def. Solids **126**, 105 (1993)
9. D.A. Young, Nature **183**, 375 (1958)
10. E. Silk, R. Barnes, Phil. Mag. **4**, 970 (1959)
11. M. Toulemonde, W. Assmann, C. Dufour, A. Meftah, C. Trautmann, Nucl. Instrum. Meth. B **277**, 28 (2012)
12. D. Groult, M. Hervieu, N. Nguyen, B. Raveau, J. Sol. State Chem. **76**, 248 (1988)
13. M. Toulemonde, F. Studer, Phil. Mag. A **58**, 799 (1988)
14. C. Houpert, F. Studer, D. Groult, M. Toulemonde, Nucl. Instrum. Meth. B **39**, 720 (1989)
15. L.A. Bursill, G. Braunshausen, Phil. Mag. **62**, 395 (1990)

16. C. Träholt, J. Wiesner, H.W. Zandbergen, H. Fuess, G. Wirth, J.G. Wen, Physica C **268**, 161 (1996)
17. J. Zhang, M. Lang, R.C. Ewing, R. Devanathan, W.J. Weber, M. Toulemonde, J. Mater. Res. **25**, 1344 (2010)
18. I. Joswik-Biala, J. Jagielski, B. Arey, L. Kovarik, G. Sattonnay, A. Debelle, S. Mylonas, I. Monnet, L. Thomé, Acta Mater. **61**, 4669 (2013)
19. F. Thibaudau, J. Cousty, E. Balanzat, S. Bouffard, Phys. Rev. Lett. **67**, 1582 (1991)
20. D.D.N. Barlo Daya, A. Hallen, J. Eriksson, J. Kopniczky, R. Papaléo, C.T. Reimann, P. Hakansson, B.U.R. Sundqvist, A. Brunelle, S. Della-Negra, Y. Le Beyec, Nucl. Instrum. Meth. B **106**, 38 (1995)
21. J. Ackermann, N. Angert, R. Neumann, C. Trautmann, M. Dischner, T. Hagen, M. Sedlacek, Nucl. Instrum. Meth. B **107**, 181 (1996)
22. I.H. Wilson, J.B. Xu, R.A.B. Devine, R.P. Webb, Nucl. Instrum. Meth. B **118**, 473 (1996)
23. L.P. Biro, J. Gyulai, K. Havancsak, Nucl. Instrum. Meth. B **122**, 476 (1997)
24. M. Yamamoto, N. Yasuda, M. Kurano, T. Kanai, A. Furukawa, N. Ishigure, K. Ogura, Nucl. Instrum. Meth. B **152**, 349 (1999)
25. C. Müller, K.O. Voss, M. Lang, R. Neumann, Nucl. Instrum. Meth. B **212**, 318 (2003)
26. N. Khalfaoui, C.C. Rotaru, S. Bouffard, M. Toulemonde, J.P. Stoquert, F. Haas, C. Trautmann, J. Jensen, A. Dunlop, Nucl. Instrum. Meth. B **240**, 819 (2005)
27. D. Schwen, E. Bringa, J. Krauser, A. Weidinger, C. Trautmann, H. Hofsäss, Appl. Phys. Lett. **101**, 113115 (2012)
28. S. Moll, L. Thomé, L. Vincent, F. Garrido, G. Sattonnay, T. Thomé, J. Jagielski, J.M. Costantini, J. Appl. Phys. **105**, 023512 (2009)
29. V.A. Skuratov, S.J. Zinkle, A.E. Efimov, K. Havancsak, Nucl. Instrum. Meth. B **203**, 136 (2003)
30. C. Scott, R. Smith, K.E. Sickafus, Nucl. Instrum. Meth. B **269**, 1625 (2011)
31. E. Dartyge, J. Phys. **39**, 1287 (1978)
32. D. Albrecht, P. Armbruster, R. Spohr, M. Roth, K. Schaupert, H. Stuhrmann, Appl. Phys. A **37**, 37 (1985)
33. K. Schwartz, C. Trautmann, C. Steckenreiter, O. Geiss, M. Krämer, Phys. Rev. B **58**, 11232 (1998)
34. B. Afra, M.D. Rodriguez, C. Trautmann, O.H. Pakarinen, F. Djurabekova, K. Nordlund, T. Bierschenk, R. Giulian, M.C. Ridgway, G. Rizza, N. Kirby, M. Toulemonde, P. Kluth, J. Phys.: Condens. Matter **25**, 045006 (2013)
35. A. Meftah, F. Brisard, J.M. Costantini, J.M. Hage-Ali, J.P. Stoquert, M. Toulemonde, Phys. Rev. B **48**, 920 (1993)
36. L. Thomé, J. Jagielski, L. Nowicki, A. Turos, A. Gentils, F. Garrido, Vacuum **78**, 401 (2005)
37. V. Chailley, E. Dooryhée, M. Levalois, Nucl. Instrum. Meth. B **107**, 199 (1996)
38. G. Sattonnay, M. Lahrichi, A. Benyagoub, J.M. Costantini, F. Garrido, L. Thomé, C. Trautmann, Nucl. Instrum. Meth. B **257**, 476 (2007)
39. A. Audouard, E. Balanzat, G. Fuchs, J.C. Jousset, D. Lesueur, L. Thomé, Europhys. Lett. **5**, 241 (1988)
40. J.M. Costantini, F. Brisard, A. Meftah, M. Toulemonde, Rad. Eff. Def. Sol. **126**, 233 (1993)
41. M.C. Busch, A. Slaoui, P. Siffert, E. Doorhyhee, M. Toulemonde, J. Appl. Phys. **71**, 2596 (1992)
42. S. Sorieul, J.M. Costantini, L. Gosmain, L. Thomé, J.J. Grob, J. Phys.: Condens. Matter **18**, 5235 (2006)
43. S. Sorieul, J.M. Costantini, L. Gosmain, G. Calas, J.J. Grob, L. Thomé, J. Phys.: Condens. Matter **18**, 8493 (2006)
44. M. Toulemonde, G. Fuchs, N. Nguyen, F. Studer, D. Groult, Phys. Rev. B **35**, 6560 (1987)
45. C. Trautmann, J.M. Costantini, A. Meftah, K. Schwartz, J.P. Stoquert, M. Toulemonde, Mater. Res. Soc. Symp. Proc. **504**, 123 (1998)
46. M. Toulemonde, W. Assmann, C. Dufour, A. Meftah, F. Studer, C. Trautmann, Mat. Fys. Medd. **52**, 263 (2006)

47. A. Audouard, E. Balanzat, S. Bouffard, J.C. Jousset, A. Chamberod, A. Dunlop, D. Lesueur, G. Fuchs, R. Spohr, J. Vetter, L. Thomé, Phys. Rev. Lett. **65**, 875 (1990)
48. A. Barbu, A. Dunlop, D. Lesueur, R.S. Averback, Europhys. Lett. **15**, 37 (1991)
49. A. Dunlop, P. Legrand, D. Lesueur, N. Lorenzelli, J. Morillo, A. Barbu, S. Bouffard, Europhys. Lett. **15**, 765 (1991)
50. H. Dammak, A. Barbu, A. Dunlop, D. Lesueur, N. Lorenzelli, Phil. Mag. Lett. **67**, 253 (1993)
51. H. Dammak, A. Dunlop, D. Lesueur, A. Brunelle, S. Della-Negra, Y. Le Beyec, Phys. Rev. Lett. **74**, 1135 (1995)
52. S. Furuno, H. Otsu, K. Hoju, K. Izui, Nucl. Instrum. Meth. B **107**, 223 (1996)
53. M. Angiolini, H. Dammak, A. Dunlop, Phil. Mag. Lett. **82**, 81 (2002)
54. C. Dufour, A. Audouard, F. Beuneu, J. Dural, A. Hairie, M. Levalois, E. Paumier, M. Toulemonde, J. Phys. Cond. Matter **5**, 4573 (1993)
55. Z.G. Wang, C. Dufour, B. Cabeau, J. Dural, G. Fuchs, E. Paumier, F. Pawlak, M. Toulemonde, Nucl. Instrum. Meth. B **107**, 175 (1996)
56. S. Bouffard, C. Leroy, S. Della-Negra, A. Brunelle, J.M. Costantini, Phil. Mag. A **81**, 2841 (2001)
57. G. Jaskierowicz, A. Dunlop, R. Jonckheere, Nucl. Instrum. Meth. B **222**, 213 (2004)
58. S. Miro, D. Grebille, D. Chateigner, D. Pelloquin, J.P. Stoquert, J.J. Grob, J.M. Costantini, F. Studer, Nucl. Instrum. Meth. B **227**, 306 (2005)
59. J. Liu, U.A. Glasmacher, M. Lang, C. Trautmann, K.O. Voss, R. Neumann, G.A. Wagner, R. Miletich, Appl. Phys. A **91**, 17 (2008)
60. P. Schouwink, R. Miletich, A. Ullrich, U.A. Glasmacher, C. Trautmann, R. Neumann, B. P. Kohn, Phys. Chem. Miner. **37**, 371 (2010)
61. C. Weikusat, U.A. Glasmacher, B. Schuster, C. Trautmann, R. Miletich, R. Neumann, Phys. Chem. Miner. **38**, 293 (2011)
62. A. Perez, E. Balanzat, J. Dural, Phys. Rev. B **41**, 3943 (1990)
63. K. Schwartz, G. Wirth, C. Trautmann, T. Steckrenreiter, Phys. Rev. B **56**, 10711 (1997)
64. C. Trautmann, M. Toulemonde, J.M. Costantini, J.J. Grob, K. Schwartz, Phys. Rev. B **62**, 13 (2000)
65. M. Kumar, F. Singh, S.A. Khan, V. Baranwal, S. Kumar, D.C. Agarwal, A.M. Siddiqui, A. Tripathi, A. Gupta, D.K. Avasthi, A.C. Pandey, J. Phys. D Appl. Phys. **38**, 637 (2005)
66. C. Müller, A. Benyagoub, M. Lang, R. Neumann, K. Schwartz, M. Toulemonde, C. Trautmann, Nucl. Instrum. Meth. B **209**, 175 (2003)
67. K. Schwartz, A.E. Volkov, M.V. Sorokin, C. Trautmann, K.O. Voss, R. Neumann, M. Lang, Phys. Rev. B **78**, 024120 (2008)
68. T. Wiss, Hj. Matzke, C. Trautmann, M. Toulemonde, S. Klaumünzer, Nucl. Instrum. Meth. B **122,** 583 (1997)
69. Hj. Matzke, P.G. Lucuta, T. Wiss, Nucl. Instrum. Meth. B **166–167**, 920 (2000)
70. F. Garrido, S. Moll, G. Sattonnay, L. Thomé, L. Vincent, Nucl. Instrum. Meth. B **267**, 1451 (2009)
71. T. Sonoda, M. Kinoshita, N. Ishikawa, M. Sataka, A. Iwase, Nucl. Instrum. Meth. B **268**, 3277 (2010)
72. J.M. Costantini, C. Trautmann, L. Thomé, J. Jagielski, F. Beuneu, J. Appl. Phys. **101**, 073501 (2007)
73. G. Sattonnay, M. Lahrichi, M. Herbst-Ghysel, F. Garrido, L. Thomé, J. Appl. Phys. **101**, 103516 (2007)
74. M. Lang, J. Lian, F. Zhang, B.W.H. Hendriks, C. Trautmann, R. Neumann, R.C. Ewing, Earth Planet. Sci. Lett. **274**, 355 (2008)
75. A. Meftah, F. Brisard, J.M. Costantini, E. Doorhyee, M. Hage-Ali, M. Hervieu, J.P. Stoquert, F. Studer, M. Toulemonde, Phys. Rev. B **49**, 12457 (1994)
76. N. Khalfaoui, C.C. Rotaru, E. Jacquet, H. Lebius, M. Toulemonde, Nucl. Instrum. Meth. B **209**, 165 (2003)

77. O. Pena-Rodríguez, J. Manzano-Santamaria, A. Rivera, G. Garcia, J. Olivares, F. Agullo-Lopez, J. Nucl. Mater. **430**, 125 (2012)
78. G.A. Kachurin, S.G. Cherkova, D.V. Marin, V.G. Kesler, V.A. Volodin, V.A. Skuratov, Nucl. Instrum. Meth. B **282**, 68 (2012)
79. K. Nomura, T. Nakanishi, Y. Nagasawa, Y. Ohki, K. Awazu, M. Fujimaki, N. Kobayashi, S. Ishii, K. Shima, Phys. Rev. B **68**, 4106 (2003)
80. K. Awazu, X. Wang, M. Fujimaki, T. Komatsubara, T. Ikeda, Y. Ohki, J. Appl. Phys. **100**, 044308 (2006)
81. A. Berthelot, S. Hémon, F. Gourbilleau, C. Dufour, B. Domengès, E. Paumier, Phil. Mag. A **80**, 2257 (2000)
82. B. Canut, A. Benyagoub, G. Marest, A. Meftah, N. Moncoffre, S.M.M. Ramos, F. Studer, P. Thévenard, M. Toulemonde, Phys. Rev. B **51**, 12194 (1995)
83. T. Aruga, Y. Katano, T. Ohmichi, S. Okayasu, Y. Kazumata, Nucl. Instrum. Meth. B **166–167**, 913 (2000)
84. S.J. Zinkle, V.A. Skuratov, D.T. Hoelzer, Nucl. Instrum. Meth. B **191**, 758 (2002)
85. V.A. Skuratov, A.E. Efimov, K. Havancsak, Nucl. Instrum. Meth. B **250**, 245 (2006)
86. V.A. Skuratov, G. Bujnarowski, Y.S. Kovalev, J. O'Connell, K. Havancsak, Nucl. Instrum. Meth. B **268**, 3023 (2010)
87. V.A. Skuratov, N.S. Kirilkin, Y.S. Kovalev, T.S. Strukova, K. Havancsak, Nucl. Instrum. Meth. B **286**, 61 (2012)
88. A. Kabir, A. Meftah, J.P. Stoquert, M. Toulemonde, I. Monnet, Nucl. Instrum. Meth. B **266**, 2976 (2008)
89. A. Kabir, A. Meftah, J.P. Stoquert, M. Toulemonde, I. Monnet, M. Izerrouken, Nucl. Instrum. Meth. B **268**, 3195 (2010)
90. S. Hémon, C. Dufour, A. Berthelot, F. Gourbilleau, E. Paumier, S. Bégin-Collin, Nucl. Instrum. Meth. B **166–167**, 339 (2000)
91. C. Houpert, M. Hervieu, D. Groult, F. Studer, M. Toulemonde, Nucl. Instrum. Meth. B **32**, 393 (1988)
92. M. Treilleux, G. Fuchs, A. Perez, E. Balanzat, J. Dural, Nucl. Instrum. Meth. B **32**, 397 (1988)
93. F. Studer, C. Houpert, D. Groult, J.Y. Fan, A. Meftah, M. Toulemonde, Nucl. Instrum. Meth. B **82**, 91 (1993)
94. S.J. Zinkle, V.A. Skuratov, Nucl. Instrum. Meth. B **141**, 737 (1998)
95. D. Simeone, C. Dodane-Thiriet, D. Gosset, P. Daniel, M. Beauvy, J. Nucl. Mater. **300**, 151 (2002)
96. D. Gosset, D. Simeone, M. Dutheil, S. Bouffard, M. Beauvy, J. Eur. Ceram. Soc. **25**, 2677 (2005)
97. L. Thomé, J. Jagielski, A. Gentils, L. Nowicki, F. Garrido, Nucl. Instrum. Meth. B **242**, 643 (2006)
98. T. Yamamoto, M. Shimada, K. Yasuda, S. Matsumura, Y. Chimi, N. Ishikawa, Nucl. Instrum. Meth. B **245**, 235 (2006)
99. K. Yasuda, T. Yamamoto, M. Shimada, S. Matsumura, Y. Chimi, N. Ishikawa, Nucl. Instrum. Meth. B **250**, 238 (2006)
100. N. Pellerin, C. Dodane-Thiriet, V. Montouillout, M. Beauvy, D. Massiot, J. Phys. Chem. B **111**, 12707 (2007)
101. K. Yasuda, T. Yamamoto, S. Seki, K. Shiiyama, S. Matsumura, Nucl. Instrum. Meth. B **266**, 2834 (2008)
102. A. Quentin, I. Monnet, D. Gosset, B. Lefrançois, S. Bouffard, Nucl. Instrum. Meth. B **267**, 980 (2009)
103. K. Yasuda, T. Yamamoto, M. Etoh, S. Kawasoe, S. Matsumura, N. Ishikawa, Int. J. Mater. Res. **2011**(09), 1082 (2011)
104. M. Tang, P. Kluth, J. Zhang, M.K. Patel, B.P. Uberuaga, C.J. Olson Reichhardt, K.E. Sickafus, Nucl. Instrum. Meth. B **268**, 3243 (2010)
105. M. Tang, T.A. Wynn, M.K. Patel, J. Won, I. Monnet, J.C. Pivin, N.A. Mara, K.E. Sickafus, J. Nucl. Mater. **425**, 193 (2012)

106. M. Lang, F. Zhang, W. Li, D. Severin, M. Bender, S. Klaumünzer, C. Trautmann, R.C. Ewing, Nucl. Instrum. Meth. B **286**, 271 (2012)
107. C.L. Tracy, M. Lang, J. Zhang, F. Zhang, Z. Wang, R.C. Ewing, Acta Mater. **60**, 4477 (2012)
108. M. Lang, J. Lian, J.M. Zhang, F.X. Zhang, W.J. Weber, C. Trautmann, R.C. Ewing, Phys. Rev. B **79**, 4105 (2009)
109. J.M. Zhang, M. Lang, J. Lian, J. Liu, F.X. Zhang, C. Trautmann, S. Delle-Negra, M. Toulemonde, R.C. Ewing, J. Appl. Phys. **105**, 113510 (2009)
110. M. Lang, F.X. Zhang, J.M. Zhang, J.W. Wang, J. Lian, W.J. Weber, B. Schuster, C. Trautmann, R. Neumann, R.C. Ewing, Nucl. Instrum. Meth. B **268**, 2951 (2010)
111. G. Sattonnay, S. Moll, L. Thomé, C. Decorse, C. Legros, P. Simon, J. Jagielski, I. Joswik, I. Monnet, J. Appl. Phys. **108**, 103512 (2010)
112. S. Moll, G. Sattonnay, L. Thomé, J. Jagielski, C. Decorse, P. Simon, I. Monnet, W.J. Weber, Phys. Rev. B **84**, 064115 (2011)
113. G. Sattonnay, C. Grygiel, I. Monnet, C. Legros, M. Herbst-Ghysel, L. Thomé, Acta Mater. **60**, 22 (2012)
114. D. Bourgault, D. Groult, S. Bouffard, J. Provost, F. Studer, N. Nguyen, B. Raveau, M. Toulemonde, Phys. Rev. B **39**, 6549 (1989)
115. D. Bourgault, M. Hervieu, S. Bouffard, D. Groult, B. Raveau, Nucl. Instrum. Meth. B **42**, 61 (1989)
116. L. Civale, A.D. Marwick, T.K. Worthington, M.A. Kirk, J.R. Thompson, L. Krusin-Elbaum, Y. Sun, J.R. Clem, F. Holtzberg, Phys. Rev. Lett. **67**, 648 (1991)
117. M. Konczykowski, F. Rullier-Ablenque, E.R. Yacoby, A. Shaulov, Y. Yeshurun, P. Lejay, Phys. Rev. B **44**, 7167 (1991)
118. H. Watanabe, B. Kabius, K. Urban, B. Roas, S. Klaumünzer, G. Saemann-Ischenko, Physica C **179**, 75 (1991)
119. B. Chenevrier, S. Ikeda, H. Kumakura, K. Togano, S. Okayasu, U. Kazumata, Jpn. J. Appl. Phys. **31**, L777 (1992)
120. M. Leghissa, T. Schuster, W. Gerhaüser, S. Klaumünzer, M.R. Koblischka, H. Kronmüller, H. Kuhn, H.W. Neumuüller, G. Saemann-Ischenko, Europhys. Lett. **19**, 323 (1992)
121. W. Gerhauser, G. Ries, H.W. Neumuller, W. Schmidt, O. Eibl, G. Saemann-Ischenko, S. Klaumunzer, Phys. Rev. Lett. **68**, 879 (1992)
122. R.C. Budhani, M. Suenaga, S.H. Liou, Phys. Rev. Lett. **69**, 3816 (1992)
123. Y. Zhu, Z.X. Cai, R.C. Budhani, M. Suenaga, D.O. Welch, Phys. Rev. B **48**, 6436 (1993)
124. H. Dai, S. Yoon, J. Liu, R.C. Budhani, C.M. Lieber, Science **256**, 1552 (1994)
125. J. Wiesner, C. Troeholt, J.G. Wen, H.W. Zandbergen, G. Wirth, H. Fuess, Physica C **268**, 161 (1996)
126. A.K. Pradhan, S.B. Roy, P. Chaddah, D. Kanjilal, C. Chen, B.M. Wanklyn, Phys. Rev. B **53**, 2269 (1996)
127. R. Kumar, S.B. Samanta, S.K. Arora, A. Gupta, D. Kanjilal, R. Pinto, A.V. Narlikar, Sol. State Comm. **106**, 805 (1998)
128. D.X. Huang, Y. Sasaki, S. Okayasu, T. Aruga, K. Hojou, Y. Ikuhara, Phys. Rev. B **57**, 13907 (1998)
129. D.X. Huang, Y. Sasaki, Y. Ikuhara, Phys. Rev. B **59**, 3862 (1999)
130. N. Ishikawa, A. Iwase, Y. Chimi, O. Michikami, H. Wakana, T. Kanbara, J. Phys. Soc. Jpn. **69**, 3563 (2000)
131. M. Sasase, S. Okayasu, H. Yamamoto, H. Kurata, K. Hojou, Jpn. J. Appl. Phys. **46**, 783 (2007)
132. R. Biswal, J. John, D. Behera, P. Mallick, S. Kumar, D. Kanjilal, T. Mohanty, P. Raychaudhuri, N.C. Mishra, Supercond. Sci. Technol. **21**, 085016 (2008)
133. N.M. Strickland, E.F. Talantsev, N.J. Long, J.A. Xia, S.D. Searle, J. Kennedy, A. Markwitz, M.W. Rupich, X. Li, S. Sathyamurthy, Physica C **469**, 2060 (2009)
134. R. Biswal, J. John, P. Mallick, B.N. Dash, P.K. Kulriya, D.K. Avasthi, D. Kanjilal, D. Behera, T. Mohanty, P. Raychaudhuri, N.C. Mishra, J. Appl. Phys. **106**, 53912 (2009)

135. R. Biswal, D. Behera, D. Kanjilal, P.V. Satyam, N.C. Mishra, Physica C **480**, 98 (2012)
136. P. Hansen, H. Heitmann, Phys. Rev. Lett. **43**, 1444 (1979)
137. P. Hansen, H. Heitmann, P.H. Smit, Phys. Rev. B **26**, 3539 (1982)
138. G. Fuchs, F. Studer, E. Balanzat, D. Groult, J.C. Jousset, B. Raveau, Nucl. Instrum. Meth. B **12**, 471 (1985)
139. J. Jensen, A. Dunlop, S. Della-Negra, M. Toulemonde, Nucl. Instrum. Meth. B **146**, 412 (1998)
140. A. Fnidiki, J. Juraszek, F. Studer, Appl. Phys. Lett. **75**, 1296 (1999)
141. J.M. Costantini, J.M. Desvignes, A. Perez, F. Studer, J. Appl. Phys. **87**, 1899 (2000)
142. J.M. Costantini, J.M. Desvignes, M. Toulemonde, J. Appl. Phys. **87**, 4164 (2000)
143. J.M. Costantini, F. Studer, J.C. Peuzin, J. Appl. Phys. **90**, 126 (2001)
144. A. Meftah, J.M. Costantini, N. Khalfaoui, S. Boudjadar, J.P. Stoquert, F. Studer, M. Toulemonde, Nucl. Instrum. Meth. B **237**, 563 (2005)
145. M. Izerrouken, A. Meftah, M. Nekkab, Nucl. Instrum. Meth. B **258**, 395 (2007)
146. M. Izerrouken, R. Bucher, A. Meftah, M. Maaza, Radiat. Eff. Defects Solids **166**, 513 (2011)
147. P.M. Ossi, R. Pastorelli, Nucl. Instrum. Meth. B **122**, 566 (1997)
148. R. Gupta, A. Khandelwal, D.K. Avasthi, K.G.M. Nair, A. Gupta, J. Appl. Phys. **107**, 33902 (2010)
149. A. Audouard, A. Dunlop, D. Lesueur, N. Lorenzelli, L. Thomé, Europ. Phys. J. Appl. Phys. **3**, 149 (1998)
150. E. Zelaya, A. Tolley, A.M. Condo, G. Schumacher, J. Phys. Condens. Matt. **21**, 85009 (2009)
151. E. Kuzmann, G. Principi, C. Tosello, K. Havancsak, S. Stichleutner, I. Gerocs, Z. Homonnay, A. Vertes, Nucl. Instrum. Meth. B **183**, 425 (2001)
152. S. Mechler, C. Abromeit, N. Wanderka, M.P. Macht, T. Zumkley, G. Schumacher, S. Klaumünzer, Nucl. Instrum. Meth. B **245**, 133 (2006)
153. A. Gentils, L. Thomé, J. Jagielski, L. Nowicki, S. Klaumünzer, F. Garrido, M. Beauvy, Nucl. Instrum. Meth. B **218**, 457 (2004)
154. T. Sonoda, M. Kinoshita, Y. Chimi, N. Ishikawa, M. Sataka, A. Iwase, Nucl. Instrum. Meth. B **250**, 254 (2006)
155. K. Shimizu, S. Kosugi, Y. Tahara, K. Yasunaga, Y. Kaneta, N. Ishikawa, F. Hori, T. Matsui, A. Iwase, Nucl. Instrum. Meth. B **286**, 291 (2012)
156. M.K. Patel, V. Vijayakumar, D.K. Avasthi, S. Kailas, J.C. Pivin, V. Grover, B.P. Mandal, A. K. Tyagie, Nucl. Instrum. Meth. B **266**, 2898 (2008)
157. G. Sattonnay, S. Moll, L. Thomé, C. Legros, M. Herbst-Ghysel, F. Garrido, J.M. Costantini, C. Trautmann, Nucl. Instrum. Meth. B **266**, 3043 (2008)
158. M.K. Patel, V. Vijayakumar, S. Kailas, D.K. Avasthi, J.C. Pivin, A.K. Tyagie, J. Nucl. Mater. **380**, 93 (2008)
159. S. Moll, G. Sattonnay, L. Thomé, J. Jagielski, C. Legros, I. Monnet, Nucl. Instrum. Meth. B **268**, 2933 (2010)
160. M.K. Patel, D.K. Avasthi, P.K. Kulriya, S. Kailas, J.C. Pivin, A.K. Tyagie, V. Vijayakumar, Nucl. Instrum. Meth. B **268**, 42 (2010)
161. S. Hémon, V. Chailley, E. Dooryhée, C. Dufour, F. Gourbilleau, F. Levesque, E. Paumier, Nucl. Instrum. Meth. B **122**, 563 (1997)
162. S. Hémon, A. Berthelot, C. Dufour, F. Gourbilleau, E. Dooryhée, S. Begin-Colin, E. Paumier, Europ. Phys. J. B **19**, 517 (2001)
163. A. Benyagoub, F. Levesque, F. Couvreur, C. Gilbert-Mougel, C. Dufour, E. Paumier, Appl. Phys. Lett. **77**, 3197 (2000)
164. C. Gilbert-Mougel, F. Couvreur, J.M. Costantini, S. Bouffard, F. Levesque, S. Hémon, E. Paumier, C. Dufour, J. Nucl. Mater. **295**, 121 (2001)
165. A. Benyagoub, F. Levesque, Europhys. Lett. **60**, 580 (2002)
166. A. Benyagoub, Phys. Rev. B **72**, 094114 (2005)
167. A. Benyagoub, Nucl. Instrum. Meth. B **268**, 2968 (2010)

168. F. Lu, J. Wang, M. Lang, M. Toulemonde, F. Namavar, C. Trautmann, J. Zhang, R.C. Ewing, J. Lian, Phy. Chem. Chem. Phys. **14**, 12295 (2012)
169. D. Simeone, J.L. Bechade, D. Gosset, A. Chevarier, P. Daniel, H. Pilliaire, G. Baldinozzi, J. Nucl. Mater. **281**, 171 (2000)
170. D. Simeone, G. Baldinozzi, D. Gosset, M. Dutheil, A. Bulou, T. Hansen, Phys. Rev. B **67**, 064111 (2003)
171. B. Schuster, M. Lang, R. Klein, C. Trautmann, R. Neumann, A. Benyagoub, Nucl. Instrum. Meth. **267**, 964 (2009)
172. B. Schuster, F. Fujara, B. Merk, R. Neumann, T. Seidl, C. Trautmann, Nucl. Instrum. Meth. **277**, 45 (2012)
173. H. Nagabhushana, B.M. Nagabhushana, B.N. Lakshminarasappa, F. Singh, R.P.S. Chakradhar, Sol. State Comm. **149**, 1905 (2009)
174. H. Rath, P. Dash, T. Som, P.V. Satyam, U.P. Singh, P.K. Kulriya, D. Kanjilal, D.K. Avasthi, N.C. Mishra, J. Appl. Phys. **105**, 074311 (2009)
175. B. Balamurugan, B.R. Mehta, D.K. Avasthi, F. Singh, A.K. Arora, M. Rajalakshmi, G. Raghavan, A.K. Tyagi, S.M. Shivaprasad, J. Appl. Phys. **93**, 3304 (2002)
176. M. Lang, F.X. Zhang, J.M. Zhang, J.W. Wang, B. Schuster, C. Trautmann, R. Neumann, U. Becker, R.C. Ewing, Nature Mater. **8**, 793 (2009)

Chapter 9
Swift Heavy Ion Irradiation of Crystalline Semiconductors

Werner Wesch and Claudia S. Schnohr

Abstract In this chapter the structural modification of crystalline semiconductors due to swift heavy ion (SHI) irradiation induced high electronic excitation is discussed. After a short description of the energy deposition processes, experimental results on ion track and damage formation in various semiconductors are presented. The results highlight the different susceptibility of the materials to SHI induced damage formation and the existence of material specific threshold values of the electronic energy deposition for track formation. The results are discussed in the framework of existing models and it is shown that the experimental data can be well described using an extended inelastic thermal spike model.

9.1 Introduction

The interaction of swift heavy ions (SHI) with solids is characterised by a high excitation of the electronic system in a narrow cylinder around the ion path with a few nanometers in diameter. This extreme non-equilibrium process may cause cylindrical structure modification of the material along the ion trajectories, so called ion tracks. In Chap. 8 it is shown that in crystalline insulators and metals irradiation with monoatomic ions or cluster ions leads to the formation of amorphous tracks if the electronic energy deposition per ion and unit length, S_e, exceeds a certain critical value. With increasing ion fluence these isolated amorphous zones accumulate to form a continuous amorphous layer. For the description of track formation in these materials the inelastic thermal spike (i-TS) model (Chap. 2) has been used successfully. In this model the electronic energy is assumed to be

---

W. Wesch (✉) · C.S. Schnohr
Institut für Festkörperphysik, Friedrich-Schiller-Universität Jena,
Max-Wien-Platz 1, 07743 Jena, Germany
e-mail: werner.wesch@uni-jena.de

C.S. Schnohr
e-mail: c.schnohr@uni-jena.de

© Springer International Publishing Switzerland 2016

W. Wesch and E. Wendler (eds.), *Ion Beam Modification of Solids*,
Springer Series in Surface Sciences 61,
DOI 10.1007/978-3-319-33561-2_9

transferred to atomic motion via various processes of electron-phonon coupling connected with heating of a narrow region along the ion trajectory. If the temperature within such a cylinder exceeds the melting temperature of the material, a molten zone is formed which may be quenched into the amorphous phase during rapid solidification.

Whereas in crystalline insulators and metals the process of track formation seems to be widely understood, the situation is more varied and complex in semiconductors. In some materials such as Si, Ge, GaP, GaAs, AlAs and SiC only point defects and point defect complexes are formed by monoatomic irradiation up to S_e values of about 29 keV nm^{-1}. In contrast, clear evidence for the formation of damaged or amorphous tracks by monoatomic ion beams was found in InP, InSb, GaSb, InAs, GaN and InN. As in the case of insulators and metals, amorphous layers are formed by agglomeration or overlap of individual damaged tracks at sufficiently high ion fluences. With cluster ions such as e.g. C_{60}, however, tracks are easily formed even in Si, Ge and GaAs due to the higher electronic energy deposition compared to monoatomic ions. Semiconductor alloys also show differing responses to SHI irradiation. While damage formation is readily observed in SiGe and InGaP, only little damage was found in case of InGaAs. It should be mentioned that beside damage and track formation, irradiation induced annealing of damage was also observed in some of these semiconductors.

After a short review of the energy deposition processes under SHI irradiation, the present chapter will summarise the experimental findings on damage and track formation in semiconductors. The attempts to model the experimental data both with simple estimates and within the framework of various modifications of the inelastic thermal spike model will be described. Problems related to the different approaches as well as the competition between irradiation induced damage formation and annealing will be discussed.

9.2 Energy Deposition

An ion penetrating a solid suffers a successive loss of its energy by interaction with the target until it finally comes to rest at a certain depth inside the material. In principle, the energy transfer to the solid may be caused by elastic or inelastic collisions with the target atoms or their individual components. Inelastic collisions with the electrons lead to the emission of bremsstrahlung radiation while inelastic collisions with the target nuclei result in nuclear excitation and/or reaction. Both these processes, however, can be neglected in the cases discussed in this section. Consequently, the two main components of energy loss to be considered here are elastic collisions with the target atoms, the so called “nuclear stopping” or “nuclear energy deposition”, and inelastic interactions with the target atoms caused by elastic collisions with the target electrons called “electronic stopping” or “electronic energy deposition”. Nuclear energy deposition causes displacements of atoms from their regular positions. If sufficient energy is transferred, these atoms may

themselves interact with other target atoms leading to so-called collision cascades. In contrast, electronic energy deposition results in excitation and ionization of the electronic system. These processes are described by the depth dependent energy depositions per ion and unit length $S_n(s) = (dE/ds)_n$ *and* $S_e(s) = (dE/ds)_e$ for nuclear and electronic interaction, respectively, where E represents the projectile energy and s denotes the path length. $S_n(s)$ and $S_e(s)$ can be calculated using the SRIM (Stopping and Ranges of Ions in Matter) Monte Carlo code [1]. Generally, the ratio S_e/S_n increases when increasing the ion energy E from the keV to the MeV region. A more detailed description of the ion-solid interaction processes is given in Chap. 1 of this book. For all SRIM calculations of the nuclear and electronic energy loss presented here density values ρ from [2] and values of the displacement energy E_d from [3] were used.

The two contributions to the energy loss show very different dependence on the projectile energy. This is illustrated in Fig. 9.1a which plots the calculated nuclear and electronic energy depositions, S_n and S_e, respectively, as a function of ion energy E for Au ion irradiation of InP. It is clearly to be seen that in the keV to low MeV energy region nuclear energy deposition dominates while for ions with energies above ≈50 MeV electronic interaction processes are dominant. As the ion gradually slows down when travelling through the material its energy and thus the ratio of electronic and nuclear energy loss change as a function of depth z as illustrated in Fig. 9.1b for InP irradiated with 185 MeV Au ions. Figure 9.2 plots the same data for InP, InAs, GaP, GaAs, and Ge, all irradiated with 185 MeV Au ions, highlighting the near surface region by a break in the depth scale [4]. It is apparent from both figures that over the first few micrometers the energy transfer is clearly dominated by electronic interaction and nuclear stopping is negligible. In the depth region of $0 < z < 0.5$ µm in particular, S_e is nearly constant and approximately two orders of magnitude larger than S_n (see Fig. 9.2). In contrast, at depths larger than $z \approx 10$ µm the ions have lost sufficient kinetic energy to undergo ballistic collisions with the target atoms such that comparable values for both energy

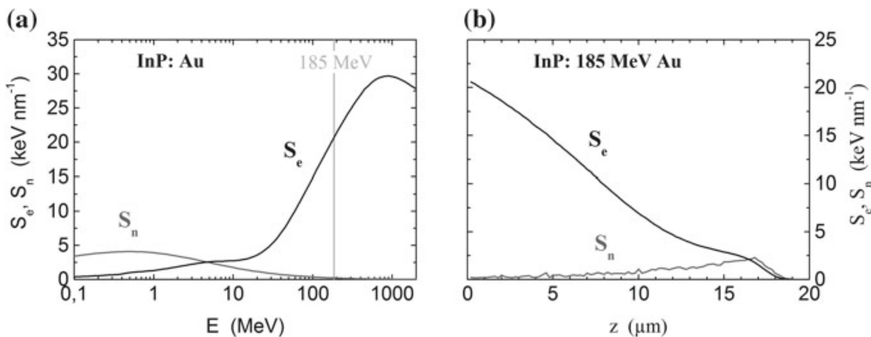

Fig. 9.1 **a** Nuclear and electronic energy deposition, S_n and S_e, respectively, as a function of ion energy E for Au irradiation of InP. **b** S_n and S_e versus depth z for InP irradiated with 185 MeV Au under normal incidence. Values were calculated using the SRIM2008 code [1]

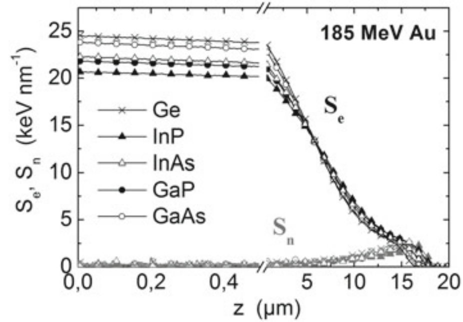

Fig. 9.2 Nuclear and electronic energy loss, S_n and S_e, respectively, versus depth z for Ge, InP, InAs, GaP and GaAs irradiated with 185 MeV Au. Values were calculated with SRIM2008 [1]. Note the break in the depth scale at $z = 0.5$ µm

loss processes are reached at $z \approx 15$ µm and nuclear interaction dominates the energy transfer. The Au ions with an initial energy of 185 MeV finally come to rest at a depth $z \approx 17$ µm below the sample surface.

Furthermore, it is obvious from Fig. 9.2 that the values of both nuclear and electronic energy loss are very similar for all five materials over the whole ion range. Average values of S_n and S_e over the first 0.5 µm from the surface are listed in Table 9.1 for various semiconductors subjected to 185 MeV Au irradiation. In all materials the near surface electronic energy loss exceeds the nuclear one by approximately two orders of magnitude. The values for S_e range from approximately 20–24 keV nm^{-1} except for AlAs and Si which exhibit slightly smaller values. The electronic energy deposition close to the surface thus exceeds the threshold value $S_{et} \approx 13$ keV nm^{-1} reported for track formation in InP [5, 6] for all materials listed in Table 9.1. Nevertheless, their response to SHI irradiation is remarkably diverse and distinctly different from the behaviour observed under irradiation with ions in the keV to low MeV region. Thanks to the dominating contribution of the electronic energy deposition to the total energy loss in the near surface region, SHI irradiation thus allows an almost separate study of the influence of ionization processes on damage formation and transformation in semiconductor materials.

Table 9.1 Nuclear and electronic energy loss, S_n and S_e, respectively, averaged over the first 0.5 µm from the surface for various semiconductors irradiated with 185 MeV Au. Values were calculated with SRIM2008 [1]

Material	S_n (keV nm^{-1})	S_e (keV nm^{-1})
Si	0.15	15.7
Ge	0.28	24.2
SiC	0.21	24.1
AlAs	0.20	18.4
GaP	0.23	21.5
GaAs	0.28	23.5
GaSb	0.26	22.0
InP	0.23	20.4
InAs	0.25	22.0
InSb	0.26	20.7

9.3 Track and Damage Formation

During the last two decades the growing interest in the use of high energy ion irradiation to produce thick or buried modified layers has stimulated numerous studies of damage evolution due to high excitation of the electronic system in various semiconductors (see e.g. [7–9] and references therein). All these studies have shown that while some materials are easily damaged due to electronic energy deposition others are surprisingly resistant to damage and ion track formation. In this section, experimental results on SHI irradiation of semiconductors will first be presented for materials resistant to damage formation including Si, Ge, GaAs, GaP, AlAs, SiC, BN and AlN followed by a review of studies on materials susceptible to damage formation, namely InP, InAs, InSb, GaSb, GaN and InN. As a more or less arbitrary criterion for this distinction we have used the threshold values of the electronic energy deposition for track formation to be reachable by monoatomic ions with accelerators available at present. Besides, experimental findings for SHI irradiated semiconductor alloys and cluster irradiation of semiconductors will be presented together with a discussion of the experimentally determined threshold values for damage and track formation due to high electronic energy deposition.

9.3.1 Materials with High Radiation Resistance

9.3.1.1 Track Formation

The first papers dealing with SHI irradiation of Si, Ge, GaAs (see [7] and references therein) and SiC [10] were published in the early and mid 1990s. The motivation for the early studies of these technologically relevant materials was mainly to investigate the modification of the electrical properties under the conditions of high electronic excitation. In all these materials and in GaP no indication for visible track formation by monoatomic ion irradiation was found up to an electronic energy deposition of $S_e \approx 29$ keV nm^{-1}. Irradiation of BN and AlN up to electronic energy depositions of $S_e = 17.6$ and 33 keV nm^{-1}, respectively, also did not result in track formation [11, 12]. For AlN, a threshold value for track formation of $S_e > 34$ keV nm^{-1} was deduced from SHI irradiation experiments with higher electronic energy depositions [13]. However, it has been shown by in situ optical absorption measurements that high electronic energy deposition in AlN causes the formation of point defects, i.e. S_e is not completely inefficient with respect to defect formation in this material [14].

For electronic energy depositions sufficiently in excess of 29 keV nm^{-1} irradiation of GaAs, GaP and Ge with swift monoatomic heavy ions (Au, Pb, Bi) results in extremely discontinuous tracks [15–17]. In case of Ge irradiated with 710 MeV Bi ($S_e = 37$ keV nm^{-1}) and 2.7 GeV U ($S_e = 42$ keV nm^{-1}), for example, single randomly distributed dot-like defects as well as discontinuous tracks consisting of

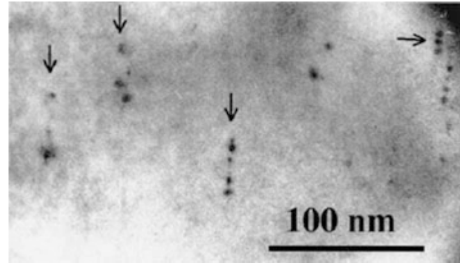

Fig. 9.3 Bright-field plan-view TEM image of a $Si_{0.5}Ge_{0.5}$ layer irradiated with 1.3 GeV U ions. The *arrows mark* the tracks [18]

individual defect clusters arranged along the ion trajectory were registered [16]. The discontinuity of the tracks and the fact that under these irradiation conditions not each impinging ion produces a visible track indicate that these S_e values are only slightly above the threshold value for the formation of visible tracks. The internal structure of the discontinuous tracks is explained by fluctuations of the ion charge state along the trajectories which periodically increases the electronic energy deposition above the threshold value for defect formation resulting in the observed intermittent structure of the tracks. From the distance between the individual defects within the tracks a periodic simultaneous loss of three electrons corresponding to an increase of the electronic energy deposition by 4–6 keV nm^{-1} is estimated. From this it is concluded that the formation of continuous tracks in Ge requires an electronic energy deposition of 46–49 keV nm^{-1} which cannot be reached with monoatomic ions (for details see [16]). A similar damage formation as in Ge was also observed in $Si_{0.5}Ge_{0.5}$ alloy layers irradiated with 1.3 GeV U ions ($S_e \approx 34$ keV nm^{-1}) which is illustrated in the bright-field plan-view (PV) transmission electron microscopy (TEM) image in Fig. 9.3 [18, 19]. The density of the isolated dot-like defects together with the discontinuous tracks is in good agreement with the ion fluence. Contrary, the total number of extended tracks consisting of three or more dots is about one order of magnitude lower than the ion fluence used [18] which is similar to the behaviour found for Xe irradiation of InP (see Sect. 9.3.2).

Irradiation of $Si_{0.5}Ge_{0.5}$ with 0.8 and 2.7 GeV U ions results in nearly the same value of the electronic energy deposition ($S_e \approx 32$ keV nm^{-1}), but the ion velocities differ by a factor of about two (2.5 and 4.3×10^7 ms^{-1}, respectively) [19]. The density of defect clusters registered by TEM is more than one order of magnitude higher at 0.8 compared to 2.7 GeV irradiation, and the morphology of the damage structure is also different. This shows that both the density and the morphology of the defects are not only governed by the value of the electronic energy deposition, but are also affected by the velocity of the projectiles [19]. The influence of this velocity effect on track formation was clearly demonstrated for yttrium iron garnet $Y_3Fe_5O_{12}$ [20] (Chap. 8) and is commonly ascribed to the deposited energy density which decreases with increasing velocity. The damage cross-section is therefore larger at low velocities and more damage is produced.

The technologically relevant II-VI semiconductor CdTe is known to possess a high resistance to defect formation due to nuclear energy deposition even at low

temperatures [21]. Similarly, no point defects or amorphous ion tracks have been observed in crystals irradiated with swift heavy ions up to electronic energy depositions of $S_e \approx 28$ keV nm^{-1} (see [22] and references therein). However, the formation of extended defects in a very thin surface layer detected at the highest energy deposition and ion fluence is evidence for defect creation caused by the high electronic energy deposition. As in case of damage formation due to nuclear processes, the observed behaviour is ascribed to the high instability of the created defects which is a consequence of the high iconicity of the CdTe lattice [21] and which, together with the high defect mobility, obviously results in a nearly perfect recrystallization of the damage produced along the ion trajectory and to the creation of extended defects at high fluences.

In contrast to irradiation with monoatomic ions, irradiation of cluster ions with energies of several 10 MeV leads to the formation of amorphous tracks in Si, Ge, GaAs [23–26] and AlN [12]. Although there is a certain theoretical uncertainty regarding how to calculate the electronic energy deposition of cluster ions correctly, additivity of the S_e values of the n individual ions, $S_e(n) = n\ S_e(1)$, is commonly assumed, yielding extremely high values of S_e not available with monoatomic heavy ions. For the investigation of damage formation in Si, Ge and GaAs the fullerene C_{60} with energies between 20 and 40 MeV was used [23–26]. After irradiation of Si single crystals with 30 and 40 MeV C_{60} corresponding to $S_e \approx 47$ and 57 keV nm^{-1}, respectively, continuous amorphous tracks with a density almost agreeing with the ion fluence were registered by means of high-resolution (HR) TEM [23, 24]. The track diameters of about 10 nm at the surface in case of the 30 MeV irradiation remains constant down to a depth of ≈80 nm and then gradually decreases as a consequence of an increasing spatial separation of the cluster constituents due to Coulomb repulsion between the charged fragments and multiple scattering in elastic collision processes. Furthermore, at the end of the tracks a series of aligned droplets of damaged material was found [23]. These findings were confirmed in another study [24] where track diameters of 8.4 and 10.5 nm were determined for 30 and 40 MeV irradiation, respectively.

Amorphous tracks were also detected in C_{60}-irradiated Ge and GaAs [25, 26]. The electronic energy depositions in the energy region from 20 to 40 MeV vary between about 37 and 51 keV nm^{-1} for Ge and about 38 and 52 keV nm^{-1} for GaAs. The diameter of the tracks increases with increasing energy of the cluster ions, i.e. with increasing electronic energy loss which is illustrated in Fig. 9.4 for the example of GaAs. Track diameters d determined from conventional TEM images were about 6, 12.5 and 15 nm in GaAs irradiated with 20, 30 and 40 MeV, respectively [26]. From the extrapolation of the dependence of the experimental cross-sections $\sigma_{exp} = \pi d^2/4$ on S_e the threshold values for track formation due to C_{60} ion irradiation were obtained as $S_{et} = 36$ keV nm^{-1} for GaAs, 33 keV nm^{-1} for Ge and 28 keV nm^{-1} for Si [26]. Contrary, irradiation of Ge with fast Bi, Pb and U ions resulting in similar or higher electronic energy depositions produced no or only extremely discontinuous tracks as discussed above [16]. In AlN irradiated with fullerene ions at electronic energy depositions ranging from $S_e = 38$ to 59 keV nm^{-1} amorphous tracks with diameters between 1.8 and 2.5 nm were registered [12].

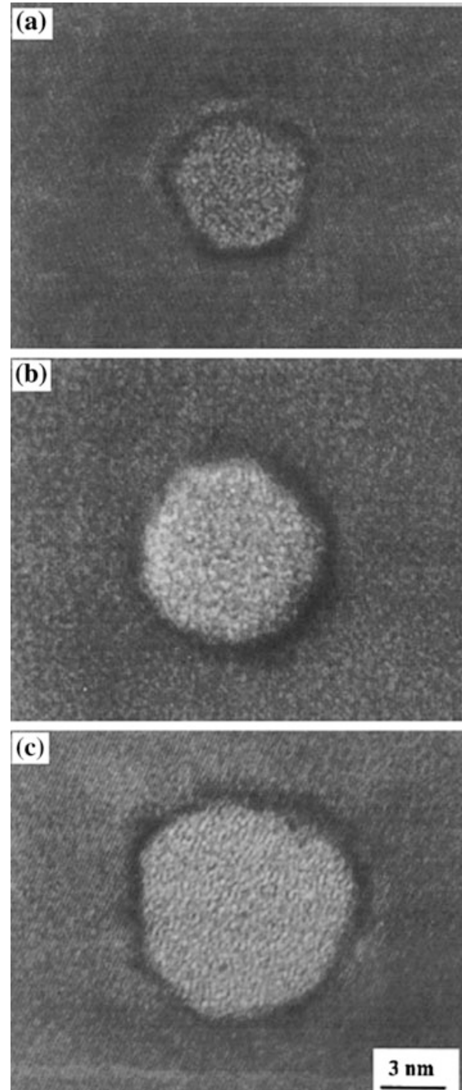

Fig. 9.4 High-resolution TEM images of GaAs single crystals irradiated with **a** 20 MeV, **b** 30 MeV and **c** 40 MeV C_{60} ions [26]

The phenomenon that slow fullerene ions form continuous amorphous tracks while monoatomic fast ions with comparable or higher electronic energy depositions do not has to be ascribed to the significantly lower ion velocity of the cluster ions compared to the monoatomic ones: the reduced velocity $\beta = v/c$ (v–ion velocity, c-velocity of light in vacuum) amounts to about 10 % in case of swift monoatomic ions and is only in the order of about 0.8–1.1 % for 20–40 MeV fullerenes [26]. As a consequence of this velocity effect, the electronic energy is deposited into a smaller volume in case of the low velocity cluster ions leading to a higher energy density and, therefore, to a higher damage cross-section (see Sect. 9.4).

9.3.1.2 Damage Accumulation

In the previous section, the effect of the electronic energy transferred to the lattice of various semiconductors as a result of irradiation with single monoatomic or cluster ions has been described. Now the accumulation of damage as a function of the ion fluence will be discussed.

A suitable and effective structural method to analyse damage formation and the crystalline-to-amorphous phase transition is Rutherford backscattering spectrometry (RBS) in combination with the channelling technique (see Chaps. 1 and 5, [27, 28]). Virgin and damaged samples are irradiated with light ions (H, He) under both random and aligned incidence. From the energy spectra of the backscattered ions the difference in minimum yield $\Delta\chi_{min}$ can be calculated which is related to the amount of defects in the damaged samples. Using the Monte Carlo code DICADA [29], the relative concentration of displaced lattice atoms, n_{da}, can then be determined with $n_{da} = 1$ corresponding to the amorphous state. A comparison of the results obtained for various irradiation conditions is possible when recalculating the ion fluence into the number of displacements per lattice atom, n_{dpa}, according to $n_{dpa} = N*_{displ} N_I/N_0$ which represents the nuclear energy deposition. Here $N*_{displ}$ is the number of displacements per ion and unit depth calculated by the SRIM code, N_I the ion fluence and N_0 the atomic density of the target.

RBS analyses of SHI irradiated Si, Ge, GaP, GaAs [7, 15] and AlAs [30, 31] confirm that in these semiconductors SHI irradiation with an electronic energy deposition S_e below ≈33 keV nm^{-1} leads only to the formation of point defects and point defect complexes. This is illustrated in Fig. 9.5 which shows the relative defect concentration, n_{da}, versus the ion fluence for 593 MeV Au irradiation of Ge (S_e = 32.8 keV nm^{-1}), GaP (S_e = 29.3 keV nm^{-1}) and GaAs (S_e = 33.3 keV nm^{-1}) [15]. For comparison, the curves for InSb (S_e = 30.4 keV nm^{-1}) and InP (S_e = 28.9 keV nm^{-1}) are included. In case of Ge, GaP, and GaAs, the defect concentration increases with the ion fluence until a saturation is reached at very low defect concentrations which do not exceed values of n_{da} ≈ 0.05, i.e. only 5 % of the atoms are displaced from their regular positions, indicative for the formation of various types

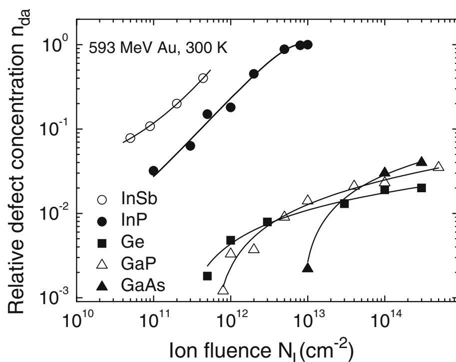

Fig. 9.5 Relative defect concentration n_{da} taken at a depth of 0.2 μm versus the ion fluence N_I for 593 MeV Au irradiation of InSb, InP, GaAs, GaP and Ge. The experimental data are fitted by sigmoidal curves [15]

of point-like defects. Identical behaviour was also observed in case of AlAs [30]. Contrary to the behaviour of these materials, InP and InSb are rendered amorphous under the same irradiation conditions and a comparable S_e value indicating their smaller resistance to damage formation which is discussed in detail in Sect. 9.3.2. It should be mentioned that under the conditions of dominant nuclear energy deposition all these materials are amorphised (see Chap. 5).

The higher radiation resistance observed in Ge, GaAs and GaP is in agreement with the result, that in this range of the electronic energy deposition no tracks were detected. For the formation of extremely discontinuous tracks electronic energy depositions well above 33 keV nm^{-1} are required (see Sect. 9.3.1.1).

While SHI induced track formation and amorphization do not occur in Si single crystals, amorphization due to SHI irradiation was recently reported in electro-chemically produced porous Si layers [32, 33]. By means of Raman spectroscopy it is shown that the initially crystalline columnar structure of the porous layers is rendered amorphous with increasing SHI fluence. In contrast to the regime with dominant nuclear energy deposition where the collision processes between the ions and the lattice atoms induce a densification of the porous layer and thus its destruction [34], the samples remain porous even at full amorphization in case of electronic energy deposition. Furthermore, the thermal conductivity of the porous layer further decreases with increasing amorphous fraction [32, 35]. The surprisingly different behaviour of porous Si compared to bulk single crystals is mainly attributed to the low thermal conductivity of the former being two to three orders of magnitude smaller than that of the bulk material and approaching that of dielectric materials. The authors argue that, according to the thermal spike model, this low thermal conductivity may lead to melting of the material after electron-phonon coupling and thus to amorphous track formation along the ion path [33, 35].

The conclusion from the RBS studies that the damage in the radiation resistant materials consists of point defects is confirmed by electrical measurements. In these early studies *n*- and *p*-doped Si, Ge and GaAs single crystals were irradiated with various ion masses ranging from oxygen to uranium. The energy per nucleon was varied from 3 to 60 MeV/u corresponding to electronic energy depositions S_e between about 1 and 28 keV nm^{-1}. In most cases, the electrical properties were analysed by means of in situ resistivity and Hall mobility measurements. In some cases, these measurements were further supported by additional ex situ deep level transient spectroscopy (DLTS), photo luminescence (PL), optical absorption, electron paramagnetic resonance (EPR), and X-ray diffraction (XRD) techniques. In *n*-Si and *n*-GaAs the mobility decreases and the resistivity increases with increasing ion fluence until saturation values are reached indicative for carrier compensation [36–39]. This is illustrated in Fig. 9.6 for the example of 5.2 GeV Kr irradiation of *n*-Si [39].

The behaviour of *n*-Ge differs from that of *n*-Si as can be seen in Fig. 9.7 for the example of 880 MeV Pb irradiation. Here the resistivity decreases after having passed a maximum, and the initially negative Hall mobility becomes positive with rising ion fluence. This is a clear indication of a type conversion from *n*- to *p*-type.

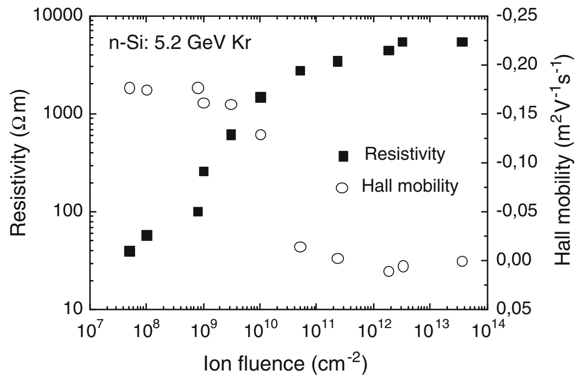

Fig. 9.6 Resistivity ρ and Hall mobility μ_H of n-Si ($n = 7 \times 10^{11}$ P cm^{-3}) irradiated with 5.2 GeV Kr ions versus the ion fluence (data from [39])

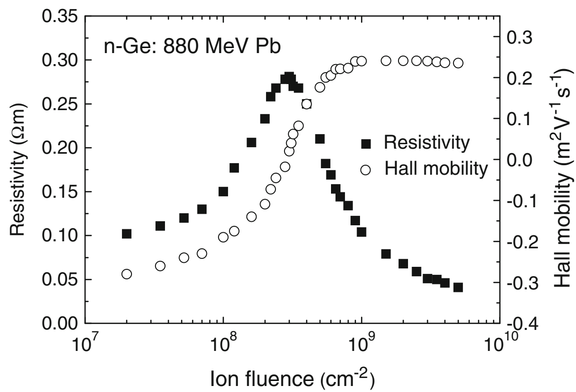

Fig. 9.7 Resistivity ρ and Hall mobility μ_H of n-Ge ($n = 2.4 \times 10^{14}$ Sb cm^{-3}) irradiated with 880 MeV Pb ions versus the ion fluence (data from [39])

In p-Ge, on the other hand, the conductivity and majority carrier density increase with increasing ion fluence [40].

Detailed analysis of DLTS, PL and TEM measurements has shown that the modifications of the electrical parameters observed in Si, Ge and GaAs have to be ascribed to the formation of point defects during SHI irradiation which cause the compensation of free carriers in n-Si and n-GaAs and a type conversion of n-Ge to p-Ge [36–39]. When comparing the results of SHI irradiated samples with those of proton, electron and neutron irradiated samples it is obvious, that the defects are similar in all cases. The most frequent defect complexes in Si and Ge are the A-centre (vacancy-oxygen complex), the E-centre (vacancy-doping impurity complex) and the divacancy [36, 41–44]. In GaAs the dominating defect produced by SHI irradiation is the As vacancy [39].

It is not yet completely clear in what way the electronic energy deposition contributes to the observed defect formation in the radiation resistant materials. For Si [36, 45] and Ge [40] it has been reported that at lower values of S_e the defect production rate scales with the nuclear energy deposition. With increasing S_e (heavier ions) the defect production rate decreases indicating in situ annealing of

defects due to the higher electronic energy deposition [36, 40, 45]. Defect annealing due to high electronic excitation was also observed in GaAs for S_e values ranging from ≈15 to 20 keV nm^{-1} [7, 46]. Consequently, in Si, Ge and GaAs the low defect concentration produced during SHI irradiation can mainly be ascribed to the effects of nuclear interaction, and these defects may also anneal during the irradiation due to the electronic energy loss of the impinging ions.

For SiC only a few studies on radiation damage formation due to high electronic excitation do exist (see [47] and references therein). 3C-, 4H- and 6H-SiC single crystals were irradiated with various ions and electronic energy depositions up to $S_e \approx 33$ keV nm^{-1}. The damage evolution was analysed using mainly optical (optical absorption, PL) and Raman spectroscopy. From optical measurements it is concluded that SHI irradiation does not produce remarkable damage. The results of the Raman spectroscopy further suggest that SHI irradiation only produces point defects while the formation of amorphous regions can be excluded. The small amount of defects produced is predominantly located at the end of the ion range and can therefore be ascribed to nuclear collisions [47, 48]. Additionally, annealing of pre-existing defects was observed under SHI irradiation which is based on enhanced migration and recombination of defects (ionization-enhanced diffusion, IED) [47–50]. Obviously, during SHI irradiation of SiC a competition between damage accumulation and IED occurs, which has also been discussed previously for other semiconductors [7].

Recent studies of SHI irradiation of SiC layers pre-damaged by nuclear energy deposition showed a dependence of damage recovery on the degree of pre-damage [51, 52]. Both 3C- and 4H- SiC fully amorphous layers irradiated with 870 MeV Pb ions ($S_e = 33$ keV nm^{-1}) [51] and 167 MeV Xe ions ($S_e = 20$ keV nm^{-1}) [52] undergo recrystallization at the amorphous-crystalline (a-c) interface reducing the thickness of the amorphous layer by around 10 nm (ion beam induced epitaxial crystallization, IBIEC). Contrary, in partly amorphous layers damage annealing over the entire damaged layers was observed. The difference in the recrystallization kinetics observed for the different damage levels are ascribed to differences in the structure of the defective layers, i.e. to differences in defect nature and density [51]. MD calculations, which very well describe the experimental findings, indicate the high energy density deposited by the SHI along their path to be responsible for the defect annealing observed (for more details see [51]).

9.3.2 *Materials with Low Radiation Resistance*

From the ion fluence dependence of the number of displaced atoms, n_{da}, in Fig. 9.5 of Sect. 9.3.1.2 it is obvious that various semiconductors show a completely different damaging behaviour under identical irradiation conditions and for similar electronic energy depositions per ion and path length. Whereas Ge, GaP and GaAs show saturation of n_{da} at relatively low values, InP and InSb are rendered amorphous. The transition to the amorphous phase may be explained by the formation of

individual amorphous or heavily damaged tracks which accumulate or overlap, respectively, to a complete amorphous layer. In this section the conditions for track formation and amorphization in various semiconductors with low radiation resistance will be discussed in more detail.

9.3.2.1 Track Formation

TEM may yield detailed information on the morphology and kind of defects in the irradiated layers. It should, however, be mentioned that defects can anneal under electron irradiation in the microscope so that the analysis of the real structure of heavily damaged or amorphous regions is complicated and may lead to misinterpretations especially in case of high-resolution imaging [53, 54]. In the following an overview about results on the formation of visible tracks in semiconductors being susceptible to damage formation under SHI irradiation will be given.

In InP irradiated with 250 and 340 MeV Xe ions at fluences $N_I \leq 5 \times 10^{12}$ cm^{-2}, no visible tracks were detected (or could be resolved under the experimental conditions used) by means of cross-section TEM (XTEM). In these cases the layers probably contain high concentrations of point defects or point defect complexes which is in accordance with the small relative defect concentrations $n_{da} \leq 0.2$ measured by RBS [7, 53]. At higher ion fluences discontinuous and partially continuous tracks were detected the concentration of which increases with the ion fluence until a completely amorphous surface layer is formed [5, 6].

The morphology of damage produced in the irradiated layers changes significantly with depth. In case of 250 MeV Xe irradiation to an ion fluence of 7×10^{12} cm^{-2} (corresponding to $n_{dpa} = 0.003$ dpa and $n_{da} = 0.37$ at the depth $z = 0.3$ μm), a ≈ 35 nm thick slightly damaged layer is followed in the XTEM images by a layer containing tracks of isolated spherical or elongated cylindrical defect clusters along the ion trajectory extending down to ≈100 nm. Then a region with dark contrast continuous and discontinuous straight lines extends to a depth $z \approx 10$ μm. The shape of the cross-section of the continuous tracks is nearly circular, and the diameters were estimated to be about (7–15) nm. Electron diffraction analyses indicate the inner structure of the tracks to consist of amorphous InP and a small amount of fine polycrystalline grains [6]. The depth region between ≈10 and 16 μm is crystalline and contains small clusters of point defects while a layer with a high concentration of defect clusters is observed between ≈16 and 21 μm.

A comparison with the depth dependence of nuclear and electronic energy deposition allows the conclusion that the near surface damage within the first 10 μm is caused by the electronic energy loss, whereas the heavily damaged buried layer is a consequence of nuclear energy deposition with its maximum value at the depth $z \approx 21$ μm. The depth extension of the track region and the existence of a crystalline region behind the tracks suggest the existence of a critical value of the electronic energy deposition S_e for track formation which is exceeded only for $z < 10$ μm (maximum depth of track region) corresponding to $S_{et} \approx 13$ keV nm^{-1} (for details see [6, 7]). The existence of a threshold value of S_e in this order of

magnitude is also confirmed by the result that 140 MeV Kr irradiation with $S_e \approx 12$ keV nm^{-1} does not result in track formation in InP [53]. It also explains the lower defect concentration in the immediate surface area ($z < 0.1$ μm) observed in the XTEM studies. The impinging ion has a low initial charge state corresponding to an electronic energy deposition well below the threshold value S_{et}. As the ion traverses the sample, the charge state increases towards the equilibrium value thereby raising S_e above the threshold value for track formation [55].

At a Xe ion fluence of $N_I = 5 \times 10^{13}$ cm^{-2} both surface and buried damage layers are amorphized due to agglomeration of the individual tracks and the buried damage clusters, respectively. The ion fluence $N_I = 5 \times 10^{13}$ cm^{-2} corresponds to $n_{dpa} = 0.55$ dpa in the maximum of the nuclear energy deposition ($z \approx 21$ μm) which leads to amorphization of InP also for conventional ion energies [56, 57].

It should be mentioned that not each impinging 250 MeV Xe ion produces a visible track. For an ion fluence of 7×10^{12} cm^{-2} a track density of 2×10^{11} cm^{-2} was estimated. This is an indication that at least under these irradiation conditions pre-damaging is necessary for track formation. In order to proof this, a buried layer containing a high concentration of point defects was produced in crystalline InP by conventional ion implantation. Afterwards the sample was irradiated with 250 MeV Xe ions to an ion fluence of $N_I = 7 \times 10^{11}$ cm^{-2} which is far below the value at which in single crystalline InP visible tracks are formed. In the bright-field XTEM image taken at this sample discontinuous tracks consisting of defect clusters arranged like a string of pearls along the ion trajectory were detected solely in the buried pre-damaged region, but not in the surrounding crystalline areas [6]. However, it has been shown that SHI irradiation may also induce defect annealing in pre-damaged InP [58] and GaAs [59]. The electronic energy deposition, the ion fluence and the concentration of defects in the damaged region then determines which of the competing processes, damage formation or annealing, dominates.

As in the case of the Xe irradiations, irradiation of InP with 200 MeV Au ions results in the formation of widely discontinuous tracks [60, 61]. However, in this case each impinging ion forms a track, i.e. no pre-damaging is required for track formation. Furthermore, electron diffraction and HR-TEM analyses reveal no evidence that the individual track cores are amorphous which may be a consequence of homoepitaxial regrowth [61]. 593 MeV Au irradiation with its still higher electronic energy deposition in InP results in continuous amorphous tracks the number of which corresponds to the ion fluence as in the case of the 200 MeV irradiation [15, 53]. A comparison of differences in track morphologies is illustrated in Fig. 9.8 which shows bright-field PV-TEM images of InP irradiated with 375 MeV Xe and with 573 MeV Au ions [15].

In another study track formation in InP, InAs, InSb and GaSb irradiated with Pb ions with specific energies ranging from 1.85 to 10 MeV/u was investigated using RBS and TEM [62]. According to the TEM results, isolated cylindrical tracks were produced at low ion fluences in all materials in the investigated energy range. In all cases the number of tracks is in reasonable agreement with the ion fluence indicating each ion to have formed a visible track. Whereas in InP and GaSb the tracks were amorphous, those found in InSb were completely recrystallized. In the case of

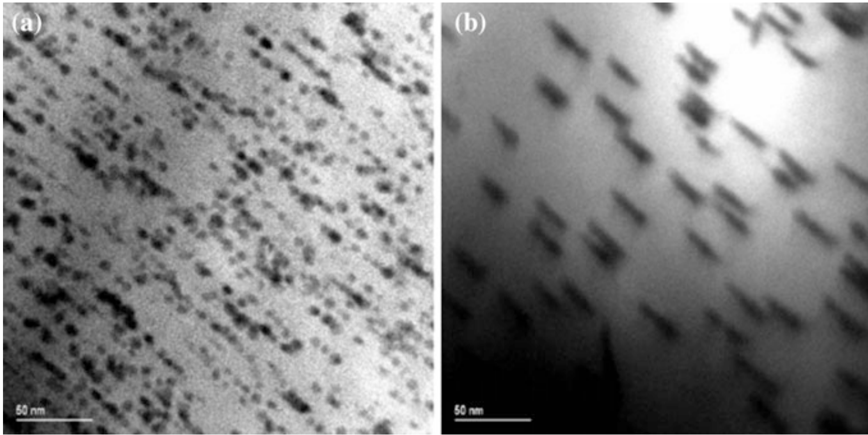

Fig. 9.8 Bright-field plan-view TEM images of InP irradiated at room temperature with **a** 375 MeV Xe up to the ion fluence $N_I = 8.4 \times 10^{11}$ cm^{-2} and **b** 573 MeV Au up to the ion fluence $N_I = 1 \times 10^{11}$ cm^{-2}. The samples were tilted off the <100> axis in the microscope [15]

InP the mean radii of isolated tracks of ≈3.3 nm are in good agreement with those determined by means of RBS [5, 53, 62] (see Sect. 9.3.2.2).

InP has also been irradiated with C_{60} cluster ions with energies from 23 to 40 MeV corresponding to electronic energy depositions between ≈37 and 48 keV nm^{-1}, respectively [63]. The resulting tracks show average diameters of ≈17 to 21 nm, respectively, corresponding again to a threshold value of $S_{et} \approx 13$ keV nm^{-1} for track formation in InP [15].

In both GaN and InN single ion irradiation with electronic energy deposition above $S_e = 24$ and 15 keV nm^{-1}, respectively, results in visible track formation [11, 12, 64]. From the comparison of the track length determined from XTEM images and SRIM calculations of the depth dependence of the electronic stopping power, S_e, the threshold value for track formation in both materials was determined to $S_{et} = 15$ keV nm^{-1} [12]. In the region of lower S_e the tracks are discontinuous, and the degree of discontinuity decreases with increasing S_e. Whereas in GaN in case of lower S_e values the tracks consist of a heavily damaged but not amorphous core and a surrounding less damaged halo [64], at least the continuous tracks seem to be amorphous [12]. In InN the contrast in the TEM images of the nearly continuous tracks observed at higher S_e values is heterogeneous indicating dissociation of InN into nitrogen bubbles and metallic indium or indium oxide [12] as it was also observed during low energy ion irradiation [65].

9.3.2.2 Damage Accumulation and Amorphization

An ion fluence dependent damage accumulation and amorphization was first reported for single crystalline InP irradiated with 250 MeV Xe ions at room

temperature [5] and later confirmed for other irradiation conditions [6, 62, 66] as well as for other semiconductors [4, 15, 62, 64]. The damage accumulation with increasing ion fluence was studied by means of RBS.

For all ion energies investigated, the relative defect concentration n_{da}, i.e. the relative concentration of displaced lattice atoms calculated from the RBS spectra, remains constant over the depth accessible with RBS analysis ($z \leq 0.5$ µm for the conditions used). This is consistent with the nearly constant value of the electronic energy deposition S_e in the near surface region of the samples (see Fig. 9.2 in Sect. 9.2). As already mentioned in Sect. 9.3.2.1, a very thin layer at the immediate sample surface retains a lower defect concentration [5, 6] which is attributed to charge state effects of the impinging ions [55].

Figure 9.9 shows a comparison of the relative defect concentration n_{da} obtained for InP irradiated with different ion species and different ion energies. In order for the data to be comparable, the ion fluence N_I has been recalculated into the number of displacements per lattice atom n_{dpa} due to nuclear energy deposition. It is clearly to be seen in Fig. 9.9 that in case of 340 and 250 MeV Xe irradiation with electronic energy depositions of $S_e = 19.5$ and 18.8 keV nm^{-1}, respectively, n_{da} quickly reaches a value of one, i.e. amorphization is already attained for n_{dpa} 0.008 and 0.016 dpa, respectively. In order to render InP amorphous by nuclear energy deposition using for example 300 keV Se or 100 keV B ions, $n_{dpa} = 0.2$ or 1 dpa are required, respectively [56, 67] (see Chap. 5). Furthermore, only values of $n_{da} < 0.05$ follow for a nuclear energy deposition of $n_{dpa} = 0.016$ dpa when using conventional ion energies of several 100 keV to a few MeV. Therefore, the amorphization by swift Xe irradiation has to be ascribed to the high electronic energy loss starting at the surface and extending to depths of several micrometers.

In case of Kr irradiation, n_{da} is approximately described by the same dependence on n_{dpa} for both ion energies (see Fig. 9.9). For 150 MeV irradiation with $S_e = 12.5$ keV nm^{-1} only weak damage close to the surface is produced up to

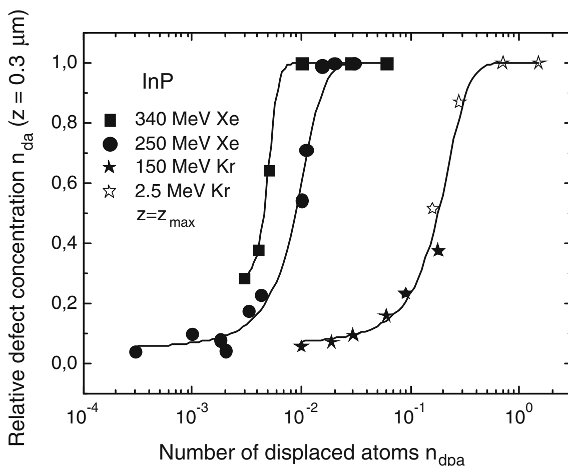

Fig. 9.9 Relative concentration of displaced lattice atoms, n_{da}, at a depth $z = 0.3$ µm versus the number of primary displacements per lattice atom resulting from nuclear interaction, n_{dpa}, for 340 and 250 MeV Xe and 150 MeV Kr irradiation in InP at room temperature. For comparison, the values for 2.5 MeV Kr irradiation at the maximum of the defect concentration profiles are included [7]

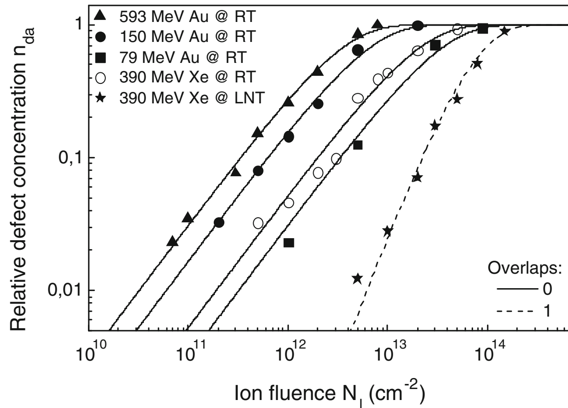

Fig. 9.10 Relative concentration of displaced lattice atoms n_{da} taken at a depth of $z = 0.2$ µm in InP versus the ion fluence [58]

$n_{dpa} = 0.2$ dpa. In case of 2.5 MeV Kr ions, on the other hand, where damaging is caused by nuclear processes, the formation of amorphous material requires n_{dpa} 0.6 dpa. From these results it can be concluded that the damage evolution observed in InP irradiated with 150 MeV Kr is a consequence of nuclear energy deposition. Comparison with the results of the swift Xe irradiations then shows that there exists a threshold value of the electronic energy deposition in order to form remarkable damage.

The formation of amorphous layers at critical ion fluences has also been observed in InP for room temperature (RT) Au irradiation with energies between 64 and 593 MeV (electronic energy depositions S_e from ≈11 to 29 keV nm^{-1}) [4, 53], for 593 MeV Au and 390 MeV Xe irradiation at liquid nitrogen temperature (LNT) [53, 58] and for 593 MeV Au irradiation at RT in InSb (S_e = 30.4 keV nm^{-1}) [15]. In Fig. 9.10 some examples of the dependence of the relative defect concentration n_{da} on the ion fluence N_I are shown for InP irradiated with Au and Xe ions of varying energies at RT and LNT.

It is obvious that the critical ion fluence for complete amorphization shifts to higher values with decreasing ion energy and ion mass. The solid and dashed lines are the result of the analysis of the fluence dependences in the framework of the overlap damage model introduced by Gibbons [68] (see Chap. 3). In this model it is assumed that heavily damaged or amorphous material is produced either directly by a single incoming ion or by multiple overlap of slightly damaged regions. Fitting the corresponding fluence dependences yields the number of overlaps m necessary to amorphize the material and the area A_I damaged by a single ion which corresponds to the damage cross-section (for details see Chap. 3). But it should be mentioned that the quantity n_{da} determined from RBS measurements gives the total concentration of displaced lattice atoms and therefore contains information about point defects, point defect complexes and amorphous regions, i.e. it overestimates the amorphous fraction. Therefore, the area A_I and the corresponding radius of material damaged by an individual ion does not necessarily correspond to the radius of a heavily damaged or amorphous track observed by TEM investigations. As can

be seen in Fig. 9.10, in case of the RT irradiation the fluence dependences can be fitted with an overlap number $m = 0$, i.e. each single ion directly creates a heavily damaged area along its trajectory. Contrary, the damage evolution curves in case of the LNT irradiations with 390 MeV Xe (Fig. 9.10) and 593 MeV Au ions [53] can be fitted only by assuming $m = 1$, i.e. one overlap of individual damaged zones is necessary to form heavily damaged or amorphous material. Obviously, at low irradiation temperature an incoming ion produces less damage than at room temperature. This behaviour is in contrast to that observed in case of damage formation by nuclear energy deposition (see Chap.5) and presents a clear indication for the completely different damage formation mechanisms occurring due to high electronic excitation of the lattice atoms.

In GaN irradiated with SHI at an electronic energy deposition of $S_e = 34$ keV nm^{-1} a fluence dependent damage accumulation was also observed [64]. The RBS yield increases with the ion fluence up to a saturation value of around 80 % of total amorphization at an ion fluence of $N_I \approx 2 \times 10^{12}$ cm^{-2}. The damage evolution curve up to this fluence could be described by the overlap damage model [68] with an overlap number of $m = 0$ and a track diameter of $d = 9$ nm (corresponding to a damage cross section $\sigma_{dam} = 6.4 \times 10^{-13}$ cm^2), which is in good agreement with the track diameter determined from the TEM images. This is an indication for direct impact disordering, i.e. no spatial overlap of tracks is necessary for lattice disordering. However, the observed deviation of the theoretical curve from the experimental data at fluences above $\approx 2 \times 10^{12}$ cm^{-2} indicates that the overlap damage model cannot satisfactorily describe the complex process of damage evolution in GaN. That the material is not rendered completely amorphous even at high ion fluences was also confirmed in another study by means of TEM investigations [12]. Probably, overlapping of ion tracks at higher ion fluences leads to partial damage annealing, i.e. a competition between ion track creation and annealing may occur thus preventing complete amorphization.

Given the strikingly different response of different binary semiconductors, e.g. InP and GaP, the question arises of how a ternary alloy such as $Ga_{1-x}In_xP$ would react. The effect of high electronic energy deposition on the damage evolution is illustrated in Fig. 9.11 for the examples of $Ga_{0.50}In_{0.50}$ P and $Ga_{0.47}In_{0.53}As$ and the related binary compounds for 185 MeV Au irradiation [4, 9].

As apparent, the binary In compounds exhibit considerable but different damage under SHI irradiation. While InP is rendered amorphous at an ion fluence of $N_I \approx 2 \times 10^{13}$ cm^{-2}, InAs exhibits much lower defect concentrations even at fluences as high as $N_I \approx 1 \times 10^{14}$ cm^{-2}. The binary Ga compounds are only slightly damaged as discussed already in Sect. 9.3.1.2. In contrast, damage accumulation in $Ga_{0.50}In_{0.50}P$ is similar to that of InP, but to amorphize the ternary a slightly higher ion fluence is required. This is obviously a consequence of the high radiation resistance of GaP leading to a change in damage susceptibility in the ternary compound compared to pure InP. Further experiments are necessary to determine whether this change comes abruptly at a certain stoichiometry or gradually over a large compositional range. But from the results it is clear that a ternary alloy with equal parts of In and Ga behaves much more like InP than like

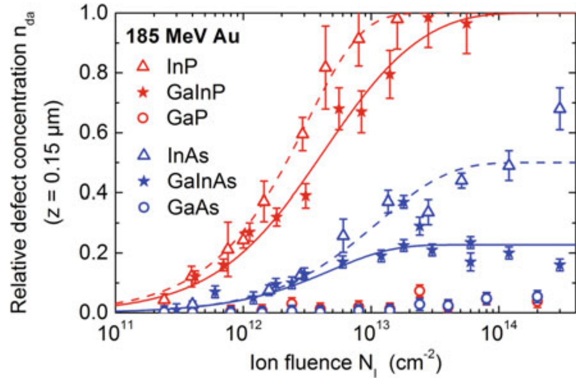

Fig. 9.11 Relative defect concentration n_{da} versus ion fluence N_I for 185 MeV Au irradiation of binary and ternary III–V compounds. The dashed and solid curves represent fits for the In binaries and ternaries, respectively, using a modified defect interaction and amorphization model (data from [4])

GaP. In $Ga_{0.47}In_{0.53}As$ damage formation is identical to that in InAs at lower ion fluences but for $N_I > 2 \times 10^{13}$ cm^{-2} the relative defect concentration saturates at $n_{da} \approx 0.20$. Thus, the ternary As compound exhibits damaging behaviour intermediate to that of InAs and GaAs.

The slower increase of the relative defect concentration with ion fluence for $Ga_{0.50}In_{0.50}P$, InAs and $Ga_{0.47}In_{0.53}As$ compared to InP can be interpreted in terms of a competition of damage formation and annihilation. Therefore the damage evolution curves cannot be fitted by means of the overlap damage model which does not consider any defect annealing. Instead, a modified defect interaction and amorphization model is used [69] which yields the cross-sections σ_{dam} and σ_{ann} for damage formation and annealing, respectively. The results of the fits are summarised in Table 9.2 and plotted in Fig. 9.11.

The observed amorphization of InP is consistent with the high damage cross-section σ_{dam} and an annealing cross-section $\sigma_{ann} = 0$. For $\sigma_{ann} = 0$ the model is identical with the overlap damage model by Gibbons [68]. The damage formation cross-section of $Ga_{0.50}In_{0.50}P$ is only slightly lower than that of InP, but the high annealing cross-section not present in InP reflects the higher fluence necessary to amorphize the ternary. Damage formation in InAs is characterized by a damage formation cross-section almost one order of magnitude less than that for InP reflecting the reduced susceptibility of InAs to SHI-induced damage formation.

Table 9.2 Damage formation and annealing cross-sections σ_{dam} and σ_{ann}, respectively, obtained from fitting the relative defect concentration n_{da} with the modified defect interaction and amorphization model [4]

	σ_{dam} (10^{14} cm^2)	σ_{ann} (10^{14} cm^2)
InP	32 ± 1	0
$Ga_{0.50}In_{0.50}P$	25 ± 3	21 ± 5
InAs	5 ± 1	10 ± 2
$Ga_{0.47}In_{0.53}As$	5 ± 1	22 ± 5

At the same time, SHI-induced damage annealing is also present in InAs. In $Ga_{0.47}In_{0.53}As$ the damage formation cross-section is equal to that of InAs. However, the annealing cross-section is twice as large as in InAs and explains the lower defect concentration measured at higher ion fluences in the ternary alloy.

9.3.3 Threshold Values

All experimental data on SHI-induced damage and track formation in semiconductors available till now indicate the existence of a threshold value of the electronic energy deposition, S_{et}, necessary to create visible tracks and amorphization of the material. For the determination of threshold values various methods are used. The comparison of the extension of individual tracks into depth obtained from XTEM images with the depth distribution of the electronic energy deposition yields the value of S_{et} directly [5]. Besides, S_{et} can be obtained from damage cross sections measured for different values of the electronic energy deposition. The damage cross sections are either calculated from track radii obtained from PV-TEM images or by fitting the fluence dependences of the RBS damage concentration in the framework of the overlap damage model [68] as described in the previous section. However, different experimental methods may yield quite different track radii and cross sections which explains the dispersion of the S_{et} values found for a given material in various sources. This problem is also reflected in calculations of S_{et} in the framework of the i-TS model which require at least one experimental S_{et} value for one material in order to fix calculation parameters (for details see [53]).

In Fig. 9.12 damage cross sections σ_{dam} for InP irradiated with Xe, Au and Pb ions are depicted versus the electronic energy deposition S_e.

The data points for Au and Pb with their nearly equal masses and those for Xe with smaller mass lie on two separate straight lines. In both cases the damage cross section increases linearly with the electronic energy deposition. Furthermore, the cross

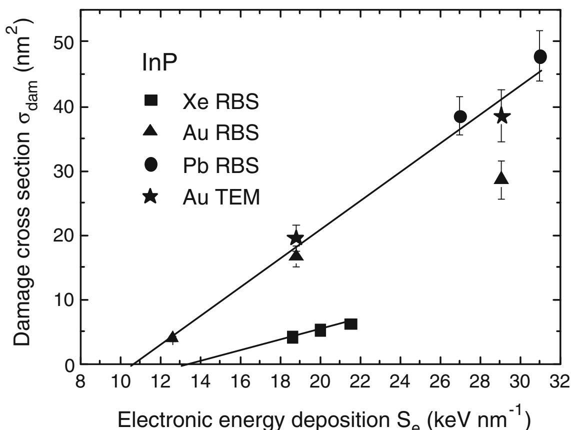

Fig. 9.12 Experimental damage cross sections, $\sigma_{dam,}$, determined from RBS and TEM analyses for InP irradiated with Xe, Au and Pb ions versus the electronic energy deposition S_e. The values for Xe and Au irradiation are taken from [53], those for Pb irradiation from [62]. The continuous *straight lines* are to guide the eye

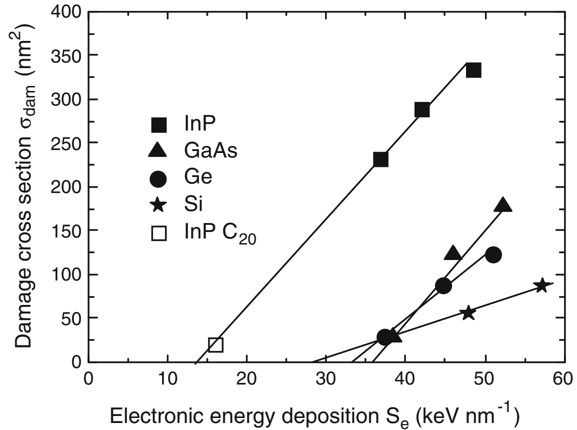

Fig. 9.13 Damage cross sections, σ_{dam}, of various semiconductors irradiated with cluster ions C_{60} and C_{20}, respectively. The cross sections were calculated from TEM track radii. The data are taken from [63] (InP), [26] (GaAs), [23] (Ge) and [25] (Si). The continuous *straight lines* are to guide the eye

sections for Au irradiation determined from TEM are in good agreement with those determined by means of RBS within the experimental uncertainty. The intersection of the lines with the abscissa yields threshold values S_{et} = 10.5 keV nm^{-1} in case of Au and Pb irradiation and 13.2 keV nm^{-1} in case of Xe irradiation. Note that from XTEM images a value of ≈13 keV nm^{-1} was estimated for InP irradiated with Xe ions (see Sect. 9.3.2.1). Although the result of i-TS calculations of the threshold value is influenced by the experimental value used, the calculated threshold values of S_{et} = 12 and 14.8 keV nm^{-1} for Au and Xe irradiation are in the same order of magnitude as those determined experimentally [53]. The results clearly show that there is no universal energy loss threshold valid for irradiation of all ions into InP, but the value significantly depends on the ion mass (velocity effect).

The damage cross sections of various semiconductors irradiated with fullerene ions are shown in Fig. 9.13 as a function of the electronic energy deposition. The threshold value for InP of ≈13.8 keV nm^{-1} is in good agreement with that obtained in case of monoatomic ion irradiation. For Si, Ge and GaAs with the cross sections given in literature [25, 26] one obtains threshold values of 28, 33 and 36 keV nm^{-1}, respectively. These values exceed those obtained for InP significatly reflecting the higher radiation resistance of these semiconductors compared to InP.

In Table 9.3 threshold values S_{et} for damage and track formation in various semiconductors irradiated with monoatomic and cluster ions are summarised. All semiconductors exhibit threshold values S_{et} > 10 keV nm^{-1} being significantly larger than those found for many insulators, amorphous materials and high-T_c superconductors [8]. While InP and InAs show damage and track formation for S_{et} ≈ 10–15 keV nm^{-1} the track formation threshold in GaP, GaAs, Si and Ge exhibits values in excess of ≈30 keV nm^{-1}.

The various semiconductors investigated show striking differences in damage behaviour under SHI irradiation even in case of irradiation with similar values of the electronic energy deposition S_e. The analysis of all data shows that neither the energy deposition per ion and unit path length nor the total energy deposition per unit volume alone can describe SHI irradiation effects in semiconductors. Instead,

Table 9.3 Threshold values of the electronic energy deposition, S_{et}, for damage and track formation in various semiconductors

Material	S_{et} (keV nm^{-1})		References
	Single ions	Cluster ions	
Si		28	[25]
Ge	46–49	33	[16], [25], [26]
$Si_{0.5}Ge_{0.5}$	34		[18]
GeS	19		[70]
InP	≈10.5–14	13.8	[53], [63]
InAs	16		[4]
InN	15		[12]
GaP	>29		[15]
GaAs		36	[25], [26]
GaN	15		[12]

velocity effects as well as the radial distribution of the energy deposition which should depend on both ion species and ion energy play an important role [53, 58]. In the following section damage formation induced by electronic energy deposition will be discussed in the framework of theoretical models described in Chap. 2.

9.4 Modelling of Track Formation

Because of the complexity of the energy relaxation processes involved in track and damage formation due to high electronic energy deposition a complete description of ion-solid interactions during swift heavy ion irradiation still does not exist [71–73]. However, in literature several models of damage formation due to electronic interactions are discussed: Coulomb explosion [74], lattice relaxation (athermal melting) [75] and the inelastic thermal spike (i-TS) model [76]. The appropriateness of the various models is still under debate. However, whereas Coulomb explosion has been ruled out as track formation mechanism at least for metals and semiconductors [72, 73], the thermal spike model as the most elaborated one currently seems to be the only model to provide approximate predictions on ion track formation in numerous conducting and non-conducting materials. A detailed overview of the existing models and their limitations is given in Chap. 2. In the following, results of some qualitative estimations as well as calculations in the framework of the i-TS model will be presented.

9.4.1 *Qualitative Estimations*

The different susceptibility of various semiconductors to SHI induced damage formation even for similar S_e values must be a consequence of differences in the processes induced by the high electronic energy deposition. As estimations on the

Table 9.4 Macroscopic parameters of various III–V compounds, Si and Ge (E_g-band-gap energy with (**d**) and (**i**) denoting a direct or indirect gap, respectively; ν_{LO}-long-wavelength longitudinal optical phonon frequency; C_a-heat capacity per unit volume of the atomic system; T_m-melting temperature; $Q = C_a (T_m - T_0)$-energy required to heat a unit volume to the melting point with T_0 being the temperature of irradiation (in this case room temperature); data from [2])

Material	E_g (eV)	ν_{LO} (THz)	Ca (J cm^{-3} K^{-1})	T_m (K)	Q (J cm^{-3})
Si	1.12 (i)	15.57	1.65	1687	2333
Ge	0.66 (i)	9.02	1.76	1210	1649
GaP	2.26 (i)	12.07	1.28	1730	1865
GaAs	1.43 (d)	8.54	1.76	1513	2182
GaSb	0.72 (d)	6.99	1.91	991	1371
InP	1.35 (d)	10.38	1.53	1335	1625
InAs	0.36 (d)	7.24	1.98	1210	1855
InSb	0.17 (d)	5.72	2.02	797	1058

basis of various models show [62, 77], there is no clear correlation of damage and track formation with main macroscopic parameters of the materials such as band-gap energy E_g or melting temperature T_m (see Table 9.4).

The lattice relaxation model (also called athermal melting model) [75, 77] assumes that structural instability results from the dense excitation of electrons from bonding states in the valence band to anti-bonding states in the conduction band. Consequently, for a given S_e value an increase in susceptibility to damage formation with decreasing band-gap energy E_g could be anticipated. Indeed, for all group-V species the increase of E_g for the Ga containing materials compared to the In compounds is accompanied by a decrease of the sensitivity to damage formation (cp. Fig. 9.11 and Table 9.4). Contrary, InP with its four times higher value of E_g compared to InAs is much more easily amorphized than InAs which contradicts the prediction of the model. Additionally, within the lattice relaxation model it is also argued that materials with higher phonon frequencies ν_{LO} of the lattice atoms show stronger instability within a given time after the excitation than those with lower ν_{LO} values [75]. Regarding the In compounds, InAs shows the lowest susceptibility to damage formation yet its phonon frequency is intermediate to those of InP and InSb in clear contradiction to the prediction of the model. Altogether, the evaluation of the validity of the lattice relaxation model for III–V compounds needs additional calculations as performed in [75] for Si.

In the framework of the i-TS model the sensitivity to damage formation is related to the electron-phonon coupling strength g which gives the efficiency of the energy transfer from the electronic system to the lattice. For inorganic insulators it was reported that higher band-gap energies yield larger g values [78]. Consequently, materials with high gap energy should be more susceptible to damage formation because for higher g values a higher fraction of the electronic energy deposition S_e is transferred to the lattice atoms thus causing a more pronounced damage formation. This is opposite to the predictions of the lattice relaxation model discussed above and completely disagrees with the experimental findings. For all group-V species, the Ga

containing material has a significantly higher gap energy than the corresponding In compound yet the latter is more easily damaged (Fig. 9.11). Among the In compounds, InAs shows the lowest susceptibility to damage formation yet its band-gap is intermediate to those of InP and InSb similar to the phonon frequencies discussed above. Additionally, both Si and Ge with their significantly differing gap energies exhibit a high radiation resistance confirming that E_g is not the only measure for the degree of susceptibility to SHI-induced damage formation.

In another estimation based on the analytical thermal spike (a-TS) model [79] the energy Q necessary to heat different semiconductors to their melting points is calculated [4, 62]. In this a-TS model the threshold energy S_{et} necessary to create visible tracks is proportional to the energy $Q = C_a\,(T_m - T_0)$, with C_a being the heat capacity per unit volume of the atomic system and T_m and T_0 denote the melting and irradiation temperature, respectively (see Table 9.4). Furthermore, S_{et} is predicted to be inversely proportional to the electron-phonon coupling efficiency γ which is the ratio between the electronic energy transferred to the atomic system and the total deposited electronic energy S_e. On the basis of this relation and the experimental results on track formation it can be concluded that low Q-values are advantageous for track formation. Indeed, in Si, Ge and GaAs with their high values of Q no tracks were detected after single ion irradiation, whereas in InSb, GaSb and InP with lower Q values track formation is observed (see Sect. 9.3). Additionally, for all group-V species, Q is higher for the Ga containing material than for the In compound, which is primarily caused by the difference of the melting temperature and which agrees with the higher radiation resistance of the Ga compounds. Furthermore, for a given group-III species, Q is largest for the As compound and smallest for the Sb compound again in agreement with the observed high and low radiation resistance, respectively. This trend in the influence of Q on damage formation thus qualitatively agrees with the experimentally observed damage formation behaviour and indicates that, similar to the case of insulators, a reasonable theoretical description of the damage formation in semiconductors due to high electronic energy deposition should be possible on the basis of a thermal spike mechanism. However, the agreement between Q and the observed susceptibility to damage formation is only qualitative. While InP and InAs exhibit Q values equal to those of Ge and GaP, respectively, the behaviour under SHI irradiation is fundamentally different demonstrating that a more complex thermal spike model is needed in order to successfully describe the damage formation in semiconductors.

9.4.2 Application of the Inelastic Thermal Spike (i-TS) Model

As already mentioned, the thermal spike model assumes that the energy deposited into the electronic system is transferred to atomic motion via electron-phonon coupling [76]. As a consequence, the thermal motion of the lattice atoms leads to

melting of the material along the ion path if the temperature exceeds the melting point. During the following rapid resolidification the molten zone may be quenched into the amorphous phase. The evolution of the thermal spike is usually described by two coupled non-linear differential equations, as discussed in detail in Chap. 2.

$$\begin{aligned} C_e(T_e)\frac{\partial T_e}{\partial t} &= \frac{1}{r}\frac{\partial}{\partial r}\left[rK_e(T_e)\frac{\partial T_e}{\partial r}\right] - g(T_e - T_a) + A(r,t) \\ C_a(T_a)\frac{\partial T_a}{\partial t} &= \frac{1}{r}\frac{\partial}{\partial r}\left[rK_a(T_a)\frac{\partial T_a}{\partial r}\right] + g(T_e - T_a) \end{aligned} \tag{9.1}$$

where C_e, K_e and C_a, K_a are the heat capacity per unit volume and the thermal conductivity of electronic and atomic system, respectively. T_e and T_a are the electronic and atomic temperatures, respectively, r is the radial distance from the ion trajectory, t denotes the time, g stands for the electron-phonon coupling strength and $A(r,t)$ represents the energy density deposited into the electronic system by the incident ion. The first equation thus describes the temperature evolution in the electronic system and the second that in the lattice. The coupling term, $g(T_e - T_a)$, describes the energy transferred from the electronic system to the lattice via electron-phonon coupling.

The electron-phonon coupling strength, g, originally derived for metals [80] can be calculated according to

$$g = \frac{\pi m_e n_e v_s^2}{6\tau_e(T_e)T_e} \tag{9.2}$$

where n_e is the volume concentration of free electrons, v_s is the sound velocity, and $\tau_e(T_e)$ is the mean free time between two collisions of an electron at the temperature T_e (see Chap. 2). Because hot electrons in the conduction band of non-metallic solids behave like hot electrons in a metal [81, 82], (9.2) can also be used for semiconductors. The only unknown parameter in this equation is $\tau_e(T_e)$ which can be estimated from experimental data on track formation (for details see [53] and references therein).

Another scenario to determine the electron-phonon coupling strength is to use the electron-phonon mean free path, λ, which is connected with g and the electron-phonon mean free time τ_e according to

$$\lambda^2 = D_e\tau_e = \frac{D_e C_e}{g},\ \tau_e = \frac{C_e}{g} \tag{9.3}$$

where C_e and D_e are the specific heat and the diffusivity of the electrons, respectively [78, 83, 84] (see Chap. 2). This method has been successfully applied to a number of insulators, mainly amorphizable oxides, where the electron-phonon coupling strength at high electronic excitations is not known [85]. Fitting the evolution of the experimental track radii of the insulators with S_e in the framework

of the i-TS model yields a monotonic decrease of λ as a function of the gap energy E_g [78]. This reference curve $\lambda_{ref}(E_g)$ has also been used for the discussion of track formation in semiconductors [12]. While these two approaches do not a priori contradict each other, very different values for τ_e, λ and g are reported in the literature that vary by several orders of magnitude (see e.g. [12, 53] and Chap. 2). A general description of track and damage formation in SHI-irradiated semiconductors on the basis of the i-TS model is thus still lacking as discussed in more detail below.

Another important term in (9.1) is the energy deposited into the electronic system, $A(r,t)$, which is the driving force for the evolution of the thermal spike. An extension of the i-TS model for semiconductors suggested by Kamarou et al. [53] mainly concerns this term which contains the information about the initial process of the energy transfer from a SHI to the electronic system, the so called "ionization spike". As a result of the treatment of this very first energy deposition stage, the time dependence of $A(r,t)$ is assumed to be Gaussian, while the spatial distribution consists of a "core" region given by the zone of primary ionization and a "halo" region defined by the range of the most energetic electrons produced.

Using this extended i-TS model, the maximum atomic temperature at the track axis, T_{max}, and the maximum radius of the molten zone, r_{sim}, were calculated for single crystalline InP irradiated with various ions at RT and LNT. The electron-phonon coupling strength was calculated using (9.2) with $\tau_e(T_e)$ estimated from experimental track data (for details see [53] and references therein). It is clearly to be seen in Fig. 9.14 that for RT irradiations with Pb, Au and Xe the calculated maximum atomic temperatures exceed the melting point T_m = 1335 K for InP within characteristic ranges of the ion energy. Conversely, for RT irradiations with Kr where the electronic energy deposition is smaller than the threshold value, $S_e < S_{et}$, and for all LNT irradiations where $S_e > S_{et}$, the maximum atomic temperatures do not reach the melting temperature of InP. Additionally, the calculated maximum temperatures reached at the track axis differ by about 800 K for RT and LNT irradiations despite the same value of S_e. This is due to the difference

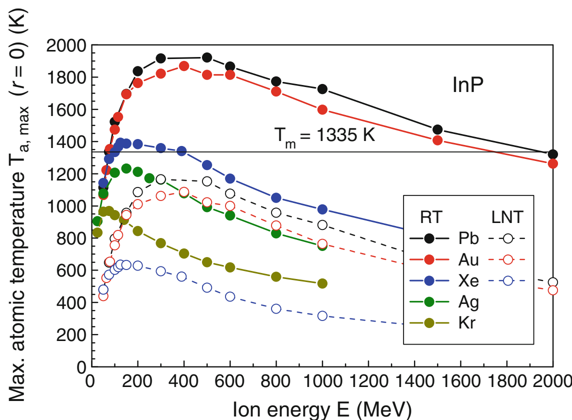

Fig. 9.14 Dependence of the maximum atomic temperature $T_{a,max}$ at the ion track axis (r = 0) on the ion energy for InP irradiated with various ions at room temperature (RT) and liquid nitrogen temperature (LNT) [53]

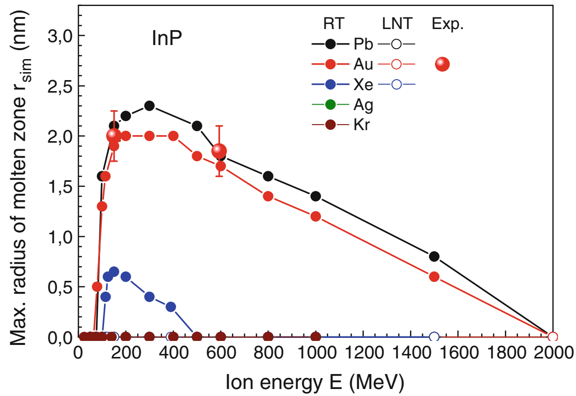

Fig. 9.15 Maximum radius of the molten zone r_{sim} for InP irradiated with various ions as a function of the ion energy. The experimental track radii for Au irradiation determined with TEM are also marked [53]

in the thermal conductivity which is about seven times larger at LNT than at RT. Consequently, the heat is transported away from the track much more efficiently at LNT so that, according to the calculations, melting is not possible in virgin crystalline material.

The calculated maximum radii of the molten tracks r_{sim} are depicted in Fig. 9.15 versus the ion energy. In case of RT irradiation the calculated radii clearly vary with ion species and ion energy. However, for Xe irradiation the maximum radius does not exceed a value of about 0.6 nm which is close to the lattice constant of InP of 0.587 nm. Consequently, under these conditions no tracks are formed but obviously point defects and point defect clusters are created. This small value of r_{sim} correlates with the calculated maximum temperature T_{max} which only slightly exceeds the melting temperature in a narrow region of the ion energy (Fig. 9.14). Additionally, for Ag and Kr irradiation at RT and for all LNT irradiations $r_{sim} = 0$ which also correlates with the energy dependence of the maximum temperature which does not exceed the melting point in these cases.

Altogether, the thermal spike calculations confirm the experimental results obtained for track and damage formation in SHI irradiated InP (see Sect. 9.3.2). In accordance with the energy dependence of the maximum temperature, Au irradiation leads to the formation of continuous tracks in the energy region where the melting temperature is exceeded, and the track radii determined from TEM analyses ($r_{TEM} \approx 2$ nm for 150 and 593 MeV Au) agree well with the calculated radii (see Fig. 9.15). In case of Xe irradiation at low ion fluences no visible tracks are detected, but with increasing ion fluence more or less discontinuous tracks are found the number of which is smaller than the ion fluence. As mentioned before, this can be explained by an increasing number of point defects with increasing ion fluence. This leads to a stronger interaction of the excited electrons with the atoms which causes an enhanced energy transfer to the lattice atoms thus favouring visible track formation. In the framework of the thermal spike model, a more efficient transfer of energy from the excited electrons to the lattice is equivalent to a higher electron-phonon coupling strength g. In order to get a qualitative estimation of the

influence of this effect on track formation in InP, track radii r_{sim} were calculated with the same parameters but with the g value multiplied by a factor α_g. $\alpha_g = 1$ corresponds to irradiation into perfect InP, $\alpha_g > 1$ stands for irradiation into pre-damaged material. For example, in case of 250 MeV Xe irradiation the calculated radius approximately corresponds to that determined from TEM analyses, $r_{sim} \approx r_{TEM} \approx 2.3$ nm, for $\alpha_g \approx 2$ [53]. This suggests that the energy transfer from the electronic system to the lattice is twice as effective in pre-damaged material as in virgin InP.

Recently, a unified i-TS model was presented by Mishra et al. [86] which is based on the extended i-TS model [53] and takes into account the influence of the nuclear energy deposition, S_n, on damage formation in SHI irradiated semiconductors, similar as it was done earlier for silica [87] and metals [88]. Using this model and additionally taking into account the latent heat of fusion at the melting point, the existing experimental data on SHI irradiation of InP [53] were re-evaluated. With assumptions previously made for metals [84, 89] the electron-phonon coupling strength in this study is expressed as

$$g = \frac{\pi^4 (k_B n_e v_s)^2}{18 K_a(T_a)} \tag{9.4}$$

with the temperature dependent thermal conductivity $K_a(T_a)$ of the semiconductor. In this expression the only free parameter is the volume concentration of the free electrons, n_e. For details of the calculation and the parameters used the reader is referred to [86]. The simulations show that for a concentration of free electrons of $n_e = 2\,N = 7.92 \times 10^{22}$ cm^{-3}, with N being the atomic density of InP, the temperature of the atomic system exceeds the melting temperature for all irradiations with electronic energy depositions above the threshold value for track formation ($S_{et} \approx 14$ keV nm^{-1}). This is in agreement with [53] even without considering S_n. The calculated track radii are in good agreement with the experimentally determined ones [53], and there is no remarkable difference between the radii determined with and without considering the contribution of the nuclear interaction. Consequently, track formation and amorphization at electronic energy depositions $S_e > S_{et}$ are caused by the high value of S_e and can be described in the framework of the i-TS model without considering the nuclear stopping. But in case of irradiation with S_e values close to or below the threshold value S_{et} damage accumulation is also influenced by nuclear interaction [55]. The latter may lead to the formation of point defects and to a more efficient transfer of energy from the excited electrons to the lattice atoms, as discussed above.

To study the influence of nuclear energy deposition in the subthreshold irradiation regime, the time evolution of the lattice temperature of InP irradiated with 64 MeV Au ($S_e = 10.7$ keV nm^{-1}), 82 MeV Xe ($S_e = 13.5$ keV nm^{-1}) [49] and 100 MeV Ag ($S_e = 13.5$ keV nm^{-1}) was simulated using the unified i-TS model [86]. In all cases the melting temperature is not reached when only the effect of S_e is taken into account in the model which corresponds to the result obtained in [53].

However, when considering both, S_e and S_n, the lattice temperature exceeds the melting temperature indicating the possible occurrence of a molten zone. When additionally considering the latent heat of fusion an incomplete phase transformation and a partly molten phase are observed. However, the radius of the partly molten zone caused by a single ion is considered to be too small to create a stable track in the material. Therefore it is assumed that heavily damaged layers observed experimentally at high ion fluences [53] are formed by accumulation and overlap of the residual defects in the damaged regions produced by the individual ions [86]. Altogether the simulations show that for irradiations with $S_e < S_{et}$ consideration of only S_e or both S_e and S_n in the i-TS model indicate different mechanisms of damage formation. However, for a still better understanding of the combined effect of nuclear and electronic energy deposition during SHI irradiation further experimental and theoretical work seems to be necessary.

Contrary to InP, no visible amorphous tracks are formed in Si, Ge, GaP and GaAs by single swift ions whereas cluster ion irradiation clearly results in track formation (see Sect. 9.3.1). Using the experimental track radii determined for cluster ion irradiation of Si, Ge, [23–26] as well as InP [63] the extended i-TS model was applied to calculate the maximum atomic temperatures for InP, Si and Ge irradiated with 593 MeV Au ions at RT [15].

It is clearly to be seen in Fig. 9.16 that, in contrast to InP, in both Ge and Si the maximum atomic temperature within the ion track does not reach the corresponding melting temperatures by far. For Si this was recently confirmed by calculations using a unified i-TS model suggested by Lazanu [90] that also takes into account the effect of both nuclear and electronic energy deposition on damage formation as well as by Monte Carlo calculations of the early stages of track formation [91]. These results explain why no continuous tracks were detected in crystalline Si and Ge and only discontinuous ones were observed in Ge at very high ion fluences [16] (see Sect. 9.3.1.1). In this latter case the increasing point defect concentration enhances the electron-phonon coupling strength until sufficient energy is transferred to the lattice atoms to induce melting. The observed discontinuity of the tracks can

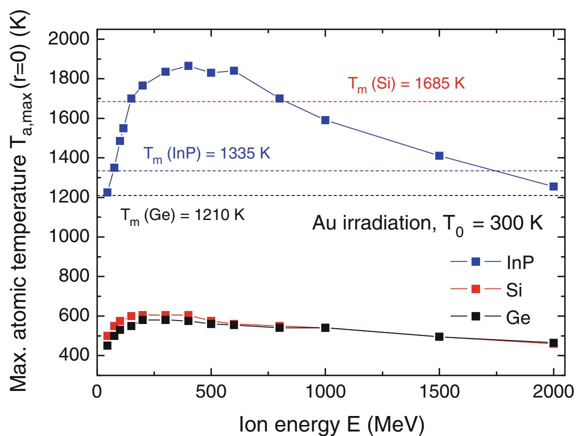

Fig. 9.16 Maximum atomic temperature $T_{a,max}$ at the ion track axis ($r = 0$) versus ion energy for InP, Si and Ge irradiated with 593 MeV Au ions at room temperature. The *dashed lines* indicate the melting temperatures of the three materials [15]

be explained by either (i) dynamic fluctuations of the ion charge due to electron capture and loss processes if the electronic energy deposition is close to the threshold value for melting [55, 92] or by (ii) breaking of the liquid phase into droplets due to surface tension (Rayleigh instability). The latter process is facilitated if the mass density in the liquid state is higher than that in the solid state, which holds for InP, InSb, GaAs, Ge and Si [15].

For the analysis of SHI induced damage and track formation in III-N semiconductors in the framework of the i-TS model [12] the approach to estimate the electron-phonon coupling strength by the electron-phonon mean free path, λ, was used [78, 85]. With the λ values achieved from fits of the track sizes experimentally determined for the various materials and irradiation conditions track radii were calculated as function of S_e and compared with the experimental data. At least in case of GaN and InN the experimental results well agree with the model predictions for the evolution of the track radii with the electronic energy deposition. Deviations observed in case of AlN are due to experimental uncertainties. However, for discontinuous tracks a comparison of the experimental radii with theoretical predictions is not straightforward since neither statistical fluctuations nor Rayleigh instabilities are included in the i-TS model [12].

With the same approach experimental data previously published for cluster ion irradiation of Si, Ge, GaAs and InP [24–26, 63] were analysed. In these materials calculations in the framework of the i-TS model also well reproduce the dependences of the track radii on the electronic energy deposition [12].

The λ values obtained from the analysis of the various semiconductors are plotted in Fig. 9.17 versus the gap energies and compared with the reference curve obtained for oxides (solid black line).

It is obvious that the values for InN, InP and GaN match very well with the reference curve, whereas those for Si, Ge, GaAs and AlN are far from agreeing with this relation. A fit of the data (blue dotted line) indicates higher λ values for some semiconductors with small E_g compared to those of the oxides, but the value for AlN completely deviates from both dependences. These results show that a uniform description of track formation in semiconductors with the i-TS model is obviously

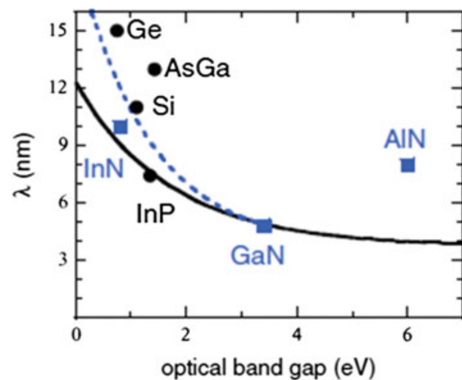

Fig. 9.17 Evolution of the electron-phonon mean free path, λ, versus the gap energy, E_g, for various semiconductors. The *solid black curve* represents the relation achieved for oxides (λ_{ref}) [78, 85], and the *blue dotted line* is a fit of the data for semiconductors [12]

not possible if the electron-phonon coupling strengths are reduced to the electron-phonon mean free path λ, i.e. to a dependence only on the gap energy E_g (see also Sect. 9.4.1).

It should also be mentioned here that the λ values for semiconductors calculated with (9.3) and D_e and τ_e values from literature remarkably deviate from those shown in Fig. 9.17. In case of InP, for example, with the mean time between two electron collisions, $\tau_e = 8.5 \times 10^{-17}$ s, calculated by Kamarou et al. [53], one obtains $\lambda = 0.2$ nm. Using the electron-phonon mean free time $\tau_e = 0.1 \times 10^{-12}$ s obtained from fs laser experiments and used in the calculations of Toulemonde (see Chap. 2.3.5) yields $\lambda = 7$ nm which approximately corresponds to the value given in Fig. 9.17. According to (9.3), the values of the electron-phonon coupling strength g derived with $\lambda \approx 7$ nm deviate from those obtained by Kamarou et al. [53] with full i-TS calculations ($\lambda = 0.2$ nm) by two to four orders of magnitude. These differences are obviously the consequence of the uncertainty in the interpretation of the physical meaning of the interaction time τ_e.

In order to describe SHI induced structural modifications observed in non-amorphizable insulators, as e.g. CaF_2, the same approach for the electron-phonon coupling strength as described above was used, but additionally the occurrence of a vapour phase along the ion path was considered in the i-TS model [90]. This modification of the thermal spike model and its discussion in literature will not be treated here in detail, and the interested reader is referred to [12, 78, 93–96] and the references therein as well as to Chaps. 2 and 8 of this book. However, applying this model to the description of damage and track formation in semiconductors did also not result in a satisfactory explanation of the differences in track formation between oxides and semiconductors on the one hand and between different semiconductors on the other [12]. Obviously the measured tracks do not reflect all atomic motion induced by the excited electrons. Concerning the semiconductors, for example, a thermally stimulated solid-phase epitaxial growth (SPEG) being different for the various materials might explain the different susceptibility to track formation as it was suspected for InAs and InP [4].

In conclusion, many aspects of track and damage formation due to high electronic excitation of semiconductors can be adequately reproduced in the framework of the i-TS model. However, none of the existing modifications of the i-TS model seems to be able to provide a general description of track formation due to SHI irradiation in all materials indicating that additional experimental and theoretical work is necessary.

9.5 Summary and Discussion

It is obvious that various semiconductors exhibit different sensitivity to damage formation by high electronic excitation even for comparable values of the electronic energy deposition. In InP, InSb, GaSb, InAs, GaN, and InN heavily damaged or amorphous tracks were registered by means of TEM after monoatomic ion

irradiation above certain threshold values of the electronic energy deposition. With increasing ion fluence an increase of the damage concentration until complete amorphization was observed in these materials. Contrary, in Si, Ge, GaAs, AlAs, and SiC, tracks as well as amorphization do not occur in the electronic energy loss regime available for monoatomic ion beams. However, cluster ions with their significantly higher electronic energy deposition compared to monoatomic irradiation easily form tracks in Si, Ge and GaAs.

As possible reasons for the low radiation sensitivity of some semiconductors it may be suspected that either SHIs do not create significant damage upon impact or damage is produced and then annealed immediately thereafter or during subsequent irradiation. A combination of material-specific damage formation and annealing may of course also be operative. Unfortunately, with the experimental techniques available the irradiated material is probed long after the ion energy has been dissipated which makes it impossible to distinguish between the two scenarios. Here molecular dynamics simulations could provide useful insight into the processes. Nevertheless, for SHI irradiation of pre-damaged InP and GaAs clear evidence of damage annealing has been found. In GaAs, which in its crystalline phase is not sensitive to monoatomic SHI induced damage and track formation, SHI irradiation into pre-damaged layers causes significant damage annealing which increases with increasing ion fluence [59]. Similar as in GaAs, SHI irradiation in pre-damaged InP with electronic energy depositions below the threshold for track formation leads to remarkable annealing of damage, whereas above-threshold irradiation essentially increases the initial damage concentration [58, 59]. The latter is in accordance with the behaviour of virgin InP under SHI irradiation where amorphous tracks are formed above the threshold value of electronic energy deposition.

In InAs significant damage is formed under SHI irradiation but the defect concentration increases much more slowly than for InP and amorphization is not reached for reasonable ion fluences. This can be explained by significant damage annealing during irradiation which also plays a role in the ternary compounds $Ga_{0.47}In_{0.53}As$ and $Ga_{0.50}In_{0.50}P$ [4]. It should be mentioned that in the nuclear stopping regime both InP and InAs can be amorphized but the fluence necessary to render InAs amorphous is approximately two orders of magnitude larger than for InP demonstrating pronounced dynamic damage annealing in InAs [97]. Furthermore, thermally stimulated solid-phase epitaxial growth operative much below the melting temperature was observed at amorphous-crystalline interfaces in III–V compounds [98]. The growth rate at a given temperature is approximately four orders of magnitude higher for InAs than for InP so that the heat dissipated after the ion impact could lead to much stronger annealing of damaged tracks in InAs relative to InP. However, since the growth rates for GaAs and InP are very similar, thermally induced epitaxial growth alone cannot describe the differences in the damaging behaviour of the various materials. Still, all these results allow the conclusion that the resulting damage concentration formed as a consequence of high electronic excitation is more or less the result of competing processes of damage formation and annealing. Whether damage is formed in the first place and which of the two processes dominates depends mainly on the material.

In general, no clear correlation exists between damage and track formation in various semiconductors and their macroscopic material parameters such as the thermal conductivity, melting temperature or gap energy. For the description of damage and track formation due to high electronic energy deposition four competing mechanisms are discussed: Coulomb explosion, shock waves, lattice relaxation (athermal melting) and inelastic thermal spikes (for details see Chap. 2). Among them the thermal spike model is the most elaborated one and currently seems to be the only model being able to provide approximate predictions on track formation in various conducting and nonconducting materials. It has been successfully applied to some metals, intermetallic compounds and dielectrics (see Chap. 8). Estimations in the framework of the a-TS model confirm that melting along the ion trajectory is very likely involved in the track formation process in semiconductors. They show that the trend in the experimental data follows the energy necessary to heat the materials to the melting point indicating the applicability of the thermal spike formalism to track formation. However, clear and direct experimental evidence for the occurrence of melting during the passage of a SHI through a semiconductor does not exist.

Indirect evidence of melting can be obtained from intermixing experiments at interfaces of layered structures using above threshold SHI irradiation where the threshold value of the electronic energy deposition is determined by the more radiation resistant material of the structure [99]. That means, efficient intermixing occurs if both sides of the interface are locally molten. This effect is governed by very efficient interdiffusion of the constituent atoms [100, 101]. Diffusion coefficients from 10^{-4} to 10^{-2} cm^2 s^{-1}, i.e. values several orders of magnitude greater than those observed in the solid state, are characteristic for liquid state diffusion and support the idea that under these conditions interface mixing results from transient interdiffusion in the molten tracks [102]. Indeed, experimental evidence for efficient intermixing not explainable by solid-phase diffusion was found at the interface between a Bi layer and InP after SHI irradiation whereas no remarkable interdiffusion occurred at the Bi/GaAs interface under the same conditions [15]. Bi with its low melting temperature belongs to the metals with low radiation resistance with respect to SHI irradiation [83, 84, 103]. Therefore, in combination with InP melting occurs in both materials under SHI irradiation leading to significant interdiffusion in the liquid phase. Contrarily, absent intermixing in the Bi/GaAs system is a consequence of the low sensitivity of GaAs to SHI induced track formation. Intermixing experiments have also been performed in Si-metal layers in order to prove possible melting of Si under SHI irradiation. Intermixing at the Ni/Si interface, for example, was considered to be an indication of melting of the silicon substrate [94]. However, this interpretation is questionable because the electronic energy deposition necessary to melt Ni is in excess of ≈ 60 keVnm^{-1} [84]. Therefore the observed intermixing in this system cannot be explained as a process which proceeds in the liquid phase. Instead, it is more likely a solid state reaction of silicide formation which occurs at temperatures far below the melting temperature of silicon (the different nickel silicide phases are formed between 250 and 450 °C; for details see [104]).

The question whether molten tracks are formed in Si under SHI irradiation is thus very difficult to answer experimentally. Simulations using an extended thermal spike model, however, do provide some valuable insight on this topic. The experimental data available on SHI irradiation of semiconductors allow the conclusion that the thermal spike mechanism is the dominating process in SHI induced track formation also in semiconductors. In accordance with that, calculations of maximum atomic temperatures and radii of molten zones in the framework of an extended i-TS model confirm the experimental findings. In InP, where visible tracks were found, the melting temperature is exceeded for irradiation above the threshold value of the electronic energy deposition [53]. The calculated radii of the molten zones are at least in the same order of magnitude as the measured track radii. However, the calculated values are generally smaller than those determined from RBS or TEM investigations. This is understandable because the calculated radii are exclusively those for perfectly ordered material. In contrast to that the radii determined from RBS are averaged values resulting from point defects, point defect clusters and tracks, i.e. RBS overestimates the real track radii. Finally, the track diameters determined by TEM cover a broad range consisting of narrow tracks formed by single ions hitting undamaged crystalline areas and wider ones produced by a number of ions hitting the same area. Nevertheless, in cases where each ion is supposed to produce a track, the calculated values are close to the lower limit of those measured by TEM. In contrast to InP, the calculated maximum atomic temperature in Si and Ge is far below the corresponding melting temperatures indicating that no molten zones are formed in the first place. This contradicts earlier discussions assuming melting of Si and subsequent resolidification into the crystalline state as it is known to occur during pulse laser irradiation of amorphous Si layers on top of crystalline Si substrates.

However, it should be mentioned here that various modifications of the i-TS model, as for example concerning the estimation of the electron-phonon coupling strength, the effect of nuclear energy deposition, the consideration of the latent heat of fusion or the introduction of a “boiling criterion” did not yield deeper insight into the processes of SHI induced damage formation compared to those obtained when using the extended thermal spike model, at least in cases of above threshold irradiation.

In summary, all experimental findings on SHI induced damage formation in semiconductors as well as the results of various calculations can be understood in the framework of the thermal spike model. Apart from the legitimate criticism (see e.g. [73] and references therein) concerning its applicability to non-equilibrium processes such as SHI irradiation, it is currently the only model that allows to perform calculations and to make predictions on track formation also in semiconductors. Especially the large influence of the irradiation temperature on the track radii and the internal structure of visible tracks supports the thermal spike mechanism and seems to contradict the others, at least for above threshold irradiations. Additionally, the results of intermixing of Bi/InP and Bi/GaAs layered structures support local melting within the ion tracks and are a further argument for the thermal spike model of track formation. But this does not mean that other non-thermal processes, presumably the lattice relaxation mechanism, as well as

processes triggered by the small contribution of nuclear energy loss may contribute to damage and track formation. In case of subthreshold irradiation such processes may be the dominating ones, as e.g. shown in [91] for Si.

However, the completely different response of semiconductors with similar properties to SHI irradiation is still an open question and discussed in literature. Various approaches that relate the radiation resistance of materials to their geometrical structure (e.g. [105]) or to certain chemical and physical properties, such as ionicity, density, elastic moduli, melting point (e.g. [106]) were discussed. But none of these models is able to describe all different materials self consistently. Further calculations using more elaborate models are therefore needed to obtain a more comprehensive picture. Unfortunately, such attempts are often hindered by missing material parameters and the lack of experimental data on track radii. Renewed efforts with regard to both theoretical calculations and experimental studies are thus required in order to fully understand damage formation in semiconductors due to high electronic excitation.

Acknowledgements The authors thank S. Klaumünzer, A. Kamarou and M.C. Ridway and his group for their valuable collaboration and the German Research Council (DFG), the Federal Ministry for Education and Research of Germany (BMBF) and the German Council for Academic Exchange (DAAD) for financial support.

Furthermore, the authors are very grateful to Marcel Toulemonde for valuable discussion concerning the applicability of the inelastic thermal spike model to describe track formation in semiconductors.

References

1. J.F. Ziegler, J.P. Biersack, U. Littmark, *The Stopping and Range of Ions in Solids* (Pergamon, New York, 2003)
2. S. Adachi, *Properties of Group IV, III-V and II-VI Semiconductors* (Wiley, New York, 2005)
3. E. Wendler, Nucl. Instr. Meth. B **267**, 2680 (2009)
4. C.S. Schnohr, P. Kluth, R. Giulian, D.J. Llewellyn, A.P. Byrne, D.J. Cookson, M.C. Ridgway, Phys. Rev. B **81**, 075201 (2010)
5. O. Herre, W. Wesch, E. Wendler, P.I. Gaiduk, F.F. Komarov, S. Klaumünzer, P. Meier, Phys. Rev. B **58**, 4832 (1998)
6. W. Wesch, O. Herre, P.I. Gaiduk, E. Wendler, S. Klaumünzer, P. Meier, Nucl. Instr. Meth. B **146**, 341 (1998)
7. W. Wesch, A. Kamarou, E. Wendler, Nucl. Instr. Meth. B **225**, 111 (2004)
8. N. Itoh, D.M. Duffy, S. Khakshouri, A.M. Stoneham, J. Phys. Condens. Matter **21**, 474205 (2009)
9. W. Wesch, E. Wendler, C. Schnohr, Nucl. Instr. Meth. B **277**, 58 (2012)
10. M. Levalois, I. Lhermitte-Sebire, P. Marie, E. Paumier, J. Vicens, Nucl. Instr. Meth. B **107**, 239 (1996)
11. S. Mansouri, P. Marie, C. Dufour, G. Nouet, I. Monnet, H. Lebius, Nucl. Instr. Meth. B **266**, 2814 (2008)
12. M. Sall, I. Monet, F. Moisy, C. Grygiel, S. Jublot-Leclerc, S. Della-Negra, M. Toulemonde, E. Balanzat, J. Mater. Sci. **50**, 5214 (2015)
13. S.J. Zinkle, V.A. Skuratov, D.T. Hoelzer, Nucl. Instr. Meth. **191**, 758 (2002)

14. M. Sall, I. Monnet, C. Grygiel, B. Ban D`Etat, H. Lebius, S. Leclerc, E. Balanzat, Europhys. Lett. **102**, 26002 (2013)
15. A. Kamarou, W. Wesch, E. Wendler, A. Undisz, M. Rettenmayr, Phys. Rev. B **78**, 054111 (2008)
16. F.F. Komarov, P.I. Gaiduk, L.A. Vlasukova, A.J. Didyk, V.N. Yuvchenko, Vacuum **70**, 75 (2003)
17. F.F. Komarov, L.A. Vlasukova, V.N. Yuvchenko, T.V. Petlitzkaya, P. Zukowski, Vacuum **78**, 353 (2005)
18. P.I. Gaiduk, A. Nylandsted Larsen, C. Trautmann, M. Toulemonde, Phys. Rev. **B 66**, 045316 (2002)
19. P.I. Gaiduk, A. Nylandsted Larsen, J. Lundsgaard Hansen, C. Trautmann, M. Toulemonde, Appl. Phys. Lett. **83**, 1746 (2003)
20. A. Meftah, F. Brisard, J.M. Costantini, M. Hage-Ali. J.P. Stoquert, F. Studer, M. Toulemonde, Phys. Rev. **B 48**, 920 (1993)
21. C.W. Rischau, C.S. Schnohr, E. Wendler, W. Wesch, J. Appl. Phys. **109**, 113531 (2011)
22. T. Steinbach, Th Bierschenk, S. Milz, M.C. Ridgway, W. Wesch, J. Phys. D Appl. Phys. **47**, 065301 (2014)
23. A. Dunlop, G. Jaskierowicz, S. Della-Negra, Nucl. Instr. Meth. B **146**, 302 (1998)
24. B. Canut, N. Bonardi, S.M.M. Ramos, S. Della-Negra, Nucl. Instr. Meth. B **146**, 296 (1998)
25. A. Colder, O. Marty, B. Canut, M. Levalois, P. Marie, X. Portier, S.M.M. Ramos, M. Toulemonde, Nucl. Instr. Meth. B **174**, 491 (2001)
26. A. Colder, B. Canut, M. Levalois, P. Marie, X. Portier, S.M.M. Ramos, J. Appl. Phys. **91**, 5853 (2002)
27. W.-K. Chu, J.W. Mayer, M.-A. Nicolet, *Backscattering Spectrometry* (Academic Press, New York, 1978)
28. G. Götz, K. Gärtner (eds.), *High Energy Ion Beam Analysis of Solids* (Akademie-Verlag, Berlin, 1988)
29. K. Gärtner, Nucl. Instr. Meth. B **132**, 147 (1997)
30. W. Wesch, A. Kamarou, E. Wendler, S. Klaumünzer, Nucl. Instr. Meth. B **242**, 363 (2006)
31. W. Wesch, A. Kamarou, E. Wendler, A. Undisz, M. Rettenmayr, Nucl. Instr. Meth. B **257**, 283 (2007)
32. P.J. Newby, B. Canut, J.-M. Bluet, S. Gomes, M. Isaiev, R. Burbelo, K. Termentzidis, P. Chantrenne, L.G. Frechette, V. Lysenko, J. Appl. Phys. **114**, 014903 (2013)
33. B. Canut, M. Massoud, P. Newby, V. Lysenko, L. Frechette, J.M. Bluet, I. Monnet, Nucl. Instr. Meth. B **327**, 99 (2014)
34. A. Simon, F. Paszti, A. Manuaba, A.Z. Kiss, Nucl. Instr. Meth. B **158**, 658 (1999)
35. M. Massoud, B. Canut, P. Newby, L. Frechette, P.O. Chapuis, J.M. Bluet, Nucl. Instr. Meth. B **341**, 27 (2014)
36. M. Levalois, P. Bogdansky, M. Toulemonde, Nucl. Instr. Meth. B **63**, 14 (1992)
37. P. Bogdansky, P. Marie, M. Toulemonde, Nucl. Instr. Meth. B **62**, 388 (1992)
38. R. Carin, R. Madelon, D. Julienne, F. Cruege, A. Hairie, Nucl. Instr. Meth. B **63**, 21 (1992)
39. M. Levalois, P. Marie, Nucl. Instr. Meth. B **156**, 64 (1999)
40. M. Levalois, J.P. Girard, G. Allais, A. Hairie, M.N. Metzner, E. Paumier, Nucl. Instr. Meth. B **63**, 25 (1992)
41. P. Marie, M. Levalois, E. Paumier, J. Appl. Phys. **79**, 7555 (1996)
42. A. Colder, M. Levalois, P. Marie, J. Appl. Phys. **88**, 3082 (2000)
43. A. Colder, M. Levalois, P. Marie, Eur. Phys. J AP **13**, 89 (2001)
44. J. Fage-Pedersen, A. Mesli, A. Nylandsted, Larsen. Phys. Rev. B **62**, 10116 (2000)
45. V.S. Varichenko, A.M. Zaitsev, N.M. Kazutchits, A.R. Chelyadinskii, N.M. Penina, V.A. Martinovich, Ya.I. Latushko, W.R. Fahrner, Nucl. Instr. Meth. **B 107**, 268 (1996)
46. M. Mikou, R. Carin, P. Bogdansky, R. Madelon, Nucl. Instr. Meth. B **107**, 246 (1996)
47. S. Sorieul, X. Kerbiriou, L. Gosmain, G. Calas, C. Trautmann, J. Phys. Condens. Matter **24**, 125801 (2012)
48. A. Benyagoub, A. Audren, Nucl. Instr. Meth. B **267**, 1255 (2009)

49. A. Debelle, M. Backman, L. Thomé, W.J. Weber, M. Toulemonde, S. Mylonas, A. Boulle, O.H. Pakarinen, N. Juslin, F. Djurabekova, K. Nordlund, F. Garrido, D. Chaussende, Phys. Rev. **B 86,** 100102(R) (2012)
50. A. Benyagoub, A. Audren, J. Appl. Phys. **106**, 083516 (2009)
51. A. Debelle, M. Backman, L. Thomé, K. Nordlund, F. Djurabekova, W.J. Weber, I. Monnet, O.H. Pakarinen, F. Garrido, F. Paumier, Nucl. Instr. Meth. B **326**, 326 (2014)
52. J.H. O´Connell, V.A. Skuratov, A.S. Sohatsky, J.H. Neethling, Nucl. Instr. Meth. **B 326**, 337 (2014)
53. A. Kamarou, W. Wesch, E. Wendler, A. Undisz, M. Rettenmayr, Phys. Rev. B **73**, 184107 (2006)
54. I. Jenčič, E.P. Hollar, I.M. Robertson, Philos. Mag. **83**, 2557 (2003)
55. A. Kamarou, E. Wendler, W. Wesch, J. Appl. Phys. **97**, 123532 (2005)
56. W. Wesch, E. Wendler, T. Bachmann, O. Herre, Nucl. Instr. Meth. B **96**, 290 (1995)
57. E. Wendler, T. Opfermann, P. Müller, W. Wesch, Nucl. Instr. Meth. B **106**, 303 (1995)
58. A. Kamarou, W. Wesch, E. Wendler, S. Klaumünzer, Nucl. Instr. Meth. B **225**, 129 (2004)
59. W. Wesch, A. Kamarou, E. Wendler, K. Gärtner, P.I. Gaiduk, S. Klaumünzer, Nucl. Instr. Meth. B **206**, 1018 (2003)
60. A.S. Khalil, D.J. Llewellyn, M.C. Ridgway, A.M. Stewart, A.P. Byrne, L.T. Chadderton, Microsc. Microanal. 10, Sppl. **2**, 580 (2004)
61. A.S. Khalil, L.T. Chadderton, A.M. Stewart, M.C. Ridgway, D.J. Llewellyn, A.P. Byrne, Radiat. Meas. **40**, 770 (2005)
62. G. Szenes, Z.E. Horvath, B. Pecz, F. Paszti, L. Toth, Phys. Rev. B **65**, 45206 (2002)
63. S. Dhamodaran, A.P. Pathak, A. Dunlop, G. Jaskierowicz, S. Della Negra, Nucl. Instr. Meth. **B 256**, 229 (2007)
64. S.O. Kucheyev, H. Timmers, J. Zhou, J.S. Williams, C. Jagadish, G. Li, J. Appl. Phys. **95**, 5360 (2004)
65. B. Lacroix, M.P. Chauvat, P. Ruterana, K. Lorenz, E. Alves, A. Syrkin, J. Phys. D Appl. Phys. **44**, 295402 (2011)
66. P.I. Gaiduk, F.F. Komarov, V.S. Tishkov, W. Wesch, E. Wendler, Phys. Rev. B **61**, 15785 (2000)
67. E. Wendler, T. Opfermann, P.I. Gaiduk, J. Appl. Phys. **82**, 5965 (1997)
68. J.F. Gibbons, Proc. IEEE **60**, 1062 (1972)
69. W.J. Weber, Nucl. Instr. Meth. B **166–167**, 98 (2000)
70. G. Szenes, Nucl. Instr. Meth. B **269**, 2075 (2011)
71. E.M. Bringa, R.E. Johnson, Phys. Rev. Lett. **88**, 165501 (2002)
72. G. Schiwietz, K. Czerski, M. Roth, F. Staufenbiel, P.L. Grande, Nucl. Instr. Meth. B **226**, 683 (2004)
73. S. Klaumünzer, Matematisk-fysiske Meddelelser **52**, 293 (2006)
74. R.L. Fleischer, P.B. Brice, R.M. Walker, J. Appl. Phys. **36**, 3645 (1965)
75. P. Stampfli, K.H. Bennemann, Phys. Rev. B **49**, 7299 (1994)
76. M. Toulemonde, C. Dufour, E. Paumier, Phys. Rev. B **46**, 14362 (1992)
77. P. Stampfli, Nucl. Instr. Meth. B **107**, 138 (1996)
78. M. Toulemonde, Ch. Dufour, A. Meftah, E. Paumier, Nucl. Instr. Meth. B **166–167**, 903 (2000)
79. G. Szenes, Phys. Rev. B **51**, 8026 (1995)
80. M.I. Kaganov, I.M. Lifshitz, L.V. Tanatarov, Sov. Phys. JETP **4**, 173 (1957)
81. A. Meftah, J.M. Costantini, M. Djebara, N. Khalfaoui, J.P. Stoquert, F. Studer, M. Toulemonde, Nucl. Instr. Meth. B **122**, 470 (1997)
82. J.A. Baranov, YuV Martinenko, S.O. Tsepelevich, YuN Yavlinski, Sov. Phys. Usp. **31**, 1015 (1988)
83. C. Dufour, A. Adouard, F. Beuneu, J. Dural, J.P. Girard, A. Hairie, M. Levalois, M. Levalois, E. Paumier, M. Toulemonde, J. Phys. Condens. Matter. **5**, 4573 (1993)
84. Z.G. Wang, Ch. Dufour, E. Paumier, M. Toulemonde, J. Phys. Condens. Matter **6**, 6733 (1994)

85. M. Toulemonde, W. Assmann, C. Doufur, A. Meftah, F. Studer, C. Trautmann, Ion Beam Sci. **52**, 263 (2006)
86. S. Mishra, S. Hooda, D. Kabiray, A. Roy, Vacuum **119**, 136 (2015)
87. M. Toulemonde, W.J. Weber, G. Li, V. Shuttanandan, P. Kluth, T. Yang, Y. Wang, Y. Zhang, Phys. Rev. B **83**, 054106 (2011)
88. H.D. Mieskes, W. Assmann, F. Gruner, H. Kucal, Z.G. Wang, M. Toulemonde, Phys. Rev. B **67**, 155414 (2003)
89. M. Toulemonde, C. Dufour, Z.G. Wang, E. Paumier, Nucl. Instr. Meth. **B 112**, 26 (1996)
90. I. Lazanu, S. Lazanu, Nucl. Instr. Meth. B **268**, 2241 (2010)
91. M. Murat, A. Akkerman, J. Barak, Nucl. Instr. Meth. B **269**, 2649 (2011)
92. H.-D. Betz, Rev. Mod. Phys. **44**, 465 (1972)
93. M. Toulemonde, A. Benyagoub, C. Trautmann, N. Khalfaouri, M. Boccafuso, C. Dufour, F. Gourbilleau, J.J. Grob, J.P. Stoquert, J.M. Costantini, F. Haas, E. Jacquet, K.O. Voss, A. Meftah, Phys. Rev. B **85**, 054112 (2012)
94. A. Chettah, H. Kucal, Z.G. Wang, M. Kac, A. Meftah, M. Toulemonde, Nucl. Instr. Meth. B **267**, 2719 (2009)
95. G. Szenes, Phys. Rev. B **87**, 056101 (2013)
96. S. Kadid, A. Meftah, Can. J. Phys. **92**, 1632 (2014)
97. Z.S. Hussain, E. Wendler, W. Wesch, G.J. Foran, C.S. Schnohr, D.J. Llewellyn, M.C. Ridgway, Phys. Rev. B **79**, 085202 (2009)
98. C. Licoppe, Y.I. Nissim, C. Meriadec, P. Hénoc, Appl. Phys. Lett. **50** (11987) 1648
99. W. Bolse, B. Schattat, Nucl. Instr. Meth. B **190**, 173 (2002)
100. W. Bolse, B. Schattat, A. Feyh, T. Renz, Nucl. Instr. Meth. B **218**, 80 (2004)
101. B. Schattat, W. Bolse, Nucl. Instr. Meth. B **225**, 105 (2004)
102. S.K. Srivastava, D.K. Avasthi, W. Assmann, Z.G. Wang, H. Kucal, E. Jacquet, H.D. Carstanjen, M. Toulemonde, Phys. Rev. B **71**, 193405 (2005)
103. Z.G. Wang, C. Dufour, M.D. Hou, G.M. Jin, Y.F. Yin, E. Paumier, M. Toulemonde, Nucl. Instr. Meth. B **135**, 265 (1998)
104. C. Lavoie, C. Detavernier, P. Besser, in : L.J. Chen (Ed.), *Silicide Technology for Integrated Circuits*, Inst. Emg. Technology, London, UK, 2004, Chapter 5, p. 95
105. K.E. Sickafus, L. Minervini, R.W. Grimes, J.A. Valdez, M. Ishimaru, F. Li, K.J. McClellan, T. Hartmann, Science **289**, 748 (2000)
106. K. Trachenko, J. Phys. Condens. Matter **16**, R1491 (2004)

Chapter 10
Swift Heavy Ion Irradiation of Amorphous Semiconductors

Werner Wesch, Tobias Steinbach and Mark C. Ridgway

Abstract In this chapter, the interaction of swift heavy ions (SHIs) with amorphous semiconductors is reviewed. While *crystalline* Si and Ge are insensitive to SHI irradiation, the higher electron-phonon coupling efficiency of their *amorphous* counterparts can result in ion track formation due to transient melting along the ion path. The cumulative effect of multiple SHI irradiations can then lead to plastic deformation and porous layer formation. After a review of plastic deformation in amorphous materials (including a theoretical description), results for ion track formation, plastic deformation and porous layer formation in selected amorphous Group IV and III-V materials are summarized. Complementary molecular dynamics simulations provide additional understanding and in combination with experiment enables new mechanistic insight at the atomic scale.

10.1 Introduction

The effects of swift heavy ion (SHI) irradiation on crystalline semiconductor substrates have been described in the previous chapter. In this chapter, we consider the amorphous counterpart and now review the interaction of SHIs with amorphous semiconductor substrates. The interaction of SHIs with either crystalline or amorphous forms of material is dominated by inelastic processes (electronic energy

---

Mark C. Ridgway: Deceased December 2015

W. Wesch (✉) · T. Steinbach
Institut für Festkörperphysik, Friedrich-Schiller-Universität Jena,
Max-Wien-Platz 1, 07743 Jena, Germany
e-mail: werner.wesch@uni-jena.de

T. Steinbach
e-mail: Tobias-Steinbach@t-online.de

M.C. Ridgway
Research School of Physics and Engineering, Australian National University,
Canberra, ACT 2601, Australia

© Springer International Publishing Switzerland 2016
W. Wesch and E. Wendler (eds.), *Ion Beam Modification of Solids*,
Springer Series in Surface Sciences 61,
DOI 10.1007/978-3-319-33561-2_10

deposition) involving the incident ion and substrate electrons such that substrate atoms are excited and/or ionised. The elastic processes (nuclear energy deposition) that lead to the displacement of substrate atoms at much lower incident ion energies are negligible in the SHI irradiation regime. Following the deposition of ion energy in the electronic subsystem, the efficiency with which this energy is transferred to the atomic subsystem is governed by electron-phonon coupling, a parameter that can vary significantly between crystalline and amorphous materials. For the latter, the reduced electron mobility yields a reduced thermal conductivity. The energy deposition is confined to a smaller volume and, as a consequence, the maximum lattice temperature attained subsequent to SHI irradiation is typically greater in the amorphous phase. The heat diffusion in and between the electronic and atomic subsystems is well described by the inelastic thermal spike (i-TS) formalism and two-temperature model (TTM) which is described in detail in Chap. 2 of this book. Therein coupled differential equations for the two subsystems use temperature, specific heat and thermal conductivity as variables with the electron-phonon coupling strength as the only free parameter. In this chapter, we show how differences in electron-phonon coupling lead to differences in the response of crystalline and amorphous materials to SHI irradiation. For example, while *crystalline* Si and Ge substrates may be insensitive to SHI irradiation for a given set of irradiation parameters, ion tracks resulting from transient melting along the incident ion path are readily formed in *amorphous* Si and Ge substrates. Thereafter, the cumulative effect of multiple SHI impacts can lead to plastic deformation and porous layer formation.

After a review of plastic deformation in amorphous materials and a theoretical description in the framework of a viscoeleastic model, we shall summarize the experimental results on track formation, plastic deformation and porous layer formation in amorphous Si and Ge (a-Si and a-Ge), respectively. We show that the experimental findings on track and porous layer formation are confirmed by molecular dynamics (MD) computer simulations.

10.2 Plastic Deformation in Amorphous Materials

All experiments on very thin free-standing dielectric and metallic glasses have shown that samples under perpendicular ion incidence shrink parallel and grow perpendicular to the direction of the ion beam under conservation of volume, i.e. no change of mass and density occurs (Fig. 10.1) [1–4]. As the ion beam in this case phenomenologically acts like a “hammer”, the effect is commonly named “ion hammering effect”.

The macroscopic deformation resulting from the cumulative effect of multiple SHI irradiation is characterized by the deformation state $\underline{\underline{\varepsilon}}_p$ and deformation rate $\dot{\underline{\underline{\varepsilon}}}_p$

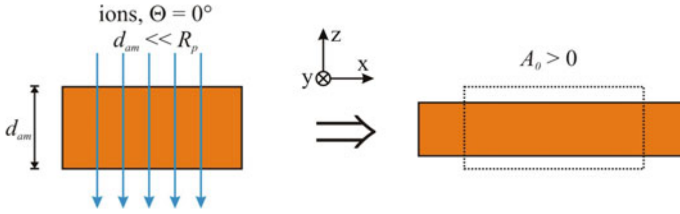

Fig. 10.1 Schematic illustration of the anisotropic plastic deformation of amorphous samples under perpendicular ion incidence ("ion hammering effect") for $A_0 > 0$

which can be described by a linear connection with the ion fluence $N_I = \Phi t$ or the ion flux Φ according to

$$\underline{\underline{\varepsilon}}_p = \underline{\underline{A}}(N_I - N_{I_o}) \quad \rightarrow \quad \dot{\underline{\underline{\varepsilon}}}_p = \underline{\underline{A}}\Phi \quad with \quad \underline{\underline{A}}(\Theta = 0^\circ) = A_0 \begin{pmatrix} 1 & 0 & 0 \\ 0 & 1 & 0 \\ 0 & 0 & -2 \end{pmatrix} \tag{10.1}$$

with t the time, $N_{Io} \approx 10^{12}$ cm^{-2} the threshold ion fluence below which no measurable deformation occurs and Θ the angle of incidence. The effect of a single ion is characterised by the deformation yield A_0, and the anisotropic deformation at perpendicular ion irradiation is described by the tensor $\underline{\underline{A}}$ [5, 6]. The trace of the deformation tensor $\underline{\underline{\varepsilon}}_p$ is equal to zero

$$\frac{dV}{V} = tr(\underline{\underline{\varepsilon}}_p) = tr(\underline{\underline{A}}) = 0, \tag{10.2}$$

which ensures volume conservation of the material during the irradiation, i.e. the volume change $dV/V = 0$. The ion irradiation induced modification of the sample dimension l_{xyz} is given by the scalar deformation yield per ion, A_0, in (10.1). The relative change of the length l_x and the area $l_x\ l_y = F$ of the irradiated sample are then

$$A_0 = \frac{1}{l_x}\frac{\partial l_x}{\partial N_I} \text{ and } 2A_0 = \frac{1}{F}\frac{\partial F}{\partial N_I}, \tag{10.3}$$

respectively [7].

The deformation yield A_0 generally depends on the irradiation temperature T_0, the initial stress state and the electronic energy deposition S_e. An effect of nuclear energy deposition on plastic deformation in amorphous materials can be excluded (for example, see [2, 7–9]). Systematic studies of the effect of electronic energy deposition S_e have shown that above a material-specific and temperature-independent threshold value $S_{et} \approx$ (2.5–23) keV nm^{-1} all amorphous materials

investigated show a linear increase of the deformation yield A_0 with the electronic energy deposition S_e [9–11],

$$A_0(S_e) = \alpha(S_e - S_{et}), \quad \alpha = \partial A_0/\partial S_e. \tag{10.4}$$

Furthermore, A_0 is maximal at low temperatures and decreases significantly when thermally activated atomic rearrangements take place.

The observed macroscopic deformations at high ion fluence could be attributed to a multitude of local plastic deformations, and the threshold value of the ion fluence N_{Io} (cp. 10.1) corresponds to a stationary state for which a substantial part of the sample volume with plastically deformed regions (corresponding to the ion tracks) exists. It should be mentioned that no correlation between the deformation yield with the glass transition temperature, the crystallization temperature, the electron-phonon coupling strength, or the thermal expansion coefficient at room temperature has been observed. This indicates that a local temperature rise along the ion path seems not to play a dominant role for the ion-beam induced dimensional changes. A more detailed discussion can be found, for example, in [7].

Contrary to perpendicular ion incidence, irradiation with $\Theta > 0°$ causes shearing of the irradiated sample (Fig. 10.2).

For the description of this process the tensor $\underline{\underline{A}}(\Theta = 0°)$ in (10.1) for the description of the ion hammering effect is transferred to its general form by a similarity transformation with the rotational matrix D and the converted rotational matrix D^T [5]:

$$\underline{\underline{A}}(\Theta) = D \cdot \underline{\underline{A}}(\Theta = 0°) \cdot D^T = A_0 \begin{pmatrix} 1 - 3\sin^2\Theta & 0 & 3\sin\Theta\cos\Theta \\ 0 & 1 & 0 \\ 3\sin\Theta\cos\Theta & 0 & 1 - 3\cos^2\Theta \end{pmatrix} \tag{10.5}$$

Because of the anisotropy of the energy deposition along the ion path, the tensor $\underline{\underline{A}}(\Theta)$ contains non-diagonal elements leading to shear components in the deformation tensor $\underline{\underline{\varepsilon}}_p$. These induce macroscopic angular changes in the free-standing amorphous layers, as illustrated in Fig. 10.2 for deformation yields $A_0 > 0$.

In amorphous layers with thicknesses significantly larger than the penetration depth of the ions, the variation of the electronic energy deposition S_e with the ion path length z causes a depth-dependent deformation yield $A_0(S_e(z))$. The situation is similar for a thin amorphous layer on top of a thick inert crystalline substrate (Fig. 10.3). In both cases the effect of ion hammering is mechanically constrained by the more or less non-deformable surrounding which leads to bending of free-standing samples [12, 13] and to a surface shift of amorphous layers on crystalline substrates as illustrated in Fig. 10.3 for non-perpendicular ion incidence and deformation yield $A_0 > 0$. In this case the surface shifts in the positive x-direction, i.e. along the projection of the ion beam to the sample surface. It should be mentioned that the opposite behaviour of the deformation is to be expected for materials with $A_0 < 0$.

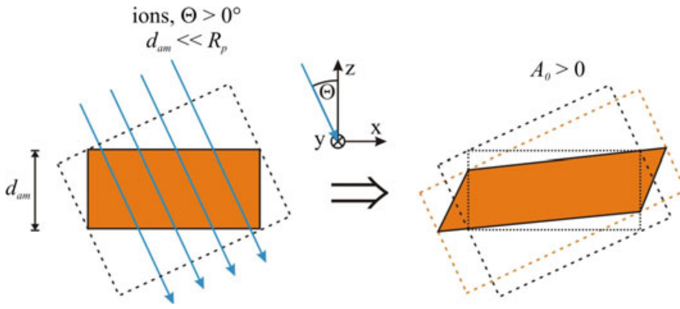

Fig. 10.2 Schematic illustration of the anisotropic plastic deformation of amorphous samples under non-perpendicular ion incidence (Θ > 0°) and for $A_0 > 0$

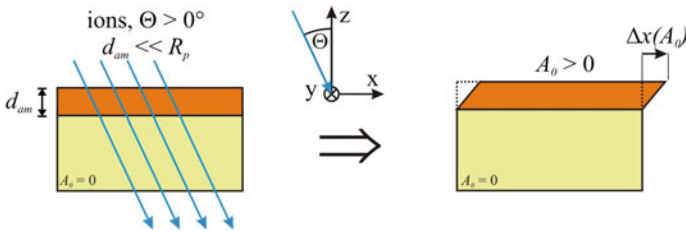

Fig. 10.3 Schematic illustration of the anisotropic plastic deformation of a thin amorphous layer on top of a thick inert crystalline substrate for non-perpendicular ion incidence (Θ > 0°) and $A_0 > 0$

The reason for this behaviour is in both cases the build-up of mechanical stress $\underline{\underline{\sigma}}^{layer}$ in the irradiated regions. For a full description of the deformation state $\underline{\underline{\varepsilon}}^{layer}$ of the amorphous layer, elastic and viscous properties of the amorphous layer have to be considered. A description is possible in the framework of a modified Maxwell model as a linear superposition of all components of deformation [4, 5, 14, 15]

$$\dot{\underline{\underline{\varepsilon}}}^{layer} = \dot{\underline{\underline{\varepsilon}}}^{elas} + \dot{\underline{\underline{\varepsilon}}}^{vis} + \dot{\underline{\underline{\varepsilon}}}^{ion}$$
$$\dot{\underline{\underline{\varepsilon}}}^{layer} = \frac{1}{2G}\frac{d}{dt}\left[\underline{\underline{\sigma}}^{layer} - \frac{v}{v+1}tr\left(\underline{\underline{\sigma}}^{layer}\right)\right] + \underline{\underline{\underline{k}}}(S_e(z))\Phi\left[\underline{\underline{\sigma}}^{layer} - \frac{tr\left(\underline{\underline{\sigma}}^{layer}\right)}{3}\underline{\underline{I}}\right] + \underline{\underline{A}}\,\Phi \quad (10.6)$$

with G the shear modulus, v the Poisson number, and $\underline{\underline{\underline{k}}}$ the fluidity tensor. The first term in (10.6) describes the elastic deformation according to Hook's law, the second stands for the relaxation of the induced stress $\underline{\underline{\sigma}}^{layer}$ due to viscous flow, and the third one considers the hammering effect. Without irradiation the layer behaves like a

totally elastic medium, i.e. $\underline{\underline{\dot{\varepsilon}}}^{layer}(\Phi = 0) = \underline{\underline{\dot{\varepsilon}}}^{elas}$. Additionally, quasi-static mechanical equilibrium has to be assumed, so that for small deformation velocities v_i

$$div\underline{\underline{\sigma}}^{layer} = 0 \tag{10.7}$$

is valid. With the corresponding boundary conditions and with the assumption of small shear values the deformation velocity v_i and the mechanical stress $\underline{\underline{\sigma}}^{layer}$ characterizing the deformation and stress state can be calculated using (10.6). For non-perpendicular irradiation and far away from the boundaries of the sample one obtains as a solution a homogeneous plastic flow along the projection of the ion beam to the surface (Fig. 10.3). The shear velocity $v_x(z)$ for a thin amorphous surface layer of thickness d_{am} amounts to

$$v_x(z) = 3\Phi sin(2\Theta)A_0(S_e)\,(z + d_{am}) \tag{10.8}$$

The maximum shear velocity at the surface, $z = 0$, is then given by

$$v_x(z = 0) = 3\Phi d_{am}A_0(S_e)sin(2\Theta) \tag{10.9}$$

and with the irradiation time t the surface shift of the irradiated sample can be calculated according to

$$\Delta_x(z = 0) = v_x(z = 0)t = 3N_I d_{am}A_0 sin(2\Theta). \tag{10.10}$$

If the surface shift can be measured (10.10) allows to calculate the value of the deformation yield A_0.

Whereas the plastic deformation of amorphous materials under SHI irradiation can be macroscopically described by the constitutive (10.6), its microscopic origin, however, is still the object of discussion. Various models have been suggested based on different concepts, such as radial Coulomb explosion and recombination of free volume [2], plastic flow and inverse relaxation of the cooled matter [16], local viscous flow of the amorphous matter during cooling of the ion track [17], or macroscopic momentum transfer from the ion to the solid [18, 19]. These as well as a modified thermal spike model (analytical thermal spike (a-TS) model) [20–23] (see also Chap. 2) which explains the ion hammering effect in amorphous materials by a continuous production and recombination of defects along the ion trajectory have more or less deficiencies with respect to the agreement with the experimental data and will not be discussed here.

The most promising approach for the description of ion-induced plastic deformation of amorphous materials seems to be the viscoelastic model by Trinkaus and Ryazanov [24–28] which is based on the a-TS model and attributes anisotropic growth and ion beam-induced creep to a deformation caused by a relaxation of shear stress within a hot and low-viscosity ion track on the ps time scale. In the framework of an effective flow temperature (EFT) approximation which is an asymptotic borderline case of a viscoelastic field theory, the experimental results could be

successfully described. Within the a-TS model the energy dissipation around the ion trajectory is treated by classical thermodynamics. The solution of the two-dimensional heat conduction equation is a Gaussian distribution of the temperature increase $\Delta T(r, t)$ with respect to the sample temperature T_0 around the ion trajectory (see Chap. 2) [21]. The model considerations start with the temperature distribution $T(r, t)$ after the energy transfer from the electronic subsystem to the lattice is finished, i.e. after $t_0 \approx 1$ ps. In the EFT approximation, it is assumed that for sufficiently high electronic energy deposition, $S_e \gg S_{et}$, temperatures above an effective flow temperature T^* are reached at which the material along the ion trajectory transforms into a low-viscosity zone and the thermally-induced shear stress relaxes [24]. The temperature T^* corresponds to the melting temperature T_m in the case of irradiation of crystalline material and to the glass transition temperature T_g during the relaxation time τ_s of the shear stress in the case of amorphous material. The value of T^* defines the track radius or the radius of the low-viscosity zone R. The relaxation time is defined by the temperature-dependent shear viscosity, $\eta(T)$, and the high frequency shear modulus G of the corresponding solid amorphous phase, $\eta(T) = \tau_s G$. The shear stress is completely reduced if the life time of the low-viscosity zone is large compared to the relaxation time, $t_v \gg \tau_s$, i.e. η approaches zero, $\eta \rightarrow 0$, for the low-viscosity zone with $T > T^*$, and infinity, $\eta \rightarrow \infty$, outside the fluid zone of the track with $T < T^*$, respectively. The temperature dependence of the anisotropic deformation is shown schematically in Fig. 10.4.

As a consequence of the temperature rise in the track region the low-viscosity zone suffers an isotropic thermal eigenstrain and possibly a density change due to the phase transition resulting in an average effective eigenstrain $\varepsilon^*(T(r, t))$ within the low-viscosity zone. The cylindrical low-viscosity zone can now be considered as a borderline case of a homogeneous ellipsoidal thermoelastic inclusion. Details of the theoretical treatment of elastic inclusions and their consequences on plastic deformation and induced stress fields can be found in [29]. In case of a cylindrical inclusion (ion track), the relaxation of shear stresses for $T > T^*$ under the condition of volume conservation leads to a non-isotropic stress field containing axial, radial and circumferential eigenstress. That means, during the relaxation time τ_s, the shear stress relaxation causes the formation of axial, radial and circumferential relaxation

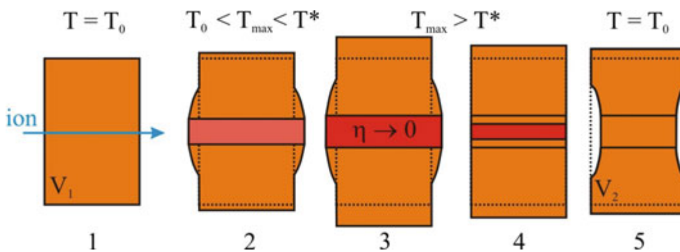

Fig. 10.4 Illustration of mechanical effects induced by a cylindrical spike: energy deposition (*1*), elastic deformation by local heating (*2*), viscous deformation by shear stress relaxation (*3* and *4*) and (*5*) strained spike region and associated deformation in the frozen state (after [28])

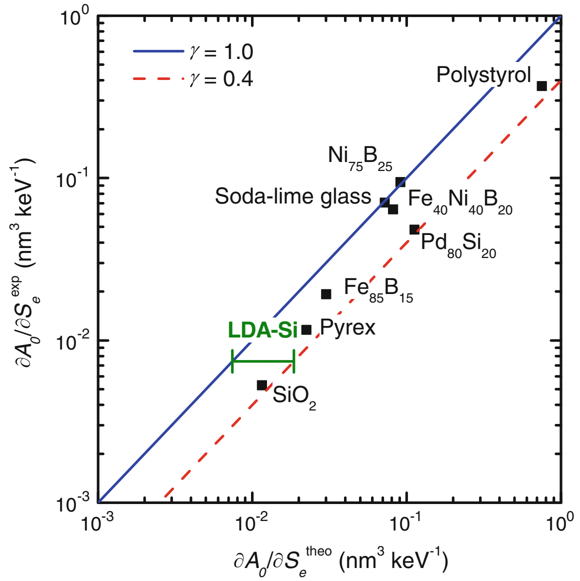

Fig. 10.5 Comparison between experimentally observed values ∂A_0^{exp} with the theoretical values ∂A_0^{theo} for various materials irradiated at low temperature [6, 30]. The theoretical values have been calculated in the framework of the viscoelastic model for ion hammering (10.11) [24] using electron-phonon coupling efficiencies of γ = 1.0 and γ = 0.4 [6, 30]

strain, i.e. the elastic energy is freed as relaxation deformation via viscous flow. During cooling down of the viscous or fluid zone these relaxation strains freeze in at the solidification front leaving behind a permanent deformation around the ion track (Fig. 10.4).

Assuming the eigenstrain to be determined only by the thermal expansion with a constant and linear thermal expansion coefficient α^{th} a linear dependence of the deformation yield A_0 on the electronic energy deposition S_e follows, which is for high electronic energy deposition independent of the temperature T^*,

$$A_0(S_e) = 1.164\frac{1+v}{5-4v}\frac{\alpha^{th}\gamma S_e}{\mathrm{e}\rho C} \tag{10.11}$$

with γ the fraction of S_e transferred to the lattice (cp. Chap. 2), ρ the mass density, v the Poisson number, C the specific heat per unit mass and e = 2.4 Euler's number [24].

For metallic glasses, values of the deformation yield A_0 are reported ranging between 2×10^{-2} and 2 nm^2 [7]. The good agreement of the experimentally observed and theoretically calculated values of $\partial A_0/\partial S_e$ for different materials shown in Fig. 10.5 confirms the adequate description of the irradiation-induced plastic deformation process by the viscoelastic model.

10.3 Structural Modification in Amorphous Silicon (a-Si)

10.3.1 Ion Track Formation in a-Si

We first consider the interaction of single SHIs with the substrate then, in subsequent sections, examine the effects of multiple ion impacts. We begin with the formation of an ion track wherein the energy coupled to the lattice following the passage of a SHI is sufficient to increase the lattice temperature above that required for melting. As a consequence, a thin cylinder of molten material is formed along the ion path. The rapid thermal quench that ensues can produce remnant structural modifications within the resolidified material and thus an ion track is formed.

Crystalline Si (c-Si) is generally radiation resistant such that the formation of a continuous ion track with single SHIs has, to our knowledge, not been reported. Only at the extremes of electronic energy deposition ($\sim$37 keV nm^{-1}) achievable with molecular ions (in this case fullerenes) has continuous ion track formation been observed [31–33]. For a-Si, predictions of ion track formation by SHI irradiation preceded by a decade experimental determinations due to the difficulty in distinguishing an amorphous track from an amorphous matrix using the same analytical technique (TEM) which yielded such beautiful images of ion tracks in c-Si [32]. For example, the report of a glass transition in a-Si by Hedler et al. [30] was entirely predicated on the formation of an ion track. Only with the recent application of the synchrotron-based method of small-angle X-ray scattering (SAXS) has the characterisation of ion tracks in amorphous semiconductors been enabled.

Figure 10.6 shows the calculated a-Si lattice temperature as a function of post-irradiation time for different radial distances measured outward from the incident ion path. Full details of the calculation are provided in [34]. The lattice temperature was extracted from MD simulations using input derived from a Monte Carlo (MC)—TTM approach [35–38]. These calculations were first performed for a-Ge and then subsequently scaled for a-Si using the ratio of the electronic energy deposition in the two materials [34]. Figure 10.6 shows the maximum lattice temperature is attained at 2 ps and is comparable to that required for vapourisation (3173 K [39]). Melting (1420 K [40]) is achieved to a maximum radial distance of 6.3–8.4 nm. Note the experimentally measured ion track diameter is typically considered indicative of the maximum melt radius [41, 42] though controversy does exist in the case of Si [42].

Figure 10.7 shows SAXS results for ion tracks in a-Si induced by SHI irradiation [34]. Details of the sample preparation and characterisation are given in [34]. The upper right inset shows the detector image recorded with the sample surface normal (and the ion tracks) oriented at 10° with respect to the x-ray beam. For 0° orientation, the image is isotropic (not shown) with the ion tracks imaged end-on while at 10° orientation, the image is anisotropic as the projection of long, narrow cylinders (ion tracks) yields the observed image contraction in the x-ray/surface

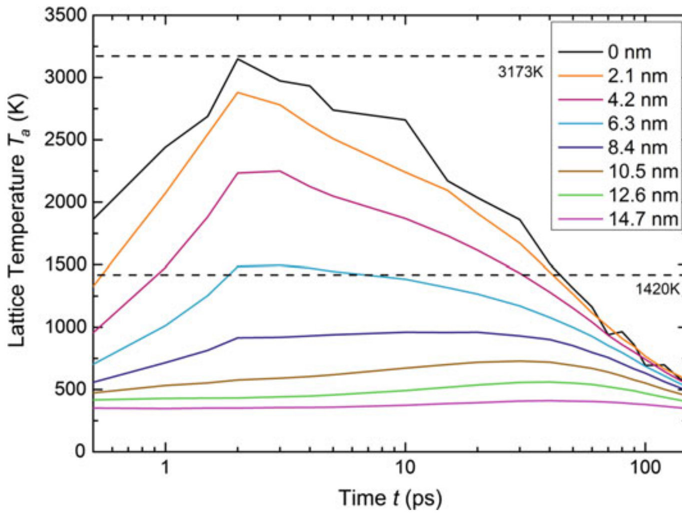

Fig. 10.6 a-Si lattice temperature as a function of post-irradiation time for different radial distances as extracted from MD simulations (data from [34])

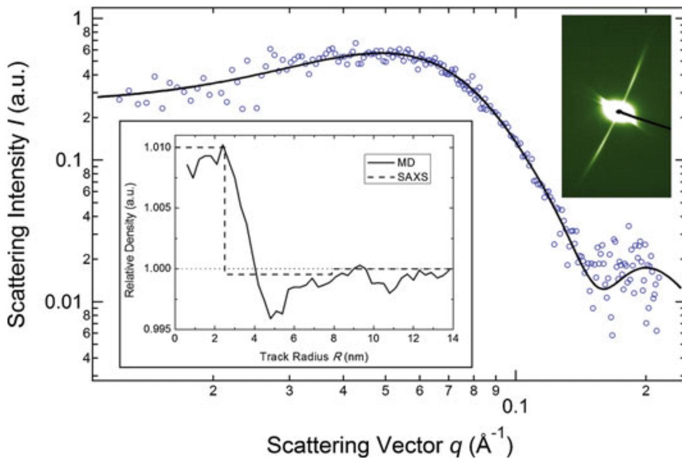

Fig. 10.7 SAXS spectrum for ion tracks in a-Si following SHI irradiation with 185 MeV Au^{+13} ions to a fluence of 1×10^{11} cm^{-2}. The *upper right* and *lower left insets* are the detector image and radial density distribution across the ion track, respectively. The latter compares SAXS and MD at 200 ps post-irradiation when resolidification is complete (data from [34])

normal plane. Tilting the sample is an effective means of separating the scattering contributions from ion tracks and unirradiated material.

In Fig. 10.7, the SAXS spectrum of intensity I as a function of scattering vector q, isolated and background subtracted, was recorded for a low SHI fluence such that ion-track overlap was negligible. Higher SHI fluences caused the well-defined

oscillations to be progressively washed out (not shown). The SAXS spectrum was fit with a core-shell model [41] as successfully applied to both a-SiO_2 [41] and a-Ge [43] in the past. Alternative models, such as a simple cylinder, yielded inferior fits [34]. The width of the ion track, summing core radius (2.5 ± 0.1 nm) and shell thickness (5.4 ± 0.3 nm), was 7.9 0.4 nm for the given irradiation conditions. The lower left inset in Fig. 10.7 shows the radial density distribution determined from SAXS using the core-shell model. For comparison, MD results are also included. Qualitative agreement between experiment and simulation is readily apparent. With respect to unirradiated material, the core is over-dense while the shell is under-dense. Given the core and shell dimensions listed above, this radial density distribution yields a net densification within the ion track. Note that SAXS can deduce the magnitude of the density difference but not the sign (given the scattering intensity is proportional to the square of the scattering amplitude). In the present case, a negative value of the core-to-shell ratio yields two possibilities: over-dense core and under-dense shell *or* vice versa. Below we justify our assertion that it is the core that is over-dense.

Molten Si is metallic and approximately six-fold coordinated with a density greater than that of a-Si [44]. These high-density liquid (HDL) and low-density amorphous (LDA) phases must be linked by a low-density liquid (LDL) phase if, as proposed by Hedler et al. [30], Si exhibits a glass transition. The over-dense core of an ion track in a-Si may thus represent remnants of the HDL phase frozen-in during the rapid post-irradiation thermal quench leading to the observed over-dense core in an a-Si ion track. McMillan et al. [45] have also reported a metastable, pressure-induced high-density amorphous phase in a-Si. Note that similar SAXS core-shell model analyses of ion tracks in a-SiO_2 [41] and a-Ge [43], the latter described below, concluded the ion-track core was under-dense for both materials, the opposite to that reported for a-Si. The under-dense core/over-dense shell reported for the radial density distributions for these two materials were attributed to radially outward material flow induced by rapid heating and thermal expansion along the ion track core that is then frozen-in by the ensuing thermal quench. While such a scenario could also be envisioned for a-Si, the similarity of the experimental (SAXS) and simulated (MD) radial density distributions supports an over-dense core/under-dense shell in the case of a-Si.

10.3.2 Plastic Deformation of a-Si

In the previous section the structural modification in individual ion tracks produced by low-fluence SHI irradiation of a-Si has been described. With increasing ion fluence, accumulation and overlap of tracks leads to a collective structural modification process resulting in plastic deformation of amorphous materials. In Sect. 10.2 it was shown that all glasses under high-fluence SHI irradiation above a certain value of the electronic energy deposition show plastic deformation with a positive deformation yield. The experimental results can be well described in the

framework of the viscoelastic model by Trinkaus and Ryazanov [24] and Trinkaus [25–28]. In the case of SHI irradiation of a-Si the situation is different. Because the mass density of a-Si is by about 10 % lower than that of liquid Si (l-Si) [46, 47], the viscoelastic model predicts a plastic deformation with negative deformation yield if a simple liquid-solid phase transition (first-order phase transition) between the HDL and LDA Si phases is assumed. However, based on experimental and theoretical studies a second scenario is discussed in the literature implying the existence of a HDL and a low-density tetrahedrally coordinated liquid (LDL) Si phase within the supercooled liquid region of the track [48–51]. During cooling of the low-viscosity zone a first-order phase transition between the HDL and LDL phases and a kinetic blocked LDL-LDA glass transition at the edge of the low-viscosity zone are proposed. This would result in a positive deformation yield as in glasses (see [30] and references therein). The verification of one of the two scenarios is possible by measuring the plastic flow of SHI irradiated thin LDA Si layers. With respect to the timescales, SHI irradiation is comparable with pulse laser irradiation but the excitation volumes are different in both cases. Whereas laser irradiation produces a penny-shaped excitation volume, several micrometers wide and a few nanometers thick, high-energy ions generate a needle-like plasma, the ion track, with a diameter of a few nanometers and a length of several tens of micrometers. The plastic deformation resulting from high fluence SHI irradiation contains information about eigenstrain and fluidity of the hot ion track existing on the ps time scale which is frozen in in this particular excitation volume. Therefore, with this technique, contrary to *in situ* analysis of the effect of short laser pulses [52], more detailed information about the phase transition between l-Si and a-Si can be obtained [30].

For the investigation of the plastic deformation, LDA Si layers produced by high-fluence Si implantation into c-Si at low temperature were irradiated with high-energy Au and Xe ions (electronic energy deposition 15.8 keV nm^{-1} $\leq S_e \leq$ 21.3 keV nm^{-1}) at 80 and 300 K and under 0° and 45° ion incidence (for the irradiation geometry, see Fig. 10.3 in Sect. 10.2). To enable a measurement of the surface shift, a 40 nm thick Au grid was evaporated on the samples and during SHI irradiation part of the sample was covered with a mask. As an example, Fig. 10.8 shows a micrograph of the surface shift Δx of a sample irradiated with 350 MeV Au ions.

It is clear that the irradiated surface is shifted with respect to the unirradiated material, and that the shift occurs in the direction of the projection of the ion beam onto the surface. This positive surface shift, which was observed for all values of the electronic energy deposition and temperature investigated, is in agreement with the behaviour of glasses under SHI irradiation (e.g. [14, 53]) and in contradiction to the predictions of the viscoelastic model for a-Si.

At the irradiation temperature T_0 = 80 K, the surface shift Δx increases linearly with the ion fluence N_I as in glasses and is larger for higher values of the electronic energy deposition S_e. This is illustrated in Fig. 10.9 [30]. As a consequence of the lateral mass transport, a ditch and dike structure appear at the x-boundary to the unirradiated material (not shown). Moreover, the cross sections of the ditch and

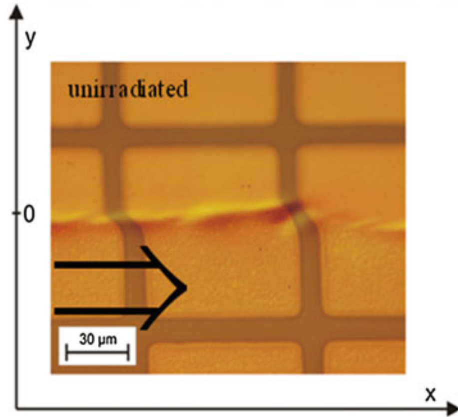

Fig. 10.8 Micrograph of the surface of an a-Si layer irradiated with 350 MeV Au ions (S_e = 18.8 keV nm^{-1}) at 80 K, an ion fluence of $N_I = 1.7 \times 10^{15}$ cm^{-2} and an ion incidence angle of $\Theta = 45°$ [30]

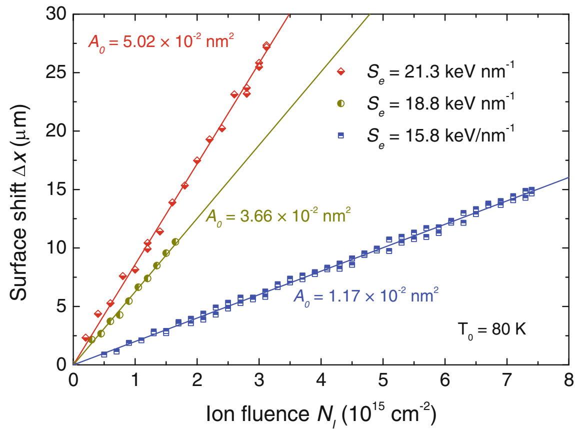

Fig. 10.9 Surface shift Δx of a-Si as a function of the ion fluence N_I for different electronic energy depositions at low temperature and under an angle $\Theta = 45°$. The corresponding deformation yields are also given [30]

dike are equal, because the plastic flow process conserves volume and density, i.e. the process occurs without material loss [53].

For room-temperature irradiation and low fluences, the linear behaviour holds well, but the surface shift Δx shows a non-linear fluence dependence for ion fluencies $N_I \geq (1–4) \times 10^{15}$ cm^{-2} depending on the energy deposition (Fig. 10.10) [53, 54].

The super-linear increase of Δx for higher ion fluences is accompanied by a disintegration of the Au marker layer and a strong volume expansion of the irradiated part of the sample. The corresponding surface elevation Δz at the irradiated/unirradiated boundary is shown in Fig. 10.11. It increases exponentially with the ion fluence without saturation within the investigated ion fluence range of $N_I \leq 3 \times 10^{15}$ cm^{-2} [54, 55].

In the case of c-Si, the volume expansion is negligible, the elevation reaches only a saturation value of $\Delta z \approx 150$ nm at $N_I = (6–7) \times 10^{14}$ cm^{-2}. Given the

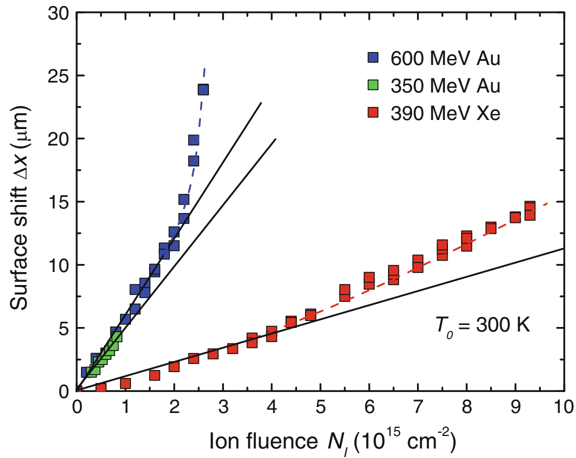

Fig. 10.10 Surface shift Δx of a-Si as a function of the ion fluence N_I for different irradiations at room temperature and under an angle $\Theta = 45°$ (data from [54])

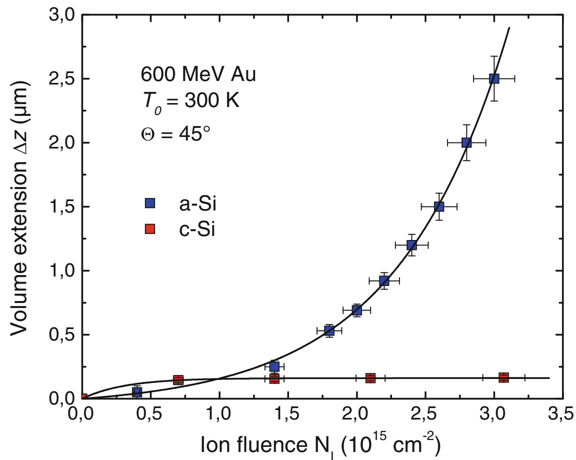

Fig. 10.11 Volume expansion Δz of an a-Si layer and a c-Si reference sample with respect to the corresponding unirradiated parts as a function of the ion fluence $N_I = \Phi t$ for irradiation under $\Theta = 45°$ [54, 55]

insensitivity of c-Si with respect to damage formation by SHI irradiation (see Chap. 9), this small volume expansion has to be attributed to the nuclear energy deposition S_n of the SHIs. According to SRIM calculations [56], more than one displacement per lattice atom is created at the ion projected range which therefore caused the formation of a buried amorphous layer at this depth. The mechanically-constrained density change of about 1.8 % due to the amorphization [47] leads to the measurable elevation at the surface.

In contrast to off-normal SHI irradiation of a-Si, perpendicular irradiation results in an exponential saturation behaviour of the surface elevation, and the values of Δz within the experimental error agree with those measured for pure c-Si samples under otherwise identical irradiation conditions. Because of this identical behaviour of c-Si and a-Si it must be concluded that no volume expansion of the a-Si surface

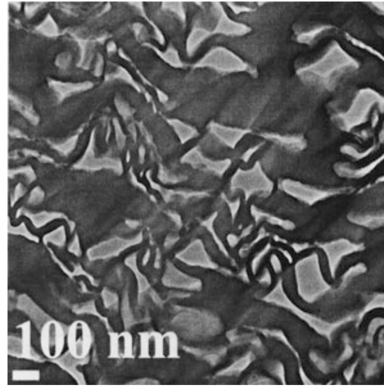

Fig. 10.12 TEM image of a-Si irradiated with 600 MeV Au at 300 K and Θ = 45° to an ion fluence of $N_I = 3 \times 10^{15}$ cm^{-2} [55]

layer occurred under perpendicular ion incidence. Hence, in both cases the small elevation of the surface is a consequence of a volume expansion of the Si substrate as discussed above. The existence of this buried a-Si layers was also proven by infrared reflection (IR) spectroscopy [55].

The reason for the swelling effect of a-Si in the case of non-perpendicular irradiation at room temperature is the transformation of the initially homogeneous a-Si layer into a sponge-like porous layer. This is illustrated by the TEM image in Fig. 10.12 for a sample irradiated with 600 MeV Au ions to an ion fluence of $N_I = 3 \times 10^{15}$ cm^{-2}. The image shows irregularly shaped voids with a size of several 100 nm which are not aligned along a preferred orientation. High-resolution TEM imaging demonstrates that the network still has an amorphous structure. The formation of such a structure explains the observed disintegration of the Au marker layer (Au diffuses into the porous layer as proven by RBS analysis) and the change of the optical reflectance of the irradiated regions [55].

Under the assumption that the plastic flow of the a-Si layers is not accompanied by a volume change of the layers, i.e. the surface shift Δx shows a linear dependence on the ion fluence, the deformation yield A_0 can be calculated in the framework of the viscoelastic model using (10.10) in Sect. 10.2. In the case of low-temperature irradiation, this assumption holds well in the whole ion fluence range (Fig. 10.9) and for room temperature irradiation for $N_I \leq (1\text{–}4) \times 10^{15}$ cm^{-2} (Fig. 10.10). In Fig. 10.13 the calculated deformation yield A_0 is depicted as a function of the electronic energy deposition S_e for irradiation at T_0 = 80 and 300 K [30, 54]. Beyond a threshold of S_{et} = 14.2 keV nm^{-1}, which is independent of T_0, the deformation yields increase linearly with S_e. As in the case of glasses the deformation yield A_0 is larger for lower temperatures (Fig. 10.13). As a consequence the slope $\partial A_0/\partial S_e = 7.4 \times 10^{-3}$ nm^3 keV^{-1} for T_0 = 80 K is larger than that for T_0 = 300 K, $\partial A_0/\partial S_e = 5.5 \times 10^{-3}$ nm^3 keV^{-1}.

From Figs. 10.10 and 10.13 it follows that ion hammering of LDA Si shows all the characteristics of ion hammering of glasses [1–3]. The energy deposition threshold for LDA Si lies in the same order of magnitude as that measured previously for glasses (S_{et} = 2.5 keV nm^{-1} for vitreous silica [3], 13 keV nm^{-1} for the

Fig. 10.13 Calculated deformation yield A_0 versus electronic energy deposition S_e for irradiation of a-Si at T_0 = 80 and 300 K [30, 54]

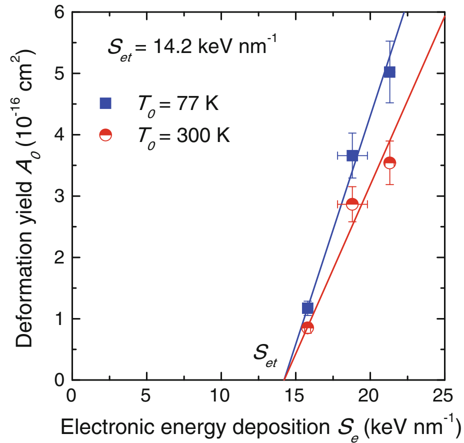

metallic glass $Fe_{85}B_{15}$ [9, 11], and 23 keV nm^{-1} for glassy $Pd_{80}Si_{20}$ [3]). The threshold value S_{et} = 14.2 keV nm^{-1} corresponds to an excitation energy density $\gamma S_{et}/\pi R^2 \approx 40$ kJ cm^{-3} for typical values of the electron-phonon coupling efficiency of $\gamma \approx 0.5$ and track radii of $R \approx 3$ nm. For comparison, to achieve sub-picosecond non-thermal melting of LDA Si by a femtosecond laser with a photon energy of 2 eV and a pulse duration of 100 fs, the laser intensity has to exceed 0.23 J cm^{-2} corresponding to an excitation energy density in the electronic subsystem of about 14 kJ cm^{-3} [57–59]. This value is obviously easily surpassed by SHI irradiation.

Given the experimentally observed positive deformation yield, the phase transition in Si cannot be explained by a liquid-amorphous first-order phase transition which would cause a negative deformation yield. According to the viscoelastic model, a low-viscosity zone did exist if the deformation yield is different from zero, $A_0 \neq 0$. Moreover, if the deformation yield is positive, $A_0 > 0$, a low-density liquid (LDL) phase must have existed. The two scenarios are schematically illustrated in Fig. 10.14. Should a LDL Si phase not exist, the low-viscosity zone would consist of a highly-coordinated metallic l-Si melt which on undercooling would transform into the metastable HDL Si phase. At the edge of the low-viscosity zone this HDL Si phase would solidify via a first-order phase transition into the surrounding semiconducting LDA Si phase (Fig. 10.14 left). However, because of the large difference in the mass densities of the two phases (ρ = 2.550 g cm^{-3} for l-Si at the melting temperature [46] and ρ = 2.287 g cm^{-3} for LDA Si produced by ion implantation [47]) the low-viscosity zone over a large temperature range has a negative eigenstrain, $\varepsilon^*(T) < 0$. As a consequence, the shear stress relaxation within the low-viscosity HDL Si zone proceeds in the opposite direction than in glasses. This leads to freezing-in of the corresponding relaxation deformation at the HDL-LDA Si interface with opposite sign causing a negative deformation yield A_0.

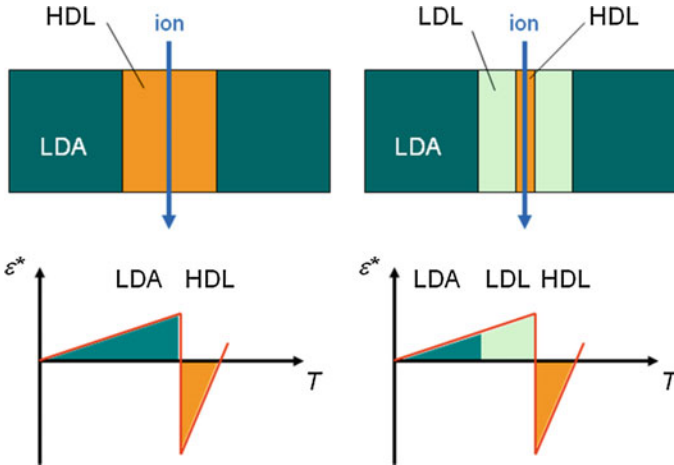

Fig. 10.14 Schematic illustration of the track region and the temperature dependence of the eigenstrain ε* for a first-order phase transition LDA-HDL Si (*left*) and a two-step process involving a HDL-LDL Si glass transition (*right*)

In the case of the existence of a metastable tetrahedral semiconducting LDL Si phase, the low-viscosity zone at the edge consists of this LDL phase and, depending on the temperature, of the HDL Si phase (l-Si melt) in the core of the ion track (Fig. 10.14 right). During cooling a first-order phase transition between HDL and LDL Si and a kinetic blocked glass transition between LDL and LDA Si at the edge of the low-viscosity zone could occur. Because the LDL phase structurally corresponds to the LDA phase, the low-viscosity zone would contain a high contribution of positive eigenstrain, $\varepsilon^* > 0$. This would allow the deformation to freeze-in at the solidification front with the same sign as in the case of glasses resulting in a positive deformation yield A_0. Indeed this scenario exactly corresponds to the experimental findings. The LDL Si phase obviously provides a natural source for a positive relaxation strain as it is required for a positive value of the deformation yield. Moreover, this scenario quantitatively accounts for the measured value of the slope of the deformation yield $\partial A_0/\partial S_e$ which is in good accordance with the theoretical value calculated in the framework of the viscoelastic model although the calculation yields only a line (see Fig. 10.5 in Sect. 10.2) because of the additional free parameter T^*. A detailed description of the theoretical considerations can be found in [30].

As the results clearly demonstrate, the semiconductor LDA Si shows the same behavior as metallic and insulating glasses after quenching on the nanometer length scale (see Sect. 10.2). The positive sign of the deformation yield proves the existence of a LDL Si phase and is an indication for the existence of liquid polymorphism in Si. At the low-temperature side this liquid transforms to solid LDA Si through a glass transition.

10.4 Structural Modification in Amorphous Germanium (a-Ge)

10.4.1 Ion Track Formation in a-Ge

While the Group IV elements Si and Ge have many similarities, the effects of SHI irradiation are much more pronounced in a-Ge relative to those described previously for a-Si. Crystalline Ge (c-Ge) is relatively insensitive to SHI irradiation such that ion-track production necessitates very-high electronic energy deposition S_e values. Like c-Si, the formation of continuous ion tracks in c-Ge has only been achieved with cluster-ion irradiation (S_e = 37–51 keV nm^{-1}) yielding ion tracks of diameter 5–15 nm [60]. In contrast, a-Ge is rendered porous under SHI irradiation for $S_e > \sim 10$ keV nm^{-1} [61] (see Sect. 10.4.2). These observations are consistent with greater electron-phonon coupling in the amorphous phase and ion-track formation was suggested as the origin of the porosity induced in a-Ge by SHI irradiation [61, 62]. Experimental and theoretical studies of ion-track formation in a-Ge are now described including physical characterisation using SAXS and TEM combined with a multi-time-scale theoretical approach.

The creation and evolution of ion tracks in a-Ge induced by SHI irradiation was characterised via MD simulations as achieved via three interconnected stages. The first included the excitation of electrons due to the ion energy deposition. The electron dynamics were then followed with a MC-TTM combination [35–38] where the TTM describes the energy transport within the electronic and lattice subsystems. Using the MC-TTM approach, the rate of energy transfer between the electronic and lattice subsystems (the electron-phonon coupling efficiency) was determined and then used as input for the MD simulations by continuously depositing kinetic energy in a random direction on the lattice atoms until the two subsystems were in equilibrium at 3 ps. MD simulations were performed with the PARCAS code [63] using the Stillinger-Weber and Tersoff potentials [64, 65]. Details of the calculations and simulations are provided in reference [43].

Figure 10.15 shows the calculated a-Ge lattice temperature as a function of post-irradiation time for different radial distances measured outward from the incident ion path [43]. The maximum temperature ($\sim$4600 K) is attained at 2–3 ps and that required for vapourisation (3093 K) is achieved for radial distances of less than 3.3–5.4 nm. Clearly the melting temperature (965 K) is exceeded for radial distances of less than 9.6–11.7 nm. Beyond $\sim$300 ps, resolidification is complete and the lattice has cooled to a temperature below the melting point. Note that to better enable the comparison of calculation, simulation and experiment, the MC-TTM input was scaled so the width of the molten ion track extracted from MD was consistent with that determined from SAXS. In the absence of scaling, the molten track width deduced from MD was half that measured experimentally, an extraordinary result given the absence of fitted parameters.

Figures 10.16 show SAXS results for low-fluence SHI irradiation of an a-Ge layer on a c-Si substrate [43]. Details of the sample preparation and characterisation

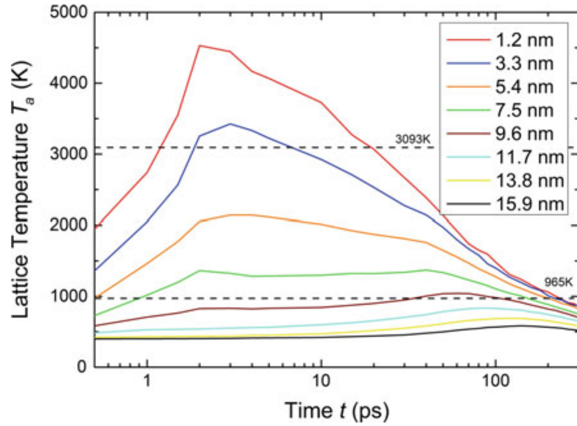

Fig. 10.15 a-Ge lattice temperature as a function of post-irradiation time for different radial distances as extracted from MD simulations (data from [43])

are given in [43]. The detector images (upper right insets) are now comprised of two anisotropic scattering components that are separable by tilting the sample relative to the x-ray direction. The components that appear as streaks and mirrored hemispheres result from ion tracks and voids, respectively. The scattering intensity I as a function of the scattering vector q, isolated and background subtracted, is shown for the ion tracks and voids in Figs. 10.16a, b, respectively. The well-defined oscillations in Fig. 10.16a are only apparent at low fluences ($<\sim 10^{11}$ cm^{-2}) where ion track overlap is negligible. Like a-Si [34], the spectrum was fit with a core-shell model from which the total track radius, comprised of core radius (4.7 ± 0.1 nm) plus shell thickness (6.5 ± 0.1 nm), was 11.1 ± 0.2 nm. Again, a negative value of the core-to-shell density ratio indicates core and shell

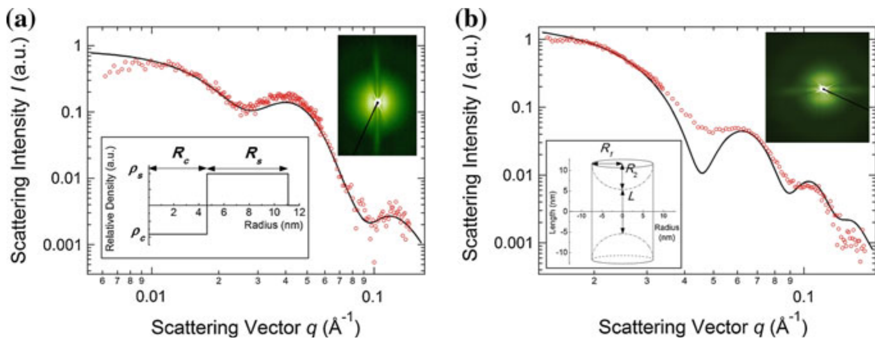

Fig. 10.16 **a** SAXS spectrum recorded at a surface normal/x-ray direction angle of 10° for ion tracks in a-Ge following SHI irradiation with 185 MeV Au^{+13} ions to a fluence of 1 × 10^{11} cm^{-2}. The *upper right* and *lower left insets* are the detector image and radial density distribution across the ion track, respectively, and **b** SAXS spectrum recorded at a surface normal/x-ray direction angle of 5° for voids in a-Ge following SHI irradiation with 185 MeV Au^{+13} ions to a fluence of 1 × 10^{11} cm^{-2}. The *upper right* and *lower left insets* are the detector image and void geometry with L, R_1 and R_2 set at 10.6, 7.4 and 6.6 nm, respectively, for the fitting (data from [43])

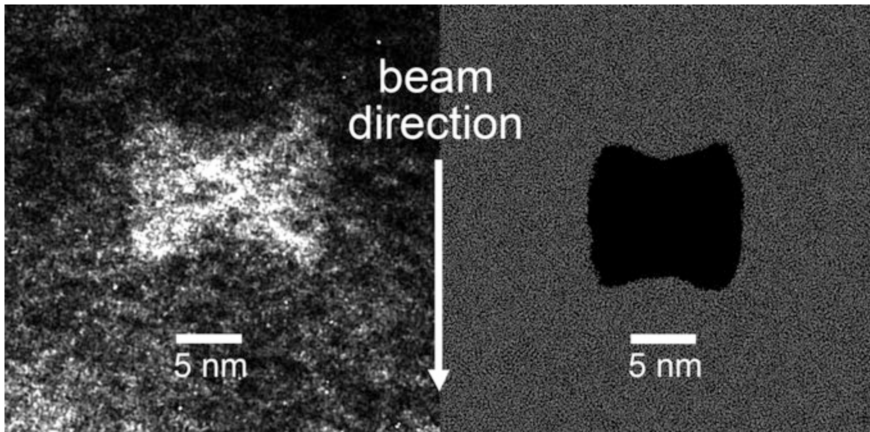

Fig. 10.17 (*left*) TEM image from a-Ge following SHI irradiation with 185 MeV Au^{+13} ions to a fluence of 6×10^{10} cm^{-2} and (*right*) MD simulation of the void geometry following resolidification (300 ps) [43]. Reprinted figure with permission from M.C. Ridgway, T. Bierschenk, R.Giulian, B. Afra, M.D. Rodriguez, L.L. Araujo, A.P. Byrne, N. Kirby, O.H. Pakarinen, F. Djurabekova, K. Nordlund, M. Schleberger, O. Osmani, N. Medvedev, B. Rethfeld and P. Kluth, Phys. Rev. Lett. 110, 245502, 2013. Copyright (2013) by the American Physical Society. http://link.aps.org/abstract/PRL/v110/p245502

have a density lower and higher, respectively, than the surrounding matrix (*or* vice versa). Assuming the core-shell structure is the result of frozen-in radially-outward material flow from the ion-track core following a thermal spike, the shell must thus be over-dense. The relative radial density distribution across the ion track derived from SAXS measurements is also included in Fig. 10.16a as the lower left inset. Like a-Si, this distribution yields a net volume contraction which is accommodated by the creation of open volume in the form of voids.

Figure 10.16b shows the scattering contribution from the irradiation-induced voids. The spectrum was fit with the bow-tie shape shown in the inset as determined from TEM observations such as that shown in Fig. 10.17. TEM through-focus analysis confirmed these features were less dense than the matrix with an average width and length of ~ 14 and 10–20 nm, respectively. The parallel sides of the void are aligned with the incident ion direction which suggests their formation mechanisms are correlated. Despite a limited number of voids to image in the microscope, clear qualitative agreement is apparent for the SAXS and TEM measurements.

Like molten Si, molten Ge is also metallic with a density greater than the amorphous solid [66]. MD simulations readily demonstrated the LDA-to-HDL phase transformation along the ion track. The animation of [43] shows spherical voids appear at ~ 10 ps as a consequence of the volume contraction induced by the solid-to-liquid phase transformation (though inter-atomic potential dependent). Void agglomeration then ensues and prior to resolidification, the void shape is prolate ellipsoid with the major axis aligned with the incident ion direction. Upon cooling, the transformation from HDL Ge to LDA Ge is observable (though again

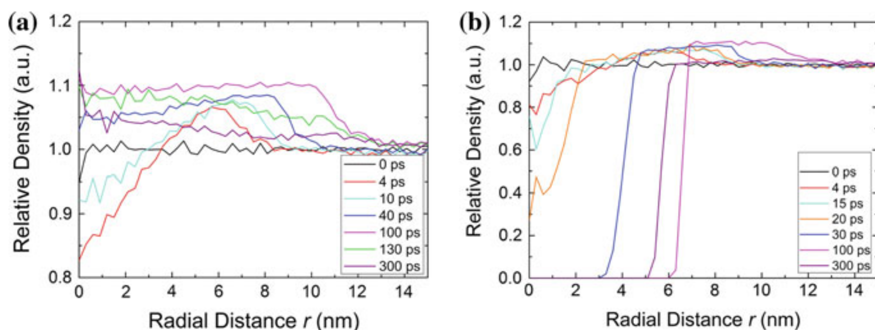

Fig. 10.18 MD simulations of relative density as a function of radial distance across **a** an ion track and **b** a void in a-Ge [43]

inter-atomic potential dependent) and the voids assume their bow-tie shape as a result of radially-inward cooling. As the molten ion track progressively solidifies from the maximum melt radius toward the ion-track core, the expanding volume of the solidified material compresses the residual molten material necessitating axial motion toward the void. The innermost volume experiences the greatest effect and a bow-tie shaped void results. Figure 10.17 demonstrates remarkable agreement between experiment and simulation.

Figure 10.18 shows time-dependent MD results for a-Ge of the radial density distribution across (a) an ion track (between voids) and (b) a void, respectively. Across the ion track, the development of the core-shell structure is rapid with the greatest density ratio achieved ~4 ps after the ion energy deposition. At approximately the same time, the maximum temperature was achieved within the ion track (~4600 K), a temperature beyond that required for vapourisation (3093 K). The maximum melt radius (~11 nm) was reached at 100 ps and the presence of HDL Ge spanning the ion track is readily apparent. Thereafter, the ion-track radial density distribution relaxes toward LDA Ge. Across the void, formation begins in the vapour phase (10 ps) but evolves fully in the liquid phase (>25 ps). The maximum radii of the void and molten track (~6.5 and ~11 nm, respectively) are achieved at the same time (100 ps) again suggesting their formation is correlated. Relaxation yields a slight narrowing of the void with the radial density distribution constant for ≥200 ps.

For the given irradiation conditions, the energy transferred from the electronic to lattice subsystems was clearly sufficient to induce melting and the formation of a molten cylinder of radius ~11 nm. The greater density of HDL Ge relative to LDA Ge then necessitated a volume contraction within the ion track as accommodated by void formation. The size and shape of the latter evolved in the liquid phase. Upon cooling, remnants of the core-shell structure were quenched into the ion track and radially-inward resolidification yielded the bow-tie shape of the voids. Independent calculations of the number of voids per unit track length using data from SAXS (2.8 ± 0.5 voids μm^{-1}) and TEM/swelling measurements (~2.1 voids μm^{-1}) has

led to the suggestion that such voids represent the embryonic precursors to the porous structure induced in a-Ge by SHI irradiation [41], as discussed in the section that follows.

The ion-track dimensions in a-Ge have also been characterised as a function of electronic energy deposition by Bierschenk et al. [67]. On the low-energy side of the Bragg peak (where the “Bragg peak” is the electronic energy deposition maximum), the ion-track dimensions scaled with S_e, as expected. In contrast, on the high-energy side of the Bragg peak, at a S_e value of 32.7 keV nm^{-1} (2.19 GeV Au ions), the ion-track dimensions were comparable to those referred to above (the low-energy side of the Bragg peak with a S_e value of 23.6 keV nm^{-1} (185 MeV Au ions)). This result is a demonstration of the so-called “velocity effect” [68]. The higher ion velocity above the Bragg peak yields an increased spread of the electron cascade and hence a decreased energy deposition density. Thus for equal values of S_e on either side of the Bragg peak, smaller ion-track dimensions are measured for the higher ion velocity/energy.

Ion tracks have thus been identified in both a-Si and a-Ge. For identical irradiation conditions, ion tracks in a-Si were of lesser width and did not contain voids consistent with the lower electronic energy deposition, higher melting temperature and higher electron mean free path [38] relative to a-Ge. A core-shell structure was determined for the radial density distributions across ion tracks in both a-Si and a-Ge. However, these distributions were inverted (core and shell were over- and under-dense, respectively, for a-Si while the opposite was calculated for a-Ge). Despite such differences, both radial density distributions yielded a net densification across an ion track in both a-Si and a-Ge, a result consistent with MD simulations in both materials for times beyond that required for resolidification. Note that ion track formation in a-Si and a-Ge has recently been reviewed by Ridgway et al. [69].

10.4.2 Porous Layer Formation (Multiple-Ion Irradiation)

As shown in Sect. 10.4.1, single SHI irradiation of a-Ge leads to structural modifications along each single ion path. After ion penetration, the material within the ion track is characterized by a core-shell structure in the radial direction, i.e. the cylindrical ion track consists of a low-density core and a high-density shell [43]. Such structural modifications caused by SHIs are observed in other materials as well (e.g., [41]). However, in a-Ge well separated nanometer sized bow-tie-like shaped regions are formed along the ion track with extremely low density or even voids (Sect. 10.4.1, Fig. 10.17). The fundamental mechanism underlying both effects (core shell structure and extreme density decrease) can be attributed to a radially-outward directed pressure wave and the solid-to-liquid phase transformation caused by the induced thermal spike (Sect. 10.4.1).

The previous section dealt solely with the modification of a-Ge caused by single ion irradiation. In the present section the focus is on the influence of multiple ion track overlap on void formation in a-Ge and the dynamics of void interaction or

void stability at high ion fluence irradiation. Moreover, the experimental results are compared with results obtained from MD simulations in which the formation, interaction and evolution of voids was also studied as a function of high electronic energy deposition.

Systematic high fluence investigations reveal—independent of the irradiation conditions—that the induced voids are generally stable, i.e. the small voids do not disappear, so that with increasing ion fluence a continuous formation of nanometer sized voids takes place [61, 62]. In the ion fluence range of 10^{11} cm^{-2}, nearly spherical voids with radii of several nanometers have been formed and are randomly distributed over the whole amorphous layer. With further SHI irradiation the initially homogeneous and void-free amorphous surface layer transforms into a void-rich porous layer which is shown exemplarily in Fig. 10.19. In addition, the effective formation of extended voids due to the coalescence of local void agglomerations leads to a significant expansion of the irradiated amorphous regions. Moreover, a macroscopic vertical volume expansion Δz of the irradiated relative to the unirradiated region occurs due to the formation of many extended voids at high ion fluences. This becomes clear in Fig. 10.19, in which the right part of the sample was masked during the SHI irradiation and consequently no voids were generated. With further increasing ion fluence the voids grow continuously in size until the initial a-Ge layer is transformed completely into a sponge-like porous structure. At this state, the voids themselves are irregularly shaped and have sizes of several hundreds of nanometers (cp. Fig. 10.20). Electron diffraction patterns (cp. inset in Fig. 10.20) of such porous structures show diffuse concentric rings demonstrating the still amorphous character of the Ge material surrounding the voids [61].

In contrast, no voids are formed in the underlying c-Ge substrate [61, 62]. After SHI irradiation, the Ge substrate is still crystalline without defects as demonstrated by electron microscopy and electron diffraction analysis, respectively. This result is in good agreement with conclusions drawn from studies concerning high electronic energy deposition in c-Ge, where neither track formation nor defect formation are observed after single and multiple ion irradiation (for a detailed

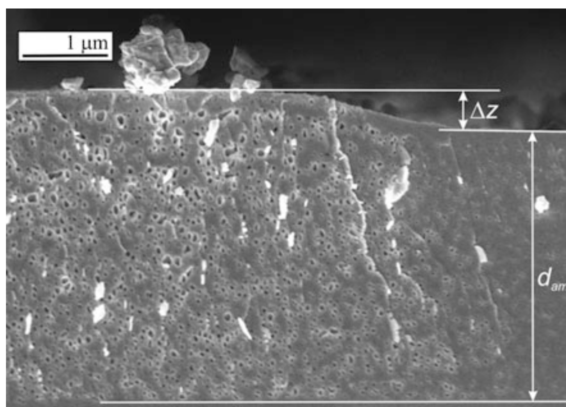

Fig. 10.19 The *left side* of the cross-section-SEM image demonstrates the formation of stable voids in a-Ge and the vertical volume expansion Δz as a consequence of the irradiation with 185 MeV Au ions under an angle of $\Theta = 45°$ with a fluence of 7.0×10^{12} cm^{-2} at room temperature [61, 62, 70]

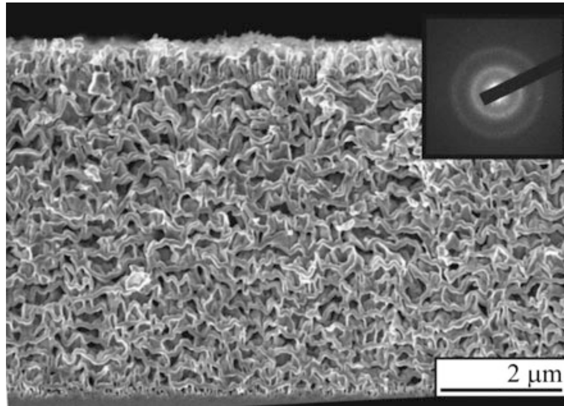

Fig. 10.20 Cross-section-SEM image showing the complete transformation of the initially homogeneous a-Ge layer into a sponge like porous structure caused by irradiation with 185 MeV Au ions under an angle of Θ = 45° with a fluence of 1.0 × 10^{14} cm^{-2} at room temperature [62]

discussion, see Chap. 9). Hence, only in the a-Ge phase, ion irradiation with sufficiently high electronic energy deposition leads to structural modification like the formation, accumulation and growth of stable voids [61, 62].

These experimental results are confirmed by MD simulations in which a multitude of energy deposition cycles were performed on different stochastically determined positions of the MD cell (for details see [70]). The snapshots of a MD cell after a certain number of ion impacts are shown in Fig. 10.21. The simulation reveals that the structural evolution is basically characterized by three processes: (A) the formation of voids around the ion impact position as well as (C) the growth or (D) shrinking of pre-existing voids [70]. Finally, for multiple energy deposition cycles the initially homogeneous MD cell ends up in a sponge-like porous structure as exemplarily shown in Fig. 10.21d. The temporal and thermal stability of such structures were verified by means of annealing experiments with temperatures up to 1000 K. It was demonstrated that the porous structures are stable long term and only for increased temperatures small local rearrangements are observed at the void interfaces [70].

As a consequence of the irradiation-induced structural modification, the surface morphology changes and the surface roughness significantly increases [61]. According to the morphological change, the optical appearance or reflectivity of SHI irradiated regions changes with increasing ion fluence. In Fig. 10.22, the optical light microscope image demonstrates that the bright silver (unirradiated) a-Ge surface changes to grey (low ion fluences) over dark grey to black (high ion fluences) corresponding to the irradiation-induced structural changes like the formation of small craters (low ion fluence), extended holes and the final collapse to a porous structure (high ion fluence). At the final stage, i.e. for sponge-like porous structures, the irradiated surface appears completely black and does not change with further irradiation [61].

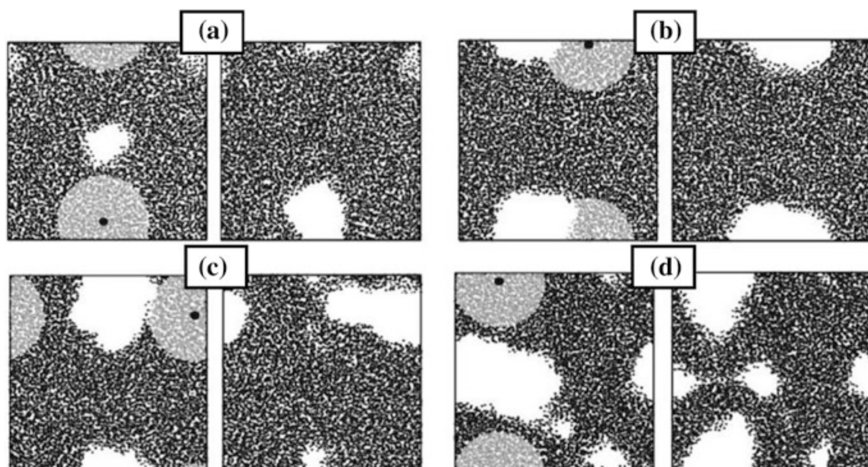

Fig. 10.21 Snapshots of the a-Ge MD cell: before energy deposition (*left image* initial situation, position of impact and deposition cylinder defined by the black dot and the highlighted area, respectively) and after energy deposition (*right image* final structure, before the next deposition cycle starts). The evolution of the MD cell is shown for 3 (a), 5 (b), 7 (c) and 17 (d) ion impacts [70]

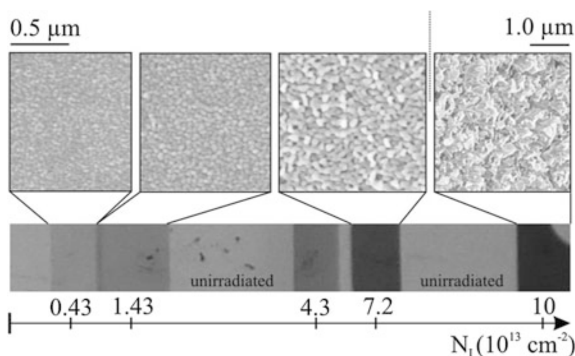

Fig. 10.22 Light microscope image showing the optical appearance/reflectivity of SHI (185 MeV Au ions, Θ = 45°) irradiated Ge for different ion fluences. The corresponding plan-view SEM images demonstrate the irradiation-induced morphological change at the surface

In general, SHI irradiation-induced structural modifications are observable for a multitude of different ion species including Ag, I, Xe, Au, Pb and U ions [61, 62, 71, 72]. For sufficiently high electronic energy deposition values (S_e = 14–40 keV nm^{-1}) extended voids are formed in a-Ge independent of the ion energy (E = 89–1000 MeV) or ion velocity and ion incidence angle (Θ = 0°–60°) [61]. As shown in Sect. 10.4.1, one single ion caused the formation of single nanometer sized voids along its path, however, a void-induced vertical volume expansion Δz cannot be verified for ion fluences below 10^{11} cm^{-2}. Using for example two- or three-dimensional optical surface profilometry, the volume expansion Δz becomes evident and can be investigated systematically. Hence, in the following, Δz is taken as a parameter to characterize the irradiation-induced formation and growth of voids

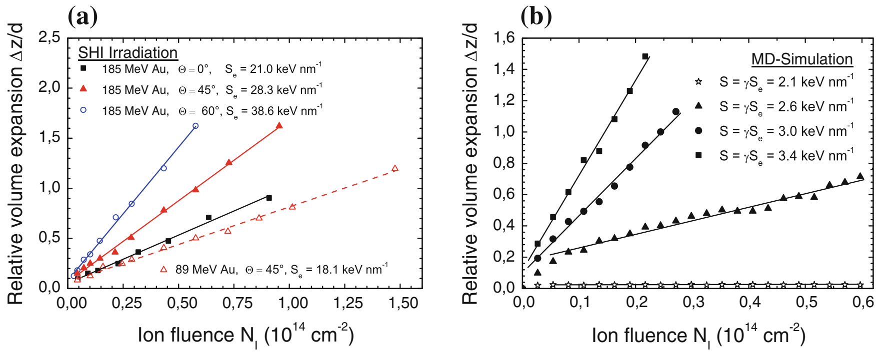

Fig. 10.23 Irradiation-induced relative volume expansion in a-Ge as a function of the ion fluence for different energy depositions: experimental data (**a**) and results of MD simulations (**b**) [61, 70]

and their accumulation to a porous and sponge-like layer as function of the irradiation conditions. The experimental [61] and simulation results [70] are summarized in Fig. 10.23. In case of the MD simulations the total amount of the kinetic energy transferred to the atoms within the deposition cylinder is $\Delta E_{kin} = Sd$ with $S = \gamma S_e$, where S is the part of the electronic energy loss per ion and path length, S_e, which is converted into atomic motion and d is the extension of the MD cell in z-direction. The ratio of the transferred energy, γ ($\gamma < 1$), is used as a free parameter. The transferred energy S has been varied between 1.7 and 3.4 keV nm^{-1}. For more details of the MD simulations the reader is referred to [70]. As can be seen in Fig. 10.23, both the measured and calculated relative volume expansion $\Delta z/d$ (d refers to the amorphous layer or MD cell thickness) continuously increases with increasing ion fluence which means that the SHI irradiation leads to a continuous void formation process and the nanometer sized voids observed in Fig. 10.17 are generally stable. Moreover, local agglomerations of such voids continuously coalesce with increasing irradiation forming extended voids as demonstrated in Fig. 10.19. Even when a sponge-like porous layer has been formed, SHI irradiation still yields continuous void growth due to the absorption of new nanometer-sized voids formed within the amorphous material surrounding the voids. For all ion fluences studied, no saturation of the volume expansion was observed so far, i.e. no final stage of the irradiation-induced structural modification was reached [61].

Furthermore, the volume expansion and therefore the void formation show a linear dependence on the ion fluence (see Fig. 10.23): $\Delta z/d = \alpha \cdot N_I$. This linearity is independent of the electronic energy deposition values S_e caused by the variation of ion species, ion energy and ion incidence angle. However, the strength of the expansion, i.e. the gradient α, changes with S_e: The higher the energy deposition, the higher the gradient $\alpha(S_e)$. This becomes clear in Fig. 10.24, where the gradient is shown as a function of the electronic energy deposition S_e. In good agreement, the experiments (Fig. 10.24a) and the MD simulations (Fig. 10.24b) reveal the

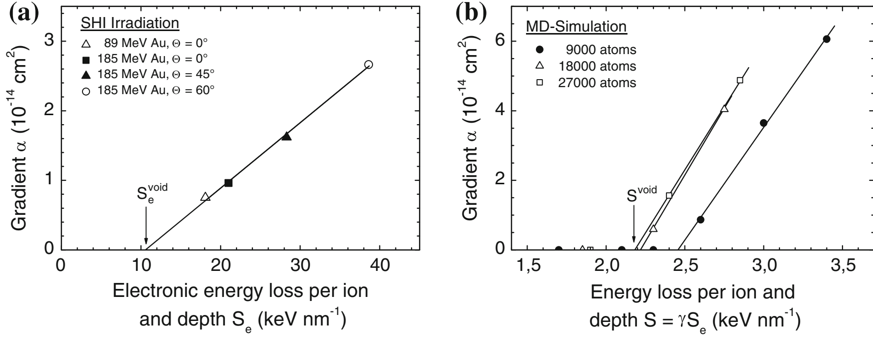

Fig. 10.24 Gradient α as a function of the electronic energy deposition S_e [61, 67]. In both experiment (**a**) and simulation (**b**), a threshold value $S^{void} = \gamma \cdot S_e^{void}$ (with $\gamma = 0.21$) for the void formation was determined

existence of a material-specific threshold value S_e^{void} above which the gradient $\alpha(S_e)$ increases linearly with increasing energy deposition: $\alpha(S_e) \propto [S_e - S_e^{void}]$. The energy deposition threshold determined from the experiments amounts to $S_e^{void} = (10.5 \pm 0.5)$ keV nm^{-1} (Fig. 10.24a) [61]. The MD simulations show a dependence of the threshold value on the size of the MD cell illustrated in the dependence of the gradient α on the electronic energy loss S in Fig. 10.24b. For larger MD cells the curves shift to smaller values of S, but for the two larger cells the shifts are equal indicating a convergence of the threshold value of S for void formation with respect to the extension of the MD cell in z direction which amounts to $S^{void} = 2.2$ keV nm^{-1}. From this value and the experimentally determined threshold value S_e^{void} follows $\gamma = 0.21$ for the relative part of the electronic energy loss (electron-phonon coupling efficiency) transferred to the atoms. This value is in the same order of magnitude as the values of the electron-phonon coupling efficiency reported in literature e.g. for III–V semiconductors [23]. From the experimental and theoretical results it follows that only if $S_e > S_e^{void}$ single-ion irradiation causes the formation of stable voids, which accumulate with increasing ion fluence to form complex and permanent sponge-like porous structures as shown in Fig. 10.20. A significant influence of the nuclear energy deposition S_n on void formation during SHI irradiation can be excluded because in the near-surface region the nuclear energy deposition is very low and therefore negligible. Moreover, at low ion energies, i.e. for $S_n > S_e$ and $S_e \ll S_e^{void}$, void formation takes place only at high ion fluences in the range of $N_I > 1 \times 10^{15}$ cm^{-2} [73–84] and can be explained by agglomeration of irradiation-induced vacancies caused by nuclear collisions [76, 77, 83] (for the formation of porous amorphous layers in Ge due to nuclear energy loss see Chap. 6.3.2).

Compared to a-Ge, the irradiation of c-Ge with high ion fluences causes neither a formation of voids in the near surface region (Fig. 10.25a, $z < 4$ µm) nor defect formation, amorphization or ion track formation as confirmed by different analysis

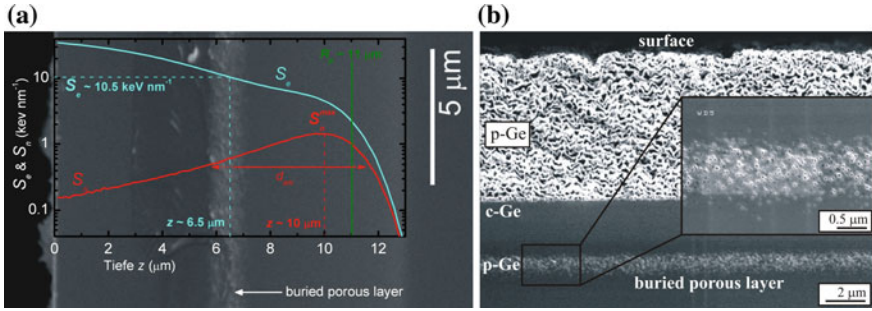

Fig. 10.25 Cross section SEM of c-Ge (a, $N_I = 1.5 \times 10^{14}$ cm^{-2}) and a-Ge (b, $N_I = 1.0 \times 10^{14}$ cm^{-2}) samples irradiated at an incidence angle of 45° with 185 MeV Au ions showing the formation of a buried porous layer. SRIM calculations of electronic S_e (*solid blue line*) and nuclear S_n (*solid red line*) energy deposition versus depth z are included for direct comparison [61, 62]

methods including RBS and high-resolution TEM [61]. The surface layer shown in Fig. 10.25a is still crystalline after SHI irradiation. However, the irradiation to high ion fluences causes the formation of a buried porous layer consisting of single isolated voids (cp. Fig. 10.25a, b) [61, 62, 71, 72]. The comparison of the depth profile with the corresponding depth distribution of the energy deposition $S_e(z)$ and $S_n(z)$ (Fig. 10.25a) reveals, that the voids do not occur in the depth region where S_n (or S_e) have its maximum or at the depth R_p where the ions come to rest. Hence, the formation of a buried porous layer cannot be attributed to void formation due to S_n or chemical processes based on the implanted ions, because no voids are observed in depth regions around S_n^{max} or R_p, respectively. However, in depth regions where the nuclear energy deposition becomes dominant, defects are generated due to elastic collisions between the ions and Ge atoms, which finally lead to the formation of a buried amorphous layer at high ion fluences. This irradiation-induced crystalline-to-amorphous transformation leads to a low but continuous volume expansion due to the density change during the amorphization process [61]. Nevertheless, it was demonstrated that buried voids are formed in the depth z_p where the electronic energy deposition is $S_e(z_p) \approx 10.5$ keV nm^{-1} [61, 71, 72]. Hence $S_e(z_p)$ is in good agreement with the experimentally determined threshold for void formation (cp. Fig. 10.24a). To conclude, in c-Ge buried porous layers are formed if the initial crystalline material was amorphized due to S_n **and** S_e exceeds the threshold necessary for void formation (cp. Fig. 10.25a). At depths $z > z_p$ no voids are observed in the amorphous phase because the electronic energy deposition is lower than the threshold value needed for void formation. In addition, the experiments demonstrate that electronic energy deposition $S_e < 10$ keV nm^{-1} does not have any influence on void formation which confirmed the proposed mechanism for void formation under low ion energy irradiation is based solely on nuclear processes [61].

In case of SHI irradiated a-Si, void formation was observed only for extreme irradiation conditions, like high ion fluxes, high ion fluences and only at room

temperature (see Sect. 10.3.2). As outlined above, in a-Ge the ion flux and the ion fluence are not key parameters because stable nanometer-sized voids are already formed in the case of single-ion irradiation (see Sect. 10.4.1). SHI irradiations of a-Ge under identical irradiation conditions but different sample temperatures ranging from 50 to 300 K show a linear volume expansion with increasing ion fluence independent of the irradiation temperature [70]. Nevertheless, the void induced volume expansion decreases with decreasing temperature. However, the ratio of the volume expansion for two temperatures $\Delta z_{LT}/\Delta z_{RT}$ is still constant over the whole fluence range (e.g. $\Delta z_{LT=50K}/\Delta z_{RT=300K} = 0.6$). This experimentally-proven temperature behaviour and even the ratio $\Delta z_{LT}/\Delta z_{RT}$ are in good agreement with results obtained by means of MD simulations [70]. Electron microscopic investigations reveal that SHI irradiation of a-Ge even at low temperatures leads to effective void formation and a transformation into a sponge-like porous layer which shows no structural difference to the porous layers obtained at room temperature irradiation.

Independent of the irradiation temperature, a thin void-free layer close to the sample surface is observed (see Fig. 10.19). Furthermore, all investigations show a sharp transition between this void-free surface layer and the void-rich layer underneath. The thickness of this layer z' amounts to several tens of nanometers and decreases with increasing electronic energy deposition. This leads to the conclusion that the electronic energy deposition in the near-surface region is lower than the threshold value required for void formation, i.e. $S_e(z < z') < S_e^{void}$. A reduced energy deposition value in the near-surface region can be attributed to fluctuations of the electronic energy deposition along the ion path due to the change of ion charge state q, $S_e(q, E) \propto q^2$[85]. After penetration into the material, the initial charge state q (and $S_e(q)$) of SHIs increases until an equilibrium charge state $\bar{q} > q$ is reached and a constant electronic energy deposition occurs along the ion path. Hence, the existence of a thin void-free layer close to the surface further confirms the existence of an electronic energy deposition threshold for irradiation-induced void formation in a-Ge.

In summary, irradiation-induced void formation in a-Ge and the transformation of a void-rich into a sponge-like layer are nearly independent of the irradiation conditions. Single-ion irradiation alone causes the formation of nanometer-sized voids and even at low temperatures effective void formation and void agglomeration into a sponge-like porous structure takes place. Systematic investigations prove that the electronic energy deposition dominates the structural modification and a material-specific threshold value S_e^{void} must be exceeded for void formation to be operative.

10.4.3 Plastic Deformation of a-Ge

As described in Sect. 10.3.2, the irradiation-induced plastic deformation process can be simply characterized by the observation of the surface shift Δx at the sample

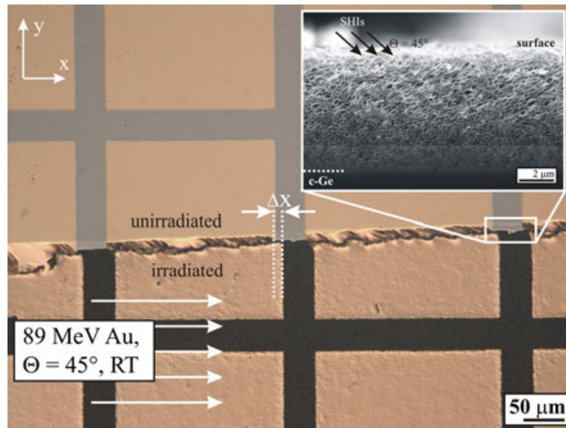

Fig. 10.26 Optical microscope image: Compared to the unirradiated reference (upper part of the sample) the irradiation-induced plastic deformation and volume expansion become evident. The lower part of the sample was irradiated at room temperature with 89 MeV Au ions under an angle of $\Theta = 45°$ from the left with an ion fluence of $N_I = 1.45 \times 10^{14}$ cm^{-2}. Inset: cross-section-SEM image: plastic flow process is directly reflected by the void alignment [61, 62]

surface. As an example, Fig. 10.26 shows a representative light microscopy image of a Ge surface, with an evaporated grid, a portion of which was irradiated with SHIs [61, 62]. A shift of the irradiated surface in the positive x-direction is clearly visible by means of the thin gold squares spanning the irradiated-unirradiated interface. Far from any boundaries, this irradiation-induced deformation was reported in a-Ge for all non-perpendicular ion irradiations and for different ion species (Xe, Au, Pb and U ions) [61]. Furthermore, the irradiation-induced plastic deformation is also directly visible by means of electron microscopy investigations using a sample cross section parallel to the direction of the surface shift as shown in the inset of Fig. 10.26 [61]. In this cross section geometry, it becomes apparent that the extended voids are well oriented within the porous layer but their alignment does not appear to correspond to the direction of the ion path along which the electronic energy is deposited. The orientation rather reflects the lateral mass transport along the projection of the ion beam direction on the surface due to the irradiation-induced plastic flow process.

The positive sign of the surface shift $\Delta x > 0$ proves that the SHI irradiated a-Ge surface layer flows plastically on the c-Ge substrate along the projection of the ion beam direction on the surface. According to (10.10) in Sect. 10.2, the plastic deformation of a-Ge is characterized by a positive deformation yield $A_0(\Delta x) > 0$ similar to that reported for SHI irradiated a-Si (cp. Sect. 10.3.2). For all ion irradiation conditions used, no irradiation-induced plastic deformation is observed in the y-direction, i.e. $v_y = \Delta y = A_0 = 0$. Moreover, irradiation of a-Ge at perpendicular ion incidence did not lead to any surface shift [61].

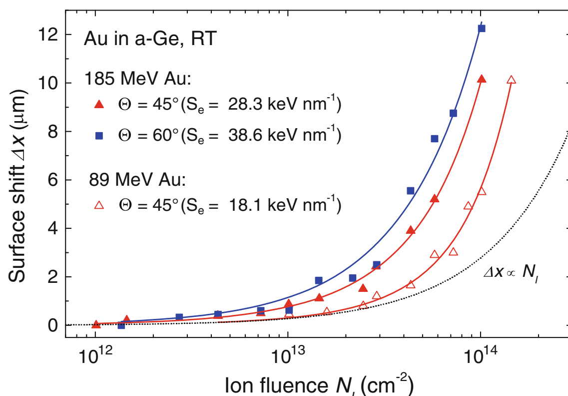

Fig. 10.27 Surface shift Δx as a function of the ion fluence obtained for a-Ge surface layers as a result of different non-perpendicular irradiation conditions. The *solid lines* are fits to the data using (10.12) and for comparison purposes, the *dotted line* represents a linear function [61]

In electron microscopy investigations, the anisotropic plastic deformation in the x-direction can be characterized as a function of the irradiation parameters, i.e. electronic energy deposition $S_e(E, \Theta)$ and ion fluence N_I [61, 62]. As shown in Fig. 10.27, the surface shift Δx increases continuously with increasing ion fluence, which means that a-Ge behaves similarly under SHI irradiation as demonstrated for conventional glasses [1, 2, 5, 15, 86] and a-Si [30, 53]. However, unlike the latter, the plastic deformation of SHI irradiated a-Ge shows a superlinear behavior of Δx in contrast to the expected linear dependence $\Delta x \propto N_I$ (see Sect. 10.2, (10.10)). This non-linear behavior can be attributed to the superimposed effect of the void-induced volume expansion in the z-direction which also becomes apparent in Fig. 10.26. Nevertheless, the influence of the electronic energy deposition on the plastic deformation $\Delta x(S_e) \propto S_e(E, \Theta)N_I$ can be discussed by means of Fig. 10.27: the higher the electronic energy deposition the greater the surface shift at the same ion fluence [61]. Moreover, non-perpendicular irradiation of a-Ge at low temperature (T = 50 K) leads also to a non-saturating anisotropic plastic deformation with a positive sign and is characterized by a superlinear behavior of Δx due to transformation into a porous structure (cp. Sect. 10.4.2).

In summary, under SHI irradiation, a-Ge shows a similar plastic deformation process with a positive deformation yield as observed for many conventional glasses [1, 2, 5, 15, 86] and a-Si [30, 53]. However, the expected steady state of the plastic flow or rather a linear shift of the surface with increasing ion fluence were not observed for a-Ge, which prevents a quantification of the deformation yield according to (10.10) in Sect. 10.2. A fundamental condition to describe the plastic deformation in the framework of the modified viscoelastic Maxwell model is the conservation of the volume and density of the deforming layer [5, 15]. This is obviously not the case for SHI irradiated a-Ge which was transformed into a sponge-like porous layer (see Sect. 10.4.2). Therefore, it was assumed that the continuous modification of the amorphous to a porous layer causes a continuous increase of the effective deformation yield A_{eff} [61]:

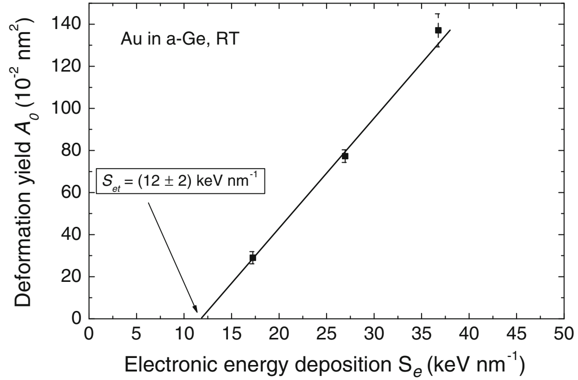

Fig. 10.28 The dependence of the deformation yield A_0 on the electronic energy deposition S_e. The extrapolation of the linear regression indicates the existence of an electronic energy deposition threshold of $S_{et} = (12 \pm 2)$ keV nm^{-1} for irradiation-induced plastic deformation in a-Ge [61]

$$\Delta x = 3d_{am} \sin(2\Theta) A_{eff} N_I \text{ with } A_{eff} \propto A_0[1 + \beta(\alpha) N_I]. \tag{10.12}$$

The parameter β is a free fit parameter. Fits based on (10.12) show an excellent agreement with the experimentally observed surface shift depicted in Fig. 10.27 (solid lines). Thus, the influence of the void formation on the plastic deformation can be functionally described by an additional quadratic term $\Delta x \propto N_I^2$, where the linear term $\Delta x \propto N_I$ corresponds to the conventional plastic flow process induced at constant volume. The deformation yield A_0 derived with (10.12) is depicted in Fig. 10.28 as a function of electronic energy deposition. It is evident that with increasing energy deposition the deformation yield increases linearly with a slope $\lambda(T)$ if a threshold value S_e for irradiation-induced plastic deformation is exceeded [61]:

$$A_0(S_e, T) = \lambda(T)[S_e - S_{et}] \text{ with } S_{et} = (12 \pm 2) \, \text{keV nm}^{-1}. \tag{10.13}$$

The dependence of the deformation yield on the electronic energy deposition (10.13) shows all the characteristic features of the ion hammering effect as described in Sect. 10.2 (cp. (10.4)). Furthermore, the threshold for the irradiation-induced plastic deformation of Ge is in the same order of magnitude as the threshold reported for Si (cp. Section 10.3.2). Following the theoretical description of the plastic deformation by means of the EFT model introduced by Trinkaus (see Sect. 10.2), this threshold S_{et} can be interpreted as an energy deposition required for the formation of low-viscosity zones around each ion path. However, the postulated phase transition from the LDA Ge to the HDL Ge phase observed in equilibrium is characterized as a first order transition. It is obvious that the difference in density between the HDL and LDA phase ($\rho_{HDL}^{Ge}/\rho_{LDA}^{Ge} > 1$) leads to a negative eigenstrain $\varepsilon^* < 0$ which directly causes a deformation with negative sign as predicted by Trinkaus, i.e. $A_0(\varepsilon^*) < 0$ [16, 24–28]. Nevertheless, for a-Si

($\rho^{Si}_{HDL}/\rho^{Si}_{LDA} > 1$, see Sect. 10.3.2) it was clearly demonstrated that a positive deformation yield $A_0 > 0$ can only be explained by a liquid-liquid phase transition assuming a LDL phase during the cooling process [30, 53]. Similar to the discussion for Si, a LDL phase has to exist for Ge to explain the results mentioned above, i.e. $A_0(\Delta x > 0) > 0$ [61, 62]. Hence, if the LDL Ge phase exists this phase would act as a source for positive thermoelastic strain, which has a cylindrical symmetry due to the cylindrical geometry of the energy deposition and the corresponding radial temperature distribution $T(r, t)$ (cp. Chap. 2). However, in order to achieve mechanical equilibrium the axial, radial and circumferential stresses relax if the temperature is larger than the effective flow temperature T^*. According to the viscoelastic model, this shear-stress relaxation causes a positive relaxation strain. The corresponding deformations permanently freeze in at the solidification front LDL to LDA when the temperature falls below T^* during the cooling process (see schematic illustration in Sect. 10.3.2, Fig. 10.14).

The positive deformation yield observed in both a-Si and a-Ge is a clear indication of the existence of a LDL phase in both materials. This result is of importance to other thetrahedrally coordinated networks with similar equilibrium melting curves, such as water or silica, and to all materials in which liquid polymorphism has been suggested to occur [50] or observed in experiments [87].

10.4.4 Structural Modification in Other Amorphous Semiconductors

While the current chapter clearly focuses on a-Si and a-Ge, other amorphous semiconductors have also been investigated. For example, the amorphous Si_xGe_{1-x} (a-Si_xGe_{1-x}) alloys are, not surprisingly, sensitive to SHI irradiation just like their mono-elemental components. Ion tracks induced by SHI irradiation were apparent across the entire alloy composition range [88]. The ion-track structural parameters, and their dependence on stoichiometry, are currently under study [88]. Void formation induced by SHI irradiation was also observed for the a-Si_xGe_{1-x} alloys. Figure 10.29 shows SEM images of a series of a-Si_xGe_{1-x} alloys for a given SHI mass and energy [89]. The origin of the intriguing layered structure has yet to be identified but we speculate that there is a characteristic length associated with the segmentation of the ion track as the high density molten phase undergoes volume contraction with one end of the first segment pinned to substrate surface. A stoichiometry dependence, particularly on void shape, is apparent and quantification of the plastic deformation in the a-Si_xGe_{1-x} alloys is also currently under study [90].

In contrast to the amorphous Group IV substrates, the amorphous Group III–V substrates appear insensitive to SHI irradiation for the same irradiation conditions.

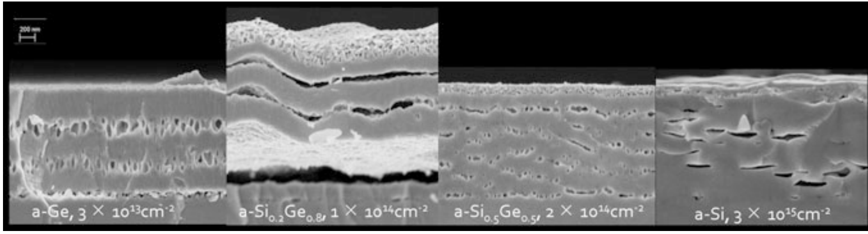

Fig. 10.29 Cross-section SEM images of a-Ge_xSi_{1-x} alloy layers on c-Si substrates following SHI irradiation with 185 MeV Au^{+13} ions. Alloy stoichiometries and ion fluences are listed on the figure [89]

Ion tracks were not observed in amorphous GaP or GaAs (a-GaP and a-GaAs, respectively) for irradiation conditions identical to those used successfully to produce ion tracks in a-Si, a-Ge and the a-Si_xGe_{1-x} alloys [91]. These irradiation conditions must thus be below the electronic energy deposition threshold for ion track formation in the two III–V materials. Note that for a given incident ion mass and energy, the electronic energy deposition for GaP will be very similar to GeSi while that for GaAs will be essentially equal to Ge. The insensitivity to SHI irradiation exhibited by these amorphous Group III–V substrates may thus stem from weaker electron-phonon coupling in these materials and/or differences in melting temperature. (For example, a crude estimate using crystalline phase values shows the melting temperatures for c-GaP and c-GeSi are 1740 and ~1448 K, respectively, while those for c-GaAs and c-Ge are 1511 and 1209 K, respectively.) Note that for these same irradiation conditions, plastic deformation in a-GaAs has been investigated but not observed [92], consistent with the lack of a measureable ion track.

We note that in another III–V compound semiconductor, in this case GaSb, the formation of nanoporous structures due to high electronic energy deposition has been reported [93]. The threshold value for void formation was S_e^{void} = 10 keV nm^{-1}. Void formation and porosity development were accompanied by swelling of the surface that increased linearly with ion fluence without saturation in bulk samples. A threshold fluence of 9×10^{12} cm^{-2} was required for measureable swelling, indicative of the necessity of a certain pre-damage before significant porosity forms. Interestingly, randomly oriented crystallites were observed within the amorphous material and their random orientation suggests they potentially formed during a quench from the melt. Complete amorphisation is thus not a prerequisite for the formation of porosity in GaSb, in contrast to Ge. However and surprisingly, no ion tracks were measureable with SAXS. Finally, while both GaSb and InSb can be rendered porous via nuclear energy deposition [94, 95], the morphology of the porous layers was different from that formed by electronic energy depositon.

10.5 Summary

SHIs readily interact with the amorphous Group IV semiconductors, potentially yielding ion track formation, plastic deformation and/or porous layer formation. In contrast, the amorphous Group III–V semiconductors appear insensitive to SHI irradiation under identical irradiation conditions. In this chapter, such phenomena have been reviewed with the inclusion of synergistic experiment, modelling and simulation results that yield new understanding of ion-solid interactions in the SHI irradiation regime.

Acknowledgements MCR thanks P. Kluth, T. Bierschenk, K. Nordlund, F. Djurabekova, O. Pakarinen, M. Schleberger, O. Osmani, N. Medvedev and B. Rethfeld for their valued collaboration and the Australian Research Council and Australian Synchrotron for financial support. MCR also acknowledges access to NCRIS and AMMRF infrastructure at the Australian National University including the Australian National Fabrication Facility, the Heavy Ion Accelerator Capability and the Center for Advanced Microscopy.

WW and TS thank S. Klaumünzer, A. Hedler, K. Gärtner, R. Giulian, L.L. Araujo, D.J. Sprouster, P. Kluth and C.S. Schnohr for their valuable collaboration and the Federal Ministry for Education and Research of Germany (BMBF) and the German Council for Academic Exchange (DAAD) for financial support.

References

1. S. Klaumünzer, G. Schumacher, Phys. Rev. Lett. **51**, 1987 (1983)
2. S. Klaumünzer, M. Hou, G. Schumacher, Phys. Rev. Lett. **57**, 850 (1986)
3. S. Klaumünzer, Mat. Sci. For. **97–99**, 623 (1992)
4. S. Klaumünzer, Multisc. Phenom. In Plast. **367**, 441 (2000)
5. A. Gutzmann, S. Klaumünzer, P. Meier, Phys. Rev. Lett. **74**, 2256 (1995)
6. S. Klaumünzer, Nucl. Instr. Meth. B **225**, 136 (2004)
7. Ming-dong Hou, S. Klaumünzer, G. Schumacher, Phys. Rev. B **41**, 1144 (1990)
8. M. Hou, S. Klaumünzer, G. Schumacher, Nucl. Instr. Meth. B **19/20**, 16 (1987)
9. A. Adouard, E. Balanzat, G. Fuchs, J.C. Jousset, D. Lesueur, L. Thomé, Europhys. Lett. **3**, 327 (1987)
10. S. Klaumünzer, Mat. Sci. For. **97–99**, 623 (1992)
11. A. Adouard, E. Balanzat, J.C. Jousset, D. Lesueur, L. Thomé, J. Phys. Condens. Matter **5**, 995 (1993)
12. A. Adouard, E. Balanzat, J.C. Jousset, G. Fuchs, D. Lesueur, L. Thomé, Nucl. Instr. Meth. B **39**, 18 (1989)
13. A. Gutzmann, S. Klaumünzer, A. Benyagoub, D. Nagengast, Rad. Eff. Def. Solids **126**, 133 (1993)
14. A. Gutzmann, S. Klaumünzer, Nucl. Instr. Meth. B **127**(128), 12 (1997)
15. S. Klaumünzer, Nucl. Instr. Meth. B **215**, 345 (2004)
16. A.I. Ryazanov, A.E. Volkov, S. Klaumünzer, Phys. Rev. B **51**, 12107 (1995)
17. V.A. Borodin, A.E. Volkov, D.N. Korolev, Nucl. Instr. Meth. B **209**, 122 (2003)
18. L. Cliche, S. Roorda, M. Chicoine, R.A. Masut, Phys. Rev. Lett. **75**, 2348 (1995)
19. M. Chicoine, S. Roorda, L. Cliche, R.A. Masut, Phys. Rev. B **56**, 1551 (1997)
20. G. Szenes, Mat. Sci. For. **97–99**, 647 (1992)

21. G. Szenes, Phys. Rev. B **51**, 8026 (1995)
22. G. Szenes, Nucl. Instr. Meth. B **107**, 150 (1996)
23. G. Szenes, Z.E. Horvath, B. Pecz, F. Paszti, L. Toth, Phys. Rev. B **65**, 045206 (2002)
24. H. Trinkaus, A.I. Ryazanov, Phys. Rev. Lett. **74**, 5072 (1995)
25. H. Trinkaus, J. Nucl. Mat. **223**, 196 (1995)
26. H. Trinkaus, Nucl. Instr. Meth. B **107**, 155 (1996)
27. H. Trinkaus, J. Nucl. Mat. **246**, 244 (1997)
28. H. Trinkaus, Nucl. Instr. Meth. B **146**, 204 (1998)
29. J.D. Eshelby, Proc. R. Soc. Lond. Sect. A **241**, 37 (1957)
30. A. Hedler, S. Klaumünzer, W. Wesch, Nat. Mater. **3**, 804 (2004)
31. B. Canut, N. Bonardi, S.M.M. Ramos, S. Della-Negra, Nucl. Instr. Meth. B **146**, 296 (1998)
32. A. Dunlop, G. Jaskierowicz, S. Della-Negra, Nucl. Instr. Meth. B **146**, 302 (1998)
33. A. Kamarou, W. Wesch, E. Wendler, A. Undisz, M. Rettenmayr, Phys. Rev. B **78**, 054111 (2008)
34. T. Bierschenk, R. Giulian, B. Afra, M.D. Rodriguez, D. Schauries, S. Mudie, O.H. Pakarinen, F. Djurabekova, K. Nordlund, O. Osmani, N. Medvedev, B. Rethfeld, M.C. Ridgway, P. Kluth, Phys. Rev. B **88**, 174111 (2013)
35. N.A. Medvedev, A.E. Volkov, N.S. Shcheblanov, B. Rethfeld, Phys. Rev. B **82**, 125425 (2010)
36. M.I. Kaganov, I.M. Lifshitz, L.V. Tanatarov, Sov. Phys. JETP **4**, 173 (1957)
37. S.I. Anisimov, B.L. Kapeliovich, T.L. Perel'man, Sov. Phys. JETP **39**, 375 (1974)
38. M. Toulemonde, C. Dufour, E. Paumier, Phys. Rev. B **46**, 14362 (1992)
39. http://www.webelements.com/silicon/physics.html
40. M.G. Grimaldi, P. Baeri, M.A. Malvezzi, Phys. Rev. B **44**, 1546 (1991)
41. P. Kluth, C.S. Schnohr, O.H. Pakarinen, F. Djurabekova, D.J. Sprouster, R. Giulian, M.C. Ridgway, A.P. Byrne, C. Trautmann, D.J. Cookson, K. Nordlund, M. Toulemonde, Phys. Rev. Lett. **101**, 175503 (2008)
42. A. Chettah, H. Kucal, Z.G. Wang, M. Kac, A. Meftah, M. Toulemonde, Nucl. Instrum. Meth. B **267**, 2719 (2009)
43. M.C. Ridgway, T. Bierschenk, R. Giulian, B. Afra, M.D. Rodriguez, L.L. Araujo, A.P. Byrne, N. Kirby, O.H. Pakarinen, F. Djurabekova, K. Nordlund, M. Schleberger, O. Osmani, N. Medvedev, B. Rethfeld, P. Kluth, Phys. Rev. Lett. **110**, 245502 (2013)
44. N. Jakse, L. Hennet, D.L. Price, S. Krishnan, T. Key, E. Artacho, B. Glorieux, A. Pasturel, M.-L. Saboungi, Appl. Phys. Lett. **83**, 4734 (2003)
45. P.F. McMillan, M. Wilson, D. Daisenberger, D. Machon, Nat. Mat. **4**, 680 (2005)
46. S.V. Stankus, R.A. Khairulin, P.V. Tyagelskii, High Temp. **37**, 529 (1999)
47. J.S. Custer, M.O. Thompson, D.C. Jacobson, J.M. Poate, S. Roorda, W.C. Sinke, F. Spaepen, Appl. Phys. Lett. **64**, 437 (1994)
48. L.I. Aptekar, Sov. Phys. Dokl. **24**, 993 (1997)
49. S.K. Debb, M. Wilding, M. Somayazulu, P.F. McMillan, Nature **414**, 528 (2001)
50. P.F. McMillan, J. Mater. Chem. **14**, 1506 (2004)
51. S. Sastry, C.A. Angell, Nat. Mater. **2**, 739 (2003)
52. A. Hedler, S. Urban, F. Falk, H. Hobert, W. Wesch, Appl. Surf. Sci. **205**, 240 (2003)
53. A. Hedler, S. Klaumünzer, W. Wesch, Phys. Rev. B **72**, 054108 (2005)
54. A. Hedler, S. Klaumünzer, W. Wesch, Nucl. Instr. Meth. B **242**, 85 (2006)
55. A. Hedler, S. Klaumünzer, W. Wesch, unpublished
56. J.F. Ziegler, J.P. Biersack, U. Littmark, *The Stopping and Range of Ions in Solids* (Pergamon, New York, 2003)
57. S.K. Sundaram, E. Mazur, Nat. Mater. **1**, 217 (2002)
58. A. Cavalleri, K. Sokolowski-Tinten, J. Bialkowski, M. Schreiner, J. Appl. Phys. **85**, 3301 (1999)

59. P.L. Silvestrelli, A. Alavi, M. Parrinello, D. Frenkel, Phys. Rev. B **56**, 3806 (1997)
60. A. Colder, O. Marty, B. Canut, M. Levalois, P. Marie, X. Portier, S.M.M. Ramos, M. Toulemonde, Nucl. Instrum. Meth. B **174**, 491 (2001)
61. T. Steinbach, C.S. Schnohr, W. Wesch, P. Kluth, R. Giulian, L.L. Araujo, D.J. Sprouster, M.C. Ridgway, Phys. Rev. B **83**, 054113 (2011)
62. W. Wesch, C.S. Schnohr, P. Kluth, Z.S. Hussain, L.L. Araujo, R. Giulian, D.J. Sprouster, A.P. Byrne, M.C. Ridgway, J. Phys. D Appl. Phys. **42**, 115402 (2009)
63. K. Nordlund, M. Ghaly, R.S. Averback, M. Caturla, T. Diaz de la Rubia, J. Tarus, Phys. Rev. B **57**, 7556 (1998)
64. M. Posselt, A. Gabriel, Phys. Rev. B **80**, 045202 (2009)
65. J. Tersoff, Phys. Rev. B **39**, 5566 (1989)
66. J. Koga, T. Yamaguchi, Phys. Chem. Glasses **46**, 425 (2005)
67. T. Bierschenk, B. Afra, M.D. Rodriguez, R. Giulian, C. Trautmann, S. Mudie, M.C. Ridgway, P. Kluth, Nucl. Instr. Meth. B **326**, 113 (2014)
68. M. Toulemonde, W. Assmann, C. Dufour, A. Meftah, F. Studer, C. Trautmann, C. Mat, Fys. Medd. **52**, 263 (2006)
69. M.C. Ridgway, F. Djurabekova and K. Nordlund, Curr. Op. Sol. State Mat. Sci., Focus Issue: Ion Beam Modification of Materials **19**, 29 (2015)
70. K. Gärtner, J. Jöhrens, T. Steinbach, C.S. Schnohr, M.C. Ridgway, W. Wesch, Phys. Rev. B **83**, 224106 (2011)
71. H. Huber, W. Assmann, R. Grötzschel, H.D. Mieskes, A. Mücklich, H. Nolte, W. Prusseit, Mat Sci. Appl. Ion Beam Techn. **248**, 301 (1997)
72. H. Huber, W. Assmann, S.A. Karamian, A. Mücklich, W. Prusseit, B. Gazis, R. Grötzschel, M. Kokkoris, E. Kossionidis, H.D. Mieskes, R. Vlastou, Nucl. Instr. Meth. B **122**, 542 (1997)
73. I.H. Wilson, J. Appl. Phys. **53**, 1698 (1982)
74. B.R. Appleton, O.W. Holland, J. Narayan, O.E. Schow, J.S. Williams, K.T. Short, E. Lawson, Appl. Phys. Lett. **41**, 711 (1982)
75. O.W. Holland, B.R. Appleton, J. Narayan, J. Appl. Phys. **54**, 2295 (1983)
76. B.R. Appleton, O.W. Holland, D.B. Poker, J. Narayan, D. Fathy, Nucl. Instr. Meth. B **7**(8), 639 (1985)
77. L.M. Wang, R.C. Birtcher, Phil. Mag. A **64**, 1209 (1991)
78. B. Stritzker, R.G. Elliman, J. Zou, Nucl. Instr. Meth. B **175**, 193 (2001)
79. T. Janssens, C. Huyghebaert, D. Vanhaeren, G. Winderickx, A. Satta, M. Meuris, W. Vandervorst, J. Vac. Sci. Tech. B **24**, 510 (2006)
80. L. Ottaviano, A. Verna, V. Grossi, P. Parisse, S. Piperno, M. Passacantando, G. Impellizzeri, F. Priolo, Surf. Sci. **601**, 2623 (2007)
81. L. Romano, G. Impellizzeri, M.V. Tomasello, F. Giannazzo, C. Spinella, M.G. Grimaldi, J. Appl. Phys. **107**, 084314 (2010)
82. B.L. Darby, B.R. Yates, N.G. Rudawski, K.S. Jones, A. Kontos, R.G. Elliman, Thin Solid Films **519**, 5962 (2011)
83. T. Steinbach, J. Wernecke, P. Kluth, M.C. Ridgway, W. Wesch, Phys. Rev. B **84**, 104108 (2011)
84. T. Steinbach, W. Wesch, Nucl. Instr. Meth. B **319**, 112 (2014)
85. G. Schiwietz, K. Czerski, M. Roth, F. Staufenbiehl, P.L. Grande, Nucl. Instr. Meth. B **225**, 4 (2004)
86. S. Klaumünzer, Ch. Li, S. Löffler, M. Rammensee, and G. Schumacher, Nucl. Instr. Meth. B **39**, 665 (1989)
87. S. Aasland, P.F. McMillan, Nature **369**, 633 (1994)
88. T. Bierschenk, M.C. Ridgway, P. Kluth, to be published
89. T. Bierschenk, Ph.D. Thesis, Australian National University, 2014
90. M.C. Ridgway, unpublished
91. M.C. Ridgway, M. Rodriguez, P. Kluth, unpublished
92. W. Wesch, T. Steinbach, M.C. Ridgway, unpublished

93. P. Kluth, J.J. Sullivan, W. Li, R. Weed, C.S. Schnohr, R. Giulian, L.L. Araujo, W. Lei, M.D. Rodriguez, B. Afra, T. Bierschenk, R.C. Ewing, M.C. Ridgway, Appl. Phys. Lett. **104**, 023105 (2014)
94. S.M. Kluth, J. Gerald, M.C. Ridgway, Appl. Phys. Lett. **86**, 131920 (2005)
95. A. Perez-Bergquist, S. Zhu, K. Suu, X. Xiang, Y. Zhang, L. Wang, Small **4**, 1119 (2008)

Part IV
Selected Applications of Ion Irradiation

Chapter 11
Ion-Shaping of Nanoparticles

Giancarlo Rizza and Mark C. Ridgway

Abstract Since its discovery in the early 2000s, the ion-shaping technique has emerged as a powerful tool to engineer real three-dimensional architectures in the form of embedded nanostructures with tunable morphology and spatial orientation. The technique has been proven to be particularly well adapted for sculpting metal-glass nanocomposites. We analyze the body of experimental research that has been carried out until now. We review progress made over the years into this unique yet poorly understood process operative only at extreme electronic energy loss. Moreover, we describe and critically analyze the models and simulations that have been developed so far. The aim is to gain a fundamental atomistic insight into the elongation phenomenon. Finally, this chapter presents recent trends in the fabrication of ion-shaped nanoparticles and possible future applications.

11.1 Introduction

Nanotechnology was born in the early 1980s. Its emergence was mainly driven by two factors: the publication of Drexler's book *Engines of creation*: *the coming era of nanotechnology*, which helped to popularize the concept of nanoscience as a means to assemble matter at the nanoscale [1] and the realization of two breakthrough characterization methods: the scanning tunneling microscope (STM) and the atomic force microscope (AFM). In the scientific excitement stirred by the awareness that these techniques suddenly provided an access to the nanoworld,

Mark C. Ridgway (deceased December 2015)

G. Rizza (✉)
Laboratoire des Solides Irradiés, Ecole Polytechnique, CEA/DRF/IRAMIS,
CNRS, Université Paris-Saclay, 91128 Palaiseau Cedex, France
e-mail: giancarlo.rizza@polytechnique.edu

M.C. Ridgway
Research School of Physics and Engineering, Australian National University,
Canberra, ACT 2601, Australia

© Springer International Publishing Switzerland 2016

W. Wesch and E. Wendler (eds.), *Ion Beam Modification of Solids*,
Springer Series in Surface Sciences 61,
DOI 10.1007/978-3-319-33561-2_11

other techniques and approaches swirled into a rapid growth process. This is e.g. illustrated by the continuous developments of techniques associated with transmission electron microscopy, photo-lithography, electron-beam lithography, and colloidal chemistry.

The swift heavy-ion (SHI) community was hit by the waves of this new science from the late 1990s onwards. Indeed, if a lot of work had already been done to understand the ion-matter interaction in the regime of pure electronic energy deposition, most of the experiments had been performed either on macroscopic samples or polycrystalline samples with a mean grain size exceeding a micrometer. At that time, it became clear that one way to obtain a deeper insight into the SHI-matter interaction was to reduce the size of the target. Among these pioneering works, we can mention the study of the cubic-to-monoclinic phase transformation observed in Y_2O_3 sub-micrometric powders [2] and of the irradiation of Sn oxide nanograins [3].

In the wake of this new research field, in a series of seminal papers published between 2000 and 2006, Polman's group demonstrated the feasibility to use SHI irradiation as a tool to sculpt matter at the nanoscale [4–10]. By combining chemical synthesis and ion-irradiation, they demonstrated that it was indeed possible to produce a new class of amorphous colloidal ellipsoids of continuously variable shape, as illustrated in Fig. 11.1. The anisotropic deformation of these colloidal nanoparticles (NPs) is the counterpart on the nanoscale of the ion hammering effect observed in irradiated amorphous macroscopic materials [11]. Inspired by this innovative approach, D'Orléans, Stoquert and collaborators studied how the properties of embedded metallic NPs were modified when submitted to sustained swift heavy-ion irradiation. Indeed, in a series of articles from the years 2003–2004 [12, 13] they reported that Co NPs embedded in a silica matrix changed shape, from spheres to rods, under the influence of swift heavy-ion irradiation, Fig. 11.2a, b. Interestingly, while van Dillen's experiments [6–10] showed that the silica colloids became oblate, i.e. the deformation was normal to the beam direction, in D'Orléans's experiments the metallic NPs became prolate, i.e. the major axis of the elongated nanoparticles was aligned parallel to the incident ion direction. The ion-shaping process was discovered. This surprising finding rapidly attracted

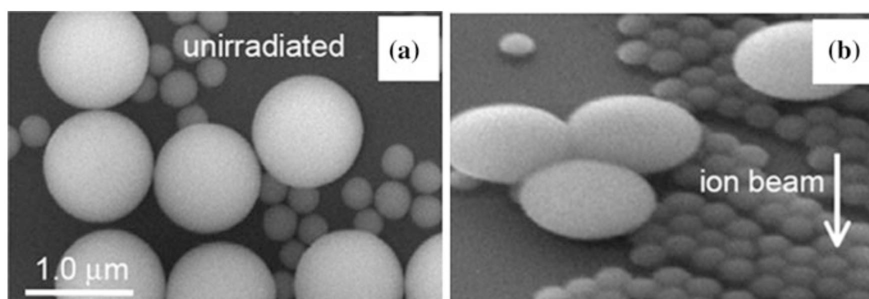

Fig. 11.1 Scanning electron microscopy (SEM) images of **a** non irradiated spherical silica colloids, and **b** ion hammering of silica colloids after 4 MeV Xe irradiation at a fluence of 3×10^{14} cm^{-2}, at an angle of 45° relative to the surface normal, at 90 K. Reproduced with permission from [4]

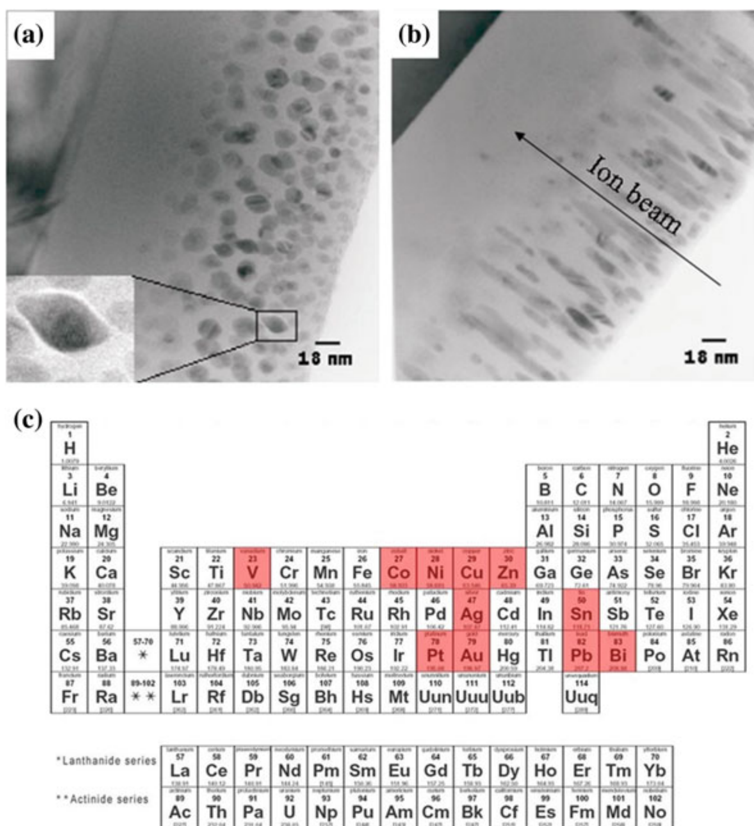

Fig. 11.2 First experimental evidence for the existence of the ion-shaping mechanism. Co NPs embedded in silica after irradiation with 200 MeV I ions shown at **a** 1×10^{13} cm^{-2}, and **b** 1×10^{14} cm^{-2}. Reproduced with permission from [13]. Copyright 2004 American Physical Society. **c** Elemental metals for which the shape transformation has been reported

the attention of an important number of groups worldwide, and has been intensively studied ever since, under a variety of conditions and for a variety of metals (for example, see Fig. 11.2c) [14–46].

It is interesting to note that in the first paper by D'Orléans et al. [12] the elongation effect was not particularly highlighted in the title: *Irradiations of implanted cobalt nanoparticles in silica layers*. However, in their following manuscript they introduced the term of *anisotropic deformation* [13]: *Anisotropy of Co nanoparticles induced by swift heavy ions*. The same year, this terminology was adopted by Roorda et al. [37] and Penninkhof et al. [39]. Schmidt et al. [44] were in 2007 the first to introduce the term *ion-shaping* in order to describe the deformation of Ge NPs embedded within a silica matrix. Nowadays, this term is widely accepted in the community. It currently indicates the irradiation-induced transformation of spherical nanoparticles into prolate nanostructures, e.g. [21, 22].

11.2 Ion-Matter Interaction for a Metal-Dielectric Nanocomposite

When an energetic ion penetrates a substrate and eventually comes to rest, it deposits energy via elastic and inelastic processes, see *Part I*. The former process, called *nuclear energy loss* and noted S_n, involves the ballistic displacements of substrate atoms in a billiard-ball like manner while the latter, called *electronic energy loss* and noted S_e, includes the excitation and ionization of substrate atoms. These two processes exhibit distinctly different ion energy dependencies as apparent from Fig. 11.3a which shows SRIM calculations for Au ions incident on SiO_2 [47, 48]. Clearly S_n and S_e are dominant at low and high ion energies, respectively, and the maximum amplitude of the electronic energy loss is much larger than that of its nuclear counterpart. Reducing the incident-ion mass shifts the maxima for both energy loss processes to lower ion energies. The magnitude of both processes is also lowered. When an embedded NP is irradiated in the nuclear stopping regime, displacement cascades favor the ballistic displacement of the metallic species into the host matrix and the formation of a halo of satellite clusters in the surroundings of the *mother* NP, Fig. 11.3a, see Chap. 4. On the other hand, when the embedded NP is irradiated in a regime where the magnitude of the electronic stopping power dominates the nuclear stopping power, NP elongation is observed, Fig. 11.3a. Here, a fraction of the energy deposited into the electronic subsystem is subsequently transferred to the atomic subsystem of the matrix and the objects embedded therein through electron-phonon (*e-p*) coupling, see Chap. 2. Thus, in this regime the energy transfer is governed by the *e-p* coupling strength *g*. For instance, for a given material, the electron mean free path is smaller in the amorphous phase than in the crystalline one, thus $g_{amorphous}$ typically exceeds $g_{crystalline}$. The transfer of energy to the lattice induces rapid heating such that molten material is formed when the temperature exceeds the melting temperature. The subsequent rapid quenching of this transient phase leads to residual disorder in the form of a so-called *ion track* [49].

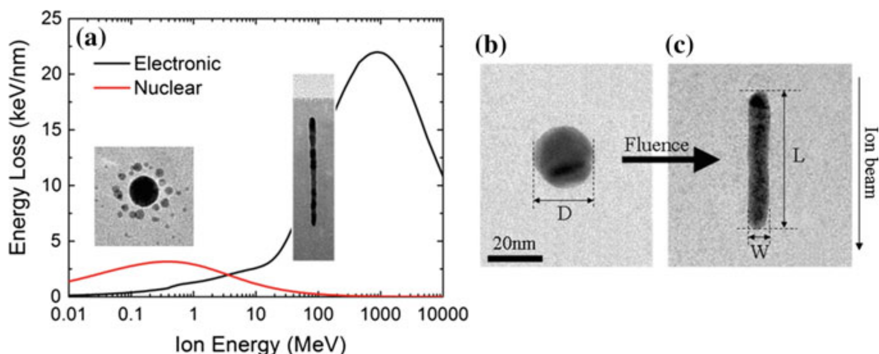

Fig. 11.3 **a** Nuclear (S_n), and electronic (S_e), energy loss processes as a function of the incident energy for Au ions in SiO_2. **b** As prepared Au NP of diameter *D*. **c** Ion-shaped NP of length *L* and width *W*

To unveil the underlying mechanisms of an unknown phenomenon it is worth establishing simple relationships between sample properties and experimental parameters. In its simplest description, the ion-shaping is the transformation of a spherical NP of diameter *D* into a cylinder of width *W* and length *L*, Fig. 11.3b, c. Thus, a great deal of effort has been made hitherto to correlate the host matrix and NP properties to the irradiation conditions (ion energy, flux, fluence and temperature). In the following, we will first describe the influence of the embedding matrix on the ion-shaping process, after which the role played by the NPs will be highlighted. Finally, the current understanding of the ion-shaping process is reported, whereby it has to be admitted that a fully consistent description of the operative mechanism is still wanting.

11.3 Influence of the Embedding Matrix

After its discovery in 2001, ion-shaping has always been observed in nanocomposite systems where NPs are confined within a host matrix. However, the necessity of the embedding matrix in the elongation process was convincingly demonstrated only in a series of articles published during the years 2004–2006 [37–39]. Since the early 1980s, it is known that amorphous materials undergo ion-hammering, which means that the irradiated material shrinks in the direction of the ion beam and expands perpendicular to it [50]. Conversely, metallic NPs that were not embedded and only simply adhered to a substrate surface have never been observed to undergo such a change in shape. Motivated by this entirely different behavior, Penninkhof et al. studied the deformation effect on core-shell colloidal assemblies, i.e. particles comprised of a Au core (fixed 14 nm diameter) and a silica shell (variable thickness up to 70 nm), Fig. 11.4a. From Fig. 11.4b, it is readily apparent that the presence of

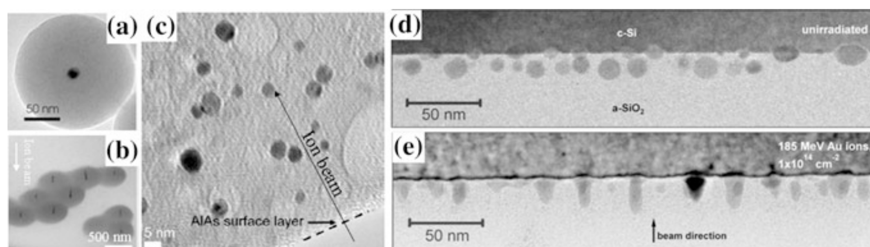

Fig. 11.4 **a** Scanning electron microscopy (SEM) image of an as-prepared Silica-Au core-shell colloid. **b** After irradiation with 30 MeV Cu ions at 5×10^{14} cm^{-2}. Reproduced with permission from [39]. **c** TEM micrograph of Au NPs embedded within a AlAs matrix and irradiated with 30 MeV Cu ions at a fluence of 5×10^{13} cm^{-2}. Reproduced with permission from [51]. TEM micrographs of Sn NPs at or in close proximity of the SiO_2/Si interface, **d** before and **e** after irradiation with 185 MeV Au ions up to a fluence of 1×10^{14} cm^{-2}. Reproduced with permission from [52]. Copyright 2010 American Physical Society

an embedding shell allows the deformation of the metallic NP even though the deformation is different for the two materials. Indeed, their major axes deform in a direction that is parallel and perpendicular to the incident ion direction, respectively. These studies demonstrated that a minimal threshold for the thickness of the embedding matrix must exist. Indeed, the elongation of the embedded Au NPs is observable only for particles whose silica shell thickness is larger than approximately 20 nm. An additional observation, rather similar in nature, is that the deformation of the metal core of core-shell particles with equal sizes and shell thicknesses depends on the local environment of the colloids: particles that are stacked two or three layers thick and are in contact before irradiation exhibit significantly larger deformation of the metal core than isolated particles. These two independent experiments (based on varying the shell thickness and the colloid contact, respectively) led to the conclusion that the NP core deforms more efficiently when more silica surrounds it.

However, the presence of an embedding matrix alone is not a sufficient condition for ion-shaping to be an effective process. A second condition to be fulfilled is that the embedding matrix is amorphous, or at least amorphisable. Available experiments indicate indeed that ion-shaping is not observed in crystalline radiation-resistant matrices. A first example illustrating this point is the crystalline matrix of the semiconductor AlAs [51]. This material is extremely radiation-resistant both in the nuclear and electronic energy loss regimes. Concomitantly it does not develop ion tracks. Spherical Au NPs obtained by ion implantation in AlAs failed to deform when subjected to swift heavy-ion irradiation, demonstrating that ion-track formation is a necessary ingredient for obtaining a transformation of the shape, Fig. 11.4c. Another elegant example is illustrated in Fig. 11.4d, e which show the behavior of Sn NPs positioned at a $SiO_2/c{-}Si$ interface when they are subjected to swift heavy-ion irradiation [52]. Such a sample with a heterostructure enables a direct comparison of the elongation process in two different matrices. In the present case, the Si matrix is crystalline. Like AlAs, crystalline Si is also radiation-resistant to swift heavy-ion irradiation such that ion-track formation is not observed under the given irradiation conditions, see Chap. 9. The TEM image of Fig. 11.4e shows that as expected, the NP elongates in the amorphous SiO_2, while this is not the case in crystalline Si.

11.3.1 Influence of the Ion-Hammering

Amorphous materials submitted to ion-irradiation undergo a non-saturable deformation at constant volume. The sample expands normal to the beam direction and shrinks parallel to the beam direction, see Chap. 10. This phenomenon, known as *ion-hammering* was discovered by Klaumünzer et al. [50] and described by Trinkaus and Ryazanov [53–56]. This model is nowadays known as the effective-flow-temperature approach (*EFTA*). The basic idea of the EFTA model is to describe an ion-track as a visco-elastic inclusion using Eshelby's theory [57]. The rapid thermal expansion about the ion path produces shear stresses that relax by viscous flow.

Rapid cooling of the hot cylindrical ion-track freezes in viscous strains. The resulting strained track represents the basic mesoscopic defect responsible for the ion-hammering. The terminology *ion-hammering* highlights in a vivid way the role played by each impinging ion: it is as though each ion acts like a little hammer deforming the sample. The overall effect is due to the sum of all the frozen-in viscous strains produced by the individual ion impacts. In particular, the ion-hammering is associated with a build up of in-plane stress σ within the matrix [56]:

$$\sigma = -1.16\frac{1+\nu}{1-\nu}G\alpha\Delta T \sim -0.3\ \text{GPa}, \tag{11.1}$$

where ν is the Poisson ratio, G the shear modulus and α is the linear thermal-expansion coefficient.

The effect of σ in the transformation process has been discussed by several authors [37, 42, 46, 58]. In particular, it has been supposed that the in-plane stress acting on the NP may favor the flow of the metallic species in the out-of-plane direction, i.e. along the beam direction [37]. However, its necessity has also been questioned. For instance, Klaumünzer pointed out that the magnitude of σ alone is not sufficient to drive the deformation of a solid NP [42] such that the NP must also play an active role in the transformation process. This means that the NP must be in a molten phase. A possible solution of this problem could be the fact that the efficiency of the ion-hammering—and thus the extent of the in-plain stress—decreases when the matrix temperature is increased. Hence, the NP elongation process may progress at a lower rate at higher matrix temperatures. The pertinence of this idea could be checked experimentally. However, up to now such experiments have never been performed. More recently, combining results from experiments and simulations, Amekura et al. [58] and Leino et al. [46] have come to a similar conclusion that the amorphous matrix does not play any active role. This point will be discussed in more detail in Sect. 11.5.

11.3.2 Influence of the Ion Track

Insights on the elongation process have been gained from detailed studies of ion-track formation. Although the average structural properties of ion tracks can often be inferred from macroscopic measurements, it remains extremely difficult to retrieve information about the inner track structure. This is due to the lack of sufficient contrast inherent to most of the observation techniques. This is particularly true in the case of amorphous materials. However, this experimental difficulty has recently been overcome by Kluth et al. [59] who used the small angle x-ray scattering (SAXS) technique to determine how the density of the material changes as a function of the distance from the ion trajectory.

In the following examples we show how the ion-shaping process is influenced by the radial density distribution across an ion track. Figure 11.5 shows Au NPs

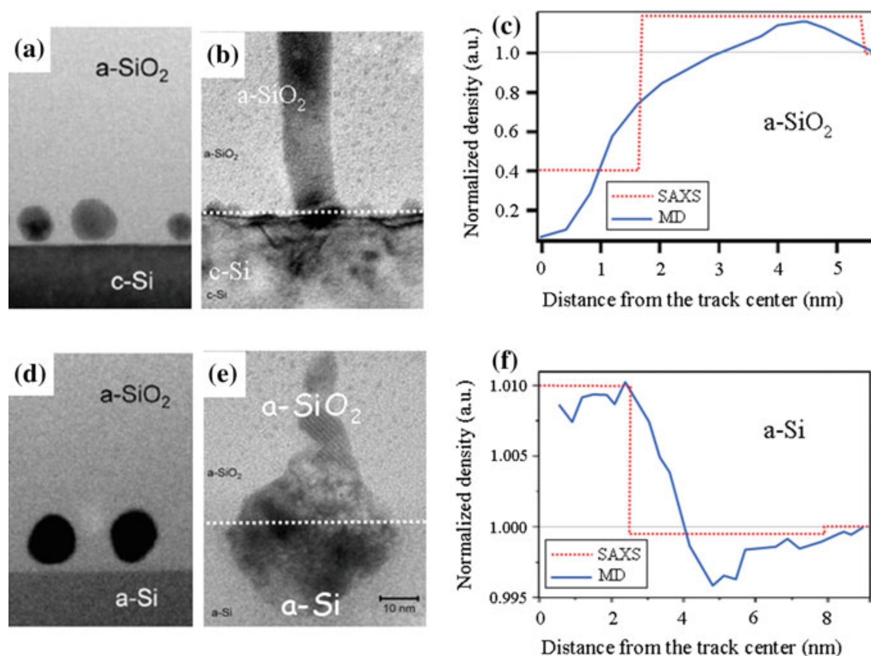

Fig. 11.5 TEM micrographs of Au NPs at $SiO_2/c-Si$ interface. **a** As-prepared. **b** Irradiated sample. TEM micrographs of Au NPs at $SiO_2/a-Si$ interface. **d** As-prepared. **e** Irradiated sample. In both cases irradiation was performed with 185 MeV Au ions at a fluence of 1×10^{14} cm^{-2}. SAXS measurements (*solid line*) and MD simulations (*dashed line*) of the radial density distribution across an ion track in **c** a-SiO_2 substrate. Reproduced with permission from [59]. Copyright 2008 American Physical Society, and **f** a-Si substrate. Reproduced with permission from [60]. Copyright 2013 American Physical Society

positioned at or close to the SiO_2/Si interface. In these experiments two different silicon substrates have been used, i.e. crystalline (c-Si), Fig. 11.5a and amorphous (a-Si), Fig. 11.5d. The TEM image of Fig. 11.5b shows that the NP elongates in SiO_2 as expected, while this is not the case in crystalline Si. Figure 11.5c shows SAXS measurements and molecular dynamic (MD) simulations for the radial density distribution across an ion track in silica. It consists of a low-density core, surrounded by a high density shell. The core has a density that is significantly lower than that of a non-irradiated material. The structure is consistent with the existence of a frozen-in pressure wave originating from the center of the ion track, produced by a thermal spike. On the other hand, no tracks are formed within the crystalline Si matrix. This demonstrates that the shape transformation cannot take place without the prior formation of an ion-track. One might thus intuitively expect that the presence of the under-dense core may facilitate the motion of metal atoms during the process of shape transformation.

A crystalline-to-amorphous phase transition of the Si gives rise to differences that are easy to observe. The TEM image of Fig. 11.5e demonstrates that some Au

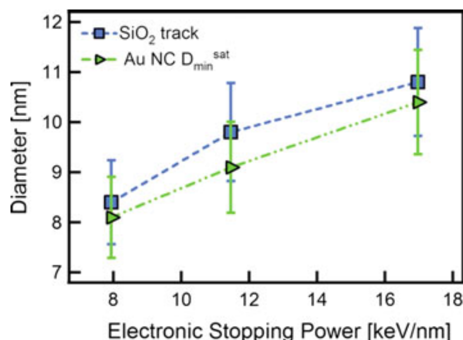

Fig. 11.6 Comparison of ion track diameter in silica and width of the elongated Au NP as a function of electronic energy loss. Reproduced with permission from [21]

migrates into the amorphous Si, possibly forming an Au–Si alloy, but *conventional* elongation is not apparent. Ion-track formation in amorphous Si has only recently been identified [60] and its radial density distribution explains this unanticipated phenomenon: the core-shell structure of an ion track in amorphous Si consists of an over-dense core and an under-dense shell. This is the opposite to what has been observed in amorphous SiO_2. MD simulations support the assumption that there exists a core that is more dense and a shell that is slightly less dense than the non-irradiated a-Si of the matrix. This is consistent with the existence of frozen-in structural remnants of the high-density liquid phase, Fig. 11.5e.

A further indication of the role played by the ion track is illustrated in Fig. 11.6. Here, the ion track diameter is compared to the width of the elongated Au NPs. Clearly both parameters scale near linearly with electronic energy loss where the diameter of the ion track in silica always exceeds the width of the elongated NP. This indicates that the ion track constrains the size of the NP during the shape transformation process.

These experiments demonstrate the following: *not only is the formation of an ion track a prerequisite for the NP elongation*, *but it must have an under-dense core. The latter favors the motion of the molten metal*, *while simultaneously constrains the width of the rod-like NPs.*

11.4 Influence of the Nanoparticles

Ion-shaping is generally observed for NPs which are metallic. On the periodic table in Fig. 11.2c the ensemble of the ion-shaped NPs can be categorized in two main groups. The first group comprises elements that belong to the class of transition metals, which includes groups 3–12 of the periodic table, in other words V, Fe, Co, Ni, Cu, Zn, Ag, Pt and Au and their alloys AgAu and FePt. In particular, swift heavy-ion irradiation of FePt nanoclusters embedded within an amorphous alumina $(FePt)_{47}\,(Al_2O_3)_{53}$ film, has been reported to cause particles inside the film to become elongated. Thereby the particle center became enriched in Pt, while the Fe was slightly redistributed to the

periphery [19]. Similarly, irradiation with 74 MeV Kr ions elongates NPs that are made of the alloy $Ag_{0.5}Au_{0.5}$ and are embedded in a SiO_2 matrix. In this case, one does not observe a clear phase separation of the two metallic species and the chemical composition of the alloy does not change appreciably during the irradiation. This is most likely due to the fact that Au and Ag are miscible in all proportions such that the alloy phase is thermodynamically stable [30].

The properties of transition metals depend strongly on the electronic configuration of the electrons in the last two outer shells. The transition elements readily form alloys with themselves and with other elements. Their atomic sizes are fairly constant since the electrons in their outermost shells have similar environments. The low values of their ionization potentials imply that these elements occur in variable-valency states due to loss of electrons from the *s* and *3d* orbitals. Compounds of the transition elements can be paramagnetic (i.e. attracted by a magnetic field) or diamagnetic (i.e. not attracted by a magnetic field). Paramagnetism in the transition elements is caused by the presence of unpaired electrons in the d sub-orbital. Diamagnetism is characteristic of compounds whose electrons in the d sub-orbitals are all paired.

The second group includes post-transition metals such as Al, Sn, Pb and Bi. Physically, post-transition metals are soft (or brittle), have poor mechanical strength, and melting points lower than those of the transition metals; most also have boiling points lower than those of the transition metals. These compounds are close to the metal-nonmetal transition boundary. Their crystalline structures tend to exhibit covalent or directional bonding effects. In general they are of greater complexity or have fewer nearest neighbors than other metallic elements.

It is worth noting that in spite of the fact that the literature is dominated by reports about ion-shaping for metallic NPs, there also exist NPs that become elongated under irradiation and are semiconductors. A few examples that illustrate this point are Ge [44, 45] and CdS [61] NPs. Even though to date it remains unclear if the mechanism driving the deformation of these NPs is the same as for metallic NPs, their observations will be reported below for the sake of completeness. Schmidt et al. [44, 45] were the first to observe the deformation of Ge NPs in SiO_2 under swift heavy-ion irradiation (30 MeV I ions). In particular, they reported the existence of three different morphologies: *large* NPs remained spherical, *medium* NPs became oblate while *small* NPs became prolate. The fact that the melting of the NP is considered to be a prerequisite for the occurrence of a shape transformation, automatically leads to the idea of defining a size threshold such that NPs larger than the threshold value remained solid and spherical in shape. The authors also reported a NP crystalline-to-amorphous phase transformation and that the NP gradually dissolves with fluence. Similar results were obtained by Araujo et al. [36] using a combination of TEM and X-ray near edge spectroscopy (XANES). In particular, they observed that the crystalline-to-amorphous phase transformation always preceded the shape transformation and dissolution. The fluence necessary to complete these two steps decreased as the ion energy increased, demonstrating that electronic energy loss was responsible for the two processes. On the other hand, a consistent and definitive relation was not obtained to relate the NP size thresholds to the

dimension of the ion track in silica. Moreover, although a model was proposed for the spherical-to-oblate transformation, an explanation for the spherical-to-prolate transformation is still lacking [45]. Another interesting observation which has not yet been elucidated, is the modification of manganese-doped cadmium sulfide (CdS:Mn) NPs embedded in a flexible polymer matrix (synthetic rubber) under irradiation with 80 MeV O ions. The NPs become elongated structures such as nanoneedles and nanorods [61]. The atomic ordering that is necessary to produce nanorods has been reached around the critical fluence of 3×10^{12} cm^{-2}. The observed nanorods have an average diameter of about 4 nm and a length of about 20 nm. Beyond this critical fluence, the stability of the elongated structures is completely destroyed, leading to a disordered nano-CdS:Mn system.

11.4.1 Deformation Pathways

Right from the early experiments on, it was clear that the ion-shaping depends on the NP dimension [12, 13, 23, 24]. However, for several years, the correlation between the initial NP size and its final morphology was not clearly identified. In particular, it was observed that NPs smaller than about 8–10 nm do not deform, whereas larger NPs deform into nanorods and nanowires whose main axis is aligned with the direction of the beam. Finally, until 2009 the consensus in the literature was that NPs larger than about 20 nm could not be deformed upon irradiation, although the process was clearly observed in TEM micrographs, see e.g. Fig. 11.3a in [12], Fig. 11.4 in [26] or Fig. 11.2 in [27]. This statement was based on the results of the thermal-spike simulations which suggested the existence of a threshold size for melting of about 20 nm [12, 23]. We will see in Sect. 11.5 that this result was an artefact of the simulation and that the transition from liquid to solid configurations is not as abrupt as initially believed. Indeed, there exists a range of sizes wherein the NP only become partially molten. The second reason for the discrepancy resides in the technique that is generally used to prepare the samples, i.e. the ion beam synthesis. This technique presents several advantages, but these are partially counterbalanced by the fact that the final size dispersion of the NPs is generally large (20–50 %). This makes it difficult to give a clear correlation between the initial NP size and its final morphology.

These experimental difficulties can be overcome in an irradiation set-up whereby all the NPs have the same size and are lying in the same plane below the sample surface. There are two reasons for this. First, NPs at the same depth below the surface receive the same amounts of energy. Second, the amplitude of the irradiation effects depends on NP size. In practice, this model system can be conveniently fabricated by sandwiching monodispersed NPs between two layers. The thickness of the second layer defines the depth at which the NPs are confined. Using this approach Rizza et al. [29] clearly demonstrated that the different deformation pathways depend on the initial NP size. This is illustrated in Fig. 11.7, where the morphological evolution of the NPs is shown as a function of both their initial size

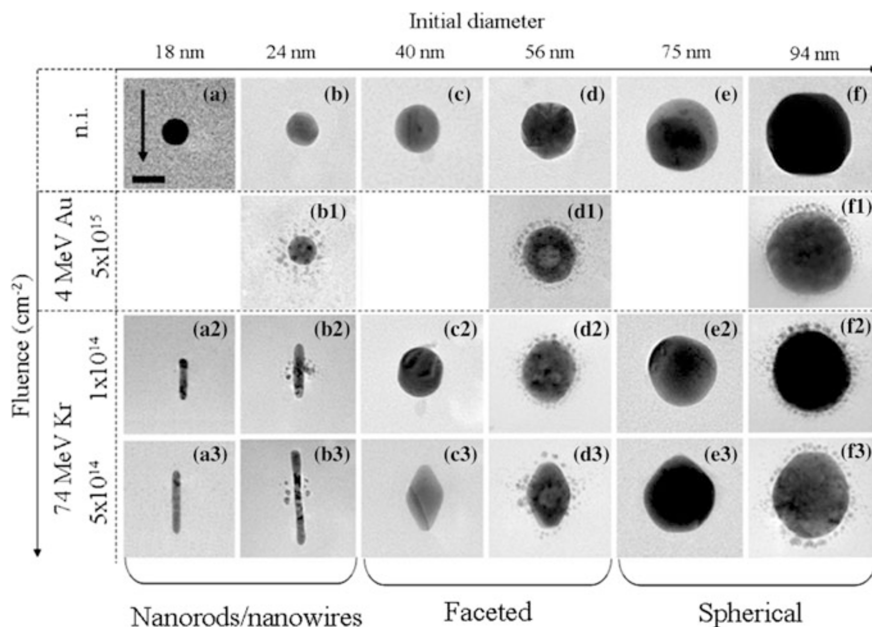

Fig. 11.7 Matrix-like diagram showing the morphological evolution of Au NPs for increasing initial size (x axis) and irradiation fluence (y axis). The length of the scale bar is 20 nm. The ion-beam direction is indicated by the *arrow*. Some of the samples [*b1*, *d1*, and *f1*] have been pre irradiated with 4 MeV Au ions at 5×10^{15} cm^{-2} to create a halo of satellites around the central NP *a2–f3*. Afterward, all the samples have been irradiated up to 5×10^{14} cm^{-2} with 74 MeV Kr ions. Reproduced with permission from [29]. Copyright 2012 American Physical Society

(x axis) and irradiation fluence (y axis). The beam direction is indicated by the arrow. NPs smaller than 10 nm have been created by pre-irradiating some of the samples with 4 MeV Au ions at a fluence of 5×10^{15} cm^{-2}, Fig. 11.7b1, d1, f1. In a second stage, the ion-beam shaping is induced by irradiating all the samples with 74 MeV Kr ions up to 5×10^{14} cm^{-2}. This reveals that the ion-shaping is not a linear process whereby all the NPs are transformed in the same way. It is rather a complicated function of initial NP size and irradiation fluence such that four different size-dependent regimes can be observed:

- NPs smaller than about 10 nm remain spherical in shape no matter what the size of the *initial parent* NP might be. There is a consensus in the literature about this fact that below a critical size NPs do not elongate. Nevertheless further details of the behavior upon irradiation depend on the metallic species. Indeed, for Au NPs the dissolution of the smaller particles is accompanied by the growth of larger particles. This process is consistent with Ostwald ripening [25, 29]. In [12] it was reported that at low fluences (3×10^{13} cm^{-2}) Co NPs remained spherical but grew in size. A more detailed study has been performed by Sprouster et al. [32] on 3.2 nm Co NPs irradiated with 185 MeV Au ions. They observe that, first, NPs

increase in size without reaching the minimum size for elongation such that they retain a spherical shape. At higher fluences, they are observed to decrease in size and to dissolve into the matrix. Finally, both Ag NPs [62] and Pt NPs [31] are observed to dissolve.

- NPs in the range 10–30 nm continuously transform into nanorods and nanowires.
- When the NP size is further increased (30–70 nm), an increasing refractoriness to deformation is observed. These NPs take more time to become ion-shaped and reveal a tendency to evolve toward faceted configurations [28].
- Finally, larger NPs (>70–80 nm) are not noticeably deformed even at the highest irradiation fluence.

As demonstrated by these observations, the variety of behaviors is large. It can be explored through the appropriate selection of the dimensions of the pristine NP. However, it is worth noticing that exotic configurations, such as faceted NPs, may occur as an intermediate step in the deformation process, while all these nanostructures evolve toward the nanorod/nanowire morphology for sufficiently long irradiation times.

11.4.2 Kinetics of the Elongation Process

As transpires readily from Fig. 11.8a, the transformation from spherical to rod-like shape indicates that the elongation is a cumulative process that requires overlapping

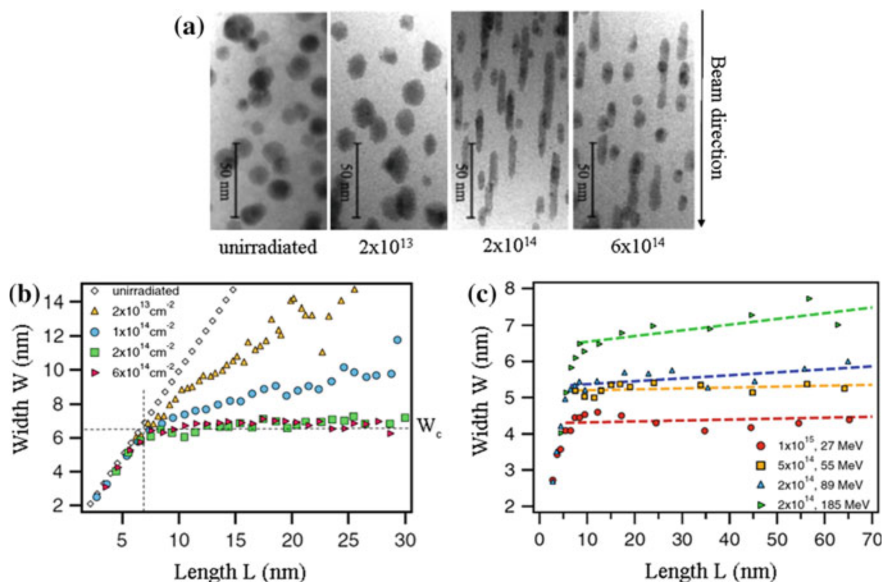

Fig. 11.8 **a** TEM micrographs of Pt NPs irradiated with 185 MeV Au ions at increasing fluences. **b** Evolution of the width-to-length ratio, W/L, with the irradiation fluence. **c** NP width saturation, W_c, for different ion energies. Reproduced with permission from [31]. Copyright 2008 American Physical Society

ion impacts, for instance about 250 impacts for a fluence of 10^{14} cm^{-2}. The ion-shaping is thus a kinetic process.

As shown in Fig. 11.8b the elongation of NPs can be followed by considering the relationship between their length, L, and width, W, as measured from TEM micrographs (each point represents the mean value of the NP width, W, for a given NP length, L ± 1 nm) [31]. As-prepared NPs are almost spherical in shape such that all the experimental data lie on a line of slope one, i.e. $W/L = 1$. At a fluence of 2×10^{13} cm^{-2}, elongation is only observed for NPs exceeding a minimum width, i.e. $W_c \sim 6.5$ nm. NPs smaller than this value remain spherical in shape whereas those that are larger elongate. Simultaneously, L increases significantly for fluences larger than 2×10^{14} cm^{-2}, yielding aspect ratios as great as ten (not shown). The elongation process continues until W saturates to a value that is close to the threshold value, i.e. $W \rightarrow W_c$. Afterward, the value of $W = W_c$ remains unchanged for higher fluences. In addition, Fig. 11.8c shows that W_c is also function of the irradiation energy. Indeed, it increases from about 4–7 nm when the ion energy is increased from 27 to 185 MeV.

While TEM has the distinct advantage of enabling a direct visual observation, it is none-the-less a destructive technique and it allows only inspecting a small portion of the sample. The results are thus statistically limited and obtaining good statistics necessitates measuring a large number of individual NPs. More reliable statistical information can be obtained by using an alternative approach such as the Rutherford Backscattering Spectrometry (RBS), see Chap. 5. RBS measurements permit probing a much larger volume and do not require a technique-specific sample preparation. As such they represent a rapid but only qualitative means of assessing the elongation of nanoparticles induced by swift heavy-ion irradiation. The combination of low-mass substrate atoms (Si and O) and high-mass nanoparticle atoms (noble metals, for example) is ideal for an analysis by RBS. From an operative point of view, the full width at half maximum (FWHM) of the RBS peak is related to the average dimension of the NPs while its broadening is related to their elongation, at least as long as the NPs remain *intact*—i.e. they are not fragmented, or in solid solution. To avoid bestowing the measured data with experimental artifacts, the size and depth distributions of the NPs must be minimized. Otherwise a further deconvolution analysis of the experimental RBS spectra becomes necessary. While this requirement cannot be met when one produces the NPs by ion beam synthesis technique, it is possible to fulfill these prerequisites by confining mono-dispersed NPs to a unique plane below the sample surface. This is clearly demonstrated in Fig. 11.9a where the fluence dependence of the broadening of the RBS peak, i.e. the FWHM of the Au depth distribution, is consistent with a progressive elongation of the embedded NPs.

RBS analysis indicates that the deformation kinetics are strongly size-dependent. This is illustrated by the data in Fig. 11.9b obtained from experiments wherein Au NPs of increasing initial size (15, 30 and 45 nm) are irradiated with 25 MeV Ag ions [34]. It is readily apparent that the smaller NPs, i.e. the Au NPs with a diameter of 15 nm, are deformed faster than the larger ones, i.e. the Au NPs with a diameter of

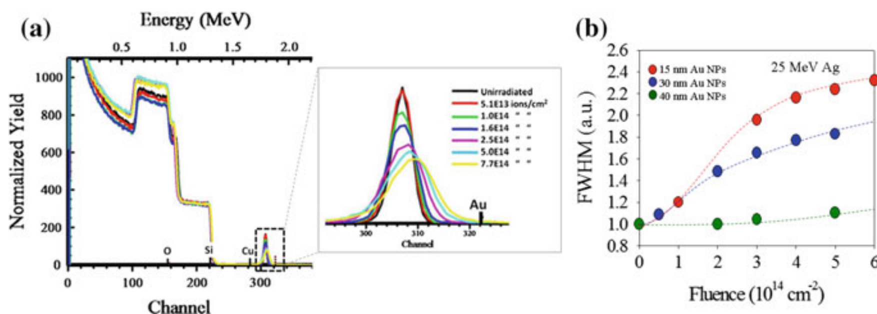

Fig. 11.9 **a** Rutherford backscattering (RBS) spectra for Au NPs (15 nm diameter) in silica on a Si substrate. The inset shows the Au peak as a function of the irradiation fluence. **b** Normalized evolution of the full-width-at-half-maximum (FWHM) of the Au peak as a function of ion fluence for three different NP sizes (15, 30 and 45 nm). Samples have been irradiated with Ag ions at 25 MeV. Reproduced with permission from [34]

45 nm. Otherwise stated, the elongation rate is observed to decrease when the NP size is increased. This being said, the deformation process evolves toward a *plateau*, whose height defines the maximum attainable length L_{max} of the ion-shaped NPs.

11.4.2.1 Threshold Fluence for Deformation

A precise determination of a threshold fluence for elongation, N_{Ic}, would provide key information to unravel the mechanism that drives the shaping process. Indeed, if a threshold fluence exists, the matrix must play an active role. On the other hand, if a single ion-impact suffices to deform an embedded NP, the matrix plays only the role of surrounding medium. Although the existence of a threshold fluence is still under debate, the available results are reported hereafter.

The existence of N_{Ic} was first evidenced by D'Orléans et al. [13] for Co NPs irradiated with 200 MeV I ions and then confirmed by Giulian et al. [31] for Pt NPs irradiated with 185 MeV Au ions and by Rizza et al. [30] for $Au_{0.5}Ag_{0.5}$ NPs irradiated with 74 MeV Kr ions. These examples indicate that N_{Ic} ranges between 10^{13} and 10^{14} cm^{-2}. Also, the analysis of the RBS data shows that N_{Ic} decreases with an increase in deposited energy, S_e, and increases with the NP size [22, 34]. As a dielectric matrix under irradiation exhibits a compaction of about 3 % [10, 63], it has been suggested that the elongation starts only after the conclusion of the compaction stage [22]. The densification of the silica is due to the rearrangement of the SiO_2 ring network into smaller, more compact rings [64, 65]. In particular, the density of the virgin material under SHI irradiation is irreversibly modified within each individual cylindrical ion track while a subsequent ion impact in the same region does not produce any further density changes [63]. Within this framework, the fluence necessary to complete the compaction corresponds roughly to a situation where all neighboring tracks show some mutual overlap, such that the projected

perturbed volume covers the whole sample surface. This condition is reached for a fluence of about 10^{13} cm^{-2}.

However, this fact has recently been questioned by Amekura et al. [35] who used optical linear dichroism (OLD) spectroscopy to monitor the elongation of Zn NPs embedded in silica irradiated with 200 MeV Xe ions at an incident angle of 45°. A small but measurable dichroism observed at 5.0×10^{11} cm^{-2} indicates that the elongation can be induced even in the low-fluence region where the ion hammering is not active. The authors introduce a minimum size for elongation above which each ion-impact will contribute to the shaping process. Additionally, molecular dynamic simulations performed by Leino et al. [46, 66] also indicate that the matrix plays only a marginal role. This point will be further developed in Sect. 11.5.

11.4.3 Efficiency of the Ion Shaping Process: The Role of the Deposited Energy

In the literature it has been reported that the lowest energy to efficiently deform embedded NPs is 8 MeV Si ions [16]. Similar irradiation conditions are used in [17] (10 MeV Si ions) and [34] (10 MeV Cu ions). In these examples the electronic-to-nuclear stopping power ratio is about $S_e/S_n \sim 10^2$, which proves the importance of the electronic energy deposition in the shaping process. For lower ion energies, ballistic effects must be taken into account and the irradiation leads to the formation of a halo of satellites surrounding the initial NP. A detailed overview on the irradiation-induced ballistic effects in metal-dielectric nanocomposites is given in Chap. 4.

TEM micrographs of Fig. 11.10a correspond to irradiations of Pt NPs in SiO_2 for increasing values of S_e, from 4 keV nm^{-1} (25 MeV Au ions) to 17 keV nm^{-1} (185 MeV Au ions), at fixed fluence of 2×10^{14} cm^{-2} [31]. It is readily apparent that the elongation process becomes more efficient as the ion energy increases, which demonstrates that it is governed by S_e. Note that in Fig. 11.10a the length of the NP appears to reach a maximum value at the intermediate energy of 90 MeV. This is due to the NP fragmentation as described in more detail in Sect. 11.4.5. Again, RBS analysis provides a quick confirmation that the rate of elongation depends on S_e. This is shown in Fig. 11.10b for 15 nm Au NPs irradiated with Ag ions for increasing ion energies, from 12 to 54 MeV, and irradiation fluences, up to 1×10^{15} cm^{-2}. Clearly, the higher the energy of the impinging ions the longer the deformed NPs. By using the dataset displayed in Fig. 11.10b it is possible to determine the elongation rate A (cm^{-2}). The latter, is defined as the relative differential length change per unit fluence, and can be written as:

$$A = \frac{1}{FWHM}\frac{dFWHM}{dN_I} \qquad (11.2)$$

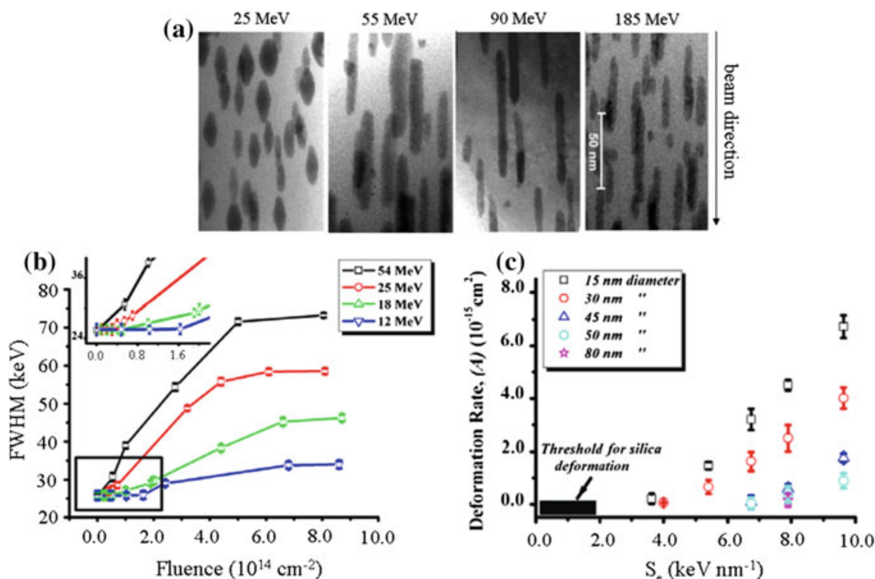

Fig. 11.10 **a** TEM micrographs of 14.5 nm Pt NPs (prior to SHI irradiation) irradiated with 2×10^{14} cm^{-2} at different energies (as shown in each panel). Reproduced with permission from [31]. Copyright 2001 American Physical Society. **b** The FWHM of the Au RBS peak as a function of fluence for 15 nm Au NPs under Ag ion irradiation for four samples with approximately identical NP areal densities. The inset represents a zoom of the region inside the selected rectangle marked in *black*. **c** The deformation rate as a function of electronic stopping in silica for Au NPs with a diameter in the range 15–80 nm after irradiation with Ag ions of different ion energies. Reproduced with permission from [34]

The value of *A* is reported in Fig. 11.10c and is found to range between 10^{-15} and 10^{-14} cm^2 ion^{-1}. By linear extrapolation to A = 0, a size-dependent stopping power threshold for elongation is established, S_{et}. Note that S_{et} is ascribed to the overall combined system Au in SiO_2. Above this threshold value, *A* gradually increases with increasing electric stopping power S_e in silica, and with decreasing NP size. Therefore, three size-dependent sub-regions can be identified:

- For 15–30 nm NPs, the value of S_{et} lies in the range between 3 and 4 keV nm^{-1}.
- For 40–50 nm NPs, the value of S_{et} is approximately 6 keV nm^{-1}.
- For 80 nm NPs, the value of S_{et} lies between 7 and 8 keV nm^{-1}.

A final point is that the minimum value of S_{et} is larger than the deformation threshold measured in a pure silica matrix, i.e. 2 keV nm^{-1}. This fact indicates that the ion-hammering effect is not uniquely responsible for the ion-shaping of the embedded NPs.

11.4.4 Elongation as a Function of the Ion Flux

In literature there exists only one work that reports on the elongation as a function of the ion flux [26]. It indicates that several morphologies can be obtained by changing the irradiation flux. However, it is not straightforward to extrapolate these results to a more general framework.

Figure 11.11a shows as-prepared Au nanopillars (diameter 40 nm and height 40 nm) obtained by electron beam lithography and confined within a silica matrix. Samples have been irradiated with 110 MeV Br ions at a constant fluence of 2×10^{14} cm^{-2} at increasing ion fluxes, Fig. 11.11b–d. At 3×10^{10} cm^{-2} s^{-1} nanopillars are transformed into a spherical core with two arms that are protruding along the beam direction, Fig. 11.11b. Doubling the ion flux to 6×10^{10} cm^{-2} s^{-1} long nanowires with an aspect ratio of about 20 are obtained, Fig. 11.11c. Finally, at the maximum flux of 1.6×10^{11} cm^{-2} s^{-1} NPs become almost completely dissolved where only small fragments are still visible, Fig. 11.11d.

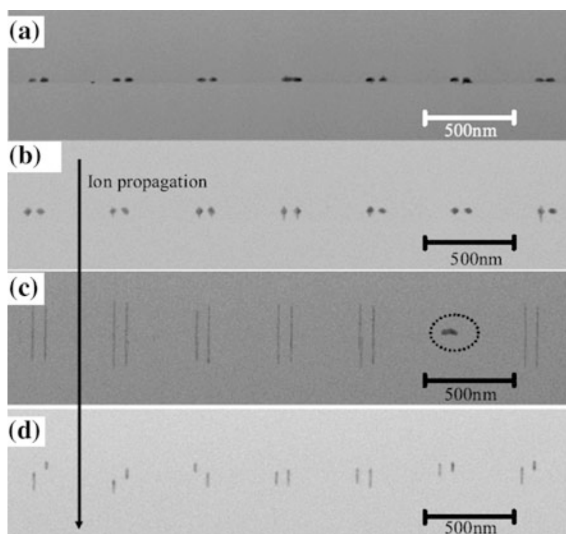

Fig. 11.11 Cross-sectional TEM micrographs. The flux dependence of the elongation of Au nanopillars with a diameter of 40 nm was examined at a constant fluence of 2×10^{14} cm^{-2}. The specimens were created with a focused ion beam. **a** Before irradiation by 110 MeV Br^{10+} ions. **b–d** Flux density of 3×10^{10} cm^{-2} s^{-1}, 6×10^{10} cm^{-2} s^{-1}1, 1.6×10^{11} cm^{-2} s^{-1}1, respectively. The direction of the ions is indicated by the arrow. Reproduced with permission from [27]

11.4.5 Elongation as a Function of the NP Concentration and Stability of the Ion-Shaped NPs

So far we have considered the ion-shaping as an individual process where the NPs do not interact one with another. In this section, we describe the elongation process when the inter-particle distance becomes sufficiently small such that diffusion-driven exchange of solute between the NPs is allowed.

Qualitative RBS analysis indicates that the NP concentration has a decisive influence on the elongation process. This is for instance shown in Fig. 11.12a for 15 nm Au NPs irradiated with 54 MeV Ag ions [22]. In this experiment the density of the NPs has been increased from 10^8 up to 10^{10} NPs cm^{-2}, such that their average distance was varied between 50 and 500 nm. The existence of two regimes is readily observed: (i) for fluences up to $1-2 \times 10^{14}$ cm^{-2} the elongation rate does not depend on the initial NP concentration—*region A* in the figure. (ii) above this threshold fluence elongation curves evolve toward a *plateau* whose value scales with the initial NP concentration—*region B* in the figure. This behavior is readily understood by observing Fig. 11.12b. Indeed, TEM micrographs reveal that the transition between these two regimes is driven by Rayleigh-like instabilities appearing at the NP surface above 1×10^{14} cm^{-2}. It has been suggested that they are generated when the width of the NP approaches a minimum width, $W(N_I) \rightarrow W_c$ [31].

This point has been clearly demonstrated by Rizza et al. [30] for 25 nm $Au_{0.5}\,Ag_{0.5}$ NPs irradiated with 74 MeV Kr ions. First, Fig. 11.12c shows that $W(N_I)$ smoothly evolves toward W_c whose value is reached for fluences larger than about $1-2 \times 10^{14}$ cm^{-2}. Second, the evolution of the normalized NP volume, $V(N_I)/V_0$, is reported in Fig. 11.12d. Clearly, when $W(N_I) > W_c, V(N_I)/V_0$ remains close to one, indicating that the ion-shaping is an *individual process*. This is, in this regime NPs are stable against irradiation and each NP is elongated into a single nanorod. Thus, the elongation process is independent on the initial NP density. On the other hand, when $W(N_I)$ approaches W_c, $V(N_I)/V_0$ becomes larger than 1. In this second regime, NPs become instable against irradiation. Their fragmentation and dissolution produces the solute necessary to the elongation of the NPs that are not fragmented. As the mass is redistributed among the NPs, the ion-shaping becomes a *collective process*. This is confirmed by the fact that the elongation scales with the initial NP density. Some insights on the diffusion process is obtained from Fig. 11.13a, where tiny satellite particles surrounding an ion-shaped nanowire are clearly visible. As these small particles were not observed in the pristine sample, they must have nucleated in the wake of the ion-NP interaction. That is, the energy deposited into the NP subsystem suffices to eject the Au atoms into solution. The ensuing solid solution may locally precipitate as a second phase as a result of local fluctuations in the solute concentration. Finally, the diffusion of the metal species through the silica matrix is triggered by the dissolution/reprecipitation processes taking place within the molten ion track.

Given small satellite clusters are absent in the pristine sample yet appear in the region surrounding the deformed NP, the elongation process is always accompanied

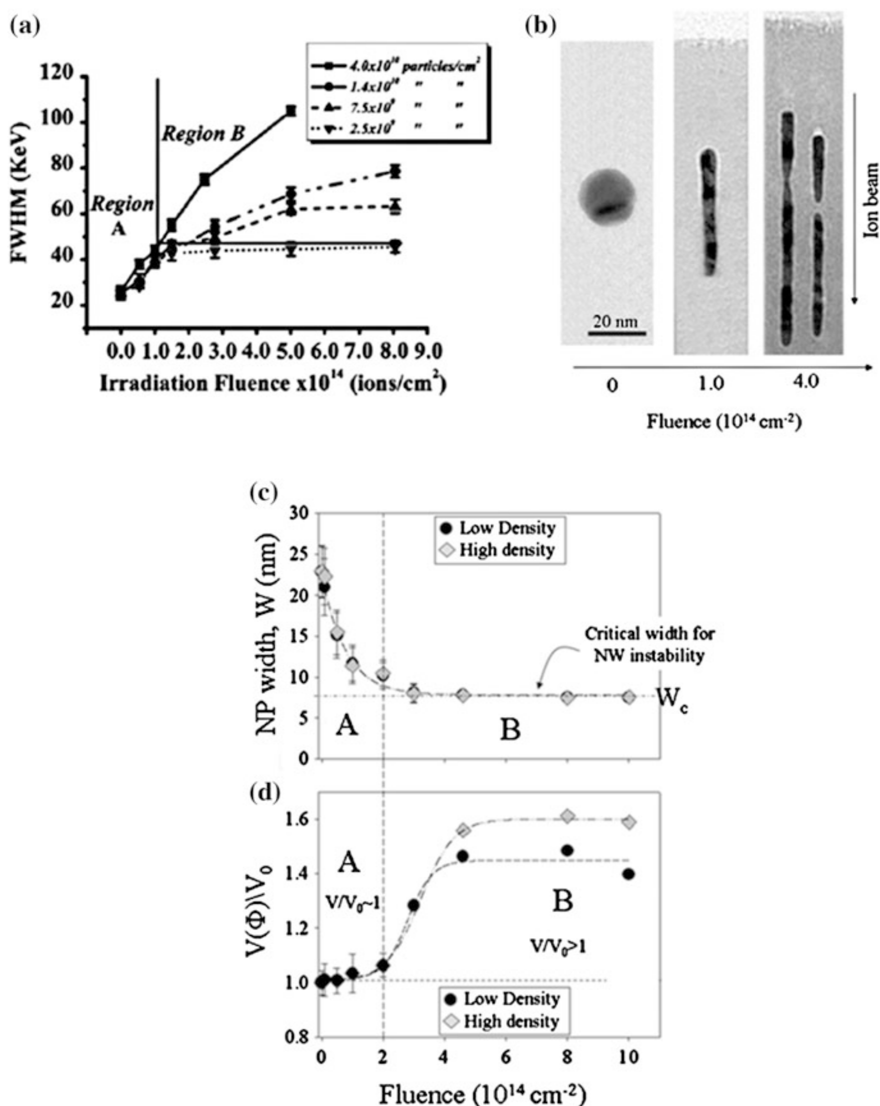

Fig. 11.12 **a** The relative change of the FWHM of the Au peak with fluence for different concentrations of 15 nm Au NPs irradiated with 54 MeV Ag^{+8} ions. The inspection of the figure clearly reveals the existence of two regions: In *region A*, NPs elongate irrespective of their initial concentration. In *region B*, the deformation effect increases when one increases the initial in-plane density of the NPs. Reproduced with permission from [22]. **b** TEM micrographs showing the elongation and fragmentation of NPs for increasing irradiation fluences. **c** Evolution of the minor diameters with fluence, $W(N_I)$. The *horizontal dashed line* defines the saturation width of the ion-deformed NPs, i.e. the critical width W_c at which the NW becomes unstable. **d** Evolution of the normalized volume $V(N_I)/V_0$ with the fluence. The *horizontal dotted line* corresponds to $V(N_I)/V_0$. The transition from the first to the second regime can be interpreted in terms of a Rayleigh-like instability under irradiation, where the critical diameter is given by the saturation width for the ion-shaped NPs. The *vertical long-dashed line* shows the passage from the individual (I) to the collective regime (II). Reproduced with permission from [30]

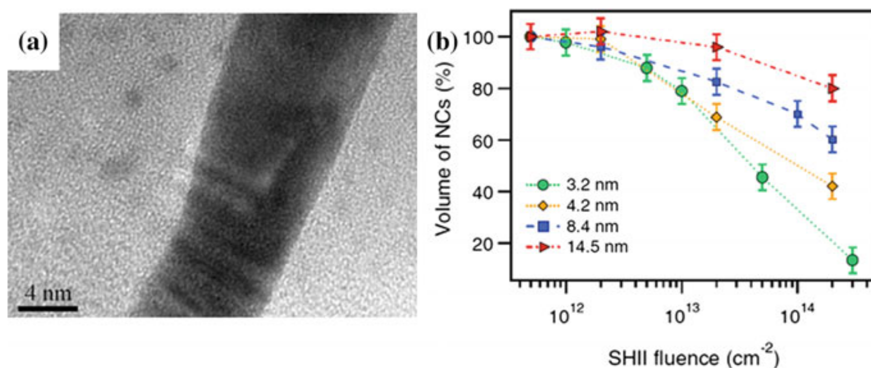

Fig. 11.13 **a** High resolution micrograph of an ion-shaped NP at a fluence of 4.6×10^{14} cm^{-2}. Reproduced with permission from [30]. **b** Volume percentage of remaining NPs as a function of SHI fluence. The values are relative to those that prevail in the unirradiated samples and the calculations are based on the total volume occupied by the particles according to the analysis of an SAXS experiment. Reproduced with permission from [31]. Copyright 2008 American Physical Society

by a loss of matter. This result has been corroborated by Sprouster et al. [32] using x-ray absorption near-edge spectroscopy (XANES) and by Giulian et al. [31] using small angle x-ray scattering (SAXS). These authors have demonstrated that high-fluence ion irradiation leads to the progressive dissolution of metal NPs embedded in silica. The loss of matter during the deformation process is shown in Fig. 11.13b for Pt NPs in the range 3.2–14 nm and irradiated with 185 MeV Au ions. It is readily apparent that the total volume of the NPs decreases as a function of increasing irradiation fluence. In particular, the dissolution rate increases when the NP size is reduced. For instance, at a fluence of 3×10^{14} cm^{-2} this rate is only 20 % for 14 nm Au NPs, but about 90 % for 3.2 nm Au NPs.

11.4.6 Role of Thermodynamics in the Shape Transformation

As discussed in Sect. 11.4.2, the shape transformation proceeds gradually as a function of irradiation fluence with the width-to-length ratio progressively approaching zero, $\mathrm{W}(N_I)/\mathrm{L}(N_I) \rightarrow 0$, see e.g. Fig. 11.8b. This indicates that all elongated NPs eventually attain a common width, W_c, which only depends on the ion energy, Fig. 11.14a, and is independent of their length, Fig. 11.8c. This result suggests that W_c is the key parameter to characterize the elongation of NPs. In order to better relate these data to the thermodynamic properties of the NP and matrix, Ridgway et al. [33] have determined the W_c values for ten different metals. Results are plotted in Fig. 11.14b as a function of the energy density per atom needed to

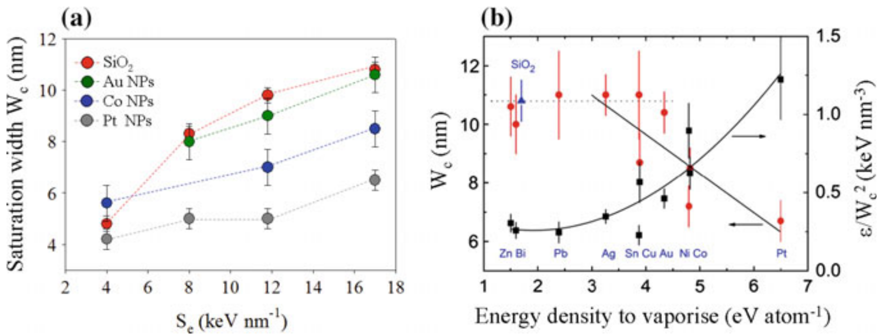

Fig. 11.14 **a** Evolution of the saturation width, W_c, with the electronic stopping power, S_e for three different metal NPs (Au, Co and Pt). The evolution of the ion-track diameter in a-SiO_2 is also reported. **b** W_c and ε/W_c^2 as a function of the energy density per atom that is required to induce vaporization. The *horizontal line* is a plot of the diameter of the molten ion-track in a-SiO_2. Reproduced with permission from [33]. Copyright 2011 American Physical Society

vaporize the bulk metal (E_{vap}). Here, two distinct trends are apparent: W_c is effectively constant at low values of E_{vap}, but decreases approximately linearly at higher values.

From Fig. 11.14a, b it is readily evident that W_c never exceeds the track diameter in a-SiO_2 (dotted blue line). This confirms the fact that the saturation width, W_c, is restricted to the diameter of the molten ion track in a-SiO_2 and suggests that metal NPs can melt and subsequently flow within the molten ion track that has been formed within the matrix. It suggests also that these processes are intrinsic to the shape transformation of metal NPs in a-SiO_2. Furthermore, the density of the deposited energy per atom, E_{dep}, scales as approximately $1/W_c^2$. Thus, as the NPs increase in length and decrease in width, the deposited-energy density per atom necessarily increases. Consequently, W_c represents the minimum sustainable width of an elongated NP under ion irradiation. Below this value, the fraction of E_{dep} transferred to the metal lattice exceeds that required for vaporization and the elongated NP is vaporized. Therefore, the minimum width in the second regime is governed by the energy density per atom required for vaporization of the metal. This requires a phase transition from the liquid (molten metal) to vapor (gaseous metal) state whereby the latter must remain confined to the ion track in the matrix and might be accommodated by the under-dense core.

11.5 Toward a Phenomenological Description

Even though a rational description of the ion-shaping mechanism is still lacking, it will be attempted in this section to describe the historical evolution of its theoretical understanding from early discussions to the latest insights. The elucidation of a new

phenomenon is always a complicated task and the early steps are often undertaken against the background of the knowledge accumulated already elsewhere. The case of the ion-shaping does not make an exception to this rule. Indeed, the first phenomenological model proposed by D'Orléans et al. [12, 13]—we are in 2003—is largely based on the idea proposed in 1998 by Berthelot et al. [3]. In this study, the fragmentation of Sn oxide (SnO_2) micro-powders by irradiation with swift heavy ions is explained by considering the large shear forces generated as a result of their thermal expansion. In D'Orléans's model, the melting of the embedded NP in the wake of the projectile generates a thermal pressure. The latter drives the elongation of the molten NP through a creep mechanism [13]. NPs can thus undergo a creep deformation due to the fact that the pressure is higher in the NP than in the surrounding matrix.

On the basis of the results obtained in Au/SiO_2 core-shell systems [37–39]. Roorda et al. [37] proposed in 2004 an indirect deformation mechanism whereby the melting of the NPs does not enter the considerations. Here, the ion-shaping is driven by the in-plane mechanical stress, generated by the ion-hammering of the silica shell, and acting on the radiation-softened Au NP. This mechanism favors the flow of the metallic species in the out-of plane direction, i.e. along the direction of the ion beam.

In a paper published in 2006, Klaumünzer tried to address the question if the conclusion that ion-shaping forcedly implies the melting of the NP, is inevitable or otherwise [42]. First, he was able to exclude deformation mechanisms based on dislocations or grain boundary diffusion. Then, the velocity of radial shrinkage of a void (which represents the most deformable passive cluster) was estimated $(1.4 \times 10^{-13}\ \mathrm{m\ s^{-1}})$ and compared to the experimentally measured radial shrinkage for a Co NP, which is about $10^{-12}\ \mathrm{m\,s^{-1}}$. The larger shrinkage rates that are measured for metallic NPs indicate that the passive deformation mechanism can be ruled out and that the NP must play an active role in the deformation process, i.e. it must melt and it is thus subjected to a large thermal pressure. Interestingly, this paper contains the following statement: *Particles with dimensions larger than 20 nm are expected not to melt*. We have already mentioned in Sect. 11.4.1, that until 2009 this assertion stood in marked contrast with the available experimental results, while it was in agreement with the results of simulations based on the inelastic thermal-spike (i-TS) model.

At that time the source of the problems encountered in trying to understand the phenomena observed was thus the model used to interpret the experimental results. As pointed out by Klaumünzer [67], the existing i-TS models were based on a series of drastic approximations even if they were quite successful in describing a large amount of SHI experiments. Some of these approximations can be mentioned in this context: (i) TS models were based on a bi-dimensional approximation, (ii) simulating the thermal evolution of nanocomposites composed of embedded NPs was impossible, (iii) the boundary conditions used precluded the diffusion of heat through the metal/dielectric interface, and (iv) the target electrons in the dielectric matrices were considered to behave like a free electron gas, even though this approximation is only valid when the temperature exceeds the band-gap energy, according to the relation $T > T_g = k_B/E_g$.

To make progress toward a coherent description of the ion-shaping phenomenon, it was thus necessary to overcome the aforementioned intrinsic limitations of the TS model. The first success of that of Awazu et al. [23]. They extended the i-TS model to account for the thermal evolution of a nanocomposite material. The latter was simulated by two cylindrical regions centered on the ion trajectory, where the inner region represents the metal NP, and the outer region the silica matrix. The energy of the swift heavy ion is first deposited into the electronic sub-system of the metal NP. Then, it diffuses to peripheral electrons by electron-electron interactions and to the lattice by electron-phonon coupling, crossing the boundary between the two materials at the metal-silica interface. The model maintains all the approximations used in the standard i-TS model [49]. As a case in point, only two-dimensional simulations are performed such that only the heat flow in the plane normal to the ion beam was taken into account. However, the spatial energy distribution was modified to account for the presence of two materials around the ion path. The model sought a correlation between the ion-shaping and the melting of the NPs. The main result is that the melting (and thus the shaping) only occurs for NPs smaller than 25 nm. Despite its improvements, the code failed thus in accounting for the deformation of larger NPs ($D > 25$ nm), see e.g. Fig. 11.7.

The main problem with the *classical*, two-dimensional, TS models was that they only provided a two-pathway solution for the thermal evolution of the irradiated NP. Indeed, above 10 nm, NPs could only exist either in a solid or in a molten phase. However, the reality has turned out to be slightly more complicated. In this sense, a real breakthrough was achieved by Khomenkov, Dufour and collaborators [43]. In a paper published in 2012, they introduced several major improvements to the existing i-TS codes. The first one consists in implementing the code in three dimensions and for a real nanocomposite material, i.e. the code allows to simulate all possible NP shapes, where only coaxial cylinders could be considered in Awazu's model. Secondly, following the work of Daraszewicz and Duffy [68], they extended the TS model to insulators. Indeed, the number of electrons involved in the thermal process, n_e, is considered to be proportional to the electronic temperature, T_e as long as T_e is lower than the band-gap temperature, T_g. Thirdly, the diffusion of heat through the matrix/metal interface is explicitly taken into account.

Abandoning the oversimplified idea that in insulators the electrons would behave like in metals and allowing the heat to diffuse through the matrix/metal interface, have proved to be the ingredients that are crucial in identifying the mechanism behind the ion-shaping process observed for larger NPs.

A phenomenological description of the physics behind the simulation results is obtained by using the schematic diagram of Fig. 11.15a. Silica possesses a low electronic thermal conductivity, K_e, and a high value for the electron-phonon coupling, g. Thus, the energy deposited remains spatially localized within the ion trajectory where it is rapidly thermalized, resulting in a narrow and hot ion track. In contrast to silica, Au possesses a high value for the electronic thermal conductivity and a weak electron-phonon coupling. Thus, the deposited energy is swiftly smeared out over the electronic subsystem while it is only weakly coupled to the

atomic subsystem. This results in a rapid increase of the electronic temperature but in a limited rise of the lattice temperature. In the study of Au NPs embedded within a silica matrix an interesting effect is encountered. The energy transferred to the electrons of a Au NP diffuses rapidly outwards to the surface. When this energy reaches the Au/SiO_2 interface, it is transferred to the electrons of the neighboring silica matrix. Here, the large electron-phonon coupling results in the formation of a hot silica layer. Thus, the dielectric matrix acts as a barrier for the diffusion of the electronic energy, allowing, at the same time, its transformation into heat. Then, in a further stage the heat diffuses back toward the center of the NP. Thus, we can conclude that the irradiation-induced heating of a Au NP (high K_e, low g) confined within a silica matrix (low K_e, high g) can be seen as an indirect mechanism wherein both the NP and the surrounding matrix are participating in the process. Due to this indirect-heating mechanism, the temperature profile within the NP becomes strongly size-dependent, Fig. 11.15b. In particular, complete melting is observed for NP diameters up to 30 nm. For larger sizes, the efficiency of the process decreases and the molten region no longer reaches the core of the NP such that it remains solid. This way, these larger NPs are only partially molten upon irradiation. Furthermore, the thickness of the liquid layer is observed to decrease with the NP size. In a companion paper published in 2012, Rizza et al. [29] give a rational description of the ion-shaping mechanism. First, a matrix-like diagram is

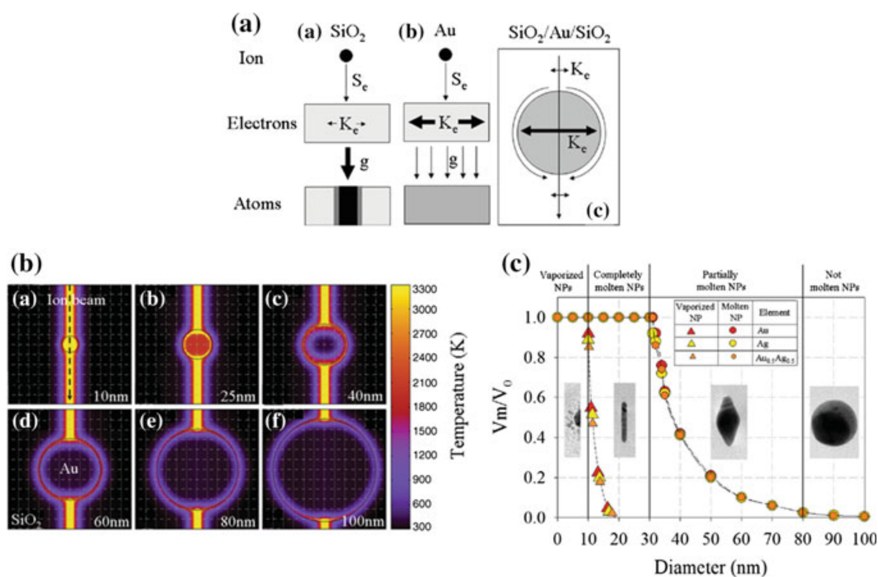

Fig. 11.15 **a** Schematic diagram for the swift heavy ion-matter interaction for **a** bulk silica, **b** bulk gold, and **c** gold NPs confined within a SiO_2 matrix. **b** Each panel represents the 3D-TS simulation corresponding to the highest temperature reached within Au NPs of increasing sizes. The ion trajectory is indicated by the *dotted arrow*. **c** The size versus shape diagram used to rationalize the ion-shaping process for all NP sizes. Four temperature-dependent regions can be defined (see text). Reproduced with permission from [29]. Copyright 2012 American Physical Society

built to correlate the final ion-beam-shaped morphology to the initial NP size and the irradiation fluence, see e.g. Fig. 11.7. In a second step, 3D TS simulations are used to obtain the dependence of the vaporized/molten fraction on the initial NP size, Fig. 11.15c. Finally, the direct comparison between experimental results and simulations enables the precise characterization of four deformation regimes whose extension depends on both NP composition and irradiation parameters:

- Completely vaporized NPs (0–10 nm) remain spherical in shape upon irradiation. Most likely, these NPs are first dissolved in the wake of the projectile and successively reprecipitate into the matrix.
- Completely molten NPs (10–35 nm) transform into nanorods and subsequently into nanowires, if the fluence is further increased.
- Partially molten NPs (35–70 nm) transform into facetted NPs and subsequently into nanowires, if the fluence is further increased.
- Very large NPs (>70 nm) do not melt and are not deformed, or their deformation rate is very low.

Although, the papers of Dufour et al. [43] and Rizza et al. [29] represent a step forward toward the comprehension of the ion-shaping mechanism, the fundamentals of the deformation process remain to be elucidated. The main limitation of the TS models is that they can only simulate the timescales of the heat exchange between the electronic to the atomic subsystems and thus, as such, cannot be used to describe the transport of material. To bridge this gap and include mass transport in the modeling, Leino et al. [46, 66] used Molecular Dynamics (MD) simulations coupled with the two-temperature TS model [69, 70]. These simulations indicate that the elongation is only driven by the thermal expansion of the molten NP and not a consequence of the ion-hammering effect or of any diffusion-like processes. As the thermal expansion remains spatially confined to the molten ion track in silica, the metallic species can only flow inside the under-dense track core. This allows to define the critical width of the elongated NPs, W_c, as the diameter of the under-dense core in silica, such that NPs that are smaller than this diameter can expand isotropically without becoming deformed. The progression of the elongation is shown in snapshots of Fig. 11.16 for a Au NP (diameter 10 nm) confined into a SiO_2 simulation cell (23 nm width). Simulations are shown for increasing numbers of 164 MeV Au ion impacts, labeled from 0 to 11. In the unirradiated cell the Au NP is spherical and crystalline (*label 0*). The first ion impact results in the formation of an under-dense core and an over-dense shell track within the silica. Meanwhile, the deposited energy causes the melting of the NP. In this configuration, the liquified NP is allowed to expand along the beam direction into the molten under-dense track. After about 20 ps the track solidifies and the NP deformation stops irrespectively of the NP temperature. Finally, the fast quenching rate results in the amorphization of the NP (*label 1*). In this configuration, subsequent impacts did not yield further elongation. This point demonstrates that the driving force for the elongation is the pressure due to the rapid heating of the NP. In this sense, a crystalline structure is a prerequisite for the NP elongation as the smaller thermal

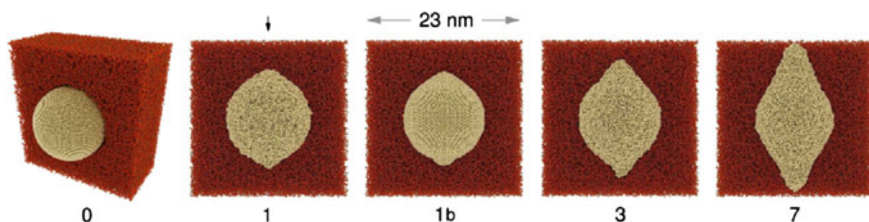

Fig. 11.16 Snapshots of MD simulations as a function of the number of ion impacts (0–7) for Au NP elongation in SiO_2 following the passage of a swift heavy ion (*vertically*). Reproduced with permission from [46]

expansion of the amorphous structure inhibits the deformation process. Therefore, a recrystallization step was implemented in MD simulation (*label 1b*) prior to the next impact. Even though after multiple impacts (*label 7*) the transformation into a nanorod was not yet accomplished, the NP presents a morphological transformation into lemon-like shape in agreement to what has been experimentally observed at low irradiation fluences, see e.g. Fig. 11.2a.

11.6 Conclusion and Outlook

In the past decade, ion irradiation at the extremes of electronic energy loss has been demonstrated to be a versatile and flexible method for sculpting matter at the nanoscale while controlling the spatial orientation of the embedded NPs. In this chapter we have presented an overview of the body of experimental research that is now available. With ion track formation as a common binding thread a great deal of effort has been devoted to unveiling the role played by the host matrix and by the NPs in the elongation process. First, the influence of the embedding matrix on the ion-shaping process has been described, then the role played by the NPs has been highlighted. Finally, an historical overview of the evolution of the theoretical comprehension of the ion-shaping processes has been traced from the first tentative steps to the present state-of-the art description of the phenomenon.

Future research directions will focus less on the elongation of new NPs, and more on developing new classes of materials with new properties. For the great majority of the potential applications, it will be critical to control both the dimension and the spatial orientation of the ion-shaped NPs. For instance, Fig. 11.17a, shows an array of elongated Au NPs with a length of 200 nm and a pitch of 100 nm has been obtained after irradiation with 74 MeV Kr ions at 5×10^{14} cm^{-2}. The plasmonic properties of the elongated NPs render their potential applications in the field of nano-optics very attractive. Indeed, as spherical NPs can be ion-shaped into NWs whose length can be as large as 400–500 nm, the spectrum of the corresponding plasmon resonances can range from the visible to the near-mid infrared, Fig. 11.17b. Thus, a broadband region of the optical spectrum

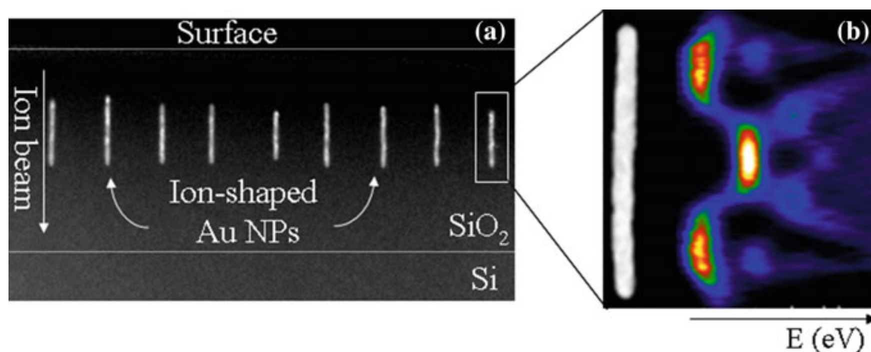

Fig. 11.17 **a** TEM micrograph of an ion-shaped nanocrystal formed by an array of elongated Au NPs of length 200 nm and a pitch of 100 nm. The sample has been obtained after irradiation with 74 MeV Kr ions at 5×10^{14} cm^{-2}. **b** Plasmon mapping of a single ion-shaped nanoantenna obtained from electron energy loss spectroscopy (EELS) using the method developed in [77]

can be explored. In this field, plasmon-based biosensors and hyperbolic meta-materials represent two promising applications. A plasmon-based biosensor is based on the fact that the refractive index of the immediate environment that surrounds the nanostructure is modified, when a bio-molecular binding event occurs close to the surface of a noble-metal nanostructure [71, 72]. A possible scheme for a sensor that would be able to detect low concentrations of molecules could be based on the idea that the tips of the ion-shaped NPs are situated either slightly below the sample surface or touching it. This way, bio-molecular interactions at the surface of the nano-structures may lead directly to changes in the local refractive index; these changes can then be monitored via the wavelength shift of the localized surface plasmon resonance (LSPR) peak. On the other hand, plasmonic meta-materials are tailor-made nanocomposites. They are combinations of metallic and dielectric materials that can be designed to obtain optical properties that do not occur in nature, [73–75]. Hyperbolic meta-materials are a sub-class of plasmonic meta-materials displaying hyperbolic (or indefinite) dispersion, [76]. This dispersion occurs when one of the principal components of the electric effective tensor has the opposite sign of the other two principal components. Such anisotropic structured materials exhibit distinctive properties, including a strong enhancement of their spontaneous emission, a diverging density of states, a negative refraction index and enhanced super-lensing effects. Arrays of spatially oriented ion-shaped NPs may display such a hyperbolic behavior.

Acknowledgments GCR acknowledges access to IRRSUD beam line at the GANIL Facility through EMIR network. GCR also thanks Pierre-Eugène Coulon for his valuable help and Gerrit Coddens for many fruitful discussions. MCR acknowledges access to NCRIS and AMMRF infrastructure at the Australian National University including the Australian National Fabrication Facility, the Heavy Ion Accelerator Capability and the Center for Advanced Microscopy. We also thank the Australian Research Council and Australian Synchrotron for support.

References

1. K.E. Drexler, *Engines of Creation: The Coming Era of Nanotechnology* (Doubleday, New York, 1986). ISBN 0-385-19973-2
2. S. Hémon, Ch. Dufour, F. Gourbilleau, E. Paumier, E. Dooryhée, S. Bégin-Colin, Nucl. Instr. Meth. B **146**, 443 (1998)
3. A. Berthelot, S. Hémon, F. Gourbilleau, C. Dufour, E. Dooryhée, E. Paumier, Nucl. Instr. Meth. B **146**, 437 (1998)
4. E. Snoeks, A. van Blaaderen, C.M. van Kats, M.L. Brongersma, T. van Dillen, A. Polman, Adv. Mat. **12**, 1511 (2000)
5. E. Snoeks, A. van Blaaderen, T. van Dillen, C.M. van Kats, M.L. Brongersma, A. Polman, Nucl. Instr. Meth. B **178**, 62 (2001)
6. T. van Dillen, E. Snoeks, W. Fukarek, C.M. van Kats, K.P. Velikov, A. van Blaaderen, A. Polman, Nucl. Instr. Meth. B **175**, 350 (2001)
7. T. van Dillen, A. Polman, C.M. van Kats, A. van Blaaderen, Appl. Phys. Lett. **83**, 4315 (2003)
8. T. van Dillen, E. van der Giessen, P.R. Onck, A. Polman, Phys. Rev. B **74**, 132103 (2006)
9. T. van Dillen, *Ion Irradiation-Induced Anisotropic Plastic Deformation*, Ph.D. Thesis, Utrecht University, 26 Apr 2004 (www.erbium.nl)
10. T. van Dillen, M.Y.S. Siem, A. Polman, Appl. Phys. Lett. **85**, 389 (2004)
11. S. Klaumünzer, Nucl. Instr. Meth. B **215**, 345 (2004)
12. C. D’Orléans, J.P. Stoquert, C. Estournès, C. Cerruti, J.J. Grob, J.L. Guille, F. Haas, D. Muller, M. Richard-Plouet, Phys. Rev. B **67**, 220101 (2003)
13. C. D’Orléans, J.P. Stoquert, C. Estournes, J.J. Grob, D. Muller, J.L. Guille, M. Richard-Plouet, C. Cerruti, F. Haas, Nucl. Instr. Meth. B **216**, 372 (2004)
14. C. Harkati Kerboua, J.M. Lamarre, M. Chicoine, L. Martinu, S. Roorda, Thin Solid Films **527**, 186 (2013)
15. B. Joseph, J. Ghatak, H.P. Lenka, P.K. Kuiri, G. Sahu, N.C. Mishra, D.P. Mahapatra, Nucl. Instr. Meth. B **256**, 659 (2007)
16. A. Oliver, J.A. Reyes-Esqueda, J.C. Cheang-Wong, C.E. Roman-Velazquez, A. Crespo-Sosa, L. Rodriguez-Fernandez, J.A. Seman, C. Noguez, Phys. Rev. B **74**, 245425 (2006)
17. V. Rodriguez-Iglesias, O. Pena-Rodriguez, H.G. Silva-Pereyra, L. Rodriguez-Fernandez, J.C. Cheang-Wong, A. Crespo-Sosa, J.A. Reyes-Esqueda, A. Oliver, Opt. Lett. **35**, 703 (2010)
18. Y. Yang, C. Zhang, Y. Song, J. Gou, L. Zhang, Y. Meng, H. Zhang, Y. Ma, Nucl. Instr. Meth. B **308**, 24 (2013)
19. M. Shirai, K. Tsumori, M. Kutsuwada, K. Yasuda, S. Matsumura, Nucl. Instr. Meth. B **267**, 1787 (2009)
20. J.C. Pivin, F. Singh, O. Angelov, L. Vincent, J. Phys. D Appl. Phys. **42**, 025005 (2009)
21. P. Kluth, R. Giulian, D.J. Sprouster, C.S. Schnohr, A.P. Byrne, D.J. Cookson, M.C. Ridgway, Appl. Phys. Lett. **94**, 113107 (2009)
22. E.A. Dawi, G. Rizza, M.P. Mink, A.M. Vredenberg, F. Habraken, J. Appl. Phys. **105**, 074305 (2009)
23. K. Awazu, X. Wang, M. Fujimaki, J. Tominaga, H. Aiba, Y. Ohki, T. Komatsubara, Phys. Rev. B **78**, 054102 (2008)
24. M.C. Ridgway, P. Kluth, R. Giulian, D.J. Sprouster, L.L. Araujo, C.S. Schnohr, D.J. Llewellyn, A.P. Byrne, G.J. Foran, D.J. Cookson, Nucl. Instr. Meth. B **267**, 931 (2009)
25. D.K. Avasthi, Y.K. Mishra, F. Singh, J.P. Stoquert, Nucl. Instr. Meth. B **268**, 3027 (2010)
26. K. Awazu, X. Wanga, M. Fujimaki, J. Tominaga, S. Fujii, H. Aiba, Y. Ohki, T. Komatsubara, Nucl. Instr. Meth. B **267**, 941 (2009)
27. K. Awazu, X. Wang, T. Komatsubara, J. Watanabe, Y. Matsumoto, S. Warisawa, S. Ishihara, Nanotechnology **20**, 325303 (2009)
28. G. Rizza, E.A. Dawi, A.M. Vredenberg, I. Monnet, Appl. Phys. Lett. **95**, 043105 (2009)
29. G. Rizza, P.E. Coulon, V. Khomenkov, C. Dufour, I. Monnet, M. Toulemonde, S. Perruchas, T. Gacoin, D. Mailly, X. Lafosse, C. Ulysse, E.A. Dawi, Phys. Rev. B **86**, 035450 (2012)

30. G. Rizza, F. Attouchi, P.E. Coulon, S. Perruchas, T. Gacoin, I. Monnet, L. Largeau, Nanotechnology **22**, 175305 (2011)
31. R. Giulian, P. Kluth, L.L. Araujo, D.J. Sprouster, A.P. Byrne, D.J. Cookson, M.C. Ridgway, Phys. Rev. B **78**, 125413 (2008)
32. D.J. Sprouster, M.C. Ridgway, Appl. Sci. **2**, 396 (2012)
33. M.C. Ridgway, R. Giulian, D.J. Sprouster, P. Kluth, L.L. Araujo, D.J. Llewellyn, A.P. Byrne, F. Kremer, P.F.P. Fichtner, G. Rizza, H. Amekura, M. Toulemonde, Phys. Rev. Lett. **106**, 095505 (2011)
34. E.A. Dawi, A.M. Vredenberg, G. Rizza, M. Toulemonde, Nanotechnology **22**, 215607 (2011)
35. H. Amekura, N. Ishikawa, N. Okubo, M. C. Ridgway, R. Giulian, K. Mitsuishi, Y. Nakayama, Ch. Buchal, S. Mantl, N. Kishimoto, Phys. Rev. B **83**, 205401 (2011)
36. L.L. Araujo, R. Giulian, D.J. Sprouster, C.S. Schnohr, D.J. Llewellyn, B. Johannessen, A.P. Byrne, M.C. Ridgway, Phys. Rev. B **85**, 235417 (2012)
37. S. Roorda, T. van Dillen, A. Polman, C. Graf, A.M. Vredenberg, A. van Blaaderen, B. Kooi, Adv. Mater. **16**, 235 (2004)
38. J.J. Penninkhof, T. van Dillen, A. Polman, C. Graf, A. van Blaaderen, Adv. Mater. **17**, 1484 (2005)
39. J.J. Penninkhof, T. van Dillen, C. Graf, A. van Blaaderen, A.M. Vredenberg, A. Polman, Nucl. Instr. Meth. B **242**, 523 (2006)
40. J.J. Penninkhof, A. Moroz, A. van Blaaderen, A. Polman, J. Phys. Chem. C **112**, 4146 (2008)
41. J.J. Penninkhof, L.A. Sweatlock, A. Moroz, H.A. Atwater, A. van Blaaderen, A. Polman, J. Appl. Phys. **103**, 123105 (2008)
42. S. Klaumünzer, Nucl. Instr. Meth. B **244**, 1 (2006)
43. C. Dufour, V. Khomenkov, G. Rizza, M. Toulemonde, J. Phys. D Appl. Phys. **45**, 065302 (2012)
44. B. Schmidt, A. Mueklich, L. Roetzsch, H.-K. Heinig, Nucl. Instr. Meth. B **257**, 3 (2007)
45. B. Schmidt, K.H. Heinig, A. Mueklich, C. Akhmadaliev, Nucl. Instr. Meth. B **267**, 1345 (2009)
46. A.A. Leino, O.H. Pakarinen, F. Djurabekova, K. Nordlund, P. Kluth, M.C. Ridgway, Mat. Res. Lett. **2**, 37 (2014)
47. J.F. Ziegler, J.P. Biersack, U. Littmark, *The Stopping Ranges and Ranges of Ions in Solids* (Pergamon Press, New York, 1985)
48. See http://www.srim.org for the code
49. M. Toulemonde, C. Dufour, E. Paumier, Phys. Rev. B **46**, 1436 (1993)
50. S. Klaumünzer, G. Schumacher, Phys. Rev. Lett. **51**, 1987 (1983)
51. C. Harkati Kerboua, M. Chicoine, S. Roorda, Nucl. Instr. Meth. B **269**, 2006 (2011)
52. R. Giulian, F. Kremer, L.L. Araujo, D.J. Sprouster, P. Kluth, P.F.P. Fichtner, A.P. Byrne, M.C. Ridgway, Phys. Rev. B **82**, 113410 (2010)
53. H. Trinkaus, A.I. Ryazanov, Phys. Rev. Lett. **74**, 5072 (1995)
54. H. Trinkaus, J. Nucl. Mater. **223**, 196 (1995)
55. H. Trinkaus, Nucl. Instr. Meth. B **107**, 155 (1996)
56. H. Trinkaus, Nucl. Instr. Meth. B **146**, 204 (1998)
57. J. D. Eshelby, *Proceedings of the Royal Society of London. Series A, Mathematical and Physical Sciences*, vol. 241 (1957), p. 376
58. H. Amekura, S. Mohapatra, U.B. Singh, S.A. Khan, P.K. Kulriya, N. Ishikawa, N. Okubo, D.K. Avasthi, Nanotechnology **25**, 435301 (2014)
59. P. Kluth, C.S. Schnohr, O.H. Pakarinen, F. Djurabekova, D.J. Sprouster, R. Giulian, M.C. Ridgway, A.P. Byrne, C. Trautmann, D.J. Cookson, K. Nordlund, M. Toulemonde, Phys. Rev. Lett. **101**, 175503 (2008)
60. T. Bierschenk, R. Giulian, B. Afra, M.D. Rodriguez, D. Schauries, S. Mudie, O.H. Pakarinen, F. Djurabekova, K. Nordlund, O. Osmani, N. Medvedev, B. Rethfeld, M.C. Ridgway, P. Kluth, Phys. Rev. B **88**, 174111 (2013)
61. D. Mohanta, G.A. Ahmed, A. Choudhury, F. Singh, D.K. Avasthi, G. Boyer, G.A. Stanciu, Eur. Phys. J. Appl. Phys. **35**, 29 (2006)

62. F. Singh, S. Mohapatra, J.P. Stoquert, D.K. Avasthi, J.C. Pivin, Nucl. Instr. Meth. B **267**, 936 (2009)
63. A. Benyagoub, S. Klaumünzer, M. Toulemonde, Nucl. Instr. Meth. B **146**, 449 (1998)
64. W. Primak, *Studies in Radiation Effects in Solids*, vol. 4 (Gordon and Breach, New York, 1975)
65. R.A.B. Devine, Nucl. Instr. Meth. B **91**, 378 (1994)
66. A.A. Leino, O.H. Pakarinen, F. Djurabekova, K. Nordlund, Nucl. Instr. Meth. B **282**, 76 (2012)
67. S. Klaumünzer, Thermal-spike models for ion track physics: a critical examination in ion beam science: solved and unsolved problems (part I, II). Med. Phys. **35**, 293 (2008)
68. S.L. Daraszewicz, D.M. Duffy, Nucl. Instr. Meth. B **269**, 1646 (2011)
69. N.A. Medvedev, A.E. Volkov, N.S. Shcheblanov, B. Rethfeld, Phys. Rev. B **82**, 125425 (2010)
70. M. Toulemonde, W. Assmann, C. Dufour, A. Meftah, F. Studer, C. Trautmann, Mat. Fys. Med. Kong. Dan. Vid. Selsk **52**, 263 (2006)
71. J.N. Anker, W.P. Hall, O. Lyandres, N.C. Shah, J. Zhao, R.P. Van Duyne, Nat. Mater. **7**, 442 (2008)
72. M.E. Stewart, C.R. Anderton, L.B. Thompson, J. Maria, S.K. Gray, J.A. Rogers, R.G. Nuzzo, Chem. Rev. **108**, 494 (2008)
73. J.B. Pendry, D. Schurig, D.R. Smith, Science **312**, 1780 (2007)
74. F. Capolino, *Metamaterials Handbook 1: Theory and Phenomena of Metamaterials* (CRC Press, Boca Raton, CA, 2009)
75. A. Boltasseva, H.A. Atwater, Science **331**, 290 (2011)
76. A. Poddubny, I. Iorsh, P. Belov, Y. Kivshar, Nat. Photon. **7**, 948 (2013)
77. J. Nelayah, M. Kociak, O. Stephan, F.J.G. de Abajo, M. Tence, L. Henrard, D. Taverna, L. Pastoriza-Santos, L.M. Liz-Marzan, C. Colliex, Nat. Phys. **3**, 348 (2007)
78. T. van Dillen, A. van Blaaderen, A. Polman, Mater. Today **7**, 40 (2004)
79. A. Leino, O.H. Pakarinen, F. Djurabekova, K. Nordlund, S. Daraszewicz, P. Kluth, M.C. Ridgway, Mater. Res. Lett. **2**, 37 (2014)

Chapter 12
Low Energy Ion Beam Modification of Nanostructures

Christian Borschel and Carsten Ronning

Abstract Nanostructures and nanomaterials with their meso-scopic properties, which can be integrated into functional devices, will enable a variety of new applications in future. They can be grown with specific properties by plenty of physical and chemical methods, and subsequent modification using ion irradiation significantly expands the potpourri of functionality of this important material class. As the ion range becomes comparable to the size of the small structures, important effects must be considered in experimental planning: reduced incorporation of implanted species, morphological changes induced by point defects, as well as strongly enhanced dynamic annealing and sputtering.

12.1 Introduction

Nanotechnology is considered to be one of the future technologies, which will strongly influence our daily life in many different aspects. Already today, it affects many industrial areas: such as computing, pharmaceuticals, cosmetics, textile, sensing, or functional coatings. The major background is not only to make materials smaller and smaller in order to store or process more and more information. Of course, this is also a very important issue and well in line with Moore's law. However, the additional key point of the nanotechnology revolution within the next decades will be the capability to make use and advantage of meso-scopic properties of such nanosized materials. These properties can strongly differ from the respective bulk counterparts due to quantum confinement or the high surface-to-volume ratio enabling new functionality of nanomaterials. Such new functionalities will be discovered and developed in future for yet unknown applications opening new

---

C. Borschel · C. Ronning (✉)
Institut für Festkörperphysik, Friedrich-Schiller-Universität Jena, Max-Wien-Platz 1, 07743 Jena, Germany
e-mail: carsten.ronning@uni-jena.de

C. Borschel
e-mail: borschel@iradina.de; chrbor@gmx.de

© Springer International Publishing Switzerland 2016

W. Wesch and E. Wendler (eds.), *Ion Beam Modification of Solids*,
Springer Series in Surface Sciences 61,
DOI 10.1007/978-3-319-33561-2_12

horizons in a variety of areas. This paradigm has been aptly called “More than Moore”.

In order to meet the above described high expectations, nanotechnology relies on the reproducible and exact design of nanomaterials either by top-down or bottom-up synthesis approaches. Top-down techniques essentially use traditional workshop or microfabrication methods, where externally controlled tools are used to mill, cut, and shape materials into the desired size and shape. The most impressive product out of this route is for example a modern multicore processor with billions of transistors on a single chip. On the other hand, bottom-up synthesis methods make use of the self-assembly ability of small building blocks (such as atoms or molecules) forming automatically hierarchy and/or complex structures—here, the most impressive example is of course the human body formed just out of one DNA molecule. Both approaches have their advantages and disadvantages, and already today a huge potpourri of different synthesis techniques is available for both routes. Ion beam techniques are also among them and an important tool for nanomaterial synthesis as outlined already in some previous chapters of this book (Chaps. 4 and 11).

Even though a huge number of different nanomaterial systems can be realized with sophisticated synthesis methods, a lot of desired nanostructures are still and will remain also in future inaccessible due to chemical and physical reasons, because most synthesis methods work close or even at thermodynamic equilibrium. Issues like solubility limits or surface reconstructions are difficult or even impossible to overcome during synthesis. One alternative option is the subsequent modification of prepared nanomaterials using energetic ion beam irradiation, which enables processes far from thermodynamic equilibrium. This can result into metastable phases of the nanomaterials/nanostructures with unusual or even exotic structural, electrical, optical or magnetic properties, which is fully in line with the desired paradigm “More than Moore”. Furthermore, ion beam implantation is a very precise and controllable doping method and a well-known standard technique in industry. It was established already in the 70s, but until lately mainly used for the electrical doping of bulk or thin film semiconductor materials.

Whereas the structural changes of buried nanomaterials using high-energetic ion beams are described in Chap. 11, this chapter focuses on doping of exposed or free nanostructures (typically lying on a supporting substrate) using ion beams in order to precisely tune their electrical, optical, and magnetic properties. For such a goal, it is therefore necessary to adjust the ion range of the implanted species to the dimension of the nanostructures. As the material sizes are so small, typical low ion energies between 1 and 100 keV are used for doping and modifying nanostructures, and thus one can assume that nuclear stopping is the major involved process while electronic stopping plays a minor role (see Chap. 1).

We will see that the subsequent dissipation of the total deposited energy (both introduced by nuclear and electronic stopping) into the confined nanostructure strongly affects the resulting structure and properties. In most cases this effect even “overwrites” the collision cascade. Furthermore, sputter yields as well as damage and implantation profiles are completely different for nanostructures compared to

the bulk or thin film situation, because of the existence of additional surfaces in lateral directions. All these effects will be described in this chapter in detail, and additionally a few examples will be presented for semiconductor nanowires and nanoparticles.

12.2 Simulations

Monte Carlo (MC) simulations are frequently used to determine the distribution of ions implanted into the target and the distribution of ion beam induced defects created in the target (vacancies, interstitials). These MC simulation codes calculate collision cascades by simulating binary collisions with a random distribution of impact parameters, see details in Chap. 1. One of the most used MC codes is TRIM (Transport and Range of Ions in Matter) [1]. There exist several variants and derivates of TRIM for special applications. Examples are `TRIM.SP` [2] for sputtering calculations, or TRIDYN [3] for calculations with dynamic variation of the target composition.

In these MC simulation codes, the structure and morphology of the target must be represented and defined. In "conventional" MC codes based on TRIM the target is defined by a stack of layers, which are flat and which usually have infinite/periodic lateral extension. This way of defining the target limits the applicability of these MC codes to the ion irradiation of bulk targets or layered targets with a flat surface and flat interfaces. Nanostructures cannot be represented in these simulation codes, which is especially a problem for *free-standing* nanostructures. Nevertheless, these bulk simulations are sometimes used when irradiating nanostructures. The simplest way of adapting bulk simulations to nanostructured targets would be to take the distribution of implanted ions or the distribution of damage from bulk simulations and "cut out" the shape of the nanostructures; however, this method does certainly not yield accurate results. A more advanced method would be to take collision cascades simulated in bulk, and apply these cascades to the nanostructure while adjusting the correct point of entry where the ions hit the nanostructure surface. This is schematically illustrated in Fig. 12.1a, b. Nevertheless, this method will also yield inaccurate distributions of implanted ions and damage, as illustrated in Fig. 12.1c: The surface of the nanoparticles cuts right through the collision cascade, but the influence of the surface *on* the collision cascade is neglected, because the cascade was simulated for bulk. Errors are caused by ions/recoils, which move out of the particle and re-enter it, as well as the neglected influence of the surface binding energy E_s at the nanoparticle surface. Consequently, the correct three-dimensional (3D) structure and surface of the target must be represented in the program already during the simulation in order to obtain accurate distributions of implanted ions and damage. This is especially true, when the size of the nanostructure is in the same range as the size of the collision cascade.

Different approaches are used to simulate the ion irradiation of nanostructures, depending on the application and the desired accuracy (see Fig. 12.2). For very

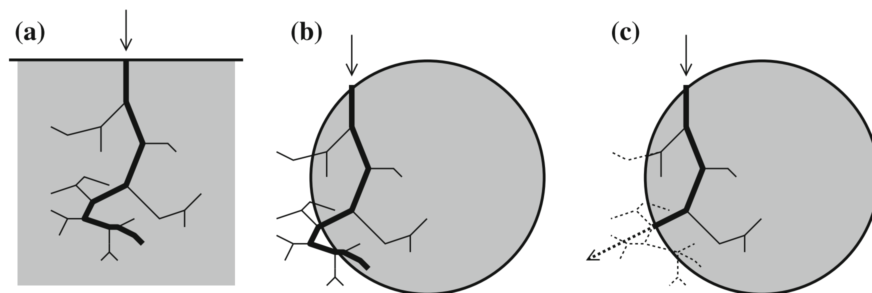

Fig. 12.1 **a** Collision cascade simulated in bulk material. *Bold line* path of the ion, *thin lines* recoils. **b** Applying the same collision cascade to a spherical nanoparticle. The cascade protrudes out of the particle. **c** In reality, parts of the cascade (*dashed lines*) would not exist in the nanoparticle

small nanostructures, full molecular dynamic (MD) simulations can be performed, as discussed in the Chap. 11. These MD simulations can inherently be much more accurate than MC simulations, because they avoid approximations like binary collisions and they can correctly simulate target temperatures above 0 K. However, the MD simulations require many orders more of computation time than MC simulations, because the equation of motion must be solved for every single target atom including all the interacting forces. Thus, MD simulations today are only feasable for small target structures of up to few tens of nanometers and only a small number of ions (a few hundred) can be simulated [4, 5].

A completely different approach is used to simulate the ion irradiation within a Focused Ion Beam (FIB) system. Here, one wants to know, how a surface or a nanostructure evolves under irradiation with a finely focused intense low-energy ion beam. There are simulation codes that calculate the evolution of the surface topography by taking into account sputtering and redeposition of sputtered atoms, (for example AMADEUS [6, 7]), see Fig. 12.2b. However, these codes are usually specialized to calculate sputter yields and related phenomena but do not perform the calculation of a collision cascade *within* the material and hence cannot be used to obtain the distribution of implanted ions or damage within nanostructures.

The third approach to simulate ion irradiation of nanostructures is using Monte Carlo simulations similar to TRIM but with a flexible 3D representation of the target (Fig. 12.2c). A versatile way to represent the target structure in the code is using a 3D rectangular grid with small rectangular cells instead of using a stack of layers, as illustrated in Fig. 12.3. Each cell can be filled with a certain material. Free standing nanostructures can be represented by setting the surrounding cells to vacuum. Furthermore, it is possible to make use of periodic boundary conditions for periodic arrays of nanostructures in order to keep the simulation volume as small as possible. The number of cells required in 3D simulations is typically much larger than the number of layers in a “conventional” MC simulation, resulting in much greater demand for memory during simulation. Furthermore, a larger number of ions has to be simulated to obtain good statistics for all cells, and additionally, for

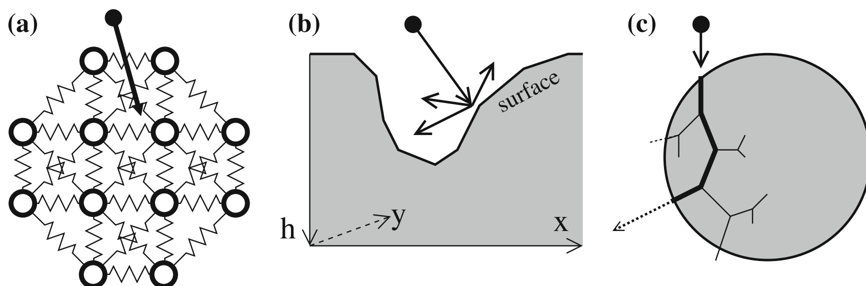

Fig. 12.2 Three approaches to simulate ion irradiation of nanostructures: **a** MD codes take into account all atoms in the target, their interaction potentials and solve the equation of motion numerically. **b** Surface evolution codes represent the target as a surface $h(x, y)$ and calculate the surface evolution due to sputtering and redeposition. **c** MC codes follow the projectiles and recoils from collision to collision

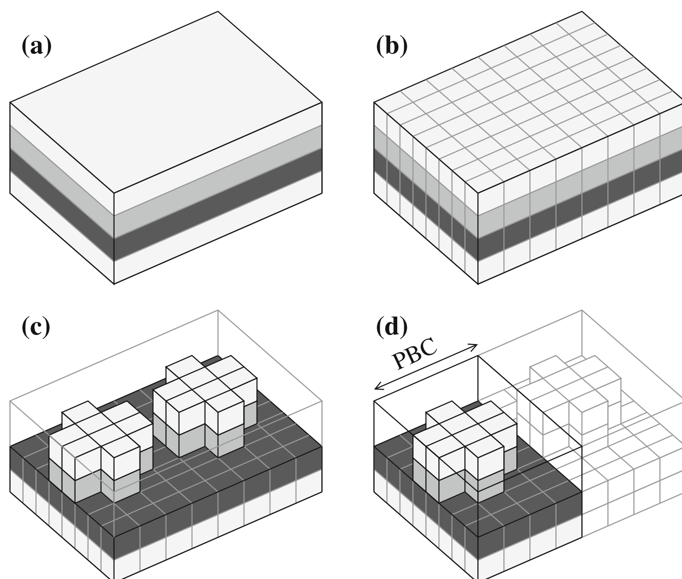

Fig. 12.3 **a** Conventional MC codes use flat, layered targets. Each layer consists of one material. **b** Division of target into rectangular cells. **c** Setting certain cells to vacuum allows representing free-standing nanostructures. **d** Periodic Boundary Conditions (PBC) can be used in order to reduce the simulation volume for periodic structures or samples with translational symmetry

small nanostructures it not possible to use large free path lengths as can be used in TRIM. In contrast, the free path lengths should be smaller than the cell size. Due to these additional requirements in computing resources, the 3D MC codes need to be optimized and often use special techniques in order to save computing resources. Examples are codes, which are used to simulate ion implantation in laterally

structured semiconductor devices, like for instance MCIMPL [8] and TOMCAT [9]. Techniques like trajectory replication, spatial octree division [9, 10], or convolution of point response functions [11] are used to save computation time. Another possibility is to speed up the simulations by avoiding the computation of transcendental functions during the simulation of the binary collisions. This can be achieved by using tabulated values for the scattering angle θ as a function of reduced energy ε and reduced impact parameter b for each combination of projectile and target nucleus Z_1 and Z_2, and combining this with clever indexing mechanisms to access the tables. This technique was first suggested by Yuan et al. [12] and later improved by Schiettekatte [13]. It is employed in the freely available 3D Monte Carlo simulation code *iradina* (**i**on **r**ange **a**nd **d**amage **i**n **na**nostructures) [14, 15], which is explained in the following and used for the simulations throughout this chapter.

Iradina uses a rectangular grid with rectangular cells to describe the target structure (as illustrated in Fig. 12.3). A list of materials can be defined in the program and one of the materials is assigned to each cell, or alternatively vacuum. The transport of ions and recoils is calculated similarly to TRIM, except that only small path lengths in the range of the average atomic distance are used and that the scattering angles in each collision are looked up from tables instead of using the MAGIC algorithm employed in TRIM, making *iradina* much faster. Whenever a projectile (ion or recoil) moves from material into vacuum or vice versa, the surface binding energy E_s is taken into account in order to calculate sputter yields appropriately. *Iradina* is intended for low energy ion irradiation where nuclear energy loss dominates, but the electronic energy loss is also taken into account using tables from SRIM [1]. *Iradina* is non-interactive and can perform simulations for other programs in the background, but a graphical user interface is available, which allows a simple object based definition of the target structure and easy use of the program.

The ion irradiation of perpendicular nanowires will be discussed in the following as an example for the usage of *iradina* and to show, why it is indeed necessary to take into account the correct 3D geometry of the target during the simulation of ion irradiation. Suppose a long cylindrical nanowire (NW) standing perpendicular on the substrate shall be irradiated from the side, as illustrated in Fig. 12.4a. It is not necessary for the simulation to represent the complete NW; instead we can take a small segment of the NW and apply periodic boundary conditions (PBC) along the nanowire axis. This leads to a nanowire of infinite length, which is a very well acceptable approximation for a long and thin nanowire. The simulation volume is always rectangular in *iradina* and is placed around the NW as illustrated in Fig. 12.4b. The simulation volume is divided into appropriate small rectangular cells; the cells inside the NW are filled with its materials, the cells outside the NW are set to vacuum, as illustrated schematically in Fig. 12.4c. The irradiation with ions is simulated. Each cell within the simulation has several counters that count the number of implanted ions, as well as the number of defects (interstitials, vacancies, displacements …) created in the cell. Figure 12.4d shows the result of an actual simulation: a grid of 40×40 cells was used for a nanowire with diameter

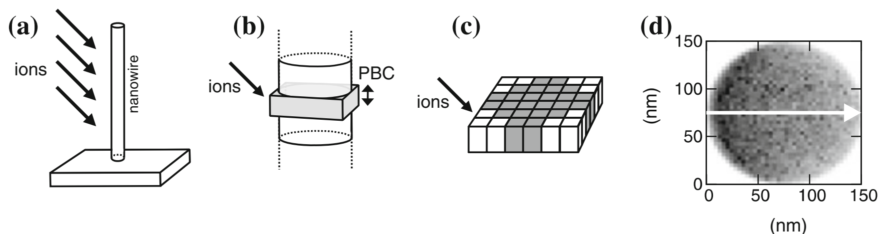

Fig. 12.4 **a** Perpendicular nanowire (NW) irradiated from the side. **b** A segment from a long NW. The *grey shaded box* shows the simulation volume. Periodic boundary conditions (PBC) mimick an infinitely long NW. **c** Simulation volume devided into rectangular cells. **d** Simulation result: each pixel corresponds to one cell (40 × 40). The concentration of implanted ions is shown in greyscale (arbitrary units)

$d = 150$ nm, and each pixel in Fig. 12.4d shows the concentration of implanted ions within one cell in greyscale (arbitrary units).

Results from these simulations with the correct 3D nanowire geometry can be compared to bulk simulations from conventional MC codes. Ion beam implantation is frequently used to dope semiconductors. In order to achieve a quasi-homogeneous doping profile, ions are usually implanted with multiple energies. The homogeneous doping profile is achieved by superposition of the implantation profiles corresponding to the individual ion energies as illustrated in Fig. 12.5a. The implantation profiles were obtained from computer simulations with a conventional MC code with flat surface. Now we use *iradina* to simulate what will happen, if the exact same ion energies and fluencies are implanted into a GaAs nanowire instead of bulk material. The result is shown in Fig. 12.5b: obviously, the concentration of

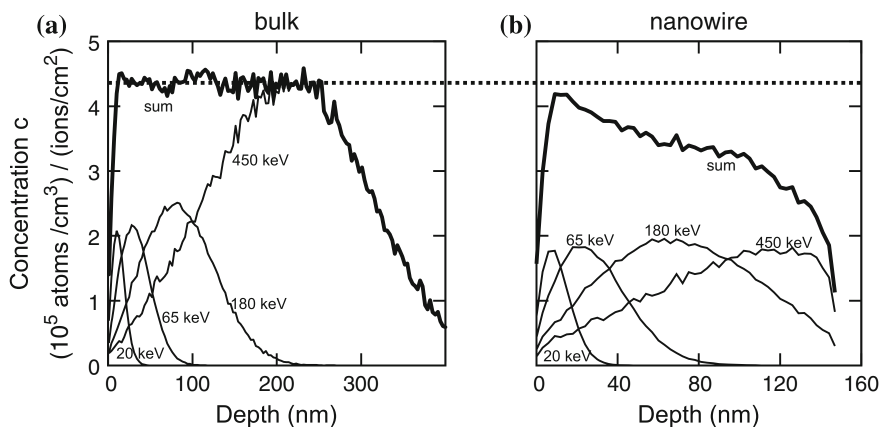

Fig. 12.5 **a** Implantation profile simulated for a bulk target (Zn implantation into GaAs). The profiles for different ion energies (*thin lines*) are superimposed to create a quasi-homogeneous sum profile (*bold line*). **b** The same profile as in (**a**), but simulated for the implantation into a nanowire. The profile corresponds to the *white arrow* in Fig. 12.4d

implanted ions is significantly less in the nanowire than in bulk. For the smallest energy of 20 keV, the profiles differ only marginally, because the ion range is much smaller than the nanowire diameter. For the higher ion energies, the ions are able to exit the nanowire at the side and the back, thus the implantation profiles differ significantly from bulk. Similar differences between bulk and nanowire occur also for the distribution of the irradiation damage. This example clearly shows the necessity to include the correct nanostructure geometry during the Monte Carlo simulation.

It is very interesting to simulate the dynamic changes in shape and structure of the target during ion irradiation. MD codes can inherently do this correctly, but MC codes often assume a static target. However, there have been dynamic MC codes for flat and layered targets for a long time, for example TRIDYN [3]. The codes update the composition of the layers according to implanted ions and ion beam induced damage, and they relax changes in the density by adjusting the layer thicknesses. In three dimensions, these relaxing processes are much more difficult to calculate, but codes for special applications have been reported [16]. More versatile dynamic 3D Monte Carlo simulation codes have only recently been developed (i.e. a 3D version of TRIDYN [17]), some examples being discussed at the end of Sect. 12.5.2. Another interesting approach in this context is the coupling of a FIB topography simulator with a MC code [18].

12.3 Enhanced Dynamic Annealing in Nanostructures

Dynamic annealing is an important effect in damage annihilation during ion irradiation: a fraction of the defects induced by the ion beam can anneal out directly during the irradiation due to the huge amount of energy deposited by the original ion and subsequent ions. Chapter 6 discusses these processes in detail.

The dynamic annealing can be significantly different when nanostructures are irradiated compared to bulk material. The reason lies in the unequal heat dissipation between nanostructures and bulk, as illustrated in Fig. 12.6. The incoming ion loses part of its energy to the target atoms via nuclear energy loss and part via electronic energy loss. Some of the target atoms in the collision cascade are displaced, but

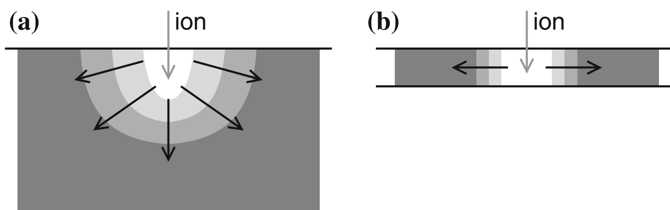

Fig. 12.6 **a** In a bulk target, the heat introduced by the ion can quickly dissipate in all directions. **b** In a nanowire, heat dissipation only proceeds in one dimension

many target atoms receive energy below the displacement threshold. This energy is converted into vibrational energy (phonons) leading to a local heating of the target and consequently possible annealing of defects. Energy transferred to electrons also goes partly into phonons through coupling of the electrons to the lattice, leading to further heating. In bulk material, the heat can quickly dissipate through heat conduction into the complete half-space of the sample. When the dimension of the target is lower, for example a quasi one-dimensional nanowire instead of a 3D bulk target, the heat can only dissipate in one dimension and the dissipation proceeds more slowly. Consequently, there is more time for defects to anneal out than in bulk material; the dynamic annealing is enhanced. A graphic illustration of this phenomenon can be found in [19] where MD simulations of ion impacts on nanowires are presented.

The effect of this enhanced dynamic annealing has been experimentally observed for example by increased amorphization thresholds in Ga ion irradiated GaN nanowires [20]. Such an increase in the amorphization threshold can be visualized directly using transmission electron microscopy (TEM). Figure 12.7a shows a TEM image of a GaAs nanowire, which was initially crystalline and has been implanted at room temperature with manganese ions of 60 keV and a fluence of 2.6×10^{15} cm^{-2} (example taken from [21, 22]). One half of the nanowire was amorphized during irradiation (the side facing the ion beam) but the back side remained crystalline. Computer simulations were performed using *iradina* in order to determine the number and distribution of displacements occuring during the ion implantation; the simulation results are shown in Fig. 12.7b. The number of displacements per lattice atom n_{dpa} obtained from the simulation is compared and overlayed to the TEM image of the nanowire. The amorphization threshold can be determined to be around $n_{\mathrm{dpa}} = 7$, as illustrated in Fig. 12.7c. Due to thinning of the

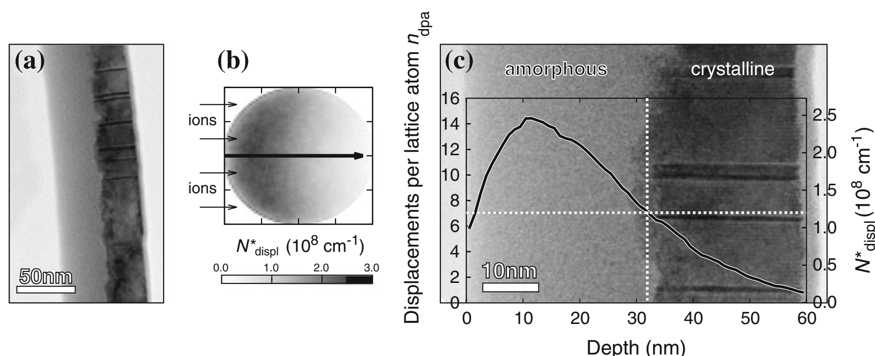

Fig. 12.7 **a** TEM image of a GaAs nanowire (NW) that has been irradiated with Mn ions from the left. Half of the NW was amorphized, the other half remained crystalline. **b** Simulation result from *iradina*: A cross section of the NW is shown, the number of displacement events are coded in greyscale. **c** TEM image of the same NW as in (**a**), but with higher resolution. A plot with the number of displacements obtained from the simulation is overlaid. The profile corresponds to the *thick black arrow* from (**b**)

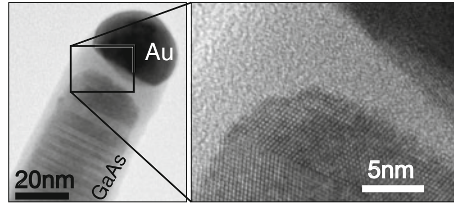

Fig. 12.8 TEM image and high resolution cut out of a GaAs nanowire (NW) that has been irradiated with Mn ions at a temperature of 100 °C and with a fluence of 2×10^{15} cm^{-2}. The dark sphere is the growth seed droplet and consists of gold. The nanowire core remains crystalline except for a thin amorphous neck close to the Au droplet

nanowire through sputtering, the actual amorphization threshold must be corrected to about $n_{\mathrm{dpa}} = 5$. An amorphization threshold of only 2 dpa would be expected from bulk irradiation at room temperature [23]. This example demonstrates the enhancement of dynamic annealing in nanostructures.

The important role of heat conductivity in the dynamic annealing of nanostructures is further shown in the following example: The GaAs nanowire together with its Au tip shown in Fig. 12.8 was irradiated with Mn ions at 100 °C. The heat dissipation is slow in the GaAs material. Consequently, the material remains hot for some time after an ion impact, enabling effective dynamic annealing in the NW core: the core remains crystalline during irradiation. However, an amorphous neck can be observed close to the Au droplet on top. The heat conductivity of the Au is about 6 times higher than of GaAs and the volumetric heat capacity of Au is larger by a factor of $\approx$1.4 [24]. When ions hit the GaAs close to the Au, the Au acts as an effective heat sink compared to the GaAs, leading to faster cooling and less effective dynamic annealing. Consequently, the neck can be amorphized, while the NW core cannot.

12.4 Semiconductor Nanowires

Semiconductor nanowires have been in the focus of intense research for the past decade, as the quasi one-dimensional structure enables them to serve as both functional unit as well as the wires that access them. Therefore, many different nano-scale applications and proto-type devices based on semiconductor nanowires have already been demonstrated, such as field-effect transistors, sensors, light-emitting diodes, and lasers [25–27]. Beside this huge success, however, full device application in electronics and photonics requires effective and controlled doping, but this is an extremely difficult task during growth of semiconductor nanowires.

In the majority of all cases, the so-called vapor-liquid-solid (VLS) mechanism is used for the growth of semiconductor nanowires, which has already been discovered for the growth of Si whiskers using Au droplets as catalysts in the 1960s [28]. However, in recent years it has been determined that this mechanism cannot fully explain the existing growth of compound semiconductor nanowires [29], because the more volatile component has almost no solubility within the catalyst used. Therefore, diffusion to the interface between catalyst and nanowires as well as

a solid catalyst particle (instead of a liquid one) were introduced in order to explain the stoichiometric semiconductor whisker growth of some III–V compounds [30, 31]. Adding further components such as possible dopants to the growth makes the prediction on the mechanism and the incorporation probability almost impossible. One theoretical work predicted that the dopants preferentially diffuse towards the surface due to low solubility limits and the high surface-to-volume ratio [32]. This effect has been experimentally confirmed for silicon and germanium nanowires below about 20 nm [33]. Another study [34] on germanium nanowires shows a clear inhomogeneous dopant distribution indicating that the vapour-solid (VS) side surface growth is responsible for dopant incorporation rather than the vapour-liquid-solid (VLS) mechanism. Furthermore, it has been observed that doping of silicon nanowires during growth could result in a significant morphological change of the wires [35].

Summarizing, doping of semiconductor nanowires during growth results often in non-uniform doping profiles and dopants accumulate at the sidewalls or surfaces of the semiconductor nanowires; thus, subsequent doping using ion implantation and annealing is a valuable alternative in order to manipulate the electrical, optical or magnetic properties [36, 37].

12.4.1 Ion Beam Doping

Silicon nanowires successfully doped via ion implantation using P and B as dopants in order to realize both n-type and p-type wires, respectively, have first been reported in [38]. The wires used in that study were rather small in diameter and featured an inner crystalline Si core (10–20 nm) and an amorphous SiO_2 shell (5–10 nm). The relatively small size of the wires was chosen with respect to Moore's law, paying regard to the on-going miniaturization in semiconductor technology. In the P implanted wires, partial amorphization took place during the implantation process and recrystallization was obtained after 30 min thermal annealing at 800 °C under high vacuum conditions, as measured by Raman spectroscopy. In the case of B doping, the wires remained crystalline during the whole process. The higher amorphization rate under P irradiation goes with the fact that amorphization is proportional to the ion mass. Fewer defects are created during implantation of the lighter element B and consequently, the enhanced dynamic annealing is sufficient to suppress amorphization. The implanted wires have been prepared as field effect transistors (FETs) for electrical measurements. The geometry with two contact leads (source, drain) to the nanowires on top of a highly doped Si/SiO_2 substrate (gate) is schematically shown in Fig. 12.9a and a typical real device can be seen in the scanning electron microscopy (SEM) image, Fig. 12.9b. The initially ambipolar nanowires show now unipolar I–V characteristics, as it can be clearly seen in the respective transfer curves in Fig. 12.9c, d. This can be connected to an implantation induced band-alignment and successful doping, as the sign of gate voltage (V_G) for the FET ON states is consistent with the implanted impurities. The huge hysteresis

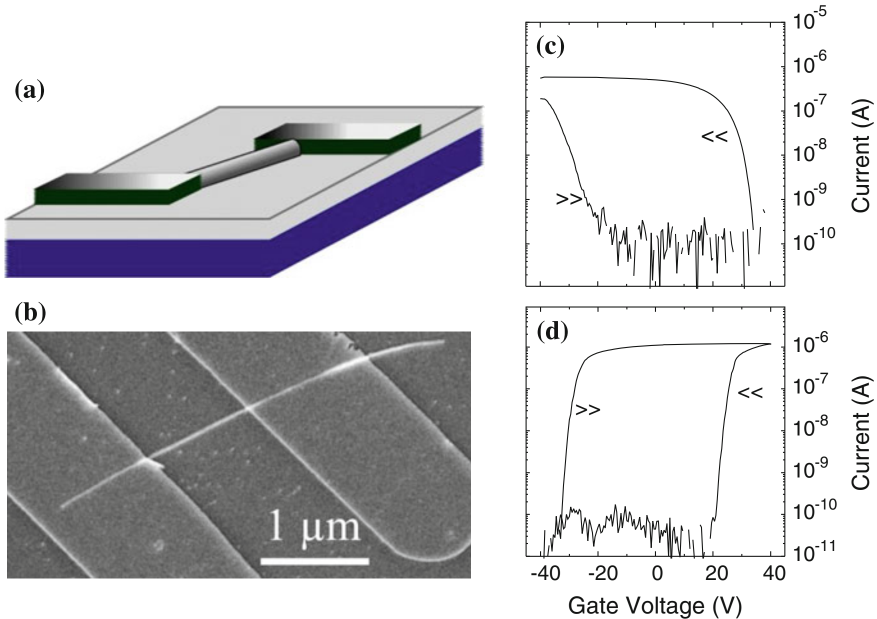

Fig. 12.9 **a** Schematic view of a semiconductor nanowire field effect transistor (FET) contacted with two leads on top of a highly doped Si/SiO_2 substrate. **b** Scanning electron microscope image of a typical FET device with a 1 μm long NW channel. Typical FET transfer curves for **c** P-implanted SiNWs and **d** B-implanted SiNWs. Consecutive gate sweeps for increasing (≫) and decreasing (≪) gate voltage (V_G) are presented. The FET ON state is found for positive V_G in panel (**d**) and for negative V_G in panel (**c**), consistently with the implanted impurities (Data taken from [38])

in the transfer curves is caused by charge traps in the oxide [38], and could be utilized for memory devices.

Ion beam doping of vertically aligned silicon nanowires has been realized [39, 40], as such upstanding nanowires have gained interest as possible building blocks of future 3-dimensional circuits. It has been further demonstrated that even pn-junctions can be realized in vertically aligned nanowires using ion beam doping [39]. Here, relatively thick (diameter 150–400 nm) and up to 500 nm long nanowires have been grown, and ion beam doping was subsequently performed with P as donor and B as acceptor. The ion energies and fluences were carefully chosen in order to realize the situation shown in Fig. 12.10a: boron ions have been implanted with higher energies to form a buried p-type layer. In a second implantation step, low energy phosphorous ions have been used to form the n-type top layer. The nanowires were contacted by a conductive PtIr tip mounted on a nanomanipulator setup inside a SEM, as shown in Fig. 12.10b. Current-voltage measurements clearly showed the rectifying behaviour of the junctions. To verify that the rectifying behaviour originates from the nanowire, electron beam induced current (EBIC) measurements have also been carried out [38]. EBIC can be used for visualization of pn-junctions, and the corresponding mapping

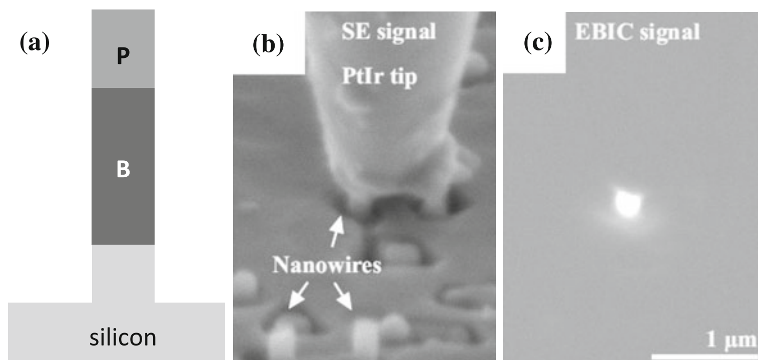

Fig. 12.10 **a** Schematic view of a silicon nanowire with an n-type (phosphorous) on top and a buried p-type (boron) region. **b**, **c** SEM and EBIC images of a nanowire implanted with a profile like shown in (**a**). The nanowires are standing at an angle of 60° with respect to the electron beam (Data taken from [39])

shown in Fig. 12.10c clearly proves that a pn-junction is inside the single silicon nanowire.

Although the optical properties of undoped semiconductor nanowires are already fascinating, doping of those nanostructures with optically active impurities can further enhance the photonic applications. The most interesting impurities are either transition metals (TM) or rare earth (RE) elements as they usually act as luminescence centres in various materials. Various attempts on doping ZnO nanowires with rare earth elements (RE = Ce, Er) during growth were reported not to be successful [41, 42] due to the high melting points of rare earth elements and their composites. Therefore, ZnO nanowires with diameters of 40–60 nm and lengths up to 10 µm were implanted with Yb, Eu, or Tm ions [43]. The majority of the implantation related damage was recovered by thermal annealing at 700 °C for 30 min in O_2 flow [44]. Figure 12.11a shows the photoluminescence of Yb-doped ZnO nanowires in the spectral range of the Yb intra-4f-luminescence. A sharp and intense luminescence peak at 1.260 eV is detected, which can be assigned to the only possible Yb^{3+} transition: ${}^2F_{5/2} \rightarrow {}^2F_{7/2}$ [45]. A successful activation of the implanted RE elements was also achieved for Eu and Tm in ZnO nanowires, as shown in the cathodoluminescence spectra in Fig. 12.11b, c, respectively. In the case of Eu, the multiple observed transitions can be assigned from the ${}^5D_0$ level to several ${}^7F_J\, J = 0, \ldots, 6$ levels [46]; whereas, for the Tm case, the emissions are due to ${}^3H_4 \rightarrow {}^3H_6$ transitions [47] and the splitting is given by different Stark levels as well as contributions from different crystal fields.

Ferromagnetic ordering can be observed in highly Mn-doped GaAs, where Mn provides the uncompensated spins as well as p-doping, allowing hole-mediated ferromagnetism [48]. These diluted magnetic semiconductors (DMS) enable electrically controllable ferromagnetism or spin-FETs for example. Whereas these DMS systems have already been realized in bulk or as thin films, all attempts in the

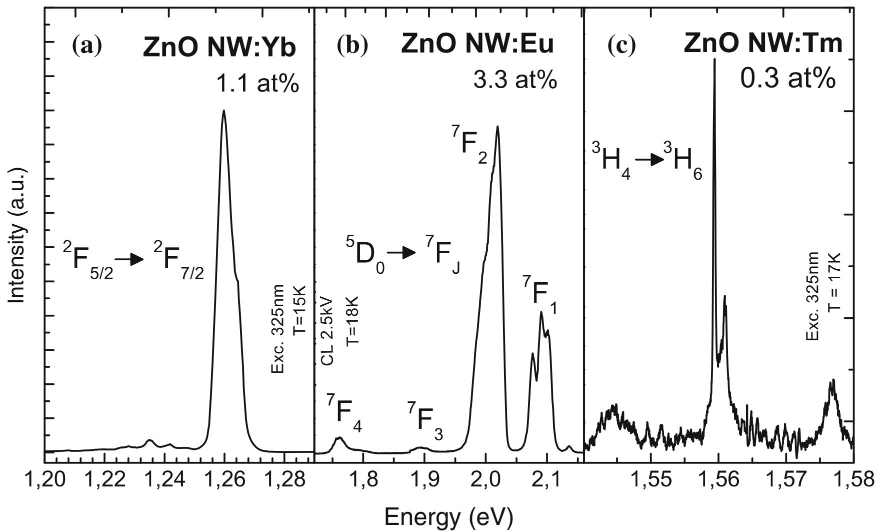

Fig. 12.11 **a** PL spectra of Yb-doped ZnO nanowires: The sharp intra-4f-luminescence of the Yb^{3+} ions originates from the $^2F_{5/2} \rightarrow {}^2F_{7/2}$ transition at 1.26 eV. **b** Intra-4f-luminescence of Eu^{3+} shows a multiplett of transitions from the $^5D_0$ to several ^7F_J levels. **c** Tm-doped ZnO nanowires showing the $^3H_4 \rightarrow {}^3H_6$ transition (Data taken from [43])

growth of highly Mn-doped GaAs nanowires failed, because of the segregation of Mn or MnAs phases during growth leading to non-ideal nanowire morphologies [22]. The only successful realization of high crystalline quality Mn-doped GaAs nanowires reports on the use of ion beam implantation [22], which allows incorporation of dopants into the target material far beyond the solubility limit. In order to minimize ion beam-induced defects different annealing routes were investigated. Post annealing of room temperature implanted and thus amorphous GaAs nanowires (see Fig. 12.7c) was not successful for nanowires, because the nanowires either decomposed or became polycrystalline within the investigated parameter space, as shown in the transmission electron micrograph in Fig. 12.12a. However, heating the sample to higher temperatures during implantation (250 °C) enabled increased dynamic annealing in addition to thermal healing, resulting into single-crystalline $Ga_{1-x}Mn_xAs$ NWs with high Mn content, as demonstrated in Fig. 12.12b. The measured Mn concentration determined by energy dispersive X-ray spectroscopy (EDX) agreed well with corresponding *iradina* simulations [22], and confirmed that respective TRIM simulations overestimate the impurity concentrations, if the nanostructure is in size comparable to the ion range. Magnetotransport measurements on such Mn-implanted and contacted GaAs nanowires (Fig. 12.12d) are displayed in Fig. 12.12c. A strong-temperature dependence of the resistance was observed in addition to a clear negative magentoresistance (MR) at low temperatures. These results indicate dilute Mn

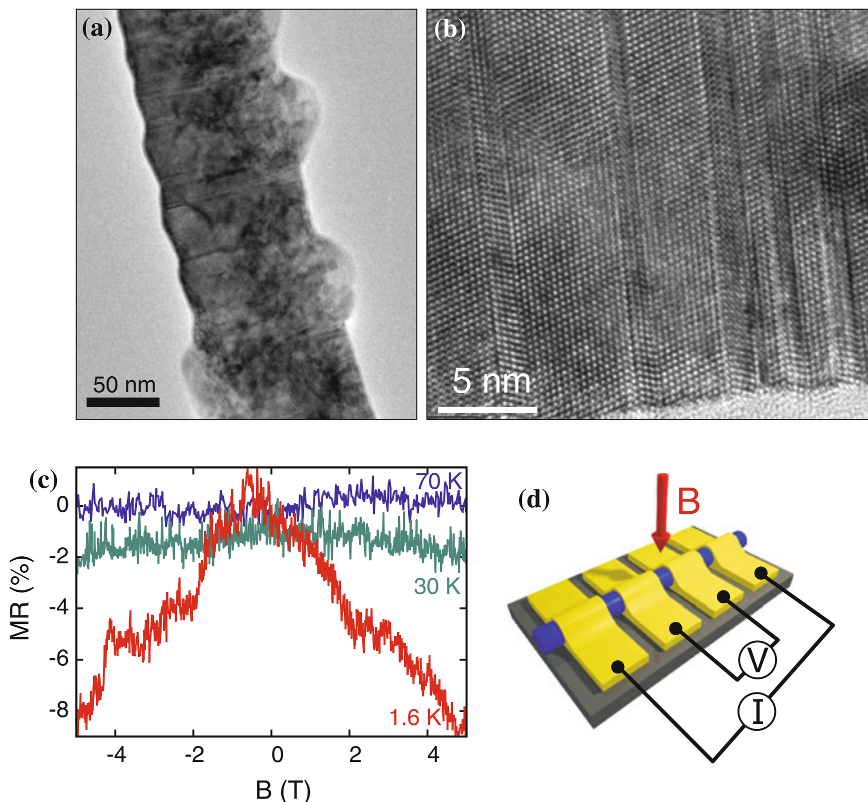

Fig. 12.12 **a** Transition electron micrograph (TEM) of a Mn-implanted GaAs nanowire after annealing in As atmosphere at 550 °C. **b** High resolution TEM micrograph of a GaAs nanowire implanted with x = 5 % Mn at 250 °C without subsequent annealing demonstrating excellent crystalline quality. **c** Plot of magnetoresistance (MR) for different temperatures; a schematic view of the measurement setup is shown in (**d**) (Data taken from [22])

incorporation and, in combination with the observed high resistance of the NWs, support the hypothesis that the implanted NWs are paramagnetic.

12.4.2 Damage Profiles and Bending of Nanowires

Ion beam doping of nanostructures is a useful alternative and tool in order to overcome the limitations of doping during synthesis of nanostructures, as nicely shown above. However, just as for bulk, the ion impact has also a major effect on the structure due to damage creation during irradiation. The effect on nanostructures can even be much more than on bulk [49], if no sufficient compensating dynamic annealing is present. The small size and the free space around nanostructures can

much more easily lead to irreversible structural and mechanical relaxation processes. This results into morphology changes; whereas, in the bulk or thin film situation, the boundary conditions to the surrounding constrain the irradiated volume.

One very interesting issue, which has been investigated in recent years, is how ion beams can shape, bend and even align nanowires [50–53]. While defect creation is mostly considered to be detrimental, the change in shape using ion beams can also be considered as a very helpful tool in controlled manipulation and alignment of nanowires.

Figure 12.13a, b illustrate the damage profiles in nanowires of two extreme situations simulated using *iradina*: the cases of shallow and deep implantation with respect to the nanowire diameter using low and high ion energies, respectively. Here, *iradina* was used in order to calculate vacancies and interstitials in each simulation cell of the nanowire. As one can assume that vacancies and interstitials in vicinity annihilate due to (enhanced) dynamic annealing, the Fig. 12.13a, b show only the value of interstitials minus vacancies for each simulation cell, thus, the number or remaining defects in each cell.

At low ion energies most of the damage is induced on the side of the nanowire that faces the incident ion beam. There is a thin layer with excess vacancies very

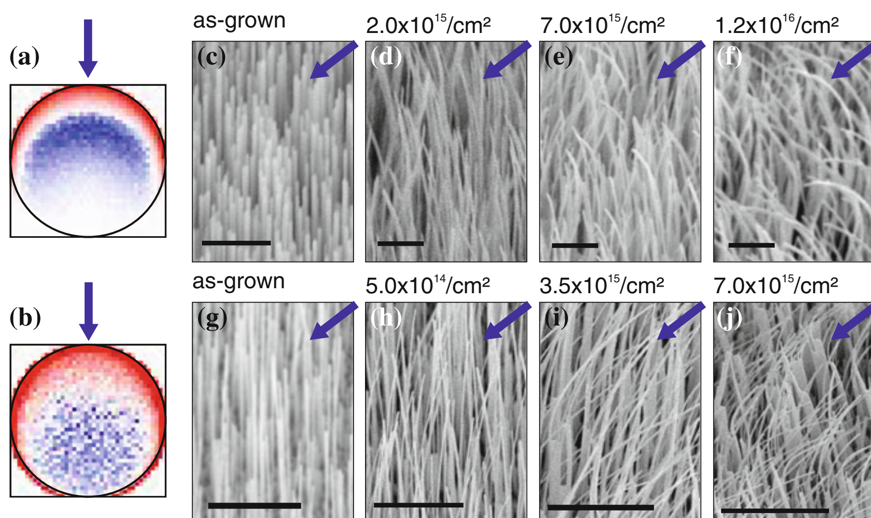

Fig. 12.13 *Iradina* Monte Carlo simulations of ion beam created damage in ZnO nanowires with **a** diameters of 60 nm and 20 keV Ar^+ ions, and **b** diameters of 90 nm and 100 keV Ar^+ ions. *Red* vacancy excess, *blue* interstitial excess. **c–f** SEM images of nanowires (typically 60 nm diameter) irradiated with increasing fluence of 20 keV Ar^+ ions (low energy situation). Scale bars denote 1 μm. **g–j** SEM images of nanowires (typically around 90 nm diameter) irradiated with an increasing fluence of 100 keV Ar^+ ions (high energy situation). Scale bars denote 5 μm. *Arrows* indicate ion beam direction (Data partly taken from [51])

close to the surface of the nanowire, which can be interpreted as removal and sputtering of material. However, most of the upper part of the nanowire is filled with excess interstitials. This additional material leads to a volume expansion of the upper part. Since the lower part is unaffected by the ion beam and not expanded, compressive stress occurs on the irradiated side, while tensile stress is induced on the non-irradiated side. Therefore, a bending moment occurs, which bends the NW away from the ion beam with increasing ion fluence, which can be clearly seen in the experimental findings displayed in the top row of Fig. 12.13.

Opposite, the complete volume of the nanowire is affected by the ion beam for the case of high energy implantation. In this case an excess of vacancies remains in the part facing the ion beam, while excess interstitials remain in the lower part. The vacancies lead to a volume reduction of the upper part of the nanowire, the interstitials to a volume expansion of the lower part. Together, this induces a bending moment, which bends the nanowire towards the incident ion beam. For high fluences, this leads to an alignment of the nanowire axis with the ion beam, as shown in the experimental findings of Fig. 12.13 (bottom row).

This very nice example demonstrates that ion beam induced point defects can have a rigorous effect on the morphology of nanostructures. However, the “negative” effects of ion beam irradiation can also be used in a very positive way: controlled tailoring of the morphology, e.g. for alignment of nanowires!

12.5 Sputtering of Nanostructures

The simulations displayed in Fig. 12.13a, b already show that a high fraction of surface atoms are sputtered, if nanowires are irradiated with ion energies in the keV range. This is obvious, as the ion range is adjusted to the small diameter of the nanowires resulting into the fact that nuclear stopping, which is mainly responsible for sputtering, is the dominating ion-solid interaction process (see above). Now, the interesting question arises, whether sputtering is enhanced for nanostructures compared to perpendicular ion impact on flat surfaces? One can clearly answer this question with “yes”, even using just a simple hand-waving argument: a significant fraction of ions hit the surface under an oblique angle and not perpendicular due to the 3D-curvature of nanostructures; and the sputter yield increases with decreasing impact angle [1]. Detailed calculations and simulations corroborate this clear statement [21, 49], but let us first present some experimental observations based on semiconductor nanowires.

Figure 12.14 shows SEM images of ZnO nanowires lying on a Si substrate, which were irradiated with low energy rare earth elements [43]. It is obvious that the morphology of the nanowires dramatically changes with increasing ion fluence. Already after an ion irradiation in the order of 10^{14}–10^{15} cm^{-2} local dimples are visible; whereas, the overall morphology still seems to be flat and unchanged. However, with increasing ion fluence the surface of the nanowires becomes more and more rough, the dimples are deeper, the nanowires become thinner, the cross

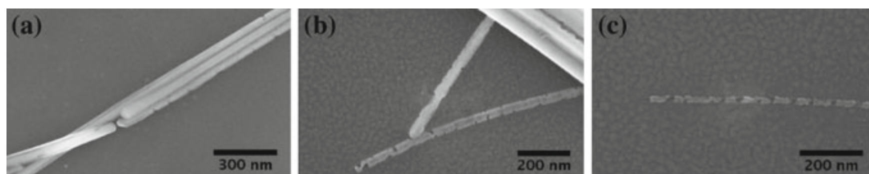

Fig. 12.14 Scanning electron microscopy (SEM) images of ZnO nanowires implanted at room temperature with low energy Eu ions and varying ion fluences: **a** 5.2×10^{14} cm^{-2}, **b** 1.7×10^{15} cm^{-2}, and **c** 5.2×10^{15} cm^{-2} (Data taken from [43])

sections are not round anymore, re-deposited material can be found on the substrate, and finally the nanowires are even cut or completely sputtered away [43, 54]. Such observations do not depend on the ion species used, and are also generally observed during focused ion beam (FIB) milling and for spherical nanoparticles [55]. In the past years, several quantitative studies on the sputter yield of nanostructures under low energy ion irradiation have been presented. It started with theoretical work and simulations, but recently experimental results became available as well. Both will be discussed below.

12.5.1 Static Sputtering Calculations

Semi-analytical models [56] can be used, as well as molecular dynamics (MD) simulations for calculating the size-dependence of the sputter yields of nanoparticles [4] or nanowires [49]. The latter shows that the yield can be up to threefold compared to bulk due to the enhanced formation of defects on or near the surface, because their formation energy is lower than in bulk. *Iradina* can also be used to simulate ion beam irradiation of nanoparticles and obtain the sputter yield as a function of nanoparticle size. In order to compare results from *iradina* to the MD method and to experimental data, we show one example: irradiation of Au nanoparticles with Ga^+ ions at energies from 0 to 30 keV (typical conditions in a focussed ion beam system).

Figure 12.15 shows the calculated sputter yield of spherical Au nanoparticles, (a) irradiated with 25 keV Ga^+ ions as a function of nanoparticle diameter, and (b) for a constant diameter as a function of ion energy. Very small NPs have a low sputter yield, which can be explained by the fact that the ions only deposit a small fraction of their energy within the nanoparticles before they leave the nanoparticle again. The sputter yield quickly increases with diameter d and reaches a maximum at about $d =$ 8–10 nm. This size is approximately the same as the projected range of the ions in bulk material (8.3 nm): the ions deposit most of their energy within the particle, but the particle is still so small, that a large fraction of the kinematic energy in the collision cascades reaches the surface of the particle. At larger diameters, the sputter yield decreases again. The reason is that now the collision cascades will

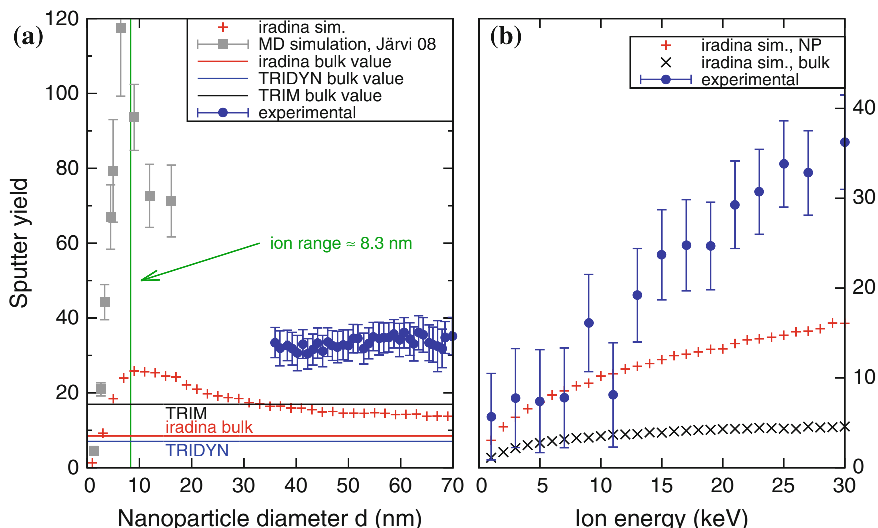

Fig. 12.15 **a** Size dependence of sputter yield for irradiation of Au NPs with 25 keV Ga^+ ions (surface binding energy $E_S = 3.8$ eV) calculated by *iradina* and measured experimentally. MD simulation results from [4] are shown for comparison. The bulk sputter yields for perpendicular incidence are illustrated as calculated by TRIM [1], TRIDYN [3] and *iradina*. **b** Energy dependence of the sputter yield for irradiation of Au NPs (diameter 50 nm) with Ga^+ ions: simulations and experimental results. Simulated sputtering for bulk material is shown for comparison (Experimental and simulated data taken from [57])

often not extend to the surface or the kinematic energy in the collision cascades is to a large extend absorbed within the particle and does not reach the surface. For very large nanoparticles with $d > 150$ nm, the sputter yield converges (not shown in the figure). Here, the nanoparticles are much larger than the projected range, thus they appear to the ions as bulk. However, the sputter yield does not reach the bulk value, which was calculated for perpendicular incidence and is similar for *iradina* and TRIDYN. The reason is simply that the incidence angles of the ions hitting the particle at different locations are always distributed between 0° and 90°, no matter how large the nanoparticle becomes and the sputter yield depends strongly on this angle of incidence, as already argued above in the hand-waving discussion.

The general behaviour and trend of the sputter yield obtained from *iradina* is similar to the MD results [4], as illustrated in Fig. 12.15a. This clearly underlines our previous hand-waiving argument that the sputter yield for nanostructures is enhanced and strongly depends on the size and shape of the nanostructures. The difference between the MC and MD simulations are the absolute sputter yields. However, one cannot expect MC and MD simulations to yield the same results. For instance, the MD simulations will be more accurate for very small nanoparticles: while Monte Carlo (MC) simulations intrinsically assume a static solid with a temperature of 0 K, the MD allows all atoms to be in motion and can represent temperatures >0 K. In the MD, heating of the nanoparticle by the ion impact and

subsequent thermal (non-ballistic) evaporation of Au atoms is possible—as opposed to MC simulations. The following estimation shows the importance of this effect: consider a small Au nanoparticle of 10 000 atoms (≈7 nm diameter). Even if an ion deposits only 1 keV into heat, this accounts for an average of 100 meV per atom, corresponding to a temperature of about 900 °C, which can lead to thermal evaporation of atoms. Furthermore, the MD can simulate emission of small Au clusters with several atoms, which requires less energy than to sputter each atom individually. The MD shows [4] indeed that about 30 % of sputtered Au is emitted in clusters of two or more Au atoms. More recent MD simulations corroborate the fact, that sputtering of nanosized objects can strongly be increased and dominated by cluster emission [5]. Nevertheless, the MD simulations allow only limited target sizes and small ion numbers due to the extremely large computation times required.

Sputter yields of Au nanoparticles irradiated with Ga ions where also investigated experimentally [57]. As shown in Fig. 12.15a, the experimental sputter yields run in parallel with the simulation results by *iradina*, but are shifted to higher values. Unfortunately, there are up to now no experimental data on smaller nano particles with diameters around 10 nm at the expected maximum in the sputter yield. There are different reasons for experimental sputter yields being higher compared to the MC simulations: as explained above, thermal effects and cluster emission, both not taken into account in the MC simulation, increase the sputter yield. Furthermore, the experiments were performed with NPs deposited on a silicon substrate while the simulations were done with free NPs neglecting NP-substrate interaction. When NPs are attachted to a substrate, on the one hand the sputter yield of the NP itself is decreased because sputtering in forward direction is suppressed, but on the other hand, the yield is increased by ions hitting the substrate close to the NP, because their damage cascades and thermal deposition of energy can reach into the NP. The experimental sputter yield as a function of ion energy, shown in Fig. 12.15b shows the same trend as the simulations but has a steeper slope for the same reasons as described above. MD simulations might fit the experimental data in the future, when sufficient computational resources become available to simulate larger nanoparticles.

12.5.2 Dynamic Sputtering Calculations

For high fluence irradiation, the assumption of a static target in Monte Carlo simulations becomes increasingly inaccurate, for different reasons: For example, when a nanowire is doped with high doses by ion beam implantation, it becomes thinner due to sputtering, which changes the implantation profiles. Furthermore, a significant change in composition due to the incorporated atoms may change the sputter yield. Another important effect is redeposition of sputtered atoms when a nanostructure is placed on a substrate, or when many nanoparticles are close to each other. In order to take all such effects into account in a simulation, the target structure and composition must be allowed to change *dynamically* during the

simulation. While MD simulations intrinsically include a dynamic target, they can (yet) only cover small target structures and small ion numbers. Dynamic Monte Carlo binary collision simulations have been possible since many years using the TRIDYN code [3]. Recently, this code was extended to fully three-dimensional targets "TRI3DYN" [17] and thus allows to simulate high fluence ion beam irradiation effects in nanostructures.

For example, high dose ion beam doping by axial implantation into nanowires has recently been studied using TRI3DYN [58]. The dynamic simulations show that the resputtering of implanted dopant atoms plays a very important role in nanostructures and quickly limits the achievable final doping concentration—an effect not accessible by static simulations. Such effects will become more important in the future, as 3D-nanostructured substrates are gaining importance in new semiconductor device concepts.

The sputtering of ZnO nanowires under Mn ion beam implantation and the incorporation of Mn dopant atoms has also been studied by pseudo-dynamic simulations using *iradina* [59]. Here, "pseudo-dynamic" means that the simulation code features a static target only, however, a number of static simulations is made incrementally to mimic a dynamic simulation: a small fluence step can be simulated with a static target, the output of the simulation can be used to construct a revised target geometry, which is then used as input for the next step in the simulation. When considering a limited set of target geometries, an alternative is to make a set of simulations for all possible geometries first and subsequently calculate a dynamic process incrementally by selecting the appropriate simulation results.

The latter approach is shown in Fig. 12.16 for ZnO nanowires implanted with manganese (and rotated during implantation) as blue squares. Sputter yields and doping efficacy were precalculated for different NW diameters and Mn/Zn ratios. The dynamic behaviour of the NW during Mn implantation was calculated step-wise, starting with a NW of 200 nm diameter, and subsequently reducing diameter and increasing Mn/Zn ratio according to the appropriate simulation results. The Mn concentration increases linearly at first and in good agreement with the experimental data (red circles in Fig. 12.16). While the NW diameter decreases due to sputtering, the Mn concentration increases slightly super-linearly in the range between 1 and 2×10^{17} cm^{-2}. With further increasing fluence and decreasing diameter, a larger fraction of the Mn ions passes through the nanowire and is not implanted anymore, leading to a saturation of the achieved Mn concentration, which can clearly be seen in Fig. 12.16. At high fluencies, the experimental data of the Mn/Zn ratio begin to deviate from the calculated values, because the simulation inaccurately presumes a homogeneous doping profile [60, 61]. However, in reality the core of the NW is enriched in Mn, because when Mn atoms come near to the surface during implantation, they have a high probability to leave the nanowire and not become implanted. Consequently, less Mn is sputtered away later and furthermore, when the nanowire is thinned, the Mn-rich core is what is left over.

In order to avoid the problems of the pseudo-dynamic simulation, a full dynamic simulation of the implantation experiment can be made. For this purpose, a special

version of *iradina* was adapted to allow a dynamic composition variation of a cylindrical nanowire. The geometry in this version is defined by nested cylinders of flexible radius instead of the static rectangular cells as described in Sect. 12.2. Since the nanowire is rotated around its axis during irradiation, full rotational symmetry is maintained at all times. Furthermore, a long nanowire can mostly be considered to be invariant under translation along its axis. Thus, the radius is the only free dimension, and the concentration profile within the nanowire can be described by a one-dimensional function. The dynamic concentration profile is then calculated in a manner similar to TRIDYN [3]: when the simulation produces interstitials and vacancies, the effective density within each cylinder changes. The radii of all cylinders are then adapted in such a way as to relax the densities to their nominal values. Note, however, that only the dynamic composition variation is one-dimensional, the ion transport simulation itself is still fully three-dimensional.

The results of this dynamic simulation are illustrated in Fig. 12.16 as a green line. For small fluencies, the resulting Mn/Zn-ratio is close to the pseudo-dynamic results. With increasing fluence, the dynamic simulation matches the trend of the experimental data more closely than the pseudo-dynamic simulation, because the dynamic simulation takes into account the inhomogeneous Mn doping profile. At very high fluencies or very small diameters, respectively, the Mn/Zn-ratio curve becomes rather unsmooth. In this case, only few material is left in the nanowire, and single ion events can have a large influence on the concentration.

This example illustrates the importance of dynamic calculations for the case of high fluence implantation in nanostructures.

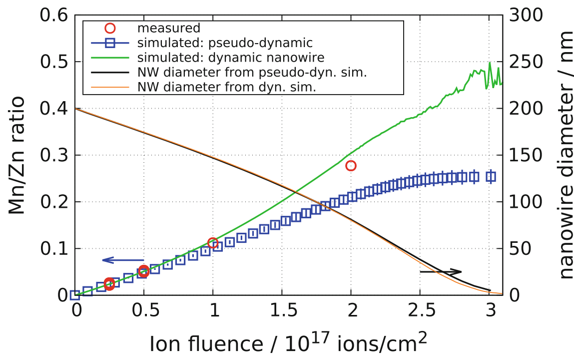

Fig. 12.16 Doping of a ZnO nanowire by 180 keV Mn ion implantation (with the NW rotated about its axis during implantation). The Mn/Zn ratio is shown as a function of ion fluence, calculated by pseudo-dynamic and by dynamic simulations using *iradina* and compared to experimental data. The *right* axis shows to calculated diameter of the nanowire to illustrate thinning by sputtering. Experimental data and pseudo-dynamic simulation results are taken from [59]

12.6 Summary

This chapter outlines the important role that ion beams play in the modification of nanostructures. Doping during growth of nanostructures is often very difficult due to thermodynamic constraints. Ion beam implantation with energies far above thermal energies is thus a very useful tool to overcome solubility limits and dope semiconductor nanostructures after growth. For example semiconductor nanowires (NW) have successfully been modified with electrically, optically, or magnetically active dopands using ion beams: NW field effect transistors have been created, pn-junctions in perpendicular NWs have been realized, optical emission from various rare earth atoms in NWs has been observed, and paramagnetic semiconductor nanowires have been created.

However, there are substantial differences when irradiating nanostructures as compared to bulk material or thin film systems, especially for free-standing nanostructures and as soon as the size of the nanostructure is comparable to the mean ion range. First of all, the distribution of the implanted ions in the target differs between nanostructures and bulk. Computer simulations of the ion irradiation of nanostructures must therefore take into account the correct 3D geometry of the target (this is for example possible using *iradina*). Furthermore, nanostructures have a large surface-to-volume ratio. This leads to strongly enhanced sputter yields reaching a maximum when the ion range is comparable to the size of the nanostructure. This increased sputtering is oberserved experimentally for nanowires and can be calculated by different methods for spherical nanoparticles. A further important difference lies in the dynamic annealing, which is enhanced in nano-structures. The reason is the slower dissipation of heat due to the confined dimensions. These differences must be taken into account when planning ion implantation experiments with nanostructured targets. In particular, the optimum implantation temperatures and annealing procedures cannot simply be adopted from bulk experiments but must be appropriately adjusted.

Special care has to be taken for high fluence irradiation of nanostructures, for example for alloying. Here, dynamic calculations are mandatory as enhanced sputtering and resputtering of implanted atoms can lead to a non-linear behaviour of dopant concentration as a function of dose and to significant changes in the target geometry.

Finally, ion beam irradiation can invoke new effects in free-standing nanostructures, which are not known from bulk irradiation. An example is the ion beam induced bending of nanowires, which is caused by an unequal distribution of ion beam induced point defects. This effect can even be used to align nanowires to a desired direction. It represents a neat example how low energy ion irradiation can be utilized to tailor the structure and morphology of nanostructures beyond "just" doping.

Acknowledgements We thank Dr. Raphael Niepelt and Dr. Sebastian Geburt for planning, performing and evaluating many of the nanowire implantation experiments presented here. Furthermore, we thank Prof. Dr. Wolfhard Möller for valuable discussion about the simulation

codes and Dr.Maria Messing for recording some of the TEM images. We acknowledge financial support for the nanowire implantation experiments by the DFG under grants Ro1198/7-3 and FOR1616.

References

1. J.F. Ziegler, J.P. Biersack, U. Littmark, *Stopping and Range of Ions in Solids* (Pergamon, New York, 1985)
2. A. Mutzke, R. Schneider, W. Eckstein, R. Dohmen, SDTrimSP version 5.00. IPP Report 12/8, Max-Planck-Institut für Plasmaphysik, Garching, Germany (2011)
3. W. Möller, W. Eckstein, Nucl. Instr. Meth. B **2**, 814 (1984)
4. T.T. Järvi, J.A. Pakarinen, A. Kuronen, K. Nordlund, Europhys. Lett. **82**, 26002 (2008). doi:10.1209/0295-5075/82/26002
5. G. Greaves, J.A. Hinks, P. Busby, N.J. Mellors, A. Ilinov, A. Kuronen, K. Nordlund, S.E. Donnelly, Phys. Rev. Lett. **111**, 65504 (2013). doi:10.1103/PhysRevLett.111.065504
6. W. Boxleitner, G. Hobler, Nucl. Instr. Meth. B **180**, 125 (2001)
7. H.B. Kim, G. Hobler, A. Steiger, A. Lugstein, E. Bertagnolli, Nanotechnology **18**, 245303 (2007)
8. G. Hobler, S. Selberherr, IEEE Trans. Comput. Aided Des. Integr. Circuits Sys. **8**, 450 (1989). doi:10.1109/43.24873
9. B.J. Obradovic, G. Balamurugan, G. Wang, Y. Chen, A.F. Tasch, in *International Electron Devices Meeting, 1998. IEDM '98 Technical Digest.* (1998), pp. 513–516. doi:10.1109/IEDM.1998.746410
10. H. Stippel, S. Selberherr, in *Proceedings of VPAD* (1993), pp. 122–123. URL http://in4.iue.tuwien.ac.at/pdfs/vpad1993/pdfs/00724750.pdf
11. A. Burenkov, K. Tietzel, A. Hossinger, J. Lorenz, H. Ryssel, S. Selberherr, in *International Conference on Simulation of Semiconductor Processes and Devices* (IEEE, 1999), pp. 55–58, 6–8 September 1999. doi:10.1109/SISPAD.1999.799258
12. B. Yuan, F. Yu, S. Tang, Nucl. Instr. Meth. B **83**, 413 (1993)
13. F. Schiettekatte, Nucl. Instr. Meth. B **266**, 1880 (2008)
14. C. Borschel, C. Ronning, Nucl. Instr. Meth. B **269**, 2133 (2011). doi:10.1016/j.nimb.2011.07.004
15. Iradina, Download page (2013). URL http://www.iradina.de
16. R. Collins, A. Prez-Martn, J. Domnguez-Vzquez, J. Jimnez-Rodrguez, Nucl. Instr. Meth. B **90**, 433 (1994). doi:10.1016/0168-583X(94)95588-3
17. W. Möller, Nucl. Instr. Meth. B **322**, 23 (2014). doi:10.1016/j.nimb.2013.12.027
18. D. Kunder, E. Baer, M. Sekowski, P. Pichler, M. Rommel, Microelectr. Eng. **87**, 1597 (2010)
19. H.M. Urbassek, R.M. Bradley, M.L. Nietiadi, W. Möller, Phys. Rev. B **91**, 165418 (2015). doi:10.1103/PhysRevB.91.165418
20. S. Dhara, A. Datta, C.T. Wu, Z.H. Lan, K.H. Chen, Y.L. Wang, L.C. Chen, C.W. Hsu, H.M. Lin, C.C. Chen, Appl. Phys. Lett. **82**, 451 (2003). doi:10.1063/1.1536250
21. C. Borschel, Ion-solid interaction in semiconductor nanowires, Dissertation, University of Jena, 2012. URL http://www.db-thueringen.de/servlets/DocumentServlet?id=20026
22. C. Borschel, M.E. Messing, M.T. Borgström, W. Paschoal, J. Wallentin, S. Kumar, K. Mergenthaler, K. Deppert, C.M. Canali, H. Pettersson, L. Samuelson, C. Ronning, Nano Lett. **11**, 3935 (2011). doi:10.1021/nl2021653
23. R.A. Brown, J.S. Williams, J. Appl. Phys. **81**, 7681 (1997). doi:10.1063/1.365347
24. Memsnet materials database (2012). URL www.memsnet.org
25. C. Lieber, Z. Wang (eds.), *Functional Nanowires*, vol. 32 (2007)
26. C. Jagadish (ed.), *Special issue on Nanowires*, vol. 25 (2010)
27. C. Ning, Phys. Stat. Sol. B **247**, 774 (2010)

28. R.S. Wagner, W.C. Ellis, Appl. Phys. Lett. **4**, 89 (1964)
29. C. Borchers, S. Müller, D. Stichtenoth, D. Schwen, C. Ronning, J. Phys. Chem. B **110**, 1656 (2006)
30. K.A. Dick, K. Deppert, T. Martensson, B. Mandl, L. Samuelson, W. Seifert, Nano Lett. **5**, 761 (2005)
31. J. Johansson, C.P.T. Svensson, T. Martensson, L. Samuelson, W. Seifert, J. Phys. Chem. B **109**, 13567 (2005)
32. M.V. Fernandez-Serra, C. Adessi, X. Blase, Phys. Rev. Lett. **96**, 166805 (2006)
33. P. Xie, Y. Hu, Y. Fang, J. Huang, C.M. Lieber, Proc. Natl. Acad. Sci. USA **106**, 15254 (2009). doi:10.1073/pnas.0906943106
34. D.E. Perea, E.R. Hemesath, E.J. Schwalbach, J.L. Lensch-Falk, P.W. Voorhees, J.L. Lauhon, Nature Nanotechnol. **4**, 315 (2009). doi:10.1038/nnano.2009.51
35. S.J. Whang, S. Lee, D.Z. Chi, W.F. Yang, B.J. Cho, Y.F. Liew, D.L. Kwong, Nanotechnology **18**, 275302 (2007). doi:10.1088/0957-4484/18/27/275302
36. C. Ronning, C. Borschel, S. Geburt, R. Niepelt, Mat. Sci. Eng. R. R. **70**, 30 (2010). doi:10.1016/j.mser.2010.07.002
37. C. Ronning, C. Borschel, S. Geburt, R. Niepelt, S. Müller, D. Stichtenoth, J.P. Richters, A. Dev, T. Voss, L. Chen, W. Heimbrodt, C. Gutsche, W. Prost, Phys. Stat. Sol. B **247**, 2329 (2010). doi:10.1002/pssb.201046192
38. A. Colli, A. Fasoli, C. Ronning, S. Pisana, S. Piscanec, A.C. Ferrari, Nano Lett. **8**, 2188 (2008)
39. S. Hoffmann, J. Bauer, C. Ronning, T. Stelzner, J. Michler, C. Ballif, V. Sivakov, S.H. Christiansen, Nano Lett. **9**, 1341 (2009). doi:10.1021/nl802977m
40. P.D. Kanungo, R. Kögler, K. Nguyen-Duc, N. Zakharov, P. Werner, U. Gösele, Nanotechnology **20**, 165706 (2009). doi:10.1088/0957-4484/20/16/165706
41. T. Hirate, S. Sasaki, W. Li, H. Miyashita, T. Kimpara, T. Satoh, Thin Solid Films **487**, 35 (2005). doi:10.1016/j.tsf.2005.01.031
42. B. Cheng, Y. Xiao, G. Wu, L. Zhang, Adv. Funct. Mater. **14**, 913 (2004). doi:10.1002/adfm.200305097
43. S. Geburt, D. Stichtenoth, S. Müller, W. Dewald, C. Ronning, J. Wang, Y. Jiao, Y.Y. Rao, S. K. Hark, Q. Li, J. Nanosci. Nanotechnol. **8**, 244 (2008). doi:10.1166/jnn.2008.N05
44. C. Ronning, P.X. Gao, Y. Ding, Z.L. Wang, D. Schwen, Appl. Phys. Lett. **84**, 783 (2004). doi:10.1063/1.1645319
45. G. Dieke, *Spectra and Energy levels of Rare Earth Ions in Crystals* (Interscience Publishers, New York, 1968)
46. C. Cascales, M.D. Serrano, F. Esteban-Betegón, C. Zaldo, R. Peters, K. Petermann, G. Huber, L. Ackermann, D. Rytz, C. Dupré, M. Rico, J. Liu, U. Griebner, V. Petrov, Phys. Rev. B **74**, 174114 (2006). doi:10.1103/PhysRevB.74.174114
47. S. Bachir, J. Ronfard-Haret, K. Azuma, D. Kouyat, J. Kossanyi, Chem. Phys. Lett. **213**, 54 (1993). doi:10.1016/0009-2614(93)85417-M
48. H. Ohno, A. Shen, F. Matsukura, A. Oiwa, A. Endo, S. Katsumoto, Y. Iye, Appl. Phys. Lett. **69**, 363 (1996). doi:10.1063/1.118061
49. W. Ren, A. Kuronen, K. Nordlund, Phys. Rev. B **86**, 104114 (2012). doi:10.1103/PhysRevB.86.104114
50. C. Borschel, R. Niepelt, S. Geburt, C. Gutsche, I. Regolin, W. Prost, F.J. Tegude, D. Stichtenoth, D. Schwen, C. Ronning, Small **5**, 2576 (2009). doi:10.1002/smll.200900562
51. C. Borschel, S. Spindler, D. Lerose, A. Bochmann, S.H. Christiansen, S. Nietzsche, M. Oertel, C. Ronning, Nanotechnology **22**, 185307 (2011). doi:10.1088/0957-4484/22/18/185307
52. L. Romano, N.G. Rudawski, M.R. Holzworth, K.S. Jones, S.G. Choi, S.T. Picraux, J. Appl. Phys. **106**, 114316 (2009). doi:10.1063/1.3267154
53. K. Jun, J. Joo, J.M. Jacobson, J. Vac. Sci. Tech. B **27**, 3043 (2009). doi:10.1116/1.3259919
54. D. Stichtenoth, Dimensionseffekte in Halbleiternanodrähten, Dissertation, University of Göttingen, 2008. URL http://webdoc.sub.gwdg.de/diss/2008/stichtenoth/
55. O. Dmitrieva, B. Rellinghaus, J. Kästner, M.O. Liedke, J. Fassbender, J. Appl. Phys. **97**, 10N112 (2005). doi:10.1063/1.1853211

56. A. Klimmer, P. Ziemann, J. Biskupek, U. Kaiser, M. Flesch, Phys. Rev. B **79**, 155427 (2009). doi:10.1103/PhysRevB.79.155427
57. H. Holland-Moritz, S. Scheeler, C. Stanglmair, C. Pacholski, C. Ronning, Nanotechnology **26**, 325301 (2015). doi:10.1088/0957-4484/26/32/325301
58. W. Möller, K.H. Heinig, Collisional transport in ion-irradiated nanowires. Personal communication (2015)
59. A. Johannes, High-fluence ion beam irradiation of semiconductor nanowires, Dissertation, University of Jena, 2015
60. A. Johannes, S. Noack, W. Paschoal, S. Kumar, D . Jacobsson, H. Pettersson, L. Samuelson, K.A. Dick, G. Martinez-Criado, M. Burghammer, C. Ronning, J. Phys. D Appl. Phys. **47**, 394003 (2014). doi:10.1088/0022-3727/47/39/394003
61. A. Johannes, S. Noack, W. Paschoal, S. Kumar, D. Jacobsson, H. Pettersson, L. Samuelson, K. A. Dick, G. Martinez-Criado, M. Burghammer, C. Ronning, J. Phys. D Appl. Phys. **48**, 079501 (2015). doi:10.1088/0022-3727/48/7/079501

Chapter 13
Modification of Structure and Properties of Optical Crystals

Feng Chen and Frank Schrempel

Abstract Amongst others, damage and distortions of optical crystals are accompanied by the modification of the materials refractive indices and chemical resistance. Thanks to the advantages of high precision and high reproducibility with respect to amount and depth distribution of defects, ion irradiation is an excellent method to modify these properties selectively. On this basis, diverse ion beam techniques have been developed to produce optical waveguide structures. The implementation of waveguides in crystals enables a number of applications in integrated optics. In this chapter, the fundamentals of ion beam induced effects in optical crystals are summarized and selected examples for refractive index engineering and photonic applications are introduced.

13.1 Introduction

Besides glasses, semiconductors and polymers, optical crystals are key materials for numerous applications in optics and photonics. In this chapter, we restrict on that class of crystalline dielectric materials. Prominent examples are non-linear crystals used for second-harmonic generation (SHG), optical parametric oscillators (OPO) and amplifiers (OPA) such as lithium niobate (LN), potassium niobate ($KNbO_3$), potassium titanyl phosphate (KTP) and β-barium borate (β-BBO). Photorefractive crystals, e.g. strontium barium niobate (SBN) or barium titanate ($BaTiO_3$), are used for refractive index modulation and laser crystals, e.g. yttrium aluminum garnet (YAG), yttrium vanadate (YVO_4) and rare earth doped sodium yttrium tungstate ($NaY(WO_4)_2$), are used in solid state lasers.

F. Chen (✉)
School of Physics, Shandong University, Jinan 250100, China
e-mail: drfchen@sdu.edu.cn

F. Schrempel
Institut für Angewandte Physik, Friedrich-Schiller-Universität Jena,
Max-Wien-Platz 1, 07743 Jena, Germany
e-mail: frank.schrempel@uni-jena.de

© Springer International Publishing Switzerland 2016

W. Wesch and E. Wendler (eds.), *Ion Beam Modification of Solids*,
Springer Series in Surface Sciences 61,
DOI 10.1007/978-3-319-33561-2_13

Since several years, ion irradiation has become a key technology for the modification of the properties of optical materials since it offers accurate control of the structural modification, which in turn enables the specific variation of optical parameters on the micro- and nanometer scale. As a result several ion beam induced techniques such as ion beam deposition, ion beam milling or etching, ion implantation, focused ion beam writing, crystal ion slicing or ion beam enhanced etching have been successfully established for the fabrication of optical and photonic devices with excellent performance in a wide range of optical materials.

One of the most important effects with respect to application in optical elements originates from the fact that ion irradiation induced damage of optical crystals is closely correlated to a change of the refractive index. Depending on the crystal structure, the kind and strength of damage, the refractive index decreases or increases, respectively. This leads to different concepts of waveguides where adjacent regions of different refractive indices confine the light and allow for the fabrication of surface or buried photonic guiding structures in planar or two-dimensional configurations.

Another method of particular interest is the combination of ion irradiation and wet etching, which enables the production of thin membranes with bulk material properties as well as the patterning on micro- and nanometer dimensions. Both applications are based on the considerable reduction of the chemical resistance due to crystal damage.

However, this chapter can neither reflect the current state of knowledge nor give an all-encompassing analysis of the literature. Therefore, as defined by the topic of the book, the content is restricted to the damage related utilization of ion beam modification. The chapter is structured as follows. Initially, very typical features of ion beam induced damage and its effects on optical crystals are presented. In the following section, the basic methods for the production of optical elements are introduced. The last section gives some prominent applications and shows the extremely high potential of ion beam techniques for the production of optical elements.

Almost all effects in this chapter are demonstrated and explained using the example of LN, one of the most popular and useful optical crystals, but can be also found in nearly all other optical materials in a more or less similar manner.

13.2 Ion Beam Induced Damage and its Effects in Optical Crystals

13.2.1 Damage Formation Due to Nuclear Energy Deposition

The damage in optical crystals caused by elastic collisions has been extensively studied and is reasonably well understood (see [1, 2] and references therein) and

simulation codes are available to describe it [3, 4]. In general, damage accumulation and its dependence on the irradiation parameters follow the rules of "normal" ion implantation as described in Part II. Typically, ion energies and fluences are between several 100 keV up to a few MeV and in the range from 10^{14} to 10^{17} cm^{-2}, respectively, whereas both depend strongly on the ion species and target materials. In this regime, defects are almost solely produced by nuclear energy loss. However, most optical materials feature high complexity regarding the number of different chemical elements and degree of crystal symmetry. Thus, damage investigations are often difficult and some specific effects occur compared to common implantation materials as e.g. semiconductors.

In the following, we describe the basic and most important effects representative for most optical crystals using the example of damage accumulation in LN (see [5, 6] and references therein). Figure 13.1 shows comparative curves of the damage formation (defect concentration as a function of ion fluence) for the irradiation of z- and x-cut LN with various kinds of ions at room and low temperature.

The damage formation can be understood as a two-stage process. For relative defect concentrations up to about 0.15, the defect concentration increases gradually with increasing fluence (pre-damage stage). For higher fluences, the defect concentration increases abruptly (heavy damage stage) up to the amorphization threshold (i.e. relative defect concentration = 1). For a given ion fluence the defect concentration at 15 K is essentially smaller than at 300 K indicating that in situ annealing due to thermal lattice vibrations is suppressed and the primary defects are stable at 15 K.

Above a critical fluence, the near-surface irradiation with light gas ions (H, He) at room temperature leads to the formation of gas bubbles in the implanted layer. Due to the associated stress, fractures occur at the corresponding depth and the surface layer flakes off. The so-called "smart cut" technique utilizes this for the production of thin membranes (see Sect. 13.3.2). However, for other applications, the effect prohibits the generation of an adequate damage, but irradiation at low temperatures avoids the formation of gas bubbles. Moreover, for some types of ions (mainly matrix ions) the defect formation at room temperature irradiation shows an atypical evolution. In these cases, the increase of damage with increasing fluence in the heavily damaged region is lower than expected (see Fig. 13.1a for irradiation with O at room temperature, for clarity data for Li are not shown). At the same time, the damaged area shifts to the surface (not shown). At low temperature, this effect does not occur leading to the assumption that the change in the chemical composition of the material in conjunction with diffusion processes is responsible for the atypical evolution.

Most pronounced in the pre-damage stage, the damage measured by Rutherford backscattering spectrometry (RBS) is much stronger for x-cut than for z-cut (see Fig. 13.1b). For the depth distribution of defects (see Fig. 13.2a), three regions exist: a weakly damaged near-surface covering layer containing point defects, a transition layer in which the defect concentration increases strongly and, depending on the ion fluence, a highly damaged or amorphous buried layer.

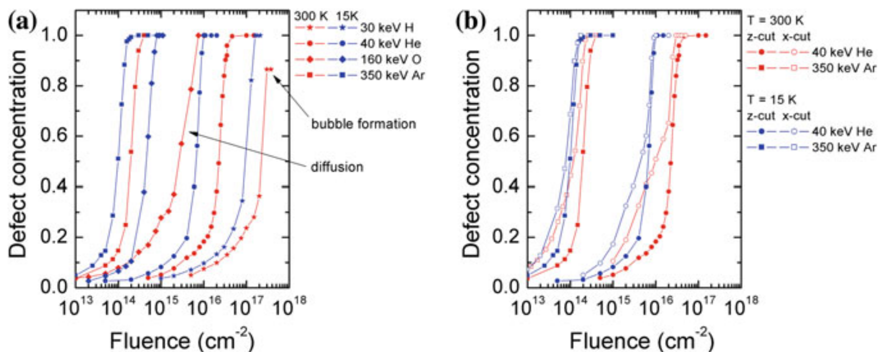

Fig. 13.1 Relative defect concentration obtained from Rutherford backscattering spectrometry as a function of ion fluence for the irradiation of z- and x-cut LN at room temperature and at a temperature of 15 K. The *left* figure **a** illustrates the dependence on the ion mass and the irradiation temperature based on z-cut LN, and the *right* figure **b** visualizes the influence of the crystal cut. Parts of the results are given in [6]

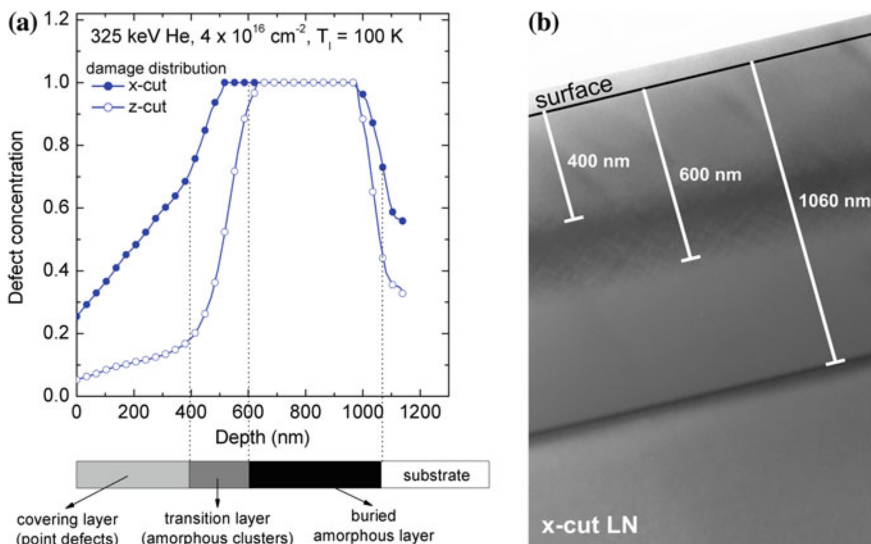

Fig. 13.2 Relative defect concentration as a function of depth for the irradiation of the x-and z-cut LN with 325 keV He ions to a fluence of 4×10^{16} cm^{-2} at T = 100 K (**a**) and TEM image of the x-cut sample (**b**)

However, transmission electron microscope (TEM) images show identical defect structures for both cuts. In particular for the irradiation with 325 keV He ions, Fig. 13.2 shows that the defect structure of x-cut estimated by TEM (Fig. 13.2b) matches the depth distribution of defects of the z-cut better than that of x-cut material measured by RBS. A more detailed view of the transition region shows

that it consists of defect clusters embedded in the crystalline matrix. At larger depths, the transition to the substrate occurs with a sharp interface.

In the pre-damage stage (compare Fig. 13.1), where the relative defect concentration corresponds to that of the covering layer of the depth distribution in Fig. 13.2, point defects are primarily generated, which lead to a preferential rearrangement of the displaced Nb atoms to vacant octahedral sites [7]. These vacant octahedral sites are located within the rows of Li- and Nb-atoms along the z-axis. Consequently, for z-cut LN the atoms of the corresponding strings shadow these sites. On the contrary, for x-cut LN these places are situated close to the center of the axial channel causing a huge backscattering yield in the RBS measurement. Assuming a mean displacement of 0.95 Å from the string, which corresponds to the preferred positions on the octahedral sites, approximately 10 % of displaced Nb-atoms occupy such sites. Hence, the apparently higher defect concentration of x-compared to z-cut is only a measurement effect caused by the different visibility of displaced atoms in the RBS measurement [6, 7]. Recent measurements performed on the same crystal from both directions proved this speculation clearly [8]. With decreasing irradiation temperature the difference of the measured defect concentration decreases between the two investigated crystal cuts (see Fig. 13.1b) leading to the conclusion that the preferred defect distribution is a result of a thermally activated process. At least for the irradiation at 15 K, the critical fluence for amorphization is almost independent of the crystal cut. However, it should be mentioned that during irradiation at low temperatures in situ annealing due to electronic energy deposition might occur [9].

In the heavy damage stage corresponding to the defect concentration in the transition layer, heavily damaged defect clusters are formed leading to a completely random distribution of the Nb atoms. For the irradiation with heavy ions (e.g. Ar) the amorphization fluence is about 10^{14} cm^{-2}, while the use of lighter ions (e.g. He) requires significantly higher fluences up to 10^{17} cm^{-2}. Besides the fact that the number of displaced lattice atoms per incident ion increases with increasing ion mass, the collision cascades of ions with larger masses are denser, which favors the formation of defects and defect complexes.

By using ion irradiation in the nuclear regime, researchers have successfully fabricated optical elements in more than 100 optical materials (see [10] and references therein) demonstrating the wide applicability and excellent control of the change of optical properties related to a specific crystal damage. Generalized and with respect to application, the ions used for the irradiation of optical crystals are basically divided into two groups, i.e. light (H and He) and heavy (atomic number no less than 6, e.g., C, N, O, Si, Ar) ions. For light-ion irradiation, the nuclear damage is dominant and the electronic contribution is negligible. Advantages of light-ion irradiation are the minor modification of the bulk material and a relatively large penetration depth (typically a few micrometers) at moderate ion energies of 400 keV up to 3 MeV. This allows the generation of buried layers as needed e.g. for waveguide barriers or slab etching (see Sect. 13.3). However, the required fluences are relatively high, which necessitates irradiation at low or elevated temperatures in order to avoid bubble formation. In this respect, heavy ions are more

effective, because typically required fluences are much lower than for light ions. Unfortunately, in order to obtain comparable depths of modification, high energies from 3 to 7 MeV are needed. Then damage due to electronic excitation may become important causing an undesired modification of the bulk crystal.

13.2.2 Damage Formation Due to High Electronic Energy Deposition

Currently growing interest emerges in the application of high energy medium mass ions (e.g. Si, O of MeV energies), where the electronic energy loss gains influence. Numerous crystalline materials are damaged according to electronic energy deposition (see Part III, Chaps. 8 and 9). In contrast to the damage formation due to nuclear energy loss, the understanding of the damage due to electronic excitations is still an evolving field. Generally, for the materials of interest in this chapter electronic damage occurs for ions having a mass number larger than 15 and energies around or above 0.1 MeV/u (swift heavy ions). By the substantiated state of knowledge, above a certain material dependent threshold of the electronic stopping power, the impact of each single ion forms an amorphous track. For LN, for example, this threshold is 5 keV nm^{-1} [11–13]. Despite the existence of several models (for details see Part I, Chap. 2), almost all experimentally observed effects could be reliably described in the framework of the thermal spike model, which assumes that the material melts along the ion trajectory [14–16]. In particular, this model provides a clear explanation for the occurrence of the well-defined stopping power threshold to generate the tracks.

For subthreshold irradiation, the situation becomes more complicated. Experimentally it has been found that defects are created as well due to electronic energy deposition, but only point defects are generated which accumulate to an amorphous layer with increasing ion fluence (see [17] and references therein). The defect concentration is strongly nonlinear dependent on the electronic energy loss. The defect accumulation has cumulative character and it is supposed that the lattice collapses if a critical defect concentration is reached. Using this process the crystal can be damaged by one irradiation from the surface to depths larger than several micrometers with fluences that are essentially smaller compared to those necessary when using the nuclear energy loss. The thermal spike model cannot describe the formation of point defects, i.e. the cumulative character of the damage and the sub-threshold damage, unless some additional processes for defect production are taken into account. In order to describe these features of damage a new model has been proposed, which explains the damage formation by the synergy between thermal spike and exciton decay (see Chap. 2 as well as [17] and references therein). In this model it is assumed that, although the material does not melt, the increase of the temperature provides the energy for trapped excitons to overcome a certain energy barrier. The following non-radiative exciton decay gives rise to

lattice displacements. This model has been successfully applied to various experimentally observed facts. In particular, it satisfactorily explains the nonlinear dependence of the damage with electronic stopping power, the thresholding effect for amorphization and the cumulative character of damage.

As before, we representatively demonstrate the basics and most important effects using the example of the damage accumulation in LN (for more information see [5] and references therein). Figure 13.3a shows the defect concentration as a function of depth for the irradiation with 5 MeV Si ions of different ion fluences at a temperature of 15 K.

The depth distributions of the electronic and nuclear energy loss are given as solid and dashed line, respectively. According to this, the damage peak at a depth of about 2 μm is clearly associated with the nuclear damage, whereas the strong damage in the surface region is attributed to the electronic part of the energy deposition. The electronic energy deposition has a maximum value of about 4.2 keV nm^{-1} at the surface and decreases with increasing depth. Correspondingly, the damage produced decreases with increasing depth. Between these regions, defects are created due to the synergy of electronic and nuclear damage. However, it has been shown that this damage is overestimated to a great amount [18].

The amount of produced damage depends not only on the depth, i.e. on the electronic energy deposition, but also on the ion fluence. The influence of the irradiation temperature on the fluence dependence of the damage formation due to electronic energy deposition is given in Fig. 13.3b. Clearly, the dependence of the defect concentration on the ion fluence is identical for stepwise irradiation and measurement (in situ) at 300 K, for irradiation of a set of samples with different fluences at 300 K and measurement after some days as well as for in situ irradiation and measurement at 15 K. From these facts, three essential conclusions can be drawn: (i) No defect annealing occurs due to the RBS-measurement as it has been

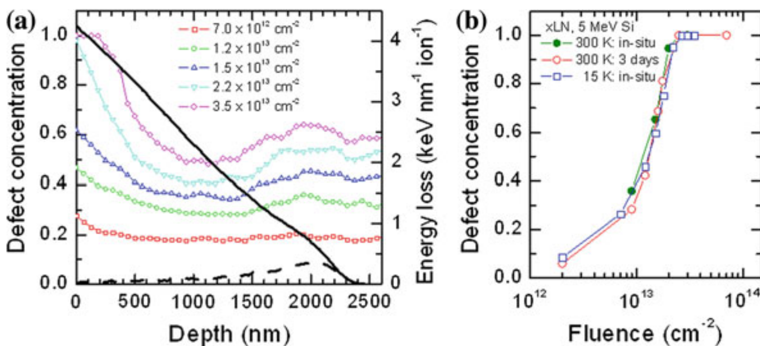

Fig. 13.3 Defect concentration versus depth for x-cut LN irradiated with 5 meV Si ions of different fluences at a temperature of 15 K (**a**) and defect concentration taken at the surface versus ion fluence for the irradiation at temperatures of 300 and 15 K, respectively (**b**). The depth distributions of electronic and nuclear energy loss are given in (**a**) as solid and dashed line, respectively. Parts of the results are given in [83]

observed for nuclear damage at 15 K [9]. (ii) For electronic damage, the primary defects are stable even at room temperature. This is completely different compared to nuclear damage, where it has been found that the primary defects are stable at 15 K, but in situ defect annealing occurs at 300 K [6]. (iii) Furthermore, no room temperature annealing of defects occurs within some days after the irradiation. The latter is in contrast to high-energy oxygen irradiation, where it has been found that the damage component induced by electronic stopping interaction is dramatically affected by room temperature aging, whereas the nuclear induced damage needs high temperature annealing to be recovered [19].

So far it is believed, that due to electronic damage of LN randomly displaced atoms and amorphous clusters are formed exclusively and, therefore, the damage formation is assumed to be independent of the crystal cut. Figure 13.4 shows the defect concentration versus ion fluence for x- and z-LN irradiated with 5 MeV Si-ions at room temperature.

Up to a defect concentration of about 0.5 x-cut LN appears significantly more damaged compared to z-cut. This cut dependence is well known for damage by nuclear energy deposition (see Sect. 13.2.1). In that case, the difference has been explained by the fact that the displaced Nb-atoms preferentially occupy vacant octahedral sites, which implicates that point defects are the most likely kind of defects. Thus, it can be concluded that for small defect concentrations equal defects are formed by both mechanisms. For defect concentrations above 0.5 x- and z-cut LN are identically damaged, i.e. no preferred positions exist anymore. In conjunction with the strong increase of the defect concentration with fluence this indicates the formation of defect clusters and amorphous domains. For nuclear energy deposition and high defect concentrations, also a sharp increase in defect concentration was observed and explained by the formation of amorphous clusters, but still there was a clear difference between the x- and z-cut LN.

The defect accumulation due to electronic energy deposition can be summarized as follows. For low defect concentrations, point defects are generated preferentially

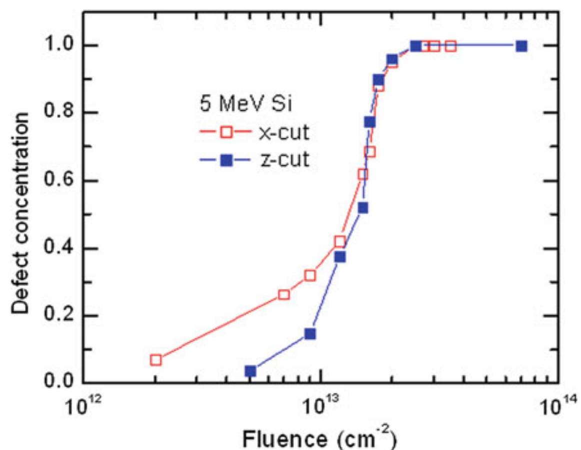

Fig. 13.4 Defect concentration versus ion fluence for x- and z-cut LN irradiated 5 MeV Si ions at room temperature

occupying vacant octahedral sites of the lattice. At a defect concentration of about 0.5 defect clusters and amorphous domains embedded in the crystalline matrix start to form. They grow with increasing ion fluence until the formation of amorphous regions. An intriguing feature of swift ions is the ultralow fluences required to achieve a certain degree of damage, which are 2–4 orders lower compared to nuclear energy deposition.

13.3 Methods for the Production of Optical Elements Based on Crystal Damage

In this section, we solely restrict to methods for the production of optical elements, which utilize the creation of defects due to ion irradiation. Without going further into it, it should be mentioned that ion irradiation creates optical absorption sites and damages somehow the original structures. Consequently, the bulk properties as well as the magnitude of electro-optical and nonlinear optical coefficients are usually not retained and light loss is increased. Therefore, in order to anneal defects, thermal treatment is commonly necessary for all ion-irradiated crystals [1]. The methods used include conventional furnace [20], rapid thermal [21] and laser beam annealing [22–24]. Depending on the kind and the amount of defects as well as on the substrate properties, thermal treatment at temperatures between 200 and 500 °C is performed for tens of minutes to several hours. The advantage of rapid thermal annealing is that defects may be annealed while avoiding undesirable diffusion processes.

But even with the above-mentioned restrictions, this chapter cannot treat all results obtained over the years comprehensively. Therefore, it is referred to some excellent review papers that summarize the contributions of various authors. The first overview of ion-implanted waveguides in insulating materials was performed by Townsend et al. [1] summarizing the early obtained results before 1993. This was followed by the review of Chen et al. [2] giving the progress between 1994 and 2006. In 2005, Levy et al. [25] summarized the crystal ion-slicing technique applied on ferroelectric crystals for producing photonic guiding membranes. Pollnau and Romanyuk [26] reviewed the fabrication of optical waveguides in laser crystals. In 2008, Olivares et al. [11] demonstrated waveguide fabrication by the irradiation with swift heavy ions and Chen [27] focused on the 2D waveguide production in insulating materials. In 2009, Chen presented a comprehensive review on LN photonic guiding structures formed by energetic ion beams [5] and 2012 on micro- and sub-micrometer waveguiding structures in optical crystals [10].

The research field is still highly active and, particularly in recent years, much work has been performed on ion-sliced photonic structures, swift heavy-ion irradiated waveguides as well as on related photonic applications by researchers worldwide.

13.3.1 Refractive Index Modulation and Waveguides

Undoubtedly, optical waveguides are of most fundamental importance for the realization of optical components, because—regardless of the purpose—for efficient performance the light must be concentrated in the active zone and transmitted between several elements. Concrete examples are low pump thresholds for waveguide lasers, fast responses for photorefractive waveguides and multiple configurations for frequency conversion [28–31]. Additionally, benefiting from the compact size, photonic components may be integrated on a small chip, realizing both passive (e.g., optical switches) and active applications (e.g., modulators, amplifiers, lasers and frequency converters) [32–35]. These guiding structures confine light by total internal reflection or photonic bandgaps (PBG) [36, 37]. Such waveguides are realized either by the distinct modification of the refractive index (planar and channel waveguides) or by 3D structuring of the material (ridge waveguides, photonic crystal waveguides). In order to get conversion efficiencies as high as possible, special attention has to be paid to the conservation of the bulk crystal properties and minimization of both light absorption and surface roughness at boundaries in order to suppress light scattering. Due to the variety of materials and configurations, numerous methods have been developed to fabricate optical elements that fit the specifications desired by the applications. These include the indiffusion of metal ions (such as Ti, Zn, Fe) [30, 38–40], ion exchange [41–44], sol gel methods [45], film epitaxy/deposition (sputtering, pulsed laser deposition (PLD), liquid phase epitaxy (LPE), etc.) [46–51], ultrafast laser writing [52–59] and optical induction (solitons, UV light irradiation, etc.) [60, 61].

Optical waveguides are defined as structures with high refractive indices surrounded by low-index layers/regions. Most studied and best known is the decrease of the refractive index caused by the reduction of the physical density that arises from nuclear damage after light ion implantation. The amount of the refractive index change is in the order of a few percent depending on material and irradiation conditions. In this way, the waveguide is between the crystal surface and a buried damaged layer acting as a waveguide barrier and is therefore often called “barrier index type” profile (see Fig. 13.5a).

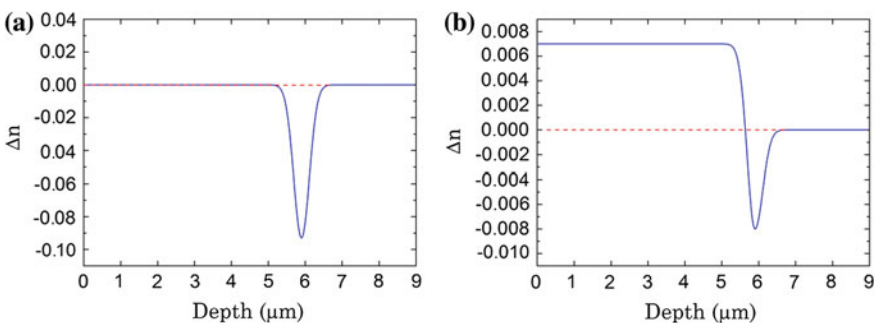

Fig. 13.5 Schematics of the refractive-index profiles of ion-beam-processed waveguides: “barrier” type (**a**), “enhanced well + barrier” type (**b**) [10]

This method has been successfully applied to many crystals [1, 2], such as LN, potassium titanyl phosphate (KTP) or lithium triborate (LBO). Indeed the barrier width obtained by a single ion implantation is relatively small so that leakage modes into the substrate may occur resulting in increased propagation losses of the waveguide. However, multiple energy irradiation broadens the barrier and improves the guiding properties.

Investigations in recent years showed that damage obtained from high electronic energy deposition due to swift heavy ion irradiation creates a buried, highly damaged or even amorphized layer allowing for the generation of wider barriers by a single irradiation step [11, 62]. An additional advantage is that the required fluence to obtain the same degree of damage is 2–4 orders of magnitude lower compared to the irradiation in the nuclear regime [63, 64]. As a third advantage, the index reduction can be as large as 10–20 %, which is several times larger than that of the barriers obtained from nuclear damage. Thus, such waveguides can confine the light field better. So far, this technique has been applied to realize waveguides in about 10 different optical crystals (see [2, 10] and references therein), including LN, potassium gadolinium tungstate (KGW), yttrium aluminum garnet (YAG), gadolinium gallium garnet (GGG), potassium lithium tantalate niobate (KLTN), a-SiO_2, gadolinium and yttrium calcium oxoborate (GdCOB, YCOB), yttrium vanadate (YVO_4) and bismuth germanium oxide (BGO).

The “barrier index type” profiles discussed above strictly hold only for heavily damaged or amorphous material. Low or pure ionization damage may otherwise increase the refractive index caused by lattice compression due to formation of damage tracks as well as change of bond polarizabilities. This allows for the generation of “enhanced well type” index profiles, where the irradiated regions act as waveguide. Examples are waveguides fabricated in BGO and YAG [65, 66]. The formation of the enhanced well is complex and closely correlated to the material properties [2]. Often, but not always changes in anisotropy and birefringence of crystals accompany the refractive index increase due to ion damage. Especially for implantation with heavy ions, but sometimes also in the case of light ions, the combination of both effects is observed. Then the regions with increased refractive index confine the light together with the waveguide barrier defining an “enhanced well + barrier type” index profile (see Fig. 13.5b). For this case, the most studied example is LN, where the ordinary and the extraordinary refractive index have a “barrier index type” and an “enhanced well + barrier type” index profile, respectively.

With respect to the theoretical explanation, the barrier model has been widely accepted to explain the barrier-type refractive index profiles of all ion-implanted waveguides in insulating optical materials. Since the change of the extraordinary refractive index is much more complicated, several groups have proposed different models: activated ion diffusion, birefringence modification, modification of spontaneous polarization, lattice damage and depolarized cluster formation (see [5] and references therein). One should note that these models are not contradictory in most cases and seem reasonable in some aspects. Depending on the material and irradiation conditions, some materials may have more complex distributions, such as buried mode wells and missing wells [5, 67]. However, with respect to application,

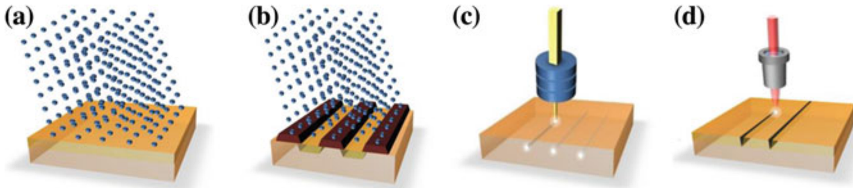

Fig. 13.6 Schematic plots of the optical waveguides waveguides produced by ion beam techniques under configurations of planar (**a**), surface channel by mask-assisted irradiation (**b**), buried channel by focused ion beam writing (**c**) and ridge by femtosecond laser ablation (**d**) [10]

the mentioned index profiles seem to be adequately precise for designing waveguide structures.

Owing to the total internal reflection, waveguides can confine light propagation within small volumes in one (1D planar configuration) or two (2D channel or ridge geometry) transversal dimensions [68]. For planar waveguides, direct irradiation is performed (Fig. 13.6a). For 2D channel waveguides, mask-assistant ion irradiation (Fig. 13.6b) or mask-free focused ion beam (H or He) writing (Fig. 13.6c) is used to construct surface or buried structures. For ridge waveguides, additional treatments, e.g., ion beam etching, chemical etching, femtosecond laser ablation (Fig. 13.6d) or diamond saw dicing must be performed to pattern the planar waveguide surface [22].

Waveguide structures are usually characterized by small dimensions, which allow the fabrication of compact optical circuits or chips for a rich variety of applications by combination of different photonic components. In addition, some properties of the substrate materials can be considerably improved in waveguide geometries with respect to the bulk platform. With those advantages, chip-scale integration of various photonic elements can be realized enabling a distinct miniaturization of optical systems [32]. Since the first ion beam produced waveguide in fused silica has been reported in 1968 [69], a vast number of waveguiding structures or devices have been developed for a wide variety of applications in the past 45 years (see [1, 2, 5, 10, 11, 25, 27] and references therein).

13.3.2 Crystal Ion Slicing (CIS)

Besides the fact that the refractive index is changed, the chemical resistance of heavily damaged optical crystals may be considerably reduced, and, as a result, the irradiated regions can be selectively removed by wet chemical etching. A technique called crystal ion slicing (CIS) utilizes this for producing thin films of materials on a substrate, commonly an insulator.

Originally developed for the production of silicon on insulator (so-called "smart cut" technique [70]), CIS is nowadays applied to a series of crystals, e.g. $LiNbO_3$

[5, 25, 71–76], $LiTaO_3$ [25], $KTaO_3$ [77], $SrTiO_3$ [78]) and diamond [79] to fabricate membranes with thicknesses from several hundred of nanometers to a few micrometers. In a two-step process, firstly a buried heavily damaged or amorphous layer is created by ion irradiation, commonly carried out with light ions. Secondly, selective etching of the damaged layer in an appropriate etchant (e.g. HF acid) is performed and the surface layer can be lifted off. Sometimes, instead of etching a thermal treatment affecting the growth of cavities and bubbles at the damaged interface is applied [74–76]. In this case, internal stress and micro cracks finally result in the detachment of the surface. Depth and width of the damage distribution defines the thickness of the resulting membrane. Because the damage is created by nuclear energy deposition, the fluences required are comparatively high, i.e. in the order of a few 10^{16} cm^{-2}.

In this way, freestanding membranes or membranes bonded on other substrates, e.g. low refractive index substrates (like fused silica), have been produced for photonic applications. Nowadays, CIS allows for the production of bulk quality membranes having wafer dimensions, which are commercially available, e.g. LN membranes bonded on fused silica (also called LNOI).

Furthermore, it has been shown that He ion irradiation in bulk LN at low temperatures can achieve membrane thicknesses down to 200 nm [80]. Figure 13.7 shows the width of the air gap as a function of the normalized ion fluence as well as SEM micrographs of membranes. The normalized ion fluence is the number of displacements per atom n_{dpa} obtained from the ion fluence N_I by $n_{dpa} = (N_I N_{displ})/N_0$ where N_{displ} and N_0 denote the number of displacements per atom calculated with SRIM [4] and the particle density, respectively. The widths obtained from the SEM images and those estimated from the damage profiles as well as from the calculation with SRIM are in good agreement. The widths of membrane and air gap can be adjusted independently over a wide range by proper adaptation of ion energy and fluence.

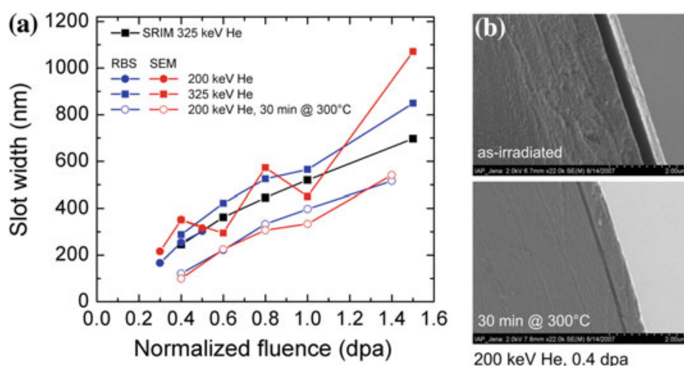

Fig. 13.7 Width of the air gap as a function of the normalized ion fluence (number of displacements per atom, see text) (**a**) and side view SEM images of membranes (**b**) fabricated in *x*-cut LN by irradiation with 200 keV He ions at 100 K. Thermal treatment was applied at 300 °C for 30 min, and etching was done in 3.7 % HF solution at 40 °C [80]

Although the low etching rates do not allow for the fabrication of large-area films, the process enables the 3D integration of advanced optical systems such as photonic crystal devices in bulk LN crystals (see Sect. 13.4.4). In this case, the achievable area depends on the configuration of openings, which enables the access of the etchant.

13.3.3 Ion Beam Enhanced Etching (IBEE)

The structuring of optical materials in the micro- and nanometer range enables complex light-matter interactions, which are particularly strong when resonances occur (photonic crystals, metamaterials and effective media). This allows both the comprehensive control of light propagation and the control of the light distribution at nanometer dimensions within the material. For example, very small electrically tunable filters and switches become realizable using crystals with electro-optical properties. Furthermore, resonant structures in nonlinear materials can be used for intensity-dependent transmission or reflection. Essential for the realization of such devices is the ability to pattern materials with very high electro-optic or nonlinear-optic coefficients (e.g. LN).

Unfortunately, the high chemical resistance of most materials complicates the manufacturing of micro- and nanostructures by standard wet-etching technologies. Therefore, a series of alternative technologies such as reactive ion etching (RIE), ion beam etching with inert and reactive ions (IBE, RIBE), direct patterning by sputtering with the Focused ion beam (FIB), laser ablation as well as wet chemical etching after previous inversion of ferroelectric domains, ion exchange or ion irradiation have been investigated and applied for structuring (see [6, 26] and references therein).

Despite all the success during the last years, all methods mentioned above exhibit limitations with respect to the desired structural properties for photonic applications. In particular, the realization of small structure sizes in the sub-micron range, high aspect ratios, small roughness of the surface and the possibility of real 3D structuring is challenging. Furthermore, there are some restrictions considering type and shape of the achievable structures (e.g. domain inversion, proton exchange). A technique often referred to as Ion Beam Enhanced Etching (IBEE), which is a combination of ion irradiation and chemical wet etching similar to the CIS technique, can fulfill the aforementioned requirements [6, 81–86]. Thereby, crystal damage is created via nuclear energy deposition at low ion energies [6, 82], electronic energy deposition in the case of swift heavy ion irradiation [83, 86] or a synergy of both effects in moderate energy regimes [84, 85]. Afterwards, the damaged material is removed by wet etching in an appropriate etchant.

The etching behavior of ion irradiated LN has been investigated thoroughly based on homogeneously damaged thick layers. As an etchant HF or KOH can be used [82, 87]. The latter is important especially for the structuring of lithium niobate on insulator (LNOI, LN on top of a SiO_2 layer being deposited on a bulk LN) substrates

because selectivity between damaged crystal membrane and substrate (SiO_2 etches in HF, but not in KOH) is obtained.

Figure 13.8a shows the mean etching rates as a function of the normalized fluence for etching of LN irradiated with Ar ions in 3.7 % HF at temperatures of 24, 40, and 55 °C, respectively. Apparently, the etching rate shows the same dependence for each temperature. The etching rate of the perfect LN crystal is below 0.1 nm min^{-1}. It increases rapidly at a normalized fluence of 0.15 dpa, and saturates at 0.4 dpa. The maximum etching rate clearly increases with increasing temperatures and amounts to 22, 130, and 200 nm min^{-1} at etching temperatures of 24, 40, and 55 °C, respectively. This yields an average increase of 5.7 nm min^{-1} K^{-1} in the range of temperature investigated. Furthermore, the etching rate is increased to 1760 nm min^{-1} using a total HF concentration of up to 40.8 % [82].

With respect to the etching process, there is a universal relationship between defect concentration and etching rate (see Fig. 13.8b). Below a defect concentration of 0.2 the etching rate is negligibly small. Above this value, it increases with increasing defect concentration and reaches a maximum value for completely amorphized material, i.e. at a defect concentration of 1. Key feature is the very high selectivity of the process resulting from the negligible etching rate of the non-irradiated material and its sharp increase with increasing ion fluence. This ensures a high contrast of the etching process. As both high selectivity and small surface roughness of the obtained structures are independent over a wide range of concentration and temperature of the etchant, the etching process can be considered extraordinarily robust and reliable.

For lateral structuring, the crystal has to be damaged starting from the surface down to the desired depth (see Fig. 13.9a). Here, a homogenously damaged—typically amorphous—layer is achieved by irradiation with ions of different energies and correspondingly adapted fluences. The use of masking techniques

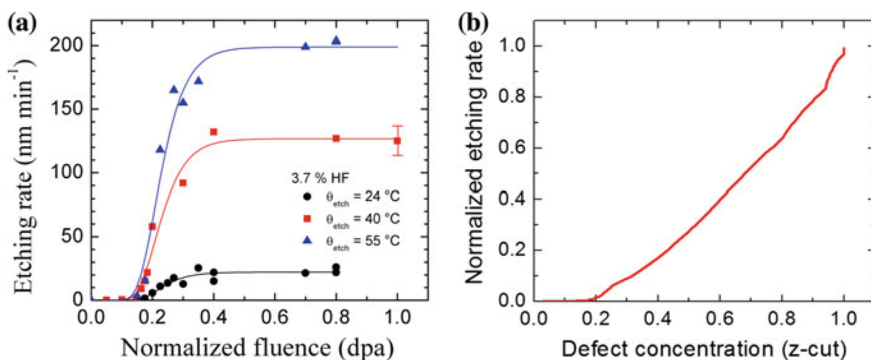

Fig. 13.8 Etching rate of Ar ion irradiated LN for etching in 3.7 % HF as a function of the normalized ion fluence (number of displacements per atom) for different etching temperatures (**a**) and normalized etching rate versus the relative defect concentration measured for x-cut LN (**b**) [82]

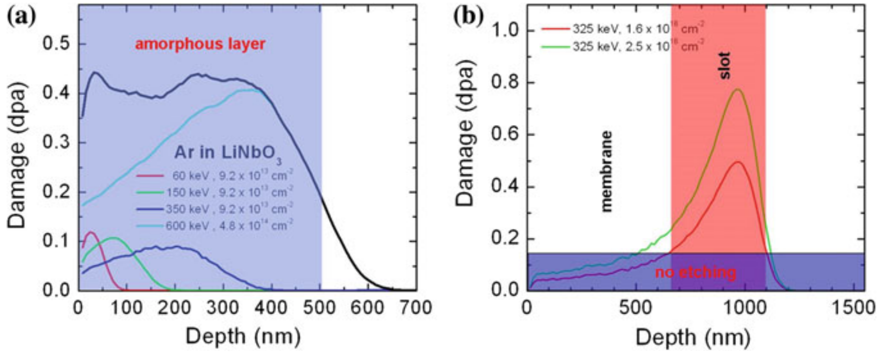

Fig. 13.9 Irradiation with ions of different energies and fluences for lateral structuring (**a**) and generation of a buried amorphous layer for membrane production (**b**). The axes gives the relative defect concentration (damage) versus the depth

accomplishes lateral selective damage, in which the accurate transfer of the mask shape to the damage of the crystal is facilitated by the high selectivity of the etching process. One difficulty is that masks with thicknesses approximately equal to the desired structural depth are required. This makes high demands on the mask technology, because the target structures with dimensions in the sub-micron range, high aspect ratios and low roughness require the production of masks with high accuracy and reproducibility. When using conventional ion implanters with acceleration voltages of 400 kV maximum structure depths between 500 nm (heavy ions, for example Ar) and 1 μm (light ions, such as He) are achieved. Structures deeper than 1 μm may be produced by repeating the process of ion irradiation and etching. A less time consuming method is the irradiation with swift heavy ions [83, 88], supported by the fact that the defect generation is done very efficiently by the electronic energy deposition of the ions (see Sect. 13.2.2).

For the production of thin membranes (~500 nm), such as those required for optical components with single mode operation and strong light guiding, a buried amorphous layer is created at the desired depth (Fig. 13.9b). Thus, light ions have to be used for irradiation since heavy ions damage the surface too much. The thickness of the membrane as well as the width of the subjacent slit can be adjusted independently with the energy and fluence of the ions (see Sect. 13.3.2).

In summary, the IBEE technique allows the realization of 3D micro- and nanostructures with high aspect ratios. The roughness of the etched horizontal surfaces is comparable to typical substrate roughnesses. On the other hand, the roughness of the structural walls is only determined by the quality of the corresponding mask. The method is not restricted to LN crystals, but can be applied to almost all optical crystals using correspondingly adjusted conditions with respect to irradiation and etching. Some examples are given in [26]. Own experiments proved the applicability of the IBEE method for the patterning of potassium titanyl phosphate (KTP), yttrium aluminum garnet (YAG), lutetium aluminum garnet

(LuAG), aluminum oxide (Al_2O_3), yttria (Y_2O_3), scandium(III) oxide (Sc_2O_3) and yttrium lithium fluoride (YLF) using hydrofluoric acid (HF) and phosphoric acid (H_3PO_4) as etchants, respectively (unpublished).

13.4 Application of Ion Beam Induced Effects for the Production of Optical Elements

In this section, selected applications of ion beam processed waveguides as electro-optical modulators, frequency doublers and waveguide lasers are described.

13.4.1 Electro-optical Modulators

Electro-optical (EO) modulators are key elements in optical communications. They utilize the electro-optical effect, i.e. the change of the refractive index of materials (usually called EO crystals) induced by external electrical fields. Consequently, phase, frequency, amplitude or polarization of light can be modulated. In the linear case, the refractive index change Δn is proportional to the amplitude of the electric field and depends cubed on the refractive index (n^3). The key material parameter is the linear EO coefficient that determines the strength of the effect.

Compared to bulk EO modulators a waveguide configuration has the advantage of long interaction lengths. However, the EO coefficient is strongly correlated to the perfection of the EO crystal lattice structures. Since the energetic ions, employed to fabricate the waveguide structures, create nuclear and electronic damage, the EO properties of the crystals may be affected. In most cases, clear degradation occurs due to the structural modification of the original lattice. This drawback somehow limits the application of as-ion-irradiated waveguides. However, appropriate post-irradiation treatment can anneal the lattice damage and remove the defects considerably, which recovers the EO properties in the irradiated regions significantly. For example, it has been reported that, after suitable annealing treatments, ion irradiated LN waveguides possess well preserved EO properties (80–90 %) of the bulk [5] and, swift heavy ion irradiated waveguides maintain about 40–60 % of the bulk EO features [5, 11]. The ion sliced freestanding LN membranes have even almost the same values of the EO coefficients as those of the bulks [5, 25].

Ion beam processed photonic waveguiding structures have been fabricated, mostly using Mach–Zehnder geometry, in several EO crystals, among them LN [25, 89] and barium borate (β-BBO) [90]. Owing to the retained bulk-level EO features, ion sliced LN modulators are of high quality at near infrared and visible light wavelengths. The β-BBO waveguide modulators mainly work in the blue light and ultraviolet (UV) regimes. Exemplarily, Fig. 13.10a visualizes an EO modulator in a BBO-crystal having the shape of a ridge waveguide (for details see [90]).

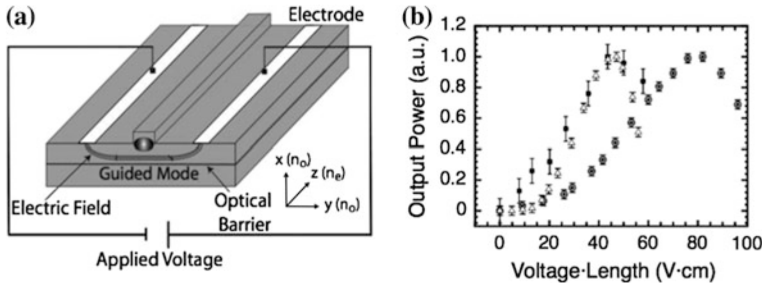

Fig. 13.10 Configuration for the EO amplitude modulator in a He implanted ß-BBO ridge waveguide (**a**) and the comparison between the measured voltage-length in modulators of different lengths at wavelengths of 257 nm (■), 373 nm (△), and 430 nm (⊙) (**b**) [90]

Figure 13.10b shows the power transmitted by the modulator as a function of the voltage-length in different modulators and at different wavelengths. The voltage-length is the product of the voltage difference between the switching states (i.e. optical state of the output switched from one to another) and the total length of the electrodes. The lower the voltage length at the maximum output power ($V_{\pi-L}$) the better. The β-BBO ridge waveguide modulators have values of $V_{\pi-L}$ = 43 V cm and $V_{\pi-L}$ = 79 V cm at wavelengths of 257 and 430 nm, respectively (see Fig. 13.10b). LN membrane modulators currently achieve 13 V cm at 1.55 μm, which means, for the device with 1cm long electrode, the driving voltage for telecommunication wavelength band is 13 V.

13.4.2 Guided-Wave Frequency Doublers

Nonlinear crystals can be used to convert light by means of second or higher-order harmonic generation. Second harmonic generation (SHG) realizes nonlinear frequency doubling from longer wavelengths to shorter ones using birefringent phase matching (PM) or quasi-phase matching (QPM) mechanisms. In waveguides, the SHG efficiency may be enhanced owing to the dedicated compact geometries of the structures, which enable high optical intensities inside the waveguides [31]. In addition, waveguides carry light in specific modes and more options to control the SHG process may be available from different modes of fundamental and second harmonics. The SHG efficiency is proportional to the square of the efficient nonlinear coefficients of the crystal, which is a parameter closely related to the perfection of the crystal lattice. For ion beam fabricated waveguides, the nonlinear coefficients usually will be affected by the nuclear and/or electronic damage resulting in a degradation of the SHG efficiency. The positive effect of a well-defined waveguide geometry and the negative effect caused by ion beam induced damage determine the final responses of the ion irradiated nonlinear waveguides.

It has been found that LN waveguides irradiated with light ions well maintain the nonlinear coefficients of the bulk. The second order nonlinear coefficient is only reduced at the barrier region due to the large disorder of the lattice induced by the nuclear collisions. In contrast, in LN waveguides irradiated with swift heavy ions the second order nonlinear coefficient within the waveguide region is reduced to 60–90 % of the bulk value [91].

A very successful example for guided-wave frequency doublers are He ion implanted potassium niobate ($KNbO_3$) waveguides providing efficient conversion of blue light SHG owing to both large nonlinear coefficients and good guiding quality [92]. The obtained maximum conversion efficiency and the maximum output power for a planar waveguide are 12.1 %/W and 320 mW, respectively. This is comparable or even higher than PM-based waveguiding SHG for a ridge waveguide. An alternative candidate for blue light SHG are He ion implanted gadolinium calcium oxoborate (GdCOB) waveguides. With planar and channel waveguides based on this material conversion efficiencies of 0.4 and 0.32 %/W at cw 822 nm pump laser power of 250 mW were demonstrated [93]. It is also possible to use QPM waveguides to generate blue light, for example, by using periodically poled lithium niobate (PPLN) waveguides. The SHG efficiency of a He-ion implanted PPLN channel waveguide reached 34.5 %/Wcm^2 [94].

For green light SHG, GdCOB waveguides can be considered as promising candidates. Figure 13.11 shows the laser spectra of the fundamental and the SHG light as well as the corresponding modal profiles of the waveguide. Under pump of pulsed laser at 1064 nm, the SHG conversion efficiencies of green light at 532 nm of swift heavy ion irradiated Nd:GdCOB reach 4.6 and 11.4 % in planar and ridge waveguide geometries, respectively [95].

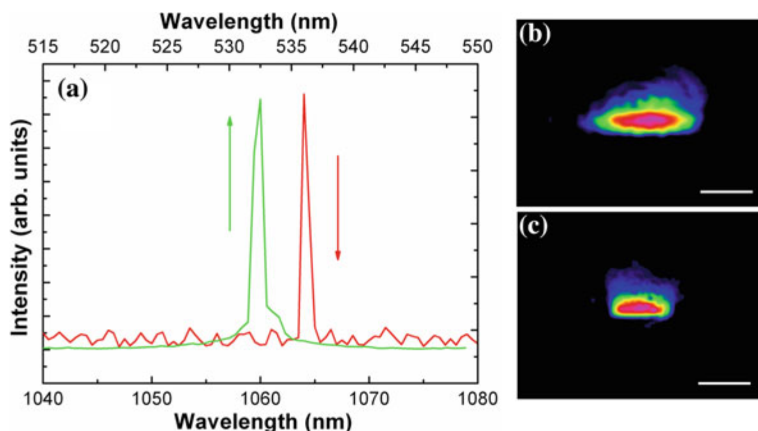

Fig. 13.11 Laser spectra of the fundamental (*red*, at 1064 nm) and SH (*green*, at 532 nm) waves from the 40-μm wide Nd:GdCOB ridge waveguide (**a**) and the related modal profiles of 1064 nm (**b**) and 532 nm (**c**) beams. The scale bar is 20 μm [95]

Waveguides in β-BBO could be also applied as frequency doublers in the UV wavelength regime. By using a ridge waveguide sample produced by He ion implantation, a maximum conversion efficiency of 0.16 %/Wcm^2 was measured at 278 nm for cw SHG, corresponding to 24 μW with input power of 153 mW [96]. In addition, the SH power of about 300 μW at 266 nm was obtained at 532 nm cw fundamental laser with input power of 650 mW corresponding to a conversion efficiency of 0.11 %/Wcm^2.

13.4.3 Waveguide Lasers

Laser crystals are optical crystals doped with active ions, such as Nd, Er, Yb, Cr, Ti etc. They are widely used as gain media for solid state laser systems. In waveguides, the active volumes are strongly compressed and, as a result, the waveguide lasers usually reach reduced lasing thresholds and efficiencies comparable to bulk laser systems [29]. A practical solution to realize waveguide lasers is to create waveguides in laser crystals and achieve in-cavity guidance of both the pump and generated laser beams. Owing to the small dimension of the waveguide elements, compact on-chip minor light sources may be available.

By using ion beam technology, waveguides with designable configurations could be fabricated in laser crystals (see Sect. 13.3.1) [1, 2, 10, 26]. However, it should be pointed out that the possibility of efficient waveguide laser generation is strongly dependent on three parameters. Firstly, the waveguide quality is determined partly by the propagation losses of light in the structures. High propagation loss is less acceptable for laser generation. For ion beam fabricated waveguides, the loss is strongly related to the bulk values. Secondly, the luminescence properties of the waveguides are of great importance for the laser performance. Most ion implanted waveguides in laser crystals preserve well the photoluminescence (PL) properties of the bulk. Significant fluorescence quenching is usually harmful and reflects the structural modification of the original lattices induced by the ion beams. The third parameter is determined by the pump system. By choosing suitable pump systems it is possible to realize high-performance waveguide lasers.

Among all the ion beam produced waveguides in laser crystals, here we focus on the most successful example, i.e. the Nd:YAG crystal. This crystal is one of the most used gain media for high-power solid-state lasers. The irradiation of many species of ions, such as H, He, C, N, O, Ar, Kr, has been applied to fabricate waveguides in this material [1, 2, 10]. The applied techniques include most suitable solutions, such as “normal” ion irradiation, proton beam writing and swift heavy ion irradiation.

The spectroscopic features of the doped Nd^{3+} ions in the YAG crystal can not only reveal the fluorescence of the waveguides but also reflect the lattice modifications due to the ion implantation. Fluorescence provides information about the local presence of disorders (through the line width), damages and defects (monitored by a fluorescence intensity reduction) and changes in the unit cell volume

(revealed by a spectral shift of the luminescence lines). From the confocal μPL emission spectra, it becomes clear that a Nd:YAG waveguide implanted with light ions suffers significant fluorescence quenching [97]. Figure 13.12 shows the spatial distribution of fluorescence intensity, spectral shift and fluorescence bandwidth of proton implanted Nd:YAG waveguides correlated to the $^4F_{3/2} \rightarrow {}^4I_{9/2}$ luminescence line of Nd^{3+} ions at around 938 nm. This wavelength has been proven to be very sensitive to any localized changes of the YAG lattice on a micrometric scale. It is obvious that the ion irradiation modifies the original lattices in the waveguide region. Within the waveguide, a clear reduction of the fluorescence intensity by roughly 20 % compared to the bulk has been generated. This is caused by the presence of ion irradiation induced defects in the waveguide's active volume (Fig. 13.12a). In addition, the peak position of the emission line shows a clear blue shift in the waveguide core (Fig. 13.12b), which may indicate a reduction in the crystal field reflecting the modification of the original matrix. Nevertheless, the obtained waveguides still show outstanding spectroscopic properties for low threshold integrated laser oscillation.

For waveguides implanted with heavy ions, the fluorescence features are well maintained without any quenching [98]. This may be because the fluence required for waveguide formation is much higher for light ions (10^{16} cm^{-2}) than that for heavy ions (10^{14} cm^{-2}). Nd-YAG waveguides produced by swift heavy ion irradiation or proton beam writing also exhibit similar μPL emission properties as the bulk suggesting potential for further laser generation [99].

The lasing properties are usually described by lasing threshold, slope efficiency (a parameter describing lasing efficiency) and maximum output power [29]. Diverse geometries of Nd:YAG waveguides have been used to construct waveguide laser systems. Planar and channel waveguides have been fabricated by using light, heavy as well as swift heavy ion irradiation and mask-patterned ion irradiation or proton beam writing, respectively. Ridge waveguides have been produced by further etching or dicing of the planar waveguide substrates. Early works focused particularly on the reduction of the lasing threshold, which was considered to be one of the most limiting features of waveguide lasers. The lowest threshold was only

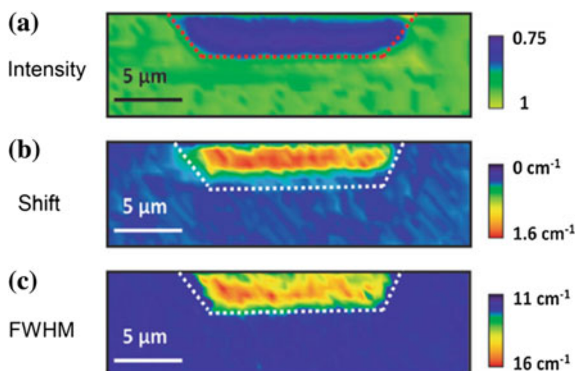

Fig. 13.12 Spatial dependence of the emission intensity (**a**), the implantation induced spectral shift (**b**), and the linewidth (FWHM) of the emission line (**c**) for a proton implanted Nd:YAG waveguide [97]. The scales give the relative intensity of the fluorescence intensity and the shift and the width of the luminescence line in wave numbers

1.6 mW [1]. However, there is a balance for all the parameters to achieve optimized waveguide laser systems. A serious drawback of the ion irradiated Nd:YAG waveguide laser systems was the very limited maximum output power, which was usually only up to a few mW. This was the result of the low coupling efficiency between the pump beam and the mode fields of the waveguides. Later work was done with more focus on the output power. The most remarkable Nd:YAG waveguide laser was produced by proton beam writing achieving an output power of 60 mW at a wavelength of 1064 nm [100].

By using fs-laser ablated ridge waveguides as gain structures, an output power of up to 21 mW at 1064 nm has been realized [101]. The laser performance of ridge waveguides shows considerable improvement compared to a planar waveguide, but it is limited by the relatively high propagation losses from the rough sidewalls of the ridge. By using diamond dicing, the roughness of the sidewalls can be significantly reduced (Figs. 13.13a and b). In addition, the modal profiles of the ridge waveguides were quite good (Fig. 13.13c). Figure 13.13d shows the dependence of the cw laser output power on the absorbed pump power for a planar (blue color) and a ridge waveguide (red color), whereat the ridge configuration is clearly advantageous. The laser threshold *P*th is smaller and the slope efficiency Φ is higher compared to the values of the planar waveguide. Based on such ridge waveguides, the maximum output power at 1064 nm reaches 84 mW corresponding to a conversion efficiency of 33 %, which is the maximum value of ion beam produced Nd:YAG waveguide systems [102].

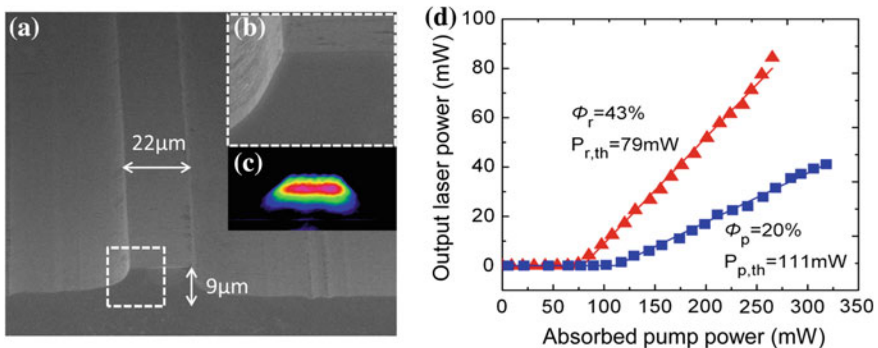

Fig. 13.13 SEM image of a cross section of a diced Nd:YAG ridge waveguide (**a**), detail of the side wall (**b**) marked by the dashed line in (**a**), measured near-field profile of the TE_{00} mode (**c**) and cw waveguide laser output powers at a wavelength of 1064 nm as a function of the absorbed light power at 808 nm (**d**). The *triangular* and *rectangular* symbols represent the data of ridge and planar waveguides, respectively [102]

13.4.4 3D Optical Micro- and Nanostructures

By means of a consequent application of the IBEE-process (see Sect. 13.3.3) an overall strategy was developed allowing the production of photonic micro- and nanostructures with high quality in the LN crystal. Figure 13.14 shows examples that demonstrate the performance of structures fabricated by this method.

Figure 13.14a shows a grating (width 400 nm, period 1 μm, depth 325 nm) realized with Ar-ion irradiation (see Fig. 13.6a) using a fused silica mask produced by electron beam lithography. With the aim to realize nanoscale waveguides, a buried damaged layer has been produced by a second irradiation with He-ions. This layer has been subsequently removed by wet chemical etching forming freestanding nanowires, which were released from the substrate in an ultrasonic bath of ethanol. For further investigation, the optical waveguide-ethanol solution was added drop-wise to appropriate substrates and dried resulting in statistically distributed nano-waveguides on the surface of the substrate. With this procedure, waveguides with widths of 50–500 nm and lengths of up to 100 μm have been realized. A waveguide with (400 × 600) nm^2 cross-sectional area and a length of 50 μm was used to excite a dye (4′,6-Diamidin-2-phenylindol, DAPI) in standard concentration for biological applications by propagated second harmonics [103, 104].

The ridge waveguides in Fig. 13.14b were produced in Zn doped LN through the eightfold application of the IBEE process using an etch-resistant chromium mask, which has been patterned by photolithography. The structure height is 3.7 μm. For the first time, ridge waveguides with smooth and simultaneously almost vertical walls were realized. Single-mode waveguiding with an attenuation of 0.9 dB cm^{-1} has been demonstrated at a wavelength of 1064 nm. Details on the manufacturing process and the optical properties are given in [105]. More ridges

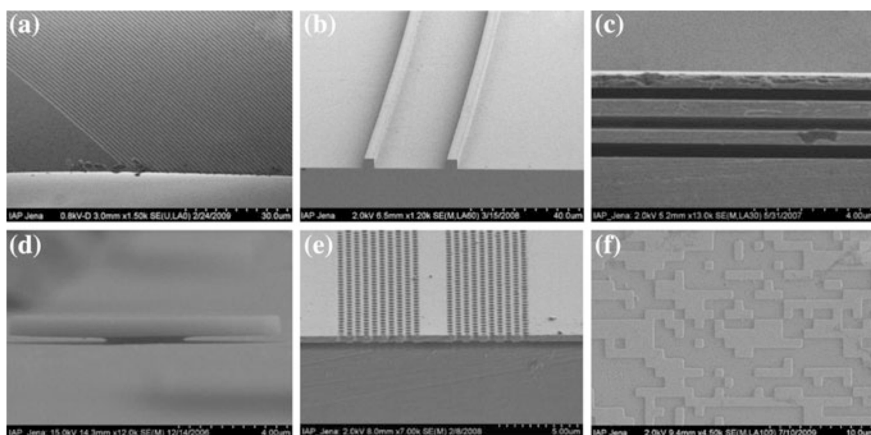

Fig. 13.14 Grating (**a**), ridge waveguides (**b**), stacks of horizontally arranged membranes (**c**), optical microresonator (**d**), photonic crystal defect waveguide (**e**) and computer generated hologram (**f**) in LN realized by means of ion beam enhanced etching (IBEE)

with heights between 3 and 7 μm have been prepared and will be used for future realization of QPM structures and the demonstration of nonlinear effects.

By irradiation with ions of different energies, stacks of membranes that can act as a Bragg filter have been realized [80]. Figure 13.14c shows the vertical arrangement of three 540 nm thick membranes, which are separated by 450 nm thick air gaps. The preparation was carried out by successive large-area irradiation at 100 K with 1.27, 0.77 and 0.29 MeV He ions and subsequent etching in 3.7 % HF solution at 40 °C for 390 min.

Figure 13.14d shows a microcavity with a diameter of 10 μm. The LN crystal was first irradiated at 100 K with 325 keV He ions. Subsequently, the lateral structuring was done by inductively coupled plasma reactive ion etching (ICP-RIE) using a chromium mask. The subsequent etching process of the 450 nm wide air gap was terminated after 60 min, so that the foot of the resonator remained standing. Due to the dry-etching the sidewalls are relatively rough and not perpendicular. The lateral structuring by means of IBEE also promises here to overcome these drawbacks. For this, however, masks have to be developed which have sufficiently smooth sidewalls. A promising solution for this issue is the use of polymer masks whose structure edge is smoothed by melting.

Photonic crystals (PhC) were prepared in 450 nm thick membranes of *x*-cut LN using different methods like IBEE and focused ion beam milling (FIB). Figure 13.14e shows PhCs that have been realized by a hexagonal arrangement of air holes (period of 620 nm, hole diameter of 350 nm). By omitting rows of holes, defect waveguides of different widths were realized simultaneously. The function of this structure as well as of resonators has been published in [106–108].

Finally, Fig. 13.14f shows a computer generated hologram fabricated with Ar-ion irradiation using a chromium mask produced by electron beam lithography that operates at a wavelength of 1064 nm while the image is displayed in the visible wavelength range at 532 nm using SHG.

13.5 Summary

By using ion irradiation, optical elements have been successfully fabricated in numerous materials showing wide applicability and excellent control of material properties combined with a well-defined crystal damage. Thereby, the fact that amongst others the refractive index and the chemical resistance can be precisely tailored is exploited. Generally and with respect to application, the ions used for the irradiation of optical crystals are basically divided into three groups, i.e. light (H and He), heavy (atomic number no less than 6, e.g., C, N, O, Si, Ar) and swift heavy ions. For light-ion irradiation, the nuclear damage is dominant and the electronic contribution is negligible. Advantages of light-ion irradiation are a minor modification of the bulk material and a relatively large penetration depth of typically a few micrometers. This allows the generation of buried layers as needed e.g. for waveguide barriers or slab etching, but the required fluences are relatively high.

In this respect, heavy ions are more effective, because typically the fluences can be much lower than for light ions. Unfortunately, in order to obtain comparable depths of modification, high energies of several MeV are needed. Therefore, damage due to electronic excitation plays an increasing role and may cause an undesirable modification of the bulk crystal. However, in many concepts for optical devices just this can be exploited. An intriguing feature of swift ions are the ultralow fluences required to achieve a certain degree of damage, which are by 2–4 orders reduced compared to nuclear energy deposition.

With these controlled damage effects, modifications in optical crystals with tailored features can be realized to construct waveguiding structures on micron and sub-micron scales. Based on these ion irradiation fabricated structures, a number of promising applications, such as electro-optical modulation, frequency conversion, waveguide lasing and 3D optical micro- and nanostructures, have been successfully implemented. Increasingly, ion irradiation controlled lattice damage becomes an intriguing solution to achieve compact device-level applications in integrated photonics.

References

1. P.D. Townsend, P.J. Chandler, L. Zhang, *Optical Effects of Ion Implantation* (Cambridge University Press, Cambridge, 1994) (Reprinted 2006)
2. F. Chen, X.L. Wang, K.M. Wang, Opt. Mater. **29**, 1523 (2007)
3. M. Nastasi, J.W. Mayer, J.H. Hirvonen, *Ion-Solid Interactions: Fundamentals and Applications* (Cambridge University Press, Cambridge, 1996)
4. J.F. Ziegler, *Ion Implantation Technology* (North-Holland, Amsterdam, 1992)
5. F. Chen, J. Appl. Phys. **106**, 081101 (2009)
6. F. Schrempel, Th. Gischkat, H. Hartung, E.-B. Kley, W. Wesch, Nucl. Instr. Meth. B **250**, 164 (2006)
7. G. Götz, H. Karge, Nucl. Instr. Meth. B **209**, 1079 (1983)
8. E. Wendler, G. Becker, J. Rensberg, S. Wolf, W. Wesch, Nucl. Instr. Meth. B (2016) (submitted)
9. Th. Gischkat, F. Schrempel, W. Wesch, Nucl. Instr. Meth. B **266**, 2906 (2008)
10. F. Chen, Laser Photonics Rev. **6**, 622 (2012)
11. J. Olivares, A. García-Navarro, A. Méndez, F. Agulló-López, G. García, A. García-Cabanes, M. Carrascosa, Nucl. Instr. Meth. B **257**, 765 (2007)
12. T. Ruiz, A. Mendez, M. Carrascosa, J. Carnicero, A. Garcia-Cabanes, J. Olivares, F. Agullo-Lopez, A. Garcia-Navarro, G. Garcia, J Phys. D **40**, 4454 (2007)
13. B. Canut, S.M.M. Ramos, R. Brenier, P. Thevenard, J.L. Loubet, M. Toulemonde, Nucl. Instr. Meth. B **107**, 194 (1996)
14. M. Toulemonde, Ch. Dufour, A. Meftah, E. Paumier, Nucl. Instr. Meth. B **166**, 903 (2000)
15. A. Meftah, J.M. Constantini, N. Khalfaoui, S. Boudjadar, J.P. Stoquert, F. Studer, M. Toulemonde, Nucl. Instr. Meth. B **237**, 563 (2005)
16. G. Szenes, Phys. Rev. B **60**, 3140 (1999)
17. F. Agulló-López, A.C. Font, Á. Munoz-Martín, J. Olivares, A. Zucchiatti, Prog. Mater Sci. **76**, 1 (2016)
18. M. Bianconi, N. Argiolas, M. Bazzan, G.G. Bentini, A. Cerutti, M. Chiarini, G. Pennestri, P. Mazzoldi, C. Sada, Nucl. Instr. Meth. B **257**, 597 (2007)

19. G.G. Bentini, M. Bianconi, M. Chiarini, L. Correra, C. Sada, P. Mazzoldi, N. Argiolas, M. Bazzan, R. Guzzi, J. Appl. Phys. **92**, 6477 (2002)
20. A. Gumennik, A.J. Agranat, I. Shachar, M. Hass, Appl. Phys. Lett. **87**, 251917 (2005)
21. M. Feuster, Ch. Buchal, E. Sneoks, A. Polman, Appl. Phys. Lett. **65**, 225 (1994)
22. P.D. Townsend, J. Olivares, Appl. Surf. Sci. **109/110**, 275 (1997)
23. P.D. Townsend, Vacuum **51**, 301 (1998)
24. M. Khanlary, D.E. Hole, P.D. Townsend, Nucl. Instr. Meth. B **227**, 379 (2005)
25. M. Levy, A.M. Radojevic, "Single-crystal lithium niobate films by crystal ion slicing", in "Wafer Bonding: Applications and Technology", ed. by M. Alexe, U. Gosele (Springer, Berlin, 2004)
26. M. Pollnau, Y.E. Romanyuk, C. R. Physique **8**, 123 (2007)
27. F. Chen, Crit. Rev. Solid State Mater. Sci. **33**, 165 (2008)
28. E. Cantelar, D. Jaque, G. Lifante, Opt. Mater. **34**, 555 (2012)
29. C. Grivas, Prog. Quantum Electron. **35**, 159 (2011)
30. D. Kip, Appl. Phys. B **67**, 131 (1998)
31. G.I. Stegeman, C.T. Seaton, J. Appl. Phys. **58**, R57 (1985)
32. E.J. Murphy (ed.), *Integrated Optical Circuits and Components* (Marcel Dekker, New York, 1999)
33. I.P. Kaminow, IEEE Trans. Microw. Theory Tech. **23**, 57 (1975)
34. J.I. Mackenzie, IEEE J. Sel. Top. Quantum Electron. **13**, 626 (2007)
35. P.G. Kik, A. Polman, MRS Bull. **23**, 48 (1998)
36. M.L. Calvo, V. Lakshminarayanan (eds.), *Optical Waveguides: From Theory to Applied Technologies* (CRC Press, London, 2007)
37. J.D. Joannopoulos, S.G. Johnson, J.N. Winn, R.D. Meade, *Photonic Crystals: Molding the Flow of Light*, 2nd edn. (Princeton University Press, Princeton, 2008)
38. J. Hukriede, D. Kip, E. Krätzig, Appl. Phys. B **72**, 749 (2001)
39. W. Sohler, H. Hu, R. Ricken, V. Quiring, Ch. Vannahme, H. Herrmann, D. Büchter, S. Reza, W. Grundkötter, S. Orlov, H. Suche, R. Nouroozi, Y. Min, Opt. Photonics News **19**, 24 (2008)
40. D. Jaque, E. Cantelar, G. Lifante, Appl. Phys. B **88**, 201 (2007)
41. R. Ramponi, M. Malangoni, R. Osellame, Appl. Phys. Lett. **78**, 2098 (2001)
42. G.L. Yip, J. Albert, Opt. Lett. **10**, 151 (1985)
43. YuN Korkishko, V.A. Fedorov, T.M. Morozova, F. Caccavale, F. Gonella, F. Segato, J. Opt. Soc. Am. A **15**, 1838 (1998)
44. L. Salavcova, J. Spirkova, F. Ondracek, A. Mackova, J. Vacik, U. Kreissig, F. Eichhorn, R. Groetzschel, Opt. Mater. **29**, 913 (2007)
45. S. Iraj Najafi, T. Touam, R. Sara, M.P. Andrews, M.A. Fardad, J. Lightwave Technol. **16**, 1640 (1998)
46. Z.Y. Yin, B.K. Garside, Appl. Opt. **21**, 4324 (1982)
47. T. Yamashiki, K. Tsuda, Opt. Lett. **28**, 316 (2003)
48. K.M. Wang, B.R. Shi, N. Cue, Y.Y. Zhu, F.R. Xiao, F. Lu, W. Li, Y.G. Liu, Appl. Phys. Lett. **73**, 1020 (1998)
49. F. Bruno, M. Guidice, R. Recca, F. Testa, Appl. Opt. **30**, 4560 (1991)
50. H. Uetsuhara, S. Goto, Y. Nakata, N. Vasa, T. Okada, M. Maeda, Appl. Phys. A **69**, S719 (1999)
51. W. Bolänos, J.J. Carvajal, X. Mateos, E. Cantelar, G. Lifante, U. Griebner, V. Petrov, V.L. Panyutin, G.S. Murugan, J.S. Wilkinson, M. Aguilo, F. Diaz, Opt. Express **19**, 1449 (2011)
52. J. Siebenmorgen, T. Calmano, K. Petermann, G. Huber, Opt. Express **18**, 16035 (2010)
53. S. Zhang, J. Yao, W. Liu, Z. Huang, J. Wang, Y. Li, C. Tu, F. Lu, Opt. Express **16**, 14180 (2008)
54. Y. Tan, A. Rodenas, F. Chen, R.R. Thomson, A.K. Kar, D. Jaque, Q. Lu, Opt. Express **18**, 24994 (2010)
55. R.R. Gattass, E. Mazur, Nat Photonics **2**, 219 (2008)

56. J. Thomas, M. Heinrich, P. Zeil, V. Hilbert, K. Rademaker, R. Riedel, S. Ringleb, C. Dubs, J.-P. Ruske, S. Nolte, A. Tünnermann, Phys. Status Solidi A **208**, 276 (2011)
57. M. Ams, G.D. Marshall, P. Dekker, J.A. Piper, M.J. Withford, Laser Photonics Rev. **3**, 535 (2009)
58. R.R. Thomson, S. Campbell, I.J. Blewett, A.K. Kar, D.T. Reid, Appl. Phys. Lett. **88**, 111109 (2006)
59. A. Benayas, D. Jaque, B. McMillen, K.P. Chen, Opt. Express **17**, 10076 (2009)
60. E. Fazio, W. Ramadan, A. Petris, M. Chauvet, A. Bosco, V.I. Vlad, M. Bertolotti, Appl. Surf. Sci. **248**, 97 (2005)
61. P. Ganguly, C.L. Sones, Y.J. Ying, H. Steigerwald, K. Buse, E. Soergel, R.W. Eason, S. Mailis, J. Lightwave Technol. **27**, 3490 (2009)
62. J. Olivares, M.L. Crespillo, O. Caballero-Calero, M.D. Ynsa, A. Garcia-Cabanes, M. Toulemonde, Ch. Trautmann, F. Agullo-Lopez, Opt. Express **17**, 24175 (2009)
63. N. Dong, F. Chen, D. Jaque, A. Benayas, F. Qiu, T. Narusawa, J. Phys. D **44**, 105103 (2011)
64. Y. Ren, N. Dong, F. Chen, A. Benayas, D. Jaque, F. Qiu, T. Narusawa, Opt. Lett. **35**, 3276 (2010)
65. S.M. Mahdavi, P. Chandler, P.D. Townsend, J. Phys. Appl. Phys. **22**, 1354 (1989)
66. S.M. Mahdavi, P.D. Townsend, Electron. Lett. **26**, 371 (1990)
67. L. Zhang, P.J. Chandler, P.D. Townsend, J. Appl. Phys. **70**, 1185 (1991)
68. G. Lifante, *Integrated Photonics: Fundamentals* (Wiley, Atrium, 2008)
69. E.R. Schineller, R.P. Flam, D.W. Wilmot, J. Opt. Soc. Am. **58**, 1171 (1968)
70. J.-P. Colinge, in *Wafer Bonding: Applications and Technology*, ed. by M. Alexe, U. Gosele (Springer, Berlin, 2004)
71. D.W. Ward, E.R. Statz, K.A. Nelson, R.M. Roth, R.M. Osgood, Appl. Phys. Lett. **86**, 022908 (2005)
72. M. Levy, R.M. Osgood Jr, R. Liu, L.E. Cross, G.S. Cargill III, A. Kumar, H. Bakhru, Appl. Phys. Lett. **73**, 2293 (1998)
73. Y.C. Yu, C.H. Chen, H. Niu, J.Y. Hsu, T.N. Yang, Nucl. Instr. Meth. Phys. Res. B **256**, 558 (2007)
74. G. Poberaj, M. Koechlin, F. Sulser, A. Guarino, J. Hajfler, P. Gunter, Opt. Mater. **31**, 1054 (2009)
75. H. Hu, L. Gui, R. Ricken, W. Sohler, Proc. SPIE **7604**, 76040R (2010)
76. Y. Seung Lee, S.-S. Lee, W.-G. Lee, and W. H. Steier, Thin Solid Films **519**, 4271 (2011)
77. T. Izuhara, R.M. Osgood, M. Levy, M.E. Reeves, Y.G. Wang, A.N. Roy, H. Bakhru, Appl. Phys. Lett. **80**, 1046 (2002)
78. R.M. Roth, D. Djukic, Y.S. Lee, R.M. Osgood, P.A. Lewis, S. Bakhru, H. Bakhru, Appl. Phys. Lett. **90**, 112913 (2007)
79. P. Olivero, S. Rubanov, P. Reichart, B.C. Gibson, S.T. Huntington, J. Rabeau, A.D. Greentree, J. Salzman, D. Moore, D.N. Jamieson, S. Prawer, Adv. Mater. **17**, 2427 (2005)
80. F. Schrempel, Th. Gischkat, H. Hartung, Th. Höche, E.-B. Kley, A. Tünnermann, Opt. Lett. **34**, 1426 (2009)
81. D.M. Gill, D. Jacobson, C.A. White, C.D.W. Jones, Y. Shi, W.J. Minford, A. Harris, J. Lightwave Technol. **22**, 887 (2004)
82. J. Reinisch, F. Schrempel, Th. Gischkat, W. Wesch, J. Electrochem. Soc. **155**, D298 (2008)
83. Th. Gischkat, H. Hartung, F. Schrempel, E.B. Kley, A. Tünnermann, W. Wesch, Microelectron. Eng. **86**, 910 (2009)
84. M. Bianconi, F. Bergamini, G.G. Bentini, A. Cerutti, M. Chiarini, P. De Nicola, G. Pennestrì, Nucl. Instr. Meth. Phys. Res. B **266**, 1238 (2008)
85. L. Wang, K.M. Wang, X.L. Wang, F. Chen, Y. Jiang, C.L. Jia, Y. Jiao, F. Lu, D.Y. Shen, H.J. Ma, R. Nie, Surf. Coat. Technol. **201**, 5081 (2007)
86. F. Nesprías, M. Venturino, M.E. Debray, J. Davidson, M. Davidson, A.J. Kreiner, D. Minsky, M. Fischer, A. Lamagna, Nucl. Instr. Meth. Phys. Res. B **267**, 69 (2009)
87. R. Geiss, J. Brandt, H. Hartung, A. Tünnermann, T. Pertsch, E.-B. Kley, F. Schrempel, J. Vac. Sci. Technol. **B33**, 010601 (2015)

88. F. Agulló-López, G. García, J. Olivares, J. Appl. Phys. **97**, 093514 (2005)
89. G.G. Bentini, M. Bianconi, A. Cerutti, M. Chiarini, G. Pennestri, C. Sada, N. Argiolas, M. Bazzan, P. Mazzoldi, Opt. Lasers Eng. **45**, 368 (2007)
90. R. Degl'Innocenti, A. Majkic, P. Vorburger, G. Poberaj, P. Günter, M. Döbeli, Appl. Phys. Lett. **91**, 051105 (2007)
91. J. Olivares, A. Garcia-Navarro, G. Garcia, A. Mendez, F. Agullo-Lopez, A. Garcia-Cabanes, M. Carrascosa, O. Caballero, Opt. Lett. **32**, 2587 (2007)
92. D. Fluck, P. Gunter, IEEE J. Sel. Top. Quantum Electron. **6**, 122 (2000)
93. B. Vincent, A. Boudrioua, J.C. Loulergue, P. Moretti, S. Tascu, B. Jacquier, G. Aka, D. Vivien, Opt. Lett. **28**, 1025 (2003)
94. Q. Huang, P. Liu, T. Liu, L. Zhang, Y. Zhou, X. Wang, Phys. Status Solidi RRL **6**, 205 (2012)
95. Y. Jia, F. Chen, J.R. Vázquez de Aldana, Sh. Akhmadaliev, S. Zhou, Opt. Mater. **34**, 1913 (2012)
96. G. Poberaj, R. Degl'Innocenti, C. Medrano, P. Günter, Opt. Mater. **31**, 1049 (2009)
97. Y. Tan, F. Chen, J. Phys. D **43**, 075105 (2010)
98. F. Chen, Y. Tan, D. Jaque, Opt. Lett. **34**, 28 (2009)
99. A. Benayas, D. Jaque, Y. Yao, F. Chen, A.A. Bettiol, A. Rodenas, A.K. Kar, Opt. Lett. **35**, 3898 (2010)
100. Y. Yao, Y. Tan, N. Dong, F. Chen, A.A. Bettiol, Opt. Express **18**, 24516 (2010)
101. Y. Jia, N. Dong, F. Chen, J.R. Vázquez de Aldana, Sh. Akhmadaliev, S. Zhou, Opt. Mater. Express **2**, 657 (2012)
102. Y. Jia, Ch.E. Rüter, Sh. Akhmadaliev, Sh. Zhou, F. Chen, D. Kip, Opt. Mater. Express **3**, 433 (2013)
103. A. Sergeyev, R. Geiss, A.S. Solntsev, A. Steinbrück, F. Schrempel, E.-B. Kley, T. Pertsch, R. Grange, Opt. Express **21**, 19012 (2013)
104. R. Geiss, S. Saravi, A. Sergeyev, S. Diziain, F. Setzpfandt, F. Schrempel, R. Grange, E.-B. Kley, A. Tünnermann, T. Pertsch, Opt. Lett. **40**, 2715 (2015)
105. H. Hartung, E.-B. Kley, A. Tünnermann, Th. Gischkat, F. Schrempel, W. Wesch, Opt. Lett. **33**, 2320 (2008)
106. R. Geiss, S. Diziain, R. Iliew, C. Etrich, H. Hartung, N. Janunts, F. Schrempel, F. Lederer, T. Pertsch, E.-B. Kley, Appl. Phys. Lett. **97**, 131109 (2010)
107. S. Diziain, R. Geiss, M. Zilk, F. Schrempel, E.-B. Kley, A. Tünnermann, T. Pertsch, Appl. Phys. Lett. **103**, 51117 (2013)
108. S. Diziain, R. Geiss, M. Zilk, F. Schrempel, E.-B. Kley, A. Tünnermann, T. Pertsch, Appl. Phys. Lett. **103**, 251101 (2013)

Index

A

Activation energy, 204, 250, 261, 269, 272, 282
Activation energy for amorphization, 266
Activation energy for IBIEC, 254, 258
$Al_xGa_{1-x}As$, 272, 282
$Al_xGa_{1-x}N$, 274, 282
Aligned spectra, 194, 196, 225
Alignment of nanowires, 490
Alloying, 165
AlN, 274
Aluminium arsenide (AlAs), 245, 273
Amorphization, 106, 120, 158, 190, 191, 195, 196, 198, 200, 208, 209, 210, 212, 214, 218, 220, 222, 224, 227, 228, 232, 234–237, 243, 245, 246, 248, 250–252, 259, 261, 264, 268, 277, 279, 321, 329, 332, 336, 338, 429
Amorphisation fluence, 128
Amorphization in InAs, 272
Amorphization kinetics, 125, 250, 265, 282
Amorphization kinetics in SiC, 269
Amorphization threshold, 483
Amorphous core, 123, 336
Amorphous cylinders, 342
Amorphous fraction, 121
Amorphous phase, 373, 376, 389
Amorphous regions, 195
Amorphous track, 329, 331, 332, 338
Amorphous zones, 197
Analytical thermal spike (a-TS) model, 75, 76, 388, 408
Angular distribution, 49
Angular straggling, 25
Anisotropic deformation, 405
Annealing, 200, 205, 211, 216, 218
Arrhenius equation, 180
Arrhenius plot, 142, 161
Athermal melting, 387
Atomic force microscope (AFM), 326, 443
Atomic mobility, 157
Avrami nucleation and growth model, 124
Axial channeling, 55

B

B2 defect, 182
Backscattering, 191
Ballistic diffusion coefficient (Dbal), 181
Ballistic mixing models, 148
Bethe-Bloch formula, 35, 37, 43, 45
Binary collisions, 22, 53, 55, 58, 477
Binary multilayers, 245
Binary semiconductors, 382
Bond defects, 252
Bond weakening, 69, 71, 99
Born-Oppenheimer approximation, 179
Box-like profile, 168

C

Cadmium telluride (CdTe), 245
Calcite-vaterite phase transformation, 349
Carrier density, 375
Cathodoluminescence, 109
Cavity, 173
Channeling, 13, 51, 58, 59, 193
Channelling irradiation, 258
Charge state, 378, 380, 431
Chemical disordering, 120
Chemical patterning, 151
Chemical synthesis, 176
Cluster beams, 331
Cluster ion, 81, 365, 371, 379, 396, 420
Coexistence region, 140
Collision cascade, 191, 206, 209, 212, 217, 214, 215, 219, 226, 227, 232, 238
Colloidal NPs, 444
Columnar defects, 341
Composite model, 132

© Springer International Publishing Switzerland 2016
W. Wesch and E. Wendler (eds.), *Ion Beam Modification of Solids*,
Springer Series in Surface Sciences 61,
DOI 10.1007/978-3-319-33561-2

Compositional patterning, 151
Compound target, 26
Computer simulation, 52, 54, 58
Conductivity, 375, 397
Continuous tracks, 370, 377, 379, 393
Core-shell model, 421
Corrosion-like process, 173
Cosmic radiation, 108
Cotunnite-like structure, 351
Coulomb explosion, 69, 70, 71, 95, 99, 386, 397, 408
Coulomb-explosion models, 323
Coulomb potential, 12, 15, 27, 28
Critical angle, 56, 194
Critical energy (ΔG*), 158
Critical energy density models, 252
Critical flux, 150
Critical radius (R*), 143, 153, 158
Critical temperature, 200–206, 208, 212, 217, 235
Critical temperature for amorphization (Tc), 127, 243–245
Cross-section, 11, 13, 48, 191, 204, 209, 212, 213, 214, 219, 235, 237, 238
Cross section for direct-impact amorphisation, 121
Crystal cut, 505
Crystal ion slicing, 512
Crystalline-to-amorphous transformation, 430
Crystal-TRIM, 59
Cubic-monoclinic transition, 348
Cut-off energy, 74

D
3D simulations, 479
3D structuring, 510
Damage annealing, 376, 396
Damage clusters, 378
Damage cross-section, 70, 81, 117, 204, 216, 328, 339, 370, 372, 382, 384
Damage formation, 72, 190, 191, 203, 209, 216, 217, 224, 228, 230, 232, 237, 238, 368, 369, 376, 387
Damage peak, 195, 197, 198
Damage production, 322
Damage profile, 197, 198, 218, 327
Damage-stimulated amorphisation, 123
Dangling bonds, 258
Dealloying, 173
Dechanneling, 55, 57, 58, 194, 195
Decomposition, 278
Defect, 195, 219, 246, 322
Defect accumulation kinetics, 114
Defect annihilation, 270, 277
Defect cascades, 341
Defect clusters, 115, 195, 197, 212, 219
Defect concentration, 87, 373, 381
Defect distribution, 58
Defect fraction, 110, 121
Defect fraction at saturation, 113
Defect interaction and amorphization model, 212, 383
Defect loss, 112
Defect migration, 116
Defect production, 112
Defect profiles, 230, 233
Defect rate expression, 114
Defect Reaction Rate Theory, 112
Defect recombination, 86, 198, 205, 212, 234
Defect recovery, 108
Defect sinks, 116
Deformation yield, 405, 432
Δ-like size distribution, 168
Density change, 430
DICADA, 58
Diffusion coefficient (D), 161, 178, 397
Diluted magnetic semiconductors (DMS), 488
Direct backscattering, 194
Direct-impact amorphisation, 121
Direct impact model, 352, 354
Discontinuous tracks, 369, 370, 378, 391
Dislocation loops, 205, 212, 219, 231, 232, 236, 246, 334, 346, 352
Dislocations, 228, 352
Displaced lattice atoms, 194, 195, 197, 202, 205, 226, 231, 233, 235, 376, 380
Displacement, 106, 110, 112, 149, 289, 290, 297–299, 301, 302, 312–314
Divacancies, 251, 252
Doping, 476
Driven system, 147
Dynamical phase diagram, 147
Dynamic annealing, 244, 246, 250, 260, 274, 277, 482, 483
Dynamic simulation, 495, 496

E
E' defect, 182
Effective flow temperature (EFT), 408, 435
Effective temperature criterion, 150
Effective thermal jump frequency, 126
Eigenstrain, 410
Elastic collisions, 322, 326, 329, 430
Elastic strain field, 335

Electrical resistivity measurements, 327
Electron beam induced current (EBIC), 487
Electron beam lithography (EBL), 176
Electron density, 5, 6, 12, 20
Electron gas, 36, 39, 43, 51
Electronegativity, 163
Electronic energy deposition, 65, 68, 77, 78, 82, 86, 88, 98, 322, 348, 365, 366, 368–371, 374, 376, 380, 384, 385, 387, 390, 394, 395, 398, 411, 414, 417, 420, 424, 506–508
Electronic energy loss, 89, 108, 321–323, 333, 446
Electronic excitation, 321, 329, 332, 334, 335, 342, 344, 346, 355
Electronic stopping, 107, 168, 289, 290, 297
Electronic straggling, 36
Electron-phonon coupling, 64, 75, 83, 84, 87, 88, 90, 93, 95, 98, 99, 366, 387, 388, 391, 393, 404, 420, 446
Electron-phonon mean free path, 83, 88–92, 95, 96, 98, 389, 394
Electro-optical effect, 517
Electro-optical modulators, 517
Elementary targets, 26
Energy deposition, 287, 289, 290, 292, 298, 307, 312, 313
Energy deposition threshold, 429
Energy-depth conversion, 193
Energy loss, 16, 23, 367
Energy loss distribution, 46, 48
Enthalpy of mixing, 171
Erosion, 275
Etching rate, 515
Eutectic phase diagram, 140
Eutectic salt, 170
Excitation, 19, 30
Exciton decay, 506
Exciton decay model, 76, 93
Exciton Self-trapping, 72
Extended defects, 131, 197, 206, 212, 214, 219, 222, 224, 226, 227, 231–234, 236
Extended i-TS model, 390, 393, 398

F
Ferromagnetic ordering, 488
Field effect transistors (FET), 485
Fission, 108
Fluorescence, 520
Flux effect, 265
Focused ion beam (FIB), 478
Free energy formation criterion, 162
Free surface, 153
Frenkel defects, 111
Frequency doublers, 518, 519
Frost-Russell model, 150
Fullerene, 371, 372, 385
Fusion, 108

G
Gallium Arsenide (GaAs), 244, 264, 265, 280, 482
Gallium Nitride (GaN), 245, 274, 275, 276, 281
Gap energy, 90, 96, 387, 388, 397
Germanium (Ge), 244, 259, 260, 263, 280
Gibbons overlap model, 122, 353, 354
Gibbs free energy, 139, 140
Gibbs-Thomson equation, 142
Glass transition, 406, 411
Growth rate, 225
Growth regime, 169

H
Hall mobility, 374
Heat dissipation, 484
Heat of fusion, 84, 392, 393, 398
Heterogeneous amorphisation, 121
Heterogeneous track overlap model, 355
High-density liquid (HDL), 413
Homogeneous amorphisation, 120
Hook's law, 407

I
IBIEC Models, 257
Impact parameter, 11, 15, 17, 18, 27
Implantation, 204
Implantation depth, 154
InAs, 272
In-cascade annealing, 117
Indium phosphide (InP), 41, 244, 271, 280
Individual potential, 7, 13, 14, 58
Inelastic thermal spike (i-TS), 365, 386, 397, 404
Inelastic thermal spike (i-TS) model, 75, 82
Interaction potential, 5, 7, 53, 56
Interdiffusion, 397
Interface, 139
Intermixing, 397
Interstitial, 221, 226, 231, 232, 477
Interstitial loops, 232
Interstitial-type defect clusters, 249
Inverse coarsening, 148
Inverse Ostwald ripening, 148

Ion beam enhanced etching (IBEE), 514, 523
Ion beam induced epitaxial crystallisation (IBIEC), 226, 244, 245, 254, 256, 259, 261, 266, 271, 278, 282
Ion beam induced interfacial amorphization (IBIIA), 209, 244, 245, 249, 251, 252, 261, 266, 271, 282
Ion-beam mixing, 172, 173
Ion-beam synthesis, 152, 159
Ion flux, 110, 156, 201–206, 208, 211
Ion hammering, 406, 417
Ionicity, 236, 237
Ion implantation, 105, 190, 229
Ion-induced surface erosion, 277
Ionization, 19, 30, 288, 289, 291–293, 304–308, 313, 314
Ionization diffusion-explosion-amorphization (IDEA) model, 75
Ion-shaping, 444
Ion-solid interaction, 190, 386
Ion track, 123, 180, 321, 323–325, 327–329, 332, 333, 334, 336–341, 342, 344, 365, 369, 371, 411
Ion velocity, 68, 77, 88, 91, 96, 343, 427
Iradina, 480, 492, 495, 496
Irradiation-driven recovery rate, 126
Isochronal annealing, 159, 161
Isothermal annealing, 159

K
Kinematic factor, 192
Kinetic system, 143
Kinks, 258

L
Laser crystals, 520
Lasing properties, 521
Latent tracks, 334
Lattice relaxation, 386, 397, 398
Lattice strain, 221
Lattice temperature, 411
Lifshitz-Slyozov-Wagner model, 146
Liquid-liquid phase transition, 435
Lithium niobate, 501
Low-density amorphous (LDA), 413
Low-density liquid (LDL), 413
Low-viscosity zone, 418

M
MAGIC, 480
MARLOWE, 59
Masking, 515
Maxwell model, 407, 433
MD simulations, 420, 426, 478
Measurement of irradiation damage, 109
Melting points, 388
Melting temperature, 77, 80, 83, 84, 87, 88, 90, 387, 390, 392, 393, 396, 398, 420
Membrane, 513, 516, 523
Metastable phase, 139
Micro- and nanostructures, 523
Minimum yield, 194, 224
Miscibility, 141, 165
Mobility, 374
Molecular dynamics (MD), 327, 478, 492
Monoclinic-tetragonal phase transformation, 348, 353
Monte Carlo (MC) calculations, 66, 67, 477
Morphology, 426
Mössbauer spectrometry, 328, 342
Multilayers, 272
Multiple ion track, 424
Multiple scattering, 25

N
Nanocomposite, 138–140, 151, 166, 169
Nanoimplantation, 177
Nanomaterials, 475
Nanoparticles, 492
Nanostructured materials, 287, 288, 308, 309, 311, 314
Nanostructures, 475
Nanotechnology, 443, 475
Nanowires, 480
Non-equilibrium process, 365
Nuclear energy deposition, 52, 66, 191, 205, 225, 227, 232, 366, 370, 373, 375, 380, 392, 416, 502
Nuclear energy loss, 446
Nuclear stopping, 476
Nuclear stopping power, 107
Nucleation-limited process, 248, 252
Nucleation rate (J*), 144
Nucleation regime, 167
Nucleation threshold, 160
Nucleation volume, 153
Nucleation window, 145

O
Optical crystals, 501, 505
Optical elements, 502, 509
Optical waveguides, 510
Order-disorder phase transition, 350
Order-disorder transformations, 120
Ostwald ripening, 146, 160, 166
Output power, 521
Overlap damage model, 381, 383, 384

Oxide dispersion strengthened (ODS) ferritic steels, 174
Oxidizing atmosphere, 159, 165

P
Phase diagram, 140
Phase transformation, 321, 329, 344, 345, 348–350, 354
Phase transition, 414
Phonon frequencies, 387
Photoluminescence, 109, 487
Photoluminescence spectroscopy, 332
Photonic components, 510
Photonic crystal, 523
Planar channeling, 55
Planar defects, 276, 279
Plastic deformation, 405, 431, 432, 434
Plastic flow, 432
Pn-junctions, 487
Point defect, 76, 94, 195, 197, 202, 205, 209, 210, 212, 214, 219, 222, 225, 228, 232, 234–236, 339, 366, 369, 371, 373, 376, 377, 391, 393
Polymorphism, 419
Porosity, 244
Porous layer, 261, 263, 417
Porous structure, 259, 276, 282
Power density, 156
Pre-damage, 376, 378
Pressure wave, 424
Primary knock-on atom (PKA), 106
Projected range, 52, 233
Pseudo-dynamic, 495

R
Radial distribution, 386
Radiation damage, 105, 190, 339, 342, 343
Radiation effects, 106
Radiation resistance, 374, 377, 382, 388
Radioactive decay, 108
Radiolytic process, 170
Raman spectroscopy, 110, 327, 332, 344
Random spectra, 193, 194, 196
Rate equations, 209
Rate theory models for amorphisation, 126
Recombination, 376
Recombination rate coefficient, 113
Recovery rate constants, 126
Recrystallization, 376
Reduced electronic energy loss, 69, 73, 99
Reduced mass, 32
Reducing atmosphere, 159
Refractive index, 510
Relativistic heavy ions, 335
Relaxation strains, 410
Resistivity, 374
Resolidification, 87, 389, 398, 422
Reversal temperature, 129
Ridge waveguides, 512, 521, 523
Roughness, 426
Rutherford backscattering minimum yield, 57, 58
Rutherford backscattering spectrometry, 109, 191, 327, 344, 373
Rutherford cross section, 12

S
Scanning force microscopy, 326
Scanning tunneling microscope (STM), 443
Scattering angle, 9, 10, 11, 22, 49, 51, 53
Scattering cross-section, 193
Screening function, 7, 12
Screening length, 7, 53
Second harmonic generation (SHG), 518
Self-trapped exciton, 69, 72, 99
Semiconductor nanowires, 477, 484
Sequential Implantation, 165
Shear stress, 418
Shear velocity, 408
SHG efficiency, 518
SiGe alloys, 260
Silicide, 397
Silicon (Si), 244, 249, 257, 280
Silicon Carbide (SiC), 244, 268, 280
Simultaneous recovery processes, 125
Small angle X-ray scattering (SAXS), 327, 411
Solid solution, 169
Solubility, 170
Solubility limit, 141, 166
Solute concentration, 140
Solvus, 141, 142
Spatial distribution, 51, 54
Spinodal decomposition, 141
Sponge-like porous structure, 426, 429
Sputtering, 96
Sputtering of Nanostructures, 491
Sputtering yields, 89, 95
SRIM, 41, 44, 45, 54
Stacking faults, 212, 222, 226, 228, 232, 236
Statistical model, 5, 7, 21, 34, 40
Steady-state, 147
Step height, 263, 277
Stopping cross section, 24, 27, 28, 30, 31, 34, 38–40, 44, 179
Stopping power, 24, 36, 41, 43, 53, 193
Straggling, 154
Straggling cross section, 24, 28, 31, 38
Strain, 332

Strained zones, 342
String potential, 56
Structural transformation, 322, 344, 352
Subthreshold irradiation, 506
Superheating, 83
Supersaturation, 143, 158
Surface elevation, 415
Surface profilometry, 328
Surface shift, 406, 431
Surface tension, 161, 178
Swelling, 262, 275, 278, 336
Swift heavy-ion (SHI), 72, 88, 93, 94, 99, 107, 321, 322, 324, 327, 328, 337–340, 346, 365, 403, 444, 506, 511

T
Temperature dependence, 116
Temperature spike, 333
Ternary compound semiconductors, 245, 247, 248, 264, 268, 272, 282, 382
Ternary semiconductors, 272
Thermal annealing, 71, 86, 190
Thermal conductivity, 391
Thermal spike, 75, 93–95, 107, 330, 333, 422, 506
Thermal spike model, 69, 99, 323, 326, 342, 395, 398
Thomas-Fermi potential, 13, 49
Threshold displacement energy, 106
Threshold energies, 325
Threshold value, 80, 368, 370, 371, 377, 379, 384, 385, 396, 398
Top-down approach, 172
Track diameter, 328, 331, 335, 338
Track formation, 63, 68, 77, 94, 96, 323, 325, 327, 332
Track morphology, 325, 378
Transferred energy, 16–18, 21, 22, 27, 53
Transmission electron microscopy (TEM), 324, 344, 444, 483
Transverse energy, 13, 14, 56, 57
TRI3DYN, 495
TRIDYN, 477
TRIM, 41, 54, 477
Two-step approach, 163
Two-temperature model (TTM), 404

U
Unified i-TS model, 392

V
Vacancy, 221, 226, 252, 477
Vacancy clustering, 261
Vacancy distribution, 52, 54
Vacancy generation, 259
Vacancy-out-diffusion model, 198, 200
Vacancy release model, 264
Vapor-liquid-solid (VLS), 484
Vapourisation, 423
Velocity effect, 66, 79, 89, 324, 342, 370, 372, 385, 386, 424
Viscoelastic model, 408
Viscous flow, 407
Void formation, 424
Voids, 262, 417
Volume expansion, 415, 425, 427, 428

W
Waveguide, 519, 521
Waveguide barrier, 510
Waveguide lasers, 520
Waveguide modulators, 517
Wet etching, 514
Wetting, 171

X
X-ray diffraction, 119, 327, 331, 332, 344

Z
ZBL potential, 14, 28, 54, 59
Zinc oxide (ZnO), 245, 279–281